

Numerical Modelling of Hydraulic Free Surface Flows and Scale Effects Associated with Physical Modelling

Caterina Torres Mansilla

Submitted in accordance with the requirements for the degree of

Doctor of Philosophy

The University of Leeds

School of Civil Engineering

November 2018

Intellectual Property and Publication Statements

The candidate confirms that the work submitted is her own, except where work which has formed part of jointly authored publications has been included. The contribution of the candidate and the other authors to this work has been explicitly indicated below. The candidate confirms that appropriate credit has been given within the thesis where reference has been made to the work of others.

The work presented in Chapters 4 and 6 of this thesis has appeared in publication as follows:

Torres, C., Borman, D., Sleigh, P.A. and Neeve, D. 2017. Three-dimensional numerical modelling of full-scale hydraulic structures. In: *Proceedings of the 37th IAHR World Congress, Kuala Lumpur, Malaysia*. 13-18th August.

I was responsible for the execution of the modelling work, data processing, analysis and preparation of the manuscript. D. Borman and P.A. Sleigh contributed in the editing of the manuscript. D. Neeve was responsible for providing the experimental data.

The work presented in Chapters 6 and 7 of this thesis has appeared in publication as follows:

Torres, C., Borman, D., Sleigh, P.A. and Neeve, D. 2018. Determination of Scale Effects for a Scaled Physical Model of a Labyrinth Weir using CFD. In: *Proceedings of the 7th IAHR International Symposium on Hydraulic Structures, Aachen, Germany*. 15-18th May.

Torres, C., Borman, D., Sleigh, P.A. and Neeve, D. 2018. Investigating Scale Effects of a Physical Model with 3D CFD. In: *Proceedings of the 20th Biennial British Dam Society Conference*. 13-15th September.

I was responsible for the execution of the modelling work, data processing, analysis and preparation of the manuscript. D. Borman and P.A. Sleigh contributed in the editing of the manuscript. D. Neeve was responsible for providing the experimental data.

This copy has been supplied on the understanding that it is copyright material and that no quotation from the thesis may be published without proper acknowledgement.

The right of Caterina Torres Mansilla to be identified as Author of this work has been asserted by her in accordance with the Copyright, Designs and Patents Act 1988.

Acknowledgements

Firstly, I would like to thank my supervisors, Dr Duncan Borman and Dr Andrew Sleigh, for their instruction and help in this thesis. I would also like to extend my gratitude to my industrial supervisors, David Neeve and Mutlu Ucuncu, for their valuable guidance and suggestions.

I wish to thank the EPSRC and Arup for funding this project and giving me the opportunity to undertake this research.

My gratitude is also due to my colleagues at the University of Leeds who offered invaluable help with the learning and implementation of HPC systems for CFD at the earliest stages of this project.

I am extremely grateful to my closest friends for the immense support and for being there for me when I most needed them.

I especially wish to thank my sister, Anna, for the enormous encouragement and strength she provided me throughout the entire length of this research. I would also like to thank my parents, Paco and Teresa, for having given me an extraordinary example of hard work and dedication which enabled me to complete this thesis.

Lastly, and most importantly, I am grateful for the love, patience and support of my partner, Mark.

Abstract

The recent increase in frequency and severity of extreme weather events has resulted in the crucial need for design and rehabilitation of hydraulic infrastructure like weirs and spillways. These structures play an essential role by ensuring flood protection and security of water resources. The current scenario has triggered an increased implementation of labyrinth weirs, which enable greater efficiency where larger discharges are expected. The standard means of hydraulic modelling for the design of this type of hydraulic structures consist in scaled physical hydraulic models. The principal limitation of these experimental techniques is their associated scale effects which are induced by the impossibility to equate all force ratios in the prototype and model. Renewed research is needed in order to determine whether such distortions are present in physical models of labyrinth weirs and provide refined limits to minimise them. Moreover, in the recent years, interest in numerical modelling has grown amongst the hydraulic structures community. Several Computational Fluid Dynamics (CFD) techniques have been proposed for hydraulic modelling, enhanced by dramatic improvements in computer processing power. These approaches require further validation evidence for a wider range of structures and flow conditions to demonstrate their reliability and to inform best practice on their implementation. Determination of the extent to which the leading numerical approaches are capable of reproducing an experimental flow of interest is therefore of significant importance.

The present work includes the initial evaluation of the capability of two leading numerical techniques to reproduce an experimental free surface flow and focuses on the assessment of the Volume of Fluid (VOF) method to simulate the flow over a labyrinth weir and investigate scale effects of a physical model. The Smoothed Particle Hydrodynamics (SPH) technique and the VOF method are first tested for a dam break case over an obstacle. Subsequently, the VOF is employed in two solvers (ANSYS Fluent and OpenFOAM) to simulate the physical model of a labyrinth weir and spillway. After validation in respect of various flow aspects is undertaken, the prototype scale is simulated, and scale effects are examined. Finally, limits to minimise scale effects observed in the different flow aspects (depths and velocities in the spillway channel as well as in the labyrinth weir rating curve) are estimated based on the numerical predictions.

The VOF modelling of various flow aspects in the physical hydraulic model demonstrated the RANS $k - \varepsilon$ family models implemented with the PLIC interface capturing scheme were appropriate to characterise the flows encountered over the labyrinth weir and in the spillway channel. In order to achieve mesh independence, the VOF applied in Fluent required a minimum cell size of 8×10^{-3} m and in OpenFOAM required 4×10^{-3} m. For the lowest flow rates, the minimal discrepancies observed in the predictions from the two solvers were found to be due to the interface capturing scheme. For the largest flows, more significant differences were found between the two solvers which were due to cell size sensitivity. This study demonstrated that the 3D CFD VOF with the appropriately chosen numerical implementations is capable of reproducing the complex free surface flows over and downstream a labyrinth weir for a range of flow conditions.

Abstract

The comparison of the prototype and physical model scale VOF predictions revealed the occurrence of larger velocities and lower depths at prototype scale. The differences at the two scales were manifested in the spillway channel flows as well as in the weir rating curve and decreased for increasing flow rate. Prototype scale simulations also showed increases in the weir nappe, causing elongation of the cross-wave configuration generated by the labyrinth weir. These were found likely to be caused by differences in pressure distribution at the weir crest and were reduced for increasing flow rate. The above findings were very well correlated with existing experimental studies from the literature. In addition, the prototype scale simulations presented changes in the waves' positions, occurring even for the largest flow rates where the scale effects on depth and velocity were minimal. Simulation results of additional scales 1:50 and 1:10 indicated that the waves' displacements are reduced for decreasing scale factor of the simulation.

Limits to minimise scale effects observed in the labyrinth weir rating curve as well as in the depths and velocities in the spillway channel were estimated using the Fluent numerical predictions. The derived limits were in close agreement with existing limiting criteria found in the literature. The present work substantiates the capability of CFD as a technique to quantify scale effects induced by physical models and determine limits to minimise them.

Table of Contents

Acknowledgements	ii
Abstract	iii
Table of Contents	v
List of Figures.....	xi
List of Tables	xxiii
Nomenclature	xxvi
1. Introduction.....	1
1.1. Role and Importance of Hydraulic Structures	1
1.2. Reservoir Failures and Refurbishment Works	3
1.3. Hydraulic Modelling Methodologies	5
1.3.1. Physical Modelling.....	5
1.3.2. Numerical Modelling.....	7
1.3.3. Composite Modelling.....	8
1.4. Hydraulic Modelling of Labyrinth Weirs.....	8
1.5. Aim and Objectives	10
1.6. Structure of this Thesis	11
2. Review of Hydraulic Modelling Methodologies	14
2.1. Introduction.....	14
2.2. Physical Modelling	14
2.2.1. Background	14
2.2.2. Concepts of Model to Prototype Similitude	15
2.2.3. Scale Effects in Hydraulic Physical Models	18
2.2.4. Review of Relevant Physical Modelling Studies	22
2.3. Numerical Modelling of Hydraulic Structures	23
2.3.1. Historical Background of Numerical Simulations	23
2.3.2. Overview of Numerical Methods for Free Surface Flows.....	24
2.3.3. Current Challenges	30
2.3.4. Review of Relevant Numerical Modelling Studies	31

Table of Contents

2.4.	Composite Modelling	33
2.4.1.	Introduction	33
2.4.2.	Review of Most Relevant Studies	33
2.5.	Conclusions	34
3.	Computational Fluid Dynamics Modelling	36
3.1.	Introduction	36
3.2.	General Concepts	36
3.3.	Governing Equations	37
3.4.	Discretisation Schemes	38
3.4.1.	Finite Difference Method (FDM)	38
3.4.2.	Finite Element Method (FEM)	38
3.4.3.	Finite Volume Method (FVM)	39
3.5.	Turbulence Modelling	42
3.5.1.	RANS Models	43
3.6.	Pressure-Velocity Coupling	49
3.6.1.	The SIMPLE Algorithm	49
3.6.2.	The PISO Algorithm	49
3.7.	Meshing	50
3.8.	Uncertainty and Error in CFD Simulations	50
4.	Numerical Modelling Approaches: Description and Implementation	52
4.1.	Introduction	52
4.2.	The VOF Method	52
4.2.1.	Introduction	52
4.2.2.	Interface Capturing Schemes	54
4.3.	The SPH Method	57
4.3.1.	Introduction	57
4.3.2.	Fundamental Equations	58
4.4.	Application of the VOF and SPH	59
4.4.1.	Introduction	59
4.4.2.	VOF Modelling	60
4.4.3.	SPH Modelling	77

4.5.	Conclusions.....	87
5.	Case Study: The Eller Beck Labyrinth Weir and Spillway	89
5.1.	Introduction.....	89
5.2.	Description of the Scheme	89
5.3.	Scaled Physical Hydraulic Model of the Eller Beck Spillway	92
5.3.1.	Purpose of the Model	93
5.3.2.	Scale Factors	94
5.3.3.	Instrumentation and Measurements.....	94
5.3.4.	Scenarios Simulated and Results	94
6.	VOF Modelling of the Labyrinth Weir and Spillway	97
6.1.	Introduction.....	97
6.1.1.	Chapter Contents	97
6.1.2.	Structure of this Chapter	97
6.2.	Modelling Domains.....	99
6.3.	Meshing.....	101
6.4.	Boundary Conditions	104
6.4.1.	General.....	104
6.4.2.	Downstream Weir Height Calculations	106
6.5.	Initial Conditions	107
6.6.	Flow Equations.....	108
6.6.1.	Turbulence Modelling	108
6.6.2.	Free Surface Modelling	108
6.6.3.	Flow Aeration	108
6.7.	Numerical Implementations.....	108
6.8.	Model Assumptions and Limitations.....	110
6.8.1.	Air Entrainment.....	110
6.8.2.	Mesh Configuration and Refinement	110
6.8.3.	Roughness of Hard Boundaries	111
6.8.4.	Geometry Differences	111
6.8.5.	Model Errors.....	111
6.9.	Sensitivity Analyses	111

Table of Contents

6.9.1.	Mesh Design and Grid Convergence Index.....	111
6.9.2.	Time Step Size.....	115
6.9.3.	Turbulence Model.....	117
6.9.4.	Interface Capturing Scheme.....	120
6.9.5.	Discussion.....	121
6.10.	Modelling the Flow in the Spillway Channel.....	124
6.10.1.	Low Flow Rate: 40 m ³ /s.....	124
6.10.2.	Intermediate Flow Rate: 79.8 m ³ /s.....	129
6.10.3.	High Flow rate: 119.6 m ³ /s.....	133
6.10.4.	PMF: 159.5 m ³ /s.....	139
6.10.5.	Summary.....	146
6.11.	Prediction of the Labyrinth Weir Rating Curve.....	148
6.12.	Modelling the PMF in the Comprehensive Domain.....	149
6.12.1.	Low Tail Water Level.....	149
6.12.2.	Medium Tail Water Level.....	153
6.12.3.	High Tail Water Level.....	157
6.12.4.	Summary.....	160
6.13.	Discussion.....	160
6.13.1.	Predictions of the Flow Downstream the Weir.....	160
6.13.2.	PMF Predictions in the Comprehensive Domain.....	162
6.13.3.	Limitations.....	163
6.14.	Conclusions.....	164
7.	Comparison of Prototype and Physical Model Predictions.....	167
7.1.	Introduction.....	167
7.2.	Assumptions and Limitations.....	167
7.3.	Sensitivity to Numerical Implementations.....	168
7.3.1.	Mesh Cell Size.....	168
7.3.2.	Turbulence Model.....	170
7.3.3.	Interface Capturing Scheme.....	175
7.3.4.	Discussion.....	176
7.4.	Flow in the Spillway Channel.....	177

7.4.1.	Low Flow Rate: 40 m ³ /s	177
7.4.2.	Intermediate Flow Rate: 78.9 m ³ /s.....	182
7.4.3.	High Flow Rate: 119.6 m ³ /s.....	186
7.4.4.	PMF: 159.5 m ³ /s.....	194
7.4.5.	Summary	201
7.4.6.	Discussion	203
7.5.	Labyrinth Weir Rating Curve	219
7.5.1.	Results	219
7.5.2.	Discussion on Existing Limiting Criteria	220
7.6.	PMF in the Comprehensive Domain	221
7.6.1.	Introduction.....	221
7.6.2.	Low Tail Water Level.....	222
7.6.3.	High Tail Water Level	226
7.6.4.	Discussion	231
7.7.	Conclusions.....	232
8.	Investigation of Scale Effects and Estimation of Limiting Criteria.....	235
8.1.	Introduction.....	235
8.2.	Water Depths and Velocities.....	235
8.2.1.	Introduction.....	235
8.2.2.	Limiting Criteria	235
8.3.	Changes in Waves Positions in the Spillway Channel.....	237
8.3.1.	Introduction.....	237
8.3.2.	Changes in the Flow Characteristics in the Spillway Channel.....	238
8.3.3.	Changes in the Waves' Positions in the Spillway Channel	241
8.4.	Labyrinth Weir Rating Curve Calculations	243
8.4.1.	Introduction.....	243
8.4.2.	Determination of Minimum Height Upstream Weir.....	243
8.5.	Conclusions.....	244
9.	Conclusions and Further Work.....	247
9.1.	Summary	247
9.2.	Conclusions.....	248

Table of Contents

9.2.1.	2D and 3D VOF and SPH Modelling of an Experimental Dam Break Flow	248
9.2.2.	3D VOF Modelling of the Labyrinth Weir and Spillway Physical Model	249
9.2.3.	Comparison of Prototype and Model Scale Predictions	251
9.2.4.	Estimation of Limiting Criteria and Comparison with Established Values	253
9.3.	Implications of Key Findings	254
9.4.	Recommendations for Further Work	255
References	257
Appendix A.	OpenFOAM Investigation of Nappe Displacement.....	271
Appendix B.	OpenFOAM Investigation of Labyrinth Weir Rating Curve	274

List of Figures

Figure 1.1: Central Government total expenditure in FCERM from DEFRA (2017)	2
Figure 1.2: Example layout of a chute spillway from Khatsuria (2005) . Where (1) is the river, (2) is the earth dam, (3) is the spillway, (4) is the approach channel, (5) is the chute and (6) is the flip bucket.....	3
Figure 1.3: Diagram of a weir with main elements from Chanson (2004b)	3
Figure 1.4: a) Oroville dam failure from New York Times (2017); b) scaled physical model of the damaged dam built at the Utah Water Research Laboratory for repairing work from Utah State University (2017)	7
Figure 1.5: a) General classifications of labyrinth weirs: (A) triangular, (B) trapezoidal and (C) rectangular; b) Typical labyrinth weir with geometric parameters from Crookston (2010)	9
Figure 3.1: Diagram with FVM established notation in the vicinity of a node P	39
Figure 4.1 a) Fluids 1 and 2 represented in the mesh; b) indication of the phases for the two fluids and at the interface as implemented in the VOF method	53
Figure 4.2: a) Example distribution of the α field in cells; b) Reconstruction of the interface utilising the normal vectors shown in red; c) Final free surface reconstruction after the iterative process	55
Figure 4.3: Initial conditions for the bump test case from Biscarini et al. (2010)	60
Figure 4.4: Example mesh and enhanced scale image of the mesh bias in the z direction	61
Figure 4.5: Setup of initial conditions in Fluent	62
Figure 4.6: Setup of initial conditions in OpenFOAM	63
Figure 4.7: Experimental photograph (top) and contour plots showing the water volume fraction at 1.8 s for the 7 meshes of increasing resolution	63
Figure 4.8: a) Free surface depth time series with different numerical implementations at the top of the obstacle on Mesh 3 and b) using Mesh 6	64
Figure 4.9: Experimental photograph (top) and contour plots showing the water volume fraction at 1.8 s for the 6 meshes of increasing resolution using fixed time stepping	65
Figure 4.10: Experimental photograph (top) and contour plots showing the water volume fraction at 3 s for the 6 meshes of increasing resolution using fixed time stepping	66
Figure 4.11: Free surface depth time series using 2D meshes 1 to 6 with fixed time stepping at a) the top of the obstacle and b) $x = 3.5$ m.....	67
Figure 4.12: Experimental photograph (top) and contour plots showing the water volume fraction at 1.8 s for the 4 meshes of increasing resolution	67

List of Figures

Figure 4.13: Experimental photograph (top) and contour plots showing the water volume fraction at 3 s for the 4 meshes of increasing resolution	68
Figure 4.14: a) Free surface depth time series using 3D meshes 1 to 4 at the top of the obstacle and b) at $x= 3.5\text{m}$	68
Figure 4.15: Experimental photograph (top) and contour plots showing the water volume fraction at 1.8 s for the 4 meshes of increasing resolution using fixed time stepping	69
Figure 4.16: Free surface depth time series using 3D meshes 1 to 4 at $x= 3.5\text{ m}$ implementing fixed time stepping.....	70
Figure 4.17: Experimental photograph (top) and contour plots showing the water volume fraction at 1.8 s for the 4 meshes of increasing resolution	70
Figure 4.18: Experimental photograph (top) and contour plots showing the water volume fraction at 3 s for the 4 meshes of increasing resolution	71
Figure 4.19: Free surface depth time series using 2D meshes 1, 3 and 6 at a) the top of the obstacle and b) at $x = 3.5\text{ m}$	71
Figure 4.20: Experimental photograph (top) and contour plots showing the water volume fraction at 1.8 s for the 3 meshes of increasing resolution	72
Figure 4.21: Experimental photograph (top) and contour plots showing the water volume fraction at 3 s for the 3 meshes of increasing resolution	72
Figure 4.22: a) Free surface depth time series using 3D meshes 1 to 3 at the top of the obstacle and b): at $x=3.5\text{ m}$	73
Figure 4.23: Fluent comparison between a) free surface depth time series at $x = 3.5\text{ m}$ computed using 2D meshes 1 to 4 and the 2D CFD VOF model and b) computed using 3D meshes 1 to 4 and the 3D CFD VOF model	74
Figure 4.24: OpenFOAM comparison between a) free surface depth time series at $x = 3.5\text{ m}$ computed using 2D meshes 1 to 4 and the 2D CFD VOF method and b) computed using 3D meshes 1 to 4 and the 3D CFD VOF model.....	75
Figure 4.25: Free surface depth time series at $x = 3.5\text{ m}$ for meshes 1, 3, 4 and 6 for the 2D CFD VOF computed in a) Fluent with implementation of fixed time stepping and b) OpenFOAM.....	75
Figure 4.26: Free surface depth time series at $x = 3.5\text{ m}$ for meshes 1 to 4 with the 3D CFD VOF simulations computed in a) Fluent with fixed time stepping method, b) OpenFOAM Conclusions	76
Figure 4.27: Setup of initial conditions in DualSPHysics.....	78
Figure 4.28: Experimental photograph (top) and simulation results at 1.8 s after the dam break for the four different cases of increasing resolution	78
Figure 4.29: Experimental photograph (top) and simulation results at 3 s after the dam break for the four different cases of increasing resolution	79

Figure 4.30 Interface depth profile versus channel length at 3 s for the four simulations of increasing resolution with a reduced size graph of the entire domain 79

Figure 4.31: Experimental photograph (top) and simulation results at 8.4 s after the dam break for the four different cases of increasing resolution 80

Figure 4.32: Interface depth profile versus channel length at 8.4 s for the four simulations of increasing resolution with a reduced size graph of the entire domain 80

Figure 4.33:a) Interface depth time series for the four simulations of increasing resolution at a) the top of the obstacle and b) $x = 3.5$ m..... 81

Figure 4.34: Interface depth time series for the different numerical implementations at a) the top of the obstacle and b) $x = 3.5$ m..... 82

Figure 4.35: Experimental photograph (top) and simulation results at 1.8 s after the dam break for the four different cases of increasing resolution 82

Figure 4.36: Simulation results at 3 s after the dam break for the four different cases of increasing resolution 83

Figure 4.37: Interface depth profile versus channel length at 3 s for the four simulations of increasing resolution with a reduced size graph of the entire domain 83

Figure 4.38: Experimental photograph (top) and simulation results at 8.4 s after the dam break for the four different cases of increasing resolution 84

Figure 4.39: Interface depth profile versus channel length at 8.4 s for the four simulations of increasing resolution with a reduced size graph of the entire domain 84

Figure 4.40: Interface depth time series for the four simulations of increasing resolution at a) $x = 3.5$ m, b) the top of the obstacle and c) at 5.2 m 85

Figure 5.1: Location of the three components of the flood alleviation scheme from Brinded et al. (2014) 89

Figure 5.2: Layout of the hydraulic structures in the Eller Beck reservoir from Brinded et al. (2014) 90

Figure 5.3: Typical labyrinth weir schematic from Crookston (2010) 91

Figure 5.4: View of the labyrinth weir from the left hand side of the scheme 91

Figure 5.5: Eller Beck spillway channel from downstream with end sill at the front of the image 92

Figure 5.6: a) Layout of the flood storage reservoir with labyrinth weir and spillway from Brinded et al. (2014); b) Physical model of the labyrinth weir and spillway including surrounding terrain; c) Enhanced view of the end sill located at the tail of the spillway; d) Enhanced detail of the labyrinth weir 93

List of Figures

Figure 5.7: Labyrinth weir rating curve obtained with experimental measurements in the physical model	95
Figure 5.8: a) Physical model diagram with the location of the experimental measurements for 40 m ³ /s; b) Photograph of the flow downstream of the physical model; c) Photograph of the flow in the spillway channel.....	96
Figure 6.1: CAD drawing of the hydraulic structures and surrounding terrain	99
Figure 6.2: a) Weir domain; b) Channel domain; c) Comprehensive modelling domain.....	100
Figure 6.3: TIN of the surrounding terrain around the spillway channel, including the upstream and downstream embankments	101
Figure 6.4: Weir modelling domain mesh, with enhanced view of the first downstream apex ..	102
Figure 6.5: Plan view of the weir modelling domain mesh with a block of lower cell size in the labyrinth area and its vicinity	102
Figure 6.6: a) Prototype size spillway channel longitudinal mesh cross section (parallel to the flow) and detailed mesh configurations indicated in the rectangular area: b) appropriate for OpenFOAM and c) appropriate for Fluent; d) Plan view and side view of the mesh indicating the location of the cross sections (perpendicular to the flow) in: e) of mesh for OpenFOAM and f) for Fluent	103
Figure 6.7:a) Prototype size mesh of the comprehensive domain (top view); b) Base view; c) Cross sectional plane along the mesh.....	104
Figure 6.8: Boundary conditions for: a) weir modelling domain; b) channel modelling domain and c) comprehensive modelling domain	105
Figure 6.9: Three modelling domains corresponding to the three weir three levels overlaid	107
Figure 6.10: Setup of the initial conditions in a) the channel domain and b) comprehensive domain	107
Figure 6.11:a) Time series of free surface depth at locations A to E of the spillway channel; b) Free surface velocity profile across the channel section through point B at time 100 to 155 s once the model is stable.....	110
Figure 6.12: Location of points A, B, C and D in a physical model diagram with depths and velocities for 40 m ³ /s.....	113
Figure 6.13: Free surface velocity contour plots on weir mesh for scaled 40m ³ /s with a CFL number of 0.9 and 0.2.....	116
Figure 6.14: Interface depth time series of simulations using CFL numbers 0.2 and 0.9	116
Figure 6.15: Free surface structures and velocity contours computed with the three turbulence models and physical model diagram showing the experimental locations and configuration of cross-waves	117

Figure 6.16: Cross-sectional profiles using the three turbulence models: a) interface depth and b) interface velocity sections through point B; c) Interface depth and d) velocity profiles at section through point C..... 118

Figure 6.17: Flow areas coloured by velocity contours at sections through locations B, C, D and E of the spillway channel for the 119.6m³/s case predicted with the three turbulence models 119

Figure 6.18: Cross-sectional profiles computed with Fluent simulations using the PLIC and the CICSAM schemes; a) Interface depth at sections through points A and B and b) through C, D and E; c) Interface velocity profiles at sections through points B to E 121

Figure 6.19: Cross-sectional interface depth profiles for 119.6m³/s using Fluent CICSAM and OpenFOAM MULES at sections through points A and B 123

Figure 6.20: a) Photograph of the physical model free surface and numerically predicted with b) OpenFOAM and c) Fluent; d) Cross-wave crests indicated with red lines on physical model, e) in OpenFOAM predictions and f) in Fluent predictions; g) Photograph of the physical model spillway channel and with black lines indicating central wave; h) Physical model diagram with experimental locations and flow features; i) Numerically predicted free surface for the spillway channel and j) with location of cross-waves' crests with OpenFOAM and with Fluent for a flow rate of 40 m³/s 125

Figure 6.21: a) Wave structures showing three distances to wave crossing points from the weir crest; b) Free surface profile predicted with OpenFOAM and Fluent along distance x_1 , b) x_2 and c) x_3 126

Figure 6.22: a) Velocity-coloured free surface with the location where numerical predictions for point A are extracted and water volume fraction contour plane through point A; b) Free surface profiles at a section across point A with physical model measurements..... 127

Figure 6.23: Time-averaged values of: a) depth and b) velocity at point locations along the spillway channel predicted by the two solvers with physical model measurements 127

Figure 6.24: a) Numerical predictions of interface velocities at locations B, C, D and E with physical model measurements and; b) flow area coloured by velocity contours at the same sections in OpenFOAM 128

Figure 6.25: a) Photograph of the physical model free surface and b) with waves' crests indicated with red lines; c) Numerically predicted free surface and d) with waves' crests indicated with red lines; e) Photograph of the physical model spillway channel and with the location of the free surface features; f) Physical model diagram with experimental locations; g) Numerically predicted free surface for the complete channel and h) with the location of the free surface crests for the flow rate of 79.8 m³/s 130

Figure 6.26: a) Interface cross sectional profiles at points A and B and b) at B, D and D; c) Interface velocity profiles through points B to E and d) velocity contour planes at sections through points B, C, D and E in OpenFOAM 131

List of Figures

Figure 6.27: a) Longitudinal profile next to the spillway right wall; b) location of the longitudinal profile indicating the distance coordinates.....	132
Figure 6.28:a) Time-averaged values of: a) depth and b) velocity at point locations along the spillway channel with physical model measurements	133
Figure 6.29: a) Photograph of the physical model free surface and numerically predicted with b) OpenFOAM and c) Fluent; d) cross-wave crests indicated with red lines on physical model and e) in OpenFOAM predictions and f) in Fluent predictions; g) Photograph of the physical model spillway channel and with black lines indicating central wave; h) Physical model diagram with experimental locations and location of flow features; i) Numerically predicted free surface for the complete channel and j) with location of cross-waves' crests for a flow rate of 119.6 m ³ /s.....	134
Figure 6.30: Free surface profiles predicted with OpenFOAM and Fluent along distances: a) x ₁ , b) x ₂ and c) x ₃	136
Figure 6.31:Cross-sectional interface depth profiles at sections across: a) points A and B and b) points C, D and E; c) longitudinal profile next to spillway right wall; d) location of longitudinal profile with distance coordinates	137
Figure 6.32: a) Cross-sectional interface velocity profiles at sections across points B, C, D, E; b) Flow areas coloured by velocity contours of the different sections in OpenFOAM	138
Figure 6.33: Time-averaged values of: a) depth and b) velocity at point locations along the spillway channel predicted by the two solvers with physical model measurements	139
Figure 6.34: a) Photograph of the physical model free surface and numerically predicted with b) OpenFOAM and c) Fluent; d) Cross-wave crests indicated with red lines on physical model and e) in OpenFOAM predictions and f) in Fluent predictions; g) Photograph of the physical model spillway channel and with black lines indicating central wave; h) Physical model diagram with experimental locations and location of flow features; i) Numerically predicted free surface for the complete channel and j) with location of cross-waves' crests for a flow rate of 159.5 m ³ /s.....	140
Figure 6.35: Free surface profiles predicted with OpenFOAM and Fluent along distances: a) x ₁ , b) x ₂ and c) x ₃	141
Figure 6.36: a) Cross-sectional interface depth profiles at sections across points A and B and b) C, D and E; c) Interface depth time series at point locations A to E predicted with Fluent	142
Figure 6.37: a) Longitudinal profile next to the spillway right wall; b) location of the longitudinal profile indicating the distance coordinates.....	143
Figure 6.38: a) Cross-sectional interface velocity profiles at sections across points B, C, D, E; b) Flow areas coloured by velocity contours of the different sections in OpenFOAM; c) Interface velocity time series at point locations B to E predicted with Fluent	144
Figure 6.39: Time-averaged values of: a) depth and b) velocity at point locations along the spillway channel predicted by the two solvers with physical model measurements	145

Figure 6.40: a) Velocities measured upstream and at the crest of the physical model; b) Free surface velocity vectors predicted with OpenFOAM; c) Free surface velocity vectors predicted with Fluent 146

Figure 6.41: Rating curve of the labyrinth weir measured in the physical scale model and computed with predictions from Fluent and OpenFOAM 148

Figure 6.42: a) Physical model diagram indicating the approximate location of stilling at low tail water level with a red arrow; b) Photograph of the physical model; c) Instant representation of the numerically predicted free surface; d) Photograph of the physical scale model with red lines showing the location of the free surface; e) Instant representation of the numerically predicted free surface with red lines showing the location of the free surface 150

Figure 6.43: a) Photograph of the physical model hydraulic jump; b) and c) Instant representation of numerical model free surface coloured by velocity; d) Location of three planes to analyse the flow situation 151

Figure 6.44: Free surface depth and velocity profiles through the hydraulic jump with the corresponding water volume fraction contour planes at the same sections along: a) Plane 1, b) Plane 2 and c) Plane 3 152

Figure 6.45: Profile in the vicinity of the hydraulic jump showing velocity vectors and contours across Planes 1, 2 and 3 153

Figure 6.46: a) Physical model diagram indicating the approximate location of stilling at medium tail water level with a red arrow; b) Photograph of the physical scale model; c) Instant representation of the numerically predicted free surface; d) Photograph of the physical scale model with red lines showing the location of the free surface; e) Instant representation of the numerically predicted free surface with red lines showing the location of the free surface 154

Figure 6.47: a) instant representation of numerically predicted free surface coloured by velocity; b) enhanced detail of the free surface coloured by velocity surrounding the terrain irregularities 154

Figure 6.48: Free surface depth and velocity profiles through the hydraulic jump with the corresponding water volume fraction contour planes at the same sections along: a) Plane 1, b) Plane 2 and c) Plane 3; d) location of the three planes in the spillway 156

Figure 6.49; Profile in the vicinity of the hydraulic jump showing velocity vectors and contours across Planes 1, 2 and 3 157

Figure 6.50: a) Physical model diagram indicating the approximate location of stilling at high tail water level with a red arrow; b) Photograph of the physical scale model; c) Instant representation of the numerically predicted free surface; d) Photograph of the physical scale model with red lines showing the location of the free surface; e) Instant representation of the numerically predicted free surface with red lines showing the location of the free surface 158

List of Figures

Figure 6.51 a) instant representation of numerically predicted free surface coloured by velocity from plan view; b) Enhanced detail of the same representation illustrating the surrounding terrain irregularities from a different perspective.	158
Figure 6.52: Free surface depth and velocity profiles through the hydraulic jump with the corresponding water volume fraction contour planes at the same sections along: a) Plane 1, b) Plane 2 and c) Plane 3; d) Location of the three planes in the spillway	159
Figure 6.53: Profiles in the vicinity of the hydraulic jump showing velocity vectors and contours across Planes 1, 2 and 3	160
Figure 6.54: Water volume fraction contours at a plane perpendicular to the third downstream crest predicted for 40m ³ /s with: a) OpenFOAM and b) Fluent and for 119.6 m ³ /s with c) OpenFOAM and d) Fluent	162
Figure 7.1: Free surface structures and velocity contours computed with the three turbulence models	170
Figure 7.2: Cross-sectional profiles using the three turbulence models: a) Interface depth and b) interface velocity through point A; c) Water volume fraction contours and flow areas coloured by velocity at sections through point A	172
Figure 7.3: Cross-sectional profiles using the three turbulence models: a) Interface depth and b) interface velocity through point B	172
Figure 7.4: Cross-sectional profiles using the three turbulence models: a) Interface depth through point C; b) Interface velocity through point C; c) Interface depth through point E; d) Interface velocity through point E; e) Flow areas coloured by velocity at sections through point C and f): through point E	173
Figure 7.5: Cross-sectional profiles computed with Fluent simulations using the PLIC and the CICSAM schemes; a) interface depth at sections through points A and B and b) through C, D and E; c) interface velocity profiles at sections through points B to E	175
Figure 7.6: Scaled and prototype model predictions of wave structures and interface velocity contours predicted with: a) OpenFOAM and b) Fluent for a flow rate of 40 m ³ /s.....	178
Figure 7.7: a) Scaled and prototype wave structures showing three distances to wave crossing points from the weir crest; b) Free surface profile along distance x_1 predicted with OpenFOAM and c) with Fluent; d) Free surface profile along distance x_2 predicted with OpenFOAM and e) with Fluent; f) Free surface profile along distance x_3 predicted with OpenFOAM and g) with Fluent	179
Figure 7.8: a) Interface cross-sectional profiles at sections A, B at the two scales predicted with OpenFOAM and b) with Fluent; c) Interface cross sectional profiles at sections C, D and E predicted with OpenFOAM and d) with Fluent.....	180
Figure 7.9: Interface cross-sectional velocity profiles at sections B, C, D and E predicted by: a) OpenFOAM and b) Fluent	181

Figure 7.10: Interface velocity contours and wave structures in scaled and prototype simulations for 79.8 m³/s 183

Figure 7.11: a) Free surface profile along distance x_1 ; b) Free surface profile along distance x_2 ; c) Free surface profile along distance x_3 183

Figure 7.12: Time-averaged values of: a) interface depth and b) interface velocity magnitude at different experimental locations 184

Figure 7.13: Cross sectional profiles of interface depth at sections through: a) points A, B, and b) points C, D and E. 184

Figure 7.14: Interface cross-sectional velocity profiles at sections B, C, D and E 185

Figure 7.15: Scaled and prototype model predictions of wave structures and interface velocity contours predicted with: a) OpenFOAM and b) Fluent for a flow rate of 119.6 m³/s 187

Figure 7.16: a) Free surface profile along distance x_1 predicted with OpenFOAM and b) with Fluent; c) Free surface profile along distance x_2 predicted with OpenFOAM and d) with Fluent; e) Free surface profile along distance x_3 predicted with OpenFOAM and f) with Fluent 189

Figure 7.17: a) Physical model photograph of the free surface features at the lower section of the channel and with the dominant wave features indicated with dashed lines; b) Predictions of free surface features in the scaled and prototype cases with the main features indicated with dashed lines from OpenFOAM and c) Fluent. The impact point of the dominant wave is indicated with an “I” 190

Figure 7.18: a) Interface cross-sectional profiles at sections A, B at the two scales predicted with OpenFOAM and b) with Fluent; c) Cross sectional profiles of interface depth at sections through points C, D and E predicted in OpenFOAM and d) Fluent; e) Free surface features indicated on the scaled and prototype cases with the location of the sections 192

Figure 7.19: Interface cross-sectional velocity profiles at sections B, C, D and E predicted with: a) OpenFOAM and b) Fluent 193

Figure 7.20: Scaled and prototype model predictions of wave structures and interface velocity contours predicted with a) OpenFOAM and b) Fluent for a flow rate of 159.5 m³/s 195

Figure 7.21: a) Free surface profile along distance x_1 predicted with OpenFOAM and b) with Fluent; c) Free surface profile along distance x_2 predicted with OpenFOAM and d) with Fluent; e) Free surface profile along distance x_3 predicted with OpenFOAM and f) with Fluent 196

Figure 7.22: a) Physical model photograph of the free surface features at the lower section of the channel and with the dominant wave features indicated with dashed lines; b) Predictions of free surface features in the scaled and prototype cases and with the main features indicated with dashed lines from Fluent and c) OpenFOAM 197

Figure 7.23: a) Physical model photograph of the free surface features at the lower section of the channel and with the dominant wave features indicated with dashed lines; b) Fluent predictions

List of Figures

of free surface features in the scaled and prototype cases and with the main features indicated with dashed lines. The impact point of the dominant wave is indicated with an “I”	198
Figure 7.24: a) Interface cross-sectional profiles at sections A, B at the two scales predicted with OpenFOAM and b) with Fluent; c) Cross sectional profiles of interface depth at sections through points C, D and E predicted in OpenFOAM and d) Fluent; e) Free surface features indicated on the scaled and prototype cases with the location of the sections	199
Figure 7.25: Interface cross-sectional velocity profiles at sections B, C, D and E predicted with: a) OpenFOAM and b) Fluent	200
Figure 7.26: a) Percentage decrease in depth and b) percentage increase in velocity at the various sections for each flow rate and solver	204
Figure 7.27: a) Percentage decrease in depth in the prototype with respect to model scale; b) Percentage increase in velocity in the prototype with respect to the model scale; c) Prototype-to-model ratio of water depth; d) prototype-to-model ratio of velocity	205
Figure 7.28: a) Prototype-to-model ratio of water depth at each experimental location; b) prototype-to-model ratio of velocity at each experimental location	206
Figure 7.29: Prototype-to-model ratios of: a) Froude number at section D; b) Froude number at section E; c) Reynolds number at section D; d) Reynolds number at section E; e) Weber number at section D; f) Weber number at section E	208
Figure 7.30: Percentage elongation of distances x_1 , x_2 and x_3 in the cross-wave configuration for each flow rate and solver	209
Figure 7.31: Location of planes perpendicular to weir crests II and III utilised to examine the flow conditions upstream and downstream the labyrinth weir	210
Figure 7.32: Planes along upstream crest II coloured by velocity contours and showing vectors with flow direction at the model scale and prototype scale for 159.5 m ³ /s in OpenFOAM.....	211
Figure 7.33: Planes along crest II coloured by pressure contours at plane through crest II at model and prototype scale with an enhanced view of the pressure contours at the crest for 159.5 m ³ /s in OpenFOAM.....	212
Figure 7.34: a) Plane along crest III coloured by velocity contours at model scale and b) at prototype scale; c) Plane along crest III in the area surrounding the weir crest coloured by pressure contours at model and d) at prototype for 159.5 m ³ /s in OpenFOAM	213
Figure 7.35: Sketch of a generic labyrinth weir crest	213
Figure 7.36: a) Pressure distribution and b) velocity distribution of flow over crest II; c) Pressure distribution and d) velocity distribution of flow over crest III for 159.5 m ³ /s in OpenFOAM.....	214
Figure 7.37: a) Plane along crest II coloured by velocity contours at model scale and b) at prototype scale; c) Plane along crest III in the area surrounding the weir crest coloured by pressure contours at model scale and d) at prototype scale for 40 m ³ /s in OpenFOAM	215

Figure 7.38: a) Plane along crest II coloured by velocity contours at model scale and b) at prototype scale; c) Plane along crest III in the area surrounding the weir crest coloured by pressure contours at model scale and d) at prototype scale for 40 m³/s in Fluent..... 216

Figure 7.39: a) Plane along crest II coloured by velocity contours at model scale and b) at prototype scale; c) Plane along crest III in the area surrounding the weir crest coloured by pressure contours at model scale and d) at prototype scale for 159.5 m³/s in Fluent..... 217

Figure 7.40: Labyrinth weir rating curve computed at model and prototype scale with the two solvers 220

Figure 7.41: a) Instant representation of the free surface at model and prototype scale simulations and b) with red dashed lines indicating the location of the tail water; c) Enhanced view of the hydraulic jump 222

Figure 7.42: Instant representation of the free surface coloured by velocity contours at model and prototype scales from two different views 223

Figure 7.43: Location of planes 1, 2 and 3 in the spillway channel at model and prototype scales 223

Figure 7.44: Free surface depth and velocity profiles at the two scales at: a) and b) Plane 1; c) and d) Plane 2; e) and f) Plane 3 224

Figure 7.45: Hydraulic jump free surface time series profiles at plane 2 for: a) scaled case and b) prototype and free surface velocity time series profiles for c) scaled case and d) prototype ... 225

Figure 7.46: Water-phase profiles in the vicinity of the hydraulic jump showing velocity vectors and contours across Plane1, 2 and 3 at model and prototype scales 226

Figure 7.47: a) Instant representation of the free surface at model and prototype scale simulations and b) Enhanced scale of the hydraulic jump with red dashed lines indicating the location of the tail water 227

Figure 7.48: a), c) Instant representation of the free surface coloured by velocity contours at model and prototype scales from different views; b) Location of the three planes for analysis 228

Figure 7.49: Free surface depth and velocity profiles at the two scales at: a) and b) Plane 1; c) and d) Plane 2; e) and f) Plane 3 229

Figure 7.50: Hydraulic jump free surface time series profiles for: a) scaled case and b) prototype and free surface velocity time series profiles for c) scaled case and d) prototype 230

Figure 7.51: Water-phase profiles in the vicinity of the hydraulic jump showing velocity vectors and contours at Plane1, 2 and 3 at model and prototype scales 231

Figure 8.1: Prototype-to-model Froude number ratio versus Reynolds number 237

Figure 8.2: Wave structures predicted for the 159.5 m³/s flow rate at the four scales simulated 238

List of Figures

Figure 8.3: a) Flow areas coloured by velocity contours with velocity vectors across the spillway channel at the impact point of the dominant wave; b) Free surface features coloured by velocity; c) location of distances x_1 , x_2 and x_3	239
Figure 8.4: Flow areas coloured by velocity at: a) the first cross-wave crossing point; b) the third cross-wave crossing point	240
Figure 8.5: Interface cross-sectional profiles at sections: a) C and b) D extracted from simulations at the four scales; c) Location of the sections C and D on the free surface features at the different scales.....	241
Figure 8.6: Wave displacement at sections C and D at scales 1:50, 1:25 and 1:10.....	243
Figure 8.7: Rating curves at physical model scale (1:25) with uncertainty bands and prototype scale.....	244
Figure A.1: OpenFOAM velocity contours and vectors along upstream crest II	271
Figure A.2: OpenFOAM pressure contours along upstream crest II	272
Figure A.3: Percentage nappe displacement at crest II for the PMF case predicted with OpenFOAM.....	273
Figure B.1: a) OpenFOAM Rating curves at physical model scale (1:25), scale 1:10 and prototype scale; b) Rating curves at the three scales with uncertainty bands for scales 1:10 and 1:25 ...	274

List of Tables

Table 1.1: Mechanism of deterioration of the 99 reservoir incidents between 2004 and 2015. Source: Environment Agency (2016)	4
Table 1.2: Significant areas of concern to Inspecting Engineers at statutory reservoirs. Source: Chesterton and Warren (2016)	4
Table 4.1: Summary of meshes used for the simulation of the dam break flow	61
Table 4.2: List of fluid properties utilised in the simulations for the two phases	61
Table 4.3: Summary of numerical implementations applied in the sensitivity analysis	64
Table 4.4: Meshes used for simulations with fixed time stepping and time step sizes	65
Table 4.5: Meshes used for the fixed time step simulations and time step sizes	69
Table 4.6: Variable and fixed time step sizes in the 2D simulations of meshes 1 to 6	74
Table 4.7: Summary of simulations for different particle distances (dp)	78
Table 4.8: Summary of numerical implementations applied in the sensitivity analysis	81
Table 5.1: Classification of hydraulic jumps according to Chow (1959)	96
Table 6.1: Number of elements of the meshes created to model low, medium and high tail water levels	104
Table 6.2: Model implementations applied on the two solvers	109
Table 6.3: Characteristics of the meshes implemented for the mesh independence study in the two solvers	112
Table 6.4: Parameters for the calculation of discretisation error in OpenFOAM, scaled Simulations	115
Table 6.5: Parameters for the calculation of discretisation error in Fluent, scaled Simulations	115
Table 6.6: Averaged values of depth and velocity along sections 1 to 3 for simulations with CFL numbers 0.2 and 0.9 and percentage difference between the two simulations	116
Table 6.7: Section-averaged values of depths and velocities and percentage difference of model predictions from the RNG $k - \varepsilon$ and SST $k - \omega$ models with respect to the Standard $k - \varepsilon$...	119
Table 6.8: Minimum, maximum and averaged $y+$ values at the first and second sections occurring with the three turbulence models.	120
Table 6.9: Relative error in depth predictions in OpenFOAM and Fluent at the different experimental locations	129
Table 6.10: Relative error in velocity predictions in OpenFOAM and Fluent at the different experimental locations	129

List of Tables

Table 6.11: Relative error in depth predictions in OpenFOAM at the different experimental locations.....	133
Table 6.12: Relative error in velocity predictions in OpenFOAM at the different experimental locations.....	133
Table 6.13: Relative error in depth predictions in OpenFOAM and Fluent at the different experimental locations.....	139
Table 6.14: Relative error in velocity predictions in OpenFOAM and Fluent at the different experimental locations.....	139
Table 6.15: Relative error in depth predictions in OpenFOAM and Fluent at the different experimental locations.....	145
Table 6.16: Relative error in velocity predictions in OpenFOAM and Fluent at the different experimental locations.....	145
Table 7.1: Parameters for the calculation of discretisation error in OpenFOAM, prototype Simulations.....	169
Table 7.2: Parameters for the calculation of discretisation error in Fluent, prototype Simulations.....	169
Table 7.3: Section-averaged values of depths and velocities and percentage difference of model predictions from the RNG $k - \varepsilon$ and SST $k - \omega$ models with respect to the Standard $k - \varepsilon$ in prototype scale simulations.....	174
Table 7.4: Froude numbers and prototype-to-model Froude ratios at sections E and D calculated from scaled and prototype simulations for 40 m ³ /s.....	181
Table 7.5: Reynolds numbers and prototype-to-model Reynolds ratios at sections E and D calculated from scaled and prototype simulations for 40 m ³ /s.....	182
Table 7.6 Weber numbers and prototype-to-model Weber ratios at sections E and D calculated from scaled and prototype simulations for 40 m ³ /s.....	182
Table 7.7: Froude numbers and prototype-to-model Froude ratios at sections E and D calculated from scaled and prototype simulations for 79.8 m ³ /s.....	185
Table 7.8: Reynolds numbers and prototype-to-model Froude ratios at sections E and D calculated from scaled and prototype simulations 79.8 m ³ /s.....	186
Table 7.9 Weber numbers and prototype-to-model Froude ratios at sections E and D calculated from scaled and prototype simulations 79.8 m ³ /s.....	186
Table 7.10: Froude numbers and prototype-to-model Froude ratios at sections E and D calculated from scaled and prototype simulations 119.6 m ³ /s.....	193
Table 7.11: Reynolds numbers and prototype-to-model Reynolds ratios at sections E and D calculated from scaled and prototype simulations 119.6 m ³ /s.....	194

Table 7.12 Weber numbers and prototype-to-model Weber ratios at sections E and D calculated from scaled and prototype simulations 119.6 m³/s 194

Table 7.13: Froude numbers and prototype-to-model Froude ratios at sections E and D calculated from scaled and prototype simulations 159.5 m³/s 201

Table 7.14: Reynolds numbers and prototype-to-model Froude ratios at sections E and D calculated from scaled and prototype simulations 159.5 m³/s 201

Table 7.15: Weber numbers and prototype-to-model Froude ratios at sections E and D calculated from scaled and prototype simulations 159.5 m³/s 201

Table 7.16: Percentage difference in depth and velocity in the prototype in respect of model scale at different sections of the spillway channel..... 203

Table 7.17: Percentage of displacement in the distances x_1 , x_2 , and x_3 for all flow rates 209

Table 7.18: Summary of depth, velocity and Weber number at physical model scale 221

Table 8.1: Impact point distance from the weir and location of dominant cross-wave at sections C and D with percentage difference compared to the prototype and distance ratio at the four scales 242

Table A.1: Displacement of the nappe bottom in respect of the prototype and corresponding head over crest..... 272

Nomenclature

Symbols

α	Volume fraction	[-]
b	Width of the channel	[m]
Ca	Cauchy Number	[-]
Δ	Small variable change	[-]
E	Modulus of elasticity	[N/m ²]
Eu	Euler Number	[-]
ε	Turbulent dissipation	[m ² /s ³]
Fr	Froude Number	[-]
Fr_r	Prototype-to-model Froude number ratio	[-]
g	Gravitational acceleration	[m/s ²]
Γ	Scalar Diffusion coefficient	[m ² /s]
h	Water depth	[m]
k	Turbulent kinetic energy	[kg m ² /s ²]
L	Entity of Length	[m]
L_m	Characteristic length in the model	[m]
L_p	Characteristic length in the prototype	[m]
λ	Scale Factor	[-]
M	Entity of Mass	[kg]
μ	Dynamic viscosity	[N s/m ²]
ν	Kinematic viscosity	[m ² /s]
ω	Turbulence frequency	[1/s]
p	Pressure	[N/m ²]
ϕ	Generic scalar quantity	[-]
Q	Volumetric flow rate	[m ³ /s]
R	Hydraulic radius	[m]
Re	Reynolds Number	[-]
Re_r	Prototype-to-model Reynolds number ratio	[-]
ρ	Density	[kg/m ³]

s_{ij}	Tensor of strain rate	[-]
σ	Surface tension	[N/m]
t	Entity of Time	[s]
τ_{ij}	Tensor of stresses	[N/m ²]
τ_w	Wall shear stress	[N/m ²]
$\mathbf{u} = (u, v, w)$	Fluid velocity vector	[m/s]
V	Mean Channel Velocity	[m/s]
We_r	Prototype-to-model Weber number ratio	[-]
We	Weber Number	[-]
$W(r, h)$	Kernel weighting function	[-]
y^+	y plus	[-]
$\nabla = \mathbf{i} \frac{\partial}{\partial x} + \mathbf{j} \frac{\partial}{\partial y} + \mathbf{k} \frac{\partial}{\partial z}$	Vector field divergence	[-]

Abbreviations

ALE	Arbitrary Lagrangian-Eulerian
AOD	Above Ordnance Datum
ARC	Advanced Research Computer
CAD	Computer-Aided Design
CBC	Convection Boundedness Criterion
CFD	Computational Fluid Dynamics
CFL	Courant-Friedrichs-Lewy number
CICSAM	Compressive Interface Capturing Scheme for Arbitrary Meshes
CLSVOF	Coupled Level Set Volume of Fluid
DAS	Donor-Acceptor Scheme
DEFRA	Department for Environment, Food & Rural Affairs
DNS	Direct Numerical Simulation
FCERM	Flood and Coastal Erosion Risk Management
FDM	Finite Difference Method
FEM	Finite Element Method
FVM	Finite Volume Method
HPC	High Performance Computer

Nomenclature

HRIC	High Resolution Interface Capturing
ICOLD	International Commission on Large Dams
ISPH	Incompressible Smoothed Particle Hydrodynamics
LES	Large Eddy Simulation
LS	Level Set
MAC	Marker and Cell
MPS	Moving Particle Semi-implicit
MULES	Multidimensional Universal Limiter with Explicit Solution
NS	Navier-Stokes
NVD	Normalised Variable Diagram
PIC	Particle in Cell
PISO	Pressure Implicit with Splitting of Operators
PKW	Piano Key Weir
PLIC	Piecewise Linear Interface Construction
PMF	Probable Maximum Flow
PVOF	Partial Volume of Fluid
RANS	Reynolds-Averaged Navier-Stokes
SIMPLE	Semi-Implicit Method for Pressure-Linked Equations
SPH	Smoothed Particle Hydrodynamics
VOF	Volume of Fluid
WCSPH	Weakly Compressible Smoothed Particle Hydrodynamics
WC-MPS	Weakly Compressible Moving Particle Semi-implicit
WCD	World Commission on Dams

1. Introduction

1.1. Role and Importance of Hydraulic Structures

The construction of water storage and control structures for human use has been documented since back to the times of the earliest civilisations. Freshwater is an essential need for life, nature, and human development and increasing wealth and technology has been correlated with improvements in the capability to store and direct water (Novak *et al.* 2007). Currently our planet is facing major challenges surrounding water availability and control with less than 2.5% of the water in earth being fresh, of which under 33% is in fluid phase (WCD 2000). Whilst it is estimated that by 2030 the world will require 30 % more of fresh water than is currently used (The Royal Academy of Engineering 2010), it is also predicted that the frequency and severity of extreme flooding events will increase in the future as a consequence of climate change (Bruwier *et al.* 2015; Kvočka *et al.* 2016). The gravity of extreme rainfall events has approximately doubled over parts of the UK since 1960 (Fowler and Kilsby 2003). Due to higher concentrations of greenhouse gases, a general increase in rainfall intensity has been recorded and paired with numerous occurrences of flooding and landslide events in Europe and UK (Osborn and Hulme 2002). Flooding is the natural disaster with highest occurrence (Jonkman 2005) and action needs to be taken rapidly in order to control the danger of such incidents and mitigate the implications of increasing flooding levels. Hydraulic structures like dams, weirs and spillways play a crucial role to the environment and society by providing supply, storage and management of water resources. Flood alleviation schemes of different levels and characteristics are being implemented more often to prevent damage in developed flood-prone areas. In England, the budget allocated to Flood and Coastal Erosion Risk Management (FCERM) has increased significantly over the last decade. This was especially pronounced following the floods in summer 2007 and subsequent increased flooding episodes in winter 2013-14 (DEFRA 2017). Figure 1.1 shows the total government expenditures in FCERM and the total in real terms of present year (2017/18).

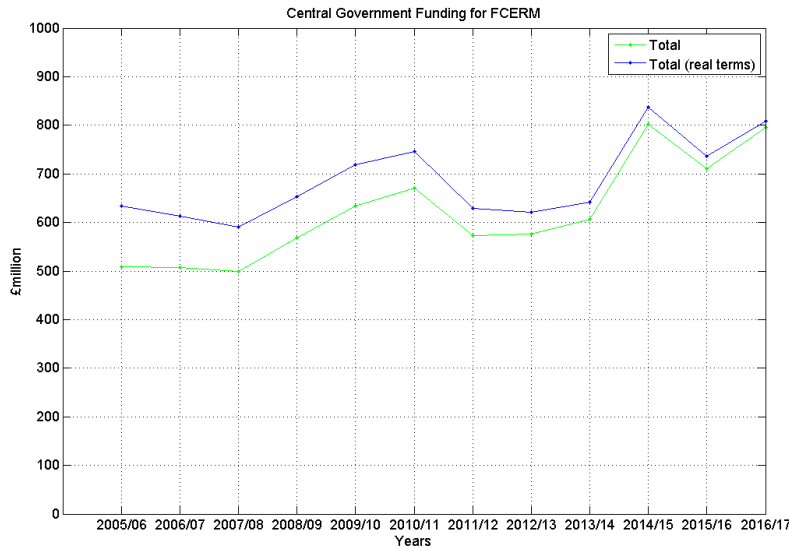


Figure 1.1: Central Government total expenditure in FCERM from DEFRA (2017)

Typical structures employed in flood alleviation schemes often involve dams and weirs. A dam is defined as a structure constructed across a valley to store water in the upstream reservoir (Chanson 2004b). Dams can be broadly classified into concrete and embankment dams. A fundamental component part of a dam is the spillway, which is a structure designed to pass the flood water and must be able to contain the design flood (usually the probable maximum flow). Spillways hence prevent dam overtopping (by waves) or overflowing (by steady flow rates) (Institution of Civil Engineers 2015) which could cause erosion and failure. Often this essential part of the dam is formed by a spillweir to control the flood, and the spillway channel, to conduct flows safely away from the dam (Novak *et al.* 2007). Spillways usually include presence of energy dissipators in order to release the kinetic energy which could erode the toe of the dam. There are several types of spillways and they can be classified according to their function, distinctive feature or control structure. A general layout of a spillway and dam structures are shown on Figure 1.2.

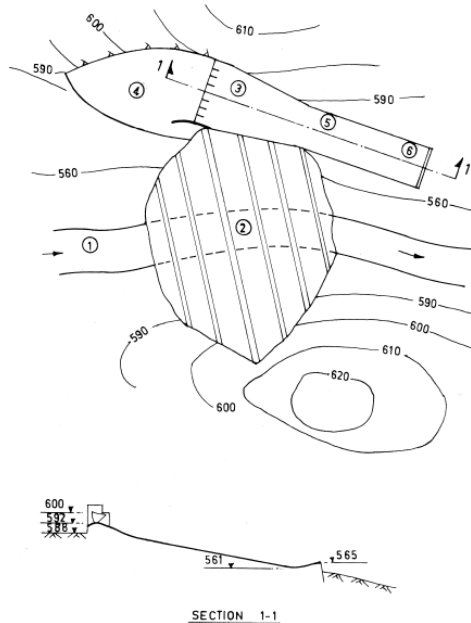


Figure 1.2: Example layout of a chute spillway from Khatsuria (2005) . Where (1) is the river, (2) is the earth dam, (3) is the spillway, (4) is the approach channel, (5) is the chute and (6) is the flip bucket

Weirs are structures built to regulate the upstream water level and discharge. There are many types of weirs and usually they also involve the presence of energy dissipators at the downstream side. Figure 1.3 shows a sketch of a weir with its main elements. In most cases there are only small differences between a small dam and a weir and frequently the two terms are interchanged. The water flow over a weir is usually defined as the nappe.

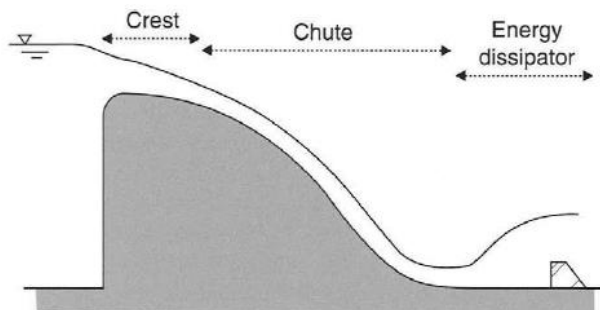


Figure 1.3: Diagram of a weir with main elements from Chanson (2004b)

1.2. Reservoir Failures and Refurbishment Works

The refurbishment of existing ageing hydraulic structures is of particular importance at the present time. In the UK serious reservoir failure incidents are still occurring regularly. According to Chesterton and Warren (2016) not all reservoir failure incidents that have occurred in the past decades have been communicated publicly. However, given the seriousness of these events, recent changes in the legislation (Reservoirs Act 1975) made their reporting currently mandatory. There were a total of 99 reported reservoir failure incidents between 2004 and 2015 (Environment Agency 2016) and the mechanism of deterioration with highest occurrence was erosion by flood overtopping with 29 cases, as shown on Table 1.1. Most cases of flood overtopping occurred in small dams following intense rainfall episodes.

Chapter 1. Introduction

Table 1.1: Mechanism of deterioration of the 99 reservoir incidents between 2004 and 2015. Source: Environment Agency (2016)

Mechanism of deterioration	Total
Damage to safety critical structures	5
Deterioration of upstream protection	3
Erosion by flood overtopping	29
Erosion from localised run-off	1
Fill deterioration	3
Foundation deterioration	2
Gates deterioration	2
Hydraulic fracture relating to internal erosion	1
Increased hydraulic loading	2
Internal erosion – adjacent to appurtenant works	9
Internal erosion – other	20
Pipework/culvert deterioration	5
Pore water pressure increase mass movement	2
Settlement/deformation	2
Structures deterioration	2
Valve deterioration	1
Wind damage – trees	1
Other	4
Not known	5

Among the reservoir failure incidents reported from 2004 and 2015, investigations were conducted and the reasons for failure in 34 cases were attributed to “inadequate performance due to original design and/or construction of a structure or through changes in loading (structural or hydraulic)”. The second cause, responsible for 24 failures was described as the “inadequate performance due to deterioration of a design element by erosion, weather, corrosion or poor management”. Therefore, the evidence shows the principal cause of dam failure is the underestimation of flood conditions which could be explained by the increasing severity of rainfall events in the recent decades as well as by inaccuracies in the design process. Measures to ensure reservoir safety were issued by Inspecting Engineers under Section 10 of the Reservoirs Act 1975 (Chesterton and Warren 2016). Based on 3,155 recommendations made in a total of 1,104 reports, the most common category of recommendation was Research, investigations and studies, which encompasses reservoir flood study as well as hydraulic analysis and modelling as main areas of importance. Measures to improve the intrinsic condition of the reservoir were the second most common recommendation and include the improvement of the spillway capacity as main subject area. Table 1.2 shows the most frequent recommendations which were advised in over 30 cases. Next to each recommendation there is the number of cases where this measure was considered appropriate and the top 3 recommendations appear underlined.

Table 1.2: Significant areas of concern to Inspecting Engineers at statutory reservoirs. Source: Chesterton and Warren (2016)

Type of measure	Significant subject areas
Research, investigations and studies	<ul style="list-style-type: none"> • <u>Reservoir flood study (203)</u> • <u>Hydraulic analysis/modelling (151)</u> • Topographic survey (123) • Stability analysis (81) • Seepage investigation (60) • Condition survey- internal structures (57) • Condition survey – CCTV (45) • Material investigation of dam fill material (43) • Condition survey – other (33) • Condition survey – surface structures (32)
Measures to improve the intrinsic condition	<ul style="list-style-type: none"> • <u>Spillway capacity improvement (213)</u> • Crest levelling (69)

	<ul style="list-style-type: none"> • Crest raising (57) • Erosion protection to the dam crest and/or downstream face (54) • Drainage improvements (49) • Other (46) • Grouting/sealing (except of dam core) (37)
Measures to address deterioration	<ul style="list-style-type: none"> • Spillway – minor repairs (117) • Gates/valves (100) • Spillway – major repairs (72) • Repairs to the dam upstream face (67) • Repairs to the downstream face (except due to internal erosion) (49) • Dam crest repair (except due to overtopping) (30)
Reservoir operation	<ul style="list-style-type: none"> • Vegetation (except grass cutting) (148) • Clear/prevent blockage/debris (102) • Water level control (46) • Access/fencing (35)
Monitoring and surveillance	<ul style="list-style-type: none"> • Reservoir records/documentation (66) • Seepage monitoring (except toe drain monitoring) (42) • Reservoir water level monitoring (32)
Risk assessment and emergency planning	<ul style="list-style-type: none"> • Emergency drawdown planning (53) • Emergency action planning (50)

The three most recommended measures are the improvement of the spillway capacity, followed by reservoir flood studies and hydraulic analysis and modelling. The first measure recommended is intrinsically linked to the second and the third; in order to improve the spillway capacity of a scheme, more accurate information on current reservoir flood levels are required, as well as hydraulic modelling for the design of the new structure. For this reason, once faithful documentation on flood levels is gathered, the design process relies on hydraulic models being able to reproduce the flow situation accurately to accomplish a design ensuring reservoir safety. A refined understanding of the currently available modelling techniques is needed in order to inform on their capabilities and limitations. In addition, new documentation informing best practice for the implementation of such modelling methodologies would constitute a valuable resource for engineers and practitioners.

1.3. Hydraulic Modelling Methodologies

1.3.1. Physical Modelling

The design of water storage structures requires appropriate hydrology conditions in the proposed area as well as the availability of hydrological studies (Chanson 2004b). The layout of hydraulic structures is decided based on the structure function and interaction with the water flow (Jeffrey et al., 2010). This includes hydraulic, structural and geotechnical studies. Therefore, a comprehensive understanding of the hydraulic processes that can occur and the ranges of flow conditions that will be present need to be considered. The process of structure design is generally iterative based on established design procedures and complemented with model studies (Tullis et al. 1995). Initially, simplified models are used to identify the most suitable type of model for the project. Then the models are refined, and results and assumptions are assessed. This process is followed for the design of new structures as well as for the assessment of existing ones (ICOLD 2013).

Free surface flows are defined as those occurring in an open channel or in a close conduit which have the presence of a free surface (Chaudhry 1993). Hydraulic modelling of free surface flows

Chapter 1. Introduction

is essential for the representation of processes that cannot be expressed by theoretical calculations. Quantification of the main forces acting on the structure in static conditions can be obtained with relatively simple calculations. However, the distribution of the pressure field with changing flow conditions as it occurs with transient flow problems, is complex and consequently challenging to determine. Typically, the hydraulic analysis approach to address this would consist in the construction of a scaled physical hydraulic model. Physical models allow the representation of the flow situation in the laboratory (Chanson 2004a) by complying with certain similarity. Generally, these are constructed based on dimensional analysis, but because when using the same fluid it is physically not possible to have equal force ratios of all forces in the prototype and model, only the most relevant force ratio is matched. If the forces which are not matched are not negligible in the physical model, scale effects occur. Scale effects are distortions due to other force ratios having significant deviations in the model and prototype (Chanson 2008). It is complex to evaluate the scale effects at all locations within a physical model and hence to determine whether their impact can be considered negligible. Scale effects in physical hydraulic models are a very relevant issue since they can result in structure failure. A particularly remarkable example of incorrect scaling consists in the catastrophic failure of the Sines breakwater in Portugal in 1978, which has been investigated in several studies, such as Baird *et al.* (1980), Burcharth (1987) or Maddrell (2005). Failure occurred as a result of extreme wave action in a storm just before construction of the scheme was completed. The studies conclude that the reasons for the failure could be attributed to a number of possible design deficiencies, as well as a combination of them. One of these included the underestimation of the structural loads due to erroneous scaling (Heller 2011). A Froude similarity physical model was utilised to model this fluid structure interaction problem and the stiffness of the structure was overestimated. Scale effects have been investigated in a multitude of studies, some examples include Erpicum *et al.* (2016) and Heller *et al.* (2007). However, it is still challenging to determine the scale effects that exist in a specific physical model and it is even more complicated to quantify the errors which these introduce in the structure design.

A particularly prominent example of a physical model for the design of spillways, and especially for refurbishment works, is the case of the Oroville dam in California, which is the tallest dam in the United States. The Oroville dam suffered spillway failure and subsequent erosion of the dam in February 2017. Researchers and engineers in the University of Utah State constructed a 1:50 scale physical model of both the failed and the newly designed spillway. The Probable Maximum Flow (PMF) of the scheme is 7843.8 m³/s. According to UPR Utah State University (2017) the refurbishment operations were based on the outcomes of such physical hydraulic models. Figure 1.4 shows an aerial picture of the failed spillway and its corresponding physical model.

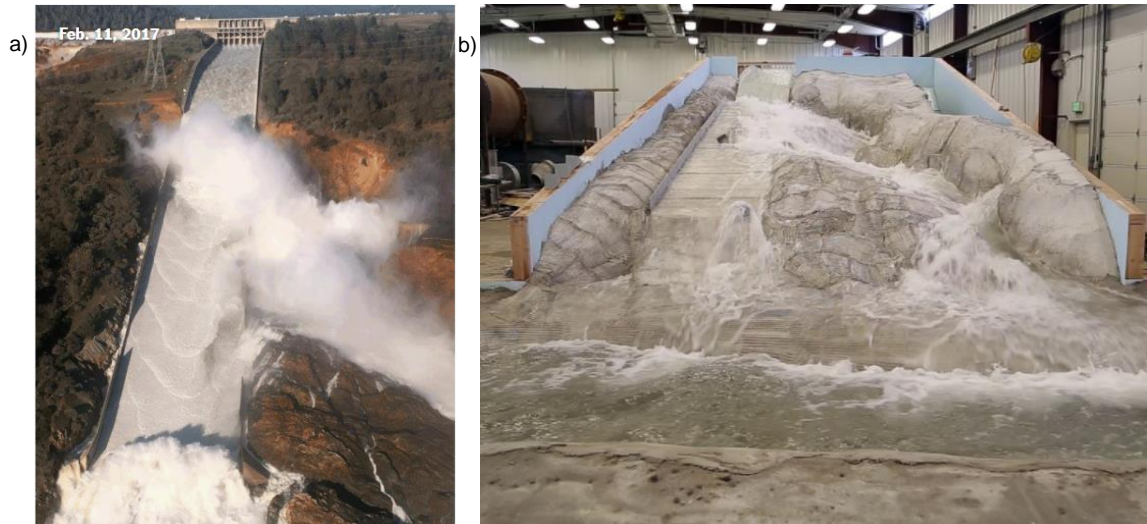


Figure 1.4: a) Oroville dam failure from New York Times (2017); b) scaled physical model of the damaged dam built at the Utah Water Research Laboratory for repairing work from Utah State University (2017)

1.3.2. Numerical Modelling

Over the recent decades the hydraulic modelling community has experienced a growing interest in the application of three-dimensional (3D) Computational Fluid Dynamics (CFD) models to simulate hydraulic free surface flows to aid structure design. CFD models have been common practice for over 50 years in other engineering fields, including the aerospace or automotive industries (Dhaubhadel 1996; Fujii 2005; Versteeg and Malalasekera 1995; Witherden and Jameson 2017). These models have progressively become more accessible and especially, advancements in computer processing power made possible their feasibility for large scale applications. Such advances also enabled substantial improvements and several numerical approaches to model complex hydraulic free surface flows have been developed. CFD consists in the analysis of fluid processes by the utilisation of computers to solve the equations that govern the fluid phenomena at numerous points of the domain and as a result, predict the fluid behaviour. Results from numerical models are able to provide highly detailed information about the field quantities, including their mapping across the entire modelling domain. In addition, with numerical models it is possible to simulate the flow conditions as they occur at the real prototype scale. CFD methods to model free surface flows can be broadly divided into three main frameworks: Eulerian, Lagrangian and Arbitrary Eulerian-Lagrangian. Eulerian methods provide analysis of the flow phenomena by using fixed elements and registering changes in the flow fields within each fixed element, which typically consists in a cell of a mesh. In the Lagrangian framework, the elements store the field quantities and move with the flow. The Arbitrary Eulerian-Lagrangian framework consists in a combination of the two, with the implementation of a Lagrangian method where there are small deformations and an Eulerian description where the deformations are large. One of the most well-known Eulerian approaches to model free surface flows is the Volume of Fluid (VOF) which was proposed by Hirt and Nichols (1981). The VOF employs a volume fraction function to differentiate between the two phases (water and air) and utilises an additional algorithm to track the position of the free surface within a cell. Lagrangian particle-based methods are recently emerging as powerful approaches to model free surface flows, with the main advantage of being

mesh-free. The most well-established Lagrangian particle-based method is the Smoothed Particle Hydrodynamics (SPH) technique. This method was initially developed to model astrophysics phenomena and it has sparked a growing interest for the modelling of free surface processes, especially fluid-structure interaction, marine structures or sloshing. CFD models have been implemented in the aerospace industry since the 1960s (Versteeg and Malalasekera 1995), and therefore they have a strong potential to become a robust tool to aid design of complex hydraulic structures. However, at the present time, the available CFD techniques have been validated in limited number of geometries and flow conditions (Chanson 2009b). Consequently, there is the need to demonstrate their reliability through extensive validation using experimental measurements (Tabbara *et al.* 2005). The development of a range of validated numerical models that reproduce complex flows over hydraulic structures is seen as a necessary evidence base for industry professionals to gain confidence in the numerical approaches. In addition, there are several phenomena which at the present day are still poorly understood, and hence no standard equations to reproduce them have been established. A well-known example of such process is air entrainment. It should also be noted that measurements and observations from physical models provide essential experimental datasets to gain understanding of complex phenomena. These are therefore crucial to generate and validate numerical models. For this reason, physical models are expected to continue to be of significant importance for coming decades (Van Os *et al.* 2004).

1.3.3. Composite Modelling

Both physical and numerical approaches present strengths and limitations. A recently proposed modelling approach consists in the combination of physical and numerical studies to obtain improved predictions of complex flow situations by merging the strength of the two methodologies to minimise the limitations. This technique has been referred to as “composite modelling” or also “hybrid modelling” and is currently an area of research. This approach has been considered in a number of studies as the potential future method for the prediction of complex flow situations (Chanson 2009b; Savage *et al.* 2016). Composite modelling has been implemented in a number of research and industry projects, for example Erpicum *et al.* (2015), Thompson *et al.* (2016), Frostick *et al.* (2011). There is currently no established methodology for the application of composite modelling. Given the promising potential of this technique, further investigation on the procedure of its implementation is clearly a matter which needs to be addressed.

1.4. Hydraulic Modelling of Labyrinth Weirs

The need to rehabilitate many ageing spillways worldwide due to dam safety issues caused an intensified interest in the implementation of labyrinth weirs over the recent decades (Khanh 2013). In the last decade it is calculated that more than 25 labyrinth weirs have been commissioned or are currently being constructed over the world (Erpicum *et al.* 2017b). Labyrinth weirs have been implemented for over 5 decades (Savage *et al.* 2016) and the recent reintroduction and global interest they triggered have mainly been caused by the increases in the frequency of extreme

flooding events and the consequent need for high-performing reliable structures (Ercicum *et al.* 2013a; Ribeiro *et al.* 2013).

These structures consist of folded weirs in plan view which makes them able to discharge larger flows with low upstream head and allow a greater storage without compromising the safety of the dam (Tullis *et al.* 1995). For this reason they offer an alternative to traditional linear weirs in cases where weir refurbishment works are needed due to increased discharges (Savage *et al.* 2004; Lopes *et al.* 2006). The labyrinth geometry generates complex fully three-dimensional flow structures which are challenging to predict using analytical approaches (Crookston *et al.* 2012).

There are different types of labyrinth weir configurations, the general classes are triangular, trapezoidal and rectangular. Figure 1.5 a) shows the geometry of these three categories. Figure 1.5 b) shows the main geometric parameters of a labyrinth weir.

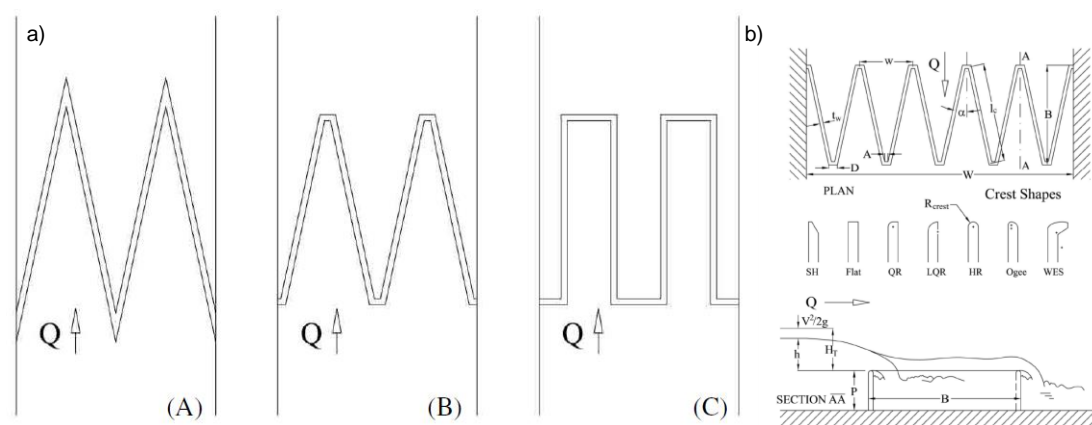


Figure 1.5: a) General classifications of labyrinth weirs: (A) triangular, (B) trapezoidal and (C) rectangular; b) Typical labyrinth weir with geometric parameters from Crookston (2010)

Several experimental studies to investigate the performance and design criteria of these structures are available in the literature, for example Tullis *et al.* (2007), Crookston (2010), Crookston and Tullis (2012a), and Crookston and Tullis (2012b). The design and research of labyrinth weirs has been mainly based on theoretical analyses and scaled physical hydraulic models. Currently, the standard hydraulic modelling approach for design of labyrinth weirs are physical hydraulic models (Tullis *et al.* 2018). In contrast with other hydraulic structures, scale effects in labyrinth weirs have been investigated in a very reduced number of occasions. The most prominent examples include Tullis *et al.* (2017) and Tullis (2018). Therefore, new research providing novel guidance on scale effects of such non-linear weirs would be remarkably valuable for designers and engineers.

Numerical modelling of labyrinth weirs has been conducted in several studies. Some available examples are Savage *et al.* (2004), Paxson and Savage (2006), Crookston *et al.* (2012), Ebner *et al.* (2016) and Savage *et al.* (2016). In most cases, the CFD simulations were performed to predict the coefficient of discharge of the weir and rating curve. Generally, both physical and numerical modelling studies have not focussed on the complex 3D pattern of cross-waves downstream the weir, especially in a full weir length. Consequently, the effects of such complex flows to the spillway channel downstream of labyrinth weirs have received little attention.

1.5. Aim and Objectives

The aim of this research is to assess the capabilities of the CFD VOF method to characterise the complex hydraulic free surface flows over and downstream of a labyrinth weir and utilise the numerical predictions to investigate the scale effects induced in a physical model.

This research is conducted in the context of the hydraulic free surface flows generated by a labyrinth weir and over a spillway which form part of a recently developed flood alleviation scheme in the town of Skipton, UK. To accomplish the research aim, the work presented in this thesis employs numerical and physical modelling techniques. Physical model measurements from a 1:25 scale Froude similarity physical model commissioned for the design of the scheme, are utilised to validate the numerical predictions. As part of this research, the VOF is initially tested together with the particle-based method SPH to reproduce a simplified experimental case with availability of measurement data from the literature.

The research aim is formed by the following objectives:

1. Investigate the capabilities of two leading CFD techniques: the VOF and the SPH to model an experimental dam break flow over an obstacle. This consists of an initial modelling test for a relatively simple geometry utilising high quality data from the literature for validation. This involves:
 - i. The creation of the geometry, mesh and modelling domain for the simulation of the dam break case.
 - ii. Conducting simulations using the CFD 2D and 3D VOF method in two solvers: ANSYS Fluent and OpenFOAM.
 - iii. Conducting simulations implementing the 2D and 3D SPH techniques in DualSPHysics.
 - iv. Undertaking sensitivity analyses in respect of various implementations in the two modelling techniques.

2. Conduct 3D VOF simulations of the free surface flow over the physical model of the labyrinth weir and spillway of study in order to assess the model performance in the prediction of various flow aspects (weir rating curve, depths, velocities and waves' features, interaction of spillway flow with tail water) using physical model measurements. This includes:
 - i. The creation of a robust workflow to extract the needed domain geometries from construction site 3D CAD drawings and build appropriate modelling domains and meshes.
 - ii. Undertaking 3D VOF simulations of several flow rates at physical model scale on ANSYS Fluent and OpenFOAM and assessing the performance of the two CFD solvers to reproduce the various flow aspects.
 - iii. Conducting sensitivity analyses in respect of cell size, turbulence model and interface capturing scheme to verify the impact of these implementations to the numerical predictions and inform best practice.

3. Conduct 3D VOF simulations of the free surface flow over the prototype scale labyrinth weir and spillway and examine the discrepancies between model scale and prototype scale predictions in different flow aspects. This is accomplished by:
 - i. Undertaking simulations at prototype scale of the previously modelled cases at physical model scale.
 - ii. Comparing simulation predictions at the two scales and recognising presence of scale effects.
 - iii. Identifying correlations between the discrepancies at the two scales and the size of the flow rate.

4. Investigate the identified scale effects in the different flow aspects simulated and estimate limiting criteria to minimise these. Compare the derived limits with available literature limits. This encompasses the following tasks:
 - i. Simulate the PMF flow rate at scales 1:10 and 1:50 in the spillway channel modelling domain to investigate changes in waves' features at the different scales.
 - ii. Examine the variations in depths and velocities along the spillway channel for the different flow rates and scales and derive a Reynolds number for which the scale effects are negligible.
 - iii. Derive the minimum head upstream the weir crest for which the labyrinth weir rating curve can be derived with a physical model with no scale effects.

1.6. Structure of this Thesis

Chapter 2: Review of Hydraulic Modelling Methodologies

In this chapter, the currently utilised methodologies for hydraulic modelling of free surface flows are described in detail. This is followed by the review of the most prominent studies that have been undertaken relevant to the aim of this research. Labyrinth weir modelling investigations with both physical and numerical modelling techniques available in the literature are examined. Furthermore, studies which employ physical modelling techniques to derive limits for scale effects are reviewed. The very limited number of studies which apply numerical approaches to determine scale effects in physical hydraulic modelling are also scrutinised. This chapter highlights the scarcity of research conducted on the modelling of the complex free surface flows downstream labyrinth weirs with physical modelling techniques but, in particular, with numerical methods. The limited attention which has been given to scale effects induced in physical modelling of labyrinth weirs is also emphasised.

Chapter 3: Computational Fluid Dynamics Modelling

This chapter deals with the description of the main principles of CFD and especially with the formulations applied to hydraulic free surface flows. The governing equations are characterised and the various discretisation schemes, turbulence models and solution methods available are outlined. The description of the various numerical aspects has special focus on the numerical

Chapter 1. Introduction

implementations utilised in this thesis. This chapter also describes the different meshing strategies as well as the error and uncertainty in CFD simulations.

Chapter 4: Numerical Modelling Approaches: Description and Implementation

In this chapter, two leading numerical techniques previously outlined in Chapter 2 are described in more detail and their capability to reproduce an experimental dam break case over a triangular obstacle is evaluated. The numerical approaches are the Eulerian VOF, which is the principal method utilised in this thesis, and the Lagrangian SPH technique, which is one of the most relevant particle-based meshless approaches utilised to reproduce free surface flows at the present time. Detailed experimental measurements of the dam break case are obtained from the literature and are utilised to validate the results predicted with the two techniques. The relatively simple geometry of this experimental case enables the modelling of 2D and 3D cases and the testing of various numerical implementations in the two techniques. The initial assessment of the VOF is essential for its subsequent application in the following chapters. Conclusions from this study will inform the decisions on numerical implementations for the modelling of a significantly more complex experimental case in Chapter 6. The evaluation of the SPH for this simple case will reveal the main capabilities and limitations of this technique for its future application in hydraulic structure modelling studies.

Chapter 5: Case Study: The Eller Beck Labyrinth Weir and Spillway

This chapter describes the case study in which this research focuses as well as the physical model commissioned for the design of the hydraulic structures. The case study is a flood storage reservoir built to alleviate floods in the town of Skipton. The scheme consists of an embankment dam, a labyrinth weir and a spillway. In this chapter, the 1:25 scale Froude similarity physical model constructed to undertake hydraulic modelling is also characterised. The different scenarios modelled, the data available from physical model measurements and instrumentation utilised are detailed.

Chapter 6: VOF Modelling of the Labyrinth Weir and Spillway

This chapter comprises the application of the 3D VOF method, previously tested on Chapter 4, to model the complex flow over the physical model of the labyrinth weir and spillway, described on Chapter 5. In order to accomplish this, the modelling domains and meshes are produced for the modelling of several flow aspects including: flow within the spillway channel, labyrinth weir rating curve and interaction of spillway flow with tail water. To model such aspects with accuracy, three modelling domains are extracted and a workflow methodology to extract and mesh the domains is described. The VOF method is implemented in the commercial package ANSYS Fluent and the open source code OpenFOAM for a series of flow rates, and performance of the two solvers is compared. The numerical predictions are assessed against experimental measurements. Sensitivity analyses in respect of cell size, turbulence model and interface capturing scheme are conducted to investigate the most appropriate implementations of the models for this case.

Chapter 7: Comparison of Prototype and Physical Model Predictions

The ability of numerical modelling techniques to reproduce phenomena at both physical model and prototype scales, enables their implementation for the investigation of scale effects. Based on this novel conceptualisation, this chapter concerns the modelling of prototype scale flows. This is undertaken once the capability of the VOF to reproduce hydraulic flows over the experimental labyrinth weir has been confirmed in Chapter 6. Prototype scale simulation predictions of the various flow aspects are compared to predictions at physical model scale. The differences in the predictions of several flow aspects at the two scales are analysed. Relationships between the size of the flow rate and discrepancies between predictions at the two scales are investigated and discussed.

Chapter 8: Investigation of Scale Effects and Estimation of Limiting Criteria

In this chapter the discrepancies at model and prototype scale identified in Chapter 7 are further investigated. Limits to minimise the observed scale effects in two principal flow aspects are estimated. A minimum Reynolds number is derived to mitigate scale effects in the spillway channel flows and a minimum upstream head over the labyrinth weir crest is estimated to ensure negligible scale effects in the prediction of the labyrinth weir rating curve. Such limits are then compared with the available values derived in the literature by experimental means. Additionally, the changes in the waves' positions occurring at various simulation scales are also examined.

Chapter 9: Conclusions and Further Work

This chapter presents a summary of the research work conducted in this thesis. The conclusions drawn in each chapter are summarised and related with the research objectives. The main implications of this research are discussed and recommended means to further develop the work conducted are also suggested.

2. Review of Hydraulic Modelling Methodologies

2.1. Introduction

This chapter presents a review of the main techniques employed for hydraulic modelling, namely physical, numerical and composite modelling. The principles of the techniques are described as well as their strengths and limitations. In the last part of each subsection, the most prominent studies where the outlined techniques are utilised for labyrinth weir research and scale effects investigations are reviewed.

2.2. Physical Modelling

2.2.1. Background

Physical hydraulic models are scaled representations of a hydraulic flow system where the major forces, boundary conditions and geometry are scaled appropriately to predict the behaviour a real flow situation. Physical modelling is a well-established modelling technique since it has been used for over 200 years (Ettema *et al.* 2000) (Hughes 1993). As such, physical models have for long been the conventional means to evaluate hydraulic designs in a broad range of hydraulic engineering problems. An interesting summary of historical milestones in hydraulic modelling is found in Hughes (1993) where it is documented that the first models for real applications were used by Smeaton in 1752 who employed scale models for water wheel experiments. The dimensional analysis was derived for the first time in 1920, and in 1947 the Hydraulic Research Station was founded in England.

The scale factor of a physical model, usually denoted as λ , is defined as the constant correlation proportions of parameters between the physical model and the prototype (Yalin 1989). Physical models are employed to reveal the insight of a complex physical process which has little description and understanding. Therefore, they are used as part of the scheme design process to include modifications and confirm the safety of the structure. Physical models are operated in hydraulic laboratories with fully controlled conditions which allow the simulation of a range of scenarios as needed by the user (Chanson 2004b). Data collection process in a physical model is conducted at reduced cost compared to field measurements, which are significantly more challenging to conduct and quantify. In recent years, instrumentation has developed, and physical models allow the simulation and recording of complicated flow situations with higher degree of sophistication. As such, they permit the modelling of complex processes which are poorly understood in controlled conditions and enable their investigation (Frostick *et al.* 2011). Physical models have the advantage of providing the visual outcomes readily available for an immediate understanding of the physical phenomena. Some authors also argue that the recent increase in popularity of numerical models will fuel the development of further physical model studies and experimental measurement techniques, since in order to describe the physical processes mathematically, it is necessary to gain in-depth knowledge and fully understand the laws of the fluid flows (Hughes 1993).

One of the main limitations of physical models are their associated scale effects, which are the discrepancies between the model and the prototype arising from the differences in several force ratios in the prototype and model. In addition, measurement effects (Heller 2011) are also a source of disagreement between measurements in the model and in the prototype, generated by the use of different sampling methodologies for data collection in the two cases. Other drawbacks of a physical scale model are the space restrictions, as well as not being able to include all items which will affect the hydraulic flow in the prototype, for example wind shear stresses acting on the free surface.

A physical model will produce reliable results only if is appropriately designed and built. A small scale representation of a physical process constitutes a correct approximation of the real process if the two are related to each other by a constant proportion, referred to as “scale” which complies with certain conditions which are the similarities (Yalin 1989). Scaling laws and different similitudes in hydraulic physical models have been described in numerous occasions, for example Hugues (1993), Ettema *et al.* (2000), and Heller *et al.* (2007).

2.2.2. Concepts of Model to Prototype Similitude

Similitude or scaling law are the formal conditions which must be satisfied by the scale between the prototype and the model in order to achieve similarity. These can be of several classes and are listed below.

2.2.2.1. Similitude by Inspectional Analysis

This approach consists in the utilisation of the equations describing the relevant forces of the physical phenomena in the prototype and in the model (Ettema *et al.* 2000) and hence requires the prototype and model to be described by strictly the same equations, for example Navier-Stokes. These governing equations are expressed in a non-dimensional form. The physical model will then be operated for specific boundary conditions. This method allows the determination of a minimum scale factor in order to avoid significant scale effects (Heller 2011).

2.2.2.2. Similitude by Calibration

This methodology is the oldest applied and can be achieved only if comprehensive information of the process in the prototype is available. It is accomplished by modifying the model in a trial and error exercise until the outcomes confirm an accurate representation of the behaviour in the prototype. Generally if there is strong agreement between the parameters in the prototype and in the model, minor scale effects are anticipated (Heller 2011). This method would be the appropriate to model a complex phenomenon with a large number of variables which would make the dimensional analysis method (described in 2.2.2.4) unviable (Hughes 1993).

2.2.2.3. Similitude by Scale Series

The scale series methodology consists in the construction of a minimum of three models at a different scales each to simulate the same process. The largest available scale is utilised as a

reference and the comparisons between the results from different models are conducted. This method is therefore capable of quantifying the scale effects, but it requires a significant experimental effort. With this procedure it is possible to derive limiting criteria in order to minimise the scale effects. An excellent example of application of this method can be found in Heller *et al.* (2007) where 7 different models were employed in order to quantify scale effects to determine limiting criteria for the modelled phenomenon.

2.2.2.4. Similitude by Dimensional Analysis

The countless number of fluid flow quantities (velocity, density, force, pressure, etc.) of interest to engineers can be reduced to three entities: length (L), time (T) and mass (M), referred to as *fundamental entities* (Yalin 1989). And hence any measurable physical quantity will be composed of a combination of the fundamental units. For example, given a quantity “*a*” which is function of the fundamental units, the units of the quantity “*a*” will be given by Eq. 2.1.

$$[a] = L^{\alpha} T^{\beta} M^{\gamma} \quad 2.1$$

Yalin (1989) then described that the units of a quantity “*a*” will be determined by the values of the exponents α, β and γ such that “*a*” is a:

- Geometric quantity if $\alpha \neq 0; \beta = 0; \gamma = 0$
- Kinematic quantity if $\alpha \neq 0; \beta \neq 0; \gamma = 0$
- Dynamic quantity if $\alpha \neq 0; \beta \neq 0; \gamma \neq 0$

And if $\alpha = 0; \beta = 0; \gamma = 0$ then the quantity “*a*” is defined as a dimensionless quantity which does not depend on the fundamental dimensions.

Dimensional analysis of a physical phenomenon is the procedure for combining physical variables into dimensionless products and hence reducing the number of variables of the problem (Hughes 1993). The dimensional analysis is based on the π -theorem of Buckingham (1914) which describes the “method of dimensions” which can be explained as follows: In a physical process with “*n*” independent variables q_1, q_2, \dots, q_n , the number of dimensionless parameters π in which it can be reduced is equal to “*n* – *r*” where “*r*” is the number of fundamental dimensions needed to describe the variables. This method is correct only if all the essential variables are included (Novak *et al.* 2010). According to this method, in a homogeneous equation (where dimensions of the terms on the left and right sides of the equality match), the variables can be replaced by the new dimensionless product parameters (or π terms).

In a similitude approach based on dimensional analysis, the dimensionless products in the prototype and in the physical model must be the same. This dictates that a model is completely similar to the prototype if it complies with mechanical similarity, which consists of geometric and dynamic (and hence kinematic) similarities (Heller 2011).

Geometric similarity is based in the similarity of form, which means that the prototype-to-model ratios of all lengths are equal. Geometrical similarity is expressed as per Eq. 2.2.

$$\lambda = \frac{L_p}{L_m} \quad 2.2$$

Where λ is the scale factor or prototype-to-model scale ratio, L_p is the characteristic length in the prototype, and L_m is that in the model. This implies, all lengths in the prototype are λ times larger than in the model, and areas and volumes in the prototype will scale with λ^2 and λ^3 respectively.

Kinematic similarity is the similarity of movement, which implies geometrical similarity in addition to equal rates of prototype-to-model characteristic velocities. This involves equal ratios of velocity, time, discharge and acceleration between prototype and model.

Dynamic similarity entails kinematic similarity in addition to equal ratios of all forces in prototype and model. In order to be able to implement dynamic similarity, the relevant variables for each problem are combined and hence simplified by implementing the π -theorem of dimensional analysis. The most essential variables, defined by Chanson (2004b) can be divided into three categories; The fluid properties and constants: density ρ ($\frac{kg}{m^3}$), dynamic viscosity μ ($\frac{Ns}{m^2}$), surface tension σ ($\frac{N}{m}$), bulk modulus of elasticity E ($\frac{N}{m^2}$), and the gravitational acceleration g ($\frac{m}{s^2}$); the channel geometry, which typically includes the characteristic length L (m); and the flow properties which involve velocity V ($\frac{m}{s}$) and pressure p ($\frac{N}{m^2}$). Applying the dimensional analysis method for these 8 basic variables which correspond to the “ n ” parameter, the 3 fundamental units which are needed to describe the problem (“ r ”) are subtracted, and it is obtained that the number of dimensionless product parameters are 5. These are outlined as per Eq. 2.3 to 2.7.

Froude number:

$$Fr = \frac{V}{(gh)^{\frac{1}{2}}} \quad 2.3$$

Reynolds number

$$Re = \frac{RV}{\nu} \quad 2.4$$

Weber number

$$We = \frac{\rho V^2 h}{\sigma} \quad 2.5$$

Cauchy number

$$Ca = \frac{\rho V^2}{E} \quad 2.6$$

Euler number

$$Eu = \frac{p}{\rho V^2} \quad 2.7$$

Where h is the water depth, R is the hydraulic radius, which is defined as: $R = \frac{y \cdot b}{(b+2y)}$ and ν is the water kinematic viscosity which is defined as $\nu = \frac{\mu}{\rho}$ and in the case of water at 20°C is equal to $1 \times 10^{-6} \text{ m}^2/\text{s}$. The definition of the Reynolds number outlined in equation 2.4 is that utilised for open channel flow (Chow 1959; Scott and Lowe 2003).

Dynamic similarity dictates that the prototype-to-model ratios of the dimensionless force ratios must be equal. However, if the same fluid is used and the scale λ is different to 1, it is impossible to satisfy dynamic (and hence mechanical) similarities. Therefore, the most important

dimensionless parameter for the phenomenon to be modelled is chosen and it must be ensured that the effects due to the forces which are not matched are minimal.

2.2.3. Scale Effects in Hydraulic Physical Models

Scale effects are the discrepancies that arise between model and prototype flows due to force ratios being unequal in the prototype and model. Physical models operate with “approximate” mechanical similarity based on the ratio of forces which are predominant or most relevant in the modelled phenomenon and neglecting the others (Novak *et al.* 2010). Therefore, it must be ensured that the effects of forces which present unequal ratios at prototype and model are negligible. The scale effects increase with increasing scale factor λ (Heller 2011).

The free surface flows occurring in hydraulic structures and open channels are mainly governed by gravity, with resistance of viscous forces and capillarity forces being minimally influent, and hence they can be disregarded. For this reason, the Froude Law of similarity is usually employed. This implies that the dimensionless parameter which will be equal in the model and prototype will be the Froude number, and the scale effects in this case will be induced by differences in viscosity and surface tension forces (if these are not negligible in the model).

The derivation of the Froude number similarity law is obtained by resolving Eq. 2.8

$$Fr_m = Fr_p \quad 2.8$$

Where Fr_m is the Froude number in the model and Fr_p is that in the prototype.

Replacing the geometrical similarity equation outlined in Eq. 2.2, to the Froude law of similarity, the velocity, time, pressure and discharge correlations are obtained as follows:

$$v_p = \sqrt{\lambda} v_m \quad 2.9$$

$$Q_p = \lambda^{\frac{5}{2}} Q_m \quad 2.10$$

$$t_p = \sqrt{\lambda} t_m \quad 2.11$$

$$p_p = \lambda p_m \quad 2.12$$

Eq. 2.9 shows the velocity equivalence, where v_m is the velocity in the model and v_p is the velocity in the prototype. Eq. 2.10 shows the flow rate relationship, where Q_m is the flow rate in the model and Q_p is the flow rate in the prototype. The time equivalence is shown in Eq. 2.11 where t_m is the time in the model and t_p is the real time. Eq. 2.12 shows the pressure equivalence where p_m is the pressure in the model and p_p is that in the prototype.

2.2.3.1. Viscosity and Surface Tension in Froude Models

When Froude number similarity is selected, the Reynolds numbers in the prototype become much larger than those in the model. This implies the turbulence levels in the model are significantly lower, while the viscosity and surface tension effects are overestimated (Chanson 2009a). This causes the predictions of air entrainment in the physical model to be lower than in the prototype

(Pfister and Chanson 2012). As highlighted by Chanson (2004a), when developing the other dimensionless parameters for the Froude similarity, the Reynolds prototype-to-model ratio Re_r takes the expression described in Eq. 2.13.

$$Re_r = \lambda^{\frac{3}{2}} \quad 2.13$$

And the Weber number ratio is shown on Eq. 2.14.

$$We_r = \lambda^2 \quad 2.14$$

As stated above, in phenomena simulated with Froude similarity, the viscosity and surface tension forces which are negligible in the prototype become more important in the physical model where low depths and velocities occur. In order to minimise the effects of such forces in Froude similarity models, some limiting values of either a dimensionless parameter or a hydraulic variable, should be ensured in the model. Heller (2011) provides a comprehensive summary of the “rules of thumb” and limiting values of parameters which should be satisfied to model multitude of phenomena including, inter alia, hydraulic jumps, impulse waves or scour.

2.2.3.2. Air Entrainment

Air entrainment or free surface aeration is described as the process of entrainment of undissolved air bubbles and air pockets which are then carried within the fluid (Chanson 2004a). This process is induced by turbulence occurring at the free surface. In turbulent flows, the air entrainment process may be by local aeration, where entrainment of air pockets is localised, or by interfacial aeration (also referred to as continuous aeration) when it occurs along the water free surface (Chanson 2004a). In hydraulic structures both types of aeration are present. Modelling air entrainment constitutes one of the main challenges of physical hydraulic modelling. The incapability of capturing air entrainment with a physical scale model is one of the main causes of scale effects (Novak *et al.* 2010). Understanding aeration is particularly important since it has the beneficial effect of preventing the existence of negative pressures and hence cavitation (Chanson 1996). As such, aeration devices are usually installed in spillways (Chanson 1989). Flow aeration also generates significant increases of the flow depth, also known as flow bulking, and therefore it needs to be investigated, well understood, and accounted for in structure design (Novak *et al.* 2007).

In Froude number similarity models, the air transport in the physical model is different from that in the prototype because the turbulence is significantly lower in the model (Chanson 2009b) and the surface tension in the model is a considerably more relevant force than in the prototype. Chanson and Murzyn (2008) and Chanson and Chachereau (2013) inspected the scale effects of a hydraulic jump with Froude similarity for various Reynolds numbers (up to 10^5) and it was found that some parameters such as bubble count rate or turbulent properties could not be extrapolated to prototype size without significant scale effects. Therefore, this has important implications in the design of prototype size schemes with high Reynolds numbers where hydraulic jumps are formed. The underestimation of the turbulence and air entrainment levels in physical models may be reduced if limits on the Reynolds and Weber numbers are applied. Pfister and

Chanson (2012) suggested that for the modelling of high speed free surface air-water flows using the Froude similitude with Froude numbers ranging between 5 and 15, it is recommended to apply either Eq 2.15 or 2.16.

$$We^{0.5} > 140 \quad 2.15$$

$$Re > 2 \times 10^5 \text{ to } 3 \times 10^5 \quad 2.16$$

The flow downstream of a weir crest is an important example of aerated flow which has potential of presenting scale effects due to incapability of the model to correctly reproduce the prototype flow process. The difficulty of this situation consists in the differences in the pressure distribution at the weir crest. In the prototype, when the discharge exceeds certain values, the flow separates from the weir downstream wall forming a free jet, whereas in the model, if minimum criteria are not in place, the flow could still be clinging from the structure. This is also referred to as the “teapot effect”. This phenomenon is due to the difference in crest pressure at the prototype and model and causes significant differences in the jet disintegration and air entrainment.

2.2.3.3. Existing Limits for Flow over Weirs

The current limits available in the literature for modelling flows over weirs are grouped in the following paragraphs according to those aimed to preserve the head-discharge relationship, i.e. the weir rating curve, and those to accurately reproduce nappe behaviour.

In order to minimise scale effects in the modelling of the head-discharge relationships with physical models Kobus and Abraham (1980) suggested a minimum upstream head above crest of 0.02 m. In Ettema *et al.* (2000) an upstream head of 0.075 m is recommended for the prediction of the rating curve. For Piano Key Weirs (PKW) Pfister *et al.* (2012) and Leite-Ribeiro *et al.* (2012) implemented a scale effects criterion based on upstream heads above 0.03 m to be considered valid to predict the rating curve. Pfister *et al.* (2013a) also investigated limitations on the head over a cylindrically-crested PKW to limit scale effects on the predictions of the rating curve. In such study, numerical simulations were undertaken to determine minimum upstream head above crest. It concludes a minimum upstream head above crest of 0.03 m should be implemented. Erpicum *et al.* (2013a) provided some guidelines to limit scale effects on PKW based on the analysis of three scaled models of the same structure at three different geometric scales. It was concluded the discharge-head relationship was correctly predicted when upstream water level was higher than 0.03 m. Erpicum *et al.* (2016) derived a required Weber number in order to ensure negligible effect of viscous and surface tension forces of 54 based on the same three physical scale models of a PKW. Crookston and Tullis (2010) suggested a minimum Weber number of 50 for labyrinth weirs. Finally, Tullis *et al.* (2017) conducted a study with three geometrically similar physical models of a single-cycled labyrinth weir at three different scales. It was found that for dimensionless heads (divided by the weir height, P) over 0.3 m results presented negligible scale effects. In Tullis (2018) such analysis was extended and minimum upstream heads for labyrinth weirs of 0.016 m to 0.008 m were derived for half round crests and from 0.007 m to 0.009 m for

quarter round crests. These values were obtained considering 5% error between prototype and model and were found to vary with the scale of the model.

Limiting values of key parameters to ensure the correct behaviour of the model flow downstream of a weir crest have been derived in several studies. Ettema *et al.* (2000) suggests a general minimum upstream head above crest of 0.06 m to correctly reproduce the nappe shape. In order to preserve the nappe behaviour in sharp-edged weirs Novak *et al.* (2010) proposed a minimum upstream head above crest to be between 0.04 and 0.06 m. For PKW, Leite-Ribeiro *et al.* (2012) suggested a minimum head of 0.05 m. Ercicum *et al.* (2013a) concluded the physical model results on nappe behaviour are similar to those in the prototype when the head upstream the weir is higher than 0.06 m. Pfister *et al.* (2013a) also examined this effect for a physical model of a cylindrically crested PKW to a significant extent. The mechanisms of jet disintegration and implications in model jets in comparison to prototype jets are explained in detail in Pfister and Hager (2012).

In addition to adjusting to limiting criteria, a further practice to minimise scale effects consists in replacing the fluid with one of a lower kinematic viscosity. For example Stagonas *et al.* (2011) used a mixture of 90% distilled water and 10% isopropyl alcohol achieving a fluid with a much lower surface tension than water (0.043 N/m as opposed to 0.072 N/m) and observed significant increases in wave energy dissipation and air entrainment. However, modifying the fluid is not always an appropriate or economical solution.

Other alternatives in the effort to mitigate scale effects include the modification of the model set up to introduce as length or roughness distortions such that geometrical similarity is not satisfied but scale effects are compensated instead (Novak *et al.* 2010).

2.2.3.4. Self-similarity

Self-similarity is a concept in mathematical physics which constitutes a powerful approach in the study of complex flows. A phenomenon is defined as *self-similar* if the spatial distributions of its properties at several different instances of time, can be obtained from one another by a similarity transformation (Barenblatt 1996; Pope 2000). Therefore, applying self-similarity it is possible to extrapolate distributions of variables such as velocity by using scale factors which depend on only one of its components, i.e. time or space (Heller 2016).

Many self-similar phenomena can be observed in nature; Mandelbrot (1983) describes the geometry of nature with terms referred to as “fractals” which are irregular shapes with statistical values of regularities and irregularities. Such shapes tend to be perfectly scaling which means their statistical values of regular and irregular features are identical at all scales. Self-similarity is of particularly relevance in the study of complex processes in fluids, such as turbulence. George and Gibson (1992) formulated a theory which demonstrates the possibility that governing equations of turbulent flows have solutions which for given initial conditions, will be self-preserving at all scales of motion.

The self-similar flow characteristics which occur on flows with large Reynolds numbers, justifies the fact that scale effects in Froude number similarity models may be reduced by imposing minimum values of the Weber and Reynolds number. Heller (2016) introduces the concept of *Reynolds invariance* which refers to the fluid conditions which become asymptotic with increasing Reynolds number. The most well-known example of Reynolds invariance is the Moody chart (Moody 1944) where the friction factor becomes Reynolds-invariant for values of Reynolds number higher than those allowing the development of complete turbulence. Heller (2016) explains that Reynolds invariance and self-similarity are two interrelated concepts since the result of their application is a simplified problem with a smaller number of variables. The two concepts appear to be useful to consider Reynolds scale effects negligible given the assumed asymptotic behaviour of turbulent characteristics for Reynolds higher than certain values.

A particularly remarkable example of self-similarity found in open channel free surface flows with high Reynolds numbers consists in the work presented by Chanson and Carosi (2007) and later on extended in Chanson (2008) using an experimental stepped chute. Such studies demonstrate a number of self-similar relationships observed at different scales in the distribution of a number of flow properties, including distributions of void fraction, interfacial velocity and turbulent levels. The relationships found presented scaling symmetry which implies these could be utilised to acquire an approximate initial estimation of the characteristics of the aerated prototype flows.

2.2.4. Review of Relevant Physical Modelling Studies

2.2.4.1. Labyrinth Weir Investigations

As previously discussed, physical hydraulic models are the current means of hydraulic modelling for the research and design of hydraulic infrastructure. In particular, the design of labyrinth weirs has been based on the hydraulic relationships derived experimentally. An interesting historical review on the developments of these structures may be found in Hager *et al.* (2015). Some of the earliest labyrinth weir investigations date back to 1970 in Hay and Taylor (1970) where the fundamental geometric and hydraulic parameters which affect weir performance were analysed. The performance of labyrinth weirs was subsequently assessed in various studies, such as Hinchliff and Houston (1984) and Magalhães and Lorena (1989). A further early study focussing on aeration of triangular labyrinth weirs is Wormleaton and Soufiani (1998) where the aeration performance of triangular labyrinth weirs was compared to that of linear weirs.

Some of the most significant studies regarding labyrinth weir design correlations were derived in Tullis *et al.* (1995) where a design method was obtained. Later on, Falvey (2003) provided comprehensive guidelines on design specifications aimed at practicing engineers. Lopes *et al.* (2006) conducted a detailed analysis where the discharge coefficients derived in various studies were compared and energy dissipation was investigated. Submerged labyrinth weirs were studied in Tullis *et al.* (2007) as well as in Crookston and Tullis (2012c). Other studies like Crookston and Tullis (2013a) revisited the earliest design relationships and presented a refined design and analysis methodology for labyrinth weirs based on a comprehensive experimental study. Staged

labyrinth weirs were analysed in Dabling and Crookston (2012), Dabling *et al.* (2013), Dabling and Tullis (2013) and then in Dabling and Tullis (2017).

Fewer studies have investigated the flow behaviour immediately downstream of the weir. Some of the most remarkable studies consist in Lopes *et al.* (2008) where air entrainment downstream of a labyrinth weir was analysed as well as the energy dissipation. Lopes *et al.* (2011) also focused on the characterisation of the flow patterns induced downstream of a labyrinth weir. Relevant features were examined, including air entrainment and shockwaves. Nappe behaviour was studied in Crookston and Tullis (2013b) which also included an analysis from the perspective of aeration and vibration and presented potential options on crest design which are directly linked to it. An additional study consist in Mohammadzadeh-Habili *et al.* (2017) where energy dissipation in a labyrinth weir was analysed and found to be approximately equivalent to the maximum possible value.

The literature shows generally all studies focus on the labyrinth weir properties at the crest and on the geometric and hydraulic parameters. There is overall little consideration for the flow downstream the weir, with a significantly reduced number of studies available.

2.2.4.2. Scale Effects in Labyrinth Weirs

Experimental studies dealing with the investigation of scale effects in weirs, and in particular in non-linear weirs have been reviewed in section 2.2.3.3. There is significantly less availability of limiting criteria to minimise scale effects in the physical modelling of non-linear weirs compared to linear weirs. Specifically in the case of labyrinth weirs, little guidance can be found in the literature. As previously noted, some of the most relevant limiting criteria to mitigate scale effects in the physical modelling of labyrinth weirs have been derived in Tullis *et al.* (2017) and Tullis *et al.* (2018). Further specifications are suggested in Crookston and Tullis (2010).

2.3. Numerical Modelling of Hydraulic Structures

2.3.1. Historical Background of Numerical Simulations

Numerical modelling of physical phenomena started developing on the 20th century. According to Roache (1998), in 1910 L. F. Richardson wrote the first well documented approach to define the bases of numerically solving partial differential equations. In such work, relevant aspects of numerical analysis were defined such as classification of time-dependent or independent problems, setting of different boundary conditions, and also estimating errors and obtaining exact solutions at “zero grid size” mesh. The definition of discretisation error by Richardson is described in more detail and applied in Chapter 6.9.1 of this thesis. Later on, in 1918 Liebmann improved the iteration and convergence of the method proposed by Richardson. In 1928 the well-known work from Courant, Friedrichs and Lewy to ensure convergence and stability of the discretised partial differential equations was published in Courant *et al.* (1928). In 1950 the work conducted for several years in Los Alamos Scientific Laboratory was published in Charney *et al.* (1950). This study comprised the first large scale numerical calculation for weather forecast. From this point in history, the interest in the potential of CFD increased significantly, particularly in the United

States and France. In 1960 the main principles of fluid dynamics, including the constitutive equations had been derived and were already well established. In the 1960's Los Alamos group started developing Lagrangian particle-based methods with the aim to reproduce shock phenomena, compiled in Fromm (1961). It was also in that decade when CFD started to be included in the design and research processes for the aerospace industry, which also coincided with the appearance of supercomputers. CFD was then further refined, and more complex discretisation schemes were proposed. Advances were mainly dependent on the development of algorithms to solve the governing equations and on the available processing power. Roache (1998) defines the start of the modern turbulence modelling time with the proposal of the bases of the model which later became the present day $k - \epsilon$ model, published for the first time on 1968 in Harlow and Nakayama (1968). In the late 1960's and 1970's CFD started to appear on text books. One of the earliest books detailing the application of CFD to model hydraulic flows is Vreugdenhil (1989). In the 1990's CFD techniques made appearance in a wider span of industries including turbomachinery, chemical, marine and environmental fields, among others.

2.3.2. Overview of Numerical Methods for Free Surface Flows

The free surface flows over hydraulic structures are multiphasic, three dimensional and highly turbulent. Given the complexity of such flows both from a numerical and physical perspective, numerous numerical approaches have been proposed to reproduce them. However, currently no standard method has been established (van Wachem and Almstedt 2003). In contrast with many other disciplines, currently in hydraulic infrastructure design, numerical methods are not the standard practice. However, at the present time, numerical approaches are progressively being implemented in more instances as complementary tool to physical models (Jeffrey *et al.* 2010).

Modelling free surface flows using CFD embraces several engineering fields, including hydraulics, mathematics and computer science (Yeoh and Tu 2010). The main complexity is caused by the presence of a distinct interface which requires special methods to locate its position and define its movement. Therefore, when attempting to reproduce these flows, it is necessary to select the appropriate numeric schemes to solve the complicated equations which describe them whilst achieving a suitable balance between accuracy and computational cost (Magoules 2011). The numerical approaches to reproduce free surface flows can be divided into three main frameworks, these are Eulerian, Lagrangian and Arbitrary Lagrangian Eulerian (Soulaimani and Saad 1998). Moreover, the interface modelling can be subdivided into front tracking and front capturing (Maitre 2006). The front tracking technique was first developed by Unverdi and Tryggvason (1992) where the free surface is tracked by a mesh that changes with the interface movement in a Lagrangian manner. In contrast, the front capturing methods simulate the interface by means of a specific function which is defined within a fixed mesh covering the whole domain. A detailed description of the interface tracking and capturing techniques may be found in Tezduyar (2004). Each of the different frameworks has strengths and drawbacks, consequently, the most appropriate approach needs to be chosen according to the nature of process simulated. In this section an overview of some of the most well-established numerical modelling approaches to simulate hydraulic free surface flows in each framework is provided. These are introduced in the following sections.

2.3.2.1. Eulerian Methods

In the Eulerian framework, the fluid processes are analysed by using a fixed mesh. The changes occurring in the fluid domain are captured within each of the mesh cells. In the modelling of free surface flows, Eulerian methods are implemented in conjunction with either an interface tracking or an interface capturing scheme to locate the exact position of the free surface. Eulerian methods combined with front capturing schemes locate the interface by defining an auxiliary function to determine presence and absence of one of the phases.

2.3.2.1.1. The Volume of Fluid Method

One of the most well-known Eulerian approaches to model hydraulic free surface flows is the Volume of Fluid (VOF) method developed by Hirt and Nichols (1981). The VOF method employs the volume fraction function with values between zero and one to distinguish between the two fluids. Cells with value zero will show presence of one of the phases, usually air, and cells with value one will contain the second phase, usually water. The interface will be confined in cells with values between zero and one. Whilst ensuring mass conservation, the VOF locates the free surface position by means of an algebraic or geometric reconstruction scheme. Numerous formulations of the VOF method and different interface capturing schemes can be found in the literature. A number of studies have been conducted to review and compare different VOF interface capturing algorithms, for example Gopala and van Wachem (2008) or Waclawczyk and Koronowicz (2008). The VOF is the main approach utilised in this thesis and a detailed description of this method is included in Section 4.2.

The VOF method has been successfully applied to model free surface flows in a wide range of flow situations, some examples are Oertel *et al.* (2012) where the VOF captured different types of flows generated in breaking waves; Biscarini *et al.* (2010) where the VOF was employed to reproduce several dam break flows, and Hieu and Tanimoto (2006) where the VOF was applied to model wave-structure interactions. The prediction of hydraulic free surface features like hydraulic jumps and wave formation have been successfully characterised using the VOF in several studies like Bayon *et al.* (2016), Xiang *et al.* (2014), and Oertel and Bung (2012). Flow over other hydraulic structures has also been accurately simulated and validated with experimental measurements in studies like Sarker and Rhodes (2004). In some instances such as Fuentes-Pérez *et al.* (2018), flow through fishways has also been well predicted with the VOF. An example of the investigation of the non-aerated region of the flow over a stepped spillway with the VOF can be found in Bayon *et al.* (2017) where several numerical implementations were tested, including various discretisation schemes and turbulence models. In that study it was found that the VOF implemented with any of the $k - \varepsilon$ model family tested with second order discretisation schemes provided predictions very well correlated with the experimental measurements.

There is a more limited number of cases where the VOF method has been tested on real flows mainly due to the high costs involved in monitoring and undertaking site measurements. Some available studies are Borman *et al.* (2014) where the VOF was employed for the prediction of the

free surface position in a white water course, and Nguyen (2015) who compared the VOF method with an Eulerian interface tracking scheme applied to model free surface flows over hydraulic structures and in natural waterways. A further example consists in Zeng *et al.* (2017) where the VOF was first tested in two benchmark cases and then applied to model a prototype scale. In that study, satisfactory agreement between numerical predictions and prototype measurements was achieved. An instance where a quasi-real scale gully and manhole were constructed in a laboratory and measurements were utilised to validate the VOF predictions is found in Beg *et al.* (2018). In such study, a close correlation was attained between the numerical predictions and the experimental measurements. An excellent investigation of some of the VOF deficiencies encountered in maritime engineering problems is found in Klaij *et al.* (2018) where the main challenges of the method are examined in detail.

2.3.2.1.2. The Level Set Method

A further Eulerian approach combined with front capturing is the Level Set (LS) method, firstly proposed in Osher and Sethian (1988). In the LS method, the free surface is defined by a function with zero level set. The level set function is assumed to be positive in one of the phases, typically water and negative in the other, typically air. The LS method does not require the application of interface capturing algorithms and the location of the interface is readily available. A detailed review of the LS method and its formulations may be found for instance in Sethian (1996). Several implementations of the LS method are presented in Sussman *et al.* (1994) and Zhang *et al.* (2009).

A number of coupled VOF with level set (CLSVOF) algorithms have also been presented in the recent years. While the VOF robustly ensures mass conservation, the LS method does not naturally establish it. Therefore, a combination of the two approaches has generally aimed at achieving simultaneous mass conservation and interface sharpness. Examples of CLSVOF methods and applications are presented in Park *et al.* (2009), Lv *et al.* (2010), Sun and Tao (2010) or Lv *et al.* (2011).

2.3.2.1.3. Other Eulerian Methods

The Marker and Cell (MAC) method is a further Eulerian approach which consists in the combination of interface tracking schemes with particles. This method was first developed by Harlow and Welch (1965) and is one of the oldest approaches to model free surface flows. The MAC is a volume marker method where the markers (particles) define the whole domain including the interface and they are moved with the flow. The particles move between cells of an Eulerian mesh with the computed velocities (Tome and McKee 1994). A detailed review of the MAC method along with recent improvements and applications is outlined in Tome *et al.* (2004). A successful application of a MAC method to model free surface flows is demonstrated for instance in Santos *et al.* (2012).

The Particle in Cell (PIC) method was introduced by Evans and Harlow (1957) and it is an additional example of particle method used in conjunction with an Eulerian mesh. This method

became a popular approach to model flows with high distortions because of its simplicity. The PIC is known for its numerical diffusion due to the transfer of velocity data from the particles to the mesh and back to the particles at each time step. A number of variations have been proposed from its first formulation to incorporate flow field information into the particles and remove the diffusion issues of the classic approach. Examples of improved PIC approaches include Kelly *et al.* (2015), Jiang *et al.* (2015) and Chen *et al.* (2015).

Another Eulerian method using interface tracking schemes is the immersed boundary method, firstly introduced by Peskin (1977) and further detailed in Peskin (2002) originally developed for biological fluids. The immersed boundary method has been refined since its initial formulation and several improved variations have been proposed. This method is based on a combination of Eulerian variables defined in a fixed mesh and Lagrangian variables to simulate an embedded flexible structure. Consequently, the boundaries of the immersed structure do not coincide with the Eulerian grid. Immersed boundary methods have seen major improvements in the recent years and have potential to increase their application in complex turbulent flows and fluid-structure interaction problems (Mittal and Iaccarino 2005).

2.3.2.2. Lagrangian Methods

In mesh-based methods in the Lagrangian framework, every element containing the field quantities in the domain moves with the fluid velocity. Therefore, Lagrangian moving-mesh methods are characterised by the movement of every point in the mesh at each time step. The interface is tracked with the moving mesh with the use of front tracking algorithms. Such methods provide an accurate representation of the free surface since the mesh coincides with the interface. However, the implementation of Lagrangian moving meshes for complex shapes can be difficult because of geometric limitations. When element distortion is too high, remeshing is needed. Complex interfaces would require a high frequency of remeshing which can make this approach computationally very expensive (Cruchaga *et al.* 2001). One of the most relevant examples of interface tracking technique is the deformable-spatial-domain/stabilised-space-time (DSD/SST) which is a moving mesh front tracking finite element formulation, successfully applied to model a number of free surface flows, for example Aliabadi and Tezduyar (1993) and Behr (2001).

Lagrangian meshless particle methods use a collection of points to represent the fluid motion. They are attractive because by computing the position of the particles, the interface is automatically defined. Meshless methods are a class of numerical approaches that do not use cell elements and were first proposed to remove the inflexibility of finite element techniques to reproduce large deformations and interface fragmentation (Idelsohn *et al.* 2001). Such methods present several advantages for simulating the complex processes present in free surface flows such as wave breaks and violent fluid phenomena. The main strength of meshless methods compared to Eulerian or Arbitrary Lagrangian Eulerian methods is that there is no need of remeshing or data transfer between the mesh and the particles (Galavís *et al.* 2008). Different approaches have been proposed in the attempt to develop mesh free techniques for both fluid

and solid mechanics, for example the Diffuse Element method (Nayroles *et al.* 1992), the Element Free Galerkin Method (Belytschko *et al.* 1994) or the Finite Point Method (Onate *et al.* 1996).

In the following sections some of the most relevant Lagrangian approaches are detailed.

2.3.2.2.1. The Smoothed Particle Hydrodynamics Technique

The oldest and currently one of the most well-known Lagrangian meshless particle formulations is the Smoothed Particle Hydrodynamics (SPH) method proposed by Monaghan (1988), originally developed for astrophysical problems. Its application to free surface flows is detailed in Monaghan (1994). This method defines the fluid by a finite number of particles storing the field quantities. The field values carried by each particle are interpolated by the use of smoothing kernels. These are weighting functions that use the values of the nearby particles to spread the information in space and thus provide continuous estimations of the physical quantities. In order to represent fluid incompressibility, two approaches have been proposed, these are the Weakly Compressible SPH (WCSPH) and the incompressible SPH (ISPH). The SPH method presents strong potential to become a key tool for the study of hydraulic free surface flows. The capability of this method has been demonstrated in several studies such as De Padova *et al.* (2013), Ferrari (2010) or Roubtsova and Kahawita (2006). In some cases, the SPH method has been found capable to reproduce complex flow phenomena more appropriately than traditional Eulerian numerical methods (Aureli *et al.* 2015). Yang *et al.* (2017) developed a two-phase SPH code with the capability of correctly reproducing the water and air interactions in aerated flows. The main limitation of such approach was found to be the restriction of the code to small scales due to computational requirements. In De Padova *et al.* (2013) a hydraulic jump was successfully characterised with an SPH formulation. An encouraging approach to capture air entrainment was more recently proposed in Wan *et al.* (2018) where accurate predictions of aerated flows were achieved, presenting agreement with experimental measurements.

However, the SPH technique still presents a number of uncertainties, mainly regarding the implementation of physically realistic boundary conditions in addition to its computationally intensive nature. Opportunities to minimise the limitations include increasing resolution of simulation with access to appropriate computing facilities and with the use of GPU capabilities.

2.3.2.2.2. The Moving Particle Semi-Implicit Technique

Another popular Lagrangian meshless particle method is the Moving Particle Semi-implicit (MPS) formulation developed by Koshizuka and Oka (1996) firstly developed to model incompressible flow. The MPS approach employs particle interaction models to calculate the differential operators. The particle interaction models are based on a weight function which take into account the interaction between neighbouring particles. The gradients of the field quantities are calculated by a weighted average of all gradients with neighbouring particles. The MPS method ensures incompressibility by solving the Poisson equation of pressure. Examples of successful applications of the MPS method to model different free surface flows are shown in Sheu *et al.* (2011) and Sun *et al.* (2015).

There is a variation of the MPS method known as weakly compressible MPS (WC-MPS) which uses an equation of state to calculate the pressure instead of using the Poisson equation. The WC-MPS method has been validated and applied in several studies to simulate hydraulic flows for example Xu and Jin (2014) where it was proven to adequately reproduce flows over hydraulic structures. In Shakibaeinia and Jin (2009) the WC-MPS method was found to successfully represent various free surface experiments.

2.3.2.3. Arbitrary Lagrangian-Eulerian Methods

The Arbitrary Lagrangian-Eulerian (ALE) methods were first proposed in Hirt *et al.* (1974) to combine the strengths of both Eulerian and Lagrangian formulations. The principle was to develop a method able to track free surfaces and interfaces while dealing with large deformations of the fluid. The method uses a Lagrangian frame where there are small deformations and a Eulerian description where the deformations are too large for the mesh to capture. This approach was initially developed to solve fluid-structure interaction problems. The ALE kinematical description is defined in Hughes *et al.* (1981). The concept of the ALE method is to employ a mesh with the initial fluid domain which will change as the fluid domain evolves. The method relies in three domains: the spatial domain, the material domain and the reference domain. The spatial domain is where the fluid is defined. The material domain is the space where the material particles are contained at the initial time, and they will occupy the spatial domain at time "t". The spatial and material domains are moving domains while the reference domain is fixed. In the Eulerian description, the spatial domain coincides with the reference domain and in the Lagrangian description the material domain coincides with the reference domain (Souli and Zolesio 2001). The moving domains are mapped at each time step to the reference domain. The mesh velocity is defined with an advection equation and is independent from the flow velocity. The mesh velocity is not zero (as for the Eulerian case) or equal to the fluid velocity (as in the Lagrangian case), it has an arbitrary value which maintains the mesh movement following the flow. Consequently, it requires the implementation of a mesh update procedure that attributes values of velocities at each point of the mesh at every time step. The method to calculate the mesh velocity is one of the main differences between the various approaches proposed of the ALE method (Nithiarasu 2005). Several methods have been proposed for the mesh update, depending on the type of flow. The constitutive equations are written in the fixed reference domain and the mesh velocity term is included (Magoules 2011). The fundamental ALE equation describes the relationship between the material time derivative and the referential time derivative (Donea *et al.* 2004). Based on this relationship the constitutive equations expressed in the ALE form are defined.

The ALE method was first proposed with finite differences and was then developed with finite elements. A finite differences approach using ALE applied to model various free surface flows is shown in Hsu *et al.* (2002). Examples of application of the ALE method with finite element discretisation for several free surface flows are presented in Soulaïmani and Saad (1998) and Duarte *et al.* (2004). The ALE method has also been combined with meshless approaches in some studies, for example Ortega *et al.* (2013).

2.3.3. Current Challenges

At the present time, all the available numerical methods proposed to reproduce hydraulic free surface flows present certain limitations. These can be attributed to different factors, mainly related to the little understanding of the complicated nature of the flows and to the restrictions associated with the available computational processing power. In the following sections some of the most significant challenges encountered in numerical techniques to model free surface flows are outlined.

2.3.3.1. Air entrainment

Modelling air entrainment in free surface flows is currently one of the main limitations of the numerical modelling techniques. In addition to increase the water depth, when air is entrained, water becomes a fluid of higher compressibility. Consequently, this would need to be taken into account into the water phase momentum conservation equation (Chanson 2013). At the present time, no air entrainment method is capable of capturing phenomena smaller than the cell size and current alternatives are based on sub-grid methods which are available in some CFD packages (for example Flow 3D). However, these require a previous calibration. The so-called Eulerian-Eulerian multiphase approaches where one set of constitutive equations is solved per phase, appear to be in some instances, an appropriate approach.

2.3.3.2. Turbulence

Free surface flows occurring over hydraulic structures are highly turbulent and of arbitrary nature. Consequently, the flow properties fluctuate in broad ranges of time and length. In order to model turbulence by means of equations which are solved with a numerical algorithm, assumptions and averages are made. The currently available turbulence models have all strengths and limitations and certain models are more appropriate than others for each flow situation. Therefore, although close approximations to real flows have been achieved with several turbulent models, there is still no practical turbulence model capable of predicting all turbulent flows of interest. To reduce uncertainty, predictions of several turbulence models are typically compared and scrutinised for each flow situation. Resolving turbulence of industrial flows at all scales of time and length, with a computationally affordable turbulence model, still remains a problem to be solved.

2.3.3.3. Computational Power

The limits in computer processing power are one of the most significant challenges currently encountered in CFD simulations. This restriction can affect numerical simulations in a number of aspects and it will have a greater or lesser impact depending on the size and characteristics of the flow situation and of the technique employed. The most evident consequence of this restriction is the impossibility to increase the number of elements and therefore conduct simulations at a sufficient resolution. If the solver enables parallelisation of the computer processes, more computationally intensive simulations can be conducted. However, increases in number of processors do not present a linear relationship with computational speed, since communications between the different processors also slow down the calculations. For this reason, even in the

case where high-performance computing facilities are available, the limiting factor would become the time. From an industry perspective, the time scales required for the CFD modelling of hydraulic problems with sufficient resolution, is, in many instances, still prohibitive.

In the case of mesh-based methods, limitations in computational resources could also cause challenges in the creation of appropriate meshes where high quality of the mesh is required. The VOF method, for instance, requires high quality of the mesh elements in order to capture the free surface features. In addition, it needs high resolution of the mesh to provide a sharp free surface. In very elaborate geometries, to achieve a mesh of high quality, with refined cells in the relevant areas, can become exceedingly time-consuming or memory restrictive.

2.3.4. Review of Relevant Numerical Modelling Studies

2.3.4.1. Labyrinth Weir Modelling

As examined in the previous subsections, CFD modelling of hydraulic structures has been in active research in recent years and efforts have been endeavoured to reproduce complex free surface behaviour with several numerical techniques. In the particular case of labyrinth weirs, more limited studies have been presented. One of the oldest consists in Savage *et al.* (2004) as well as Paxson and Savage (2006) where CFD simulations of a two-cycle physical scale labyrinth weir were conducted in order to compute the weir rating curve. The solver predictions proved to be well correlated with the physical model measurements. In Paxson *et al.* (2008) a 2D CFD model of a labyrinth weir was found to predict accurate discharge relationships compared to that of the physical model. Later on, an interesting work was conducted in Blancher *et al.* (2011) where CFD models were employed to investigate and compare efficiency of a labyrinth and PKW in terms of discharge capacity. In Salazar *et al.* (2014) an attempt was made to compare the predictions of the rating curve from a finite element-based, level set code with empirical relationships. Once close agreement was achieved, the 3D patterns generated by the weir were also analysed using the numerical predictions. In Ebner *et al.* (2016) and Thompson *et al.* (2016) CFD predictions of rating curve of an arced labyrinth weir were compared to those from the physical model and a close agreement was achieved. Moreover, in Savage *et al.* (2016) a thorough validation study including the sensitivity analysis of various turbulence models to simulate flow over a labyrinth weir was conducted. Excellent agreement was found between the discharge coefficients obtained in two geometrically similar physical models and predicted numerically.

Additionally, a comprehensive work was conducted using CFD simulations in Aydin and Ulu (2017) in order to analyse the effect of antivortex elements located in labyrinth side weirs.

The effects of nappe breakers on circular labyrinth weirs were investigated using physical and numerical models in Bilhan *et al.* (2018). Good agreement was achieved in the prediction of the weir discharge coefficients with physical and numerical modelling techniques.

The studies noted above indicate that, similarly to most physical model research, the majority of CFD investigations of labyrinth weirs focus on the weir discharge coefficients and rating curves.

In the little instances where the downstream flow behaviour has been regarded, this has not been compared with physical model measurements. There has been no occasion where 3D CFD simulations of the complex downstream weir flows have been assessed against experimental measurements and observations. Therefore, there is a significant lack of numerical studies scrutinising the capability of numerical approaches to reproduce nappe behaviour as well as the flow patterns developed immediately downstream of labyrinth weirs.

2.3.4.2. Scale Effects Investigations

The capability of CFD to model the real prototype scale offers the opportunity to compare predictions at model and prototype scales and hence investigate scale effects. This novel concept has only been put into practice in very scarce cases. Consequently, there is an extremely limited number of studies available in the literature where scale effects have been analysed by means of CFD simulations. An instance of this conceptualisation is found in Kim and Park (2005) where 2D CFD simulations were conducted to model the flow over an ogee spillway using various scales and roughness to observe their effects on the weir velocities and pressures.

An interesting study where 3D CFD was implemented to investigate scale effects on turbulence modelling and sediment scour around a bridge pier and consists in Huang *et al.* (2009). In such study simulations were undertaken at physical model scale and qualitative validation was undertaken with physical model measurements. Subsequently, the prototype scale was numerically simulated and results were compared to the model scale predictions. The CFD simulations demonstrate that not being able to simultaneously satisfy Reynolds and Froude number similarity, might induce significant errors in predicting both turbulence and scour around a large bridge pier. Considerable differences in velocity at the two scales are also highlighted.

In Aldaş and Yapıcı (2014) the scale effects induced in Reynolds number similarity models for water jet pumps were investigated for 7 different scales. The efficiency of the pump is analysed for each scale. Roughness and turbulence models were also examined for a fixed scale. The study concludes CFD proves to be a suitable tool to improve efficiency of such pumps.

Pfister *et al.* (2013a) consists in a remarkably relevant study to the research conducted in this thesis. In such work, 2D simulations of a cylindrically crested PKW were conducted at several sizes of crest radii. Effects on the rating curve as well as on the crest pressures were inspected for the various scales. The derived minimum head over crest to minimise scale effects in the rating curve presented agreement with values proposed in the literature. Such study also highlights the overestimation in pressure profiles at the weir crest occurring at the smallest crest sizes.

The four cases outlined above utilise CFD to investigate the effects of scale in the flow over three different hydraulic structures and around a bridge pier. Two of them, (Pfister *et al.* (2013a) and Kim and Park (2005)) consist in 2D simulations and there is no previous validation conducted. In Huang *et al.* (2009) qualitative validation is undertaken and in Aldaş and Yapıcı (2014) model validation is conducted using certain aspects of the flow. Therefore, there is an exceptionally limited number of studies which include an initial validation of the CFD predictions, prior to the analysis of the scale effects for a comprehensive 3D case. Additionally, in the studies where

validation of the CFD predictions is conducted, scale effects are investigated but limits to minimise them are not derived.

2.4. Composite Modelling

2.4.1. Introduction

Using the results from physical models in conjunction with the predictions from numerical simulations is a recently proposed modelling technique generally referred to as “composite” or “hybrid” modelling, defined by Frostick *et al.* (2011) as “the integrated and balanced use of physical and numerical models”. Composite modelling attempts to combine physical and numerical models in order to minimise limitations and use the strengths of both techniques (Van Os *et al.* 2004) (Kamphuis 2000). This approach is expected to provide higher confidence and less uncertainty in the predictions, allowing the model of complex problems that cannot be resolved in detail by using a single modelling approach (Gerritsen *et al.* 2011). Therefore, this combined methodology could have potential for satisfying industry and scientific specific needs. Composite modelling is still in its infancy and constitutes a promising developing research area. For this reason, a standard method for the implementation of composite modelling has not been defined yet. Composite modelling has been applied in a number of occasions where physical and numerical models have complemented and enhanced each other using various methodologies. For instance, the physical model allows the representation of detailed phenomena in a local scale and its results can be used as boundary conditions that feed into numerical models to simulate real regional scale processes. Another example is the use of numerical modelling to reduce the number of physical experiments once the numerical model is calibrated and thus save time and costs. A selection of modelling strategies is outlined in Sutherland and Barfuss (2012). A description of the technique applicability and uncertainties may be found in Frostick *et al.* (2011).

Composite modelling provides an important opportunity for comparison of the numerical and physical modelling allowing the investigation of uncertainties and limitations in both techniques, which could be critical for the future independent use of numerical models. Since this technique is still at the early stages of development, further work is needed to improve the basis of its understanding. The combination of physical and numerical modelling is not a common practice and hence there is much research work to be conducted in order to evaluate and establish how best the two approaches could work together. A detailed definition of the different approaches to apply the technique needs to be refined.

2.4.2. Review of Most Relevant Studies

One of the first applications of composite modelling was conducted and reported in Piroton *et al.* (2003) where the potential for time-saving and provision of valuable information of the numerical approaches when combined with physical models was revealed. Since then, this technique has been evolving and researchers and engineers have been implementing it in a variety of forms. Further examples of work showing the successful implementation of composite modelling include Heiner (2013), Erpicum *et al.* (2012) or Erpicum *et al.* (2015). Some studies demonstrated that

the complementary use of physical and numerical models presents substantial improvements to the assessment of hydraulic structures (Willey *et al.* 2012).

Epicum *et al.* (2017a) consists in a more recent study where three possible strategies to implement composite modelling are presented. Examples illustrating the three methodologies are also described.

Composite modelling has been regarded as a promising methodology and the potential way forward in hydraulic modelling for the design of hydraulic infrastructure in a multitude of studies, some examples include Chanson (2008), Chanson (2013), Savage *et al.* (2004), Savage *et al.* (2016). The application of composite modelling for the design of labyrinth weirs has been documented in a number of occasions, for example Ebner *et al.* (2016) Thompson *et al.* (2016), Paxson *et al.* (2008) and Ackers *et al.* (2012).

2.5. Conclusions

This chapter outlined the currently used hydraulic modelling methodologies to simulate flows over hydraulic structures. These consist in physical, numerical and composite modelling techniques. The background of each technique has been reviewed as well as the main principles behind them, their strengths and limitations. The most prominent studies relevant to the research conducted in this thesis have been outlined.

Physical modelling constitutes the most widely utilised tool for hydraulic structure research and design. At the present time, experimental techniques play a crucial role by enabling the modelling of poorly understood physical phenomena in controlled conditions and allowing their investigation. The main limitations in the utilisation of physical modelling for structure design are scale effects.

There are many numerical modelling approaches which have been proposed with the aim of reproducing the complex free surface flows occurring over hydraulic structures. All the leading techniques reviewed present certain limitations, mainly due to current lack of knowledge of the physical phenomena, and to restrictions on computational power. However, their strengths enable them to be very powerful tools to analyse free surface flow situations. The studies reviewed highlighted the remarkable potential of these techniques to predict numerous free surface flows. Further validation evidence for a wider range of hydraulic structures and flow conditions are necessary to demonstrate their capability to reliably reproduce complex flows.

Composite modelling is currently seen as a modelling strategy of significant prospects by many authors. This technique has been successfully implemented in a selection of forms to enhance understanding of multiple complicated cases. There are numerous encouraging opportunities for development which are yet to be explored. There is an extraordinary potential in the application of numerical techniques in conjunction with physical modelling.

The most prominent studies implementing physical and numerical modelling techniques to simulate flows over labyrinth weirs have been reviewed. There are several experimental studies with focus on the flows upstream labyrinth weirs, and especially on the weir geometric and hydraulic parameters. In several cases, numerical models have been applied to model flows

upstream labyrinth weirs and they have been proven to be capable of accurately predicting labyrinth weir rating curves. However, the literature shows the complex, fully 3D flows occurring downstream of labyrinth weirs have received little attention. Very scarce physical modelling studies concerning flows downstream of labyrinth weirs are available, and in even more limited occasions, these have been investigated with numerical approaches.

Studies concerning the investigation of scale effects and derivation of limits to minimise these in physical models have been scrutinised. The review of the existing research developments shows that additional research is needed to determine guidelines to minimise scale effects in physical modelling of non-linear weirs, and in particular, of labyrinth weirs. The available studies concerning scale effects in non-linear weirs have been undertaken with experimental techniques in all cases with the exception of one study, where limits to minimise scale effects were attempted with the application of a 2D CFD model.

3. Computational Fluid Dynamics Modelling

3.1. Introduction

This chapter introduces the main principles behind CFD modelling and especially describes the aspects and implementations utilised in the simulations undertaken in this thesis. Firstly, general concepts are introduced, followed by the definition of the governing equations and the available discretisation schemes employed to express the equations in algebraic form. Subsequently, the concept of turbulence and its modelling is described. Solution methods and meshing arrangements applied by the solvers used in this thesis are also characterised. Finally, potential sources of uncertainty and error present in CFD simulations are detailed.

3.2. General Concepts

CFD consists in the investigation of flow processes by the use of computer simulations (Versteeg and Malalasekera 1995). The study of flows with CFD involves the analysis of phenomena by partitioning the domain into a number of elements (for example using a mesh) covering the entire area of interest. Once the domain is divided into a finite number of elements, a set of fundamental equations which governs the fluid phenomenon is selected. In most CFD applications, the Navier-Stokes equations are solved, which comprise the transport of momentum, heat and mass, formulated in the momentum, mass and energy conservation equations. The governing equations are then expressed in algebraic terms by using approximations, such as Taylor's Series expansions. These are solved at each element using numerical algorithms. Thus, changes are captured within each element and the values of field quantities (such as velocity and pressure) are calculated at every set space of time.

The Navier-Stokes equations consist in a non-linear system of equations and therefore they require a procedure to solve them iteratively. This is undertaken by the selection of an appropriate iterative algorithm. At each iterative step the predicted solution becomes closer to the exact solution. The difference between the predicted and the exact solution is referred to as the *residual*. The residuals of the constitutive equations are set to be sufficiently small in the solver specifications, and once those values are achieved it is judged that the solution has converged. The difference between the converged solution and the real solution is referred to as the *modelling error*.

This process is implemented through a CFD solver, where the geometry of the discretised domain is embodied. The physics of the problem and the constitutive equations to solve are defined as well as the discretisation schemes and iterative algorithms required to solve them in the specified terms of time and space. The solver provides the solution residuals at each time step. Once the simulations are concluded the results are post-processed in the corresponding solver visualisation application.

Due to the size and complexity of the modelling domains present in this study, parallelisation of the simulations in the High-Performance Computer (HPC) is required. The HPC facilities utilised are part of the Advanced Research Computing (ARC) resource at the University of Leeds. In this

thesis, two of the three available CFD solvers in such clusters were employed. These consist in the commercial CFD package ANSYS Fluent and the open source solver OpenFOAM, which are regarded as leading CFD solvers for hydraulic flows at the present time.

3.3. Governing Equations

The constitutive equations for fluid motion consist in the conservation laws of mass, momentum, and energy. These form a system of equations referred to as Navier-Stokes (NS) equations. The NS equations are applied to a generic control volume located in the fluid domain. The hydraulic free surface flows in which this thesis focuses are assumed to be at constant temperature and hence the energy equation is not required. The system of governing equations solved in typical hydraulic free surface flows consists in the mass and momentum conservation equations.

The continuity equation of a compressible fluid is defined as per Eq. 3.1.

$$\frac{\partial \rho}{\partial t} + \frac{\partial(\rho u)}{\partial x} + \frac{\partial(\rho v)}{\partial y} + \frac{\partial(\rho w)}{\partial z} = 0 \quad 3.1$$

Or expressed in vector notation in Eq. 3.2.

$$\frac{\partial \rho}{\partial t} + \nabla \rho \mathbf{u} = 0 \quad 3.2$$

Where \mathbf{u} is the fluid velocity vector: $\mathbf{u} = (u, v, w)$ and ρ is the fluid density.

In the case of hydraulic flows, the water is treated as an incompressible fluid (since its compressibility is considered to be negligible). Thus, the mass conservation equation results in Eq. 3.3.

$$\nabla \mathbf{u} = 0 \quad 3.3$$

The momentum conservation equation is based on Newton's second law, which dictates that the rate of change of momentum of a fluid particle is equal to the sum of forces of the particle. The derivation of the momentum conservation equation may be found in any fluid dynamics or CFD text books, such as Versteeg and Malalasekera (1995). In a Newtonian fluid (like water), where the viscous stresses maintain a linearly proportional relationship with the rates of deformation, the viscous stresses may be written in terms of the linear deformation and volumetric deformation rates. The x, y and z components of the momentum equations are expressed in Eq. 3.4 to 3.6.

$$\rho \left(\frac{\partial u}{\partial t} + u \frac{\partial u}{\partial x} + v \frac{\partial u}{\partial y} + w \frac{\partial u}{\partial z} \right) = -\frac{\partial p}{\partial x} + \mu \left(\frac{\partial^2 u}{\partial x^2} + \frac{\partial^2 u}{\partial y^2} + \frac{\partial^2 u}{\partial z^2} \right) + \rho F_x \quad 3.4$$

$$\rho \left(\frac{\partial v}{\partial t} + u \frac{\partial v}{\partial x} + v \frac{\partial v}{\partial y} + w \frac{\partial v}{\partial z} \right) = -\frac{\partial p}{\partial y} + \mu \left(\frac{\partial^2 v}{\partial x^2} + \frac{\partial^2 v}{\partial y^2} + \frac{\partial^2 v}{\partial z^2} \right) + \rho F_y \quad 3.5$$

$$\rho \left(\frac{\partial w}{\partial t} + u \frac{\partial w}{\partial x} + v \frac{\partial w}{\partial y} + w \frac{\partial w}{\partial z} \right) = -\frac{\partial p}{\partial z} + \mu \left(\frac{\partial^2 w}{\partial x^2} + \frac{\partial^2 w}{\partial y^2} + \frac{\partial^2 w}{\partial z^2} \right) + \rho F_z \quad 3.6$$

Where p is the pressure, μ is the dynamic viscosity and F_x , F_y and F_z are the body forces acting on the fluid, which in the flows of study consist in the gravity acceleration. Equations 3.4 to 3.6 can be written in its short vectorial form presented in Eq 3.7:

$$\rho \left(\frac{\partial \mathbf{u}}{\partial t} + \mathbf{u} \nabla \mathbf{u} \right) = -\nabla p + \mu \nabla^2 \mathbf{u} + \rho \mathbf{g} \quad 3.7$$

Where \mathbf{g} is the gravity acceleration vector.

The first term in the left-hand side refers to the time derivative and the second is the advection term. On the right-hand side the first term is the pressure gradient, the second term is the diffusion term and the last one refers to the body forces acting on the fluid, which in this case is the gravity.

3.4. Discretisation Schemes

In order to solve the governing equations, these need to be expressed in algebraic form by discretising them in space and time. Three of the most well-established discretisation schemes consist in finite differences, finite elements and finite volume. In this section, the main principles of the finite differences and finite element schemes will be outlined. The finite volume scheme will be described in more detail since is the scheme implemented in this thesis.

3.4.1. Finite Difference Method (FDM)

The approximation of derivatives using the FDM is one of the oldest and simplest techniques. It consists in the definition of a domain in a set of points in a grid, with a defined space size Δx and time size Δt . The derivatives take the expressions of Taylor Series expansions of a function $f(x)$. These expressions use combinations of the function values at the neighbouring grid points so they can be forward, backward and central differences, depending on which node is utilised to derive the function derivative. Considering a grid domain of spacing Δx , a generic node “i” will have as neighbours i-1 and i+1 on the left and right-hand side respectively. For example, the approximation of a space first order derivative, the forward, backward and central differences are presented on Eq. 3.8 to 3.10.

$$\frac{df}{dx} \approx \frac{f(x+\Delta x)-f(x)}{\Delta x} = \frac{f_{i+1}-f_i}{\Delta x} \quad \text{Forward Difference} \quad 3.8$$

$$\frac{df}{dx} \approx \frac{f(x)-f(x-\Delta x)}{\Delta x} = \frac{f_i-f_{i-1}}{\Delta x} \quad \text{Backward Difference} \quad 3.9$$

$$\frac{df}{dx} \approx \frac{f(x+\Delta x)-f(x-\Delta x)}{2\Delta x} = \frac{f_{i+1}-f_{i-1}}{2\Delta x} \quad \text{Central Difference} \quad 3.10$$

The accuracy of the finite difference approximations depends on the truncation error. Backward and forward differences are 1st order accurate, while central differences are 2nd order accurate. This implies in the forward and backward schemes, the approximated value presents an error in respect of the exact value which is proportional to the grid space, while the error of central differences proportional to the square grid space. FDM can be applied to solve higher order derivatives and provide reasonable accuracy. It constitutes a generally quick method to be easily implemented, especially in simple differential equations and domains. However, it would become challenging to implement on complex phenomena and geometries.

3.4.2. Finite Element Method (FEM)

The FEM consists in a similar approach to the FDM but with the difference that a continuous representation of the solution is achieved. With FEM, the solution is obtained in a continuous form

by means of an interpolation function, referred to as shape function. The elements can have diverse shapes, depending on their dimensions (1D, 2D or 3D) and the interpolation type will be different for each of these. The FEM is a powerful method which is able to interpolate the solution over complex geometries.

3.4.3. Finite Volume Method (FVM)

The FVM is a combination of the finite difference simple formulation with the geometric flexibility of finite elements. It is based on the discretisation of the domain into of control volumes. For this reason, it is possible to apply conservation of laws of physics at each volume. The FVM is the scheme applied in most CFD solvers to simulate hydraulic free surface flows in the Eulerian framework.

In this method, the domain is divided into a number of volumes where the governing equations are to be solved. This is typically conducted with a mesh which represents the entire domain with elements. The FVM is based on a cell-centred formulation and its established naming convention in CFD is presented on Figure 3.1. It consists of a generic node point P and its neighbours to the east and west, referred to as “ E ” and “ W ” respectively. The faces of the neighbour control volumes to the east and west are identified as “ e ” and “ w ” respectively. The spacing between the nodes W and P and that between P and E are referred to as δx_{WP} and δx_{PE} respectively. The distances between the node P and the neighbour faces w and e are δx_{wP} and δx_{Pe} respectively. On Figure 3.1 the control volume extent is shown in shaded blue, with width Δx which is equal to the distance between the neighbour faces w , and e δx_{we} .

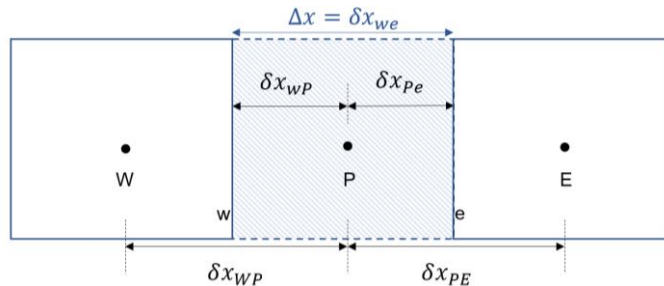


Figure 3.1: Diagram with FVM established notation in the vicinity of a node P

The main feature of the FVM is the numerical integration of the governing equations over each control volume in order to obtain the equations in an algebraic form at each node.

Considering a simple case consisting in the transport equation of a generic scalar ϕ including a time derivative, an advective and diffusion terms in one dimension, its expression is outlined on Eq.3.11.

$$\frac{\partial(\rho\phi)}{\partial t} + \frac{\partial(\rho u\phi)}{\partial x} - \frac{\partial}{\partial x} \left(\Gamma \left(\frac{\partial\phi}{\partial x} \right) \right) = 0 \quad 3.11$$

Where Γ is the diffusion coefficient.

For a control volume defined with notation terms on Figure 3.1, the integration of the transport equation 3.11 of scalar ϕ will be that presented on 3.12.

$$\frac{d}{dt} \int_V \rho\phi \, dV + \int_V \rho u\phi \, dn - \int_S \Gamma \left(\frac{\partial\phi}{\partial x} \right) \, dn = 0 \quad 3.12$$

Where V is the volume of the control volume, S is the area of the face of the volume, and n is the normal vector to the control volume face. In order to numerically solve Eq. 3.12 it will require to be expressed in algebraic terms. This is undertaken by means of discretisation schemes which will approximate the solution.

3.4.3.1. Discretisation of the Governing Equations

The governing equations need to be discretised and integrated over each control volume. Various discretisation schemes are available in the CFD solvers employed in this thesis, (ANSYS Fluent and OpenFOAM). In this section, the discretisation schemes implemented in this study will be outlined for each term of the constitutive equations.

Time derivative

First order schemes are often chosen for the time derivative providing sufficient accuracy in most problems. In this study, the first order Euler implicit scheme is implemented. The discretised form of the time derivative is shown on Eq. 3.13.

$$\frac{d}{dt} \int_V \rho \phi dV = \rho V \left(\frac{\phi^{t+1} - \phi^t}{\Delta t} \right) \quad 3.13$$

Where the superscripts indicate the time level and Δt is the time step size. Eq. 3.13 consists in an implicit formulation. This implies it is formed of a system of equations in which the current and future states are involved. The advantage of implicit schemes is that in contrast with explicit schemes they present unconditional stability regarding the time step size.

Advection Term

As previously specified, the FVM is a cell-centred formulation. This implies the discrete values of a generic scalar ϕ are stored at the volume centres. The advection term requires values to be on the face of the control volume, rather than in the centre. For example, considering the control volume defined in Figure 3.1, the advection of scalar ϕ at face e , will be described by Eq. 3.14.

$$\int_V \rho u \phi dn = \rho u_e \Delta n_e \phi_e \quad 3.14$$

Where u_e is the velocity at face e , Δn_e is the vector normal to face e (which will be a distance, an area or a vector depending on the dimensions) and ϕ_e is the ϕ value at face e , which will be obtained depending on the discretisation scheme chosen to approximate it to the face e . Therefore, the values need to be interpolated from the volume centres to the faces utilising special schemes. There are several schemes utilised to conduct this interpolation, some of the most widely employed include the First Order Upwind Scheme, Second Order Upwind Scheme, the Central Differencing Scheme or the Third Order MUSCL Scheme. In the present study the second order upwind scheme is applied.

In the first order upwind scheme, the values computed at the faces are identical to the values stored at the cell centres located upstream of each face, that is, in the opposite direction to the flow. For example, for the control volume defined in Figure 3.1, assuming a flow direction from

west to east, the value of the scalar ϕ at face e , namely ϕ_e will be equal to the value of the function at the upstream cell centre P , ϕ_P as per Eq. 3.15.

$$\phi_e = \phi_P \quad 3.15$$

The first order upwind scheme is the simplest approach and is first order accurate. This scheme can result in increased errors if the flow is not aligned with the control volumes. Therefore it is not suitable when increased accuracy in the predictions is needed (Versteeg and Malalasekera 1995).

The second order upwind scheme presents second order accuracy and consists of an interpolation from the cell centres to the faces using two upstream values. It employs Taylor Series expansion of the values at the cell centres to achieve the values at the faces. For the control volume defined in Figure 3.1, the value of ϕ_e will be calculated based on the principle outlined in Eq. 3.16.

$$\phi_e = \phi_P + \frac{(\phi_P - \phi_W) \delta x_{WP}}{\delta x_{WP}} \frac{\delta x_{WP}}{2} = \phi_P + \frac{1}{2}(\phi_P - \phi_W) \quad 3.16$$

Where ϕ_W is the value of ϕ at the centre of cell W which is the upstream cell of P . Therefore, this scheme is equivalent to the first order scheme with the addition of a correction term (second term in Eq. 3.16) in order to increase order of accuracy. The second term is based on the gradient of quantity ϕ at the upstream cells.

Diffusion Term

The discretisation of the diffusion term at face e in the one-dimensional control volume of example is presented on Eq. 3.17.

$$\int_S \Gamma \left(\frac{\partial \phi}{\partial x} \right) dn = \Gamma \Delta n_e \frac{(\phi_E - \phi_P)}{\delta x_{PE}} \quad 3.17$$

In the present study, the gradient schemes in the governing equations are approximated using Least Squares Cell-Based. This scheme is capable of producing accurate predictions, especially if the mesh is sufficiently refined.

3.4.3.2. Collocated and Staggered Grid Arrangements

In the finite volume discretisation there are two main arrangements to determine the location where the scalar and vector quantities are stored, namely collocated and staggered. In a collocated grid, the values of all fluid quantities are stored at the cell centres. In a staggered grid, all scalar variables, (such as pressure) are stored at cell centres while the vector variables are stored at the cell faces. In this thesis, both solvers utilised implement a collocated scheme.

In order to compute the values of the pressure at the faces in collocated schemes, interpolation of the values from the centres to the faces is required. The disadvantage of this arrangement is that the so-called “checker-board” pressure challenge arises in the calculation of the scalar gradients. It consists in the problem generated when a highly non-uniform pressure field occurs, which varies at every node. The calculation of the gradient can appear to be like that of a uniform

field giving zero values for the discretised gradients. This issue is mitigated by applying special interpolation schemes for the pressure field. The collocated arrangement is desirable for CFD simulations involving complex geometries.

3.5. Turbulence Modelling

Most flows of engineering interest, and especially those occurring over hydraulic structures and open channels, are of turbulent nature. Turbulent flows are characterised by a chaotic fluid motion, where the fluid particles move at erratic directions. Turbulence is therefore an unsteady state of very complex and irregular three-dimensional motion. As previously noted, the Reynolds number provides an indication of the turbulence levels of the flow, consisting in the ratio between the viscous and inertial forces. When certain Reynolds number is exceeded, complicated processes occur which induce drastic changes in the flow's nature causing it to be no longer characterised by a laminar motion. For Reynolds number values larger than 2000 the flow is generally in a turbulent regime. This may be observed in the Moody chart (Moody 1944). In turbulent flows, the flow quantities such as velocity or pressure, present complicated variations which are reflected in fluctuations. Such fluctuations are manifested at different scales of time and space.

In laminar flows, the velocity profile is defined by a parabolic velocity distribution. In turbulent flows, the velocity profile from the wall is divided into two regions; the outer and the inner region. In the outer region the velocity presents a constant profile with distance from the wall. The inner region is further subdivided into three sections. The nearest to the wall consists in a very fine region where the viscous stresses dominate referred to as the "laminar" or "viscous" sub-layer. Next to the laminar sub-layer there is the buffer layer where viscous and turbulent stresses are of similar magnitude. This layer links to the logarithmic sub-layer where turbulent stresses dominate and the velocity exhibits a logarithmic velocity profile until it becomes fully turbulent in the outer region.

Turbulence in the flow is visually exhibited in a form of rotational patterns referred to as turbulent eddies. These structures are established in a wide range of scales. The eddies with largest sizes present lower fluctuations in the flow quantities and as they reduce in size the fluctuations increase. The process by which energy is transferred from the mean flow motion into the large eddies and from these to smaller eddies is referred to as the *energy cascade*. The large eddies split into smaller eddies to which the energy is transferred. This process occurs until the size of the eddies to which energy is transferred is very small. At this point, viscous forces become relevant and the fluctuation energy is dissipated.

The previously presented NS equations are able to predict turbulent flows, however, the scales of time and space at which turbulence takes place are extremely small compared to the size of the flow domain (especially in real scale hydraulic structures). The mesh size required to resolve the smallest eddies with a sufficient number of grid points per eddy, is still at the present time, computationally restrictive to model industrial flows. This approach consists in the Direct Numerical Simulation (DNS) method, which aims to resolve all scales of turbulence. Turbulence

is therefore, in most cases dealt with by conducting additional modelling. In some instances, where considerable processing power is available, it is possible to conduct modelling of the smallest scales up to a fixed threshold and resolve the largest scales. This is performed with the Large Eddy Simulation model (LES). In this thesis, the so-called Reynolds-Averaged Navier-Stokes Equations (RANS) models are implemented, which consist in the modelling of turbulence at all scales.

3.5.1. RANS Models

RANS models are the most widely used technique to model turbulence in flows of engineering significance. These approaches model all scales of turbulence and consist in the time-averaging of the NS equations. The existing fluctuations are averaged with time, producing the averaged quantities which are the representative values of interest. This is accomplished by the so-called *Reynolds decomposition* which defines all flow properties as the mean value plus its fluctuating component. For example, for the velocity, this is expressed on Eq. 3.18.

$$u = U + u' \quad 3.18$$

Where U is the mean value and $u'(t)$ is the fluctuating component. The mean value U is the time-averaged component over a time interval which compared to the turbulent scales is large, but in relation to the mean flow time scales is small.

$$U = \frac{1}{t} \int_t u \, dt \quad 3.19$$

Eq. 3.19 shows the mean velocity component corresponds to the time-averaged value. Averaging the fluctuating velocity over the same time interval, (which is sufficiently large) the fluctuating velocity is zero. This is expressed in equations 3.20 and 3.21.

$$\bar{U} = U \quad 3.20$$

$$\bar{u}' = 0 \quad 3.21$$

The quantities are expressed in their decomposed form in the constitutive equations, where the vector \mathbf{u} is replaced by its mean and fluctuating components \mathbf{U} and \mathbf{u}' respectively, the velocity components in the y and z dimensions, as well as the pressure are also decomposed so that: $\mathbf{u} = \mathbf{U} + \mathbf{u}'$; $u = U + u'$; $v = V + v'$; $w = W + w'$ and $p = P + p'$. The equations are simplified since the time-averaged divergence of a fluctuating vector \mathbf{u} is equal to that of the mean component \mathbf{U} . The resulting time-averaged form of continuity equation is presented on Eq. 3.22 and the time-averaged x, y and z components of the momentum equation are outlined in Eq. 3.23 to 3.25 respectively.

$$\nabla \mathbf{U} = 0 \quad 3.22$$

$$\rho \left(\frac{\partial U}{\partial t} + \nabla(UU) + \nabla(\overline{u'u'}) \right) = -\frac{\partial P}{\partial x} + \mu \nabla^2 U + \rho F_x \quad 3.23$$

$$\rho \left(\frac{\partial V}{\partial t} + \nabla(VU) + \nabla(\overline{v'u'}) \right) = -\frac{\partial P}{\partial y} + \mu \nabla^2 V + \rho F_y \quad 3.24$$

$$\rho \left(\frac{\partial W}{\partial t} + \nabla(W\mathbf{U}) + \nabla(\overline{w'\mathbf{u}'}) \right) = -\frac{\partial P}{\partial z} + \mu \nabla^2 W + \rho F_z \quad 3.25$$

The time-averaging of the momentum equations introduced new terms, which consist in the product of fluctuating velocities (third term on the left-hand side). Such terms are usually written as the last term on the right-hand side. These stress terms correspond to the so-called *Reynolds stresses*. Re-arranging terms Eq. 3.23 to 3.25 can be re-written as per Eq. 3.26 to 3.28.

$$\rho \left(\frac{\partial U}{\partial t} + \nabla(U\mathbf{U}) \right) = -\frac{\partial P}{\partial x} + \mu \nabla^2 U + \rho F_x - \rho \nabla(\overline{u'\mathbf{u}'}) \quad 3.26$$

$$\rho \left(\frac{\partial V}{\partial t} + \nabla(V\mathbf{U}) \right) = -\frac{\partial P}{\partial y} + \mu \nabla^2 V + \rho F_y - \rho \nabla(\overline{v'\mathbf{u}'}) \quad 3.27$$

$$\rho \left(\frac{\partial W}{\partial t} + \nabla(W\mathbf{U}) \right) = -\frac{\partial P}{\partial z} + \mu \nabla^2 W + \rho F_z - \rho \nabla(\overline{w'\mathbf{u}'}) \quad 3.28$$

Eq. 3.22 together with Eq. 3.26 to 3.28 form the RANS equations.

An important quantity related to the Reynolds stresses consists in the turbulent kinetic energy, k which is defined in Eq. 3.29:

$$k = \frac{1}{2} (\overline{u'^2} + \overline{v'^2} + \overline{w'^2}) \quad 3.29$$

The Reynolds stresses consequently introduce 6 additional unknowns to the constitutive equations. Considering the original unknowns of the governing equations, consisting in the velocity components in the three dimensions and the pressure, there is a total of 10 unknowns. However, there are only 4 equations. This results in the need of further equations in order to close the system. The new equations employed for the closure consist in the turbulence model chosen. The turbulence model will therefore enable the solving of the RANS equations. The turbulence models are classified according to the number of transport equations which are solved with the RANS equations. All the turbulence models utilised in this study consist in two-equation models. These are presented in the following sections.

3.5.1.1. The Standard $k - \varepsilon$ model

The $k - \varepsilon$ model is one of the most widely employed to model industrial flows, and in particular in the field of hydraulic structures. This model employs two transport equations, one for the total turbulent kinetic energy k and another for its dissipation rate ε . The instantaneous kinetic energy of a turbulent flow $k(t)$ is defined as the sum of the mean kinetic energy, K and the previously defined turbulent kinetic energy k . This model was developed by Launder and Spalding (1974)

The tensor of stresses defined in matrix form, (of i rows and j columns) can be referred to as, τ_{ij} and the tensor of rate of deformation as s_{ij} . The rate of deformation of the fluid can be decomposed into its mean and fluctuating components as shown on Eq. 3.30.

$$s_{ij} = S_{ij} + s'_{ij} \quad 3.30$$

The rate of dissipation of flow kinetic energy per unit of volume is expressed as the rate of dissipation of turbulent kinetic energy multiplied by the density. The expression of the rate of

dissipation of the turbulent kinetic energy per unit of mass, ε is presented on Eq. 3.31. This term explains mathematically the dissipation of the turbulent kinetic energy which occurs in the smallest eddies, caused by the viscous stresses.

$$\varepsilon = 2\nu \bar{s}'_{ij} \cdot \bar{s}'_{ij} \quad 3.31$$

The standard $k - \varepsilon$ model presents two transport equations, one for k and one for ε . k and ε are used to characterise the velocity scale, v_s and length scale l_t of turbulence. These are defined in Eq. 3.32 and 3.33 respectively.

$$v_s = k^{\frac{1}{2}} \quad 3.32$$

$$l_t = \frac{k^{\frac{3}{2}}}{\varepsilon} \quad 3.33$$

The effective turbulent viscosity μ_t is defined in Eq. 3.34.

$$\mu_t = C_\mu \rho k^{\frac{1}{2}} l_t = C_\mu \rho \frac{k^2}{\varepsilon} \quad 3.34$$

Where C_μ is a constant.

The turbulent viscosity is also referred to as the eddy viscosity. The closure of the RANS equations is typically undertaken by making use of the Boussinesq hypothesis (Boussinesq 1887). This consist in the assumption of a dependence of the Reynolds stresses on the deformation rate tensor, similar to the relationship between the viscous stresses of a Newtonian fluid. The Reynolds stress tensor is expressed as per Eq. 3.35.

$$\tau_{ij} = -\rho \bar{u}'_i \bar{u}'_j = 2\mu_t S_{ij} - \frac{2}{3} \rho k \delta_{ij} \quad 3.35$$

Therefore, the Reynolds stresses in the RANS equations are replaced by Eq. 3.35. This introduces two new unknowns to the equations, namely k and ε , and equations for their transport need to be formulated. The transport equation for k and that for ε are presented in Eq. 3.36 and Eq. 3.37 respectively.

$$\frac{\partial(\rho k)}{\partial t} + \nabla(\rho k \mathbf{U}) = \nabla \left(\frac{\mu_t}{\sigma_k} \nabla k \right) + 2\mu_t S_{ij} S_{ij} - \rho \varepsilon \quad 3.36$$

$$\frac{\partial(\rho \varepsilon)}{\partial t} + \nabla(\rho \varepsilon \mathbf{U}) = \nabla \left(\frac{\mu_t}{\sigma_\varepsilon} \nabla \varepsilon \right) + C_{1\varepsilon} \frac{\varepsilon}{k} 2\mu_t S_{ij} S_{ij} - C_{2\varepsilon} \rho \frac{\varepsilon^2}{k} \quad 3.37$$

Where σ_k and σ_ε are constant Prandtl numbers which link the diffusivities of k and ε to the turbulent viscosity and C_μ , $C_{1\varepsilon}$ and $C_{2\varepsilon}$ are also constants. The values of such constant coefficients and Prandtl numbers are derived empirically. The recommended values for such constants, which have been derived with a range of turbulent flows, (Launder and Spalding 1974) are as follows: $\sigma_k = 1.00$; $\sigma_\varepsilon = 1.30$; $C_\mu = 0.09$; $C_{1\varepsilon} = 1.44$ and $C_{2\varepsilon} = 1.92$.

The $k - \varepsilon$ model presents a good balance between computational requirements and numerical accuracy. This turbulence model is the one of the most widely used for engineering flows, and it particularly provides accurate results in complex 3D geometries.

Chapter 3. Computational Fluid Dynamics Modelling

The $k - \varepsilon$ model is only applicable for reproducing turbulent flows with high Reynolds numbers, and hence is not capable of predicting near-wall behaviour where viscosity forces are dominant over inertial forces. Therefore, additional modelling is required for the behaviour of the flow near-wall. A method typically employed to account for the conditions near the walls with the $k - \varepsilon$ model is the implementation of the so-called wall functions. These functions apply the “law of the wall” at hard boundaries so that the model equations do not need to be integrated to the wall. The “law of the wall” consists in the formula outlined on Eq. 3.38 which is derived from a dimensional analysis.

$$u^+ = \frac{U}{u_\tau} = f(y^+) \quad 3.38$$

Eq. 3.38 shows the non-dimensional near-wall velocity, u^+ only depends on the non-dimensional distance from the wall y^+ . u_τ is the velocity scale, which is equal to the shear velocity, utilised to convert the mean flow velocity U into a dimensionless value. The shear velocity has the expression outlined on Eq. 3.39.

$$u_\tau = \sqrt{\frac{\tau_w}{\rho}} \quad 3.39$$

Where τ_w is the wall shear stress. The non-dimensional wall distance relative to the shear velocity is defined as per Eq. 3.40.

$$y^+ = \frac{\rho u_\tau y}{\mu} \quad 3.40$$

At the fluid layer next to the wall, previously described as the laminar sub-layer, the velocity profile can be approximated as linear, so that the relationship between the dimensionless near-wall velocity and distance is described as per Eq. 3.41.

$$y^+ = u^+ \quad 3.41$$

The turbulent region at the logarithmic layer, the velocity obeys an empirical logarithmic profile, outlined in Eq. 3.42.

$$u^+ = \frac{1}{\kappa} \ln(Ey^+) \quad 3.42$$

Where κ is Von Karman's Constant = 0.4187, and E is a constant value, usually $E = 9.7393$. The logarithmic layer typically is located at the region where y^+ is between 35 and 350.

The implementation of wall functions at hard boundaries is conducted by evaluating the value of y^+ at the wall by using equation 3.43.

$$y^+ = \frac{\Delta y_P}{\nu} \sqrt{\frac{\tau_w}{\rho}} \quad 3.43$$

Where Δy_P is the distance from the wall to the first node P.

If the value of y^+ is equal or lower than 11.63, the flow is assumed to be laminar and the wall shear stress considered to be of wall origin only. If the value of y^+ is greater than 11.63, the flow is turbulent, and the shear stress is calculated with the wall functions. The value of 11.63 is used

as a threshold since it is that obtained when the linear profile of the viscous sublayer intersects the logarithmic law region in a turbulent boundary layer.

In order to perform appropriately, standard wall functions are valid within a range of y^+ values. It must be ensured that the first mesh node from hard boundary is located within the logarithmic boundary layer. Typically values of y^+ should be lower than 300 to prevent the first node from being in the outer region.

3.5.1.2. The RNG $k - \varepsilon$ model

The Renormalisation Group (RNG) $k - \varepsilon$ model consist in a variant of the Standard model, firstly proposed in Yakhot and Orszag (1986) and later improved in Yakhot *et al.* (1992). It is based on a statistical technique referred to as the RNG theory. It is comparable to the Standard $k - \varepsilon$ model with several enhancements. This model is claimed to improve the accuracy for swirling flows as well as rapidly strained flows. The Prandtl numbers presented in the Standard $k - \varepsilon$ model, which consist in constant values, in the RNG $k - \varepsilon$ model are derived analytically. Therefore these are replaced with different values. A main feature of this model is that while the Standard model is only applicable to high Reynolds numbers and requires especial treatment in low Reynolds number areas, the RNG model includes an element which accounts for areas with low Reynolds number. This is achieved by using an effective viscosity term. The transport equations for the RNG $k - \varepsilon$ model are presented in Eq. 3.44 and 3.45.

$$\frac{\partial(\rho k)}{\partial t} + \nabla(\rho k \mathbf{U}) = \nabla(\alpha_k \mu_{eff} \nabla k) + \tau_{ij} S_{ij} - \rho \varepsilon \quad 3.44$$

$$\frac{\partial(\rho \varepsilon)}{\partial t} + \nabla(\rho \varepsilon \mathbf{U}) = \nabla(\alpha_\varepsilon \mu_{eff} \nabla \varepsilon) + C_{l\varepsilon} \frac{\varepsilon}{k} \tau_{ij} S_{ij} - C_{2\varepsilon} \rho \frac{\varepsilon^2}{k} \quad 3.45$$

Where μ_{eff} is the effective viscosity and is calculated as per Eq. 3.46

$$\mu_{eff} = \mu + \mu_t \quad 3.46$$

In this case the model constants take the following values: $C_\mu = 0.0845$; $\alpha_k = \alpha_\varepsilon = 1.39$; $C_{l\varepsilon} = 1.42$ and $C_{2\varepsilon} = 1.68$.

3.5.1.3. The $k - \omega$ model

The $k - \omega$ model consists in an alternative to the $k - \varepsilon$ and employs the turbulence frequency, ω defined in Eq. 3.47 as a second variable instead of ε .

$$\omega = C_\mu = \frac{\varepsilon}{k} \quad 3.47$$

When using the turbulence frequency, the length scale is calculated as per Eq. 3.48.

$$l_t = \frac{k^{\frac{1}{2}}}{\omega} \quad 3.48$$

And the eddy viscosity is provided by Eq. 3.49.

$$\mu_t = \frac{\rho k}{\omega} \quad 3.49$$

The transport equations for k and ω have the form outlined in Eq. 3.50 and 3.51.

$$\frac{\partial(\rho k)}{\partial t} + \nabla(\rho k \mathbf{U}) = \nabla \left(\left(\mu + \frac{\mu_t}{\sigma_k} \right) \nabla k \right) + P_k - \beta^* \rho k \omega \quad 3.50$$

$$\frac{\partial(\rho \omega)}{\partial t} + \nabla(\rho \omega \mathbf{U}) = \nabla \left(\left(\mu + \frac{\mu_t}{\sigma_\omega} \right) \nabla \omega \right) + \gamma_1 \left(2\rho S_{ij} S_{ij} - \frac{2}{3} \rho \omega \frac{\partial U_i}{\partial x_j} \delta_{ij} \right) - \beta \rho \omega^2 \quad 3.51$$

Where P_k is the rate of production of kinetic energy, which has the expression outlined in Eq. 3.52.

$$P_k = 2\mu_t S_{ij} S_{ij} - \frac{2}{3} \rho k \frac{\partial U_i}{\partial x_j} \delta_{ij} \quad 3.52$$

And the model constants have the following values: $\sigma_k = 2.00$; $\sigma_\omega = 2.0$; $\gamma_1 = 0.553$; $\beta^* = 0.09$ and $\beta = 0.075$.

This model resolves the boundary layer without wall functions, therefore it becomes a convenient option where wall functions cannot be applied. Similarly to the $k - \varepsilon$ model, this model also solves two equations and the transport equation of ε is replaced by the transport equation of ω , which is modelled equivalently. The $k - \omega$ model was proposed in Wilcox (1988). In contrast with the $k - \varepsilon$ model, in the $k - \omega$ model the transport equations are integrated to the wall. The value of k at the wall is zero and the value of ω will tend to infinity or an assumed sufficiently large number as described in Wilcox (1988).

3.5.1.4. The SST $k - \omega$ model

In order to improve the accuracies observed in the $k - \omega$ model, the Shear Stress Transport (SST) $k - \omega$ approach was proposed by Menter (1994). This model was intended to produce an approach which was less sensitive to assumed values from the mean stream flow, such as the $k - \varepsilon$ model, but was able to resolve the near-wall low Reynolds numbers region like the $k - \omega$. The Reynolds stresses are calculated in the same way as in the $k - \omega$. This model includes a modified term for the turbulent viscosity to consider the transport of the turbulent shear stress. The transport equation of k is the same as in the original $k - \omega$ model, however, the transport of ω is formulated by a transformation of the ε equation substituting $\varepsilon = k\omega$. Therefore, it has one extra term compared to Eq. 3.51 which appears as a result of such substitution. The transport equation for ω has the expression indicated in Eq.3.53.

$$\frac{\partial(\rho \omega)}{\partial t} + \nabla(\rho \omega \mathbf{U}) = \nabla \left(\left(\mu + \frac{\mu_t}{\sigma_{\omega,1}} \right) \nabla \omega \right) + \gamma_2 \left(2\rho S_{ij} S_{ij} - \frac{2}{3} \rho \omega \frac{\partial U_i}{\partial x_j} \delta_{ij} \right) - \beta_2 \rho \omega^2 + 2 \frac{\rho}{\sigma_{\omega,2} \omega} \frac{\partial k}{\partial x_k} \frac{\partial \omega}{\partial x_k} \quad 3.53$$

The model constants are as follows: $\sigma_k = 1.00$; $\sigma_{\omega,1} = 2.0$; $\sigma_{\omega,2} = 1.17$ $\gamma_2 = 0.44$; $\beta^* = 0.09$ and $\beta_2 = 0.083$.

This model implements the so-called blending functions, which aim to mitigate the instabilities which arise due to the different values of turbulent viscosity computed with the $k - \varepsilon$ in the outer region and that produced at the near-wall region.

3.6. Pressure-Velocity Coupling

The compressibility of water is so small that it is standard practice to consider this fluid incompressible. The assumption of incompressibility of a fluid implies the density is constant and not linked to pressure. Consequently, as previously noted, the equation of state cannot be used to acquire the pressure term for the NS equations. This generates a pressure velocity coupling condition, which is that the pressure field utilised in the momentum equation needs to provide a velocity value which satisfies the continuity equation. In order to find the values of velocity and pressure which satisfy simultaneously momentum and continuity equations, an iterative algorithm is employed.

3.6.1. The SIMPLE Algorithm

For steady calculations, a well-established option is the SIMPLE (Semi-Implicit Method for Pressure-Linked Equations) algorithm. This scheme was developed in Patankar and Spalding (1972) and is based on an iterative algorithm which uses an initially guessed value of the pressure field, which is substituted into the discretised momentum equations. The initially guessed value of the pressure enables to obtain the corresponding guessed values of the velocities. Corrections for the pressure and velocity fields are obtained and substituted into the momentum and continuity equations. The continuity equation acts as the pressure correction equation which provides the correction for the pressure value. Once the correct pressure value is known, the correct velocities can be obtained.

3.6.2. The PISO Algorithm

The SIMPLE algorithm it is not applicable to unsteady problems. The algorithm selected in this study to solve the unsteady flows consists in the PISO (Pressure Implicit with Splitting of Operators), first developed by Issa *et al.* (1986). The PISO is based on the same principle as the SIMPLE but it includes an additional corrector step for further refinement. With an equivalent approach to SIMPLE, an initial value for the pressure is assumed and the corresponding values for the initially estimated velocities are obtained. The first corrector step consists in substituting the velocity estimates into the continuity equation, which will result in the first pressure correction value. Once the pressure correction is known, the corrected value of the pressure can be substituted in the continuity equations to obtain velocity values which satisfy the continuity equation. The second correction step taken makes this algorithm different from the SIMPLE. It consists in the substitution of the corrected velocity values into the momentum equation. The substitution of the newly corrected velocities into the continuity equation provides a further refined value of the pressure. The continuity equation in this case acts as a second pressure correction equation. The twice-corrected velocity fields are then acquired by substituting the final pressure value. This is conducted until convergence is achieved.

Although the PISO requires increased processing power to solve the pressure correction equation two times, this algorithm has been found to be considerably fast and very accurate (Versteeg and Malalasekera 1995).

3.7. Meshing

The procedure by which a modelling domain is divided into the control volumes is the generation of a mesh. The meshing methodologies typically employed for the CFD modelling of complex geometries are divided into structured and unstructured arrangements. Structured meshes are also referred to as body-fitted meshes, which consist in a regular arrangement of grid point connectivity with an equal number of neighbour cells which follow a regular pattern. In an unstructured mesh, the elements are arbitrary created which leads to an irregular pattern.

Structured meshes enable the superior performance of certain algorithms, and in some occasions, particular algorithms are restricted to these arrangements. The main example related to free surface flows is the application of the VOF method, which provides significantly improved predictions of the free surface in structured meshes. In particular, the VOF is extremely sensitive to mesh quality and in certain instances it is not possible to apply it on unstructured meshes. This is also explained by the fact that structured meshes are generally aligned (or more closely aligned) to the flow direction, which enables increased accuracy and convergence, making this type of arrangement more effective. Structured meshes are remarkably complex to create, especially when high quality meshes are required in an exceedingly complex geometry. In some cases, the regular mesh topology in a very complex geometry could result in poorly shaped elements and hence in a loss of accuracy.

Unstructured meshes present the main advantage of the effortless procedure in which they are generated, which is fully automated. For this reason, they constitute the most straightforward option for complex geometries. However, their applicability will depend on the algorithms needed to be implemented since the accuracy of such arrangements is lower than that achieved with a structured mesh. In addition, unstructured meshes have the requirement of increased memory in order to store the cell connectivity.

In this thesis structured meshes are utilised in all flow situations modelled. The meshing strategies employed for each modelling domain are specified in each chapter.

3.8. Uncertainty and Error in CFD Simulations

The simulation of a real flow process by means of a model always involves presence of some form of error. According to Slater (2008), there are a number of factors which are responsible for CFD simulation predictions differing from the true values. The difference between an uncertainty and an error is that an uncertainty consists in a deficiency caused by the lack of knowledge of the process modelled while an error is not.

Uncertainty can be generated by the input factors, for example, not enough understanding of the boundary conditions, material characteristics, etc. Or can also be caused by the differences between the real and simulated flows due to inaccurate simulation of physical phenomena or model assumptions. This also includes changes in the physical model geometry due to manufacturing processes.

Other possible sources of uncertainty include the assumptions made on roughness of smooth walls. In most of CFD simulations of hydraulic flows it is often assumed the walls are perfectly smooth. However, in the real physical model or prototype there are microscopic roughness elements at the hard boundaries which might present certain roughness. Such discrepancies are considered to be minor and have negligible effects on the simulation predictions.

A possible method of determining uncertainty in a model is to conduct sensitivity analyses. For example, in CFD, one of the main uncertainties is the modelling of turbulence. At the present time turbulence is a process which is not fully understood, and for this reason there are various models to reproduce it. Testing a CFD code for various turbulence models would represent an approach of determining the uncertainty related to turbulence in a CFD model.

There are various classifications of the possible errors encountered in CFD simulations. A possible method is to divide them into numerical errors, coding errors and user errors (Versteeg and Malalasekera 1995).

Numerical errors could be considered to be the inaccuracies caused by the round-off error, iterative convergence error and discretisation error. The round-off error is that related to the number of significant digits utilised to represent real numbers in the numerical code. The iterative convergence error refers to the deficiency introduced as a result of the truncation in the number of iterations which occurs after a set value in the residuals is reached. Consequently, this error lessens with decreasing the set tolerance of the residuals. The discretisation error is induced by the higher order terms which are neglected in the Taylor's series in the discretisation procedure. Therefore, the means by which the numerical errors are lowered imply substantial increases in memory requirements and thus, a balance must be found between accuracy and computational cost.

Coding errors are those associated with the solver which are mitigated with Quality Assurance and Control procedures. User errors are reduced with increasing training and experience of the user as well as by conducting regular simulation checks.

4. Numerical Modelling Approaches: Description and Implementation

4.1. Introduction

In the first two sections of this chapter, two leading numerical techniques utilised to model free surface flows are described. These are the previously outlined Eulerian mesh-based VOF method and the Lagrangian meshless particle-based SPH technique. In the third section of this chapter, the two approaches are employed to model an experimental dam break flow. The purpose of the study conducted in this chapter is to evaluate the capabilities of the two techniques and identify best practice for their implementation in the specific solvers utilised. The initial testing of the VOF is essential to enable an efficient analysis of a more complex flow problem undertaken in Chapter 6. The testing of the SPH for this experimental case is expected to reveal the capabilities and limitations of this technique for its future application in hydraulic structure modelling studies.

An experimental case of moderate complexity with availability of high quality experimental data is chosen from the literature in order to accomplish the purpose of this first study. Ensuring a reasonably simplistic geometry with various flow situations (dam break flow, fine layer of flow traveling over a triangular obstacle, interaction of dam break flow with a pool of water, and generation of a reflective wave) provides an opportunity to compare various numerical implementations within each approach.

4.2. The VOF Method

4.2.1. Introduction

As previously noted, the VOF consists in one of the most well-established methods to simulate hydraulic free surface flows. The VOF employs a volume fraction function α with values 0 and 1 to determine the presence and absence of the two phases (water and air). The interface between the two phases is located in cells with values of the function between 0 and 1. In order to locate the exact position of the free surface, the VOF method solves a transport equation for the volume fraction function defined in Eq. 4.1 by employing interface capturing algorithms.

$$\frac{\partial \alpha}{\partial t} + \nabla(u\alpha) = 0 \quad 4.1$$

Where u is the velocity of the corresponding phase at cells where α is equal to 0 and 1, and at cells containing the interface, it corresponds to the averaged air-water velocity.

Solving such transport equation with discretisation schemes is not a trivial task. The principal challenges in the discretisation of the transport equation of α are mitigating artificial diffusion of the interface (i.e. achieving a sharp interface) and ensuring boundedness (i.e. physical values of α where changes are monotonic) (Waclawczyk and Koronowicz 2008).

The VOF method solves only one set of constitutive equations for the two phases. The values of the fluid properties at the interface are computed by using a weighting of the values of water and

air based on the value of α at each cell. For the density and dynamic viscosity this is shown in Eq. 4.2 and Eq. 4.3 respectively.

$$\rho = \rho_w \alpha + \rho_a (1 - \alpha) \quad 4.2$$

$$\mu = \mu_w \alpha + \mu_a (1 - \alpha) \quad 4.3$$

Where the subscripts w and a stand for water and air. A diagram of the two phases and their interface represented in the VOF method is illustrated on Figure 4.1

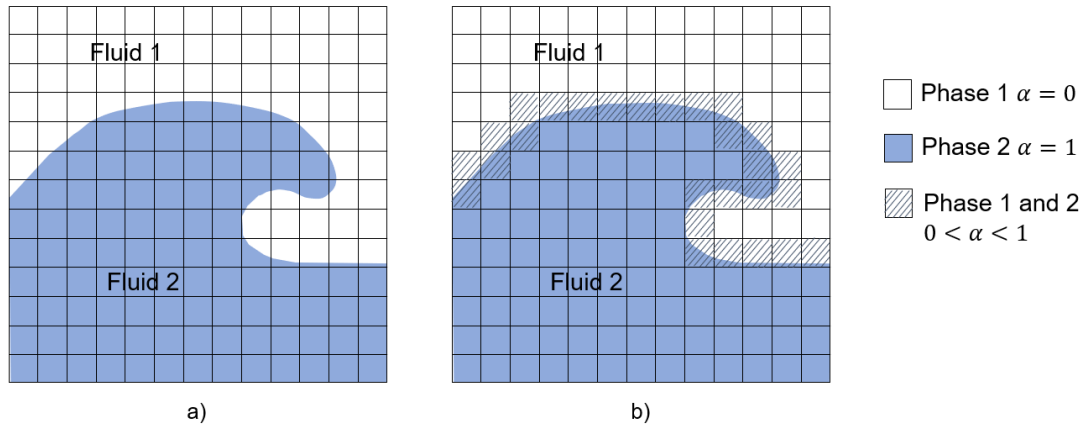


Figure 4.1 a) Fluids 1 and 2 represented in the mesh; b) indication of the phases for the two fluids and at the interface as implemented in the VOF method

The VOF formulation by Hirt and Nichols (1981) was based on the donor-acceptor scheme (DAS). This consists in the implementation of downwind differentiation to advect the volume fraction downstream, that is, using the “acceptor” cell value (the downstream cell receiving the volume fraction) from the donor cell (the cell from which the volume fraction is transported downstream). This approach considers the direction of the free surface to calculate the amount of fluid moved through the cell faces and ensures global boundedness (volume fraction values between 0 and 1). However, it does not ensure local boundedness (that is, values of α might not be bounded in relation to its neighbours once is advected).

The original VOF method as proposed by Hirt and Nichols (1981) presents slight changes compared to that applied in several codes such as the two employed in this thesis. The original VOF dictated the inclusion of three elements. The first is the definition of the volume fraction function, with values equal to 1 in one of the phases and 0 in the other phase. The second is the algorithm which solves the advection equation of the volume fraction function and enables it to define a sharp free surface. The third element was the implementation of free surface boundary conditions. In this original formulation, the VOF was only computed for the liquid phase. That is, in Eq. 4.1 the velocity is always that of the water phase. Bombardelli *et al.* (2001) argued the application of the VOF method with a solver which includes only the first and second elements can be referred to as “partial” VOF method (PVOF). Some of the disadvantages of the PVOF methods are that because the free surface velocities are computed from an average of the velocity at the two phases, it could present inaccuracies. In addition, the velocity in the air phase is not relevant and hence it could be considered a misuse of computational resources. The two solvers utilised in this thesis, ANSYS Fluent and OpenFOAM, both utilise a VOF formulation based on

the first two elements, and they do not present a boundary condition at the interface and solve the VOF for both phases. Consequently, the methods applied could be referred to as “partial” VOF.

Various algorithms have been proposed in order to locate the exact position of the free surface in the VOF formulation. These can be broadly divided into algebraic and geometric reconstruction schemes. Algebraic reconstruction schemes solve the transport equation of the volume fraction (Eq. 4.1) by employing a combination of discretisation schemes. Geometric schemes utilise a representation of the interface by using planes (in 3D) or lines (in 2D) and these are advected according to a reconstruction made from the volume fraction function flux. It has been recognised that geometric reconstruction methods are capable of providing very accurate representations of the free surface. However, in the 3D case they present significantly higher computational requirements than algebraic reconstruction techniques. In addition, geometric schemes require, in most occasions, structured meshes. Generally geometric schemes available in most CFD packages either fail or do not perform satisfactorily with unstructured meshes. In the next subsections, four of the most widely used interface capturing algorithms are described, the three first of which are employed in this thesis.

4.2.2. Interface Capturing Schemes

4.2.2.1. Piecewise Linear Interface Construction

The Piecewise Linear Interface Construction (PLIC) was first proposed by Youngs (1982). And several later versions have been developed based on the same principle. Some examples include Rider and Kothe (1998), Pilliod and Puckett (2004) or Aulisa *et al.* (2007). For unstructured meshes some PLIC approaches have also been developed, for example Huang *et al.* (2012).

The method consists in the construction of the interface by utilising planes derived from the solution of the convective term of Eq. 4.1. In order to locate the position of the interface in the cells where $0 < \alpha < 1$, the fluxes of α are calculated. The interface is reconstructed by fitting a plane normal to the flux quantity of the α field. The normal vector to each plane is calculated from the gradient computation of α . An example distribution of the volume fraction field is shown on Figure 4.2 a) and the PLIC reconstruction based on normal planes is shown on Figure 4.2 b). The translation of each plane within each control volume needs to be determined so that the volume between the plane and the cell boundaries is equal to the value of α at the cell centre. Volume conservation is enforced through the translation value. An iterative method is implemented in order to obtain a continuous free surface and minimise discontinuities in the values of α between adjacent cells. The volume fraction is advected in one direction at a time (first x, then y then z) in order to accurately advect the fluid volume from one cell to the other. The final reconstructed free surface is shown on Figure 4.2 c).

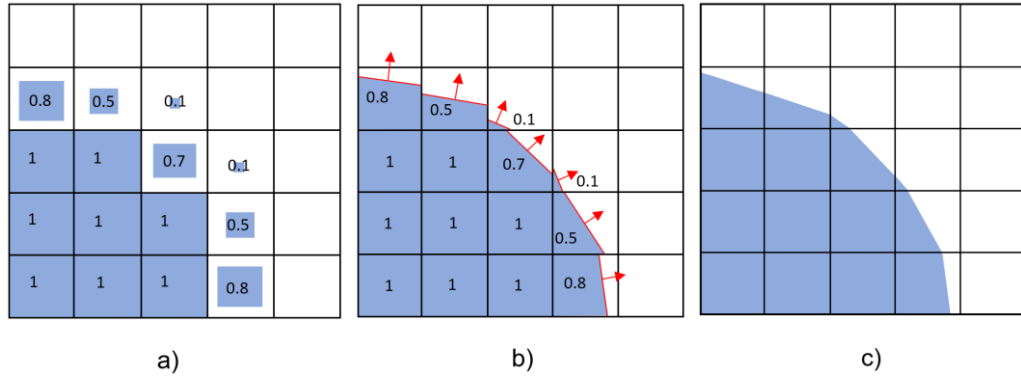


Figure 4.2: a) Example distribution of the α field in cells; b) Reconstruction of the interface utilising the normal vectors shown in red; c) Final free surface reconstruction after the iterative process

The PLIC approach is the one employed in the so-called “Geometric Reconstruction Scheme” algorithm available in ANSYS Fluent.

4.2.2.2. Compressive Interface Capturing Scheme for Arbitrary Meshes

The Compressive Interface Capturing Scheme for Arbitrary Meshes (CICSAM) consists in an algebraic scheme initially proposed by Ubbink and Issa (1999) where the method is described with comprehensive details. This scheme was designed mainly in the attempt to create an interface capturing methodology capable to deal with unstructured meshes providing a sharp interface whilst ensuring physical (bounded) values of the volume fraction function.

This method is based on the Convection Boundedness Criterion (CBC) originally proposed in Gaskell and Lau (1988) within the Normalised Variable Diagram (NVD) framework dependent on the Courant number (CFL) condition (Leonard 1991). Normalised values of α are calculated and bounds for the interpolated values of α at the cell faces are obtained. The normalised volume fraction at a generic cell face f defined between a donor and an acceptor cell is defined in Eq. 4.4.

$$\tilde{\alpha}_f = \frac{\alpha_D - \alpha_U}{\alpha_A - \alpha_U} \quad 4.4$$

Where α_D and α_U are the values of the volume fraction at the donor, acceptor and upwind cell centres.

In this scheme, in the cells with presence of interface, both fluids are treated as one, sharing the same velocity. In order to discretise the second term of Eq. 4.1, the CICSAM employs a combination of compressive schemes which ensures local boundedness of α and maintains sharpness of the interface. This is performed by switching from one differencing scheme to the other (that ensuring boundedness and that ensuring sharpness) by using a weighting factor, γ_f , which is calculated based on the angle between the interface and the direction of the fluid motion. The first differencing scheme is based on the CBC criterion. The second scheme consists in the so-called ULTIMATE QUICK (UQ) presented in Leonard (1991) based on an adaptation of the QUICK scheme, which is suggested to present less smear of the interface than the upwind differencing scheme.

The interpolated value of the normalised volume fraction at a cell face $\tilde{\alpha}_f$ will therefore be dependent on the weighting factor γ_f , as described in Eq. 4.5.

$$\tilde{\alpha}_f = \gamma_f \tilde{\alpha}_{fCBC} + (1 - \gamma_f) \tilde{\alpha}_{fUQ} \quad 4.5$$

The compressive schemes which ensure boundedness, can present instabilities and non-physical behaviour due to the scheme using the upper limit of the boundedness range (Hirt and Nichols 1981). The CICSAM scheme overcomes this issue by solving the transport of α two times, which is referred to as the “predictor-corrector step”.

4.2.2.3. Multidimensional Universal Limiter with Explicit Solution

The multidimensional Universal Limiter with Explicit Solution (MULES) is the scheme available in all versions of the OpenFOAM platform. The MULES scheme ensures boundedness and consistency by including an artificial compressive term for the discretisation of volume fraction transport equation which is only active at the interface (Greenshields 2017). Such algorithm offers the possibility to be completely explicit, where a more strict value needs to be applied in the maximum Courant number to limit the time step, or semi-implicit, which allows a greater time step and faster computation of the solution. The default of this algorithm is semi-implicit to enhance computational speed.

This scheme is based on the two-fluid Eulerian model where, the velocity of each phase is calculated based on the value of α . Hence, it is possible to write the expression of the velocity at the interface as a weighted average, as indicated in Eq. 4.6.

$$u = \alpha u_w + (1 - \alpha) u_a \quad 4.6$$

Where u_w and u_a denote velocities of the phase water and air respectively.

When Eq. 4.6 is substituted in the transport equation of α , the form outlined in Eq. 4.7 is obtained.

$$\frac{\partial \alpha}{\partial t} + \nabla(u\alpha) + \nabla[u_c \alpha(1 - \alpha)] = 0 \quad 4.7$$

Where u_c is the so-called “compression velocity” and is defined as $u_c = u_w - u_a$. Consequently, the transport equation presents an additional term, referred to as the “compression term”. This term is only in use at the interface and vanishes for values of α equal to 1 and 0. The compressive term is claimed to improve the interface resolution, and therefore there is no need to employ a further scheme to solve the convective term. The diffusion introduced by the discretisation of the convective term can be minimised by the discretisation of the compression term (Berberovic *et al.* 2009).

4.2.2.4. High Resolution Interface Capturing

The High Resolution Interface Capturing (HRIC) scheme was proposed by Muzaferija *et al.* (1998) in an attempt to simplify the CICSAM algorithm. Similarly to the CICSAM, this method is also defined within the NVD and hence utilises normalised variables. The normalised value of the volume fraction function at the cell face is estimated employing an upwind and downwind scheme.

A weighting factor is applied which depends on the angle between the interface and the direction of the fluid motion in order to switch between one scheme and the other. To prevent instabilities in the combination of the upwind and downwind schemes, a correction in respect of the CFL number is enforced. Therefore, the main differences between the HRIC and the CICSAM schemes are the point at which the CFL condition is enforced and the discretisation schemes employed (Waclawczyk and Koronowicz 2008).

4.3. The SPH Method

4.3.1. Introduction

The SPH is the oldest meshless particle-based method (Belytschko 1996) and was originally developed to solve astrophysical problems. SPH was first proposed as a tool to model free surface flows in Monaghan (1994). The Lagrangian nature of this method simplifies the modelling of free surface flows in a number of aspects. The absence of grid enables more flexibility on the treatment of the moving boundaries, with no need to employ interface capturing schemes. The SPH technique has been successfully applied and verified in several dam break cases, for example Ferrari *et al.* (2009a), Ghadimi *et al.* (2012) or Roubtsova and Kahawita (2006). Nevertheless, as previously noted, the SPH method still presents a number of uncertainties such as the implementation of physically realistic boundary conditions or the penetration of fluid particles into boundaries. Therefore, validation of the SPH approaches are still of remarkable importance.

Two approaches have been formulated to model fluid incompressibility in SPH. The first and most common is the weakly compressible algorithm (WCSPH) which uses an explicit time-stepping method. The second approach is the incompressible SPH (ISPH) which is a semi implicit approach. Some studies demonstrated that the ISPH outperforms the WCSPH in particular cases, for example Bøckmann *et al.* (2012) or Lee *et al.* (2008). However, the two approaches have not been compared in extensive detail. Hughes and Graham (2010) developed an enhanced WCSPH algorithm and obtained equivalent or improved results to those using ISPH for dam break cases. The code implemented in this thesis is based on the WCSPH approach.

A detailed description of the SPH method can be found in Monaghan (1988) and Monaghan (1994). The SPH method is based on an interpolation technique that uses movable points in space to represent fluid properties. Such points are referred to as particles. The field functions (velocity, pressure etc.) are represented with integral expressions and approximate the fluid by involving a limited number of surrounding particles. The values carried by each particle are spread in space by a smoothing kernel, which consists in a weighting function that uses the values of the nearest neighbouring particles. The main principle consists in the representation of a generic function A at a position vector \mathbf{r} , in a form of an integral interpolant as indicated in Eq. 4.8.

$$A(\mathbf{r}) = \int A(\mathbf{r}') W(\mathbf{r} - \mathbf{r}', h) d\mathbf{r}' \quad 4.8$$

Where h is the smoothing length of the weighting function and $W(\mathbf{r} - \mathbf{r}', h)$ is the weighting function. The approximation of function A at a generic interpolation point a , can be expressed in algebraic terms as per Eq. 4.9.

$$A(\mathbf{r}) = \sum_b m_b \frac{A_b}{\rho_b} W_{ab} \quad 4.9$$

Where the neighbouring particles utilised for the summation are referred to by the term b (here only one neighbouring particle is used for illustration purposes) and their inclusion is dictated by the length of the kernel h . The terms m_b and ρ_b refer to the mass and density of particle b respectively. Therefore, for the position vector $\mathbf{r} = \mathbf{r}_a$ the kernel between particles a and b will have the form of: $W_{ab} = W(r_a - r_b, h)$. The kernel function can have several forms, for example Gaussian, quadratic, cubic or quintic, also referred to as Wendland kernel, from Wendland (1995).

The cubic spline and the Wendland kernel are some of the most widely used kernel functions. These are expressed by the non-dimensional distance between particles, $q = \frac{r}{h}$ where r is the distance between particles and the smoothing length h corresponds to the radius of influence of the kernel. The definition of the cubic spline is indicated in Eq. 4.10 (Gomez-Gesteira *et al.* 2012).

$$W(r, h) = \alpha_D \begin{cases} \left(1 - \frac{3}{2}q^2 + \frac{3}{4}q^3\right) & 0 \leq q \leq 1 \\ \frac{1}{4}(2 - q)^3 & 0 \leq q \leq 1 \\ 0 & q \geq 2 \end{cases} \quad 4.10$$

Where $\alpha_D = \frac{10}{7\pi h^2}$ in the 2D and $\alpha_D = \frac{1}{\pi h^3}$ in 3D.

The Wendland spline is defined by Eq. 4.11.

$$W(r, h) = \alpha_D \left(1 - \frac{q}{2}\right)^4 (2q + 1) \quad 0 \leq q \leq 2 \quad 4.11$$

Where $\alpha_D = \frac{7}{4\pi h^2}$ in the 2D and $\alpha_D = \frac{21}{16\pi h^3}$ in the 3D case.

4.3.2. Fundamental Equations

In the SPH technique, the terms in the previously characterised constitutive equations for fluids are expressed in the SPH formulation. The main difference in the mass conservation equation is that in the SPH method used here, the fluid is considered to be weakly compressible. This enables a link between the density and the pressure and allows the use of the equation of state to calculate the pressure field. The SPH form for the mass conservation equation is described in Eq. 4.12

$$\frac{d\rho_a}{dt} = \sum_b m_b \mathbf{v}_{ab} \nabla_a W_{ab} \quad 4.12$$

The various terms in the momentum conservation equation are similarly expressed in the SPH formulation.

There are a number of alternatives to express the diffusion term in the momentum equation. The artificial viscosity, which is the simplest approach defined by Monaghan (1994) is introduced by the artificial viscosity term γ_{ab} . The viscosity term has the expression outlined in Eq. 4.13

$$\gamma_{ab} \begin{cases} \frac{-\theta C_{ab} \mu_{ab}}{\rho_{ab}} & \mathbf{v}_{ab} \mathbf{r}_{ab} < 0 \\ 0 & \mathbf{v}_{ab} \mathbf{r}_{ab} > 0 \end{cases} \quad 4.13$$

Where θ is a constant parameter which depends on the problem, $\mathbf{r}_{ab} = \mathbf{r}_a - \mathbf{r}_b$, $\mathbf{v}_{ab} = \mathbf{v}_a - \mathbf{v}_b$, $\mu_{ab} = \frac{h \mathbf{v}_{ab} \mathbf{r}_{ab}}{r_{ab}^2 + \eta^2}$, and $\eta^2 = 0.01 h^2$. And where C_{ab} is the mean speed of sound, which has the following form: $C_{ab} = 0.5(C_a + C_b)$.

The pressure gradient is expressed as per Eq. 4.14.

$$\left(-\frac{1}{\rho} \nabla P \right)_a = - \sum_b m_b \left(\frac{p_b}{\rho_b^2} + \frac{p_a}{\rho_a^2} \right) \nabla_a W_{ab} \quad 4.14$$

The momentum equation will have the form outlined in Eq. 4.15.

$$\frac{dv_a}{dt} = - \sum_b m_b \left(\frac{p_b}{\rho_b^2} + \frac{p_a}{\rho_a^2} + \gamma_{ab} \right) \nabla_a W_{ab} + g \quad 4.15$$

The artificial viscosity consists in the most widely used approach because of its simplicity. Alternatively, viscous stresses can be formulated using the so-called laminar viscosity approach or the laminar viscosity and sub-particle scale (SPS) turbulence. Comprehensive details on such approaches can be found in Gomez-Gesteira *et al.* (2012).

4.4. Application of the VOF and SPH

4.4.1. Introduction

In this section, the two numerical approaches described in the last two sections will be applied to simulate an experimental dam break case. The VOF method is applied on two different CFD packages: the commercial solver ANSYS Fluent (ANSYS 2017) and the open source platform OpenFOAM (Greenshields 2017). The Lagrangian meshless particle-base SPH is implemented on the open source code DualSPHysics described in Crespo *et al.* (2015).

The first part of this section is aimed to investigate the capability of 2D and 3D CFD VOF models to predict the experimental free surface flow situation in the two solvers. A mesh independence study is also conducted for the 2D and 3D cases and this is followed by a sensitivity analysis performed to investigate the influence of various numerical implementations in the Fluent 2D model.

The second part of this section concerns the implementation of 2D and 3D SPH models to reproduce the experimental dam break flow. In this case the influence of a number of code parameters to the numerical results is also evaluated. A study is conducted to analyse the influence of the number of particles (and initial separation) for both the 2D and the 3D SPH cases.

A sensitivity analysis with respect to a several numerical implementations is also performed for the 2D case.

The chosen experimental case consists in the study conducted by Biscarini *et al.* (2010) which provides sufficient experimental data to validate the different modelling approaches and analyse the associated numerical implementations. The experiment of the dam break over a triangular obstacle case was undertaken at the Université Catholique de Louvain (UCL) at the Laboratory of the Civil Engineering Department. The setup consists of a rectangular channel 5.6 m long and 0.5 m wide. The tank contains two water pools and a symmetrical triangular obstacle. The water in the upstream reservoir is released to simulate a dam break, flowing downstream to the triangle and to the second pool. The first reservoir is 2.39 m long and has a water level of 0.111 m. The triangular obstacle has a height of 0.065 m and it is 0.9 m long; located at $x = 4$, its peak is at $x = 4.45$. The water level at the downstream reservoir is 0.025 m. The setup is shown in Figure 4.3. The triangular shape of the obstacle as well as the existence of a pool of water downstream of the obstacle make this case an interesting free surface flow situation to initially test the CFD solvers on and examine their performance.

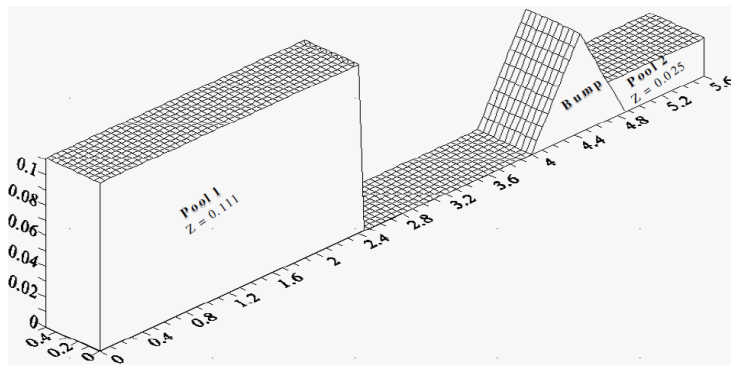


Figure 4.3: Initial conditions for the bump test case from Biscarini *et al.* (2010)

Available experimental data consist in experimental photographs and free surface depth profiles at 1.8 s, 3 s, 3.7 s, and 8 s after the dam break.

4.4.2. VOF Modelling

4.4.2.1. Meshing

Simulations were undertaken in Fluent and in OpenFOAM using a total of 7 meshes to investigate mesh independence. Meshes were created using the ANSYS Workbench Meshing tool and they were then exported to OpenFOAM. A summary of the meshes created and simulations run with each of the CFD packages is shown in Table 4.1. Parallel simulations were conducted on 8 HPC CPU processors.

Table 4.1: Summary of meshes used for the simulation of the dam break flow

Mesh ID	Number of Elements		Cell size x [m]	Cell size y [m]	Cell size z [m]	Run in Fluent		Run in OpenFOAM	
	2D	3D				2D	3D	2D	3D
1	12600	316000	2×10^{-2}	2×10^{-2}	5×10^{-3}	Y	Y	Y	Y
2	26040	885360	1.5×10^{-2}	1.5×10^{-2}	3×10^{-3}	Y	Y	N	Y
3	50400	2.52M	1×10^{-2}	1×10^{-2}	2.5×10^{-3}	Y	Y	Y	N
4	67000	3.35M	1×10^{-2}	1×10^{-2}	2×10^{-3}	Y	Y	Y	Y
5	122880		6×10^{-3}	-	1.7×10^{-3}	Y	N	N	N
6	491520		3×10^{-3}	-	8×10^{-4}	Y	N	Y	N
7	1,96M		1.5×10^{-3}	-	4×10^{-4}	Y	N	N	N

A “bias factor” was included in the z (vertical) direction of the meshes to increase resolution in the area near the base. A thin layer of flow was predicted to occur and hence the bias was put in place to enhance the capture of the flow features. An example section of a mesh outline is shown in Figure 4.4.

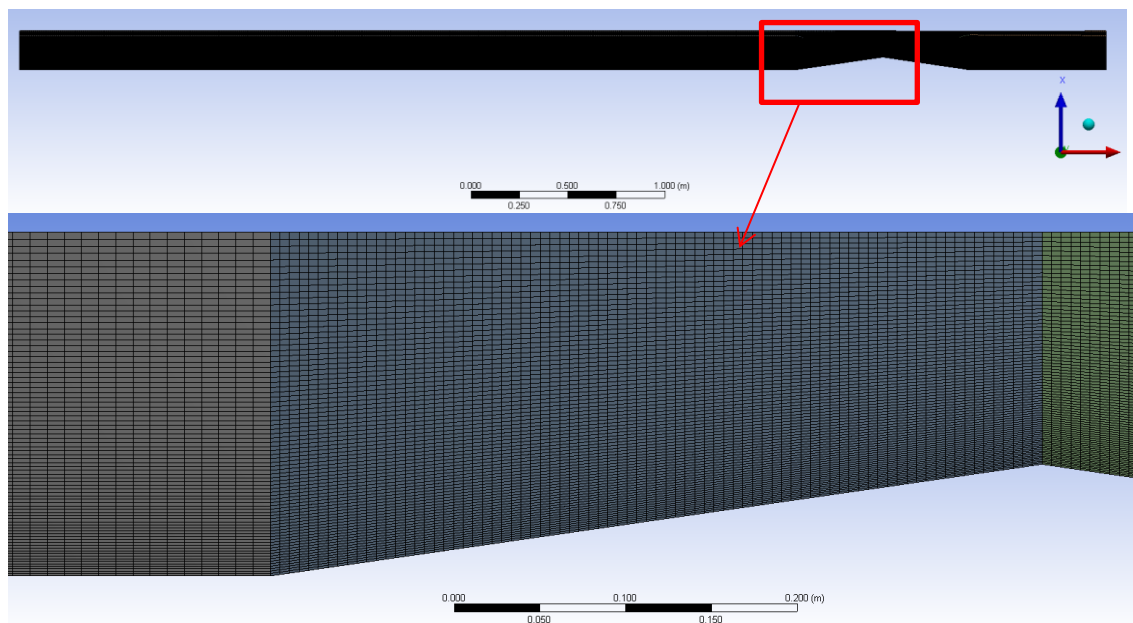


Figure 4.4: Example mesh and enhanced scale image of the mesh bias in the z direction

4.4.2.2. Flow Equations

Simulations were conducted using a collocated FVM discretisation scheme. The constitutive equations solved in the 2D and 3D simulations consist in the 2D and 3D RANS equations defined in Eq. 3.22 and Eq. 3.26 to 3.28.

All fluid properties utilised were those corresponding to a temperature of 20 °C and are presented in Table 4.2.

Table 4.2: List of fluid properties utilised in the simulations for the two phases

Water dynamic viscosity [m^2/s]	Air dynamic viscosity [m^2/s]	Air density [kg/m^3]	Water density [kg/m^3]	Water surface tension [N/m]
1×10^{-6}	1.48×10^{-5}	1.2	1000	0.07

4.4.2.2.1. Turbulence Modelling

Turbulence was modelled with the RANS Standard $k - \epsilon$ model with standard wall functions. This model was chosen since it has been widely implemented for the modelling of industrial flows and

in particular hydraulic modelling. The SST $k - \omega$ model is implemented to test the sensitivity to turbulence model in section 4.4.2.4.1.

4.4.2.2.2. Free Surface Modelling

The free surface was modelled with the VOF multiphase model described in Section 4.2. The free surface was computed at the location where the volume fraction function was equal to 0.5.

4.4.2.3. Numerical Implementations

A CFD Case was set up in Fluent generally implementing most of the default settings to examine the initial model's performance, subsequently some of the most relevant implementations were adjusted to observe their impact. Simulations were conducted for the different meshes as per Table 4.1 using variable time stepping with a global CFL (Courant Friedrichs Lewy) number of 1 so that the CFL condition presented on Eq. 4.16 is accomplished.

$$\frac{|U|\Delta t}{\Delta x} = CFL \leq 1 \quad 4.16$$

Where U is the velocity magnitude, Δt is the time step and Δx is the cell size.

The Fluent default global CFL value for the explicit VOF is 2 where the global time step is calculated by implementing a specific flux-based definition of the CFL number described in the solver's user guide (ANSYS 2009). The interface capturing scheme implemented was the PLIC algorithm. The pressure-velocity algorithm used was PISO. The case was set up and run for the 2D meshes 1 to 7 and the 3D meshes 1 to 4 using the same numerical settings. The initial conditions set up is shown in Figure 4.5.



Figure 4.5: Setup of initial conditions in Fluent

The case was set up in OpenFOAM using similar numerical implementations to those applied in Fluent. The interFoam solver was utilised with its available interface capturing scheme MULES (Greenshields 2017) with a volume fraction CFL number of 0.2 as recommended in Roenby *et al.* (2016) to ensure accuracy for this scheme. The default global CFL number restriction was 0.5 which was the default implemented in this solver. The PISO algorithm was implemented for pressure-velocity coupling. The initial conditions set up is equivalent to that in Fluent and is shown on Figure 4.6. Simulations were conducted using 2D meshes 1, 3 and 4. 3D simulations were conducted using meshes 1, 2 and 4, as detailed in Table 4.1.

Boundary conditions for the hard boundaries (walls and base) were no-slip. The upper boundary of the computational domain was defined as pressure outlet with atmospheric pressure.

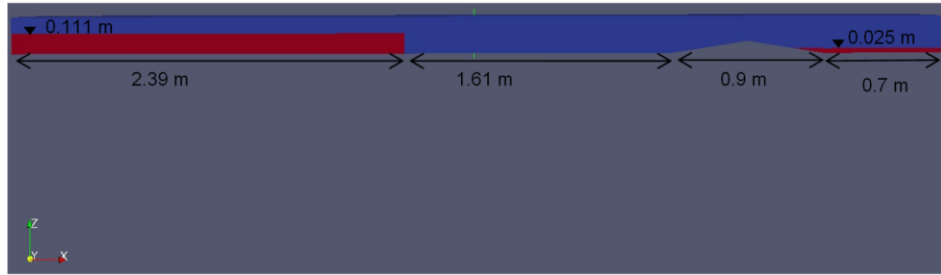


Figure 4.6: Setup of initial conditions in OpenFOAM

4.4.2.4. Experimental and Numerical Results

4.4.2.4.1. Fluent 2D VOF

As indicated in Table 4.1, 2D CFD VOF simulations were undertaken using various meshes of different resolution to assess cell size sensitivity of the model. The photograph of the experiment at 1.8 s after the dam break and the volume fraction contour plots for 1.8 s are shown on Figure 4.7.

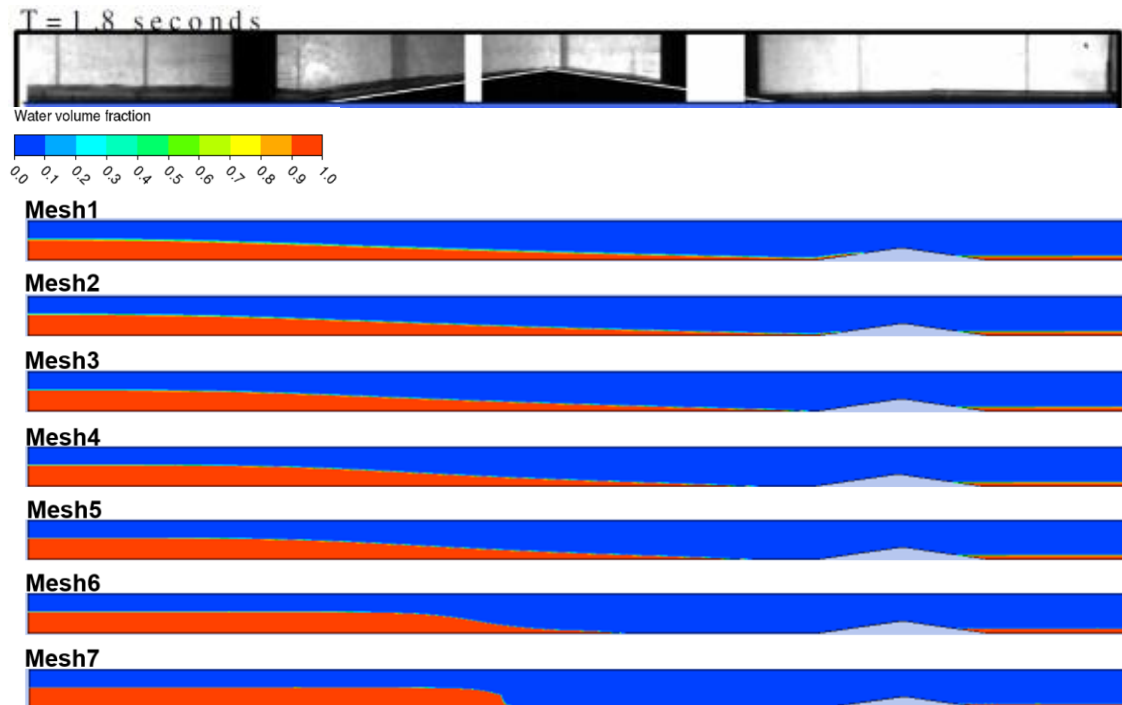


Figure 4.7: Experimental photograph (top) and contour plots showing the water volume fraction at 1.8 s for the 7 meshes of increasing resolution

At 1.8 s after the dam break, the experimental photograph shows that the flow has reached the top of triangle. The numerical predictions show this behaviour is not well reproduced. The computed results present a delay in the flow for all cases which becomes larger with increasing mesh resolution. The observed delay did not improve with simulation run time and persisted at later simulation times.

Sensitivity analyses were conducted in respect of various numerical implementations in the Fluent 2D VOF model. The different solver settings and scenarios modelled are summarised in Table 4.3.

Table 4.3: Summary of numerical implementations applied in the sensitivity analysis

Numerical Implementation	Original Case	Case I	Case II	Case III	Case IV
Turbulence Model	$k - \epsilon$	SST $k - \omega$	$k - \epsilon$	$k - \epsilon$	$k - \epsilon$
Multiphase Model	Standard VOF	Standard VOF	Eulerian-Eulerian	Standard VOF	Standard VOF
Interface Tracking Scheme	PLIC	PLIC	PLIC	CICSAM	PLIC
Bed	Dry	Dry	Dry	Dry	Wet

Sensitivity to the various solver implementations was tested with Mesh 3 and Mesh 6. The various implementations consist in the SST $k - \omega$ turbulence model, the CICSAM interface capturing scheme and the application of the Eulerian-Eulerian multiphase model to compare its performance against the VOF. In addition, the dam break case was modelled over a wet bed by including a thin layer of water between the upstream reservoir and the triangular obstacle. The time series plot of the free surface at the peak of the obstacle for the above listed cases is shown in Figure 4.8 a) and b) for Mesh 3 and Mesh 6 respectively.

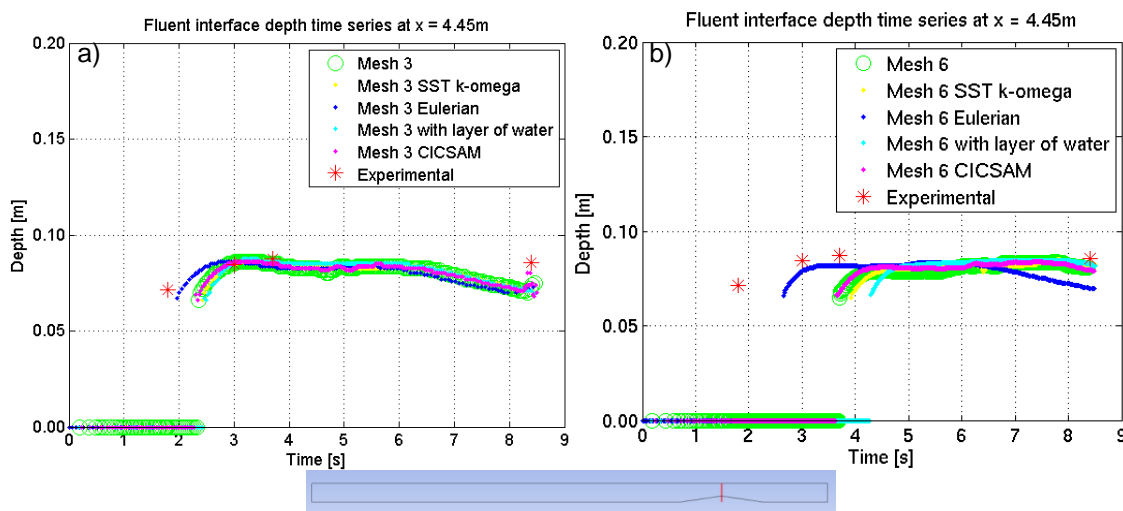


Figure 4.8: a) Free surface depth time series with different numerical implementations at the top of the obstacle on Mesh 3 and b) using Mesh 6

When applying the SST $k - \omega$ model the simulation results are very comparable to those using the $k - \epsilon$ model. The simulation using the CICSAM algorithm presents equivalent flow features to that using the PLIC scheme. Both interface capturing schemes predict similar and appropriate results for this type of problem. The Fluent Eulerian-Eulerian multiphase model was implemented in Fluent in conjunction with the “multi-fluid VOF” model which allows the use of interface tracking schemes. As shown in Figure 4.8, the predicted flow using the Fluent Eulerian-Eulerian model shows less delay than that using the VOF model. The free surface depth is well predicted in all cases. There is more time difference between simulations using VOF and Fluent Eulerian-Eulerian when resolution is increased to Mesh 6.

Simulation results with a thin layer of water show further increase in delay compared to the original setup. Crespo *et al.* (2008) conducted a similar analysis on a dam break case for dry and wet beds using a Lagrangian approach. It was found that initially the interaction between the dam break flow with the water layer slows down the horizontal velocity, and this makes the wave front to be slower than that of the dry bed. In time, the dry bed would show the slowest propagation along the channel. This is consistent with results shown in Figure 4.8 where there is an initial time difference between the dry and the wet beds and at later stages results converge.

To further investigate the observed delay on the numerical results for increasing resolution, the time stepping method was examined. Simulations with meshes 1 to 6 were conducted using fixed time stepping to compare against the previously run using variable time steps. The time step size was chosen by using an iterative method with observations of the simulation results and decreasing the time step for increasing mesh resolution. A CFL number of approximately 0.5 was observed to produce optimum results and closest to the experimental measurements. For a fixed time step the CFL values varied along the simulation time depending on the flow features occurring. The time step sizes were adjusted to achieve CFL values from 0.1 to 0.5 in all simulations. A summary of the chosen time step size for each mesh is shown on Table 4.4.

Table 4.4: Meshes used for simulations with fixed time stepping and time step sizes

2D Mesh ID	Number of Elements	Cell size x [m]	Cell size z [m]	Time Step Size [s]
1	12600	2×10^{-2}	5×10^{-3}	0.007
2	26040	1.5×10^{-2}	3×10^{-3}	0.003
3	50400	1×10^{-2}	2.5×10^{-3}	0.001
4	67000	1×10^{-2}	2×10^{-3}	0.001
5	122880	6×10^{-3}	1.7×10^{-3}	0.0005
6	491520	3×10^{-3}	8×10^{-4}	0.0001

The volume fraction contour plots using meshes 1 to 6 with fixed time stepping at 1.8 s after the dam break are shown in Figure 4.9.

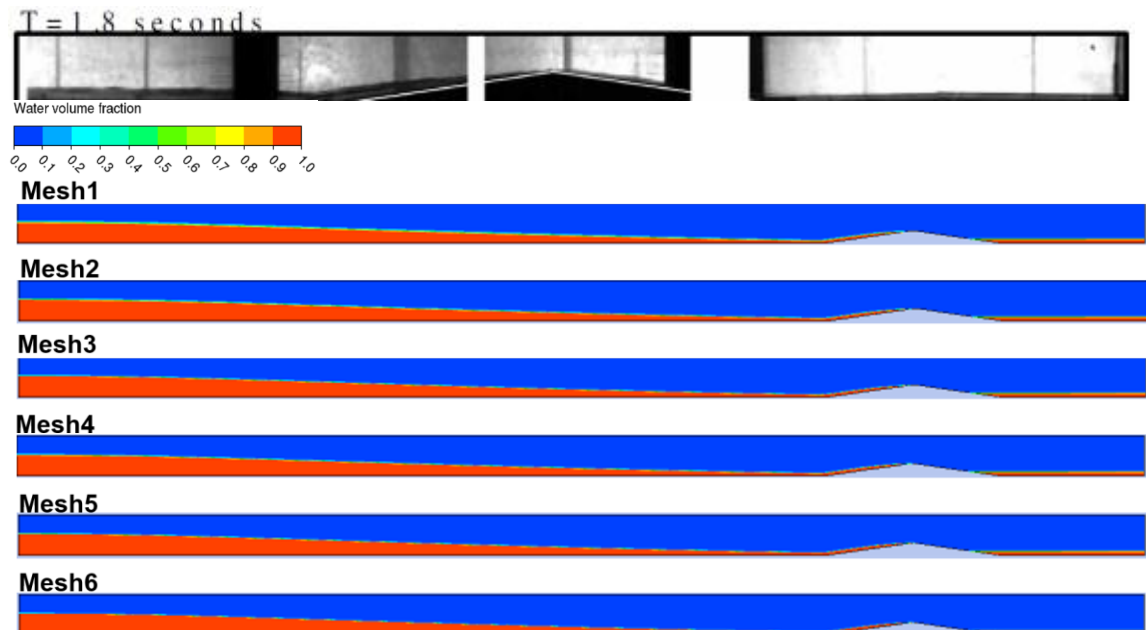


Figure 4.9: Experimental photograph (top) and contour plots showing the water volume fraction at 1.8 s for the 6 meshes of increasing resolution using fixed time stepping

At 1.8 s after the dam break, the numerical results using fixed time stepping show close agreement with the experimental photograph and consistent results for increasing resolution. The flow profile does not present delay in any simulation.

Figure 4.10 presents the experimental photograph and the volume fraction contour plots for the 6 meshes of increasing resolution using fixed time stepping at 3 s after the dam break. At this simulation stage, the experimental data indicates that the front of the wave has reached the top of the triangular obstacle and the flow is split into two parts: one reflecting upstream and the other one overtopping the obstacle. The part of the wave which overtopped the peak of the triangle has

reached the second pool. The 2D numerical results using fixed time stepping are capable of accurately reproducing the flow situation observed in the experiment. The numerical predictions show an equivalent pattern for increasing resolution and there is no delay observed in any of the simulation predictions.

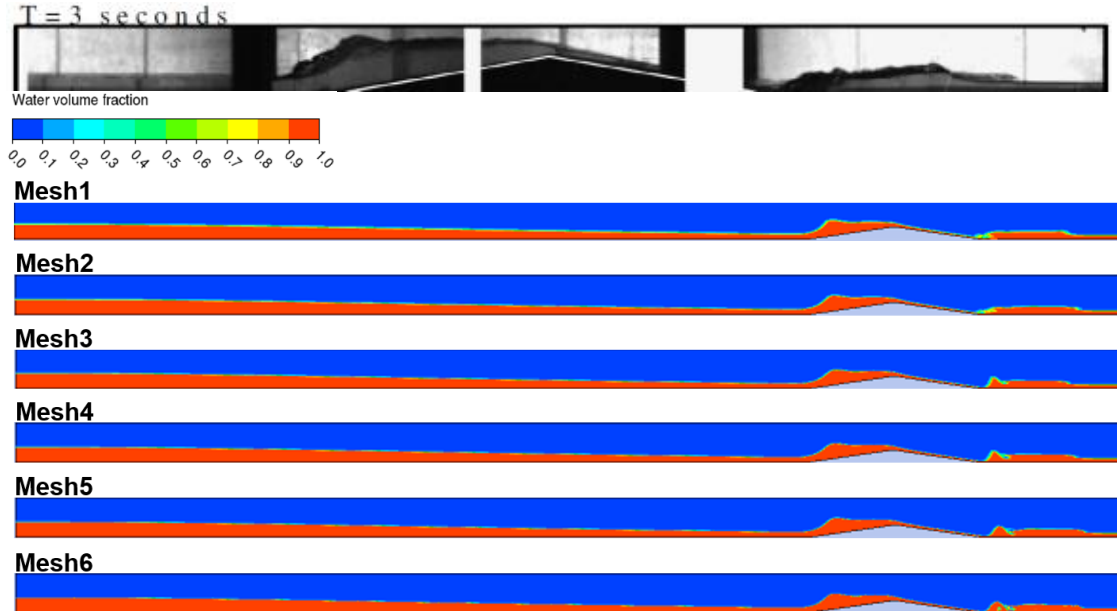


Figure 4.10: Experimental photograph (top) and contour plots showing the water volume fraction at 3 s for the 6 meshes of increasing resolution using fixed time stepping

Figure 4.11 a) and b) present the free surface depth at the top of the obstacle and at 3.5 m from the upstream wall of the upstream pool respectively. The simulation using Mesh 6 was not computed until the end of the experiment since it is possible to determine any differences in flow time by only running the simulation for the first few seconds. As observed in the volume fraction contour plots, Figure 4.11 a) and b) show that there are no flow time discrepancies between results of different resolution. There is very close agreement between the numerically predicted and the experimental free surface depth. The numerical predictions exhibit mesh independence and the flow characteristics are well captured in all simulations.

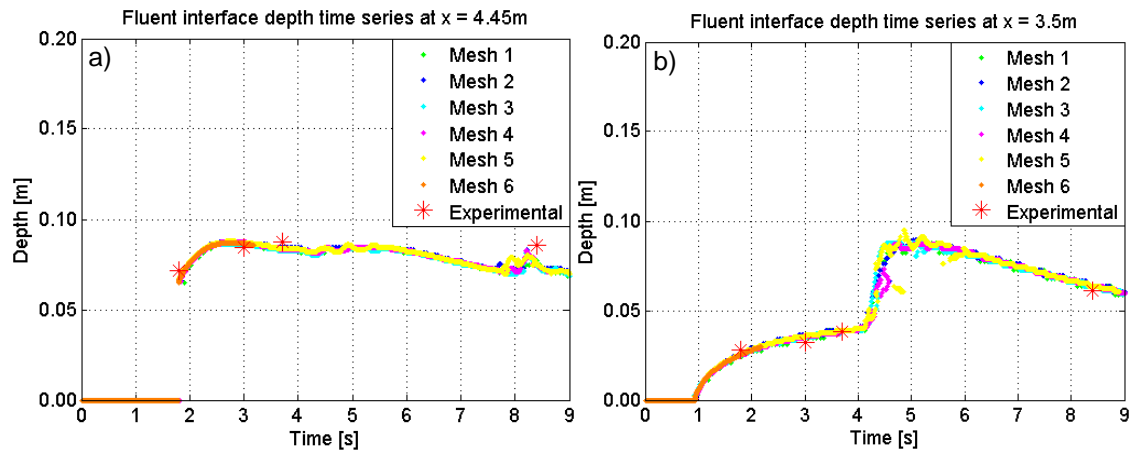


Figure 4.11: Free surface depth time series using 2D meshes 1 to 6 with fixed time stepping at a) the top of the obstacle and b) $x = 3.5$ m

4.4.2.4.2. Fluent 3D VOF

Four 3D meshes were created by adding a third dimension to the 2D meshes 1 to 4 as shown on Table 4.1. This enables the comparison between results of 3D meshes 1 to 4 and their equivalent 2D meshes. All 3D simulations were conducted using the numerical aspects specified in Section 4.4.2.2 and these were not changed at any stage of the analysis. Volume fraction contour plots at 1.8 s for 3D meshes 1 to 4 are shown in Figure 4.12.

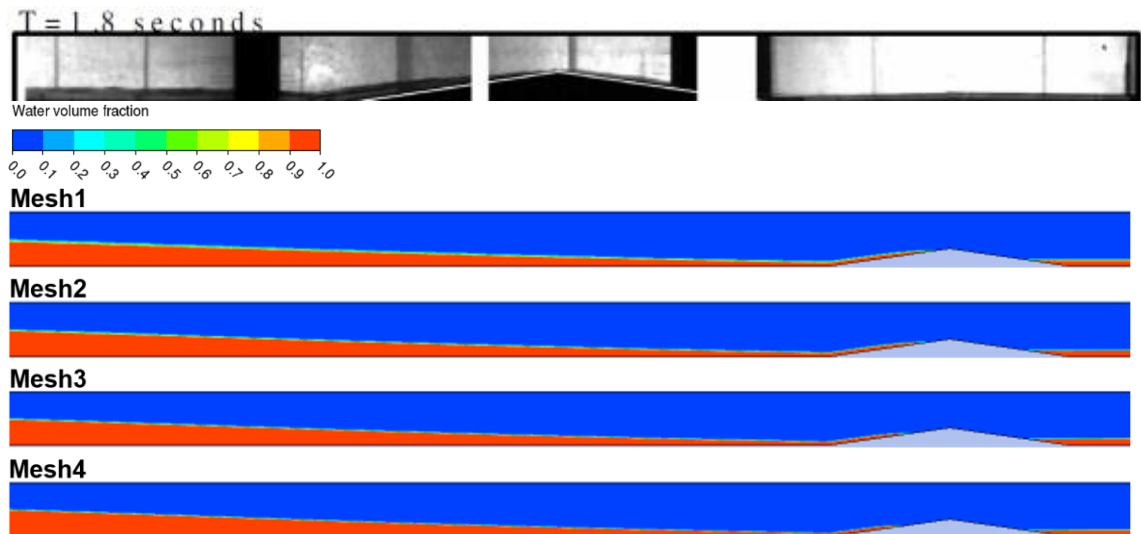


Figure 4.12: Experimental photograph (top) and contour plots showing the water volume fraction at 1.8 s for the 4 meshes of increasing resolution

The simulation predictions at 1.8 s after the dam break are well correlated with the experimental observations and measurements. The numerical results predict the flow to be moving up the upstream face of the triangular obstacle at a similar position to the flow in the experiment. Similarly to the 2D case, simulations reveal a small flow delay which increases with mesh resolution, however the time difference between the four simulations is not significant and is smaller than in the 2D case. Figure 4.13 shows the contour plots of the 3D simulations for meshes 1 to 4 at 3 s.

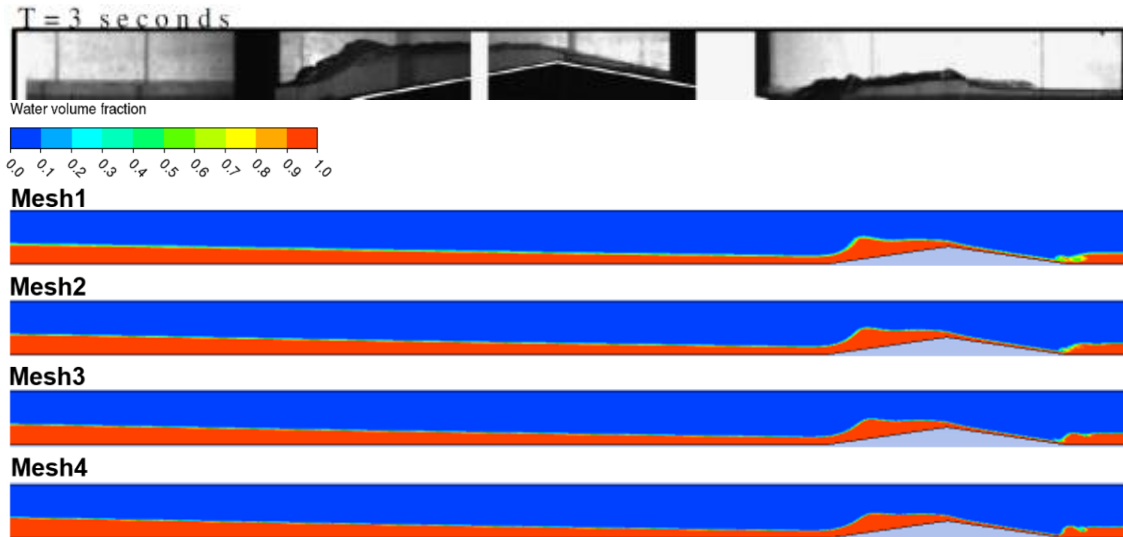


Figure 4.13: Experimental photograph (top) and contour plots showing the water volume fraction at 3 s for the 4 meshes of increasing resolution

At 3 s after the dam break, simulation results using 3D meshes 1 to 4 show close agreement with the experimental data. The numerical simulations successfully capture the flow characteristics observed in the experiment and predictions using different meshes show consistency. Figure 4.14 a) and b) show the interface time series at the peak of the obstacle and at 3.5 m.

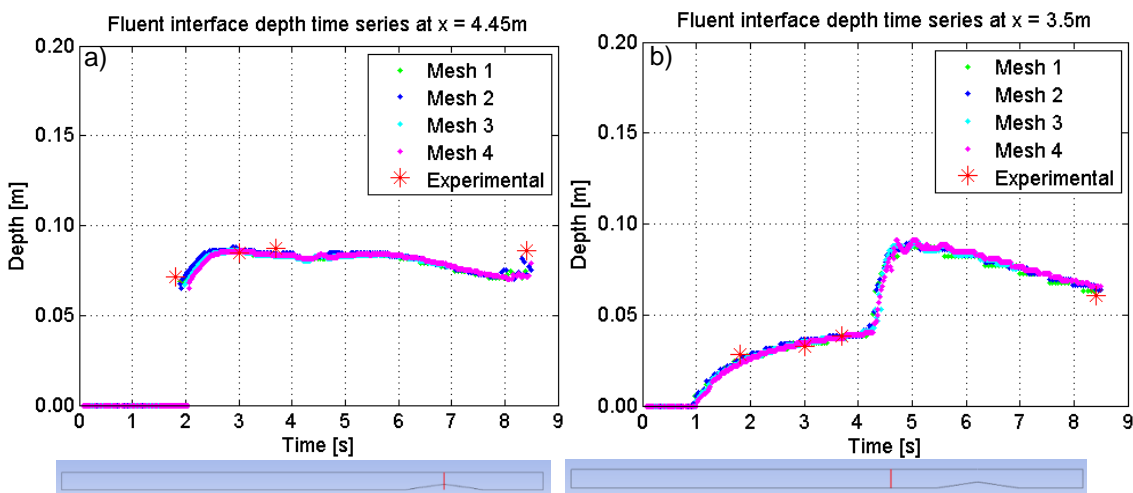


Figure 4.14: a) Free surface depth time series using 3D meshes 1 to 4 at the top of the obstacle and b) at $x = 3.5\text{m}$

Figure 4.14 shows that at early stages of the simulation results present a minimal flow delay compared to the experimental data but they exhibit certain improvement at later simulation times. The flow time difference between simulations using the four different meshes is smaller than 0.2 s. The predicted interface height is accurate for all simulations.

Similarly to the 2D case, the small flow delay is expected to be mitigated with the use of fixed time stepping. In order to confirm such hypothesis, simulations using meshes 1 to 4 were conducted with fixed time stepping. As in the 2D case, the fixed time step size was chosen based on observations of the variable time stepping simulations and decreasing it when appropriate. Informed by the experience on the 2D case, CFL numbers for these simulations were between 0.4 and 1.1. A summary of the fixed time step sizes used is shown on Table 4.5.

Table 4.5: Meshes used for the fixed time step simulations and time step sizes

3D Mesh ID	Number of Elements	Cell size x [m]	Cell size y [m]	Cell size z [m]	Time Step Size [s]
1	316000	2×10^{-2}	2×10^{-2}	5×10^{-3}	0.002
2	885360	1.5×10^{-2}	1.5×10^{-2}	3×10^{-3}	0.002
3	2524000	1×10^{-2}	1×10^{-2}	2.5×10^{-3}	0.001
4	3355000	1×10^{-2}	1×10^{-2}	2×10^{-3}	0.0005

Simulations using Meshes 3 and 4 were not run until the end of the experiment because of the long computational time that this would represent. Conducting the simulations for only several seconds was sufficient to determine whether the flow delay would persist or simulations would improve.

Figure 4.15 presents the volume fraction contour plots at 1.8 s after the dam break for the fixed time stepping simulations of increasing resolution. The contour plots show there is a very good agreement between simulations of different resolution and there is no observed time difference between the simulation results.

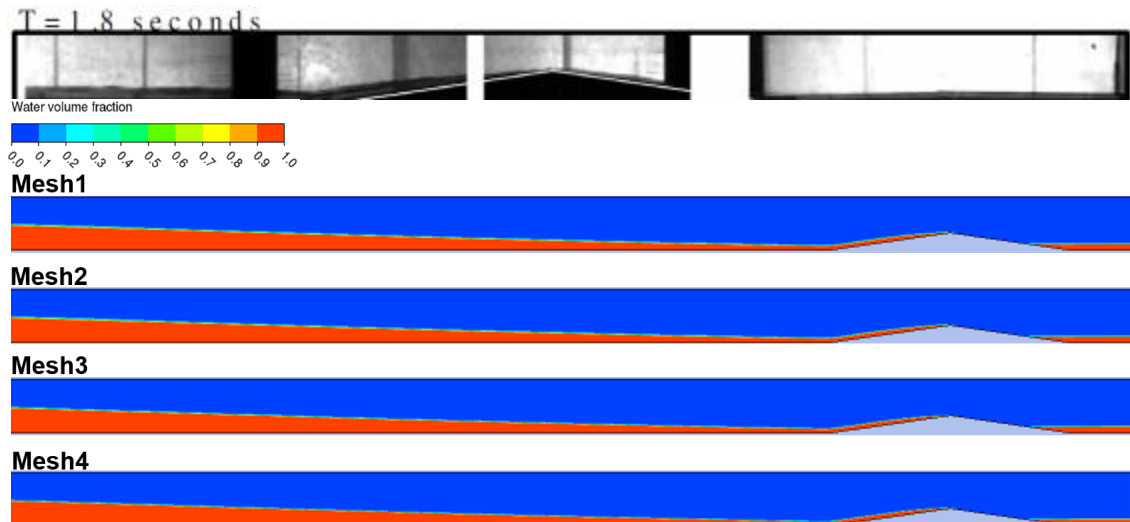


Figure 4.15: Experimental photograph (top) and contour plots showing the water volume fraction at 1.8 s for the 4 meshes of increasing resolution using fixed time stepping

Figure 4.16 indicates the depth of the water free surface at 3.5 m predicted with fixed time stepping. The numerical predictions demonstrate good agreement with the measured data and they do not show flow delay at any point with mesh refinement. The interface height and flow features are well captured and simulations using the meshes of increasing resolution confirm mesh independency.

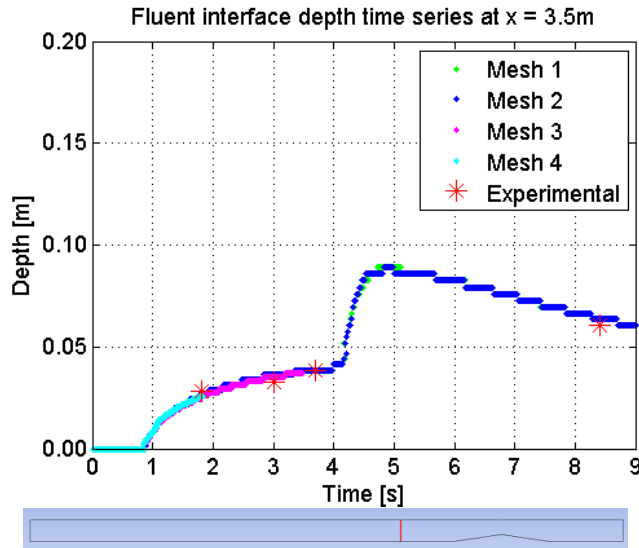


Figure 4.16: Free surface depth time series using 3D meshes 1 to 4 at $x = 3.5$ m implementing fixed time stepping

Similarly to the 2D case, the implementation of fixed time stepping in the 3D simulations provides significantly accurate results with no flow delay occurring in the simulations.

4.4.2.4.3. OpenFOAM 2D VOF

2D VOF simulations were undertaken in OpenFOAM and a mesh sensitivity analysis was conducted using meshes 1, 3, 4 and 6. Figure 4.17 shows the 2D numerical results at 1.8 s after the dam break. The numerical results using the four 2D meshes at 1.8 s after the dam break are well correlated with the experimental flow, where the front wave has reached the top of the obstacle. The numerical results present consistency in the interface features and the flow times for the different mesh resolutions.

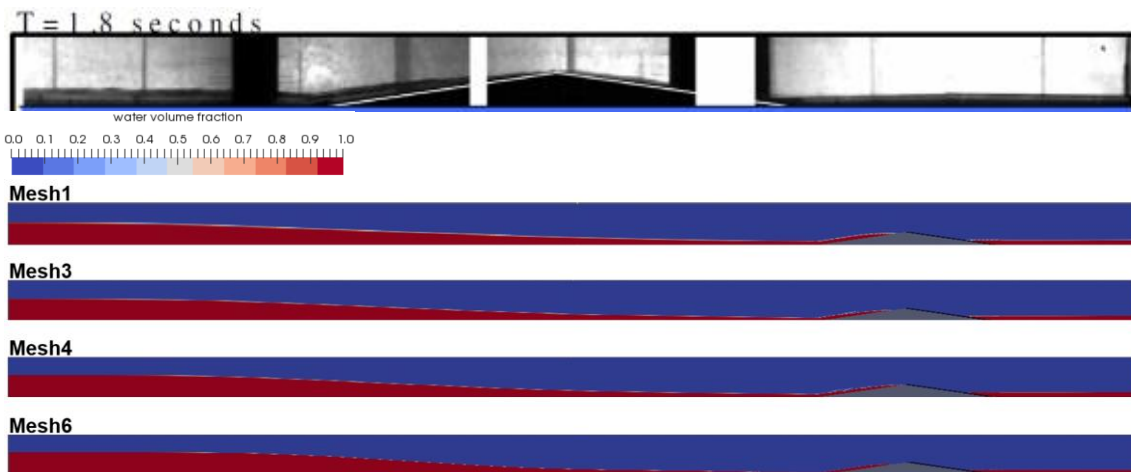


Figure 4.17: Experimental photograph (top) and contour plots showing the water volume fraction at 1.8 s for the 4 meshes of increasing resolution

3 s after the dam break the interface features and flow times are well correlated with the flow situation observed in the experiment. This is shown in Figure 4.18 where it is observed that part of the wave has reflected upstream and the other part has arrived in the second pool.

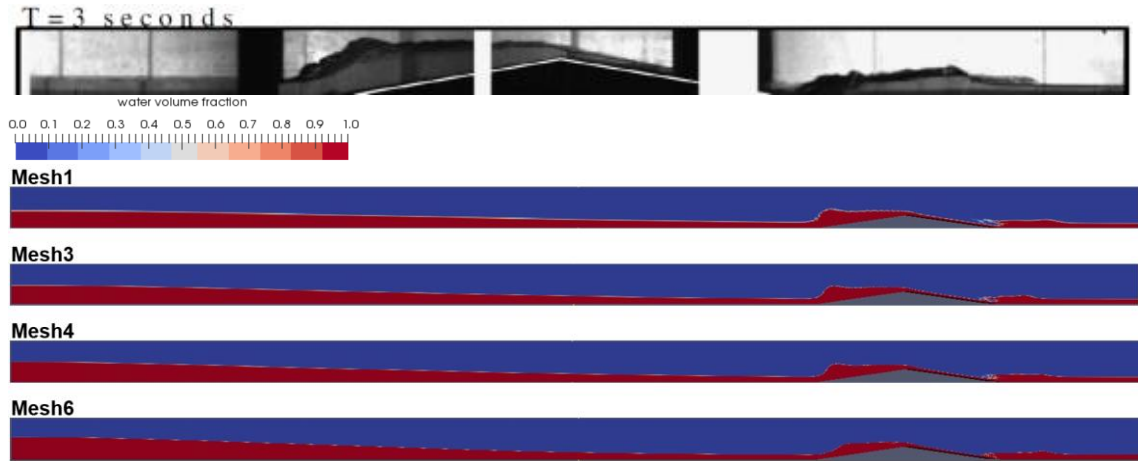


Figure 4.18: Experimental photograph (top) and contour plots showing the water volume fraction at 3 s for the 4 meshes of increasing resolution

Figure 4.17 and Figure 4.18 show that simulations using meshes 1, 3 and 4 present a very similar flow pattern. However, when increasing resolution to Mesh 6, results show a short flow delay and a slightly different interface shape compared to the rest of simulations. Figure 4.19 a) and b) indicate the interface depth against time plotted at the top of the triangle and at 3.5 m respectively.

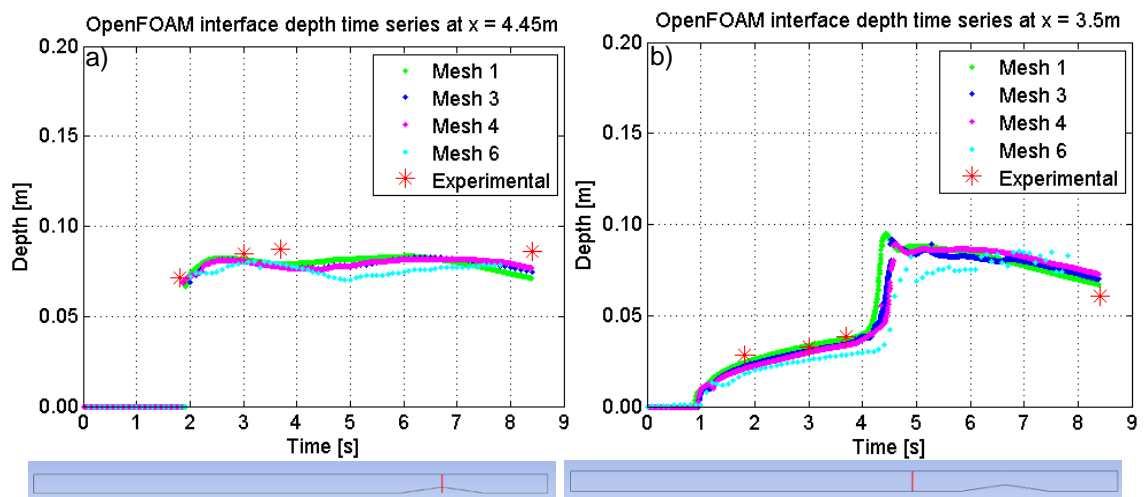


Figure 4.19: Free surface depth time series using 2D meshes 1, 3 and 6 at a) the top of the obstacle and b) at $x = 3.5$ m

The free surface depth graphs show that meshes 1 to 4 provide an appropriate representation of the flow characteristics and of the free surface depth. Results appear to become mesh independent when using Mesh 3, which shows close agreement with results from Mesh 4. However, when resolution is increased to Mesh 6, the numerical predictions present a diverging flow pattern which differs from the experimental data. Further investigation would be required in order to identify the precise reason for results becoming less accurate with Mesh 6.

4.4.2.4.4. OpenFOAM 3D VOF

3D VOF model was implemented in OpenFOAM and a mesh independence study was performed using the 3D meshes 1,3 and 4. Figure 4.20 shows the water volume fraction contour plots at 1.8 s after the dam break. The increase in mesh resolution does not have a significant impact on the results showing a comparable estimation of the flow time and interface features. According to

the experiment photographs, the flow has reached the top of the triangle and this is consistent with the numerical predictions.

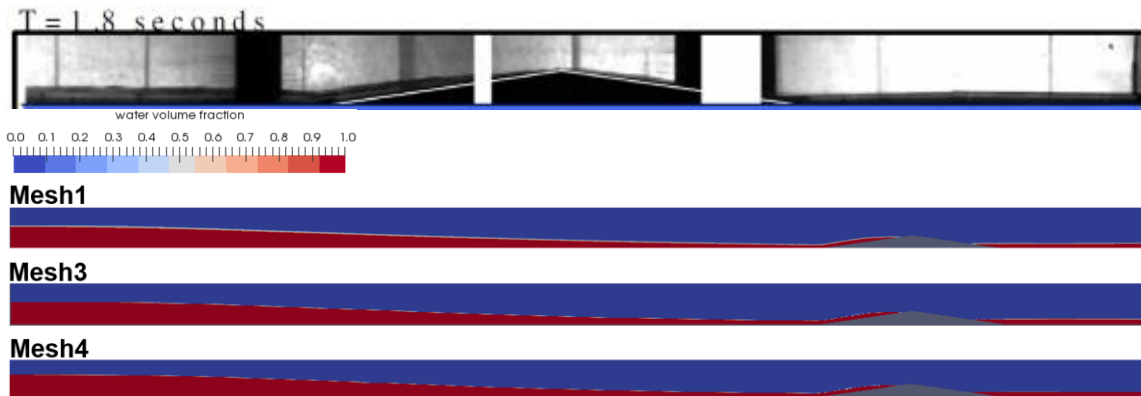


Figure 4.20: Experimental photograph (top) and contour plots showing the water volume fraction at 1.8 s for the 3 meshes of increasing resolution

The volume fraction contour plots at 3 s after the dam break are shown in Figure 4.21. Results show there are no major differences between the numerical results computed using the three different meshes. The model is capable of correctly predicting the experimental flow situation including the wave reflection and overtopping flow moving down to the downstream pool. The model exhibits a very sharp interface when using meshes 3 and 4 which present very comparable predictions. There is no flow delay observed in the numerical results compared to the experiment photograph and point data.

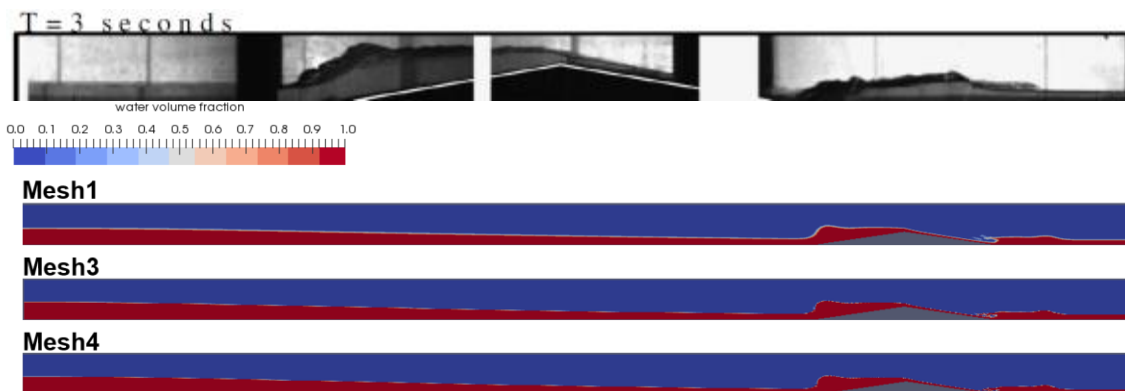


Figure 4.21: Experimental photograph (top) and contour plots showing the water volume fraction at 3 s for the 3 meshes of increasing resolution

Figure 4.22 a) and b) present the plot of the water surface depth time series at the top of the triangle and at an x distance of 3.5 m. The plots show that numerical results using meshes 3 and 4 present very comparable times and free surface features.

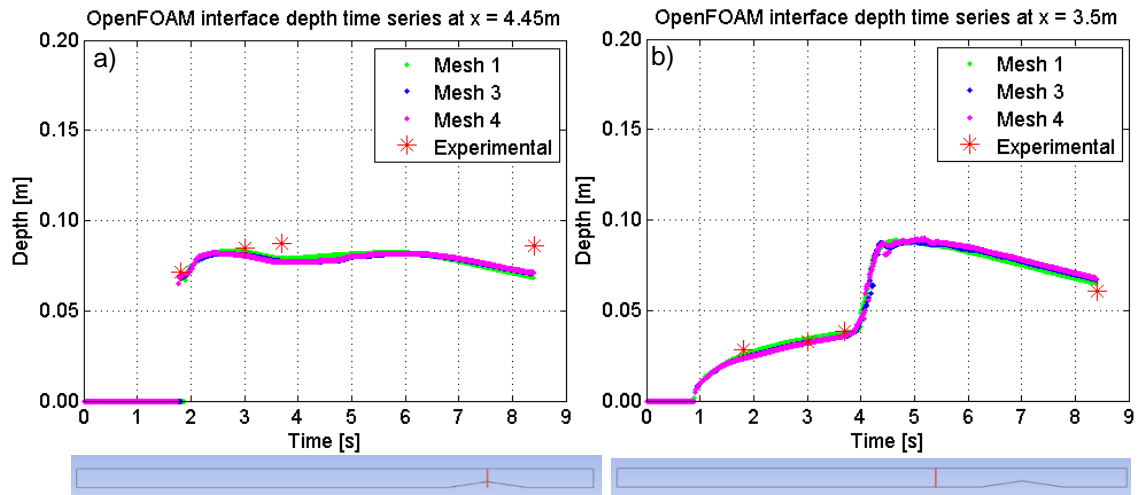


Figure 4.22: a) Free surface depth time series using 3D meshes 1 to 3 at the top of the obstacle and b): at $x = 3.5\text{ m}$

Results from the 3D VOF simulations run in OpenFOAM show a close agreement with the experimental dataset. Simulations using meshes 3 and 4 present consistent predictions in both flow time and interface depth and adequately reproduce the flow behaviour. Mesh 3 is therefore a reference for this problem since further refinement does not provide significant improvements in the numerical results.

4.4.2.5. Discussion

Results show that when implementing variable time stepping with a CFL of 1 the Fluent 2D VOF simulations present a significant delay on the flow in addition to increasing inaccurate representation of the flow features with greater mesh resolution. The Fluent 3D simulations presented less flow delay than the 2D simulations for equivalent mesh resolution. The investigation conducted in this study demonstrated the existing delay in the numerical predictions is completely corrected by using fixed time stepping. The slightly erroneous predictions when implementing variable time stepping could be due to the variable time stepping algorithm not performing appropriately for this case. A second reason could be that the variable time step sizes chosen by the solver with a CFL restriction of 1 were slightly larger than the fixed ones, (which produced CFL numbers of 0.1 to 0.5) causing certain delay. The difference in the size of time steps in the variable and fixed simulations was greatest for Mesh 5 but within the same order of magnitude in the other cases. The time step sizes for all meshes in the fixed and variable time step simulations are shown in Table 4.6.

The ANSYS Fluent guidance suggests rather large CFL numbers for the VOF model (since the code default CFL value for the explicit VOF was 2) and therefore implementing a CFL of 1 was initially considered to be sufficiently low. For this reason, the present findings provide new knowledge on the performance of this solver for VOF simulations. The obtained results indicate that for 2D simulations of the particular case modelled in Fluent, CFL values from 0.1 to 0.5 are found to be providing the most accurate predictions.

Table 4.6: Variable and fixed time step sizes in the 2D simulations of meshes 1 to 6

Mesh ID	Approximate Fluent dt (variable)	Fixed Fluent dt
1	6×10^{-3} to 7×10^{-3}	7×10^{-3}
2	5×10^{-3} to 6×10^{-3}	3×10^{-3}
3	4×10^{-3} to 5×10^{-3}	1×10^{-3}
4	3×10^{-3} to 4×10^{-3}	1×10^{-3}
5	2×10^{-3} to 3×10^{-3}	5×10^{-4}
6	6×10^{-4} to 1×10^{-3}	1×10^{-4}

Figure 4.23 a) and b) show that when using variable time stepping, the 2D case is significantly more sensitive to the mesh cell size than the 3D case with a greater difference in the flow times for increased mesh resolution. The predicted interface depth does not present variations with mesh resolution and is comparable for the 2D and 3D models.

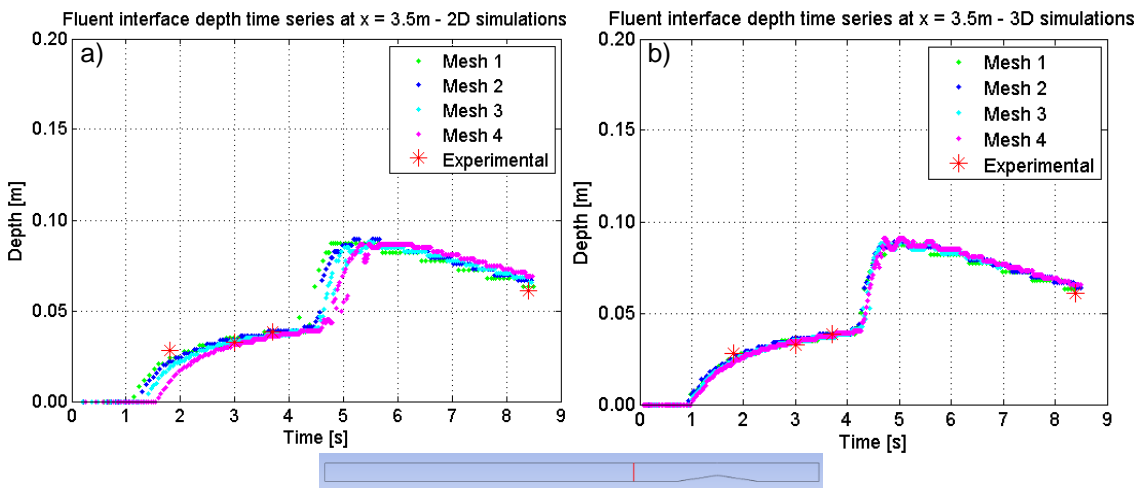


Figure 4.23: Fluent comparison between a) free surface depth time series at $x = 3.5$ m computed using 2D meshes 1 to 4 and the 2D CFD VOF model and b) computed using 3D meshes 1 to 4 and the 3D CFD VOF model

The OpenFOAM 2D VOF simulations demonstrate an accurate representation of the flow. However, the implementation of the finest mesh presents a slight delay compared to the experimental data. Figure 4.24 a) and b) show a comparison plot of the free surface time series for the 2D and 3D simulations using meshes 1, 3 and 4. The 2D model presents slight changes on the interface depth for the different resolutions. The 3D model shows almost equivalent interface depth for the different mesh sizes.

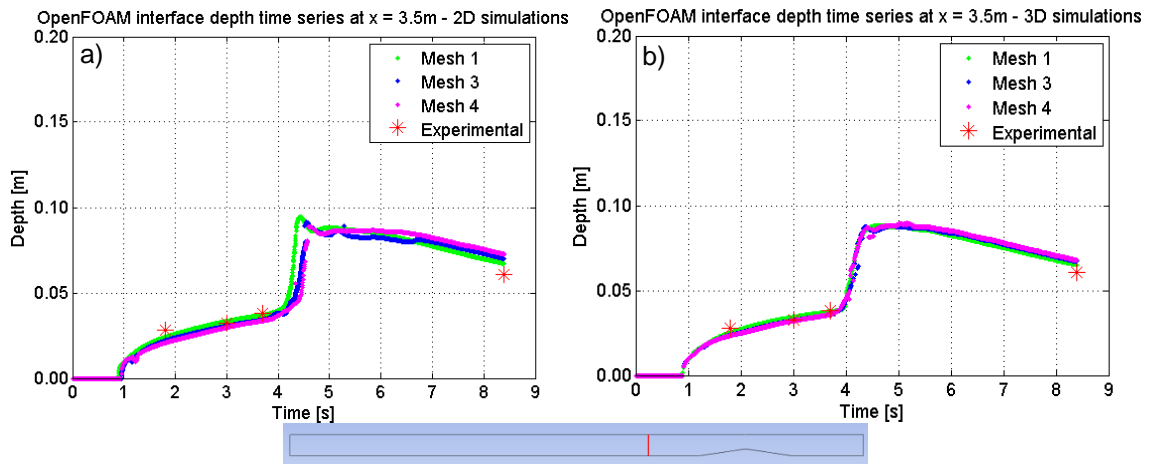


Figure 4.24: OpenFOAM comparison between a) free surface depth time series at $x = 3.5$ m computed using 2D meshes 1 to 4 and the 2D CFD VOF method and b) computed using 3D meshes 1 to 4 and the 3D CFD VOF model

Figure 4.25 a) and b) show the plots of the free surface depth over time at 3.5 m using the 2D VOF models in Fluent with fixed time stepping and OpenFOAM with variable time stepping. The fixed time step simulation results in Fluent show consistency with the OpenFOAM results as well as mesh independency and close agreement with the experimental results. Results computed with the OpenFOAM 2D VOF model present more changes in the interface depth for increasing simulation resolution but overall exhibit an accurate representation of the flow. However, when the simulation resolution is increased to Mesh 6 results show certain delay and increased distortion of the flow characteristics. Possible improvements on the OpenFOAM simulations with the mesh of highest resolution could consist in decreasing the global CFL number to 0.1.

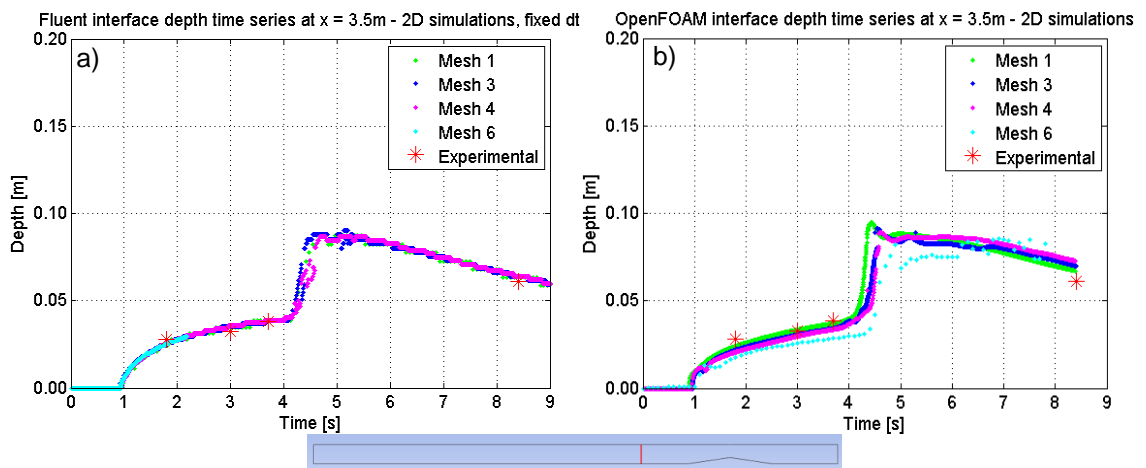


Figure 4.25: Free surface depth time series at $x = 3.5$ m for meshes 1, 3, 4 and 6 for the 2D CFD VOF computed in a) Fluent with implementation of fixed time stepping and b) OpenFOAM

Figure 4.26 a) and b) present the Fluent and OpenFOAM 3D VOF time series results at an x distance of 3.5 m. In both solvers the 3D simulation predictions accurately reproduce the flow characteristics and the results appear to be less sensitive to the cell size than in the 2D case. As stated above, the 3D Fluent simulations present a marginal flow delay for increasing mesh resolution, which is negligible compared to that generated in the 2D case. This minimal delay is completely removed when applying fixed time stepping. Overall the interface depth predictions from the two solvers are consistent and present close agreement with the experimental data. Figure 4.26 a) shows the 3D Fluent predictions for fixed time stepping, which have not run until

the end of the simulations in order to reduce computational effort. However, the available results are sufficient to reveal the fixed time predictions are more mesh independent than those with variable time stepping. In this case the small delay has been removed and results exhibit strong consistency with those from OpenFOAM.

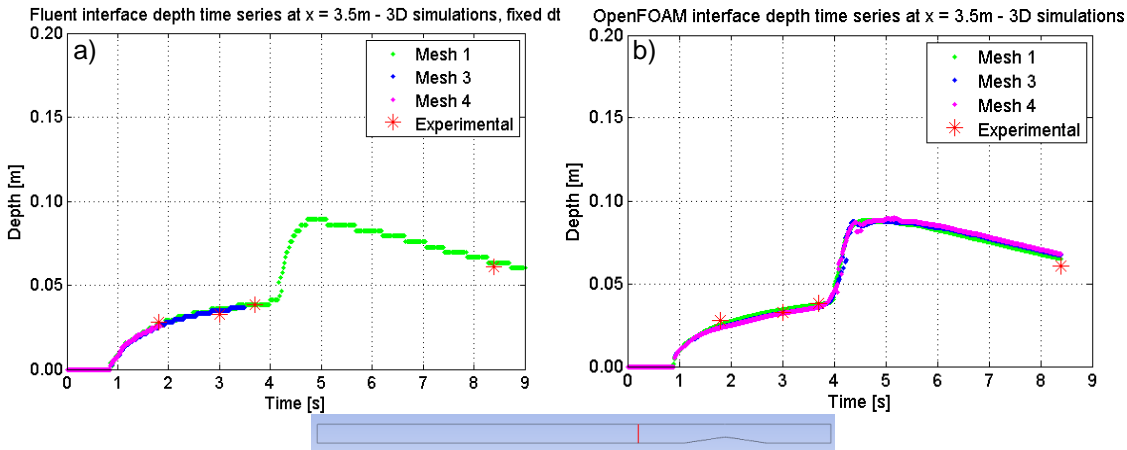


Figure 4.26: Free surface depth time series at $x = 3.5$ m for meshes 1 to 4 with the 3D CFD VOF simulations computed in a) Fluent with fixed time stepping method, b) OpenFOAM Conclusions

4.4.2.6. Conclusions

2D and 3D CFD numerical modelling studies were conducted to simulate a dam break free surface flow over a triangular obstacle using ANSYS Fluent and OpenFOAM. The RANS equations were solved with the Standard $k - \varepsilon$ turbulence model. The VOF method was used to capture the interface position by the implementation of the PLIC algorithm in Fluent and the MULES scheme in OpenFOAM. A mesh cell size independence study was conducted for every model and CFD package. A further sensitivity study was performed using the Fluent 2D model to investigate the effect of a number of numerical implementations to the numerical predictions. A time stepping study was also conducted for the Fluent 2D and 3D models to examine the effects of the time stepping method to the predicted flow timings. The relevant observations of the present work are listed as follows:

- The 2D VOF simulations undertaken in Fluent using the variable time stepping method exhibit a flow delay in the representation of the dam break experimental flow. Such delay becomes more significant for increasing simulation resolution. The delay was further investigated by changing a number of numerical aspects in addition to the time stepping method. Numerical results using the Fluent 2D VOF model with fixed time stepping are capable of appropriately reproducing the dam break flow characteristics and the interface height measured in the experiment. Predictions using the 6 meshes of increasing resolution show overall accuracy and consistency. The model does not show sensitivity to the interface capturing scheme, predicting equivalent results with the geometric reconstruction and the CICSAM algorithms. The use of the SST $k - \omega$ turbulence model did not introduce significant changes on the numerical predictions. The modelling of the dam break case over a wet bed initially induced a more pronounced delay on the wave front. At later stages of the simulation the timings of the dry and wet bed simulations

converged. The implementation of the Fluent Eulerian-Eulerian multiphase model had a considerable impact on the flow delay. The front of the wave presented a significantly shorter flow delay for the two simulations run using meshes of different resolution. Mesh 3 with cell size 1×10^{-2} m (x) by 2.5×10^{-3} m (z) and a fixed time step of 1×10^{-3} s may be considered a reference to model this particular dam break case with the 2D VOF case, since further refinement does not provide substantial improvement of the numerical results.

- The 3D VOF Fluent results demonstrate a close agreement with experimental dataset. The model correctly represents the main flow characteristics observed in the experiment. A minor flow delay is registered with increasing simulation resolution showing a small difference in the flow time predictions at each mesh refinement step. The observed changes in the increased resolution predictions are only in the flow time and the interface height does not present differences. Similarly to the 2D case, the implementation of fixed time stepping analysis for the 3D VOF model completely eliminates the flow delay occurring with variable time stepping. A time step size of 1×10^{-3} s using Mesh 3 with cell size 1×10^{-2} m (x), 1×10^{-2} m (y), 2.5×10^{-3} m (z) provides an accurate characterisation of the flow features and free surface height for the dam break case of study.
- The 2D VOF OpenFOAM simulations provide an accurate representation of the flow situation. The mesh size sensitivity analysis shows that results using meshes 3 and 4 provide the most accurate approximations. Similarly to Fluent, in this solver Mesh 3 also provides a sufficiently accurate flow approximation and may be taken as a reference.
- Simulations undertaken with the 3D VOF OpenFOAM model are well correlated with the experimental data. The mesh independence study demonstrates an accurate characterisation of the flow using Mesh 3. Both interface depth and features are successfully captured and flow times are consistent with the observed in the experiment.

4.4.3. SPH Modelling

4.4.3.1. Numerical Model

The freely available open source code DualSPHysics was utilised to conduct SPH simulations of the dam break flow. This code is formulated according to the weakly compressible algorithm (WCSPH) which is the most common approach to model fluid incompressibility (Gomez-Gesteira *et al.* 2012).

The kernel definition chosen for this study was the cubic spline and the viscosity treatment was laminar viscosity and sub-particle scale (SPS) turbulence. The time step was variable (from 1×10^{-5} to 1×10^{-4} s) with a CFL number restricted to 0.2, as recommended in the code guidance. The Symplectic time integration algorithm was employed. The Shepard density filter was included in all time steps to correct the kernel function for boundary particles. Simulations were conducted using 16 HPC CPU processors in one computer node.

To investigate the effect of number of particles on the solution, the initial particle separation was set. This is referred to as the particle distance or separation (dp) in the presentation of numerical results. A number of simulations were undertaken for different particle separation values for the 2D and 3D cases. A summary of the simulations undertaken for the different particle separations and corresponding smoothing lengths (h) is shown on Table 4.7.

Table 4.7: Summary of simulations for different particle distances (dp)

Simulation ID	2D			3D		
	dp [m]	h [m]	Number of Particles	dp [m]	h [m]	Number of Particles
1	0.0025	3.54×10^{-3}	50506	0.0075	1.30×10^{-2}	502138
2	0.0015	2.12×10^{-3}	135717	0.007	1.21×10^{-2}	643512
3	0.0010	1.41×10^{-3}	298215	0.0065	1.13×10^{-2}	768820
4	0.0005	7.07×10^{-4}	1166352	0.005	8.66×10^{-3}	1559618

The initial conditions set up in DualSPHysics are shown in Figure 4.27.

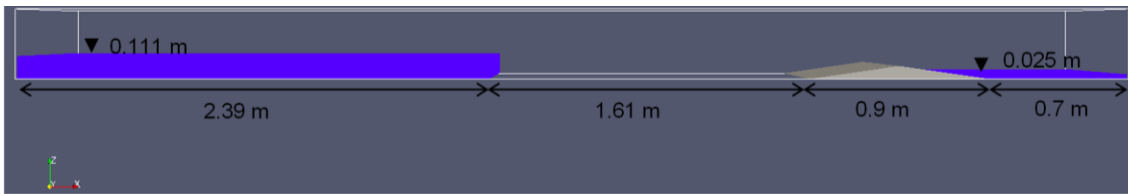


Figure 4.27: Setup of initial conditions in DualSPHysics

4.4.3.2. Experimental and Numerical Results

4.4.3.2.1. 2D SPH

A photograph of the experimental results and the numerical predictions of different resolutions at 1.8 s after the dam break is shown in Figure 4.28. The particles are coloured by particle ID in order to enhance the identification of the flow features.

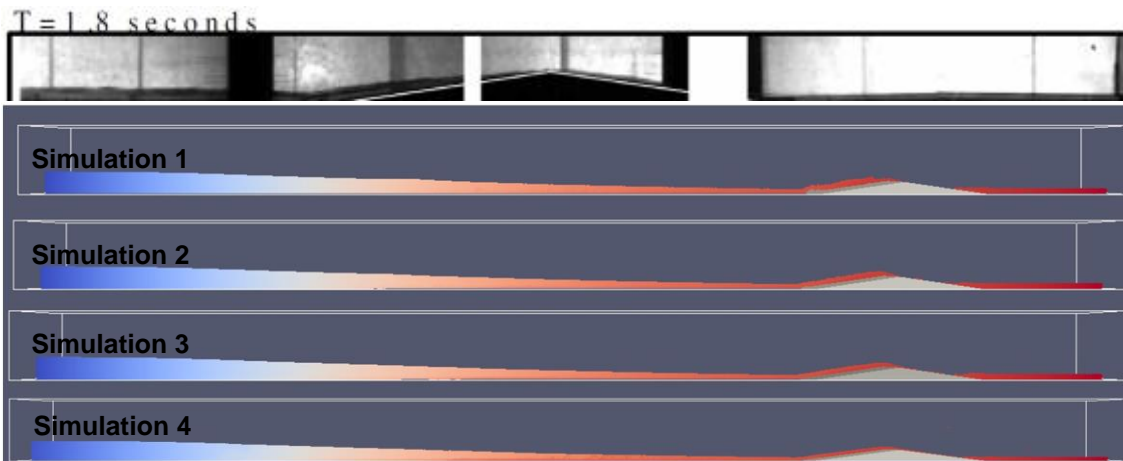


Figure 4.28: Experimental photograph (top) and simulation results at 1.8 s after the dam break for the four different cases of increasing resolution

After 1.8 s the experimental results show the flow has reached the peak of the triangular obstacle. This situation is generally well reproduced in all simulations. Simulations 3 and 4 appear to be slightly more advanced than Simulations 1 and 2, with the water front having moved slightly over the top of the triangle.

The photograph of the experimental results at 3 s after the dam break with the four simulation predictions is shown in Figure 4.29.

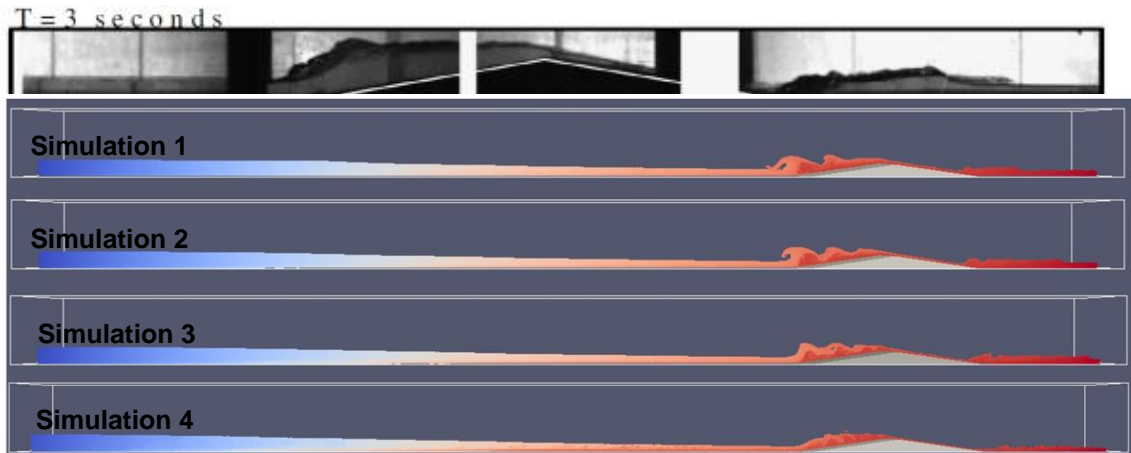


Figure 4.29: Experimental photograph (top) and simulation results at 3 s after the dam break for the four different cases of increasing resolution

3 seconds after the dam break part of the flow has arrived to the second pool and the other part has reflected upstream. This behaviour is well reproduced by the numerical predictions. The most accurate representation of the interface shape is provided by Simulation 3. Simulation 4 presents a slightly less accurate flow profile. Figure 4.30 shows an enhanced view around the triangle vicinity of the interface depth versus length of the channel at 3 s after the dam break. The free surface at the entire domain is shown in a reduced size view.

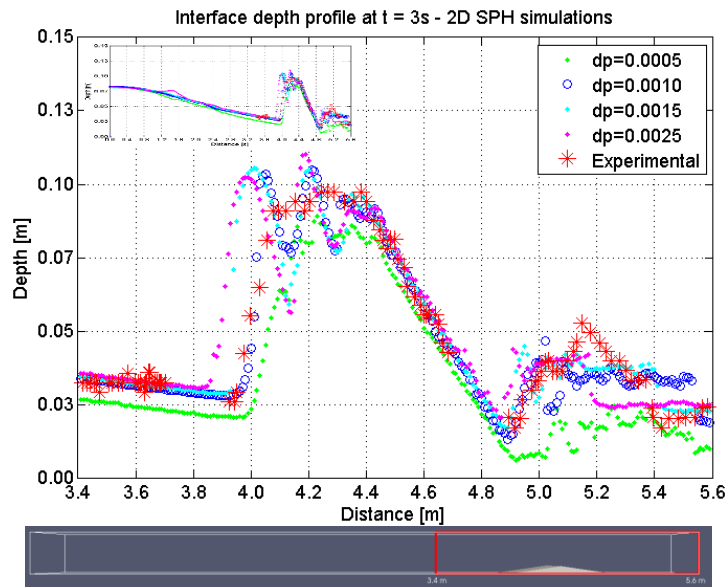


Figure 4.30 Interface depth profile versus channel length at 3 s for the four simulations of increasing resolution with a reduced size graph of the entire domain

Figure 4.30 shows that generally results from Simulations 1 to 3 are well correlated with the experimental free surface depth showing both the front wave traveling upstream and the second bore in the downstream pool moving towards the downstream wall. However, Simulation 4 does not appear to be accurately predicting the flow situation; the wave in the downstream reservoir does not appear clearly defined and the shape of the front wave reflected upstream is not consistent with the observed in the experiment. In general, the flow behaviour shown in Simulation

4 is likely to be a consequence of the water level having decreased because of particles being excluded of the domain.

A photograph of the experimental results 8.4 s after the dam break with the corresponding numerical predictions are shown in Figure 4.31.

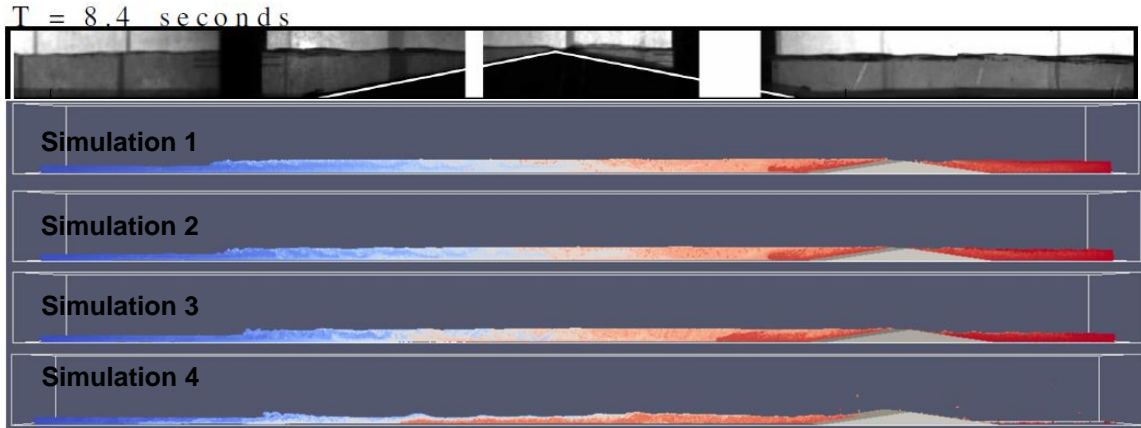


Figure 4.31: Experimental photograph (top) and simulation results at 8.4 s after the dam break for the four different cases of increasing resolution

At this later stage of the dam break, the reflection wave travelled upstream (after reflecting against the end of the tank) and at the same time the dam break flow continued to arrive to the second pool. Results generally reproduce this situation well; however, the predicted interface depth of all simulations appears to be lower than that measured in the experiment. Figure 4.32 shows that the estimated free surface depth is generally lower than the experimental, and the simulation resolution strongly affects this discrepancy. For increasing resolution, a larger number of particles appear to be excluded from the domain and this is reflected in a decrease in the water depth.

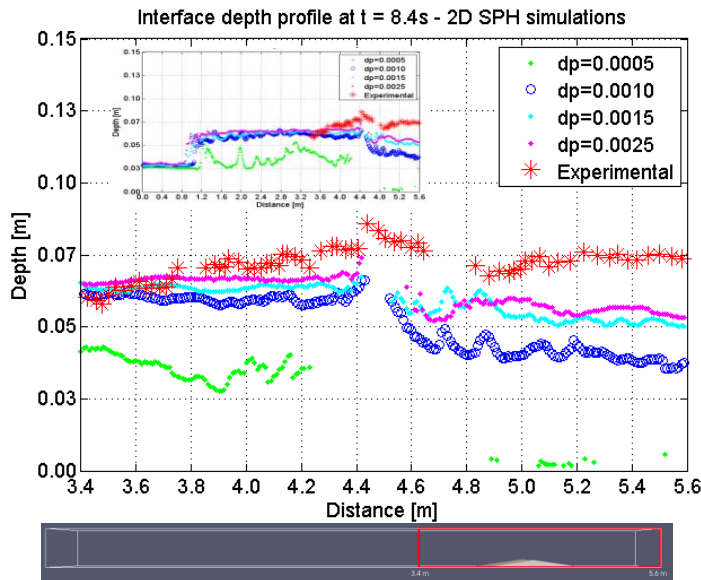


Figure 4.32: Interface depth profile versus channel length at 8.4 s for the four simulations of increasing resolution with a reduced size graph of the entire domain

Free surface time series plots at 4.45 m (top of the obstacle) and at an x distance of 3.5 m are shown on Figure 4.33 a) and b) respectively. These show that generally 2D SPH simulations of intermediate resolution are capable of correctly representing the flow characteristics and interface depth for most of the simulation time but they predict a slight drop in the interface depth at the

final stages of the simulations. Simulation 1 using the particle spacing of 0.0025 predicts the front wave to arrive to the peak of the obstacle a little later than the other two simulations, but the difference is minimal. Also, this case predicts the interface depth to be the highest. The predicted depth of the interface decreases as the simulation resolution is increased. Simulation 3 provides the best approximation of the flow situation. Further simulation refinement induces considerable particle losses which are reflected in significant free surface drops and unrealistic flow behaviour.

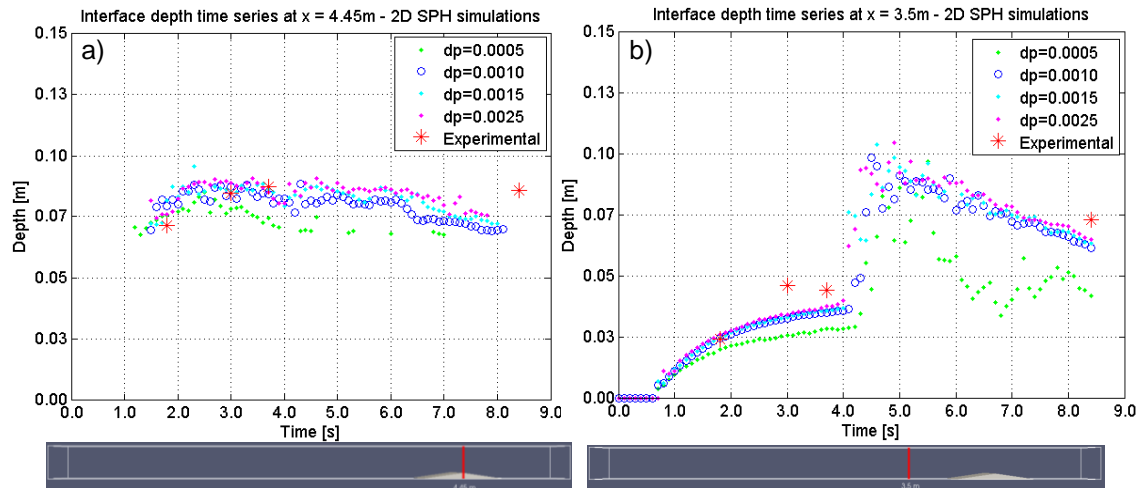


Figure 4.33:a) Interface depth time series for the four simulations of increasing resolution at a) the top of the obstacle and b) $x = 3.5$ m

Sensitivity Analysis

In order to evaluate the influence of several numerical implementations to the 2D SPH results, four variables were investigated. Simulations using a constant dp value of 0.0015 m were conducted with changes in time step algorithm, viscosity treatment and kernel definition. A summary of the specific numerical implementations used in each simulation is shown on Table 4.8.

Table 4.8: Summary of numerical implementations applied in the sensitivity analysis

Numerical Implementation	Original Settings	Case I	Case II	Case III
Time Step Algorithm	Symplectic	Verlet	Symplectic	Symplectic
Viscosity treatment	Laminar + SPS	Laminar + SPS	Artificial	Laminar + SPS
Kernel Definition	Cubic Spline	Cubic Spline	Cubic Spline	Quintic (Wendland)

The interface depth versus time at the top of the obstacle and at $x = 3.5$ m for all cases is shown in Figure 4.34 a) and b) respectively.

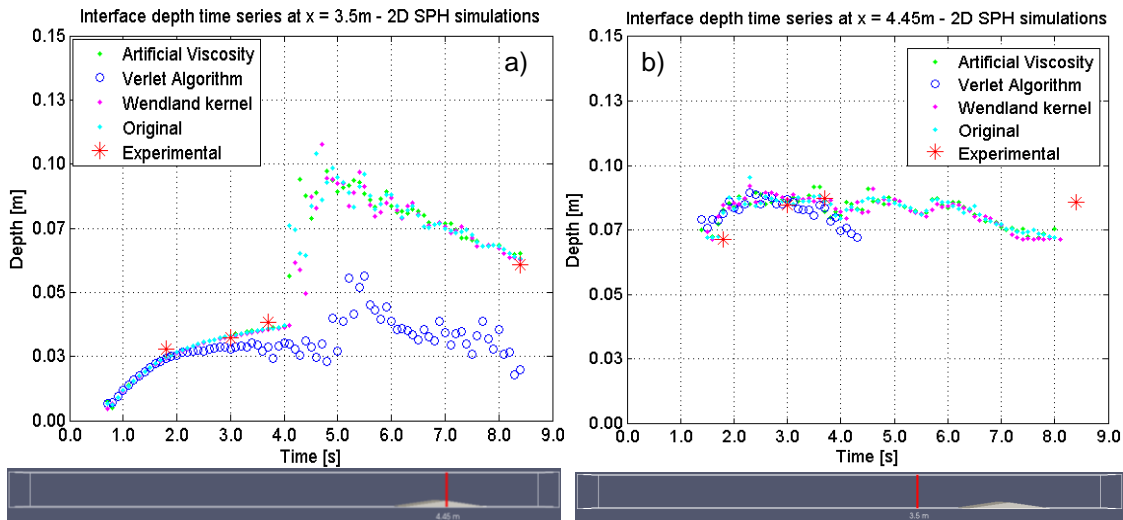


Figure 4.34: Interface depth time series for the different numerical implementations at a) the top of the obstacle and b) $x= 3.5$ m

Figure 4.34 shows that overall the 2D SPH model is not sensitive to changes in the viscosity treatment or the kernel definition. However, the model presents dramatic changes in the flow predictions when using the Verlet time step algorithm as opposed to the Symplectic algorithm. The simulation employing the Verlet time step algorithm induces a constant loss of particles. Particles are registered to escape the domain from very early stages of the simulation. This is reflected in a considerable decrease in the interface depth and hence results do not provide accurate estimations.

4.4.3.2.2. 3D SPH

3D SPH simulations were conducted using the same layout as for the 2D case. The number of particles in the four 3D simulations are shown on Table 4.7. The numerical results predicted at 1.8 s after the dam break are shown in Figure 4.35.

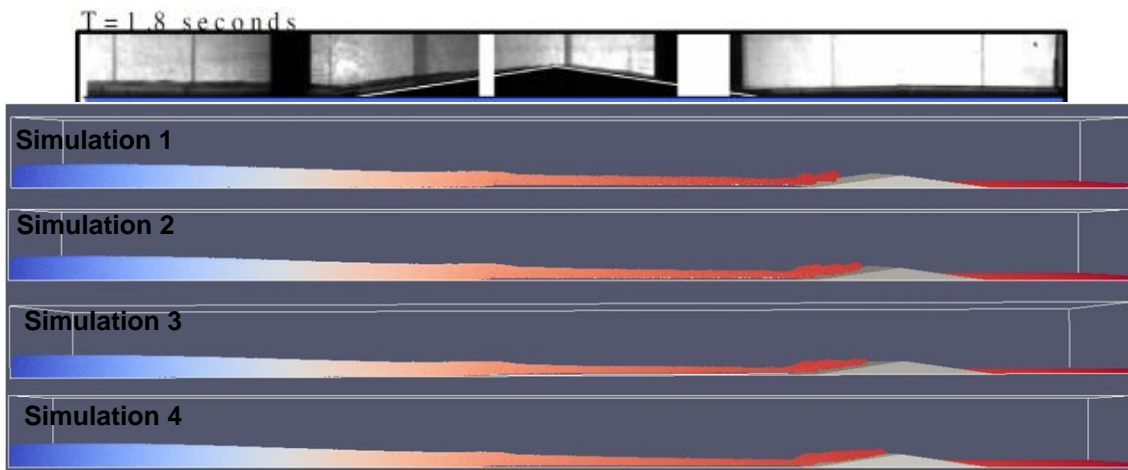


Figure 4.35: Experimental photograph (top) and simulation results at 1.8 s after the dam break for the four different cases of increasing resolution

Numerical results at 1.8 s after the dam break present a slight delay compared to the experimental data. The dam break flow appears to be moving up the upstream face of the triangular obstacle while the experimental photograph shows the front wave to be around the top of the obstacle.

The time difference is reduced with increasing simulation resolution and results improve with each refinement step. Simulation 4 presents the closest results to the experimental data.

Simulation results at 3 s after the dam break are shown in Figure 4.36.

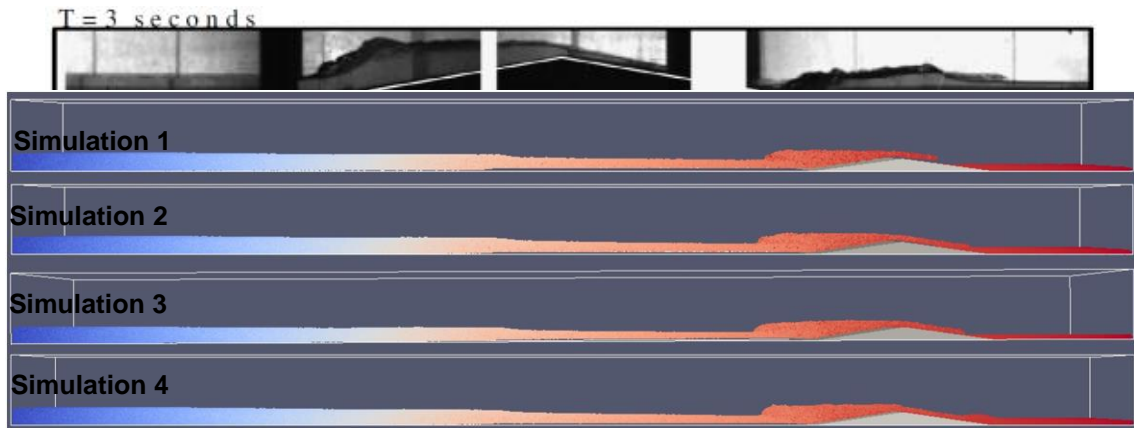


Figure 4.36: Simulation results at 3 s after the dam break for the four different cases of increasing resolution

3 s after the dam break, the experimental photograph show the front wave to have reflected upstream and a second wave generated from the dam break flow is travelling downstream in the second pool. This behaviour is not well represented by the numerical results of Simulations 1 to 3, where the front wave is just about to arrive to the second pool. Numerical results of Simulation 4 provide significant improvements, where it is observed that the front wave has entered the second pool. Figure 4.37 presents the water surface depth versus the channel length at 3 s. Simulations 1 and 2 indicate the water in the downstream pool is still flat since the front wave has not yet arrived. Interestingly, Simulation 2 presents a slightly better approximation than Simulation 3. Simulation 4 provides the most accurate results, however there is still a slight delay compared to the experimental measurements.

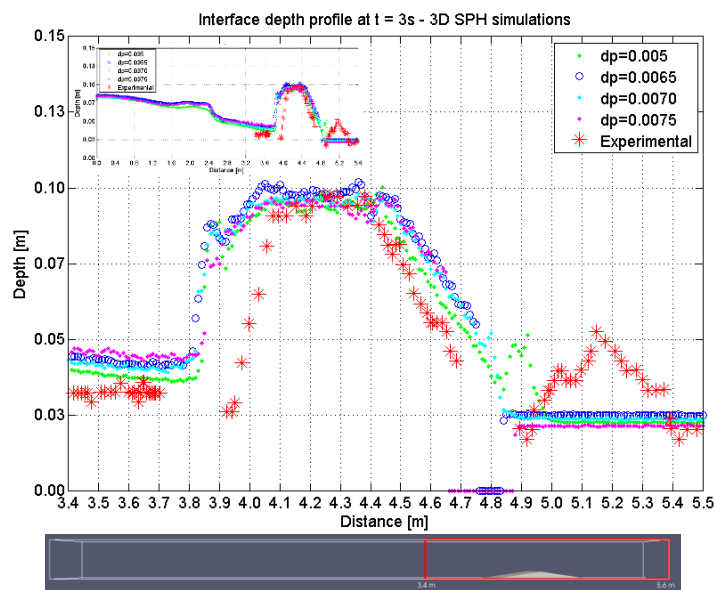


Figure 4.37: Interface depth profile versus channel length at 3 s for the four simulations of increasing resolution with a reduced size graph of the entire domain

Simulation results at 8.4 s after the dam break are shown in Figure 4.38.

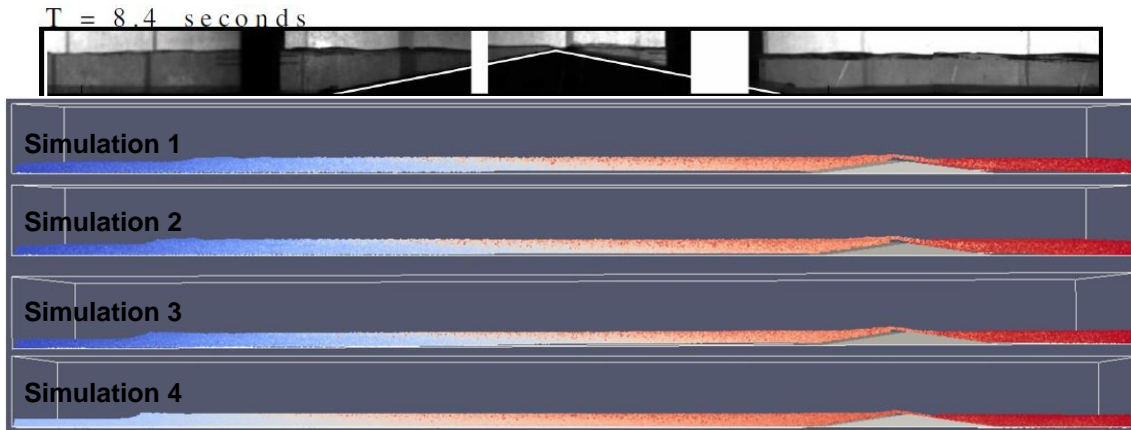


Figure 4.38: Experimental photograph (top) and simulation results at 8.4 s after the dam break for the four different cases of increasing resolution

After 8.4 s, the numerical results demonstrate an acceptable representation of the interface shape and depth, showing a generally even distribution of the flow upstream and downstream the obstacle. Figure 4.39 shows the computed depth of the free surface versus the length of the channel. Overall the water level matches that measured in the experiment; however Simulation 4 predicts a slightly lower interface depth both upstream and downstream of the obstacle compared to the rest of simulations.

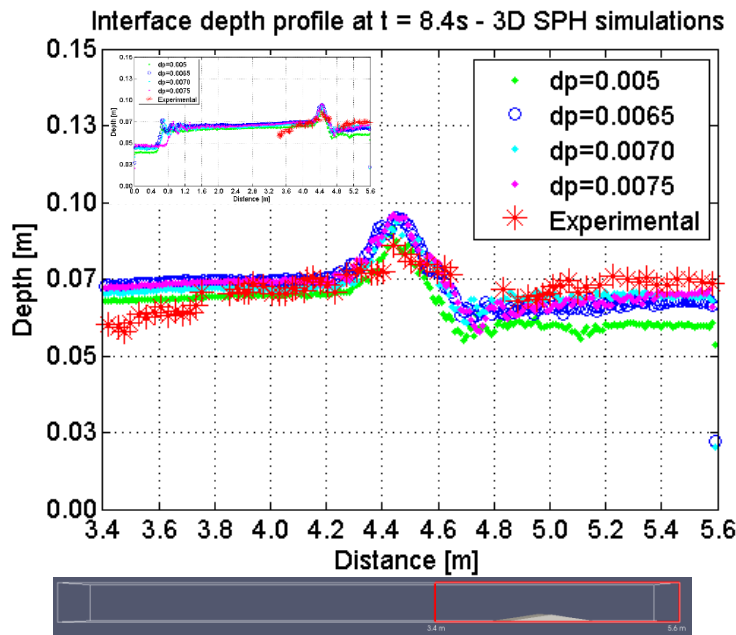


Figure 4.39: Interface depth profile versus channel length at 8.4 s for the four simulations of increasing resolution with a reduced size graph of the entire domain

Upstream of the triangle the numerical models predict the depth of the free surface to be higher than the experimental and downstream the obstacle they predict the free surface to be lower. To further investigate this, the interface depth was plotted against time at a location upstream the obstacle, $x = 3.5$ m, at the peak of the obstacle, $x = 4.45$ m and at the downstream pool, $x = 5.2$ m. These are presented in Figure 4.40 a), b) and c) respectively.

Figure 4.40 a) and b) and show that upstream and at the top of the obstacle, the 3D SPH model predicts the depth of the free surface to be slightly delayed and higher than that measured in the experiment. The height of the free surface moves closer to the experimental results with

increasing number of particles and hence with smaller flow delay. Figure 4.40 c) highlights the effects of the front wave delay downstream the obstacle. In this location the numerical results predict a lower interface height than the measured in the experiment.

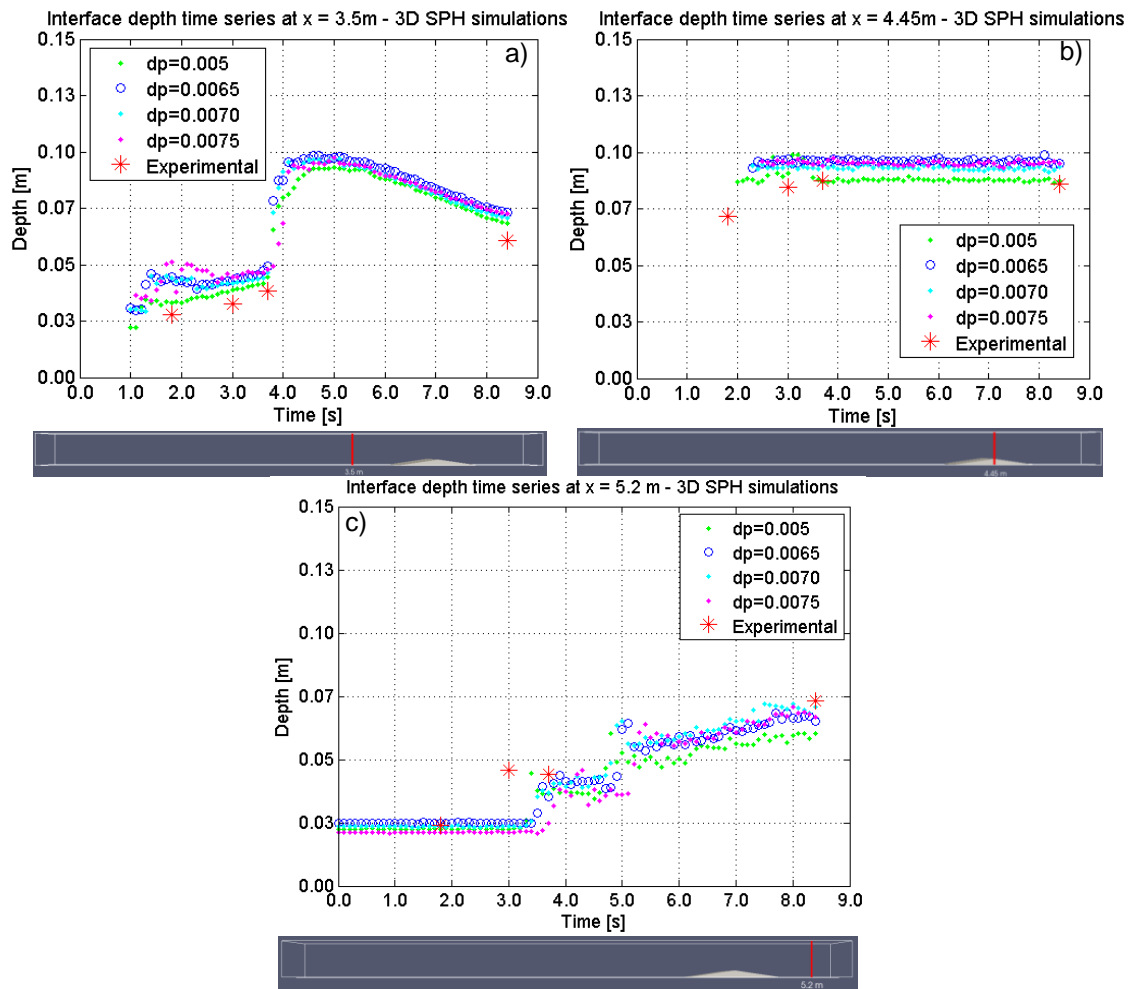


Figure 4.40: Interface depth time series for the four simulations of increasing resolution at a) $x = 3.5$ m, b) the top of the obstacle and c) at 5.2 m

4.4.3.3. Discussion

4.4.3.3.1. 2D SPH

The 2D SPH model run with highest resolution generally provides an acceptable representation of the interface height and flow characteristics at the early stages of the experiment but exhibits challenges at later stages. At 1.8 s after the dam break, Simulations 1 and 2 show a slight delay in respect of Simulations 3 and 4 which present generally accurate predictions. At 3 s after the dam break, Simulation 3 predicts the best results and Simulation 4 shows a slightly inaccurate profile with an drop in the interface depth. At later times of the experiment, all simulation results present a decrease in the interface depth compared to that measured in the experiment. This difference with experimental results increases for increasing particle number. At 8.4 s after the dam break, Simulation 1 shows the height of the interface to be closest to that measured in the experiment. The difference between the experimental and the numerically predicted interface depth increases with simulation resolution ranging from 0.02 m in Simulation 1 to 0.07 m in

Simulation 4. The results provided by Simulation 4 at 8.4 s are not considered to be appropriate due to the substantial loss of particles.

It is observed that dp has a significant impact on simulation results. It is also noted that the number of particles being excluded from the domain increases with increasing resolution. These issues are likely to be associated with the SPH implementation and require further research. A potential manner to further examine the code would be to further decrease the minimum initial time step of the simulations.

The numerical implementation sensitivity analysis highlighted that changes in viscosity treatment and kernel definition do not affect the numerical results. However, numerical predictions are dramatically influenced by changes in the time step algorithm. Using Verlet algorithm drastically reduces the computational time compared to that using the Symplectic scheme; however the predictions are not accurate. The Symplectic scheme is recommended for long-lasting simulations (Gomez-Gesteira *et al.* 2012).

4.4.3.3.2. 3D SPH

The 3D SPH requires a remarkably larger number of particles than the 2D SPH model to provide an accurate estimation of the flow characteristics. As such, the 3D simulations have been conducted with relatively higher particle spacing (dp) to manage computational resource.

The free surface predicted by the 3D SPH model appears to present a delay in all simulation results. The observed delay decreases with increasing resolution, hence Simulation 4 presents the least delayed results. Through undertaking simulations with a larger number of particles it would be possible to ascertain if the delay could be entirely removed.

At 1.8 s and 3 s after the dam break, all simulation results are delayed compared to the experiment photographs, the delay ranges from 0.2 s to 0.5 s. In addition, the predicted free surface depth is slightly higher than that measured in the experiment in Simulations 1 to 3 but it is most accurate in Simulation 4. At 8.4 s after the dam break, numerical results of Simulations 1 to 3 show an improved approximation regarding the delay observed at the earlier stages of the experiment. The predicted interface depth is still higher than that measured in the experiment. Simulation 4 presents the lowest interface depth, which agrees with the experimental data upstream of the obstacle but appears to be too low downstream the obstacle. This behaviour could be attributed to implementation uncertainties in the code that require further investigation.

In contrast with the 2D case there are no particles recorded to be excluded of the domain in any of the 3D simulations.

Additional refinements in the simulations would be likely provide results of improved precision and would allow a better understanding of the code limitations. However, it was not possible to further increase resolution as part of this study due to computational restrictions. Therefore further work would consist in the investigation of higher resolution simulations.

4.4.3.4. Conclusions

2D and 3D SPH simulations were performed to model the dam break free surface flow over a triangular obstacle. A particle number sensitivity analysis was conducted for both the 2D and the 3D SPH models. Sensitivity analyses in respect of several numerical implementations were undertaken to investigate their influence on the numerical results of the 2D model. These include the viscosity treatment, the time step algorithm and the kernel formulation.

The results of the 2D SPH model using the highest resolution provide the best representation of the flow features at the early stages of the experiment. The SPH predictions provide an accurate representation of the free surface behaviour over time, but due to some unknown implementations of the DualSPHysics code there is still further research required to obtain a comprehensive quantitative measure of its accuracy. However, the provisional results are promising. The main challenge is that the current implementation of the model presents particle loss challenges which are larger for higher resolution simulations. This appears to cause a sizeable drop in the interface depth at later stages of the simulation. Simulation 3 with a dp value of 0.0010 m overall provides the best estimation, although the free surface depth at the end of the test is slightly lower than the measured in the experimental study. There is certainly a need for further investigation of the particle loss issue in the 2D SPH model within DualSPHysics.

The numerical results of the 2D SPH model are not found to be sensitive to the viscosity treatment and kernel definition. However, results are proven to be strongly dependent on the time step algorithm. The Symplectic time step algorithm is recommended to model this dam break case.

The 3D SPH numerical results present a small delay compared to the experimental data. The delay decreases at later stages of the dam break and all simulation results become closer to the measured data. Increasing the number of particles provides significant improvements to the numerical predictions. Simulation 4 with highest resolution ($dp = 0.005$ m) although, with an initial delay of 0.2 s, is considered to provide an acceptable approximation of the interface height and features. It should be noted that increasing the particle number in the 3D SPH model also appears to provide a decrease in the free surface height, particularly at later stages of the simulation. Further increases in simulation resolution, as well as testing further model settings are expected to provide a better understanding of the existing discrepancies between the numerical and experimental data. 3D SPH results appear to be very promising, and additional simulations need to be undertaken in order to extensively confirm the capabilities of the technique.

4.5. Conclusions

In this chapter, two leading numerical approaches to simulate free surface flows were described in detail, namely the VOF and the SPH. In the second part of this chapter, an experimental dam break flow was simulated with the 2D and 3D VOF implemented in ANSYS Fluent and in OpenFOAM and with the 2D and 3D SPH technique implemented in the DualSPHysics. The modelling of this relatively simple experimental case enabled the evaluation of the numerical techniques as well as the completion of several sensitivity analyses. In the case of the VOF, various implementations were tested, including cell size, time step size, turbulence model and

interface tracking scheme. In addition, the Eulerian-Eulerian multiphase model was compared to the VOF for equivalent numerical implementations. Sensitivity analyses in the SPH simulations were conducted in respect to the time step algorithm, viscosity treatment and the Kernel definition. The outcomes of the VOF analysis provided crucial information on key numerical aspects and implementations which will be utilised in Chapter 6 where a significantly more complex hydraulic situation is modelled with the VOF. The SPH study of this experimental case constitute a valuable research work on the SPH technique implemented on DualSPHysics. The SPH predictions obtained in this study may be utilised to inform the future application of this technique in the modelling of hydraulic free surface flows.

The main conclusions from the evaluation analysis conducted with the SPH and the VOF may be summarised as follows:

- The 2D and 3D VOF predictions using Fluent and OpenFOAM accurately reproduce the flow features and the free surface depths measured in the experiment. The use of variable time stepping in the 2D and 3D VOF models provides accurate results in OpenFOAM, however it is not recommended in Fluent;
- The predictions from the two solvers confirm a mesh with cell size 1×10^{-2} m (x, y) by 2.5×10^{-3} m (z) with a fixed time step size of 1×10^{-3} s is considered to be appropriate for the dam break case modelled and the dimensions of the domain (5.6 x 0.5 x 0.1 m);
- The sensitivity analyses show no significant changes in the flow predictions when using the SST $k - \omega$ and compared to the Standard $k - \epsilon$ turbulence models;
- The model shows comparable results with the implementation of the interface capturing schemes PLIC and CICSAM;
- The use of the Fluent Eulerian-Eulerian multiphase model significantly improved the flow delay observed in Fluent when using variable time stepping and also presents an accurate representation of the flow behaviour;
- 2D SPH model using a particle spacing value (dp) of 1×10^{-3} m provides an acceptable estimation of the flow characteristics and free surface of the dam break case modelled. Numerical predictions were not found to be sensitive to viscosity treatment or kernel definition but they were strongly dependent on the time step algorithm. The Symplectic algorithm is recommended for the modelling of this type of problem. 3D SPH results present a satisfactory representation of the interface and flow features for a particle spacing value of 5×10^{-3} m. Further investigations with simulations of higher resolution would be needed in order to fully determine the capabilities of this technique.

5. Case Study: The Eller Beck Labyrinth Weir and Spillway

5.1. Introduction

In this chapter, the scheme in which this thesis focuses is described and the physical hydraulic model constructed for the design of the scheme is characterised. The purpose of the model is outlined together with the main elements and characteristics of the experimental measurements collected.

5.2. Description of the Scheme

The case study consists in a set of hydraulic structures which form a component part of the flood alleviation scheme in the town of Skipton, North Yorkshire (UK). The scheme is located in the North of the town and is designed to alleviate flooding resulting from storm events with return period up to 100 years. Skipton has experienced severe flooding in a total of six incidents from 1908 to 2007. The two contributors to flooding in Skipton are the rivers Eller Beck and Embsay Beck. The flood alleviation scheme developed for Skipton consists in the Eller Beck Flood Storage Reservoir, the Waller Hill Beck Flood Storage Reservoir and the In-town located flood defences (Brinded *et al.* 2014). This thesis focuses in the Eller Beck Flood Storage Reservoir scheme. Figure 5.1 shows the three components for the flood protection of the town of Skipton. The Eller Beck scheme is indicated with a rectangular red frame.



Figure 5.1: Location of the three components of the flood alleviation scheme from Brinded *et al.* (2014)

The Eller Beck river flows through a golf course before merging with Embsay Beck, immediately upstream of a road embankment located in the North of Skipton. The scheme to control the Eller Beck flow consists of a flood storage reservoir built across the river before the merging with Embsay Beck takes place. The reservoir is formed by an embankment dam, a culvert through the dam, a labyrinth weir and a spillway channel to pass the overflow. Figure 5.2 presents the elements composing the Eller Beck scheme. According to Brinded *et al.* (2014), in order to provide

appropriate flood defence to the town, floods over 17 m³/s are required to be stored in the reservoir. In a 100-year event, the flood storage reservoir is able to store 433000 m³ of storm water. Immediately downstream of the scheme, there is a road embankment and the water flow over the hydraulic structure will be impounded against it. Such situation will create different levels of tail water on the spillway, which will vary depending on the flood levels of both rivers.

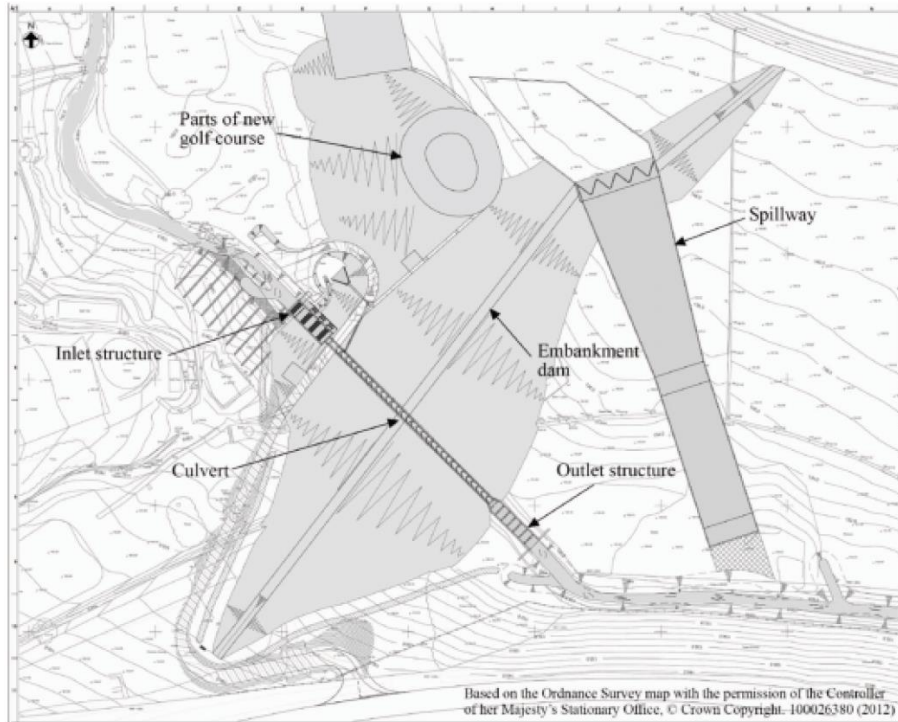


Figure 5.2: Layout of the hydraulic structures in the Eller Beck reservoir from Brinded et al. (2014)

The present study will focus in the flow processes occurring as the watercourse passes over the labyrinth weir and flows over the spillway channel.

The labyrinth weir has a trapezoidal shape and was designed based on the guidance specified in Tullis *et al.* (1995). A schematic of a generic labyrinth weir is shown on Figure 5.3 where D is the outside apex length which is 0.850 m, A is the inside apex length which is 0.485 m, α is the sidewall angle 35.15°, and w is the distance between cycles which is 7.97 m. The labyrinth weir has a total of 4 cycles (N), with three upstream apexes and four downstream apexes. The crest height is 1.8 m and the thickness of the wall, t_w , is 0.25 m, l_c is the centreline length of the sidewall, which is 5.8 m. The total width of the labyrinth, W is 31.8 m. B is the length of the apron (parallel to the flow) which is 5.12 m. L_c is the centreline length of the crest which is equal to 51.74 m, calculated as per Equation 5.1 from Crookston and Tullis (2013a).

$$L_c = N(2l_c + A + D) \quad 5.1$$

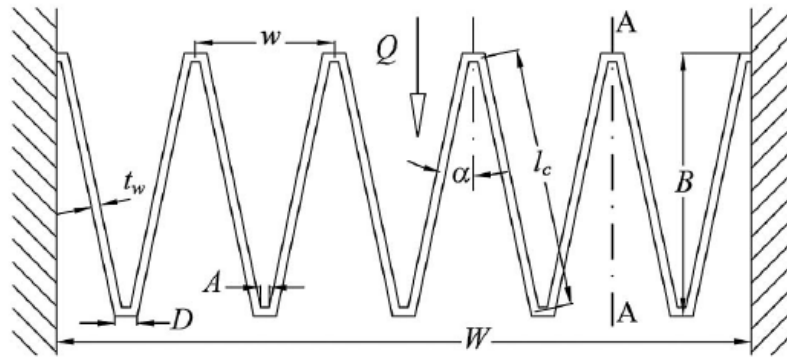


Figure 5.3: Typical labyrinth weir schematic from Crookston (2010)

The embankment dam crest level is at 143.0 m AOD and the labyrinth weir crest is at a level of 140.8 m AOD.

Figure 5.4 shows a view of the labyrinth weir and the spillway channel taken from the left side.



Figure 5.4: View of the labyrinth weir from the left hand side of the scheme

The spillway channel has a length of 150 m from the labyrinth weir to the stilling basin. The spillway channel initial width is that of the labyrinth weir, 31.8 m and it progressively narrows down until the second section. The first section of the spillway is 75 m long with a base gradient of 1.6° . In the second section the spillway channel has a total width of 20 m which is maintained constant until the end of the structure and the base gradient is increased to 14.02° . 8.8 m downstream, the spillway presents a third section with a further change in gradient, reducing to 5.71° and remains constant for 55 m until it merges with the stilling basin which has a horizontal bed. Therefore, the spillway has four different gradients along the channel. At the tail of the stilling basin there is an end sill of 1 m height to enhance energy dissipation within the concrete structure with a 0.5 m slot at the centre of the channel to allow drainage of the stilling basin after a flood event. To enhance energy dissipation, the stilling basin has a baffle block of 1 m height and 0.5 m width. A view from downstream of the spillway channel is shown on Figure 5.5.



Figure 5.5: Eller Beck spillway channel from downstream with end sill at the front of the image

5.3. Scaled Physical Hydraulic Model of the Eller Beck Spillway

A 1:25 scale physical hydraulic model based on Froude number similarity was constructed to confirm design of the Eller Beck labyrinth weir and spillway. The physical model design was specified by Arup and it was constructed and operated by the sub-contracted firm CRM Rainwater Drainage Consultancy Ltd (Bolton, UK). The model was constructed in timber and plastic resin. The physical model of the scheme includes the approach channel (from the reservoir to the weir), the upstream embankment dam, the labyrinth weir, the spillway channel, and the spillway sides of surrounding terrain. A picture of the extent of the physical model in the scheme map together with three views of the physical model are presented on Figure 5.6.

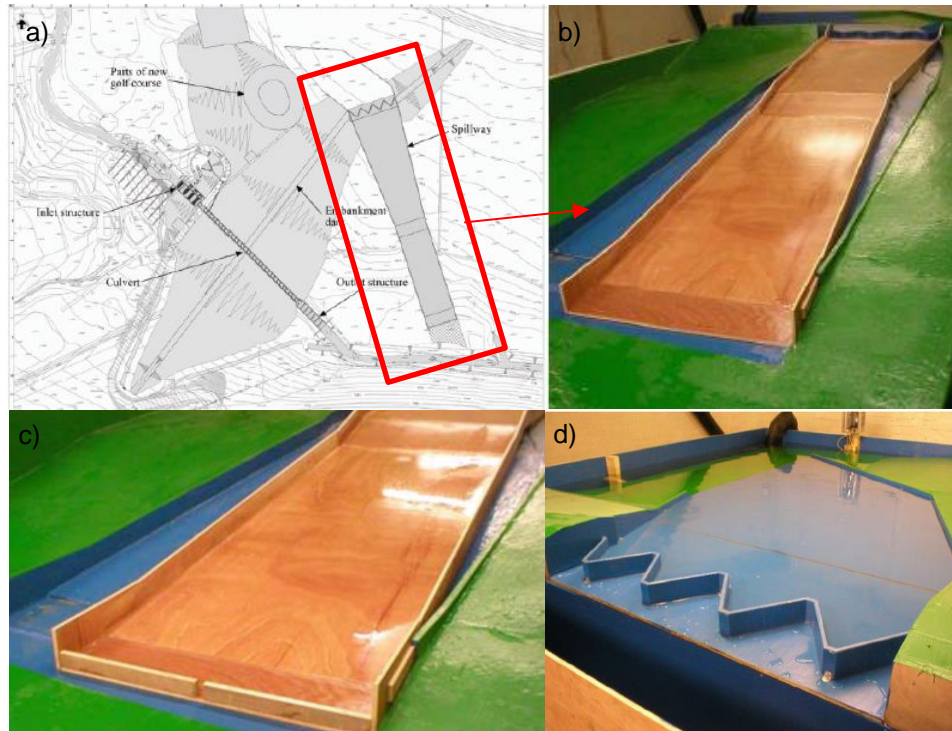


Figure 5.6: a) Layout of the flood storage reservoir with labyrinth weir and spillway from Brinded et al. (2014); b) Physical model of the labyrinth weir and spillway including surrounding terrain; c) Enhanced view of the end sill located at the tail of the spillway; d) Enhanced detail of the labyrinth weir

Figure 5.6 a) shows the extent of the physical model on a map of the entire scheme. Figure 5.6 b) shows the spillway channel in the physical model, before constructing the end sill at the tail of the channel and Figure 5.6 c) presents a view of the end of the channel with the addition of the end sill. Figure 5.6 d) shows a view of the labyrinth weir where its performance was verified against design specifications and appropriate amendments were introduced before modelling it in conjunction with the spillway channel.

The embankment dam culvert was not included in the physical model and it was modelled separately. Therefore, its modelling is not considered in this thesis.

5.3.1. Purpose of the Model

The purpose of the physical model of the labyrinth weir and spillway was to verify the initial design and ensure the general safety of the structure. There were a number of key outcomes which were needed from the physical model. Firstly, hydraulic modelling was necessary to confirm that the maximum head over the weir crest was not greater than 1.5 m in order to prevent overtopping of the embankment dam. Furthermore, the modelling of the flow over the labyrinth weir was conducted to inform optimisation of the design (with minimum height and width) and to ensure the spillway channel did not submerge the weir. The flow characteristics in the approach channel also required inspection to determine whether areas of high turbulence would be created which could pose a risk of erosion. Additionally, the physical model was required to verify that the flow stayed within the spillway channel structure. Finally, different levels of tail water were modelled to provide an insight of the interaction between the spillway flow with the various levels of tail water, and specifically, confirm velocities outside the concrete structure were sufficiently low.

5.3.2. Scale Factors

The model was constructed based on the Froude number law of similarity in a 1:25 scale. The scale factors utilised to scale the length, velocity, flow rate, time and pressure down to model scale are summarised as per Eq. 5.2 to 5.6.

$$L_p = 25 L_m \quad 5.2$$

$$v_p = \sqrt{25} v_m \quad 5.3$$

$$Q_p = 25^{\frac{5}{2}} Q_m \quad 5.4$$

$$t_p = \sqrt{25} t_m \quad 5.5$$

$$p_p = 25 p_m \quad 5.6$$

5.3.3. Instrumentation and Measurements

The flow through the physical model was simulated using a pump recirculation system and the flow rate was measured with an electromagnetic flow meter of 200 mm diameter, which was located in a section of pipes discharging to the reservoir. At the downstream end of the physical model, where the road embankment was represented, an undershot gate was introduced in order to control the discharge as well as to simulate the various levels of tail water.

Depths were measured with a steel ruler and the accuracy of the measurements is stated to be of 1 mm, which is equivalent to 25 mm in the prototype. The values of depth reported were the maximum values occurring in the experiment. When fluctuations occurred, a fluctuation range was provided. The velocity measurements were taken with a total head pitot tube. The velocity accuracy is stated to be 0.01 m/s in the physical model which is 0.05 m/s in the prototype.

Although physical model diagrams are provided with the location of the measurement points in the spillway channel, the exact coordinate of the experimental points is not available. Therefore, it is reasonable to assume that, especially in areas where the depths and velocities are highly changing, the results would have approximately 10% uncertainty. This would reduce in areas where there is less variation in water depth and velocity with changes in distance in the vicinity of the measurement points.

5.3.4. Scenarios Simulated and Results

A total of 8 flow rates were modelled, each of them with three levels of tail water on the spillway channel. The low flow rates modelled are 10 m³/s, 20 m³/s, 30 m³/s, 40 m³/s and 50 m³/s. The PMF of the site is 159.5 m³/s which was the largest flow modelled, along with 119.6 m³/s which corresponds to $\frac{3}{4}$ of the PMF and 79.8 m³/s which is $\frac{1}{2}$ of the PMF. All the physical model results are shown converted to prototype scale values by using Equations 5.2 to 5.6.

The rating curve of the labyrinth weir was obtained after the weir was calibrated to meet the design criteria. The physical model rating curve was obtained with a total of 13 points. The experimental rating curve is presented on Figure 5.7.

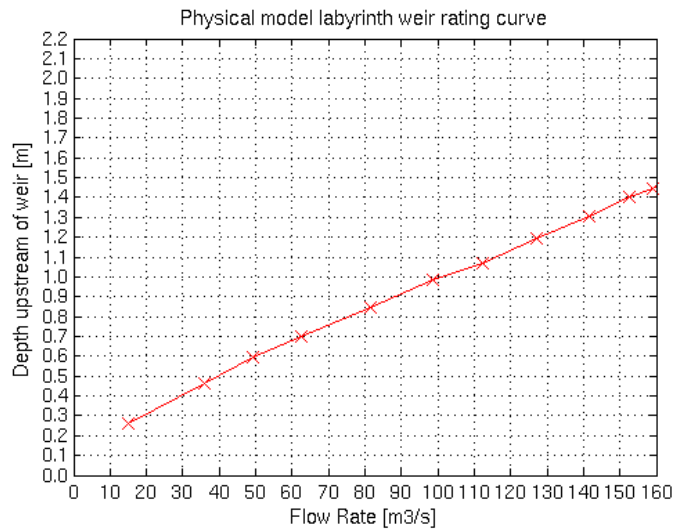


Figure 5.7: Labyrinth weir rating curve obtained with experimental measurements in the physical model. In addition to the labyrinth weir rating curve, the flow downstream of the weir and along the spillway channel was examined in the physical model. The available physical model dataset consist in point velocity and depth measurements at several locations of the spillway channel, experiment photographs and accurate representations of the waves' configurations and features. Also, for the PMF flow rate, 19 velocity measurement points at the crest of the labyrinth weir are available. Figure 5.8 a) shows the physical model diagram for 40 m³/s, including the location of the experimental points and the configuration of the cross-waves generated by the labyrinth weir. In the present research, the various measurement points have been named from A to E where point A is that located furthest upstream, and point E is located at the end of the channel, as indicated in the diagram. The experimental points aligned to those named B to E on the right side of the channel are also utilised for validation purposes and are referred to with the same name as those aligned to them on the opposite side of the channel. Figure 5.8 b) shows a picture of the physical model with the complex configuration of cross-waves developed immediately downstream of the labyrinth weir for 40 m³/s. Figure 5.8 c) shows the 40 m³/s flow over the entire spillway channel for low tail water conditions.

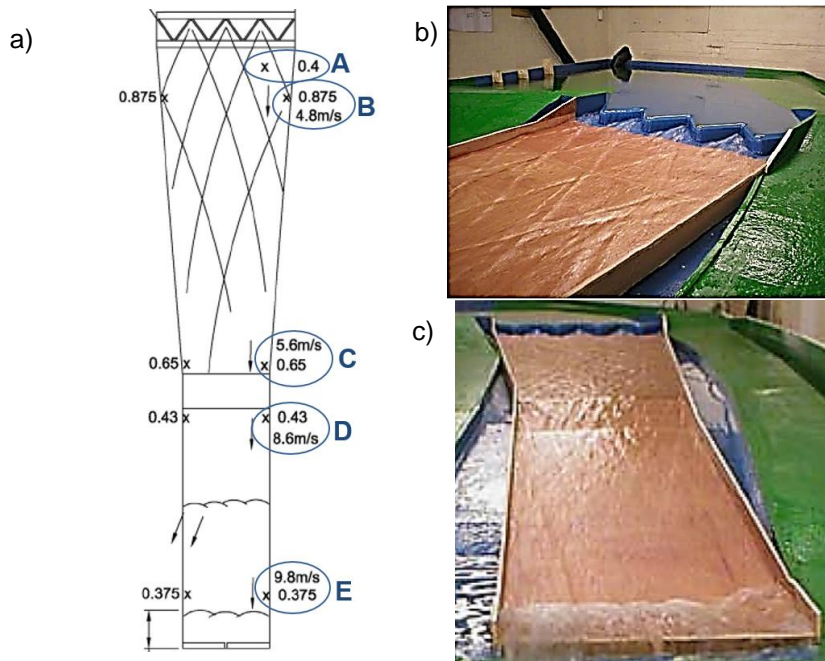


Figure 5.8: a) Physical model diagram with the location of the experimental measurements for 40 m³/s; b) Photograph of the flow downstream of the physical model; c) Photograph of the flow in the spillway channel

The three levels of tail water modelled for each flow are low, medium and high. The low tail water level corresponds to the scenario where the downstream road embankment has been eroded completely as a consequence of the storm. The medium tail water level scenario is the case where the Eller Beck river levels are those of the design storm and Embsay Beck is on base flow conditions. The high tail water level conditions occur when both rivers are experiencing the design storm conditions.

A hydraulic jump is formed where the spillway flow meets the tail water. A hydraulic jump is a highly turbulent phenomenon which is generated in a free surface flow when there is a transition from supercritical flow ($Fr > 1$) to subcritical flow ($Fr < 1$) (Chanson 2004b). Hydraulic jumps dissipate significant amounts of energy, and this consists in their main function in hydraulic structures. Hydraulic jumps are classified depending on the flow conditions upstream of the jump. Chow (1959) presents a classification of the type of hydraulic jump according to the Froude number of the incoming flow. These are presented on Table 5.1.

Table 5.1: Classification of hydraulic jumps according to Chow (1959)

Type of Hydraulic jump	Fr
Undular jump	1 to 1.7
Weak jump	1.7 to 2.5
Oscillating jump	2.5 to 4.5
Steady jump	4.5 to 9
Strong jump	>9

In this thesis, the interaction of the spillway flow with the three tail water levels are examined for the PMF flow rate only. In the PMF, the low, medium and high levels of tail water correspond to 133.0 m, 138.1 m and 139.9 m AOD.

6. VOF Modelling of the Labyrinth Weir and Spillway

6.1. Introduction

6.1.1. Chapter Contents

In this chapter, the 3D VOF model tested in Chapter 4 is applied to simulate the physical model of the hydraulic structure of study described in Chapter 5.

In the first sections of this chapter, the numerical modelling aspects for the implementation of the VOF to model the scheme of study are characterised. This includes the description of the modelling geometries and the domains utilised. In order to analyse various processes occurring in the physical model and conduct appropriate validation, three different domains are created. The meshing strategies adopted, and boundary conditions employed are also described.

In the second part of this chapter, the VOF simulation results are presented. Firstly, sensitivity analyses with respect to various numerical implementations are conducted, including mesh cell size, time step, turbulence model and interface capturing scheme sensitivity. Secondly, using a modelling domain which covers the entire spillway channel, the VOF method is applied to simulate four flow rates over the scaled physical hydraulic model of the scheme with the two previously used solvers. Thirdly, a modelling domain which comprises only the approach channel and the labyrinth weir with a limited section of the spillway channel, is utilised to compute the weir rating curve. Finally, a modelling domain embracing the entire scheme, including the upstream dam embankment as well as the spillway surrounding terrain, is employed to model the PMF flow rate with different levels of tail water. Validation of various flow aspects is undertaken using physical model measurements of depth, velocity and detailed representations of the flow features. Numerical results are discussed and conclusions on the analysis are drawn.

6.1.2. Structure of this Chapter

The information contained in this chapter is structured in the following subsections:

Sections 6.2 to 6.7: Numerical Modelling Characterisation

These subsections describe the various aspects which are involved in the setting up of the numerical CFD simulations. These include: Modelling domains, Meshing, Boundary Conditions, Initial Conditions, Flow Equations and Numerical Implementations.

Section 6.8: Model assumptions and Limitations

In this subsection the model assumptions and limitations are outlined. Justification for these and possible effects are discussed.

Section 6.9: Sensitivity Analyses

In this subsection, numerical simulations are conducted using various numerical implementations to investigate the model sensitivity to these. The different implementations examined consist in mesh cell size, time step size, turbulence model and interface capturing scheme.

Chapter 6. VOF Modelling of the Labyrinth Weir and Spillway

Three meshes with decreasing cell size are utilised to model the lowest flow rate in the spillway channel with the two solvers and the Grid Convergence Index (GCI) is calculated for the meshes which are found to be mesh independent.

Two different time step sizes are tested in the mesh of the modelling domain covering the approach channel and the labyrinth weir using values within the range of acceptable CFL numbers for numerical stability.

Three different turbulence models are tested for one of the largest flow rates including: Standard $k - \varepsilon$, RNG $k - \varepsilon$ and SST $k - \omega$. The results are compared against each other as well as against the experimental measurements and a decision is made on which model is to be applied for the rest of the simulations in this thesis.

Two different interface capturing schemes are implemented including the geometrical reconstruction approach PLIC and the compressive algebraic approach CICSAM to model the flow over the spillway channel. Predictions are compared against each other and with the experimental measurements in order to decide which algorithm is most appropriate.

Section 6.10: Modelling the flow in the spillway channel

In this subsection, the numerical modelling domain comprising the spillway channel is utilised to model four flow rates with the chosen mesh and implementations on each solver. In OpenFOAM, four flow rates are modelled, these are 40 m³/s, 79.8 m³/s, 119.6 m³/s, 159.5 m³/s. In order to compare the performance of the two solvers, Fluent simulations are undertaken of three flow rates, these are 40 m³/s, 119.6 m³/s and 159.5 m³/s. The modelling of the lowest, largest and a high flow rate in Fluent are judged to be sufficient to assess the performance of the solvers against each other. This also optimises computational and license resources.

Predictions on the spillway channel are analysed at the locations where there is availability of experimental data. Depths, velocities and wave structures are compared with those measured in the physical model and the performance of the VOF method implemented in the two solvers is evaluated.

Section 6.11: Prediction of the Labyrinth Weir Rating Curve

This subsection presents the numerical predictions of the rating curve, which are obtained with the modelling domain containing only the approach channel and the labyrinth weir, with several metres of spillway channel downstream the weir. The rating curve is simulated with the two solvers and is compared with that obtained with the physical model.

Section 6.12: Modelling the PMF in the Comprehensive Domain

In this subsection, a modelling domain comprising the entire hydraulic structure and the surrounding terrain is used to simulate the interaction with the different levels of tail water expected to be generated for the PMF case. Three tail water levels are modelled: low, medium and high, and the numerical predictions are compared with the physical model measurements and observations. The three simulations are conducted in Fluent.

Sections 6.13 and 6.14: Discussion and Conclusions

These subsections present a discussion of the results obtained in the previous sections and the conclusions for this chapter respectively.

6.2. Modelling Domains

The creation of the modelling geometry was possible given the availability of the full CAD drawings of the scheme and its surroundings which include the contour lines of the surrounding terrain with the 3D drawings of the hydraulic structures. Figure 6.1 outlines the main elements of the site. As previously noted, the embankment dam culvert is not considered for the modelling of the hydraulic situation in this work since it was not included in the physical model.

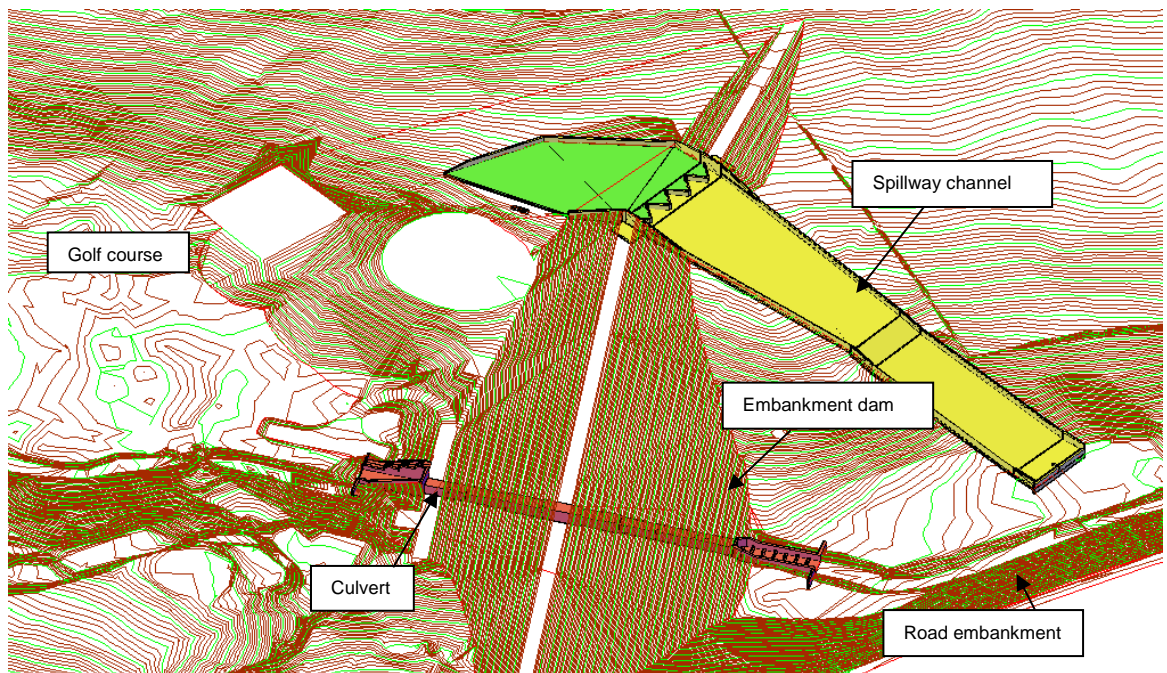


Figure 6.1: CAD drawing of the hydraulic structures and surrounding terrain

In order to conduct validation and examine different aspects of the flow, three different modelling domains were extracted. These are: a first domain comprising the approach channel, the labyrinth weir and a few metres of the spillway channel downstream of the weir; a second modelling domain comprising the areas of the first domain but also including the total length of the spillway channel and stilling basin; and a third domain covering the spillway surrounding terrain and the upstream embankment dam. The three modelling domains are presented on Figure 6.2.

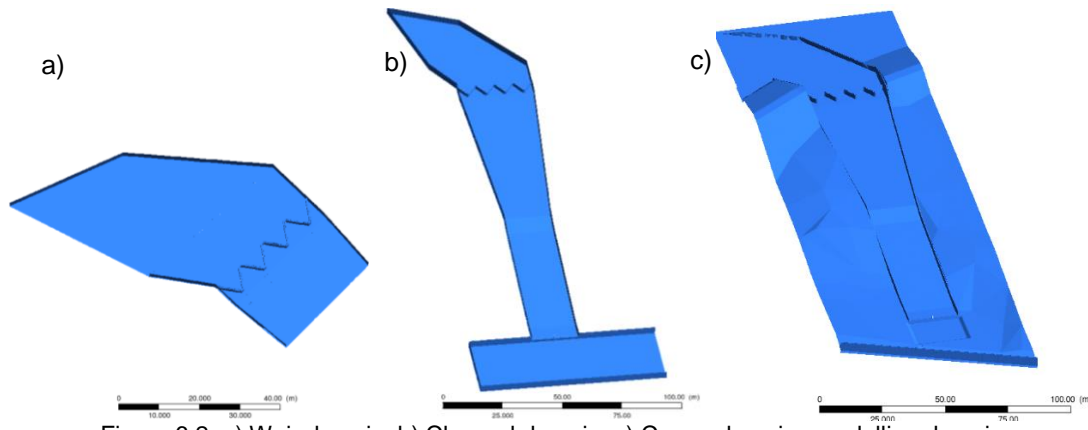


Figure 6.2: a) Weir domain; b) Channel domain; c) Comprehensive modelling domain

From this point onwards, the first, second and third modelling domains will be referred to as *weir*, *channel* and *comprehensive* modelling domains respectively. As detailed in Chapter 5, experimental measurements consist in the availability of the weir rating curve, depths, velocities and wave structures along the spillway channel and characteristics of the hydraulic jump at three different tail water levels. The weir modelling domain is created to accurately measure the flow characteristics in the approach channel and at the weir crest. This will be required for the calculation of the weir rating curve and for the extraction of the crest pressure and velocity distributions. The channel domain is intended to model the development of the water flow downstream the weir and along the channel, including predictions of water depths, velocities and wave features, which are the main aspects measured and observed in the physical model. In this geometry, an artificial box was designed adjacent to the end sill. This was to observe the behaviour of the flow along the end of the channel and stilling basin without possible disturbances induced by the outlet, by locating it further away from the channel. The comprehensive modelling domain was generated to observe the interaction of the channel flow with different levels of tail water, confirm that the water flow in the spillway channel remains in-bank and examine velocities on the sides of the spillway channel.

The creation of the modelling geometries was achieved using the Civil 3D toolbox in AutoCAD by employing various solid modelling operations. The geometries of the weir and channel domains were obtained by creating the 3D solids corresponding to the required domains by extruding the structure base and relevant areas surrounding the structure. This process created several 3D solids which were subsequently merged into one only element.

The comprehensive modelling domain required additional effort to be created, since it is not possible to extract the geometry of the irregular surrounding terrain by extruding 2D surfaces to create solids. For the creation of such domain a new methodology had to be devised. This involved a number of steps, which are outlined as follows:

- A Triangulated Irregular Network (TIN) was created to represent the surrounding terrain in a surface form using the contour lines as input.
- The produced TIN contained several millions of triangles, which required simplification in order to be able to construct a hexahedral mesh of sufficient quality based upon such geometry. The software MeshLab was utilised to simplify the TIN surface down to 300

triangles. The resulting surface obtained from the simplification process is shown on Figure 6.3.

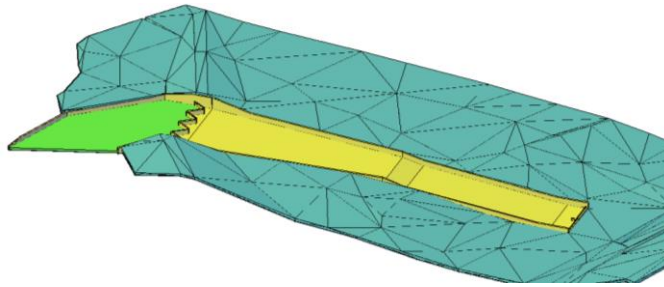


Figure 6.3: TIN of the surrounding terrain around the spillway channel, including the upstream and downstream embankments

- Once the TIN was created a method of extraction of the required modelling domain needed to be engineered, since the existing geometry was formed of the structure and terrain which are the inverse volume of the modelling domain. This was achieved by designing a 3D solid box covering the entire domain, encapsulating the complete geometry shown on Figure 6.3. The strategy applied was to create a void in such box with the shape of the structure and the terrain, and remove the parts which were not needed located under the TIN. The volumes not needed were cleared and the obtained geometry was trimmed into an optimal shape.
- The geometry with the modelling domain was then obtained with the extent of the physical model and the appropriate patches for the different boundary conditions were added. The complete prototype size extent of the comprehensive domain is 75 m x 250 m.
- In order to control the tail water level downstream the structure and conduct modelling of three different set levels, a weir was located with the model outlet. The calculations for the acquisition of the height of such weir are included on Section 6.4.2.

6.3. Meshing

Meshing was undertaken with the ANSYS Workbench Meshing application. Given the exceptional complexity of the modelling domains' geometries combined with the high quality of mesh required to implement the VOF method, where hexahedral meshes are remarkably beneficial, the Cartesian Meshing "CutCell" method was implemented. The CutCell is an Assembly Meshing method available in ANSYS Meshing for Fluent which produces a mesh for the entire model formed of hexahedral cells adapted to the given geometry. In order to achieve the purpose of each modelling domain, different meshing strategies were adopted. The weir modelling domain was meshed with a volume of equal cell size to be able to measure the flow characteristics upstream the weir with appropriate precision. The approach channel was meshed with one block of cell size 4×10^{-3} m and the labyrinth weir and its vicinity a block of cell size 2×10^{-3} m. The cell sizes of the weir domain were informed by a mesh sensitivity analysis conducted on the channel domain.

Figure 6.4 and Figure 6.5 show the mesh of the weir domain from two different perspectives. The same mesh of 9.5 M elements was implemented for simulations with the two solvers.

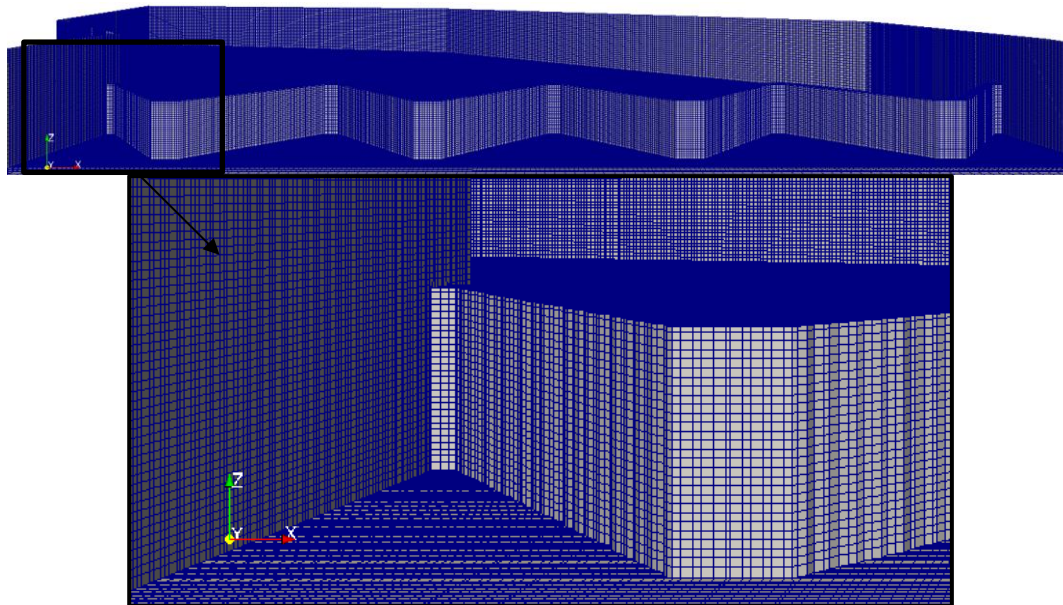


Figure 6.4: Weir modelling domain mesh, with enhanced view of the first downstream apex

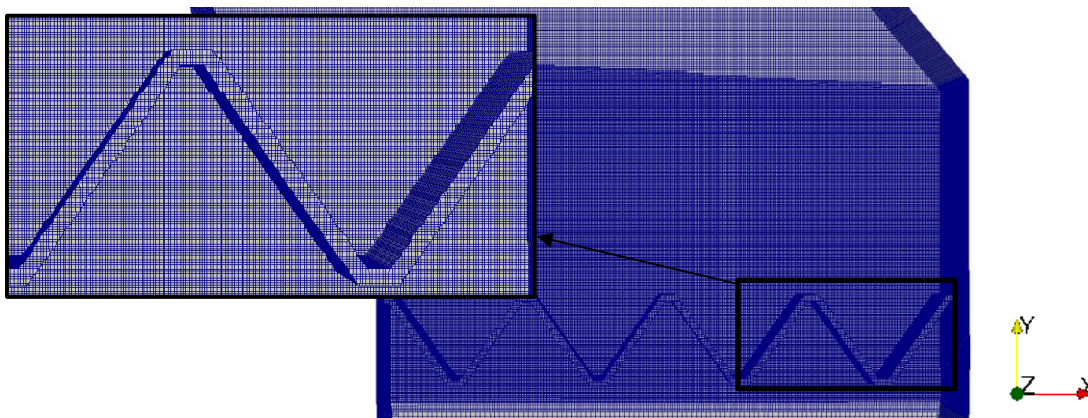


Figure 6.5: Plan view of the weir modelling domain mesh with a block of lower cell size in the labyrinth area and its vicinity

The channel and comprehensive domains were meshed with an inflation layer at the base of the spillway to accurately capture the flow features along the length of the channel.

The channel domain was meshed with two different approaches since the two solvers utilised responded differently to two different mesh configurations. Apart from the geometry of the labyrinth, the main complexity of such domain was the five different gradients of the spillway channel, including the flat gradients of approach channel and stilling basin. A channel mesh was first created with an inflation of 4 layers parallel to the spillway channel bed and simulations of the same flow rate were undertaken in Fluent and OpenFOAM. With this mesh configuration, the OpenFOAM results showed a successful representation of the complex pattern of cross-waves but the Fluent predictions were not able to appropriately reproduce it. The grid gradient change above the inflation layer produced interference and prevented the correct representation of the free surface features. The pattern of cross-waves created by the labyrinth weir is especially challenging to reproduce and requires a high resolution mesh as well as a configuration with no changes of mesh size or gradient at the free surface. A second mesh configuration was created, with the spillway channel base cell size half the size of the rest of the channel. This mesh was tested in both solvers and the Fluent results presented successful predictions of the cross-waves

as well as field quantities. The OpenFOAM results did not show an accurate representation of the flow characteristics and interface with this second mesh. Predictions exhibited a free surface which was not smooth but had the outline of the mesh cells. The meshes with the two configurations are shown on Figure 6.6 with the base mesh cell size indicated, which corresponds to the size of the cells in the area around the free surface. The two mesh configurations were created in two different cell sizes each (intermediate and fine) and a mesh independence study was conducted applying these in the two solvers. The third (coarsest) mesh had the same configuration in the two solvers. The details of the three meshes created with different resolution on the channel modelling domain are described in section 6.9.1, which comprises the mesh independence study.

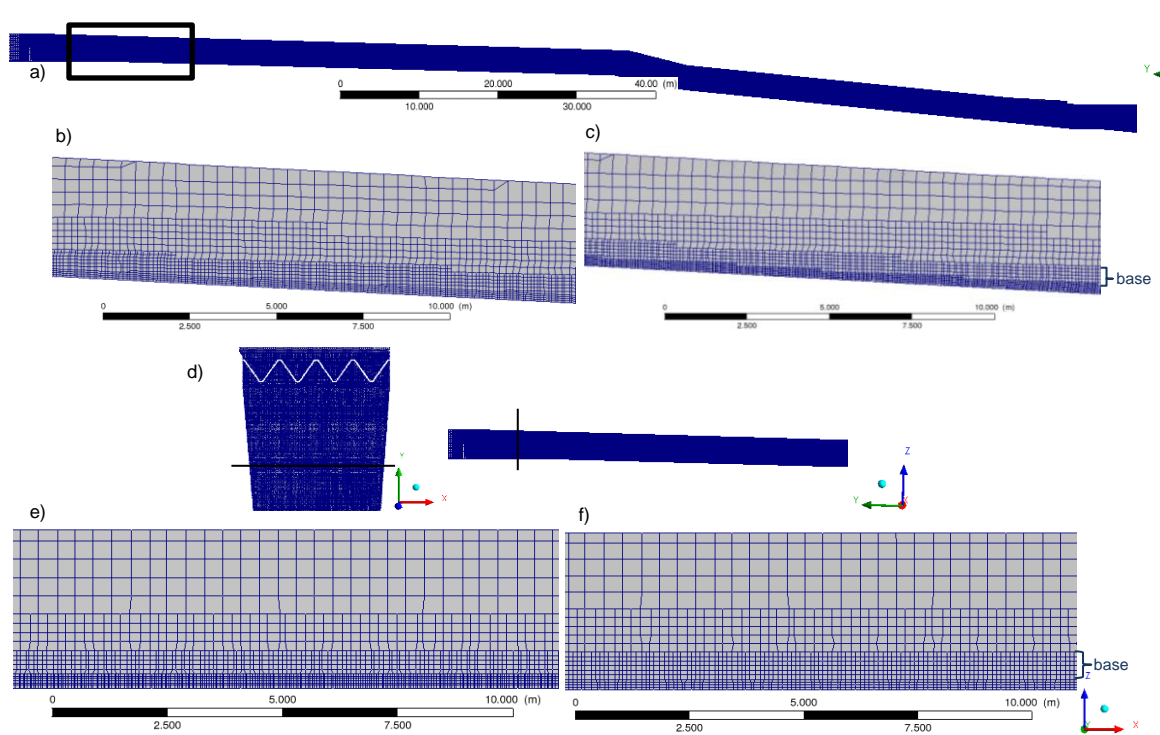


Figure 6.6: a) Prototype size spillway channel longitudinal mesh cross section (parallel to the flow) and detailed mesh configurations indicated in the rectangular area: b) appropriate for OpenFOAM and c) appropriate for Fluent; d) Plan view and side view of the mesh indicating the location of the cross sections (perpendicular to the flow) in: e) of mesh for OpenFOAM and f) for Fluent

The mesh for the comprehensive domain was created with a lower cell size at the base of the domain instead of an inflation layer, since the quality of the mesh cells improved significantly with this configuration. Figure 6.7 shows a top, side and bottom view of the low tail water level mesh. To effectively manage computational resources, the parts of the domain where water is not present, such as the upstream embankment and the spillway surrounding terrain, are meshed with a larger cell size.

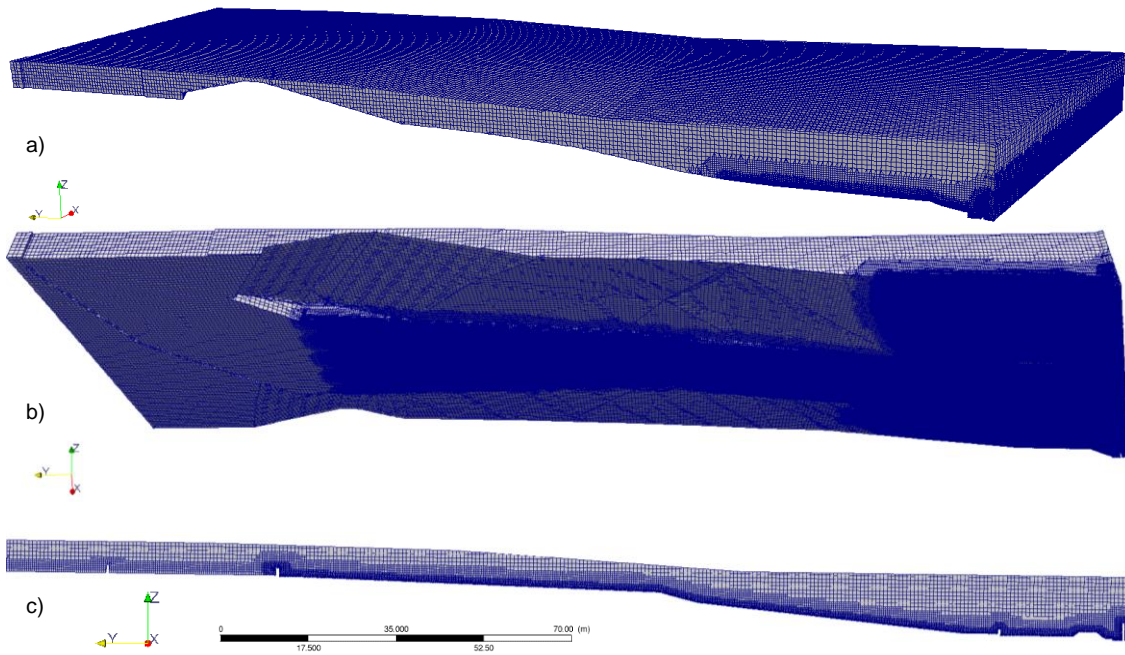


Figure 6.7:a) Prototype size mesh of the comprehensive domain (top view); b) Base view; c) Cross sectional plane along the mesh.

The cell size of the meshes of the comprehensive domains were informed by the sensitivity analyses conducted using the channel meshes, detailed in section 6.9.1. The cell size at the base of the spillway and surrounding terrain with presence of water was the same of that in the channel mesh of intermediate resolution, (4×10^{-3} m at model scale, 0.1 m at prototype scale) and similarly, the cell sizes were larger with increasing distance to the domain base, in the water depth direction.

The number of cells of the three meshes utilised to model low, medium and high tail water levels are outlined on Table 6.1.

Table 6.1: Number of elements of the meshes created to model low, medium and high tail water levels

Tail water level	Number of Elements
Low	6.25 M
Medium	7.27 M
High	7.79 M

6.4. Boundary Conditions

6.4.1. General

The boundary conditions at the inlet were the same for all modelling domains, where the flow rates $40 \text{ m}^3/\text{s}$, $79.8 \text{ m}^3/\text{s}$, $119.6 \text{ m}^3/\text{s}$ and $159.5 \text{ m}^3/\text{s}$ were scaled down according to Eq. 5.4 and kept constant throughout the simulations as executed in the physical model. The boundary conditions employed for the weir and channel domains are equivalent upstream of the labyrinth weir and they differ in the geometry and outlet downstream of the weir. In the weir domain the outlet is located 18 m downstream of the weir downstream crests. In the channel domain the outlet is located on the left wall of the artificial box designed adjacent to the stilling basin. In the comprehensive modelling domain, the location of the inlet is the same as in the other domains. The domain outlet is created on the downstream faces of the domain, and the outflow is regulated by the domain downstream weir which is designed at specific depth to control the required level of tail water. The boundary conditions at the three domains are indicated on Figure 6.8.

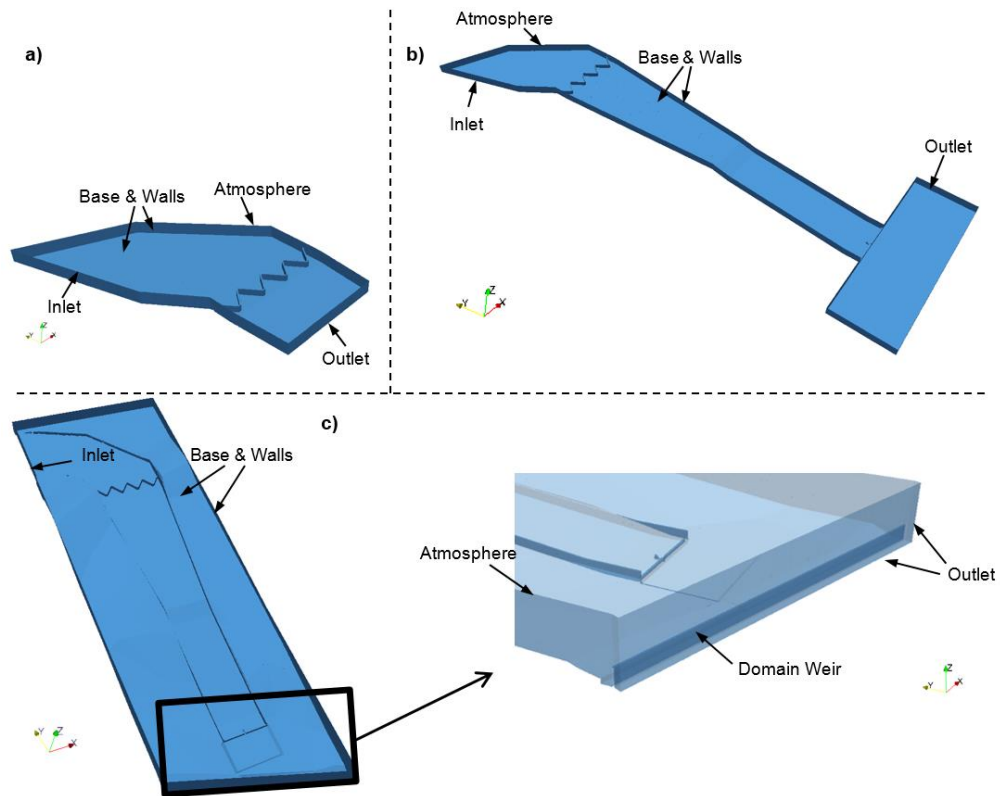


Figure 6.8: Boundary conditions for: a) weir modelling domain; b) channel modelling domain and c) comprehensive modelling domain

The boundary conditions are outlined as follows:

- Inlet

The inlet is located on the right side of the spillway, upstream the labyrinth weir as in the physical model, and as will occur in the prototype. An inflow boundary condition with constant velocity is invoked. The volume fraction function of the water at the inlet is established as 1, which implies the water inflow condition is set for the total area of the inlet. At the inlet, the pressure gradient in the flow direction is zero.

$$u = \text{constant flow rate}$$

$$\frac{\partial p}{\partial x} = 0$$

$$\alpha = 1$$

- Atmosphere

The upper boundary of the computational domain, which is the open air, was defined as pressure outlet with atmospheric pressure. The other field quantities are extrapolated from the flow in the interior.

$$\frac{\partial u}{\partial x} = 0$$

$$p = 0$$

$$\frac{\partial \alpha}{\partial x} = 0$$

- Outlet

At the model outlet a gauge pressure is given and all field quantities are extrapolated from the flow within the modelling domain. The gradient of all variables in the flow direction is set to zero.

$$\frac{\partial u}{\partial x} = 0$$

$$p = f(x)$$

$$0 \leq \alpha \leq 1$$

- Base and walls

No-slip boundary conditions are applied at the walls and the base of the spillway channel, including the weir structure. No additional wall roughness is included in the model as the wall characteristics of both scale and prototype (smooth plastic and concrete, respectively) do not indicate this would be necessary. The pressure gradient normal to walls and base is zero.

$$u = 0$$

$$\frac{\partial p}{\partial x} = 0$$

$$\frac{\partial \alpha}{\partial x} = 0$$

6.4.2. Downstream Weir Height Calculations

In the scaled physical model, the three different tail water levels downstream of the structure were set up and maintained constant in such a way that once the model reached steady state, the tail water level was the desired for each scenario. This situation needed to be reproduced in the same way in the numerical simulations.

The height required for each of the three levels of water was known. In order to achieve and maintain the tail water at such height at the steady state of the simulation a weir was created at the end of the domain which acted as a water level control. The weir crest height which would generate the desired level of tail water was not known, since the coefficient of discharge or the water height over the weir were also unknown and had to be calculated. An iterative procedure was undertaken in order to obtain the required upstream heads. A modelling domain with an initially estimated weir height was built and meshed. A simulation of the PMF flow rate was conducted and water depth predictions of the tail water were extracted once it reached steady state. Water depth values were extracted at several locations of the tail water, and they indicated the upstream head over the weir crest was 0.9 m. Therefore, for the modelling of low, medium and high tail water cases the weir crest was designed at a depth equal to 0.9 m lower than the required tail water level. In this thesis only the PMF flow rate is modelled using the comprehensive domain. The downstream weir width was 78.7 m. For the PMF case, the low, medium and high tail water design levels correspond to 133.0 m, 138.1 m and 139.9 m AOD. In order to achieve this, the downstream weir crests were located at 132.1 m, 137.2 m and 139 m AOD. The weir heights of the three different modelling domains are shown on Figure 6.9.

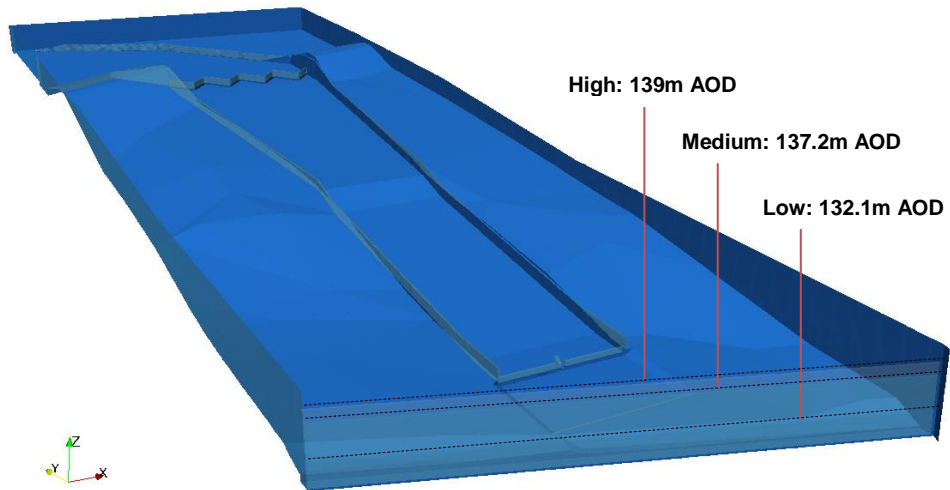


Figure 6.9: Three modelling domains corresponding to the three weir three levels overlaid

6.5. Initial Conditions

The initial conditions at the weir and channel domains were equivalent. These consisted of a pool of water of height equal to the weir crest height, created with the aim of saving computational time. Similar initial conditions were implemented in the comprehensive domains. The approach area was patched with a water pool to the height of the weir. In addition, downstream of the spillway channel, the tail water was patched up to the required level, which was equal to the height of the domain's weir. Initial conditions applied in the channel and comprehensive modelling domains are shown on Figure 6.10.

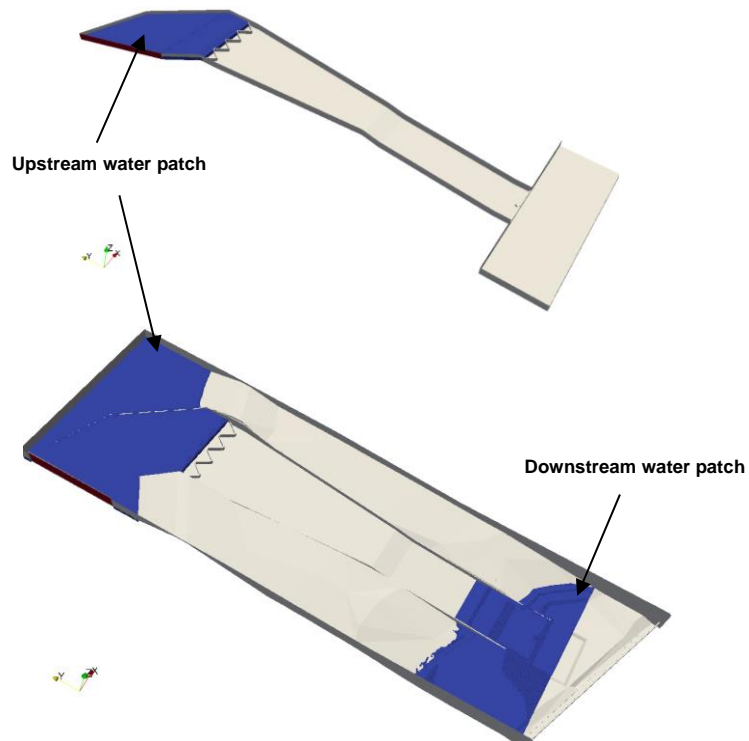


Figure 6.10: Setup of the initial conditions in a) the channel domain and b) comprehensive domain

6.6. Flow Equations

Simulations were conducted using a collocated Finite Volume Method (FVM) discretisation scheme together with the VOF approach for multiphase modelling. The two previously tested solvers in Chapter 4 were utilised again in this chapter to perform the numerical simulations and allow for performance comparison. These are the open source platform OpenFOAM 3.0.1 and the commercial CFD solver ANSYS Fluent 17.2. The three-dimensional turbulent nature of the flow required solving the 3D RANS equations comprising conservation of mass for an incompressible flow defined in Eq. 3.22 and the x, y and z conservation of momentum equations, shown in Eq. 3.26 to 3.28.

All fluid properties utilised were those corresponding to a temperature of 20 °C and are equivalent to the previously presented in Chapter 4, Table 4.2.

6.6.1. Turbulence Modelling

Turbulence was modelled with the RANS Standard $k - \varepsilon$ model with standard wall functions. The choice of this model was based on a sensitivity analysis presented on Section 6.9.3. This concluded that both the Standard and RNG $k - \varepsilon$ models were capable of accurately reproducing the flow situation.

6.6.2. Free Surface Modelling

As in Chapter 4, the free surface was modelled with the VOF multiphase model which involves solving a transport equation for the volume fraction function α defined by Eq. 4.1. The free surface was computed at the location of the volume fraction function equal to 0.5.

6.6.3. Flow Aeration

In this work the VOF method is employed to locate the free surface where the value of the volume fraction function is 0.5 and water and air are allowed to mix within a cell. No further models have been implemented to capture aeration phenomena of size smaller than the cell size.

6.7. Numerical Implementations

The model implementations applied in the two solvers are summarised on Table 6.2. The equation residuals set for all simulations were 1×10^{-5} . The main differences between the implementations in the two solvers are the time step method and the interface capturing scheme. OpenFOAM simulations were conducted on 180 HPC processors. The number of processors used in the Fluent simulations were restricted due to limits in the number of parallel licenses. These were typically from 48 to 84 processors.

Table 6.2: Model implementations applied on the two solvers

Implementation	OpenFOAM	Fluent
Turbulence Model	RANS standard k-ε	RANS standard k-ε
Wall treatment	Standard wall function	Standard wall function
Discretisation schemes: -Gradient -Divergence -Turbulent kinetic energy -Time derivative	Second order Least Squares Second order upwind Second order upwind First order (Euler)	Second order Least Squares Second order upwind Second order upwind First order (Euler)
Time Step	Variable (between 1×10^{-4} and 5×10^{-5} s)	Fixed (from 1×10^{-3} to 5×10^{-5} s)
CFL Number	0.8	0.5 to 1
Multiphase model	VOF	VOF
Interface capturing scheme	MULES	PLIC
Pressure-velocity coupling	PISO	PISO

Based on the findings from the study conducted in Section 4.4.2, the time stepping method in OpenFOAM was set as variable with a CFL limit of 0.8, and thus the time step size depended on the flow rate, which was typically between 1×10^{-4} s and 5×10^{-5} s. The time step was fixed in Fluent since it was demonstrated to provide best performance. The time step size had values from 1×10^{-3} to 5×10^{-5} s depending on the flow rate, with consequently CFL numbers of 0.5 to 1, which have been previously proven to be appropriate. Roenby *et al.* (2016) recommended a volume fraction CFL value closer to 0.1 in the use of the MULES scheme of interFoam solver in simulations where high precision is needed. The effects of the time step size (or CFL number) are investigated as part of the model sensitivity analysis and presented in Section 6.9.2.

As previously noted, in the version of OpenFOAM utilised (3.0.1) the available algorithm for interface capturing in the interFoam solver is the algebraic reconstruction scheme MULES. The geometrical reconstruction approach PLIC was utilised in Fluent and an additional simulation was conducted with the CICSAM approach to compare the differences in the predictions. This is shown on Section 6.9.4. Therefore, it is anticipated that changes in such numerical implementations might reflect in variations in the predictions from both solvers. This will be explored in Sections 6.9 and 6.10.

By extracting time series point data from the numerical simulations it was observed that steady state occurred after approximately 90 s of simulated real flow time in all flow rates. This is demonstrated on Figure 6.11 a) with the free surface depth time series at locations A, B, C, D and E of the spillway channel (of which the location is indicated on Figure 6.12) for a flow rate of $119.6 \text{ m}^3/\text{s}$. All numerical results presented in this study at point locations are time-averaged predictions extracted from the simulations at times between 95 to 120 s, when the monitored predictions had remained stable for a minimum of 5 s and hence generally within a time window of 20 to 30 s, depending on the simulation. Within such time window, the variation in the results was minimal with a standard deviation of approximately 0.001. In most cases, the results in this chapter are presented in the form of the free surface profiles plotted across the spillway channel from left to right, where the 0 m coordinate of the graph corresponds to the right wall of the spillway in all plots. Figure 6.11 b) presents a cross sectional free surface velocity profile through measurement point B at 12 different times taken every 5 s once the system is stable and variation is negligible.

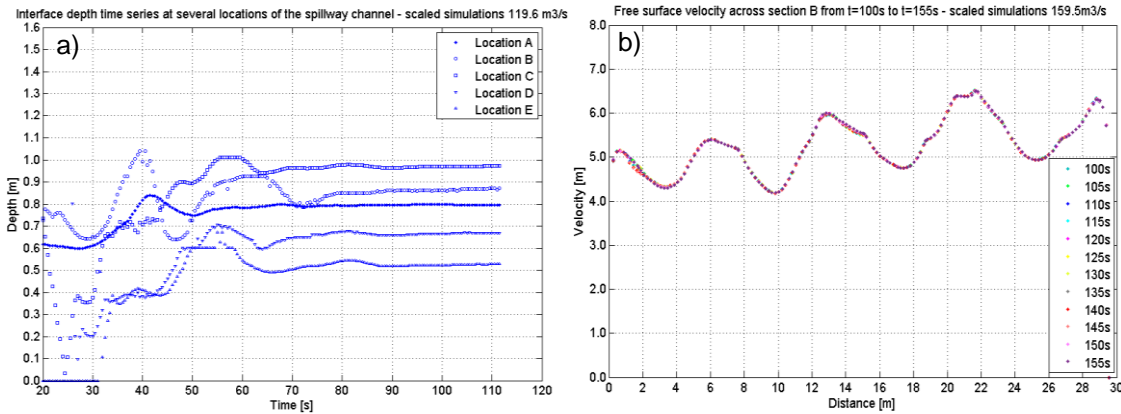


Figure 6.11: a) Time series of free surface depth at locations A to E of the spillway channel; b) Free surface velocity profile across the channel section through point B at time 100 to 155 s once the model is stable

6.8. Model Assumptions and Limitations

6.8.1. Air Entrainment

As previously discussed in Section 2.2.3.2, air entrainment is a key element of hydraulic free surface flows, causing an increase of water depth among other aspects. In this study the VOF method is implemented where water and air are enabled to mix within a cell. The exact location of the free surface is computed by the interface capturing scheme. However, no additional equations have been solved in order to model air entrainment phenomena smaller than cell size. For this reason, the amount of air entrained in the water phase is expected to be higher in the physical model than that predicted with the model scale simulations (and therefore, it is also expected to be larger in the real scale prototype than that predicted with the prototype scale simulations).

In the hydraulic structure of study, the air entrainment is relevant in two instances. These are the labyrinth weir nappe for large flow rates and in the hydraulic jump generated when the spillway flow meets the tail water. The impact of not including an additional modelling method to account for air entrainment is greatest for the largest flow rates. This is because the air entrained for the lowest flow rates, (40 m³/s and 79.8 m³/s) is negligible but it becomes more relevant for the two largest flow rates (119.6 m³/s and especially 159.5 m³/s).

6.8.2. Mesh Configuration and Refinement

The hydraulic structure of study represents a challenging modelling domain to mesh. This is given the large size and the remarkably complicated geometry of the physical model, (especially compared to the small size and simplified geometry of the dam break case modelled in Chapter 4). Because of the large geometry, it is not possible to generate meshes containing a larger number of cells, since it becomes computationally restrictive. The complicated geometry makes it very challenging to produce a mesh with the same quality to those generated in Chapter 4. The presence of multiple edges in the geometry does not make it possible to align nodes on each dimension in the same manner as previously conducted in the meshing tool utilised. For this reason, the CutCell mesh methodology was the option adopted. This meshing methodology could

lead, in some instances, to artefacts appearing in the free surface at the point in the mesh where cells change in size.

6.8.3. Roughness of Hard Boundaries

In this study it is assumed that there is no roughness in the hard boundaries, and a no-slip condition is applied. This assumption was made since the physical model was built with a timber and plastic resin which consists in a very smooth material. The same assumption is made to model the flows over the prototype structure since the real structure material consists in smooth concrete. The approximate values of the roughness height k of plastic and concrete are sufficiently low to consider this assumption acceptable. That for the plastic is from 0.0015 to 0.007 mm and that for smooth concrete is from 0.1 to 0.15 mm (Hager 1999).

6.8.4. Geometry Differences

As previously highlighted, model uncertainties can arise from differences in the physical model geometry and that in the numerical model. The numerical modelling domain was achieved directly from the 3D model of the scheme, as well as from a 3D model of the surrounding terrain. The physical model was built according to the 3D drawings of the scheme. However, minor differences in the geometry achieved in the physical and numerical models are expected, as a result of the manufacturing of the physical model and meshing of the numerical model.

6.8.5. Model Errors

As previously discussed in Chapter 5, although the approximate location of the physical model measurement points is indicated in the physical model diagram, their precise coordinate in respect of the weir or spillway walls is not of knowledge. Therefore, it is assumed that the experimental measurements carry approximately 10% of error. This value is considered to be representative of the location uncertainty as well as instrumentation error of the measurements, and has been used in other physical model studies, for example Dufresne *et al.* (2018). Consequently, in the calculation of the relative errors from the numerical models in respect of the physical model measurements, it will be considered acceptable if these are of the order of 10 %.

6.9. Sensitivity Analyses

6.9.1. Mesh Design and Grid Convergence Index

A mesh convergence study was conducted on the channel domain using 3 structured hexahedral meshes with increasing number of grid cells as shown on Table 6.3. The chosen cell sizes of such meshes were informed from the findings from Chapter 4.4.2. These meshes had the two different configurations appropriate for the two solvers as described on Section 6.3 apart from the coarsest mesh which had the same configuration.

Table 6.3: Characteristics of the meshes implemented for the mesh independence study in the two solvers

Mesh ID	Base Cell Size: Scaled/Prototype [m]	Solver to be implemented on	Number of elements
Mesh 1_Inf	$4 \times 10^{-3} / 0.1$	OpenFOAM	7.9 M
Mesh 2_Inf	$8 \times 10^{-3} / 0.2$	OpenFOAM	2.9 M
Mesh 3_Inf	$2 \times 10^{-2} / 0.5$	OpenFOAM & Fluent	0.6 M
Mesh1_B	$4 \times 10^{-3} / 0.1$	Fluent	8.1 M
Mesh2_B	$8 \times 10^{-3} / 0.2$	Fluent	3.3 M

Mesh independence was judged based on various aspects of the flow, including free surface features, depths and velocities. In order to quantify mesh independence the Grid Convergence Index (GCI) method specified by the ASME and described in Celik *et al.* (2008), was implemented. This method was developed by Roache (1994) and constitutes a standard procedure to quantify the mesh convergence. The method is based on the theory of the generalised Richardson Extrapolation, explained with extensive detail in Richardson (1910) and Richardson (1927). The method consists in calculating the predictions of a specific variable of interest f with at least three meshes of different cell size. The method assumes the solutions from the different meshes can be represented with a series expansion, with spacing equal to the mesh cell size. The generalisation of the Richardson extrapolation to the order of convergence p is described in Roache (1994). The series expansion is used to calculate an estimation of the error terms generated by the meshes of different cell sizes. In a consistent numerical study, as the mesh cell size tends to zero the solution of the discretised equations approaches the analytical solution (Elsayed and Lacor 2011).

Following the guidance for the application of the method as described in Celik *et al.* (2008) the first step is to choose a minimum of three meshes of different numbers of elements N with a representative cell size h each. These are N_1 , N_2 and N_3 which correspond to the number of elements of Mesh1, Mesh2 and Mesh3 as shown on Table 6.3. The values of h_1 , h_2 and h_3 correspond to the base cell size of each of the meshes. Therefore $N_1 > N_2 > N_3$ and $h_1 < h_2 < h_3$. Simulations are then run with the three meshes and the variable of interest f is computed for each of them. The mesh refinement factors r are calculated as per Eq. 6.1 and 6.2.

$$r_{21} = \frac{h_2}{h_1} \tag{6.1}$$

$$r_{32} = \frac{h_3}{h_2} \tag{6.2}$$

Celik *et al.* (2008) recommends a minimum value of 1.3 for the refinement factors. The mesh refinement factors r_{12} and r_{23} for the meshes of the present study are 2 and 2.5 respectively, both above the minimum recommended.

The key variables utilised for this study f_1 , f_2 and f_3 extracted from meshes 1, 2 and 3 respectively are velocities and depths at sections through measurement points A, B, C, D and E predicted by the models for a flow rate of 40 m³/s. The location of these measurement points is indicated on Figure 6.12.

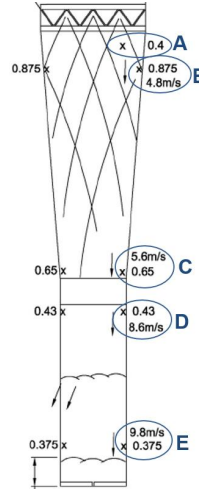


Figure 6.12: Location of points A, B, C and D in a physical model diagram with depths and velocities for 40 m³/s

The differences in the key variables computed with meshes of finest and medium refinement levels are defined in Eq. 6.3 that between the medium and coarsest refinement levels are defined in Eq. 6.4:

$$e_{21} = f_2 - f_1 \quad 6.3$$

$$e_{32} = f_3 - f_2 \quad 6.4$$

Once these variables are defined, the order of convergence of the results is calculated. Its expression is outlined on Eq. 6.5.

$$p = \frac{1}{\ln(r_{21})} \left| \ln \left| \frac{e_{32}}{e_{21}} \right| + \ln \left(\frac{r_{21}^p - s}{r_{32}^p - s} \right) \right| \quad 6.5$$

Where $s = 1 \cdot \text{sgn} \left(\frac{e_{32}}{e_{21}} \right)$

The expression of the order of convergence is implicit and therefore an iterative method needs to be employed to calculate the value of p .

The approximate relative errors in the variables between the solutions from different meshes ε are then calculated as per Eq. 6.6 and 6.7.

$$\varepsilon_{21} = \left| \frac{f_1 - f_2}{f_1} \right| \quad 6.6$$

$$\varepsilon_{32} = \left| \frac{f_2 - f_3}{f_2} \right| \quad 6.7$$

The next step is to utilise Richardson Extrapolation to obtain the value that a theoretical mesh of cell size equal to zero would give, f_{ext} also referred to as $f_{[exact]}$ in Roache (1994). Such extrapolated value of the key variable is shown on Eq. 6.8, which indicates that the exact value of the variable is equal to the variable calculated with the fine mesh plus an “error correction” term. Once the solution of the mesh of zero spacing is approximated, it will be possible to calculate the error due to mesh discretisation produced in the mesh utilised for the study.

$$f_{ext} = f_1 + \frac{f_1 - f_2}{r_{21}^p - 1} \quad 6.8$$

The extrapolated relative error of the fine mesh solution is expressed as per Eq. 6.9.

$$\varepsilon_{ext} = \left| \frac{f_{ext} - f_1}{f_{ext}} \right| \quad 6.9$$

If the mesh utilised for the analysis is not the finest but the intermediate, the correction to the intermediate mesh solution should be calculated. The expression for the mesh of zero spacing, f_{ext} in this case is calculated as per Eq. 6.10.

$$f_{ext} = f_2 + \frac{(f_1 - f_2) r_{21}^p}{r_{21}^p - 1} \quad 6.10$$

Similarly, the extrapolated relative error of the intermediate mesh solution is calculated with Eq. 6.11.

$$\varepsilon_{ext} = \left| \frac{f_{ext} - f_2}{f_{ext}} \right| \quad 6.11$$

Finally, it is possible to calculate the Grid Convergence Index for the finest mesh GCI_{21} using Eq. 6.12.

$$GCI_{21} = \frac{1.25|\varepsilon_{21}|}{r_{21}^p - 1} \quad 6.12$$

If the intermediate mesh is utilised, its index GCI_{32} needs to be reported instead, using Eq. 6.13.

$$GCI_{32} = \frac{1.25|\varepsilon_{32}|}{r_{32}^p - 1} \quad 6.13$$

Where 1.25 is a factor of safety.

It should be noted that GCI_{21} must always be lower than GCI_{32} .

The study was conducted with the two solvers. Results reveal that the VOF method implemented in OpenFOAM is more sensitive to changes in mesh size than that in Fluent. In the OpenFOAM simulations there were more noticeable changes between the finest and the intermediate mesh and hence the mesh of highest resolution was chosen. In particular, in OpenFOAM the wave features appeared defined with higher accuracy by the finest mesh. The Fluent simulations presented negligible changes between the predictions of the finest and intermediate meshes and hence the latter was chosen. This is reflected in the GCI_{21} and GCI_{32} values. Results from the study using velocities and depths averaged through sections A, C and E as key variables are shown on Table 6.4 and Table 6.5 for OpenFOAM and Fluent respectively. In the Fluent simulations the GCI_{32} of the mesh of intermediate resolution showed satisfactorily low values. The Fluent GCI_{32} values of velocities and depths at sections A, B, C, D and E of the spillway channel ranged between 0.04 and 2.7 %. The OpenFOAM GCI_{21} values for the finest mesh were between 0.2 and 11 %. These values are considered to be sufficiently low and within the expected range. Since the experimental values present an approximate error of 10 %, GCI values within 10 % are considered to be acceptable. The GCI value of 10 % is found to be in agreement with that calculated in other studies where this analysis was conducted for CFD of hydraulic structures, for example Pedersen *et al.* (2018) or Bayon *et al.* (2016).

Table 6.4: Parameters for the calculation of discretisation error in OpenFOAM, scaled Simulations

	Depth Section A	Velocity Section A	Depth Section C	Velocity Section C	Depth Section E	Velocity Section E
r_{21}	2	2	2	2	2	2
r_{32}	2.5	2.5	2.5	2.5	2.5	2.5
f_1	0.4375 m	3.1075 m/s	0.3861 m	4.4510 m/s	0.2331 m	7.9138 m/s
f_2	0.4175 m	3.1969 m/s	0.3699 m	4.492 m/s	0.228 m	7.7992 m/s
f_3	0.371 m	3.3616 m/s	0.338 m	4.5639 m/s	0.2202 m	7.6319 m/s
p	0.6928	0.4098	1.7206	1.5046	1.2435	1.1673
f_{ext}	0.47 m	2.8354 m/s	0.3931 m	4.4287 m/s	0.2369 m	8.0057 m/s
ϵ_{21}	4.5723 %	2.8759 %	4.1933 %	0.9204 %	2.2047 %	1.4477 %
ϵ_{ext}	6.9054 %	9.5948 %	1.7938 %	0.5034 %	1.5863 %	1.1486 %
GCI_{21}	9.2720 %	10.9435 %	2.2832 %	0.6261 %	2.0149 %	1.4525 %

Table 6.5: Parameters for the calculation of discretisation error in Fluent, scaled Simulations

	Depth Section A	Velocity Section A	Depth Section C	Velocity Section C	Depth Section E	Velocity Section E
r_{21}	2	2	2	2	2	2
r_{32}	2.5	2.5	2.5	2.5	2.5	2.5
f_1	0.4171 m	3.2101 m/s	0.3885 m	5.3048 m/s	0.2330 m	9.121 m/s
f_2	0.4191 m	3.1987 m/s	0.3901 m	5.2981 m/s	0.2352 m	8.8169 m/s
f_3	0.4419 m	3.0311 m/s	0.3955 m	5.2711 m/s	0.2461 m	8.309 m/s
p	2.5177	2.8538	2.7866	3.087	3.5389	1.4128
f_{ext}	0.4166 m	3.2119 m/s	0.3896 m	5.2998 m/s	0.2347 m	9.0085 m/s
ϵ_{32}	5.4324 %	5.2388 %	1.3843 %	0.5096 %	4.6763 %	5.7600 %
ϵ_{ext}	0.6043 %	0.4119 %	0.1170 %	0.0320 %	0.1904 %	2.1279 %
GCI_{32}	0.7508 %	0.517 %	0.1460 %	0.04 %	0.2376 %	2.7178 %

6.9.2. Time Step Size

The time stepping method was informed by the study undertaken in Chapter 4.4.2. In OpenFOAM variable time stepping was implemented with a CFL number of 0.9. In Fluent the time step was fixed and set to a similar size to that in OpenFOAM, which was between 1×10^{-4} s and 5×10^{-5} s, depending on the flow rate. Additional simulations were undertaken in OpenFOAM changing the global CFL number to observe and quantify its impact on the numerical outputs.

In OpenFOAM two simulations using the weir domain were conducted for the physical model scale $40 \text{ m}^3/\text{s}$ using CFL values equal to 0.2 and 0.9. These simulations were conducted with time step sizes of 4.1×10^{-5} s and 1.7×10^{-4} s respectively. Figure 6.13 shows the free surface velocity contours for the two cases taken at time equal to 90 s in both simulations. The velocity contours indicate the predictions from the two cases are very comparable.

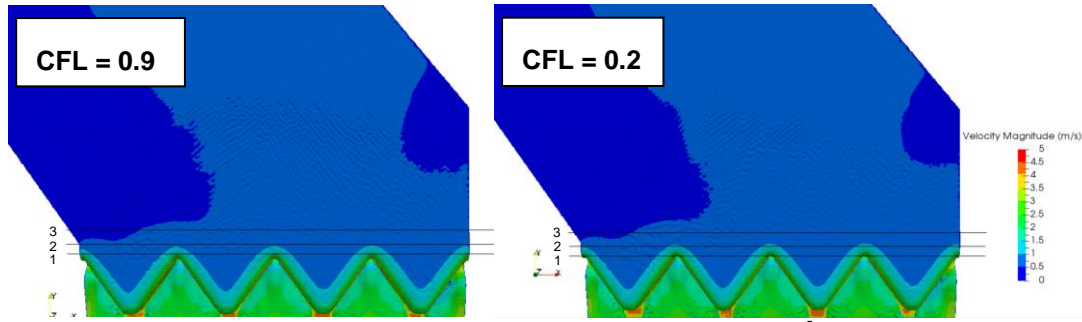


Figure 6.13: Free surface velocity contour plots on weir mesh for scaled 40m³/s with a CFL number of 0.9 and 0.2

Values of velocity and depth at sections 1, 2 and 3 upstream the weir indicated in Figure 6.13 were extracted and averaged across the section. Averaged values at each section for the two simulations and their percentage difference are shown on Table 6.6.

Table 6.6: Averaged values of depth and velocity along sections 1 to 3 for simulations with CFL numbers 0.2 and 0.9 and percentage difference between the two simulations

	CFL= 0.9 Depth	CFL 0.2 Depth	% Difference	CFL= 0.9 Velocity	CFL 0.2 Velocity	% Difference
Section 1	0.6379	0.6370	0.14	0.7335	0.7397	0.84
Section 2	0.6385	0.6390	0.07	0.5857	0.5918	1.04
Section 3	0.6361	0.6369	0.12	0.5082	0.5119	0.73

The section-averaged values show the difference in velocities and depths upstream the weir is negligible. A further inspection was made by extracting the time series depth at a point located on Plane 1, on the first upstream crest in order to contrast the variation of the results from the two simulations with time. The time series comparison obtained with the two CFL numbers is shown on Figure 6.14.

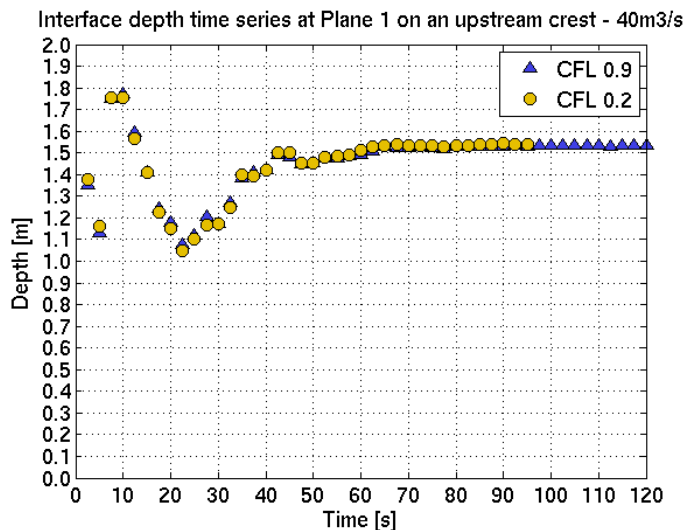


Figure 6.14: Interface depth time series of simulations using CFL numbers 0.2 and 0.9

Figure 6.14 confirms there are negligible differences between the time series predictions of the two simulations at the same location, with results indicating equivalent values once the system is stable. Therefore, this study verifies that CFL values between 0.2 and 0.9 would be acceptable, since the results do not appear to be impacted by changes in the time step within this range.

6.9.3. Turbulence Model

Simulations of the scaled $119.6 \text{ m}^3/\text{s}$ flow rate with three different turbulence models were conducted in OpenFOAM and model outputs were compared. The three models were implemented with the same wall functions available in OpenFOAM “nutkWallFunction”. Such function is the default standard for $k - \varepsilon$ and $k - \omega$ models and utilises a condition on the turbulent viscosity at the first node based on the logarithmic law of the wall using the turbulent kinetic energy value near wall. The sensitivity analysis in respect of turbulence model was conducted in one of the highest flow rates since the turbulence levels are higher and the flow structures are more complex than in the lower flows. The three models tested are the Standard $k - \varepsilon$, the RNG $k - \varepsilon$ and the SST $k - \omega$. Figure 6.15 shows the free surface wave structures and velocity contours for the three cases once the system had become stable.

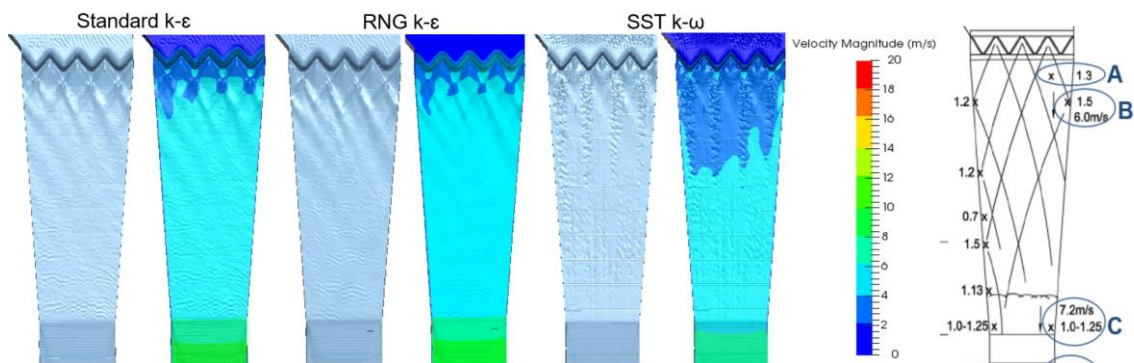


Figure 6.15: Free surface structures and velocity contours computed with the three turbulence models and physical model diagram showing the experimental locations and configuration of cross-waves

Results show the cross-waves are well reproduced by the both of the $k - \varepsilon$ models, however they do not appear as well defined when using the SST $k - \omega$ model. The velocity contours are very comparable in both $k - \varepsilon$ models and they exhibit significantly lower values in the SST $k - \omega$ case.

Cross sectional profiles of the results computed with the different turbulence models were plotted at different locations across the spillway channel. Figure 6.16 shows the depth and velocity profiles at sections through points B and C. The cross-waves generated by the weir cross for the first time at section through point A. At section through point B, the cross-waves cross for the second time, and this is indicated on Figure 6.16 a) and b). The results from the two $k - \varepsilon$ models exhibit the shapes of four sets of crests which have crossed and from this point, they move downstream in separate ways, therefore the two small crests are shown in each set. The $k - \varepsilon$ family models' predictions demonstrate significant resemblance, with the waves generally crossing at the same point apart from the third set of waves, which appears to be at its crossing point in the RNG $k - \varepsilon$ model but just downstream of it in the Standard $k - \varepsilon$ predictions. Results from the SST $k - \omega$ model appear to show a less pronounced pattern of waves, which have crossed just upstream of this section and hence it exhibits the four sets of crests with the pair of waves on each of them. The free surface depths predicted by the two $k - \varepsilon$ models show consistency, however, the depth profile predicted with the SST $k - \omega$ model appears to be about

40 % lower. Velocities are similar between the two $k - \epsilon$ models and slightly less than 1 m/s lower in the $k - \omega$ model (around 20% lower).

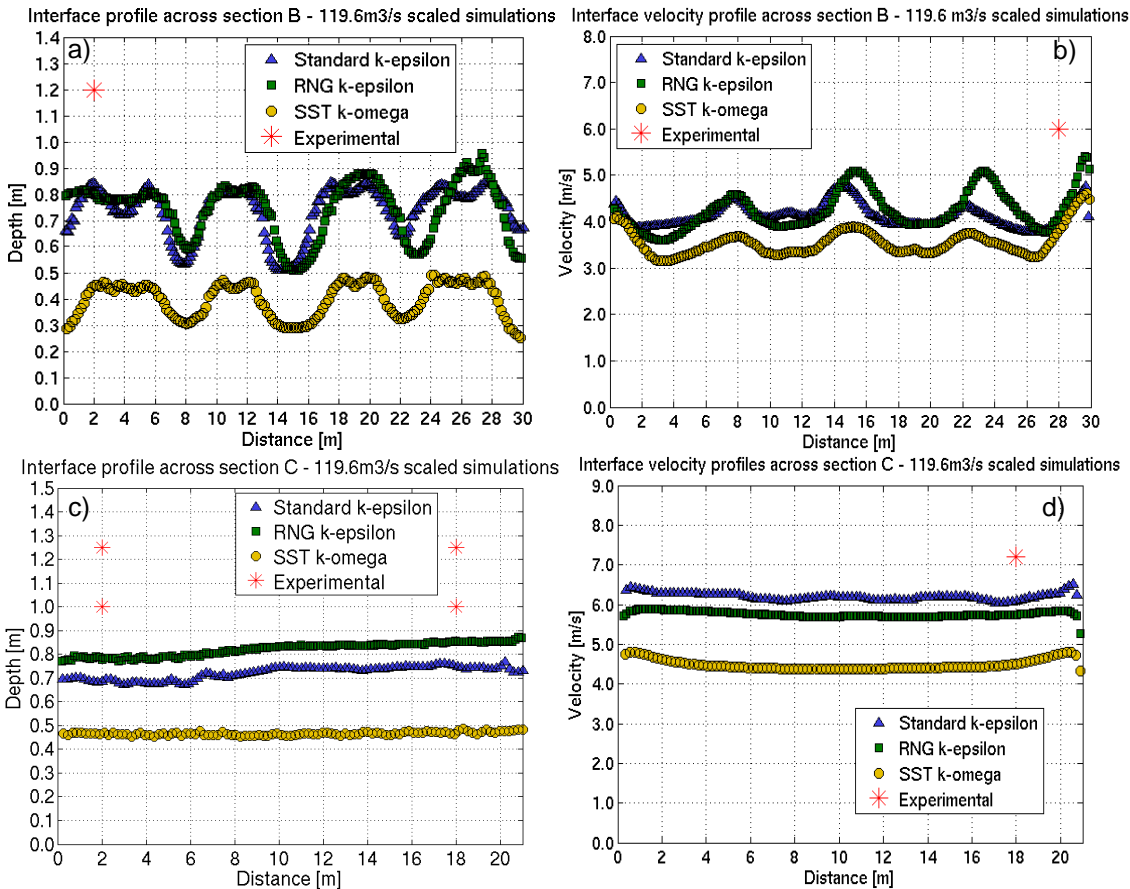


Figure 6.16: Cross-sectional profiles using the three turbulence models: a) interface depth and b) interface velocity sections through point B; c) Interface depth and d) velocity profiles at section through point C

Figure 6.16 c) and d) present the interface depth and velocity sections at section C, located just before the first change in gradient. Predictions at this section show the RNG $k - \epsilon$ model exhibits higher depths than the Standard $k - \epsilon$ by less than 0.1 m and the Standard $k - \epsilon$ shows velocities of around 0.5 m/s higher. The SST $k - \omega$ model presents significantly lower depths, from 0.2 to 0.3 m lower and about 1.5 m/s lower velocities.

The flow areas coloured by velocity were extracted at sections B, C, D and E of the spillway channel for the three cases. These are shown on Figure 6.17. It is observed that consistently in all sections the Standard $k - \epsilon$ presents the highest values of velocity, followed by the RNG $k - \epsilon$. The $k - \omega$ model presents the lowest velocity values in all sections.

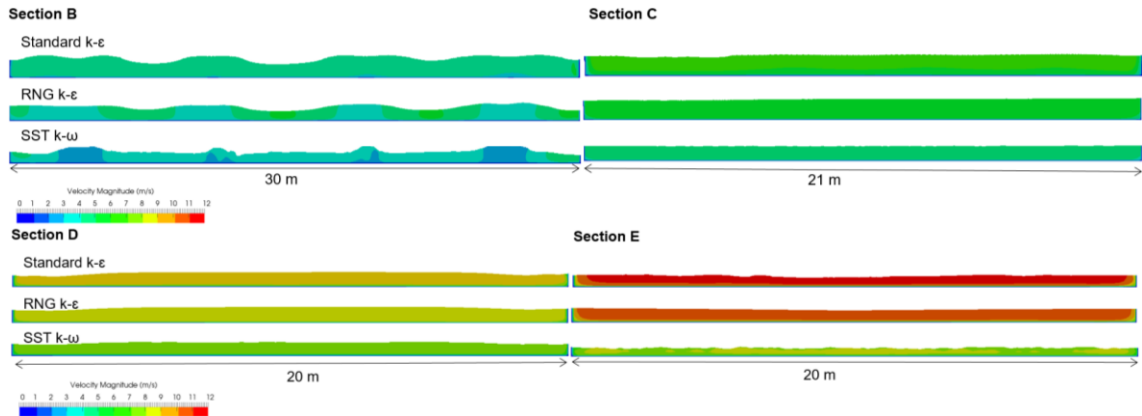


Figure 6.17: Flow areas coloured by velocity contours at sections through locations B, C, D and E of the spillway channel for the 119.6m³/s case predicted with the three turbulence models

Generally the depth predictions using the RNG $k - \epsilon$ model appear to be slightly higher than that predicted using Standard $k - \epsilon$ but the difference is less than 0.1 m. Depth profiles predicted using the SST $k - \omega$ model are significantly lower than the experimental measurements and the $k - \epsilon$ models, with approximately from 0.2 to 0.3 m difference. The velocity profiles provide overall very comparable predictions in the two $k - \epsilon$ models. Predictions from the SST $k - \omega$ model are approximately 1 to 2 m/s lower than these from the $k - \epsilon$ family models.

Table 6.7 outlines the averaged values of depth and velocity at cross-sections A to E predicted with the three models and the percentage difference in depth and velocity in the RNG $k - \epsilon$ and SST $k - \omega$ with respect to the values from Standard $k - \epsilon$. Results show the percentage difference in the predictions from the $k - \epsilon$ family are approximately from 0.2 to 10%, with generally an increase in depth and decrease in velocity in the RNG model with respect to the Standard. As already observed in the cross-sectional graphs, the differences in the $k - \omega$ model are in average of 40% decrease in depth and approximately 20% decrease in velocity.

Table 6.7: Section-averaged values of depths and velocities and percentage difference of model predictions from the RNG $k - \epsilon$ and SST $k - \omega$ models with respect to the Standard $k - \epsilon$

Section	Standard $k - \epsilon$		RNG $k - \epsilon$		SST $k - \omega$		%Diff. Standard vs RNG $k - \epsilon$		%Diff. Standard $k - \epsilon$ vs $k - \omega$	
	Depth [m]	Vel. [m/s]	Depth h [m]	Vel. [m/s]	Depth [m]	Vel. [m/s]	Depth [%]	Vel. [%]	Depth [%]	Vel. [%]
A	0.73		0.74		0.40		0.24		-44.90	
B	0.74	4.13	0.74	4.24	0.40	3.55	0.75	2.81	-46.27	-13.94
C	0.72	6.20	0.82	5.76	0.47	4.48	13.67	-7.14	-35.47	-27.67
D	0.51	9.08	0.56	8.64	0.29	7.69	8.41	-4.91	-43.70	-15.34
E	0.41	11.15	0.46	10.40	0.28	7.70	12.87	-6.74	-32.46	-30.97

Extracting the y^+ values at the first section of the spillway (where the cross-waves are located) and at the second section, (in between the first and second changes in gradient of the spillway base), it is observed that the three models present acceptable and similar values. Table 6.8 shows the minimum, maximum and average y^+ values at the first and second sections computed with the three turbulence models. In the three models the y^+ values are within the acceptable range, considering a maximum acceptable value of 300, as explained in Section 3.5.

Table 6.8: Minimum, maximum and averaged y^+ values at the first and second sections occurring with the three turbulence models.

Spillway section	Standard $k - \varepsilon$			RNG $k - \varepsilon$			SST $k - \omega$		
	Min y^+	Max y^+	Avg y^+	Min y^+	Max y^+	Avg y^+	Min y^+	Max y^+	Avg y^+
First section	27.4	175.6	57.3	32.4	138.5	73.5	29.9	133	68.5
Second section	46.8	81.8	68.3	50.9	108.3	95.1	42.8	97.8	86.4

The turbulence model study indicates either of the RANS $k - \varepsilon$ family models would be appropriate to model this case, involving complex cross-wave structures. The two $k - \varepsilon$ models present almost equivalent representations of the free surface features and with generally negligible differences in the predictions of depths and velocities. However, the RANS SST $k - \omega$ model does not appear to provide an accurate representation of such complicated features and exhibits an overall underestimation of the velocities and depths. Such underestimations are likely to be due to the nature of this model, which requires higher mesh refinement at the base of the spillway in order to correctly resolve the boundary layer. For the implementation of the $k - \varepsilon$ family, (with the implementation of wall functions), refinement in the near-wall region is believed to be sufficiently high. However, for the implementation of the SST $k - \omega$ model it is possible that a further refinement step would provide improved results. However, additional studies would be required in order to confirm this and identify the precise reason for the lower performance of this model.

From this point of the study onwards, the utilised turbulence model is the Standard $k - \varepsilon$, since it has been proven to provide an appropriate balance between computational resources and numerical accuracy.

6.9.4. Interface Capturing Scheme

In the version of OpenFOAM 3.0.1, utilised in this work, only one interface capturing scheme is available, which is the MULES algorithm previously described in Section 4.2.2.3. However, ANSYS Fluent 17.2 has a number of interface capturing schemes available. A simulation was conducted with the CICSAM scheme in Fluent to compare the predictions of this algorithm with those from the PLIC scheme for a physical model flow rate of $119.6 \text{ m}^3/\text{s}$. In case substantial discrepancies between such predictions and those using the PLIC scheme are observed, they could partly explain any differences present in the predictions from the two solvers. In Figure 6.18, the free surface depths and velocity profiles computed with the two interface capturing schemes are presented. Figure 6.18 a) shows the free surface sections through points A and B, located across the cross-wave configuration. The CICSAM scheme exhibits less prominent wave crests than the PLIC scheme. Figure 6.18 b) presents the free surface profiles at section through points C, D and E. Results show that in a reduced presence of free surface features, the two schemes exhibit similar representation of the free surface. Figure 6.18 c) indicates the interface velocity profiles at several sections of the spillway channel, and predictions from both schemes appear to be very comparable, with the only existing difference in profile through section D where the CICSAM schemes predict velocities 9% higher than the PLIC.

The PLIC scheme is shown to provide a more accurate representation of the free surface features with closer agreement with the experimental measurements. Consequently, this scheme will be implemented in all Fluent simulations unless stated otherwise.

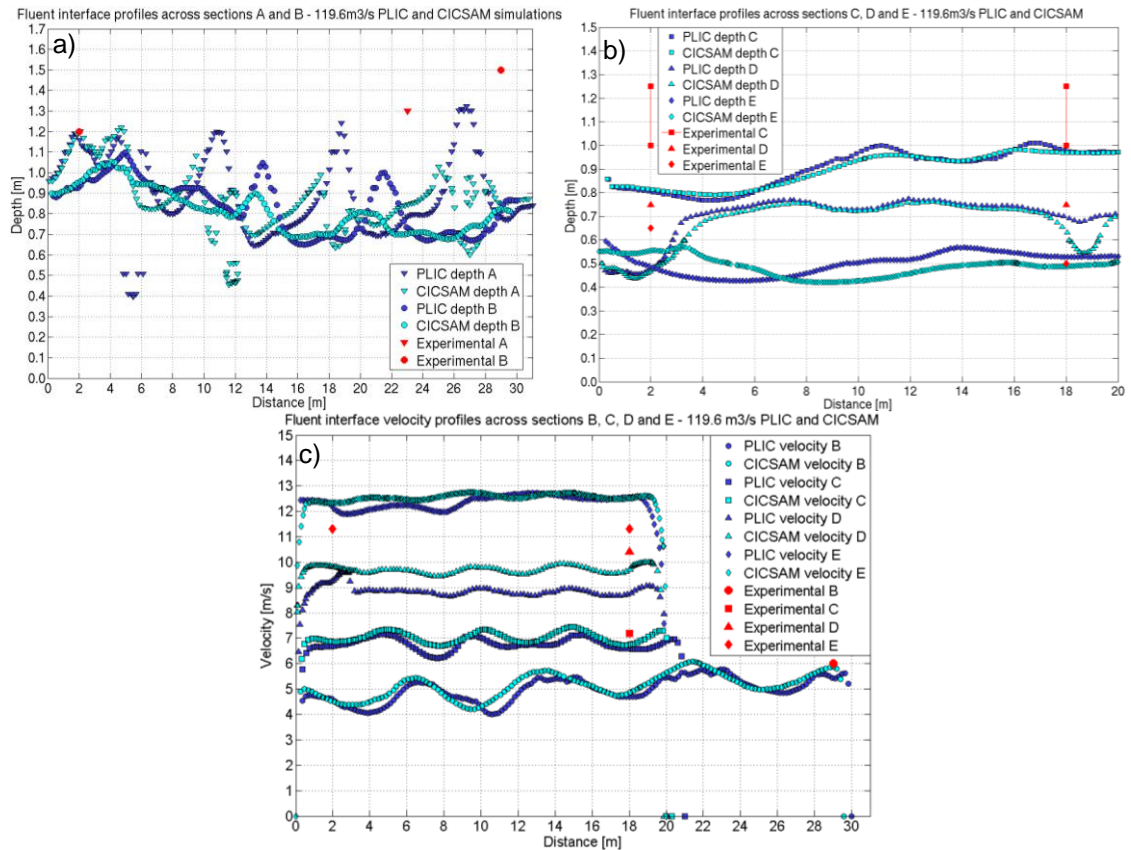


Figure 6.18: Cross-sectional profiles computed with Fluent simulations using the PLIC and the CICSAM schemes; a) Interface depth at sections through points A and B and b) through C, D and E; c) Interface velocity profiles at sections through points B to E

6.9.5. Discussion

The mesh independence study indicates that the two solvers require different levels of refinement to produce similar results for the particular flow situation simulated in this section. In OpenFOAM a mesh with main cell size 4×10^{-3} m at the free surface area is found to be appropriate to capture the complex pattern of intersecting cross-waves and represent all the free surface features. For a cell size of 8×10^{-3} m, the results do not appear to be mesh independent and the free surface exhibits a more diffuse pattern. In addition, as the CGI in OpenFOAM study demonstrates, the velocities and depths present noticeable differences. In contrast, the Fluent predictions from the intermediate mesh (8×10^{-3} m at the free surface area) are proven to be sufficiently mesh independent and are capable of capturing the free surface features with detail.

These results imply that the OpenFOAM solver, for a flow situation occurring at the scale of the process modelled in this section, (i.e. a scaled physical model) shows greater mesh sensitivity than Fluent. The higher mesh sensitivity of OpenFOAM compared to other solvers in the modelling of experimental flows has also been documented in other studies. For example Bayon *et al.* (2016) found that OpenFOAM exhibits higher sensitivity to cell size compared to the commercial solver Flow 3D.

As previously verified in Chapter 4.4.2, the Fluent 3D simulations provide a best estimation of the flow situation when using a fixed time stepping with a CFL number between 0.5 and 1. This has been observed again in this significantly more complex geometry where CFL numbers in such range provide accurate results, and there is no need to use values lower than that, which is beneficial considering computational time. Changes in the OpenFOAM time step size were not examined in Chapter 4.4.2 and the CFL number was kept low according to the code guidance. This study revealed that CFL values between 0.1 and 0.9 provide equally accurate predictions.

Three of some of the most well-known and widely implemented RANS turbulence models were employed to simulate the second largest flow rate over the labyrinth weir and the spillway. These are the $k - \varepsilon$ RNG, $k - \varepsilon$ Standard and SST $k - \omega$. Results confirmed the two $k - \varepsilon$ models implemented are capable of capturing the complexity of the hydraulic flow and they exhibit values of depth and velocity which correlate with those measured in the physical scale model. There were only minimal discrepancies in the characteristics of the flow predicted with the two $k - \varepsilon$ models, with the RNG model generally presenting minor increases in depth and decreases in velocity. In average, such differences were approximately around 5 %. However, the SST $k - \omega$ appears to consistently underestimate velocities and depths compared to the $k - \varepsilon$ family models. Bayon *et al.* (2017) also observed a similar behaviour in the modelling an experimental stepped spillway where the SST $k - \omega$ model appeared to underestimate velocities. Given the nature of the SST $k - \omega$ model, the flow behaviour predicted with this model could be due to the mesh refinement level utilised. It is possible that this model would perform more successfully if a further refinement step was taken near the hard boundaries. However, the mesh utilised to conduct the simulation with the SST $k - \omega$ model is the finest one employed in this study and refining it further would not present a feasible solution considering the time available to complete this analysis. Additional investigations would be required, for example for a wider range of flow rates in order to verify the cause of the low performance of this turbulence model.

The high performance of the $k - \varepsilon$ family in this study is in line with studies available in the literature which confirm the suitability of such models for modelling free surface flows over hydraulic structures. Some examples can be found in Bombardelli *et al.* (2010), Ferrari *et al.* (2009b) or Witt *et al.* (2015). Finally, it is important to highlight the fact that the $k - \varepsilon$ models are computationally less expensive than the SST $k - \omega$ model. Therefore, results indicate the benefit of utilising models from the $k - \varepsilon$ family for this particular case since they are capable of offering higher accuracy and at a lower computational cost.

The PLIC interface capturing scheme based on geometrical reconstruction of the volume fraction is often considered superior to the algebraic approach CICSAM in terms of accuracy and interface sharpness (Denner and van Wachem 2014). In this case this is demonstrated by the comparison of the two schemes in Fluent and with that implemented in OpenFOAM, based on a compressive approach. It has been observed that generally the very complex pattern of intersecting cross-waves is still captured with remarkable accuracy using the CICSAM (in Fluent) and the MULES (in OpenFOAM) schemes. However, for the largest flow rates, the cross-waves' patterns are particularly complicated and the PLIC scheme appears to provide slightly improved predictions of

the high peaks of the waves. The CICSAM scheme has been applied for 119.6 m³/s. As it will be further detailed in Section 6.10, this flow rate together with the PMF present the greatest difference in the predictions of the waves by the two solvers. For 119.6 m³/s the two compressive schemes present considerably resembling predictions of the free surface waves' profiles. Figure 6.19 shows the free surface profiles at sections through points A and B using the CICSAM scheme in Fluent and the MULES scheme in OpenFOAM. The waves' peaks appear to be flatter than those predicted by the PLIC scheme and hence the predictions from the two algebraic compressive schemes demonstrate agreement. However, although the models are predicting similar wave features, the OpenFOAM predictions of depth are slightly lower than those from Fluent.

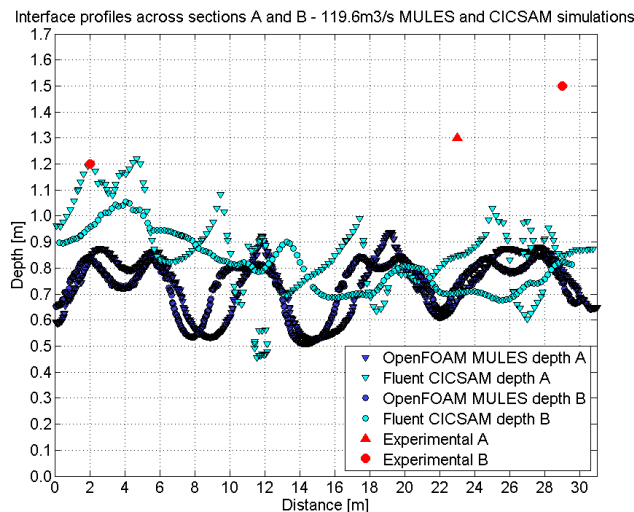


Figure 6.19: Cross-sectional interface depth profiles for 119.6m³/s using Fluent CICSAM and OpenFOAM MULES at sections through points A and B

This is interesting given that in the experimental dam break case modelled in Chapter 4 the results predicted with the PLIC and CICSAM algorithms could be considered almost identical. This shows that for a considerably simpler flow situation the schemes predict equivalent results. In addition, for 40 m³/s, (see section 6.10.1) the OpenFOAM and Fluent predictions of cross-waves' features are very comparable which means that for a low flow rate with lower depth and velocity, the MULES scheme appears to perform equally to the PLIC. When increasing the flow rate, the flow situation modelled presents higher levels of turbulence and greater complexity of the flow structures. This tests the schemes for a significantly more challenging flow situation, making it possible to reveal their slight differences. Therefore, the implementation of the CICSAM scheme for the 119.6 m³/s flow rate in Fluent, verifies that the interface capturing scheme is one of the causes of the higher differences between the two solvers for the two largest flow rates, as it will be detailed in Section 6.10.3.

The existing challenges of the interface capturing algorithm for OpenFOAM in version 3.0.1 for complex flow situations have been identified by the code developers, and a new algorithm based in geometric reconstruction, capable of ensuring boundedness and consistency was devised during the time this research was being undertaken. The new algorithm is referred to as "IsoAdvect" and it is included in OpenFOAM v1706 which is not currently available at the computer cluster used to conduct the present work. A further study to investigate the performance

of this new scheme in OpenFOAM to this flow situation would undoubtedly be of value. More details of such algorithm in addition to its comparison with the CICSAM, MULES and HRIC schemes can be found in Roenby *et al.* (2016) which concludes that significant improvements are achieved with the newly developed algorithm for the tested cases.

6.10. Modelling the Flow in the Spillway Channel

In this section, simulations on the channel modelling domain are undertaken for the four flow rates: 40 m³/s, 79.8 m³/s, 119.6 m³/s and 159.5 m³/s. Simulations were conducted using the chosen design meshes and implementations resulting from the sensitivity analyses. As indicated in Section 6.9.1, the meshes employed are Mesh1 in OpenFOAM and Mesh2 in Fluent.

6.10.1. Low Flow Rate: 40 m³/s

The physical model photograph showing the complex configuration of intersecting cross-waves generated by the labyrinth weir for 40 m³/s after the model reached steady state is presented on Figure 6.20 a). The numerically predicted with the VOF method implemented in OpenFOAM and Fluent for 40 m³/s are presented in Figure 6.20 b) and c) respectively. Figure 6.20 d), e) and f) show the cross-waves' crests indicated with numbered red lines in the physical model and predicted with the two solvers respectively. Figure 6.20 g) corresponds to a photograph of the entire spillway channel and that with black lines indicating the main features at the third section on the spillway channel. The physical model diagram is presented on Figure 6.20 h) with the locations of the experimental locations, named from A to E and the detailed flow features. It is important to note that the cross-waves crests indicated on the physical model diagram consist in qualitative information and not quantitative. That is, the diagram shows the representation of the cross-waves' arrangement observed in the physical model with no exact positioning of the crests in respect of the distance to the weir or to the spillway change in gradient. For this reason, these appear larger and more stretched compared to the physical model photograph and the numerical predictions. Despite of the minor uncertainty around the wave positioning, it is appreciable that all of the cross-waves observed in the physical model photographs and indicated in the model diagram are well predicted by the two numerical solvers as shown in Figure 6.20 i). The numerically predicted crests illustrated in the physical model diagram and observed in the physical model photograph have been indicated with dark lines on top of the free surface in Figure 6.20 j). Comparing experimental results in Figure 6.20 h) with the numerical predictions identifies that the numerical results from the two solvers present accurate capturing of the complex configuration of cross-waves generated by the labyrinth weir.

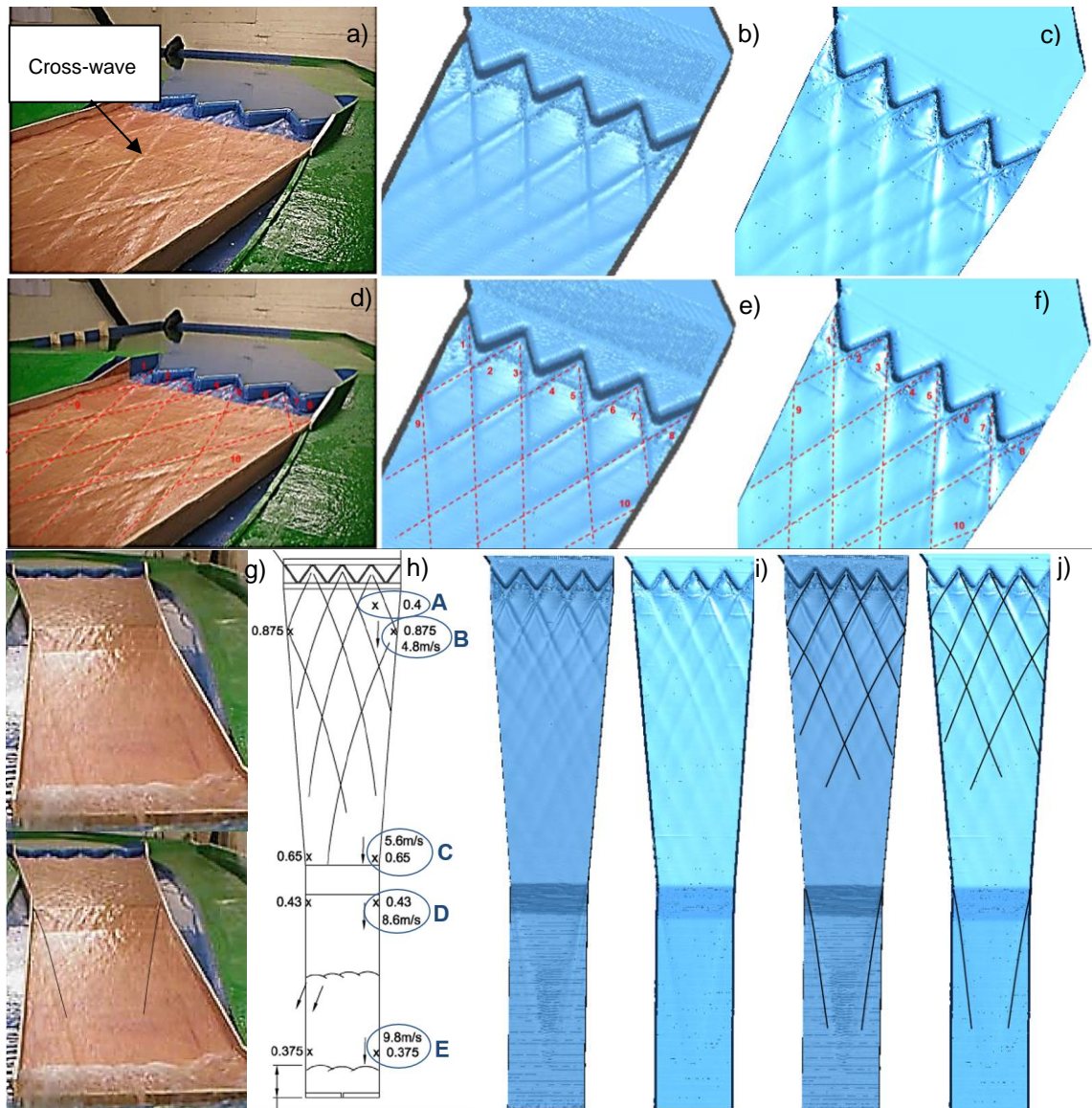


Figure 6.20: a) Photograph of the physical model free surface and numerically predicted with b) OpenFOAM and c) Fluent; d) Cross-wave crests indicated with red lines on physical model, e) in OpenFOAM predictions and f) in Fluent predictions; g) Photograph of the physical model spillway channel and with black lines indicating central wave; h) Physical model diagram with experimental locations and flow features; i) Numerically predicted free surface for the spillway channel and j) with location of cross-waves' crests with OpenFOAM and with Fluent for a flow rate of $40 \text{ m}^3/\text{s}$

The location of three cross-waves crossing points predicted with the two solvers was examined. These are referred to as x_1 , x_2 and x_3 and they correspond to the distance between the weir downstream apexes and the crossing points between cross-waves 3 and 4, 3 and 6, and 3 and 8 respectively. The distances x_1 , x_2 and x_3 are indicated on Figure 6.21 a). The free surface profiles along the three distances where the x coordinate corresponds to the weir downstream weir apex are shown on Figure 6.21 b), c) and d). Results show the greatest difference occurs in distance x_1 where Fluent shows minimal space between the weir downstream apex and the cross-wave crest crossing point and OpenFOAM shows approximately 3 m of distance before the crossing point is originated. Such difference in the two solvers is expected to be due to the different interface capturing scheme implemented in the two solvers. Distance x_2 presents approximately 0.5 m difference between the two solvers. The two solvers show consistency in the prediction of distance x_3 .

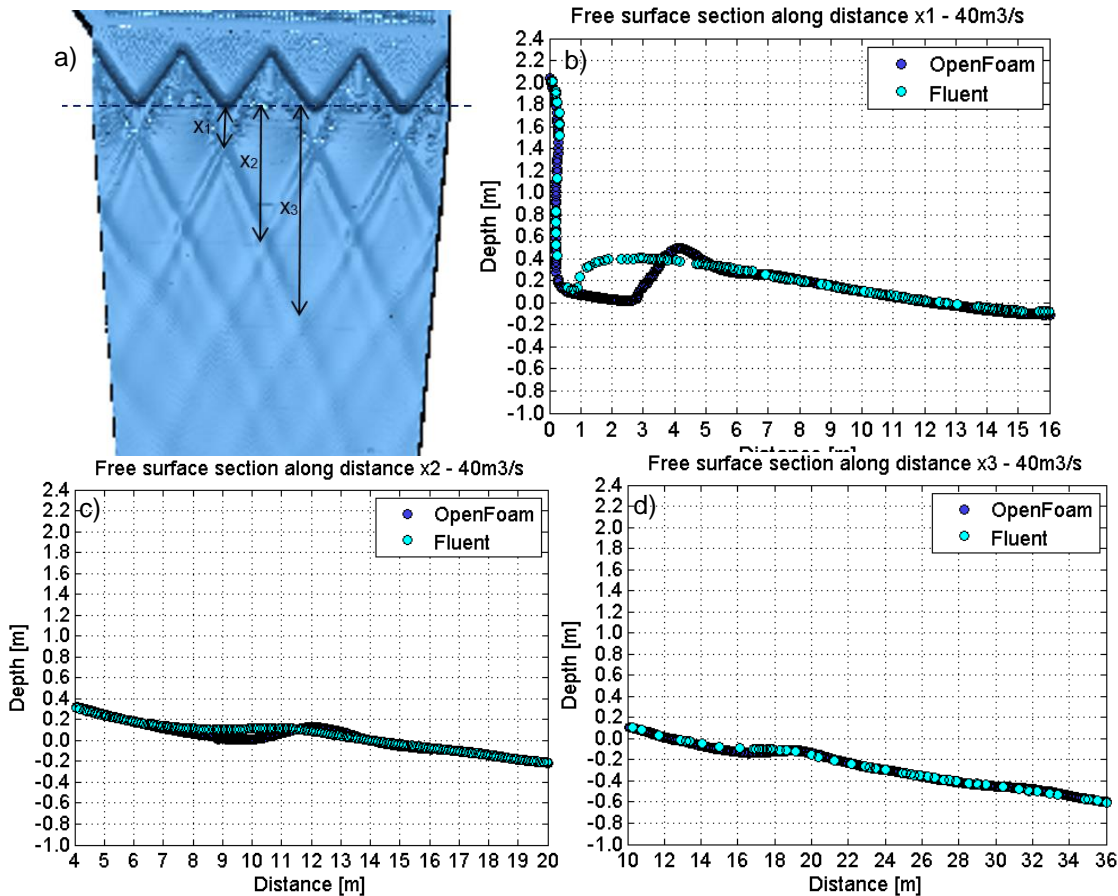


Figure 6.21: a) Wave structures showing three distances to wave crossing points from the weir crest; b) Free surface profile predicted with OpenFOAM and Fluent along distance x_1 , b) x_2 and c) x_3

In the experiment, the intersecting cross-waves generated by the weir propagate until the first change in gradient where they fade. This situation is well reproduced by the numerical predictions from the two solvers. The free surface configuration is defined by the primary cross-waves, generated from the weir upstream and downstream crests (numbered from 1 to 8) and secondary waves which are originated from the reflection of the primary cross-waves against the spillway walls (with numbers 9 and 10). Physical model representations indicate that the flow was equally distributed across the first section of the spillway channel.

As shown on Figure 6.20 h), experimental data is available at several locations along the spillway channel, which are referred to as points A to E. Coordinates of the points where experimental measurements were taken were not provided in the physical scale model report. Therefore, numerical predictions were extracted at locations in the vicinity of the measurement locations informed by their position in the physical model diagram. Figure 6.22 a) shows the location where point A is extracted from the free surface. The free surface is coloured by velocity contours which indicate velocity in the cross-waves area ranges from 2 to 4 m/s. The contours of the water volume fraction on a plane through location A are also shown with a line indicating the location of the point. In Figure 6.22 b) a graph with the experimental measurement of depth and numerical predictions of free surface profiles from the two solvers at a section through point A are presented. Point A corresponds to a dip point in between the cross-waves. The water depth at location A

when the model reaches steady state is in very good agreement with the experimental measurements. At this section, the wave structures are very well represented by the two solvers.

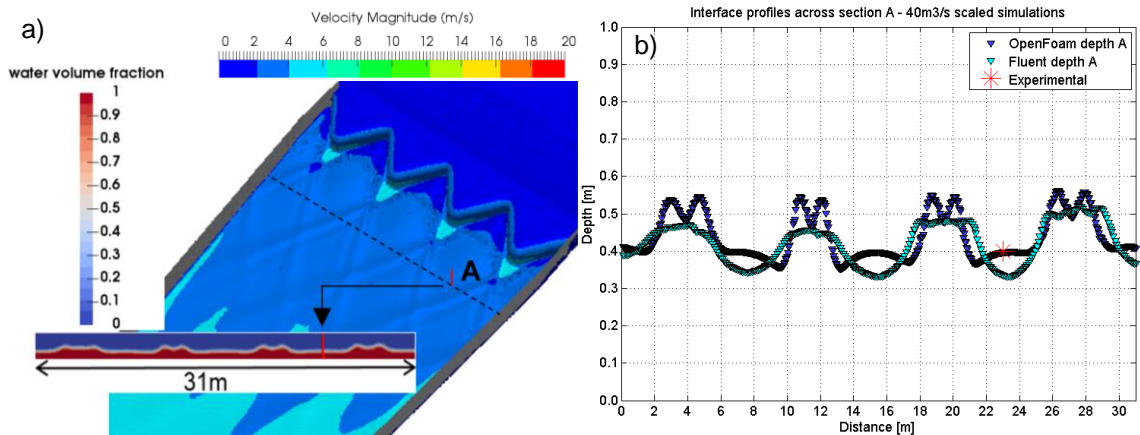


Figure 6.22: a) Velocity-coloured free surface with the location where numerical predictions for point A are extracted and water volume fraction contour plane through point A; b) Free surface profiles at a section across point A with physical model measurements

Figure 6.23 a) and b) show the time-averaged values of interface depth and velocity at all experimental point locations once the model was stable for a minimum of 10 s. The experimental values of depth presented at each location are the maximum values recorded in the in the experiment and hence these are expected to be higher than the numerical predictions. Results show there is good agreement between the velocity values at the different locations and the experimental measurements. The interface depth predictions present higher difference with the experimental measurements. Higher differences in depth are also expected given the experimental depths are the maximum recorded and also since there are higher interface depth variations across and along the spillway channel than interface velocity variations with changes in distance.

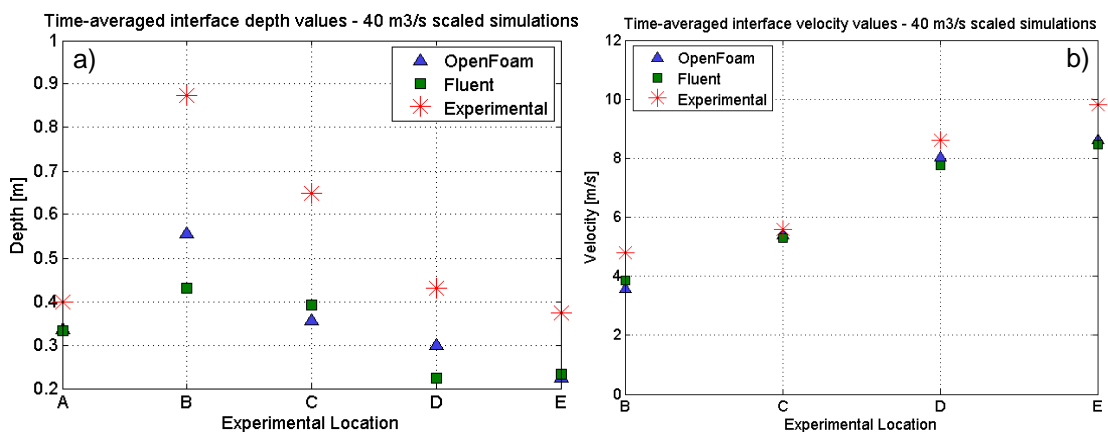


Figure 6.23: Time-averaged values of: a) depth and b) velocity at point locations along the spillway channel predicted by the two solvers with physical model measurements

The cross-sectional velocity profiles were extracted at different sections through points B, C, D and E of the spillway channel and are presented on Figure 6.24 a) together with the flow areas coloured by velocity contours in Figure 6.24 b). At all sections of the spillway the predictions from both solvers present strong consistency. Velocities at sections B and C present very good agreement with the physical model measurements. At section B, the velocity contours show the highest velocity values (of slightly over 4 m/s) occur in between the cross-waves and lowest

velocities are found at the crests of the waves and range from 2.5 to 3 m/s. The highest value of velocity in the vicinity of point B is around 4 m/s which is in good agreement with the highest predicted in the experiment of 4.8 m/s.

At section D there is a central wave generated from the symmetrical pattern of cross-waves and is present in the predictions from both Fluent and OpenFOAM. Velocity predictions at this location are in very good agreement with measurements; the average cross-sectional velocity is around 8 m/s and the maximum recorded in the experiment is 8.6 m/s. The velocity contours at D show the values are around 7.5 m/s throughout the section depth with two areas of higher velocity near the interface of 8m/s. At point E the free surface profile is generally flat with velocity values ranging from 8 to 9 m/s with the highest velocities concentrating at the centre of the channel.

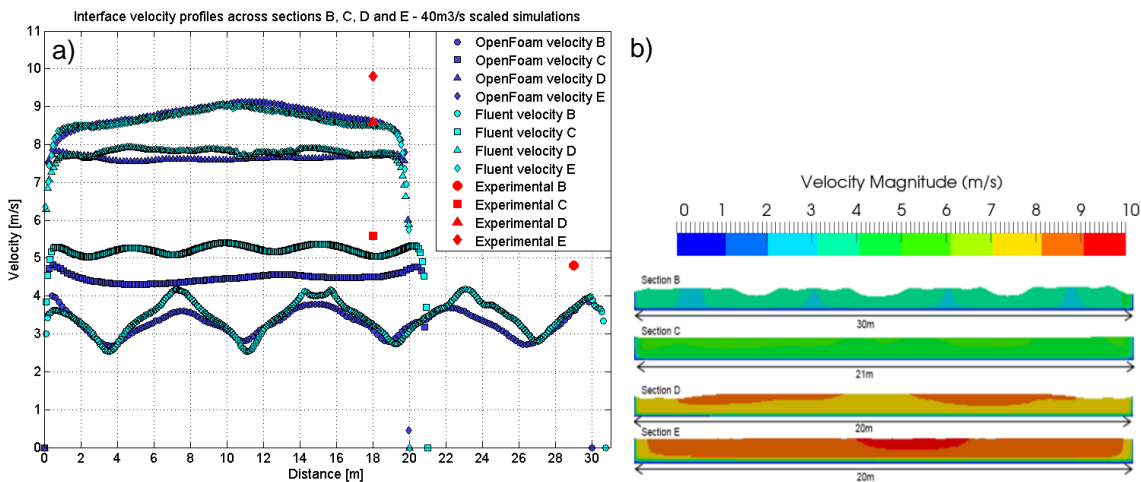


Figure 6.24: a) Numerical predictions of interface velocities at locations B, C, D and E with physical model measurements and; b) flow area coloured by velocity contours at the same sections in OpenFOAM

Overall simulations of the 40 m³/s flow rate show the free surface cross-waves are well reproduced by the two solvers. The values of water depth predicted by both solvers for this flow rate show consistency and although at some sections they show an underestimation of the free surface depth, generally they are acceptably close to the maximum values recorded in the experiment. Velocity predictions from the two solvers also present consistency and are in good agreement with the experimental values.

In order to obtain an indication of the accuracy of the numerical predictions, the values within 0.5 m in the vicinity of the extracted points were averaged in each location and the relative error of the numerical predictions was calculated. The relative error between the physical model velocity v_p and the velocity numerical predictions averaged 0.5 m around each measuring location, v_n was obtained as: $abs(v_n - v_p)/v_p$. The calculation of the relative error of depth predictions was conducted equivalently but considering the range of experimental values -10%. This was because the available physical model depth values consist in the maximum recorded and the numerical values are the time-averaged once the simulations are stable. Table 6.9 presents the relative errors in depth and Table 6.10 presents the relative errors in velocity at all experimental locations analysed. The error values are very similar in the two solvers at all locations. The errors in depth show values in average of 35 % with especially low values in point A, from 1 to 6 % and slightly higher values at point B, of up to 50 %. Consequently, the two solvers

appear to present considerable underestimations of depth. The relative errors for the velocity predictions present significantly lower values than these of depth. The maximum error values occur at location B in the two solvers, being of approximately 20 % and in average of 14% in all locations. As previously discussed, the errors in the velocity predictions are lower since there is less uncertainty in the velocity measurements of the physical model. In particular, the lower accuracy in the depth predictions at point B is expected to be caused by the highly varying free surface profile in the area of the cross-waves and the uncertainty around the precise location to extract the numerical predictions.

Table 6.9: Relative error in depth predictions in OpenFOAM and Fluent at the different experimental locations

	A	B (left)	B (right)	C (left)	C (right)	D (left)	D (right)	E (left)	E (right)
OpenFOAM relative error %	0.9	49.3	50.4	34.2	33.8	45.3	40.9	30.6	33.1
Fluent relative error %	6.3	45.1	47.9	32.4	29.6	40.5	36.0	30.7	32.9

Table 6.10: Relative error in velocity predictions in OpenFOAM and Fluent at the different experimental locations

	B	C	D	E
OpenFOAM relative error %	24.1	16.0	10.1	11.2
Fluent relative error %	21.6	5.9	10.8	12.8

6.10.2. Intermediate Flow Rate: 79.8 m³/s

As previously stated, scaled simulations of flow rate 79.8 m³/s were only conducted in OpenFOAM. The photograph of the physical model in operation is indicated in Figure 6.25 a) and that with the cross-waves crests indicated with numbered red lines is presented in Figure 6.25 b). The numerically predicted free surface features in the vicinity of the weir are shown in Figure 6.25 c) and the location of the cross-waves crests is indicated in Figure 6.25 d). A picture of the entire spillway channel in the physical model is shown on Figure 6.25 e) and the physical model diagram is shown in Figure 6.25 f). The numerically predicted free surface in the spillway channel is presented in Figure 6.25 g) and that with the location of the cross-waves' crests is outlined in Figure 6.25 h).

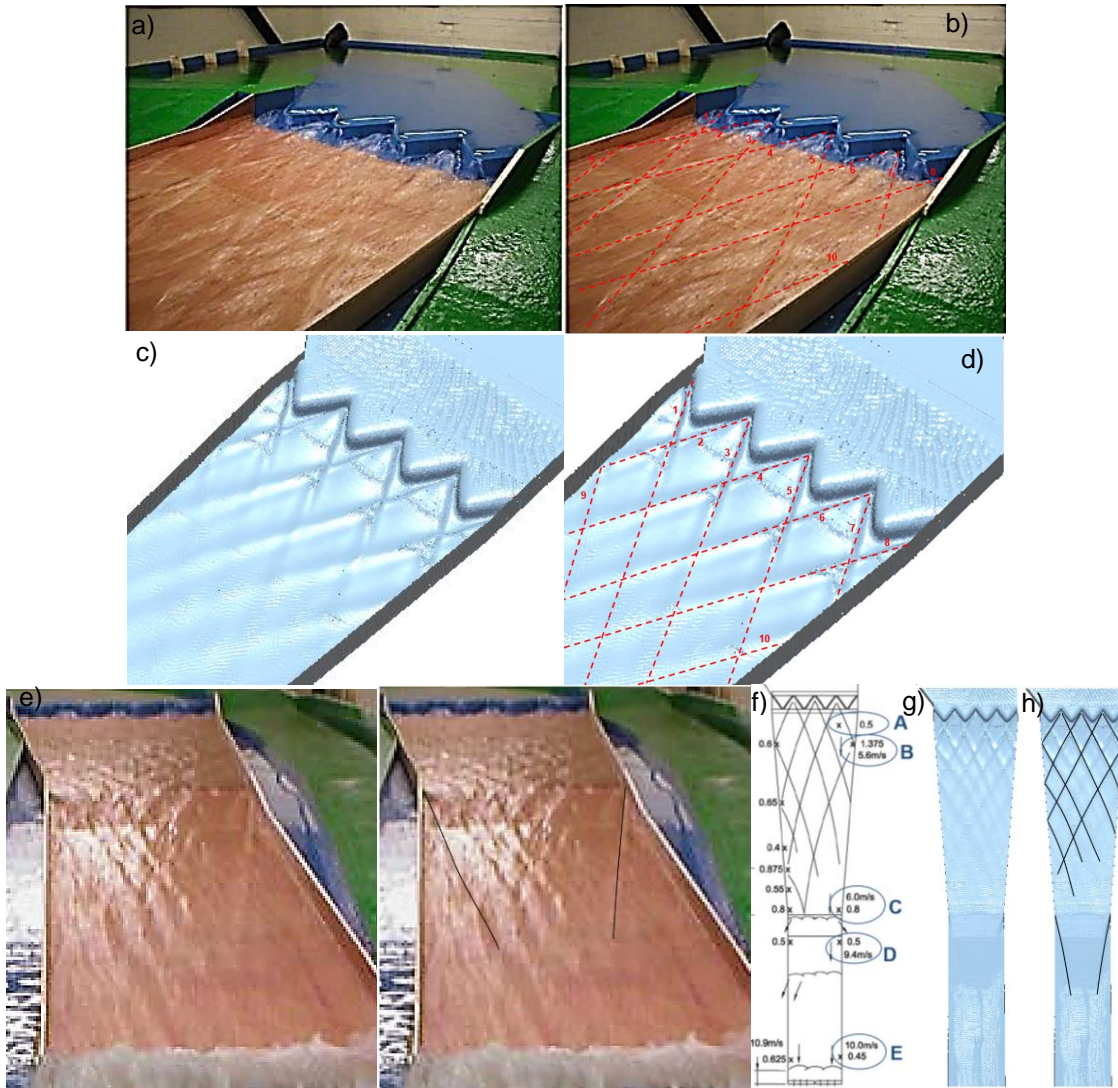


Figure 6.25: a) Photograph of the physical model free surface and b) with waves' crests indicated with red lines; c) Numerically predicted free surface and d) with waves' crests indicated with red lines; e) Photograph of the physical model spillway channel and with the location of the free surface features; f) Physical model diagram with experimental locations; g) Numerically predicted free surface for the complete channel and h) with the location of the free surface crests for the flow rate of $79.8 \text{ m}^3/\text{s}$

The numerical results show an accurate representation of free surface cross-waves generated by the labyrinth weir. In the physical model, the cross-waves extend along the spillway channel until the first spillway change in gradient, and this behaviour is generally accurately captured in the numerical predictions. The numerically predicted cross-waves fade at the first change in gradient point and the free surface becomes approximately levelled. The cross-waves' crests indicated in the model diagram are present in the numerical simulations, including the waves originating from the labyrinth weir and the secondary waves generated from the reflection of the primary waves against the spillway walls.

Cross sectional profiles of interface velocity and depth were computed at the different measurement points along the spillway channel. Figure 6.26 a) indicates the free surface profile is very well reproduced. The depth at location A which corresponds to a dip in between the crests of the cross-waves is in very close agreement with the maximum values of experimental measurements at this location. There is availability of two measuring points at the section across location B, one on the left bank and one on the right bank. Similarly to the measurement taken on

the dip of the wave (point A), the measurement on the right bank presents strong correlation with the model predictions. The measurement taken on the left bank, however appears problematic since it is over twice the height of the wave at the right bank, with 1.375 m height as opposed to 0.6 m. This recorded point appears out of line with the rest of the dataset as well as the numerical predictions and it is suspected to be the result of a recording error. Figure 6.26 b) reveals predictions of interface depth across sections C, D and E demonstrate close agreement with the maximum values of interface depth. Section C shows the average interface values to be approximately 0.7 m while the maximum experimental values are 0.8 m. Section D is approximately 0.5 m which agrees with maximum experimental values and section E is also correlated with the experimental measurements, especially that on the left side of the channel.

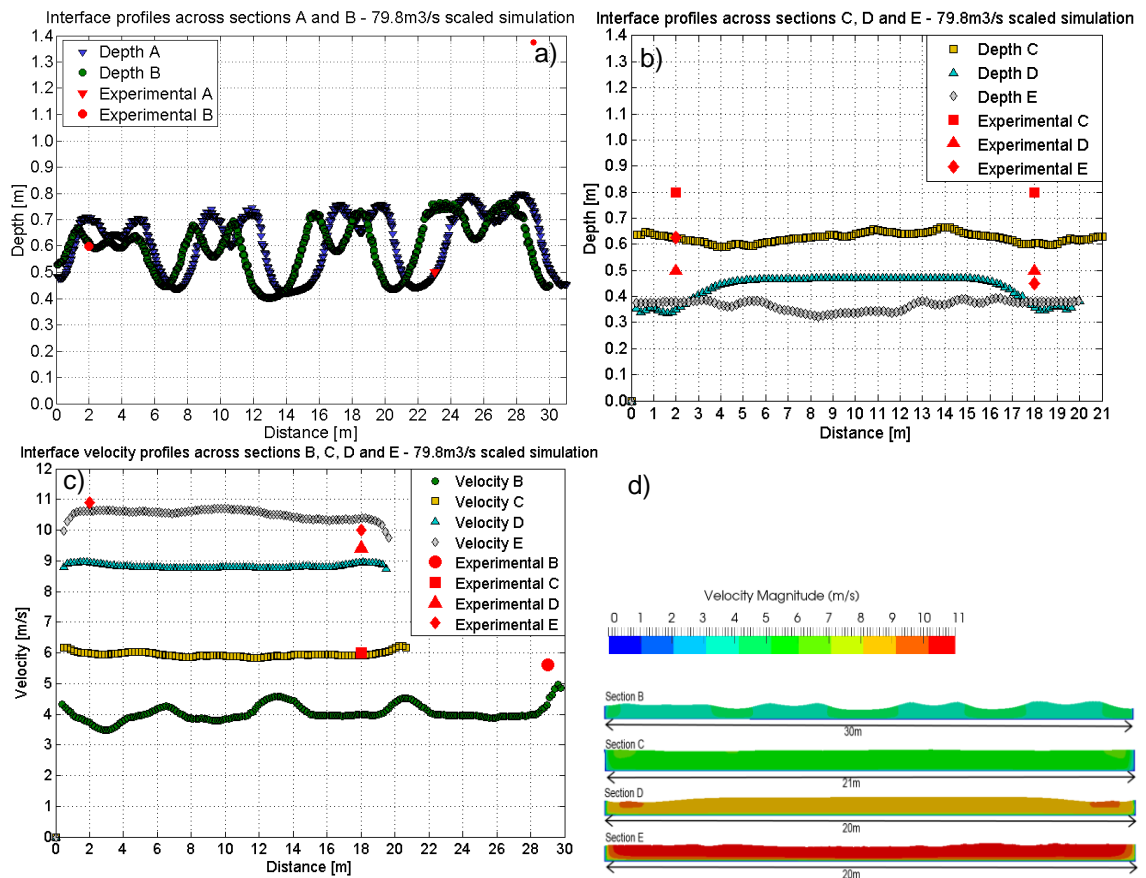


Figure 6.26: a) Interface cross sectional profiles at points A and B and b) at B, D and D; c) Interface velocity profiles through points B to E and d) velocity contour planes at sections through points B, C, D and E in OpenFOAM

Free surface velocity profiles and flow areas coloured by velocity contours at all sections are shown on Figure 6.26 c) and d) respectively. At the section through point B, the velocity measurement point coincides with one of the points of velocity in the cross-section; this is well corresponded with the value of velocity predicted in this area. This is particularly relevant when considering the aforementioned disagreement between measurement and numerical predictions of depth at this same location and it confirms the assumption that this measured depth was recorded incorrectly. Further down in the spillway channel, the velocity profiles at sections C and D show excellent agreement with values recorded in the experiment. At the end of the spillway channel, section E has availability of two measurement points across the section. The predicted

velocity profile presents a very good correlation with these, with values in between the two experimental data points.

The depth measurements taken next to the right wall of the spillway along 6 locations were plotted with the predictions of the free surface profile relative to the spillway base. These are shown in Figure 6.27 a) and the location of the profile is indicated in Figure 6.27 b). The $x=0$ coordinate was taken as the downstream outside apex of the labyrinth weir and the reference point of $z = 0$ corresponded to the weir base.

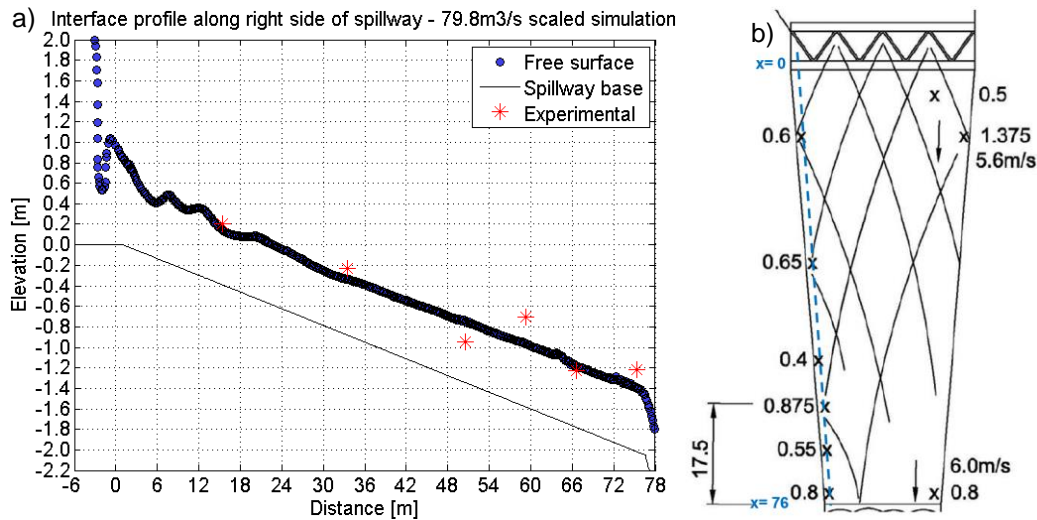


Figure 6.27: a) Longitudinal profile next to the spillway right wall; b) location of the longitudinal profile indicating the distance coordinates

Figure 6.27 a) confirms there is a close agreement between the maximum experimental depth values and the numerical predictions at the various locations along the spillway channel.

The time-averaged values of depth and velocity at the different measurement locations were extracted and plotted in Figure 6.28. There is significant depth variation in the area immediately downstream the weir where the cross-waves are present. This implies that small variations in positioning could reflect in large changes in water depth. As previously mentioned, the interface depth at location B presents higher discrepancy with the experimental data than other locations. As observed in Figure 6.26 at this point of the channel in between the cross-waves, experimental measurements range from 0.6 m to 1.375 m. The extracted depth values at points C, D and E present generally close agreement with the maximum values of experimental measurements. Velocity predictions are well correlated with the experimental values at all locations.

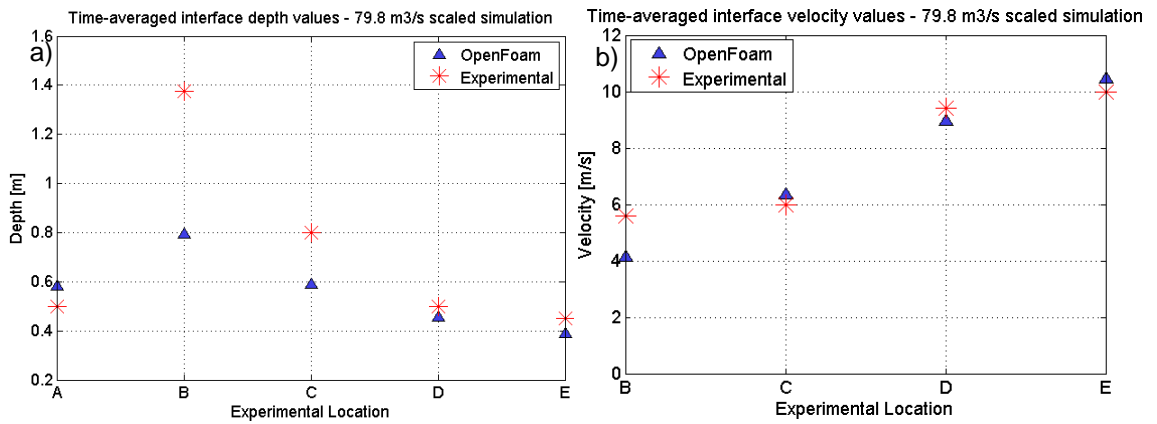


Figure 6.28:a) Time-averaged values of: a) depth and b) velocity at point locations along the spillway channel with physical model measurements

The relative error of the numerical predictions for this flow rate was calculated following the same procedure as in the previous flow rate. The relative errors in depth are shown on Table 6.11 and those for velocity are shown in Table 6.12. Similarly to the 40 m³/s case, the depth error at point A is the lowest. It is observed that in this flow rate the depth errors are lower than in the 40 m³/s case, being in average of 14 %. As previously noted, errors in velocity predictions at all locations present lower values than those for depth. These are from 2 to 5 % in locations C to E and up to 20% at B. The average error in all locations is of 6.8 %.

Table 6.11: Relative error in depth predictions in OpenFOAM at the different experimental locations

	A	B (left)	B (right)	C (left)	C (right)	D (left)	D (right)	E (left)	E (right)
OpenFOAM relative error %	0.26	41.51	2.31	13.40	12.48	5.50	14.06	6.60	32.70

Table 6.12: Relative error in velocity predictions in OpenFOAM at the different experimental locations

	B	C	D	E (left)	E (right)
OpenFOAM relative error %	20.43	2.17	5.38	3.43	2.53

6.10.3. High Flow rate: 119.6 m³/s

The photograph of the physical model free surface configuration immediately downstream the weir for 119.6 m³/s is shown on Figure 6.29 a). The equivalent view predicted numerically with OpenFOAM and Fluent are presented on Figure 6.29 b) and c) respectively. The physical model cross-wave crests indicated with numbered red lines are shown on Figure 6.29 d) and those numerically predicted with OpenFOAM and Fluent are shown on Figure 6.29 e) and f) respectively. The physical model pictures show in this case the cross-waves' crests are significantly more prominent than in the 40 m³/s and the 79.8 m³/s cases. Figure 6.29 g) presents a photograph of the spillway channel in the physical model and that with the free surface features in the third section of the channel indicated with black lines. Figure 6.29 h) shows the physical model diagram. Figure 6.29 i) presents the numerically predicted free surface with OpenFOAM and Fluent and Figure 6.29 j) shows these with the indication of the main free surface features shown in the physical model photographs and diagram.

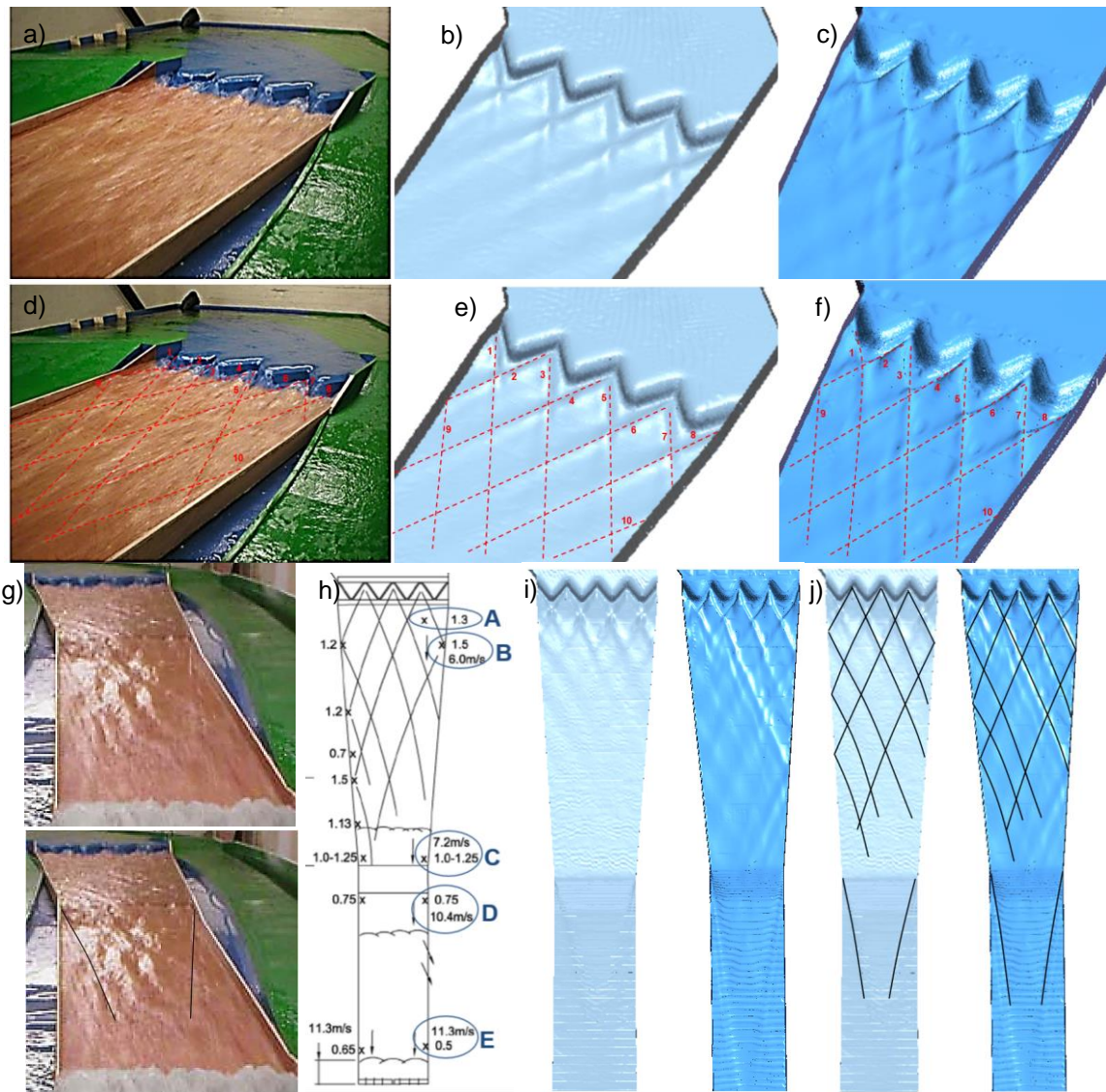


Figure 6.29: a) Photograph of the physical model free surface and numerically predicted with b) OpenFOAM and c) Fluent; d) cross-wave crests indicated with red lines on physical model and e) in OpenFOAM predictions and f) in Fluent predictions; g) Photograph of the physical model spillway channel and with black lines indicating central wave; h) Physical model diagram with experimental locations and location of flow features; i) Numerically predicted free surface for the complete channel and j) with location of cross-waves' crests for a flow rate of $119.6 \text{ m}^3/\text{s}$

Results indicate that the complex configuration of cross-waves observed in the experiment is generally reproduced by the numerical models in both solvers, but with some differences in the prominence of the cross-wave crests. The Fluent predictions exhibit higher peak height of waves and an improved definition of the waves features compared to OpenFOAM. As in the previous cases, there are several secondary wave crests which are created from the original waves reflecting on the spillway right wall and downstream the channel. These are observed in the experiment, as presented in the physical model diagram in Figure 6.29 h), well represented by Fluent and less well defined by OpenFOAM (Figure 6.29 j)).

This case exhibits certain asymmetry of the flow. Especially in the Fluent free surface features, there is the presence of a dominant cross-wave originating from the first upstream apex which is particularly distinct. This is caused by the flow inlet being located on the right hand side of the

domain. The central wave generated at the third section of the spillway channel as indicated in Figure 6.29 g) is well reproduced by the two solvers.

Figure 6.30 a), b) and c) show the free surface profiles along the previously defined x_1 , x_2 and x_3 distances from the downstream weir apex to the three cross-waves crossing points predicted with the two solvers. Results show that in this case, the differences in the wave's crossing points are greater than for the lowest flow rate. The wave's peaks predicted by Fluent are located further downstream than these in OpenFOAM. There is approximately 0.5 m difference in the location of the first crossing point in the two solvers, 3 m in the second and around 4 m in the third. Although the exact values of the distances x_1 to x_3 from the experiment are not known, the Fluent characterisation of the cross-waves is observed to be superior to that in OpenFOAM. Therefore the predictions of the distances x_1 to x_3 by Fluent are considered to be more accurate. Small differences between the two solvers are expected because of the different interface capturing scheme implemented in the two solvers, as observed in the 40 m³/s case. However, the differences in the waves' positions observed in this case are greater. The reasons for these greater differences in this flow rate are examined in more detail in Section 6.13.1. It is anticipated that apart from the interface capturing scheme, in this case, the greater differences are also due to the cell size in the area where the interface is located, which is larger. As noted in Section 6.9.1, OpenFOAM requires a lower cell size than Fluent, which was achieved in the 40m³/s mesh. However, for this larger flow, the free surface has moved to cells of larger size (equivalent to those in Fluent) which do not show to have enough resolution for this solver to capture the characteristics of the waves in detail.

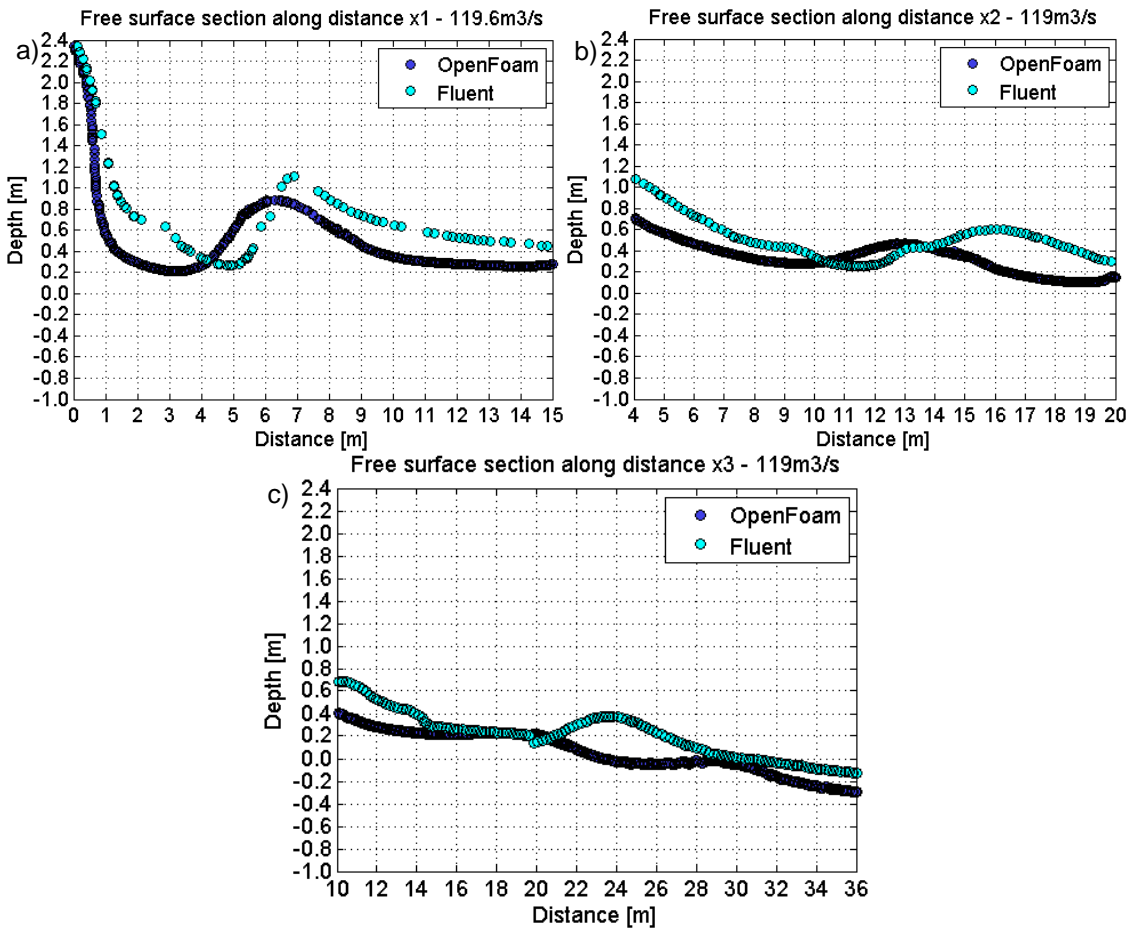


Figure 6.30: Free surface profiles predicted with OpenFOAM and Fluent along distances: a) x_1 , b) x_2 and c) x_3

Cross-sectional profiles of interface depth and velocity magnitude were plotted at the different measurement locations. Figure 6.31 a) shows the free surface profile sections through points A and B predicted using OpenFOAM and Fluent. It is observed that the waves shapes and features (particularly the peaks) are more pronounced in the Fluent predictions than those from OpenFOAM. The interface profile through A predicted by OpenFOAM is about 0.3 m lower than the maximum values of experimental data, the same situation is observed on section B. However, Fluent simulations show accurate predictions, with values of depth closer to the maximum recorded in the experiment. They also reveal the presence of an air pocket in the cross-section profile A. The measurement point next to the left bank of section B which is equal to 1.5 m appears to be slightly higher than the predictions from both solvers. However, as previously stated, in this area there are significant interface depth variations for small changes in position. Simulations from both solvers, and especially Fluent are in good agreement with the measurement point next to the right bank in section B. The discrepancies from the two solvers in the predictions of the waves features are anticipated to be due to the difference in interface capturing scheme as well as different levels of mesh sensitivity of the two solvers. These factors are discussed in further detail in the Discussion of this chapter, Section 6.13.1.

Figure 6.31 b) presents the free surface profiles at cross sections through points C, D and E predicted with OpenFOAM and Fluent. At section C the interface depth ranges from 1 to 1.25 m. The average section values predicted by OpenFOAM appear to be slightly lower than that, being

approximately around 0.8 m. The Fluent values show accurate predictions of around 0.9 to 1 m. At section D, just after the second change in gradient there is the presence of a central wave which is shown in both solvers. Predictions of depth at section through point D are very accurate in Fluent and slightly lower than the experimental measurements in OpenFOAM. Interface depth predictions at section through point E, which is located at the end of the channel, are well correlated with the measurements in both solvers, ranging from 0.4 m to 0.6 m.

Figure 6.31 c) shows the longitudinal free surface profile along a section next to the spillway right wall. The location of the section is indicated on Figure 6.31 d) with the position of the coordinate $x=0$ corresponding to the downstream crest apex and that at the end of the section, which coincide with the first change in gradient. The Fluent free surface predictions along this profile present good agreement with the values of experimental depth at the different locations. Generally all experimental measurements are well correlated apart from that occurring at around 50 m of 1.5 m depth which is shown to be higher than the predicted profile. The OpenFOAM predictions exhibit lower depths which result in slightly higher differences with the experimental measurements but generally present satisfactory agreement, especially at the centre and end of the section.

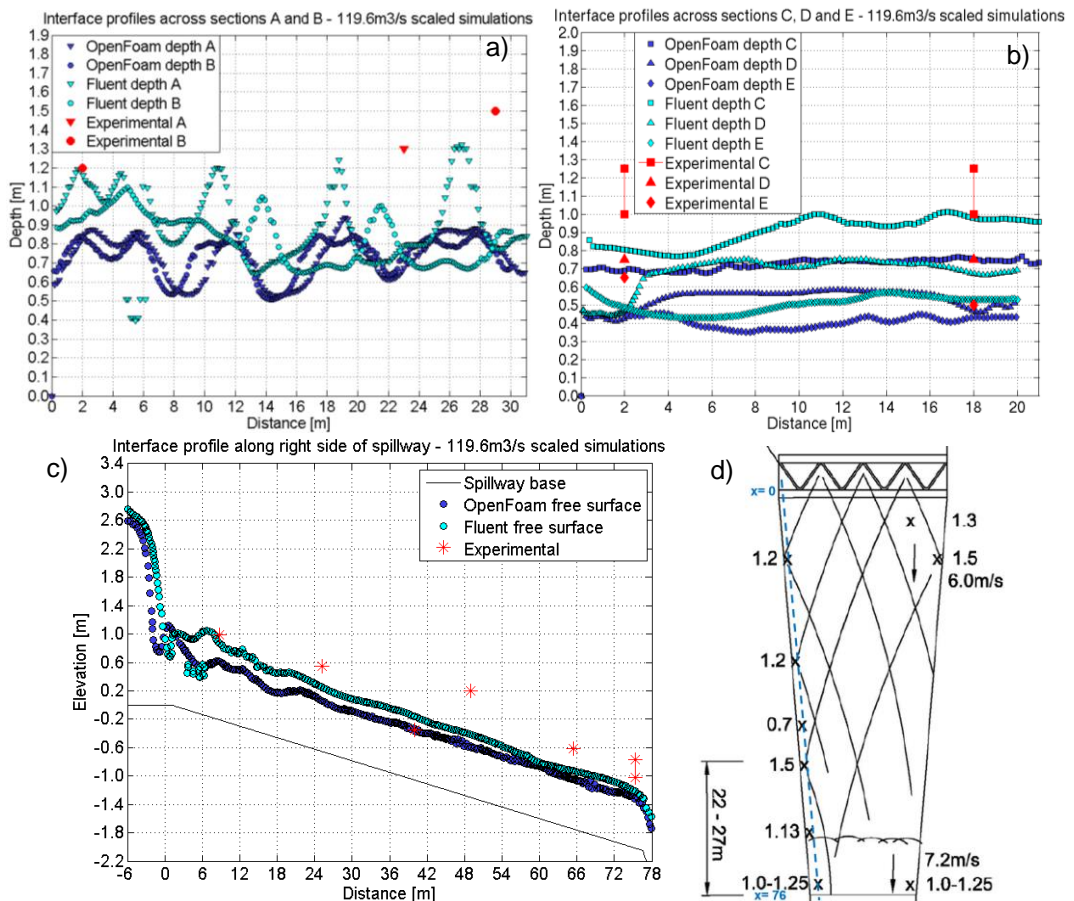


Figure 6.31: Cross-sectional interface depth profiles at sections across: a) points A and B and b) points C, D and E; c) longitudinal profile next to spillway right wall; d) location of longitudinal profile with distance coordinates

Figure 6.32 a) shows the free surface velocity magnitude profiles predicted with the two solvers at sections B, C, D and E and Figure 6.32 b) presents the contour planes of velocity magnitude across the spillway channel at the same sections. The OpenFOAM and Fluent interface velocity

profiles at all locations are in close agreement with the values measured in the experiment. Section B shows lowest values of velocities at the crests of the cross-waves and highest values in between the waves. The predictions on the vicinity of the measurement point B show very close agreement with the value of velocity at this point, especially in Fluent. Section C presents a generally uniform profile with values ranging from 6 to 7 m/s. Section D also demonstrates generally acceptable agreement with values of just over 9 m/s in both solvers and the experimental value being of 10.4 m/s. At section E, the OpenFOAM and Fluent velocity predictions are approximately around 11 m/s and 12 m/s respectively, which are both very close to the measured in the experiment of 11.3 m/s, with the Fluent predictions being reasonably higher.

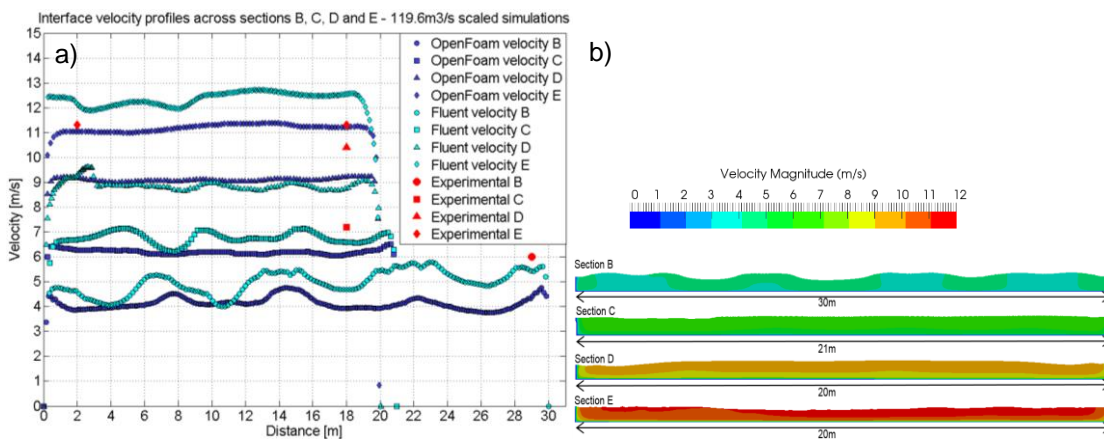


Figure 6.32: a) Cross-sectional interface velocity profiles at sections across points B, C, D, E; b) Flow areas coloured by velocity contours of the different sections in OpenFOAM

Figure 6.33 a) and b) show the time-averaged values of interface depth and velocity magnitude. The values of depth at point locations A and B show the highest difference in free surface depth compared to the maximum values recorded in the experiment. This has been previously observed in the cross-sectional graphs where there is a considerable variation in wave height in this area and therefore results highly depend on the location of the point where data is extracted. Fluent predictions of interface depth values at point C present good agreement with maximum experimental values and OpenFOAM predictions are slightly lower. Predictions of interface depth at points D and E from both solvers are in good agreement with maximum experimental values at these locations. As previously observed on the cross-sectional graphs, point data of velocity predictions at the measurement locations present very close agreement with the velocity values measured in the physical model.

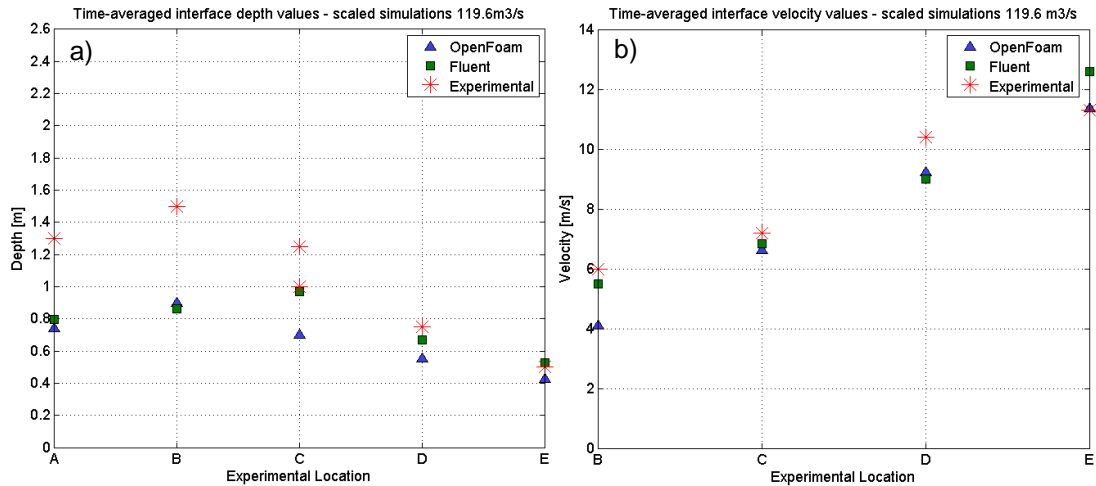


Figure 6.33: Time-averaged values of: a) depth and b) velocity at point locations along the spillway channel predicted by the two solvers with physical model measurements

The relative errors of the depth and velocity predictions from the two solvers were calculated and are presented on Table 6.13 and Table 6.14 respectively. Results show the OpenFOAM errors are slightly greater in this flow rate than for 79.8 m³/s but lower than in the 40 m³/s. The depth error average is of approximately 24 % and that for velocity is of 10%. The Fluent average errors are generally of the same order, with an average of 17% of depth and 8% for velocity. These values are also lower than for 40 m³/s.

Table 6.13: Relative error in depth predictions in OpenFOAM and Fluent at the different experimental locations

	A	B (left)	B (right)	C (left)	C (right)	D (left)	D (right)	E (left)	E (right)
OpenFOAM relative error %	40.25	37.79	23.45	16.59	22.65	20.97	30.55	4.96	23.63
Fluent relative error %	33.29	36.68	12.85	0.13	9.38	8.81	29.56	5.83	16.94

Table 6.14: Relative error in velocity predictions in OpenFOAM and Fluent at the different experimental locations

	B	C	D	E (left)	E (right)
OpenFOAM relative error %	25.80	11.41	11.19	0.57	2.25
Fluent relative error %	7.72	8.47	13.36	4.91	6.60

6.10.4. PMF: 159.5 m³/s

The largest flow rate modelled is the PMF of the scheme which has a size of 159.5 m³/s. The free surface configuration in the physical model and the numerically predicted with OpenFOAM and Fluent is shown on Figure 6.34 a), b) and c) respectively. Figure 6.34 d), e) and f) show the same views as in the previous three pictures with the indication of the cross-waves crests in numbered red lines.

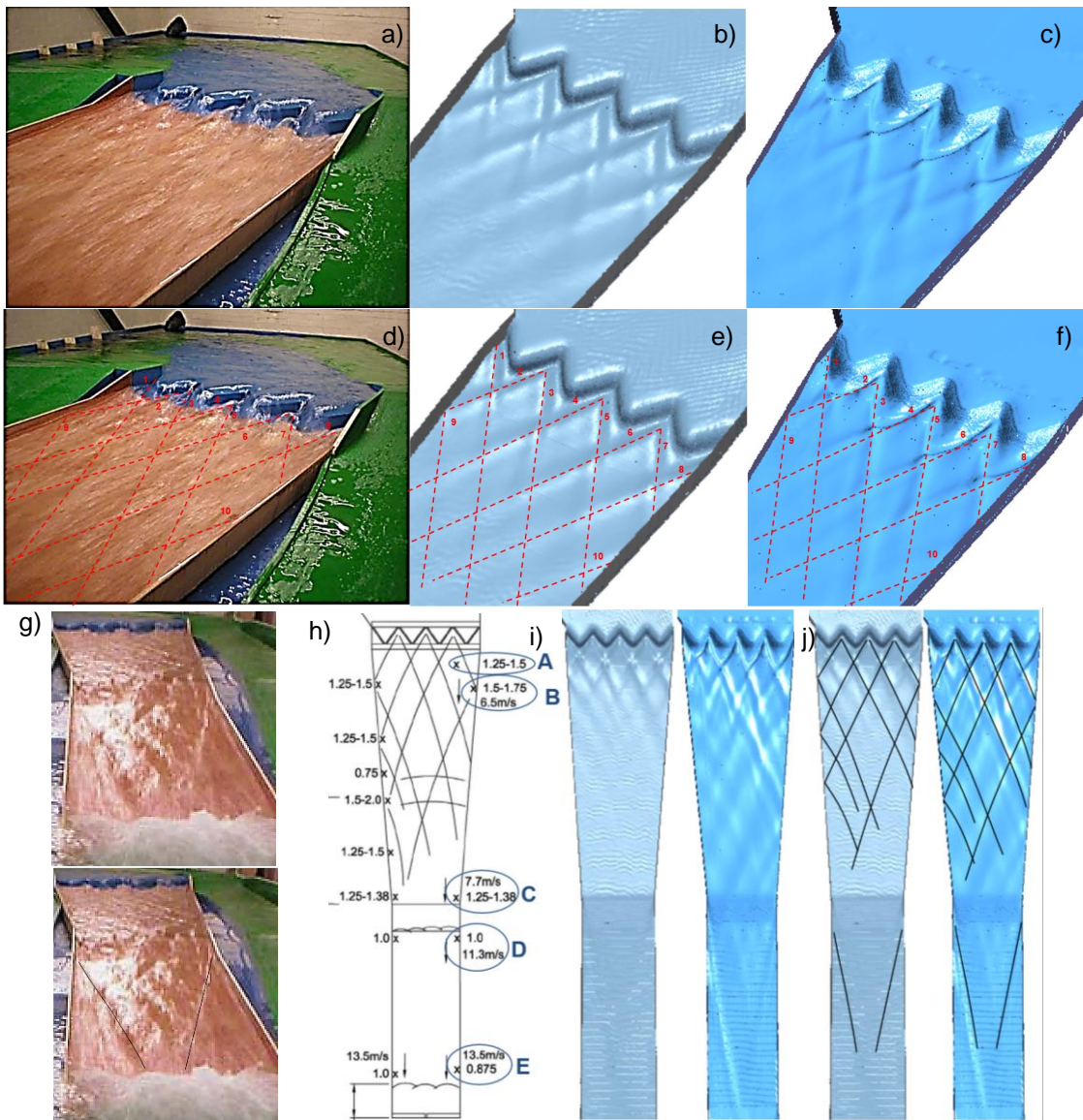


Figure 6.34: a) Photograph of the physical model free surface and numerically predicted with b) OpenFOAM and c) Fluent; d) Cross-wave crests indicated with red lines on physical model and e) in OpenFOAM predictions and f) in Fluent predictions; g) Photograph of the physical model spillway channel and with black lines indicating central wave; h) Physical model diagram with experimental locations and location of flow features; i) Numerically predicted free surface for the complete channel and j) with location of cross-waves' crests for a flow rate of $159.5 \text{ m}^3/\text{s}$

Similarly to the previously simulated flow rate, the complex cross-wave pattern created by the labyrinth weir is accurately predicted in Fluent and less well defined in OpenFOAM. In this case, in the physical model the nappe presents certain aeration, which as previously stated, it is not entirely captured in the numerical models. However, the numerical predictions present an accurate representation of the nappe shape, which is especially appreciated in the Fluent predictions. Figure 6.34 g) shows the entire physical model spillway channel and below the same picture with the lines indicating the free surface features at the third section of the channel. Figure 6.34 h) presents the physical model diagram and Figure 6.34 i) and j) show the numerically predicted free surfaces and those with the free surface features indicated with lines respectively. Comparably to the $119.6 \text{ m}^3/\text{s}$ case, the configuration of cross-waves predicted in Fluent is shown to be significantly more pronounced than that in OpenFOAM, and hence the Fluent predictions present stronger correlation with the physical model measurements. The likely reasons for the

discrepancies in the cross-waves' features in the two solvers are anticipated to be the lower resolution of the cells where the interface is located for this largest flow rate in OpenFOAM (which is now equivalent to that in Fluent) and the different interface capturing scheme employed. These are discussed in further detail in Section 6.13.1. The previously stated asymmetric pattern of the flow is in this case more perceptible and reproduced with the two solvers.

The free surface profiles along distances to the cross-waves crossing points x_1 , x_2 and x_3 are shown on Figure 6.35 a), b) and c). Results indicate that the differences between the predictions from the two solvers become greater for increasing flow rate. In this case, the Fluent distances are from 3 to 6 m longer than those predicted with OpenFOAM.

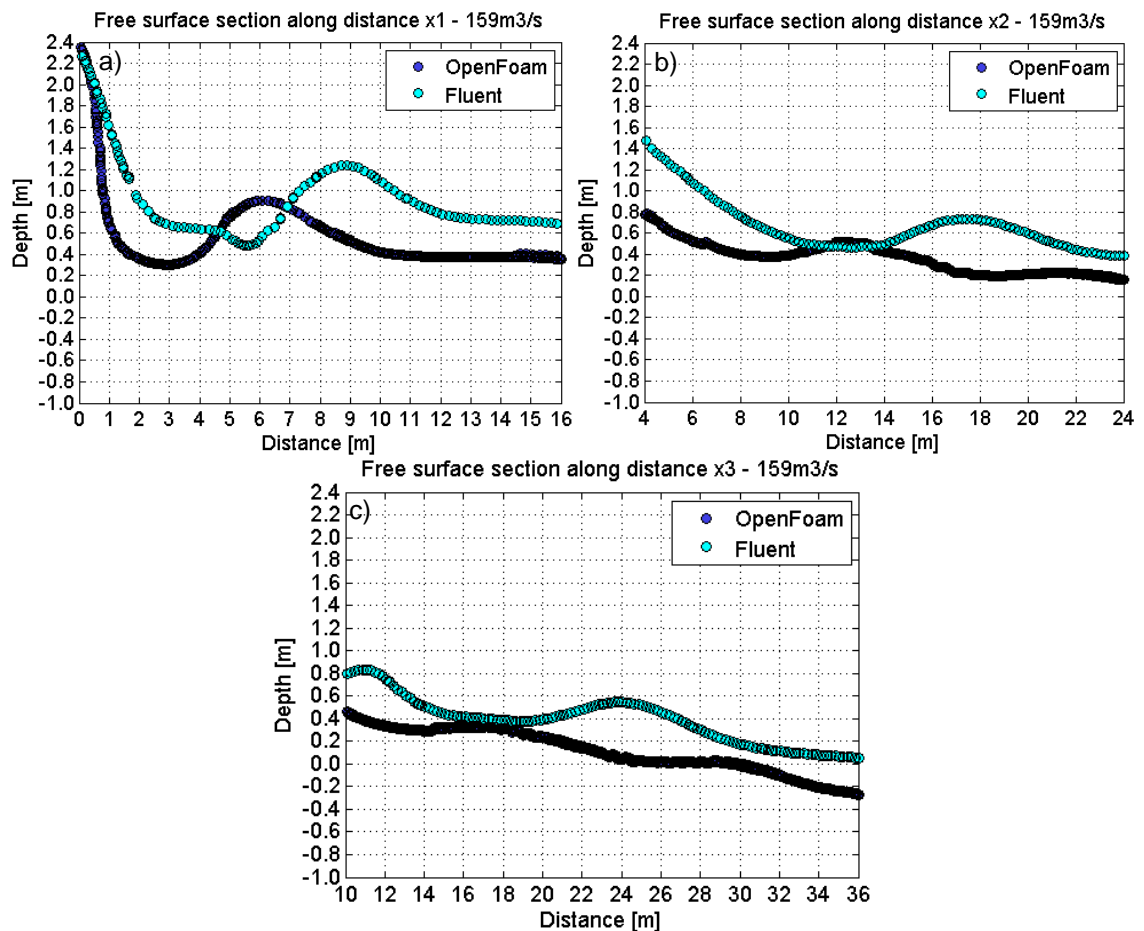


Figure 6.35: Free surface profiles predicted with OpenFOAM and Fluent along distances: a) x_1 , b) x_2 and c) x_3

The interface depth profiles across sections through points A and B with OpenFOAM and Fluent are shown on Figure 6.36 a) and those through points C, D and E are presented on Figure 6.36 b). In the modelling of this flow rate, fluctuation in depth in the physical model was observed and recorded at several locations of the spillway channel. In order to compare this with the fluctuation of the numerical predictions, depth time series of the Fluent simulations were plotted at several point locations. This is shown on Figure 6.36 c) where it is observed that overall there is a variation of approximately 0.1 m in depth at the different specific points with time. The time series predictions of depth at points A and C are well correlated with the experimental measurements which exhibit the same value at the two locations (1.25 m). Predictions at point D present slightly

lower values than the measurements. Depth predictions at locations B and E are lower at the specific point locations.

Figure 6.36 a) indicates that at point A the free surface depth fluctuates from 1.25 to 1.5 m. The values of depth at a section across point A predicted with OpenFOAM range from 0.95 to 1.05 m which is slightly lower than the maximum experimental values. The Fluent depths at section A present acceptable agreement with maximum values measured. The largest discrepancies between the free surface depth point data predictions and the physical model measurements are at location B. At section B the OpenFOAM free surface values are lower than the maximum values measured, with highest depth of approximately 0.9 m and 1.05 m on the right side of the spillway. On the right side, the Fluent values present very close agreement with the experimental values, and at the left side, the predicted values are slightly lower.

Figure 6.36 b) shows the Fluent predictions of interface depth at location C are well correlated with the maximum experimental values recorded, however those from OpenFOAM are lower. The OpenFOAM highest interface profile depth values at D and E are approximately 0.6 m and 0.5 m and the maximum recorded at these locations in the experiment are 1 m and 0.875 m respectively, which suggests the OpenFOAM predictions are considerably lower than the maximum experimental values. The Fluent predictions of interface depth at location C, D and E are generally well correlated with the physical model measurements of depth.

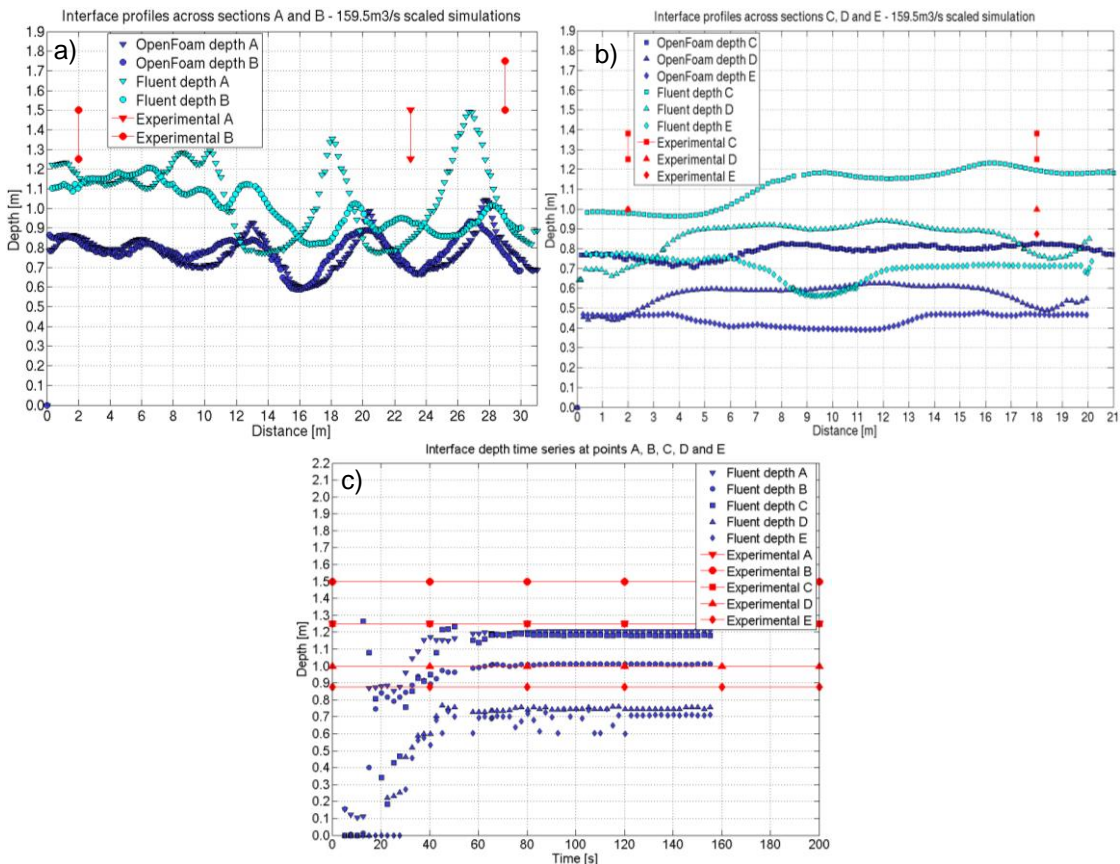


Figure 6.36: a) Cross-sectional interface depth profiles at sections across points A and B and b) C, D and E; c) Interface depth time series at point locations A to E predicted with Fluent

The free surface depths next to the right wall of the spillway were extracted and compared with the experimental measurements. These are shown on Figure 6.37 a) and the location of the cross section is shown on Figure 6.37 b). In this case there are increased differences in free surface depth predictions from the two solvers. The Fluent predictions, particularly at the two most upstream points are very well correlated with the measurements, however the OpenFOAM predictions exhibit an underestimation of the depths. The OpenFOAM predictions present improved agreement at the centre of the profile. The Fluent predictions are also well correlated with the last 3 measurement points. Similarly to the 119.6 m³/s flow rate, the height of the wave on the fourth measurement point from upstream presents greatest difference with the numerical predictions. As previously stated, such difference could be due to the position of the waves in the profile.

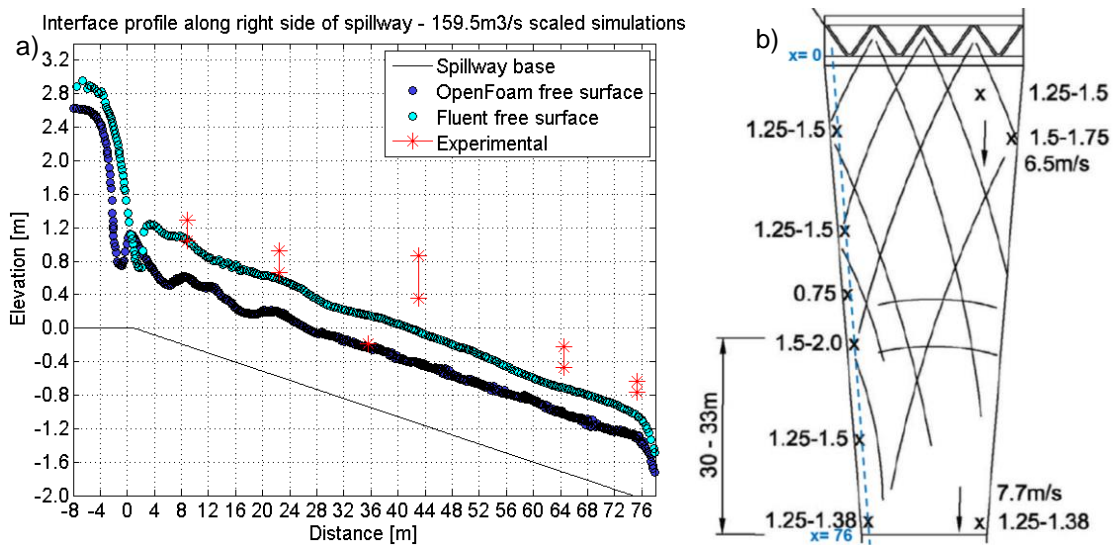


Figure 6.37: a) Longitudinal profile next to the spillway right wall; b) location of the longitudinal profile indicating the distance coordinates

Figure 6.38 a) shows interface velocity magnitude profiles at sections B, C, D and E. The contour planes at each location are presented on Figure 6.38 b) and the velocity time series at the different point locations on Figure 6.38 c). At section B the velocity predictions by both solvers present good agreement with the values recorded in the experiment of 6.5 m/s, especially those from Fluent. The values predicted by OpenFOAM are around 5 m/s while the predicted by Fluent are just over 6 m/s. At C the velocities predicted by both solvers range from 6.5 to 7.2 m/s, which correlate with experimental values of 7.7 m/s. Velocity predictions across section D are consistent in both solvers with values just over 9 m/s, which are below the experimental measurements of velocity of 11.3 m/s. At section E the OpenFOAM measurements predict values of over 11 m/s which are slightly lower than the measured of 13.5 m/s and Fluent predictions present values from 12 to 13 m/s which are in close agreement with the experimental measurements.

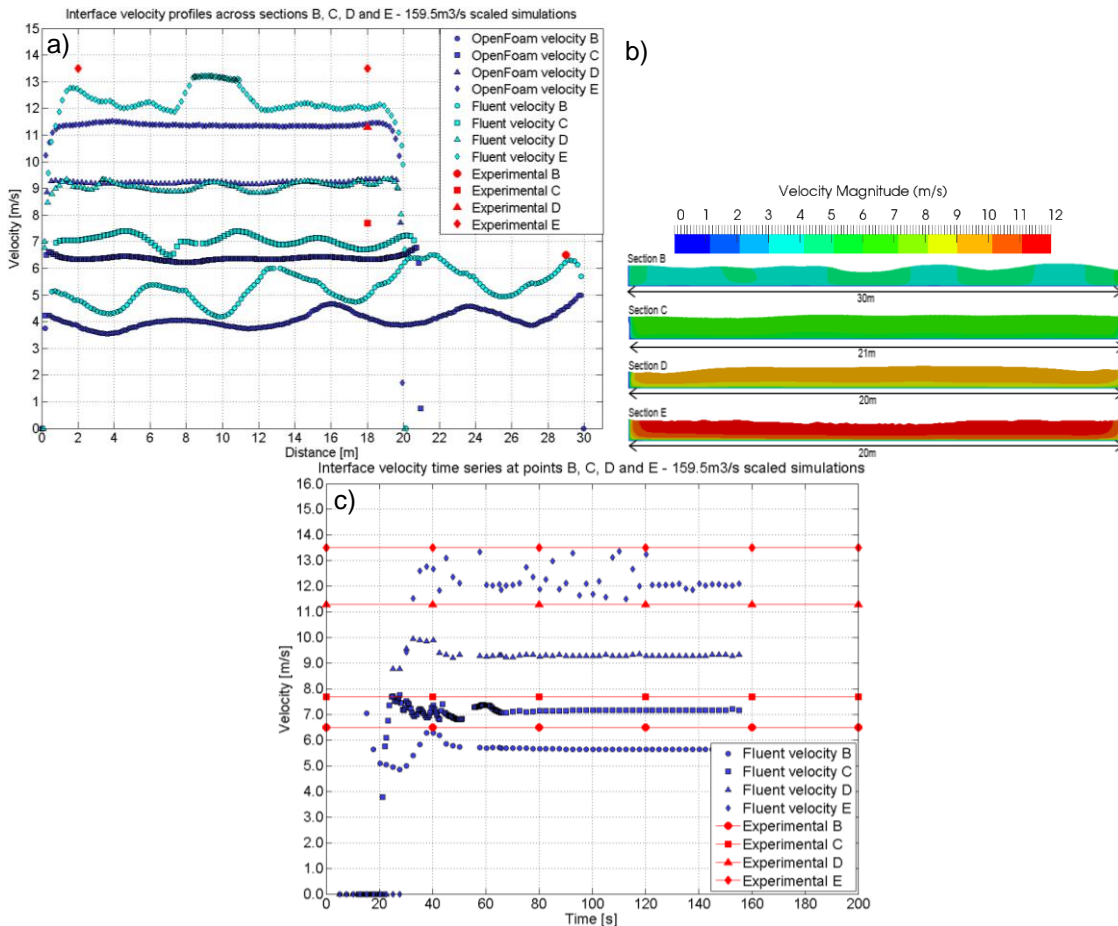


Figure 6.38: a) Cross-sectional interface velocity profiles at sections across points B, C, D, E; b) Flow areas coloured by velocity contours of the different sections in OpenFOAM; c) Interface velocity time series at point locations B to E predicted with Fluent

Time-averaged point data of depth and velocity at the different experimental locations were extracted and plotted on Figure 6.39 a) and b) respectively. As already indicated in the cross-sectional plots, locations A and B present highly varying wave height and therefore it is challenging to plot representative results in only one data point. This is illustrated by the difference in extracted depths and the maximum measured ones at points A and B. The point depth predicted with Fluent at point C is in close agreement with the maximum experimental values. As also shown on the cross-sectional plots, the depth predicted by OpenFOAM at this point is slightly lower. Interface depth at points D and E show the lowest values in the cross section of flow which are slightly lower than the maximum experimental. Velocity predictions are overall in close agreement with experimental values, with the greatest disagreement occurring at point D. As previously observed, velocity predictions are slightly lower in OpenFOAM.

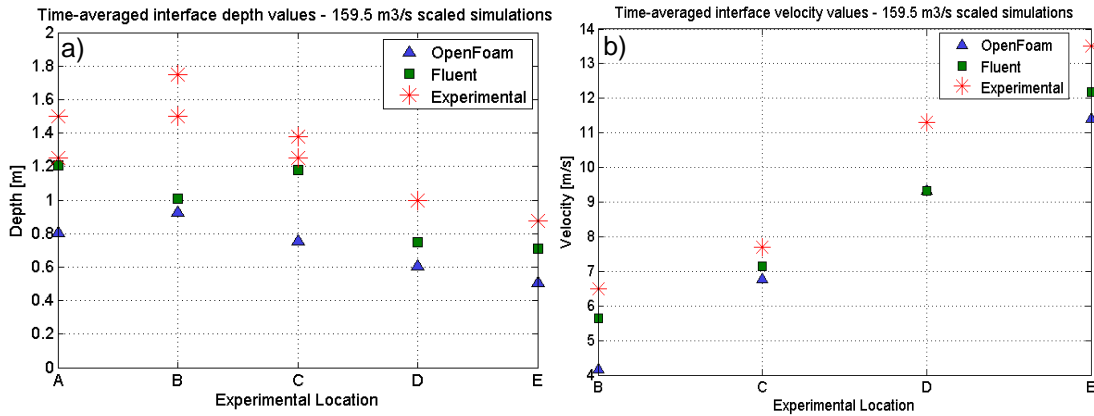


Figure 6.39: Time-averaged values of: a) depth and b) velocity at point locations along the spillway channel predicted by the two solvers with physical model measurements

The relative errors of depth and velocity predictions from the two solvers at the various locations are presented on Table 6.15 and Table 6.16 respectively. In this flow rate the OpenFOAM errors of depth and velocity are generally higher in all locations. The average OpenFOAM depth errors are around 35 % and velocity errors are approximately 18 %. Fluent presents significantly lower errors, reflecting superior agreement with the physical model measurements. The Fluent average errors of depth and velocity are 12 and 11 % respectively.

Table 6.15: Relative error in depth predictions in OpenFOAM and Fluent at the different experimental locations

	A	B (left)	B (right)	C (left)	C (right)	D (left)	D (right)	E (left)	E (right)
OpenFOAM relative error %	34.82	31.64	24.84	27.19	31.65	34.94	42.06	40.57	48.45
Fluent relative error %	13.18	26.10	0.40	3.66	12.98	6.92	19.45	9.40	14.06

Table 6.16: Relative error in velocity predictions in OpenFOAM and Fluent at the different experimental locations

	B	C	D	E (left)	E (right)
OpenFOAM relative error %	27.67	14.32	17.30	15.26	15.66
Fluent relative error %	8.53	9.88	18.15	10.74	6.29

Numerous velocity measurements were taken for the PMF case at the crest of the labyrinth weir. Measurements were collected at every upstream and downstream crest in addition to at the centre of each sidewall. Predictions from the weir modelling domain mesh were extracted and compared against these experimental measurements. The points where the numerical predictions were extracted correspond to the centre of the crest at each experimental location. The physical model outputs are presented in Figure 6.40 a). The numerical predictions of free surface velocity presented in form of velocity vectors for OpenFOAM and Fluent are shown in Figure 6.40 b) and c) respectively. Results show the velocities in the approach channel and most locations of the crest are well predicted.

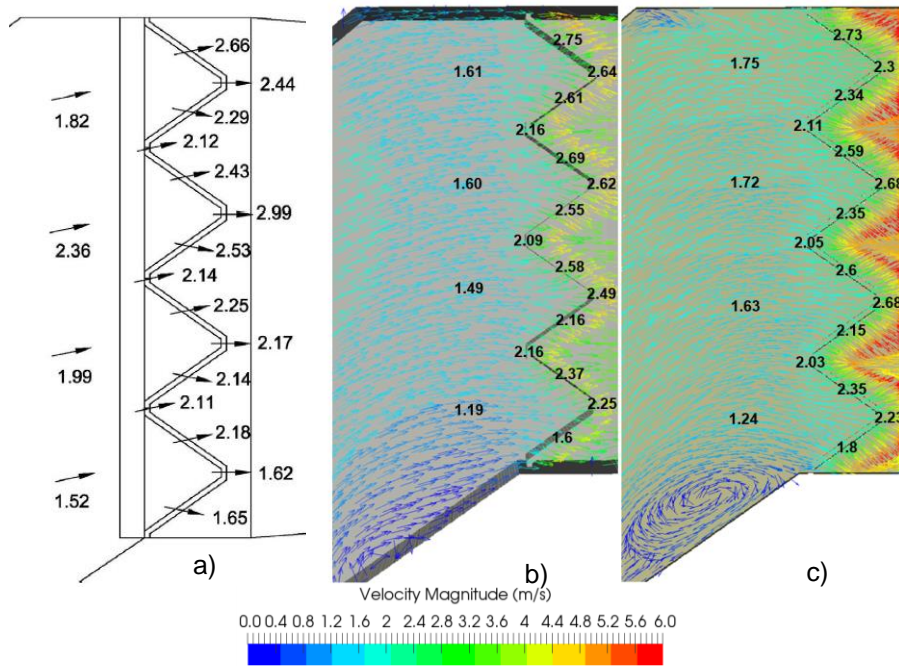


Figure 6.40: a) Velocities measured upstream and at the crest of the physical model; b) Free surface velocity vectors predicted with OpenFOAM; c) Free surface velocity vectors predicted with Fluent

The predictions from the two solvers present generally comparable velocity values and vector directions upstream the weir. Velocities are slightly larger in Fluent with differences being greater immediately downstream the weir. The main differences in the vectors occur near the approach channel walls. In the low velocity area near the right wall of the approach channel Fluent predicts the existence of a stationary vortex, while OpenFOAM shows a smaller recirculation region.

When taking into account the measurements at the crest apexes the relative errors of the free surface velocity predictions are 9 % in both OpenFOAM and Fluent. Considering all the measurement points, including those in the approach channel, the relative errors are of 12 % OpenFOAM and 13 % in Fluent. Therefore there is higher accuracy in the predictions at the weir crest than at the reservoir. This is highly likely to be due to the fact that there is more uncertainty around the exact location of the four measurement points in the reservoir, while the location of the measurement points at the crest apexes and sidewalls is known. The small underestimations are still within the order of 10 % error which is within the physical model uncertainty.

6.10.5. Summary

The modelling of the flow in the spillway channel revealed that the consistency in the predictions from the VOF implemented in two solvers varies with the size of the flow rate. For $40 \text{ m}^3/\text{s}$, the predictions from both solvers provide general agreement on the depths, velocities and configuration of cross-waves. The minor differences observed between the two solvers are expected to be due to the different interface capturing scheme implemented. Errors in the depth predictions are the highest for this flow rate and are of very similar order for the two solvers being 35 and 34 % in OpenFOAM and Fluent respectively. The velocity errors are lower than those for depth and are comparable for the two solvers, with average values of 15 and 13 % in Fluent and OpenFOAM respectively.

The 79 m³/s OpenFOAM predictions indicate a close correlation between the numerically predicted free surface and that generated in the physical model. In addition, the predictions of this flow rate exhibit significantly lower errors in depths and velocities than for the lowest flow rate, with an average error of 14 % in depth and 7 % in velocity predictions.

The 119.6 m³/s cross-wave configuration is well predicted with Fluent but slightly less well defined with OpenFOAM. In addition, the cross-waves crossing points are located further downstream in Fluent than in OpenFOAM. Consequently the solvers present less consistency than in the 40 m³/s case. The cross-wave's crossing points' heights as well as flow depths and velocities in the spillway channel are well reproduced in Fluent. However, OpenFOAM shows certain underestimations of flow depths. The average OpenFOAM and Fluent relative errors of depth predictions are 24 and 17 % respectively. The velocity averages are 10 and 8 %. Therefore, the errors are still of similar order in the two solvers, (i.e. approximately 20 % for depth and 10 % for velocity) and overall slightly lower than in the 40 m³/s case.

The 159 m³/s case reveals greater discrepancies between the predictions from the two solvers, where the cross-wave configuration is more elongated and superiorly defined in Fluent than in OpenFOAM. The free surface depths and velocities predicted with Fluent appear to be in closer agreement with the physical model measurements. The average relative depth errors are 35 and 12 % in OpenFOAM and Fluent respectively and these for velocity are 18 and 11 % in OpenFOAM and Fluent respectively. Consequently, there are more significant differences between the free surface features predictions as well as between the relative errors in the two solvers in this flow rate. This is expected to be due to the higher cell size of the cells where the free surface is located in OpenFOAM in this higher flow rate (which is equivalent to that in Fluent, and the mesh independence study showed OpenFOAM requires a lower cell size). In the prediction of free surface velocities in the approach channel and at the labyrinth weir crest, the two solvers present more similar values, with velocities slightly higher in Fluent. Such predictions are obtained with a mesh of finer cell size at the weir and approach channel in the area where the free surface is located than that of the spillway channel. Therefore the lower performance of OpenFOAM for the largest flow rate compared to Fluent is partly attributed to the higher sensitivity to cell size and requirement of higher resolution of this solver.

In summary, the Fluent predictions indicate generally a very accurate characterisation of the free surface features. The velocity errors are in the order of 10 % in all cases, which is within the uncertainty of the physical model measurements. The relative errors in the depth predictions are between 10 and 17 % in the two largest flow rates. However, these are higher for the lowest flow rate, which presents the greatest discrepancies between the physical model depth measurements and predictions from the two solvers. The OpenFOAM predictions reveal a similar trend to those from Fluent, with the exception of increased errors (up to 35 % in depth and 18% in velocity) in the largest flow rate. General differences in the two solvers are expected because of the different interface capturing scheme. Greater discrepancies between the two solvers in the largest flow rate occur due to the larger cell size where the free surface is located and higher sensitivity of OpenFOAM to cell size.

6.11. Prediction of the Labyrinth Weir Rating Curve

The rating curve of the labyrinth weir, consisting in the upstream head over the weir (relative to the crest) against the flow rate was calculated from simulations conducted on the weir modelling domain, described in Section 6.2. This modelling domain consists in the smallest geometry with a high mesh resolution at the crest of the labyrinth weir and its vicinity in order to capture the flow characteristics with sufficient detail. It is known that the physical model measurements for the rating curve were taken at a point located in the approach channel where there was no influence of the streamline curvature induced by the weir. The numerically predicted depths were also extracted in the approach channel at a point where the water heads were levelled, located 1.5 m upstream of the labyrinth weir upstream crests (30 m at prototype scale). The water head variation from the reservoir level to the weir crest was greater for increasing flow rate. The numerically predicted and experimental curves are shown on Figure 6.41.

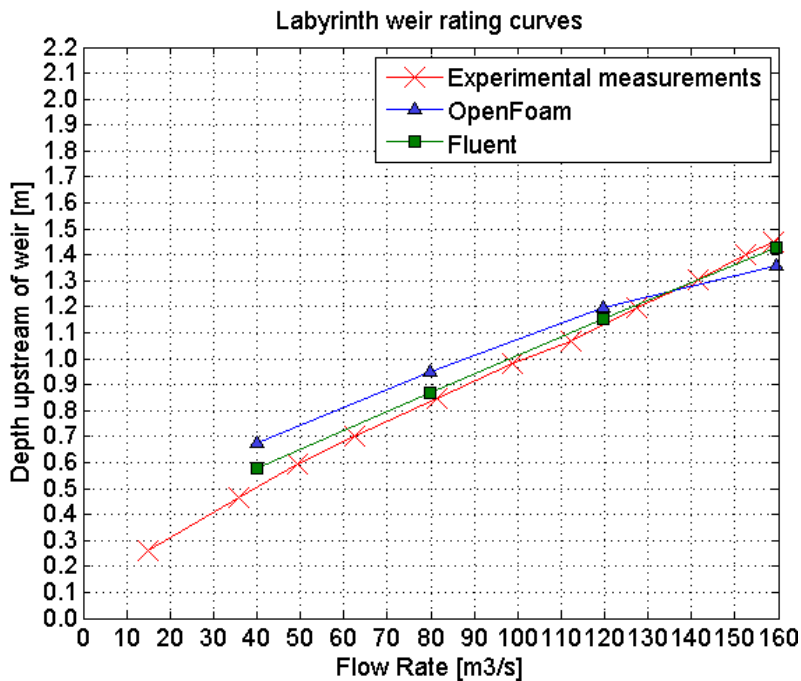


Figure 6.41: Rating curve of the labyrinth weir measured in the physical scale model and computed with predictions from Fluent and OpenFOAM

Figure 6.41 indicates there is close agreement between the numerical predictions from Fluent and the experimental measurements for all flow rates with only slightly higher predictions of head for the lowest flow. The predictions from OpenFOAM show an overestimation of the head at the lowest flow rates and slight underestimation for the PMF. The greatest difference between the predictions from the two solvers is in the lowest flow rate, where the OpenFOAM head prediction is approximately 0.1 m higher than that from Fluent. The greater differences between the numerical and physical model measurements for the lowest flow rates are in line with the fact that lower heads present higher uncertainty in the physical model, due to the increased challenges in levelling the water head (Tullis *et al.* 2017). In the intermediate flow rate data points, there is good agreement between physical and numerical results, although the OpenFOAM predictions are slightly higher. For 159.5 m³/s, the experimental curve shows an upstream water head of 1.45 m, the numerical predictions show the water head to be 1.42 m in Fluent and 1.36 m in OpenFOAM.

Therefore, the predictions from Fluent are concluded to be of significant level of accuracy. In average in the 4 points computed, the OpenFOAM relative error is of 15.2 % and that in Fluent is of 5.8 %. The existing differences between the predictions of the two solvers range from 4 to 16 % and they are mainly attributed to the different interface capturing scheme employed. However, further investigations of the solver implementations would be required in order to confirm the precise reason for the observed discrepancies between the two solvers.

6.12. Modelling the PMF in the Comprehensive Domain

Simulations of the comprehensive domain were undertaken for the three different scenarios of tail water level modelled in the physical model for the PMF flow rate. These are, low, medium and high water levels. Such simulations aimed to evaluate the capabilities of the numerical model to reproduce the interaction between the fast flow developed on the spillway channel with different levels of tail water. This is completed by comparing the numerical predictions with the physical model outputs.

In this structure, the means by which the energy is dissipated is through a hydraulic jump occurring where the spillway flow meets with the tail water. One of the objectives of the physical modelling of the different levels of tail water (and hence of the location of the formed hydraulic jump), was to predict the position of the hydraulic jump as well as the velocity values and distribution downstream of the structure. This was undertaken to help determine whether armouring of the ground surface would be necessary to withstand velocities higher than 6 m/s and prevent erosion of the embankment dam. The numerical modelling conducted here for this flow situation is used to consider the same criteria. Therefore, the technical characteristics of the hydraulic jump (bubble rate, roller lengths, etc.) are not examined since they are beyond the scope of this thesis and were nor the aim of the physical model of this scheme. In this section, the numerical predictions are compared with the predominantly qualitative experimental data recorded as part of the physical modelling.

Given the computational effort of such a large domain, simulations were only conducted in Fluent, which has previously been shown to provide an accurate characterisation of the flow within the spillway channel for this flow rate. The modelling of the channel and weir domains with the two solvers was judged sufficient to compare predictions from both solvers.

6.12.1. Low Tail Water Level

The location of the hydraulic jump in the low tail water case is indicated in the physical model diagram with a red arrow in Figure 6.42 a). The physical modelling of the low tail water conditions showed the hydraulic jump occurred approximately 10 metres upstream of the end sill with velocities decreasing significantly downstream of the concrete structures. Figure 6.42 b) shows a physical model photograph of the hydraulic jump for the low tail water scenario. Figure 6.42 c) presents an instant representation of the numerically predicted flow situation at 130 s of simulation time, once the system has become stable. Figure 6.42 d) and e) show the physical model photograph and an enhanced view of the numerical prediction with the hydraulic jump free surface

location indicated with red lines. The position of the free surface in the numerical model is well reproduced and presents good agreement with that observed in the physical model. The physical model photograph reveals that in this scenario, there is a considerable amount of air entrainment in the hydraulic jump. The free surface in the vicinity of the hydraulic jump and also downstream of it, is shown to be formed of mainly white water. Since no additional equations to model air entrainment are included in the numerical solvers, the amount of air bubbles predicted in the water phase in the numerical predictions is lower than those observed in the physical model.

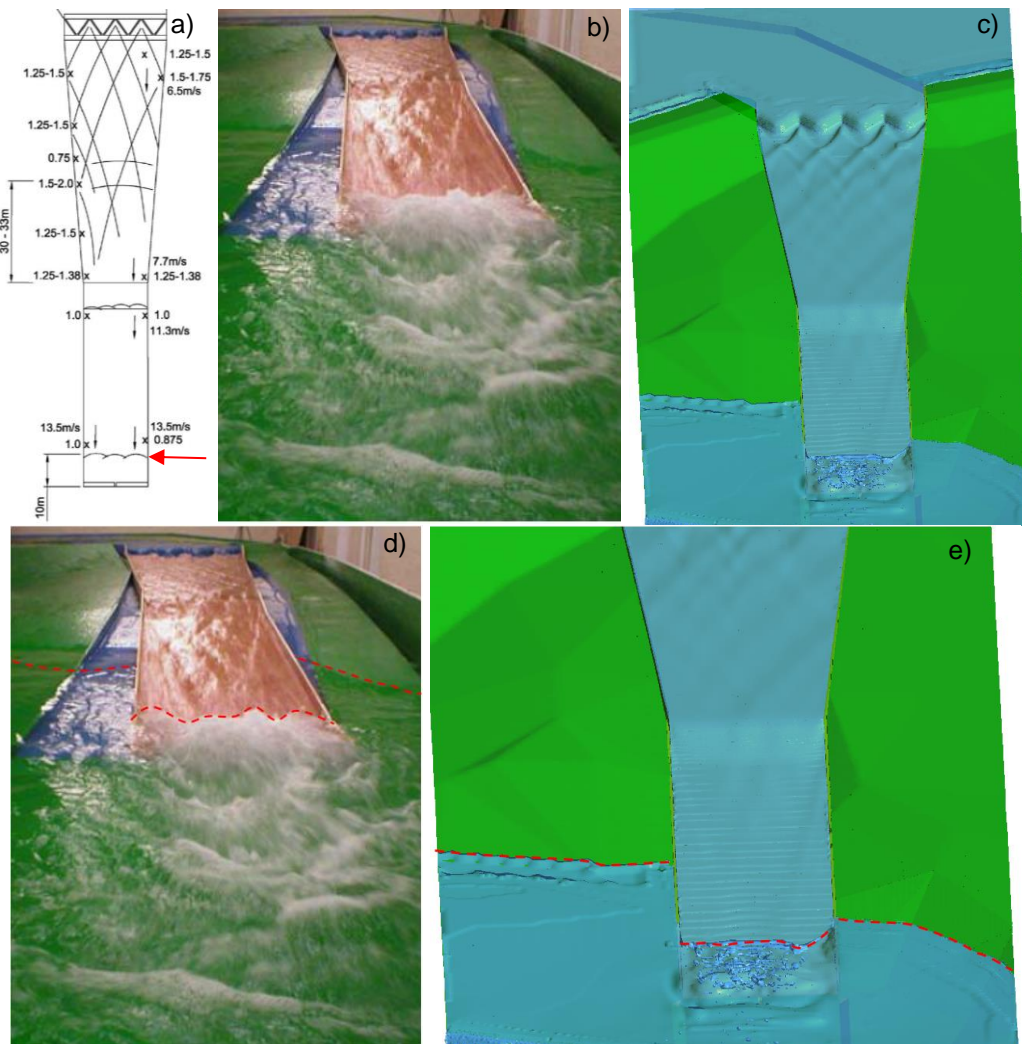


Figure 6.42: a) Physical model diagram indicating the approximate location of stilling at low tail water level with a red arrow; b) Photograph of the physical model; c) Instant representation of the numerically predicted free surface; d) Photograph of the physical scale model with red lines showing the location of the free surface; e) Instant representation of the numerically predicted free surface with red lines showing the location of the free surface

A further photograph of the physical model hydraulic jump is presented in Figure 6.43 a) and the predictions of the free surface features coloured by velocity are shown on Figure 6.43 b). It is important to note that both the position of the hydraulic jump and the velocity contours in its vicinity are stable at this point of the simulation. Therefore, the instant illustrations of the free surface are very representative of the flow situation. In order to investigate the characteristics and location of the hydraulic jump predicted by the model, the flow was analysed along three sections of the spillway channel. The location of the three planes is shown on Figure 6.43 d). Plane 2 is located

5 m to the right of the baffle block, plane 2 is located on the baffle block and plane 3 is located 5 m to the left of the baffle block.

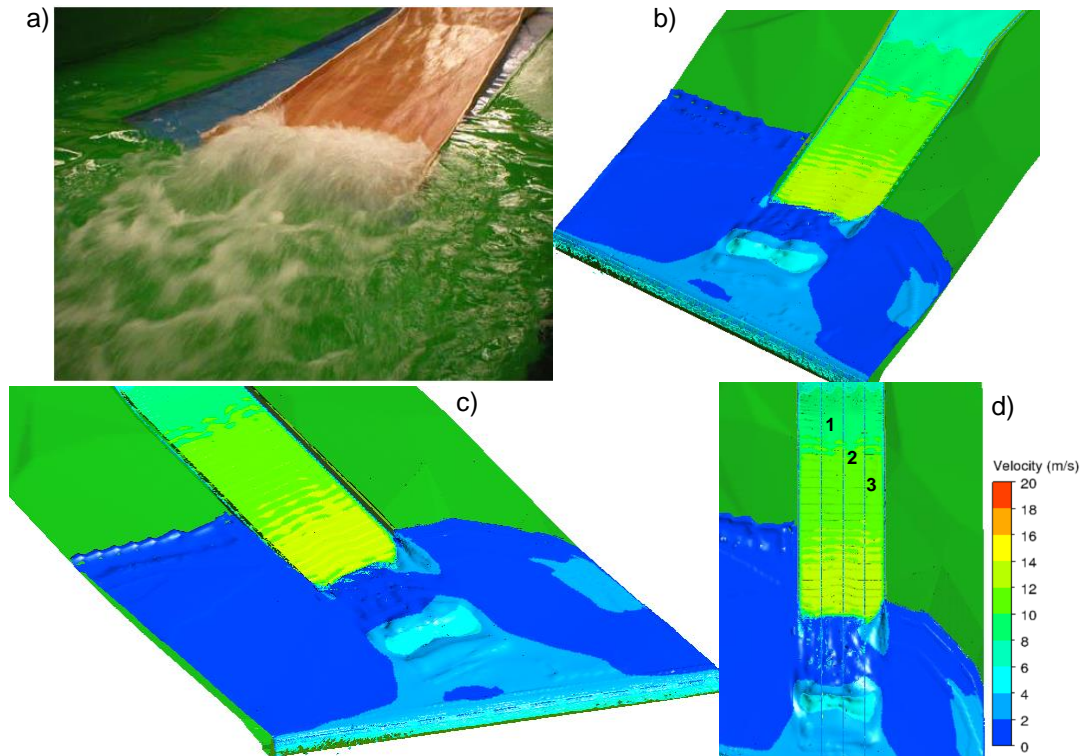


Figure 6.43: a) Photograph of the physical model hydraulic jump; b) and c) Instant representation of numerical model free surface coloured by velocity; d) Location of three planes to analyse the flow situation

Cross sectional profiles of free surface velocity and depths were extracted along planes 1 to 3 and these were plotted on the same axes along with the water volume fraction contours at each plane. These are presented on Figure 6.44 a), b) and c). In the graphs, the 0 m coordinate for the horizontal distance was set at point measurement E, situated at the end of the spillway channel. The 0 m coordinate for the depth, in the direction of the water depth, corresponds to the base of the stilling basin. Figure 6.44 indicates that the location of the hydraulic jump is well predicted, approximately at 10 m upstream of the end sill. Therefore, it confirms close agreement with the physical model results for this scenario. In addition, the velocity plots in Figure 6.44 show that the fast flow at the end of the spillway channel with a velocity of around 13 m/s meets the tail water level within the spillway channel and then the velocity decreases sharply at the hydraulic jump, which occurs within the spillway structure. Downstream of the hydraulic jump, which is also downstream of the concrete structure, velocities are just under 2.5 m/s. Therefore, in this particular scenario, the velocities in this area are safely low which is also predicted in the physical model. The free surface profiles and water volume fraction confirm that the model is capturing the inclusion of air pockets up to certain extent. This is larger at planes 1 and 2 and moderately decreases at plane 3. The free surface velocity and depth profiles are overall very comparable at the three planes. The velocity decreases along the hydraulic jump and then it exhibits a subtle peak immediately downstream the end sill. Downstream of such peak the velocity becomes even and remains stable with values of approximately 2 m/s in plane 1 and of 2.2 m/s and 2.5 m/s in plane 2 and 3 respectively.

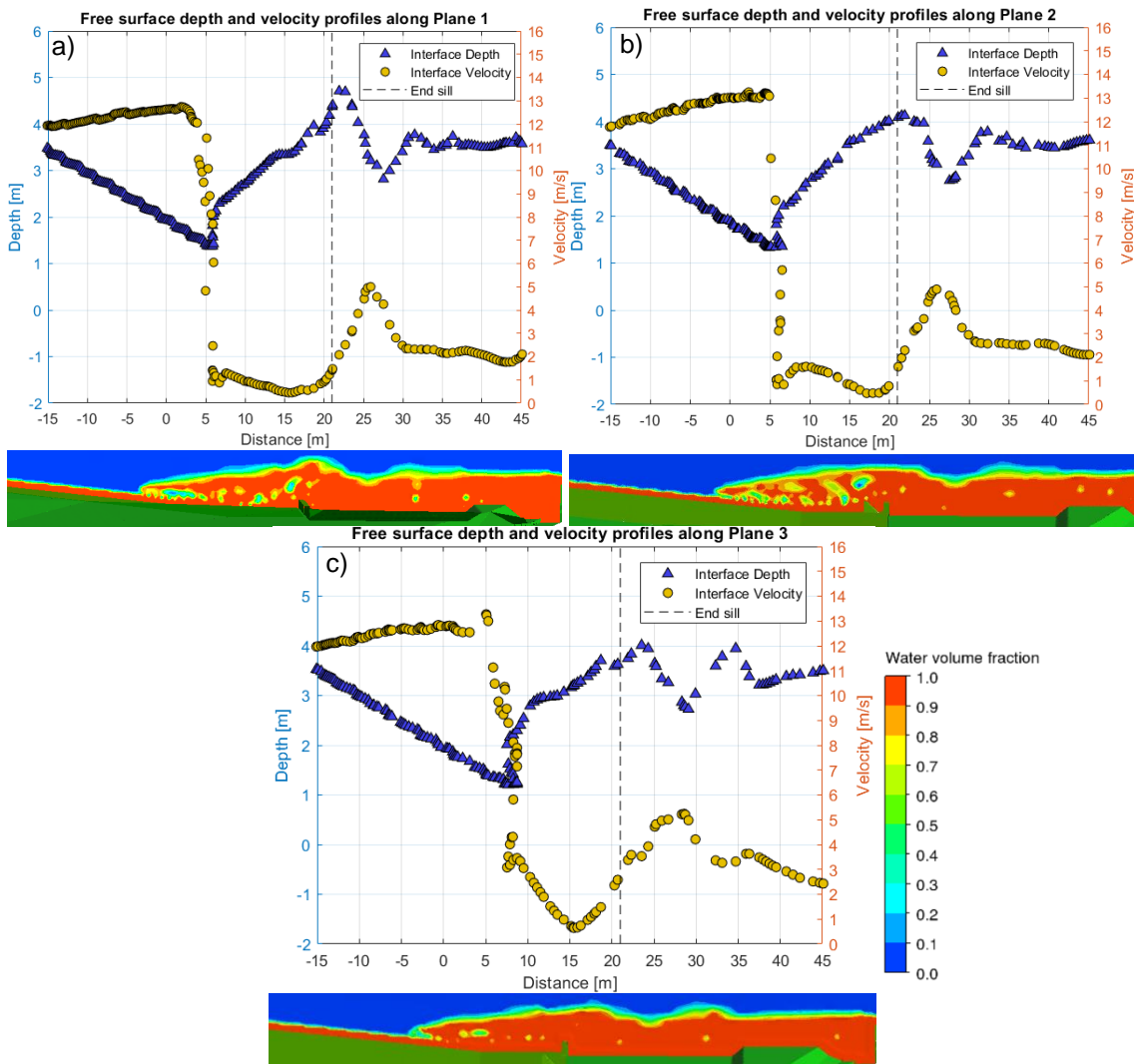


Figure 6.44: Free surface depth and velocity profiles through the hydraulic jump with the corresponding water volume fraction contour planes at the same sections along: a) Plane 1, b) Plane 2 and c) Plane 3

Figure 6.45 presents further details of the hydraulic jump across the three planes, where the velocity vectors on the water phase are indicated in each plane coloured with velocity contours. Results show the velocity contours at planes 1 and 2 are very comparable in the vicinity of the hydraulic jump as well as upstream and downstream of it. Plane 3 exhibits generally less air pockets and slightly higher velocities at the hydraulic jump than the other two planes, as has already been observed on Figure 6.44 and Figure 6.43. Therefore, velocities are marginally higher in the left side of the spillway, but differences are of approximately less than 1 m/s. Velocities at the base of the terrain downstream of the end sill do not exceed 3 m/s at any of the planes, indicating no potential problematic areas of higher velocity which would require special attention are found. This is in agreement with the physical model observations.

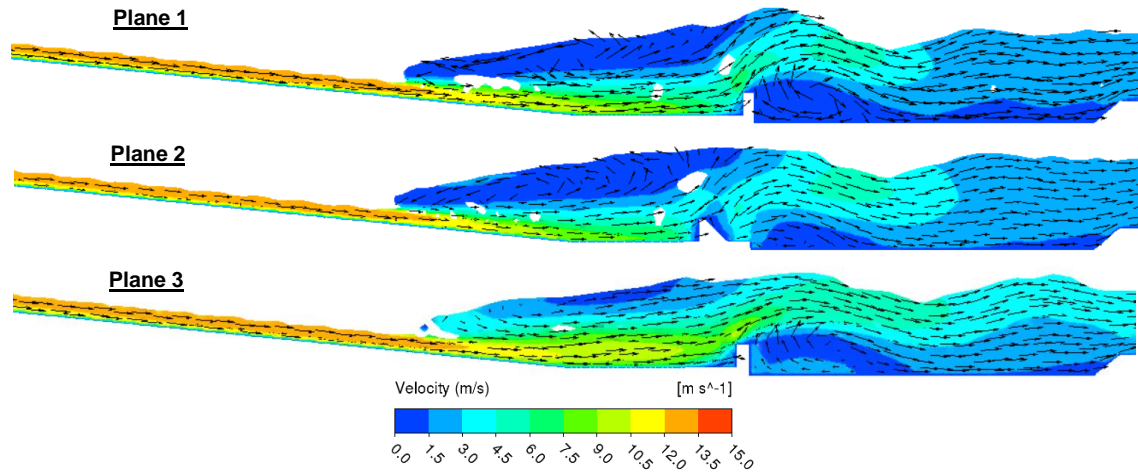


Figure 6.45: Profile in the vicinity of the hydraulic jump showing velocity vectors and contours across Planes 1, 2 and 3

6.12.2. Medium Tail Water Level

The physical model diagram and photograph of the flow situation for the medium tail water level scenario are presented on Figure 6.46 a) and b) respectively. An instant representation of the free surface features predicted with the numerical model at 200 s are shown on Figure 6.46 c). The physical model photograph with the location of the free surface is shown on Figure 6.46 d) and that on the instant representation of the numerically predicted free surface is presented on Figure 6.46 e). The physical model diagram and photograph indicate that in this case, the hydraulic jump is located in the vicinity of the second change in gradient in the spillway, shown with a red arrow. The physical model photograph also show a considerable amount of air pockets at the hydraulic jump and immediately downstream. The location of the hydraulic jump is well predicted by the numerical model. The physical model and numerical predictions of the flow are generally well correlated, but they differ in the water level on the sides of the spillway; that is, on the surrounding terrain. The physical model of the final spillway design was built on top of the initial spillway design (the latter is shown in blue in Figure 6.46 a)) In addition, the irregular surrounding terrain was not reconstructed exactly as it is in the real site. These two factors brought differences between the physical model and the numerical simulation predictions. Because the numerical model is built upon the geometry created from the real contour lines of the terrain, the mesh presents the irregularities more resemblant to those in the real site around the spillway channel. When the water level is set to the required tail water downstream, the water flows around the irregularities, making its way further upstream where the terrain is flatter. This does not occur in the physical model where the terrain surrounding the spillway is generally more levelled, which allows the water flow uniformly on both sides of the spillway. This is particularly evident on the left side of the spillway, where in the numerical model the tail water does not progress further upstream due to a slight terrain elevation but it is located further upstream on the physical model. The terrain irregularities represented in the modelling domain are shown in extended detail on Figure 6.47 b).

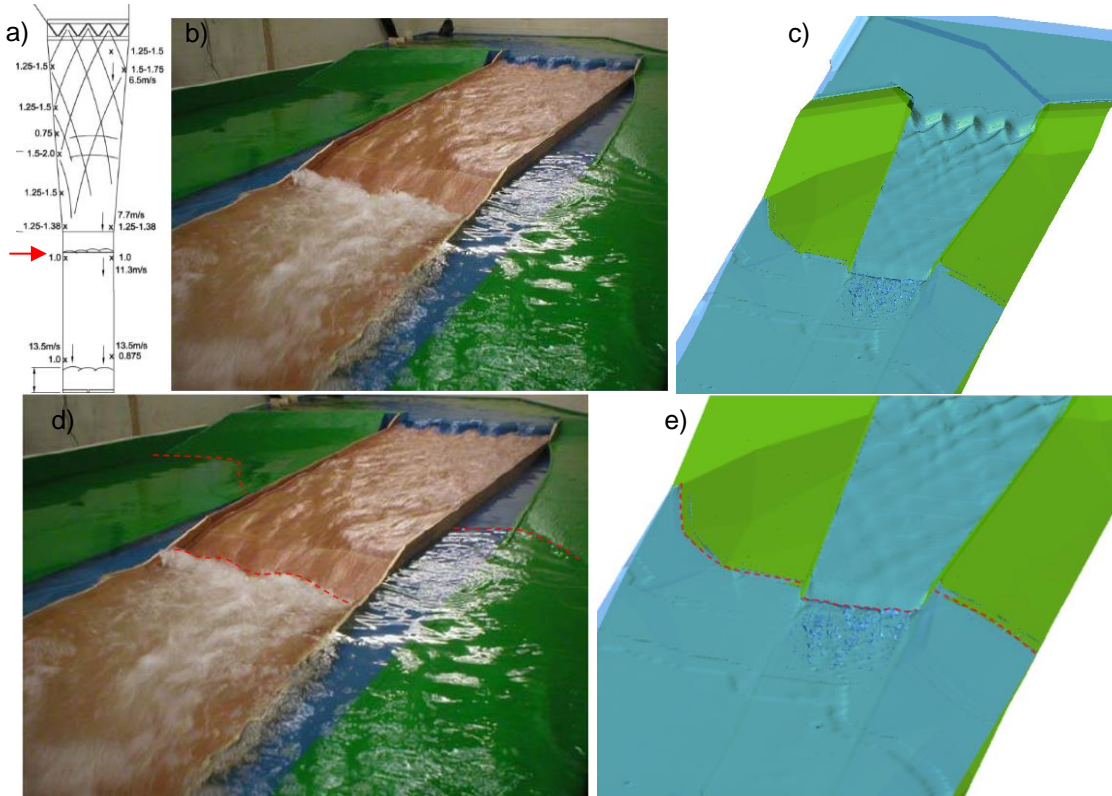


Figure 6.46: a) Physical model diagram indicating the approximate location of stilling at medium tail water level with a red arrow; b) Photograph of the physical scale model; c) Instant representation of the numerically predicted free surface; d) Photograph of the physical scale model with red lines showing the location of the free surface; e) Instant representation of the numerically predicted free surface with red lines showing the location of the free surface

The physical model indicates that velocities developing outside of the spillway structure on the tail water are sufficiently low, with all the energy being dissipated within the concrete structure before moving over the spillway right wall. These results are in line with the numerical model outcomes which show velocity values in the tail water from 0 to 2 m/s. The free surface coloured by velocity is shown on Figure 6.47 a), with an enhanced view of the right side of the tail water on Figure 6.47 b).

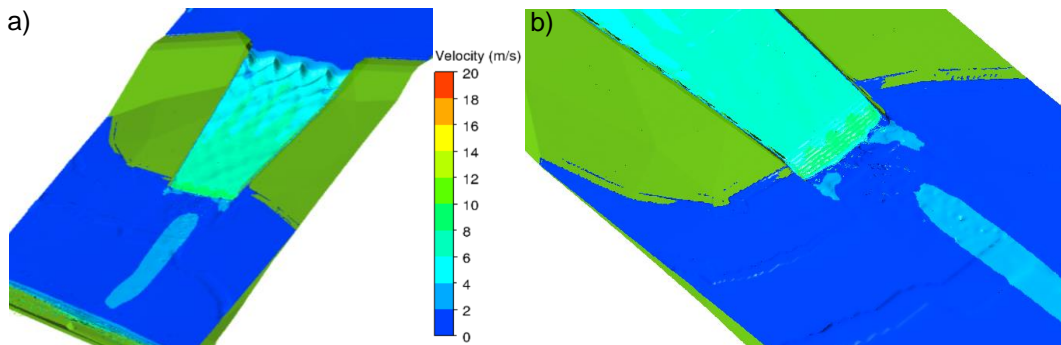


Figure 6.47: a) instant representation of numerically predicted free surface coloured by velocity; b) enhanced detail of the free surface coloured by velocity surrounding the terrain irregularities

In order to further examine the flow situation, free surface depth and velocity along planes 1, 2 and 3 as described in the low tail water case, were extracted. The location of the three planes is the same as for the previous case. In this case the coordinate $x = 0$ m corresponds to the measurement location C, which is located just before the first change in gradient. The coordinate $z = 0$ m is taken as the base of the spillway channel at location C. The free surface depth and

velocity profiles along planes 1, 2 and 3 are presented on Figure 6.48 a), b) and c) respectively. The location of the three planes in the structure is shown on Figure 6.48 d). Results extracted along the three planes show very comparable profiles of velocity and depth, which means the hydraulic jump height does not present major variations across the spillway channel width. The velocity profiles show the flow along the spillway has a velocity of approximately 9 m/s in all planes when it meets with the tail water. Downstream of the hydraulic jump velocities decrease to 1 m/s in plane 1 and to 3 m/s to 2 m/s in planes 2 and 3 respectively. As indicated on Figure 6.48 d), planes 2 and 3 are located in an area of higher tail water velocity than plane 1. The free surface plots show a significant presence of air pockets which varies in the three sections, with the greatest number appearing at plane 3. The volume fraction contour plots for each plane confirm the hydraulic jump is located immediately before the second change in gradient.

Results show that despite there being certain discrepancies in the geometry of the modelling domain in the region outside the spillway channel between the physical and numerical models, the velocities and flow characteristics present agreement in the two models. Therefore, the relevant outcomes from the physical model that were required for structure design, are correctly predicted in the numerical models. This case highlights some of the most typical challenges that physical models present to reproduce real flow situations, and in particular, to recreate an irregular terrain geometry in a physical model.

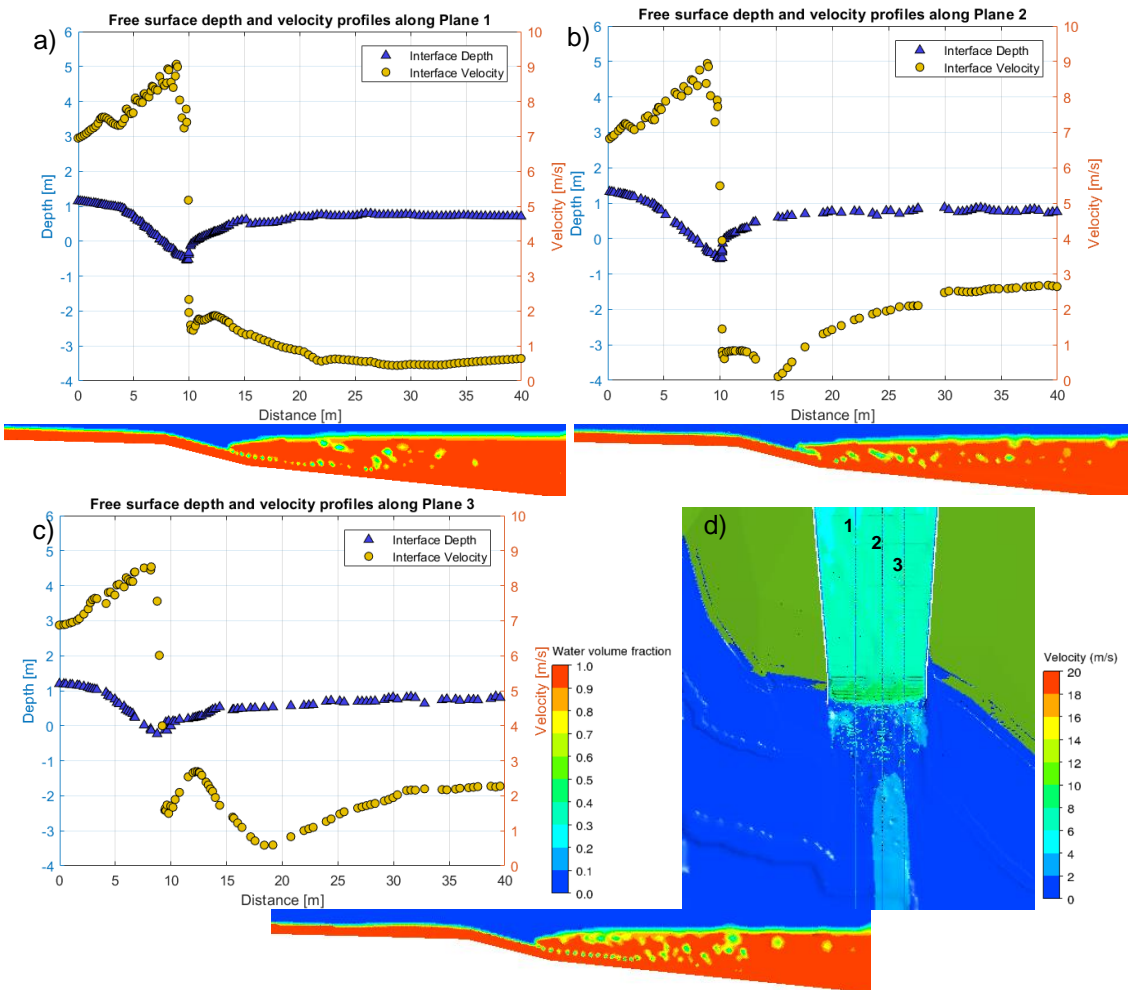


Figure 6.48: Free surface depth and velocity profiles through the hydraulic jump with the corresponding water volume fraction contour planes at the same sections along: a) Plane 1, b) Plane 2 and c) Plane 3; d) location of the three planes in the spillway

Figure 6.49 shows the water phase in the vicinity of the hydraulic jump at the three planes coloured by velocity contours and showing the velocity vectors. As previously observed on Figure 6.47, the velocities in the spillway channel flow are very comparable at all planes, however in the tail water there is an area of larger velocity at planes 2 and 3 in comparison to plane 1. In Figure 6.49 it is also shown that the location of the hydraulic jump does not vary at the different planes.

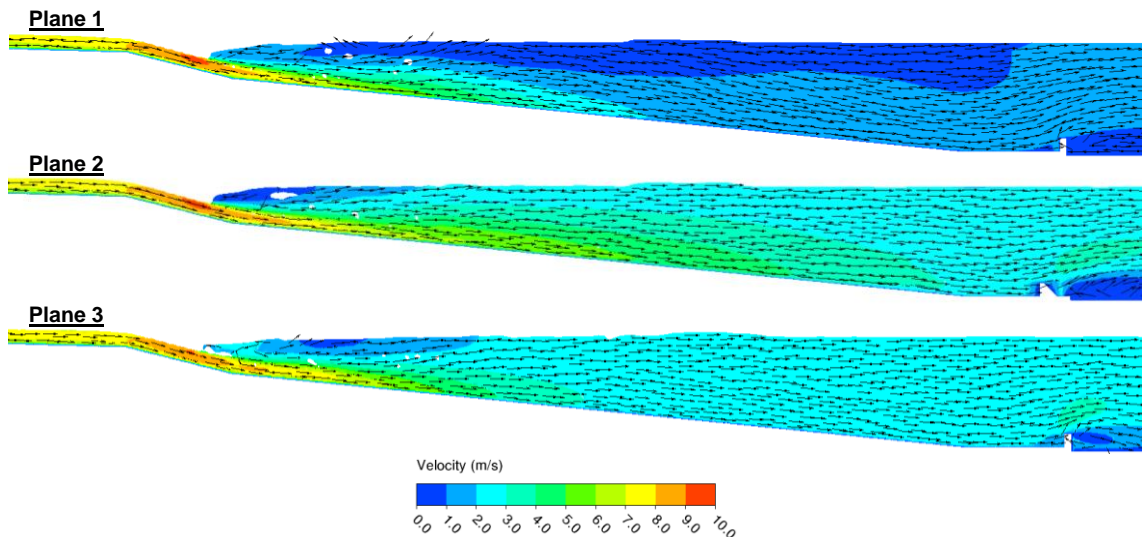


Figure 6.49; Profile in the vicinity of the hydraulic jump showing velocity vectors and contours across Planes 1, 2 and 3

6.12.3. High Tail Water Level

The schematic location of the tail water for the high tail water case on the physical model diagram is indicated with a red arrow on Figure 6.50 a). The photograph of the flow situation in the physical model is shown on Figure 6.50 b). In this case, the physical model photograph shows there is significantly less air entrainment in the hydraulic jump. The instant representation of the numerically predicted free surface at 290 s is shown in Figure 6.50 c). The tail water free surface boundaries are indicated with red lines in the physical model photograph on Figure 6.50 d) and on the numerically predicted free surface on Figure 6.50 e). The location of the hydraulic jump is generally well predicted with the numerical model. The location of the tail water on the left wall is more challenging to distinguish in the physical model photograph than in the diagram. But it is possible to approximately identify the area of the wall which is not longer submerged by the tail water, indicated with the red dashed line. Similarly to the medium tail water case, the tail water level on the spillway surrounding terrain is less advanced upstream in the numerical model predictions, given the difference in the irregularities in the physical and numerical models. This is especially more evident on the left side of the spillway channel, where the tail water in the physical model appears to be closer to the upstream embankment than that in the numerical predictions.

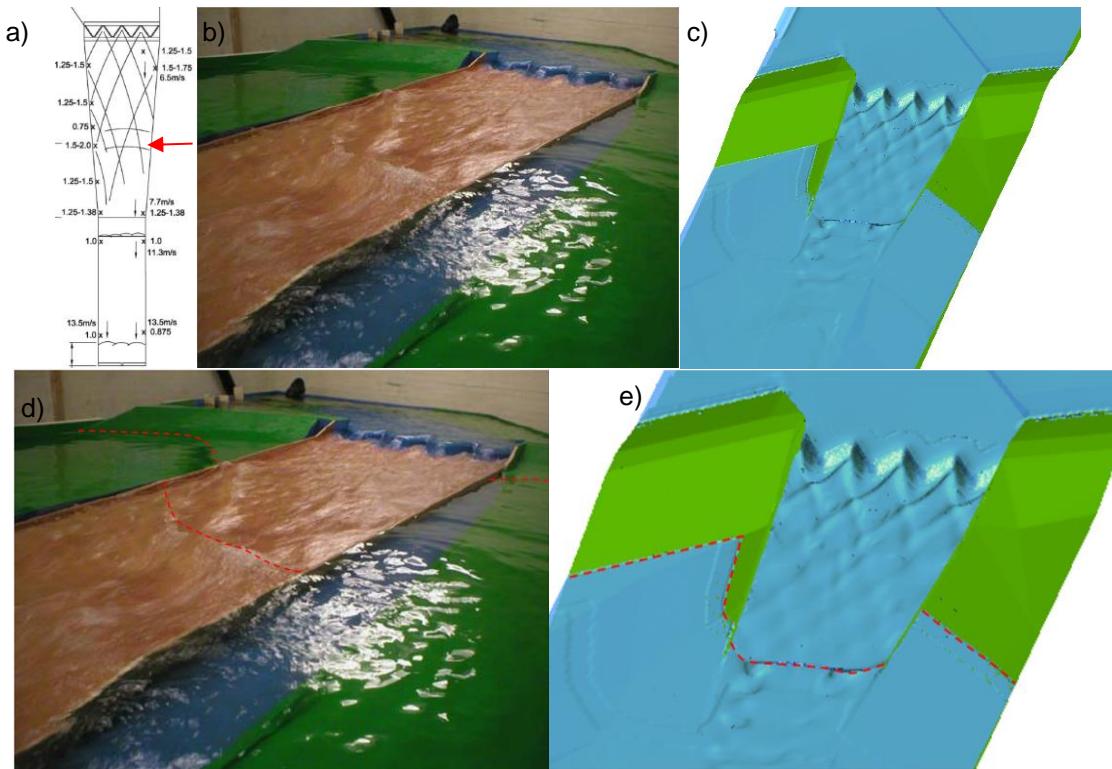


Figure 6.50: a) Physical model diagram indicating the approximate location of stilling at high tail water level with a red arrow; b) Photograph of the physical scale model; c) Instant representation of the numerically predicted free surface; d) Photograph of the physical scale model with red lines showing the location of the free surface; e) Instant representation of the numerically predicted free surface with red lines showing the location of the free surface

The instant representation of the free surface coloured by velocity is shown on Figure 6.51 a). The velocity contours indicate an area of velocities around 4 to 5 m/s at the centre of the tail water and these decrease to approximately 1.5 m/s in the area outside the spillway structure. In order to obtain a further perspective of the surrounding terrain irregularities, Figure 6.51 b) illustrates the instant free surface from a different perspective. In the left side of the spillway there is a mild elevation of the terrain which is not present in the physical model. In the right side of the spillway, the terrain adjacent to the spillway wall is also shown to have certain gradient as opposed to a more levelled surface as defined in the physical model.

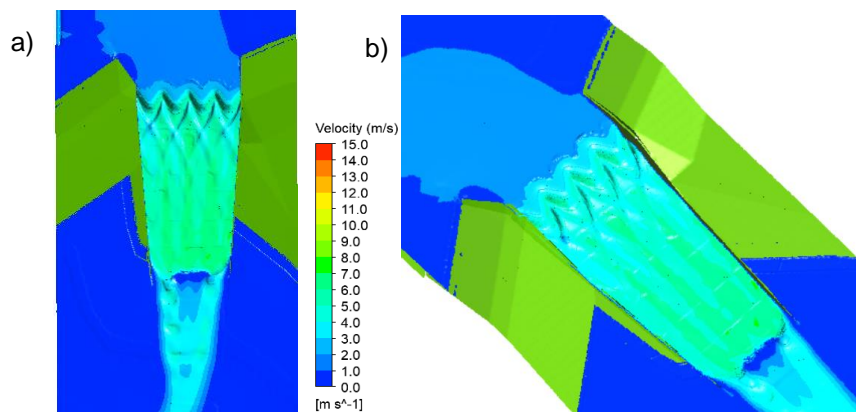


Figure 6.51 a) instant representation of numerically predicted free surface coloured by velocity from plan view; b) Enhanced detail of the same representation illustrating the surrounding terrain irregularities from a different perspective.

Figure 6.52 a), b) and c) show the free surface depth and velocity profiles at planes 1, 2 and 3 in the vicinity of the hydraulic jump with the volume fraction function of water contour planes for each case. The location of the three planes in the spillway is shown on Figure 6.52 d). In this case, the $x = 0$ coordinate was taken as that of measurement point B, and the $z = 0$ corresponds to the elevation of the base of the spillway at point B. In this case the free surface depth is similar in the three planes being of approximately 1 m at the tail water at the three locations. The velocity profiles change slightly since the higher velocities are found at the centre with values up to 5 m/s and down to 1.5 m/s on plane 3. In this case the volume fraction contours do not show presence of air pockets which agrees with the physical model photograph also showing less aeration.

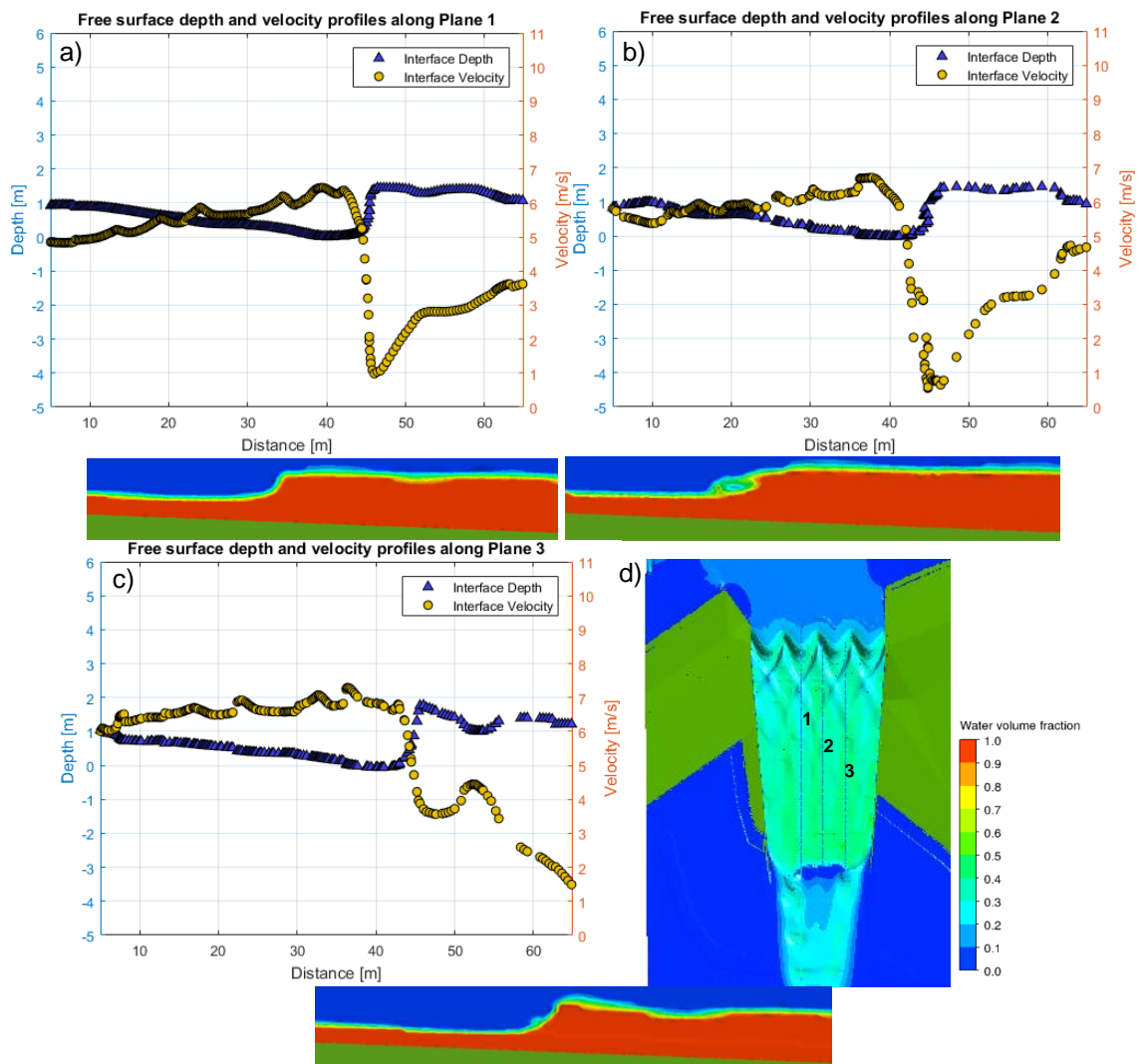


Figure 6.52: Free surface depth and velocity profiles through the hydraulic jump with the corresponding water volume fraction contour planes at the same sections along: a) Plane 1, b) Plane 2 and c) Plane 3; d) Location of the three planes in the spillway

Further flow characteristics in the vicinity of the hydraulic jump generated in this case are shown on Figure 6.53 where the velocity contours and vectors at the water phase are shown for the three planes. The velocity vectors show very comparable patterns at the three planes. The velocities at the front of the jump are lower in planes 1 and 2 and further downstream in the tail water are lower at plane 3. Overall the velocity contour planes indicate similar values at the three locations with velocity values at the base of the spillway being from 1 to 4 m/s.

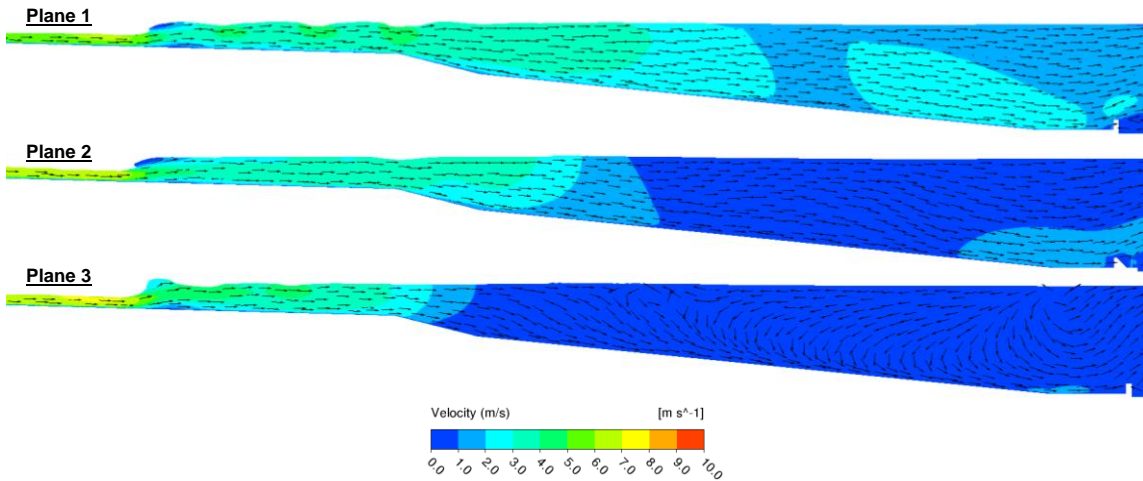


Figure 6.53: Profiles in the vicinity of the hydraulic jump showing velocity vectors and contours across Planes 1, 2 and 3

6.12.4. Summary

The modelling of the comprehensive domain revealed several valuable findings. In the low tail water scenario, the numerical model was capable of accurately predicting the location of the hydraulic jump. In addition, no potentially problematic areas of high velocity were identified in the tail water downstream or on the sides of the concrete structure, which agrees with the outcomes from the physical model. The medium and high tail water cases also indicate the location of the hydraulic jump within the spillway channel is well predicted by the numerical model. In both cases, the tail water velocities predicted on the surrounding terrain (outside the spillway structure) are safely low, as predicted with the physical model. These two scenarios highlighted one of the main discrepancies between the physical and numerical model outcomes consist in the geometry of the spillway surrounding terrain which is recreated by different means in the two models. Such differences generate variations between the location of the tail water on the irregular terrain. The other main difference between physical and numerical models is the presence of air entrainment which as previously discussed, is not being captured with any additional modelling in the VOF model applied. This assumption in the numerical models brings differences in the modelling of the hydraulic jump in the low and medium tail water levels. However, it is judged to be fully acceptable in the modelling of the high tail water level where there is negligible air entrainment observed in the physical model. Overall results show the physical model outputs required to inform the structure design requirements are possible to be acquired with the numerical predictions.

6.13. Discussion

6.13.1. Predictions of the Flow Downstream the Weir

Acknowledging the assumptions and limitations previously noted, as well as the different implementations utilised in the two solvers, it is possible to confirm the Fluent simulations are capable of reliably predicting flows in the spillway channel for all flow rates including velocities, depths and wave structures. The OpenFOAM predictions appear to be more reliable at lower

flows than at larger flows. Although they still provide the core flow features at the two largest flow rates, they underestimate flow depths and exhibit a less accurate definition of the cross-waves.

Results show the discrepancies between the predictions from the two solvers for the two largest flow rates are attributed to two possible causes. The first is the difference in the interface capturing scheme utilised in the two solvers. The second is the different sensitivity to mesh cell size that the two solvers exhibit. As discussed in Section 6.9.1, OpenFOAM demonstrates greater dependency on the mesh cell size than Fluent, meaning that at this scale this solver requires a lower cell size than Fluent to reproduce the flow situation with the same accuracy. In the 40 m³/s case (which is the flow rate utilised to conduct the cell size sensitivity analysis) the wave, velocity and depth predictions from both solvers are almost equivalent (and Mesh1 is implemented in OpenFOAM while Mesh2 is implemented in Fluent). For 79.8 m³/s results from OpenFOAM still predict the wave features with significant accuracy. However, for a larger flow rate, the free surface is not in the finest cell area but on the mesh base where the cell sizes are 8x10⁻³ m, which is the same size as the mesh implemented in Fluent. This is shown to be too large for OpenFOAM to capture the prominence of the waves, while Fluent is still reliably predicting them. The creation of a mesh with a further refinement step would thus be necessary to verify whether is possible to reproduce the waves' characteristics with higher precision in larger flow rates than the one presented here with the used numerical implementations. However, this would involve a mesh with a number of elements which would be too restrictive (approximately over 20 million elements) and hence its creation and subsequent solver simulations do not appear to be achievable with the available timescale. In order to illustrate this situation, water volume fraction contours were plotted perpendicular to the third downstream crest of the labyrinth weir for 40 m³/s and 119 m³/s with the two solvers. Figure 6.54 a) and b) indicate that for 40 m³/s the OpenFOAM free surface is within the cells of size 4x10⁻³ m while the Fluent waves are at the limit between the cells of 4x10⁻³ and 8x10⁻³ m. The size and height of such waves present consistency in the two solvers and the existing differences are expected to be due to the different interface capturing scheme implemented in the two solvers. Figure 6.54 c) and d) show that for 119.6 m³/s the free surface in OpenFOAM at the crest of the wave is located in the area of cells of size 8x10⁻³ m, while in the Fluent case the wave is completely within the 8x10⁻³m cell size zone. Therefore, although the difference in size and shape of such wave is expected to be mainly generated by the different interface capturing schemes of the two solvers, the increase in cell size in OpenFOAM for the largest flow rates is distinctly likely to have caused the greater disagreement in this case.

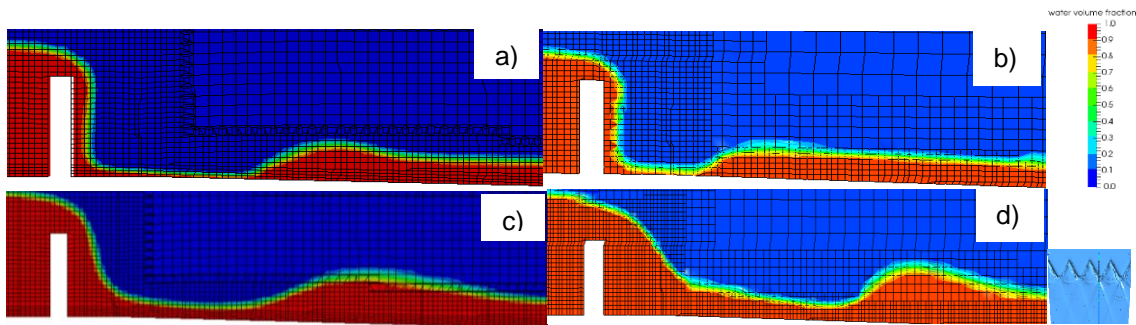


Figure 6.54: Water volume fraction contours at a plane perpendicular to the third downstream crest predicted for $40\text{m}^3/\text{s}$ with: a) OpenFOAM and b) Fluent and for $119.6\text{ m}^3/\text{s}$ with c) OpenFOAM and d) Fluent

6.13.2. PMF Predictions in the Comprehensive Domain

The numerical simulations of the comprehensive domain confirmed the methodology devised to extract the modelling domain from a real site set of contour lines and solid structures was successful. In addition, the procedure implemented to model the tail water level downstream of the spillway channel, consisting in an iterative methodology, has provided accurate results. In the modelling of the low tail water level, the numerical predictions showed accurate values of depth and velocity. The location of the hydraulic jump also presented very good agreement with that shown in the physical model. In the modelling of the medium and high tail water levels, the characteristics of the tail water present increased variations. These were caused by the existing differences in the representation of the surrounding terrain in the numerical and physical models. In the case of study, this does not have a significant impact on the outputs required from the hydraulic modelling to confirm the structure design. Hydraulic modelling of the tail water interaction with the spillway flow aimed to confirm that the water remained in the spillway channel structure before meeting the tail water. An additional objective of the physical modelling was to obtain a prediction of the channel flow behaviour with the different levels of tail water. In addition, velocities occurring outside the structure, on the embankment, were of concern since velocities higher than a given threshold would require armouring. These outputs obtained with the predictions of the numerical model show good agreement with those from and the physical model. The spillway flow interaction with the tail water is well correlated with the physical model results. Equivalently to the physical model predictions, the numerically predicted flow velocities reveal that there is no concern with the tail water velocities occurring in the embankment in the PMF case.

However, it is possible that for a different case of study, differences in the geometry of the numerical modelling domain and the physical model could lead to more significant variations between the outcomes from physical and numerical models. It is therefore important to highlight the existing challenges in accurately representing a scheme which involves the presence of an irregular terrain in physical and numerical modelling.

6.13.3. Limitations

6.13.3.1. Limits in the available experimental data

The available experimental dataset from the physical model report is recognisably not as extensive as it would have been if hydraulic modelling had been conducted for hydraulic research purposes (as opposed to structure design purposes). It is likely that in research facilities, a more detail dataset would have been gathered. An example of this is the experimental measurements collected in the dam break case analysed in Chapter 4, where the free surface of the dam break flow was measured over time and a continuous free surface data profile is available. As previously specified, the physical model utilised in this study to validate the numerical predictions was constructed with the aim of informing and confirming the scheme design. Therefore, it provides information relevant for design purposes. Thus, the dataset does not include cross sectional values of velocity and depth which would have been valuable to justify the instances where the numerically predicted depths diverged from the physical model measurements.

Mitigations for this limitation were taken by modelling of four flow rates to enhance robustness of the analysis. Modelling various flow rates and being able to validate predictions in all cases with several point measurements and flow features in each case is considered to significantly improve this situation. Moreover, the successful characterisation of the various flow aspects by the numerical models has also confirmed their capability to reliably predict the complex flows occurring in the physical model.

6.13.3.2. Limits in the mesh quality and cell size

This chapter showed that for considerably idealised flow situations like that modelled in Chapter 4, it is possible to conduct simulations employing a significant number of meshes of remarkably high quality. The experimental dam break flow simulated in Chapter 4 was modelled with 7 meshes in 2D case and 4 meshes in the 3D case. The simplicity of the geometry made possible to have a significantly higher mesh quality in the modelling of the experimental dam break case than in the physical model of the labyrinth weir and spillway. In the dam break case the cells were parallel to the base of the domain since it was possible to implement a mesh strategy based on number of nodes at each end of the domain in the z direction. A mesh density “bias” was implemented to decrease the cell size in the area near the domain base. Due to the complex geometry of the labyrinth, introducing multiple vertices across the spillway channel section, it was not possible to mesh the labyrinth weir and spillway domain employing the same meshing methodology. However, considering the existing challenges to mesh such complicated geometry, meshes of a considerable quality were produced for the three modelling domains of the hydraulic structures.

The smaller extent of the domain and the lower simulation time required to conduct model validation also enabled further mesh refinement steps in the dam break case which were not possible in the physical model case. It is likely that a further level of refinement would have

enhanced the simulation results of the largest flow rates, (119.6 m³/s and 159.5 m³/s) in OpenFOAM and provided closer agreement between the predictions from the two solvers.

6.13.3.3. Capturing air entrainment

As previously noted, a further limitation present in the numerical results is the capturing of air entrainment. In the numerical solvers implemented no additional equations were used to model air entrainment. In the flow over the labyrinth weir for low flow rates, the air entrainment in the physical model can be considered negligible. For the largest flow rates, and in the PMF in particular, there is more impact of such assumption, which results in the prediction of lower water depths than those in the physical model. The labyrinth weir nappe flow in the PMF presents higher aeration than that in the lower flow rates. Although the numerical models accurately predict the nappe shape, they do not reproduce the aeration.

The second case where this assumption affects the numerical results in greatest measure is in the modelling of the hydraulic jumps occurring in the low and medium tail water levels in the comprehensive domains. Decreasing the cell size in the area of the hydraulic jump would have increased the number of entrained air, however, (apart from having computational restrictions preventing this option) it would have not been able to capture air entrained smaller than the cell size. It is also important to mention that the modelling of air entrainment is one of the main challenges currently faced by numerical (and physical) models.

6.14. Conclusions

This chapter provided significant findings regarding the solvers' performance comparison and guidance on numerical implementations to model a 3D turbulent flow downstream of a labyrinth weir. The numerical predictions of the flow characteristics upstream the labyrinth weir and of the interaction between the channel flow with the tail water have also been assessed. The main conclusions from this chapter are summarised as follows:

- In the first section of this chapter it was discovered that the two solvers require the implementation of different mesh configurations to conduct simulations in a geometry with changes in the gradient of the domain base as well as changes in cell size. The VOF requires considerable mesh quality and hence the representation of the free surface is affected by the configuration of the cells in its vicinity. The VOF method implemented in Fluent shows best performance with a lower cell size at the base of the domain, which increases with distance from the base. In OpenFOAM, best performance is achieved with the first cells presenting a parallel layer of lower size to the spillway base.
- The mesh independence study revealed the two solvers exhibit different levels of sensitivity to cell size, with OpenFOAM requiring higher resolution than Fluent to provide mesh independent results. Fluent provides mesh independent results when the cell size is 8×10^{-3} m or lower, and OpenFOAM requires 4×10^{-3} m or lower.
- The different turbulence models employed show that for the process modelled in this chapter, consisting in a physical scale model of a labyrinth weir (therefore experimental

scale) the Standard $k - \varepsilon$ and RNG $k - \varepsilon$ models demonstrate generally equally accurate predictions of the flow phenomena, including depths, velocities and flow features. The SST $k - \omega$ model did not appear to be able to reproduce the flow behaviour as reliably as the $k - \varepsilon$ family models when using the same mesh, predicting lower depths and velocities as well as showing reduced definition of the wave features. It is expected that predictions from this model would improve with a further mesh refinement, but this would increase the computational time and resources to run the simulations. Additional investigations would be required to fully determine the cause of such comparatively poor performance.

- The model sensitivity to the interface capturing scheme was investigated for a flow rate of 119.6 m³/s by the implementation of the CICSAM scheme in Fluent. The predictions implementing the CICSAM scheme show lower peaks of the waves in the free surface area, which therefore show greater resemblance to the predictions from the MULES scheme applied in OpenFOAM. This gives support to the case that to reproduce remarkably complex flow features, like the configuration of the cross-waves for the largest flow rates, the PLIC scheme is better suited.
- Simulations of the flow on the spillway channel were conducted for four flow rates. The 3D VOF RANS Standard $k - \varepsilon$ model with the PLIC scheme implemented in Fluent generally indicates a very accurate characterisation of the free surface features for all flow rates. The Fluent velocity errors are in the order of 10 % in all cases, which is within the uncertainty of the physical model measurements. The Fluent relative errors in the depth predictions are between 10 and 17 % in the largest flow rates. However, these are higher for the 40 m³/s case, which presents the greatest discrepancies in depth between the physical model measurements and predictions from the two solvers. The 3D VOF RANS Standard $k - \varepsilon$ model with the MULES scheme applied in OpenFOAM presents similar predictions of depth and velocity to those predicted with Fluent, with the exception of increased errors (up to 35 % in depth and 18% in velocity) in the largest flow rate. The OpenFOAM predictions of the wave features become less well defined in the largest two flow rates, where the cross-wave configuration also becomes compressed compared to that in Fluent. The minor differences between the predictions from the two solvers for the lowest flow rate are expected because of the different interface capturing scheme utilised. The greater discrepancies between the predictions from the two solvers in the larger flow rates are due to the different interface capturing scheme in addition to the difference in cell size sensitivity that the two solvers exhibit.
- The numerical modelling of the labyrinth weir rating curve shows the Fluent results present very close agreement with the experimental curve, with OpenFOAM predictions being slightly overestimating the heads upstream the weir crest. Discrepancies between numerical and physical model predictions are larger for the lowest flow rates, which is expected to be due to increased uncertainty in the physical model measurements for low flow rates.

- Numerical simulations conducted in the comprehensive modelling domain confirm the methodology devised to extract the modelling geometry, the subsequently adopted meshing strategy, and the engineered boundary conditions implemented in the domain were successful and can be reapplied in the future. The numerical predictions of the comprehensive domain for the three modelled scenarios verify close agreement with the physical model measurements and observations. The three tail water scenarios confirm very good correlation with the physical model predictions of depth, velocity and location of the hydraulic jump. As expected, a reduced amount of air entrainment is exhibited in the numerical simulations in the low and medium tail water cases compared to the physical model photographs. In the high tail water level case there is negligible air entrained and hence there is effectively no impact of air entrainment assumptions. The main variation between the physical and numerical model cases consists in the outline of the irregular terrain surrounding the spillway channel, which resulted in slight changes in position of the tail water for the medium and high cases. Considering the existing discrepancies in the geometry, the numerical results are judged to be accurate and capable of providing the required outcomes for structure design.

7. Comparison of Prototype and Physical Model Predictions

7.1. Introduction

In this chapter, the flow aspects simulated in Chapter 6 at physical model scale, are simulated at prototype scale. The aim of the prototype scale simulations is to determine differences in the predictions at the two scales and thus identify scale effects. In order to quantify the influence of scale effects on the different flow aspects, prototype scale simulations are undertaken using the same modelling domains and implementations as in the previous chapter. The variations observed at the two scales are investigated and compared with existing studies in the literature. Furthermore, the same numerical implementations tested at model scale are applied at prototype scale to verify whether changes in scale would introduce variations in the model sensitivity of the various implementations.

The structure of this chapter is very similar to that of Chapter 6 with the difference that the sections describing the modelling domains, boundary and initial conditions, flow equations, numerical implementations and model assumptions are omitted since they are equivalent to those in Chapter 6. The only difference between the numerical implementations in this chapter and in the previous one is that the flow rates and the size of the domains have been scaled up to prototype scale. Prototype scale simulation results are presented in conjunction with the model scale predictions in order to observe changes occurring in the different processes at prototype scale.

In the first part of this chapter, sensitivity analyses in respect of mesh cell size, turbulence model and interface capturing schemes are conducted for the prototype scale simulations. Subsequently, the same four flow rates simulated on the spillway channel at model scale are simulated at prototype scale and predictions at the two scales are compared. In the following subsection, the prototype labyrinth weir rating curve is calculated at prototype scale and compared with the scaled curve. Finally, PMF simulations of the comprehensive modelling domain for two different levels of tail water (low and high) are undertaken at prototype scale and predictions at the two scales are compared. The discrepancies found in the different flow aspects at the two scales are investigated and discussed and conclusions on the outcomes are drawn.

7.2. Assumptions and Limitations

The numerical modelling of the prototype structure is undertaken in equivalent conditions as the numerical modelling of the physical model. Identical numerical implementations are chosen in order to be able to conduct an appropriate comparison between the simulations at the two scales. This assumption is made because the objective is to compare simulations at the two scales. This assumption could lead to certain inaccuracies, since some conditions are expected to slightly change in the real scale scheme compared to the physical model. However, these are considered to present minor influence and thus were not considered in the physical model experiment.

One of the main aspects identified is the increased roughness of the concrete spillway walls compared to that at the base of the spillway and of the labyrinth weir. The labyrinth weir and spillway base were constructed with smooth concrete while the walls had a textured surface

added to the concrete. However, being only on the spillway walls, the effects of the additional spillway roughness are considered to be negligible. The zero velocity condition applied at the walls is judged to be a good approximation to the real boundary condition, since any surface roughness will be negligible compared to the width of the channel and water depth considered.

In addition, in the modelling of the comprehensive domain, the physical model representation of the surrounding terrain consisted of a smooth surface, not taking into consideration the roughness of the grass. Consequently, the behaviour of the tail water in the real scheme is expected to present small differences compared to that observed in the physical model and numerical simulations at both scales.

A further aspect consists in the differences in the topography in the real scheme and that in the physical model. As previously specified, in the numerical simulations, the topography of the surrounding terrain resembles the prototype scheme as is built. This is because the modelling domain was created using CAD and terrain models from the site. The impact from this variation has already been observed in the previous chapter, section 6.13.2.

Moreover, the air entrainment is expected to be of significantly higher amount in the real scale prototype than that observed in the physical model. It has not been possible to validate the numerical models against air entrainment modelling at physical model scale since no specific model has been applied for it. Therefore, it is expected that the numerical predictions underestimate the amount of air entrainment occurring at the prototype structure.

Other aspects which are expected to have certain impact on the prototype structure consist in the wind and ice effects, for which there is no control over. Additional processes such as sediment transport may also occur in the prototype and generate some effects on the prototype flow compared to that in the physical model. In particular, the accumulation of driftwood in the labyrinth weir is also anticipated. Driftwood is typically transported during flood events and is a process which is especially associated with PKW and labyrinth weirs compared to in linear weirs due to the lower heads over crest for a given discharge (Pfister *et al.* 2013b). Such processes would require additional modelling in order to be appropriately investigated. In the current study, the impact of these is considered to be minimal and therefore, these are not examined.

7.3. Sensitivity to Numerical Implementations

In this section the various numerical implementations tested at physical model scale are applied at prototype scale. These are the mesh cell size, the turbulence model and the interface capturing scheme. The aim of this study is to verify whether the sensitivity of such implementations presents changes with varying scale. Once these are examined, Section 7.4 will deal with the comparison of the flows in the spillway channel at the two scales.

7.3.1. Mesh Cell Size

The mesh convergence study based on the *GCI* index as described in Section 6.9.1 was conducted at prototype scale employing the same three meshes for the two solvers. The key variables chosen for the study at this scale f_1, f_2 and f_3 extracted from meshes 1, 2 and 3

respectively are the same as those at model scale, i.e. velocities and depths at sections A, B, C, D and E extracted from a 40 m³/s flow rate simulation. Results show that for this case, the velocities, depths and wave features predicted by OpenFOAM using the meshes of finest and intermediate resolution are very comparable and, in some instances, these were almost equivalent. In Fluent the situation was similar, the predictions from the finest and intermediate resolution exhibited very close results. The differences between the predictions from the mesh of finest and intermediate resolution exhibited values of similar order or slightly higher than in OpenFOAM. Therefore the *GCI* indices and errors calculated were those for the intermediate meshes (Mesh2), since they were the ones implemented in the two solvers. The analysis results from OpenFOAM and Fluent are presented on Table 7.1 and Table 7.2.

Table 7.1: Parameters for the calculation of discretisation error in OpenFOAM, prototype Simulations

	Depth Section A	Velocity Section A	Depth Section C	Velocity Section C	Depth Section E	Velocity Section E
r_{21}	2	2	2	2	2	2
r_{32}	2.5	2.5	2.5	2.5	2.5	2.5
f_1	0.32 m	3.70 m/s	0.32 m	5.47 m/s	0.19 m	9.02 m/s
f_2	0.31 m	3.72 m/s	0.31 m	5.49 m/s	0.2 m	8.87 m/s
f_3	0.27 m	4.05 m/s	0.30 m	5.62 m/s	0.2 m	8.28 m/s
p	1.94	2.71	1.17	3.77	1.22	3.05
f_{ext}	0.32 m	3.69 m/s	0.32 m	5.49 m/s	0.19 m	8.91 m/s
ϵ_{32}	12.42 %	8.66 %	3.41 %	2.40 %	3.28 %	6.68 %
ϵ_{ext}	2.48 %	0.79 %	1.75 %	0.08 %	1.62 %	0.43 %
GCI_{32}	3.17 %	0.98 %	2.23 %	0.1 %	2.0 %	0.54 %

Table 7.2: Parameters for the calculation of discretisation error in Fluent, prototype Simulations

	Depth Section A	Velocity Section A	Depth Section C	Velocity Section C	Depth Section E	Velocity Section E
r_{21}	2	2	2	2	2	2
r_{32}	2.5	2.5	2.5	2.5	2.5	2.5
f_1	0.35 m	3.38 m/s	0.35 m	5.76 m/s	0.19 m	10.35 m/s
f_2	0.36 m	3.54 m/s	0.34 m	5.81 m/s	0.19 m	10.3 m/s
f_3	0.42 m	3.11 m/s	0.30 m	5.95 m/s	0.23 m	9.7 m/s
p	1.04	1.15	1.77	2.38	5.59	5.37
f_{ext}	0.33 m	3.77 m/s	0.34 m	5.79 m/s	0.19 m	10.30 m/s
ϵ_{32}	15.93 %	12.16 %	10.03 %	2.38 %	20.1 %	5.83 %
ϵ_{ext}	11.16 %	6.13 %	2.42 %	0.30 %	0.12 %	0.04 %
GCI_{32}	12.55 %	8.16 %	3.10 %	0.38 %	0.15 %	0.05 %

The largest discrepancies between predictions with the meshes of different resolution were found at section A, with GCI_{32} depth indices of 3.17 % in OpenFOAM and 12.55 % in Fluent. At all other sections, both the errors and the *GCI* indices for the mesh of intermediate resolution were satisfactorily low. As previously specified in Section 6.9.1, values within the range of 10 % are considered to be acceptable. At this scale the velocities are found to be less sensitive to mesh size than depths. At model scale, sensitivity of depth and velocity varied and there was no observed trend.

In summary, the GCI_{32} values calculated based on the mesh of intermediate resolution with the two solvers present satisfactorily low values, typically in the range of 10 % or lower with velocity indices generally showing lower values than those of depth. Therefore, the mesh of intermediate resolution will be implemented in the two solvers to conduct simulations at prototype scale. In Fluent, these results are generally similar to those observed with the physical model scale

simulations. However, in OpenFOAM, the results at physical model scale presented greater sensitivity to cell size, requiring the implementation of the finest mesh.

7.3.2. Turbulence Model

As previously noted, the simulations undertaken in Chapter 4.4.2 and in Chapter 6 were computed using the Standard $k - \epsilon$ turbulence model. In Chapter 4, the dam break case simulated presented generally equivalent results with the implementation of the Standard $k - \epsilon$ and the SST $k - \omega$ (see section 4.4.2.4.1). In Chapter 6 the modelling of the experimental flow over the physical model labyrinth weir and spillway demonstrated very comparable predictions when using the Standard and the RNG $k - \epsilon$ models. However, the SST $k - \omega$ model appeared to provide less accurate predictions (see section 6.6.1). In order to investigate the sensitivity to the turbulence model at prototype scale, 119.6 m³/s flow rate simulations were undertaken with the Standard, RNG $k - \epsilon$ and the SST $k - \omega$ RANS models in OpenFOAM. Figure 7.1 shows the free surface waves and velocity contours generated using the three different turbulence models once the model reached steady state. The cross-wave crests in the plan view appear to be more uniform and straight on the Standard $k - \epsilon$ simulation and the crests of the waves are wider compared to the results computed with the other two turbulence models. Simulations conducted using the RNG $k - \epsilon$ and SST $k - \omega$ present a comparable pattern of cross-waves to the Standard $k - \epsilon$. However, the wave's crests profiles predicted in the RNG $k - \epsilon$ and SST $k - \omega$ models are slightly more irregular and curly (less straight) on the plan view. This behaviour is more pronounced in the SST $k - \omega$ case than in the $k - \epsilon$ RNG. The cross-waves' crests are more distinctly defined and they extend for longer (to the spillway second change in gradient) in the simulations using the SST $k - \omega$ and the RNG $k - \epsilon$ than in the Standard $k - \epsilon$. The dominant wave generated by the impact of a cross-wave from the first upstream crest to the left spillway wall and from there downstream, is present in all simulations but less distinct in the SST $k - \omega$ case. However, from the reflection point downstream, the reflective wave is well defined by this model. Velocity values are very comparable in all simulations, with generally the highest values appearing in the RNG $k - \epsilon$ case but with only minor variations.

These numerical predictions are contrasting compared to those at physical model scale, where the SST $k - \omega$ model results exhibited a less defined pattern of cross-waves and lower velocities to those predicted by the $k - \epsilon$ family models (see Section 6.9.3).

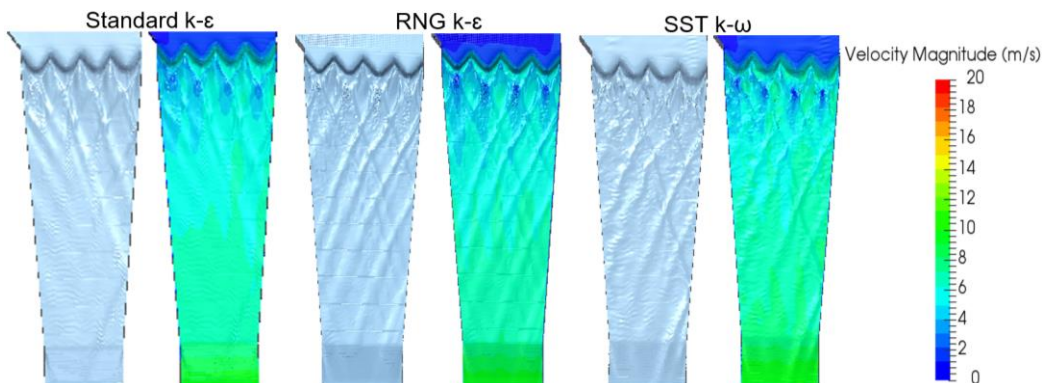


Figure 7.1: Free surface structures and velocity contours computed with the three turbulence models

In order to identify any substantial differences elsewhere in the channel, cross sections of the flow, interface depth and velocity profiles were extracted from the simulations using the three models. Cross-sectional contours of water volume fraction and velocity magnitude were also examined. The graphs corresponding to section A are shown on Figure 7.2. This section is located in the area where the waves originated from the different labyrinth weir crests cross for the first time. As indicated on Figure 7.2 a) and c) in the Standard $k - \varepsilon$ case, section A is located at the crossing point of most of the cross-waves immediately downstream the weir. As such, the Standard $k - \varepsilon$ profile shows four main wave sets with the first of them revealing that the cross-waves have just crossed upstream with two cross-waves crests travelling downstream in different directions. The RNG $k - \varepsilon$ case presents a similar profile to that of the Standard $k - \varepsilon$ with the second cross-wave set also having crossed upstream of the section, showing two small crests. The other two sets of waves appear to be just about to separate. In the SST $k - \omega$ case the section is located just downstream of the crossing points of most waves, so the interface depth graphs and water volume fraction contours show the four pairs of waves (since the cross-waves have just separated to move downstream in opposite directions). This is an interesting observation since in the scaled case (Section 6.9.3) all models predicted the waves' crossing point at the same coordinate, while in this case the SST $k - \omega$ model predicts the waves crossing points to be upstream of those predicted by the $k - \varepsilon$ family models. The volume fraction contours show there is presence of air pockets predicted in all simulations and especially in that using the RNG $k - \varepsilon$ model. The free surface depth predicted with the two $k - \varepsilon$ models at plane A is comparable, with the crests reaching up to 1.1 to 1.2 m. The interface depth predicted with the SST $k - \omega$ model is slightly lower with the maximum value of the crests being 0.7 m. The free surface shape is overall more uniform and smooth in the predictions from the Standard $k - \varepsilon$ than in the two other models which show a curlier profile at the waves' surface. Figure 7.2 b) indicates the velocity profiles of all cases are comparable with lowest values at the crests of the waves of around 3 m/s and highest values at the dips of approximately 6 m/s. The fact that the three velocity profiles are overall within the same range is a marked difference between the predictions from the three turbulence models at prototype scale and those at physical model scale.

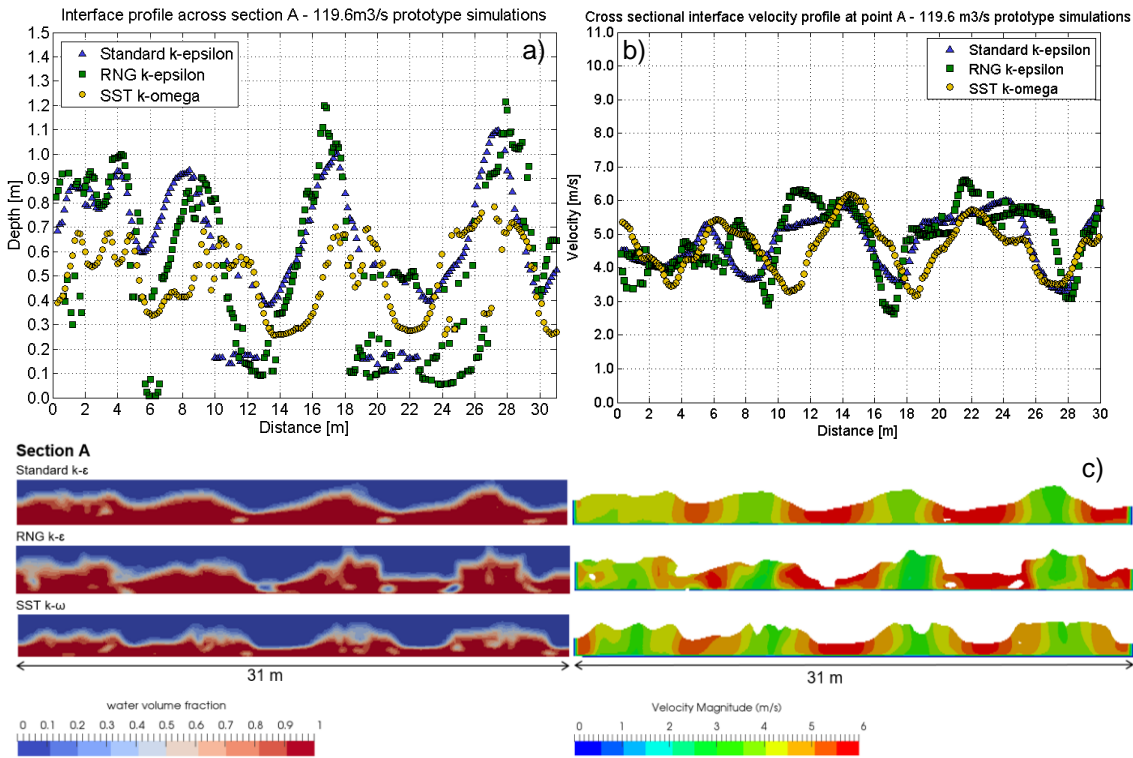


Figure 7.2: Cross-sectional profiles using the three turbulence models: a) Interface depth and b) interface velocity through point A; c) Water volume fraction contours and flow areas coloured by velocity at sections through point A

Figure 7.3 shows the interface depth and velocity profiles through point B. At this location the single cross-waves are traveling downstream after having crossed with the neighbouring ones and they are approaching the spillway walls. After impacting the walls, approximately one metre downstream of section B, they create reflection waves. The interface depth graph indicates the Standard $k - \epsilon$ presents the highest values of depth in all points in the section. The SST $k - \omega$ model shows high values of wave crests of up to 0.8 m and the RNG $k - \epsilon$ shows the lowest values for the dips between waves. Velocity profiles show overall consistency in the predictions of all simulations, with the highest values occurring in the RNG $k - \epsilon$ simulations which in some instances are over 6 m/s.

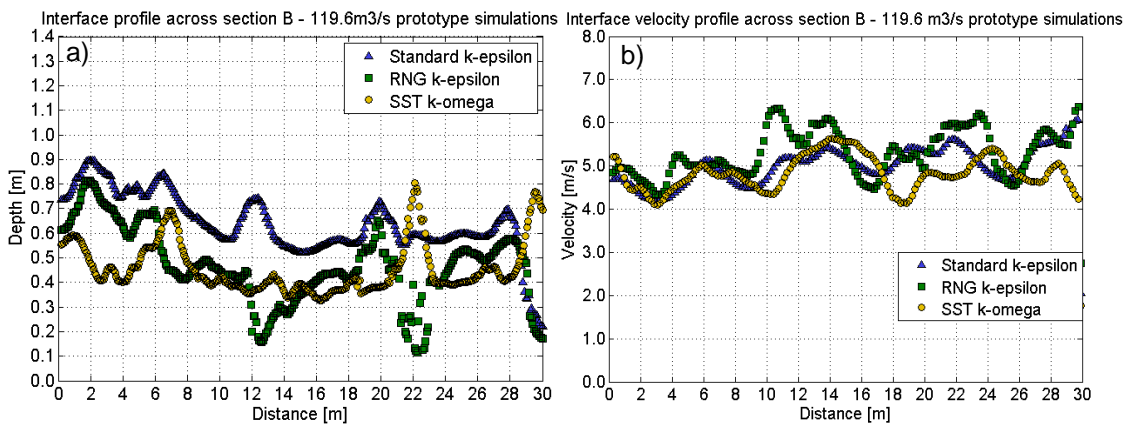


Figure 7.3: Cross-sectional profiles using the three turbulence models: a) Interface depth and b) interface velocity through point B

Figure 7.4 a) and b) illustrate the cross sectional plots of interface depth and velocity through point C which is located just before the first spillway change in gradient. Figure 7.4 e) shows the flow area coloured by velocity magnitude at this section. Interface depth and velocity profiles at

this plane present less variation than in the previous locations since at this point most of the cross-waves have flattened. The $k - \epsilon$ models show the shape of the predominant wave which travels from the left wall to the right wall of the spillway, previously observed in Figure 7.1.

This wave is more pronounced in the RNG $k - \epsilon$ model than in the Standard $k - \epsilon$, which also predicts a smaller second crest next to the dominant one. The free surface depth predicted by the SST $k - \omega$ model is from 0.1 to 0.3 m lower than that predicted by the $k - \epsilon$ models. The velocity predictions using the RNG $k - \epsilon$ model exhibit the highest values ranging from 7 to 7.5 m/s with small variations. The SST $k - \omega$ shows slightly lower velocities with maximum values occurring at the centre of the channel with mean velocity of approximately 7 m/s. The $k - \epsilon$ family models show little velocity variation across the section.

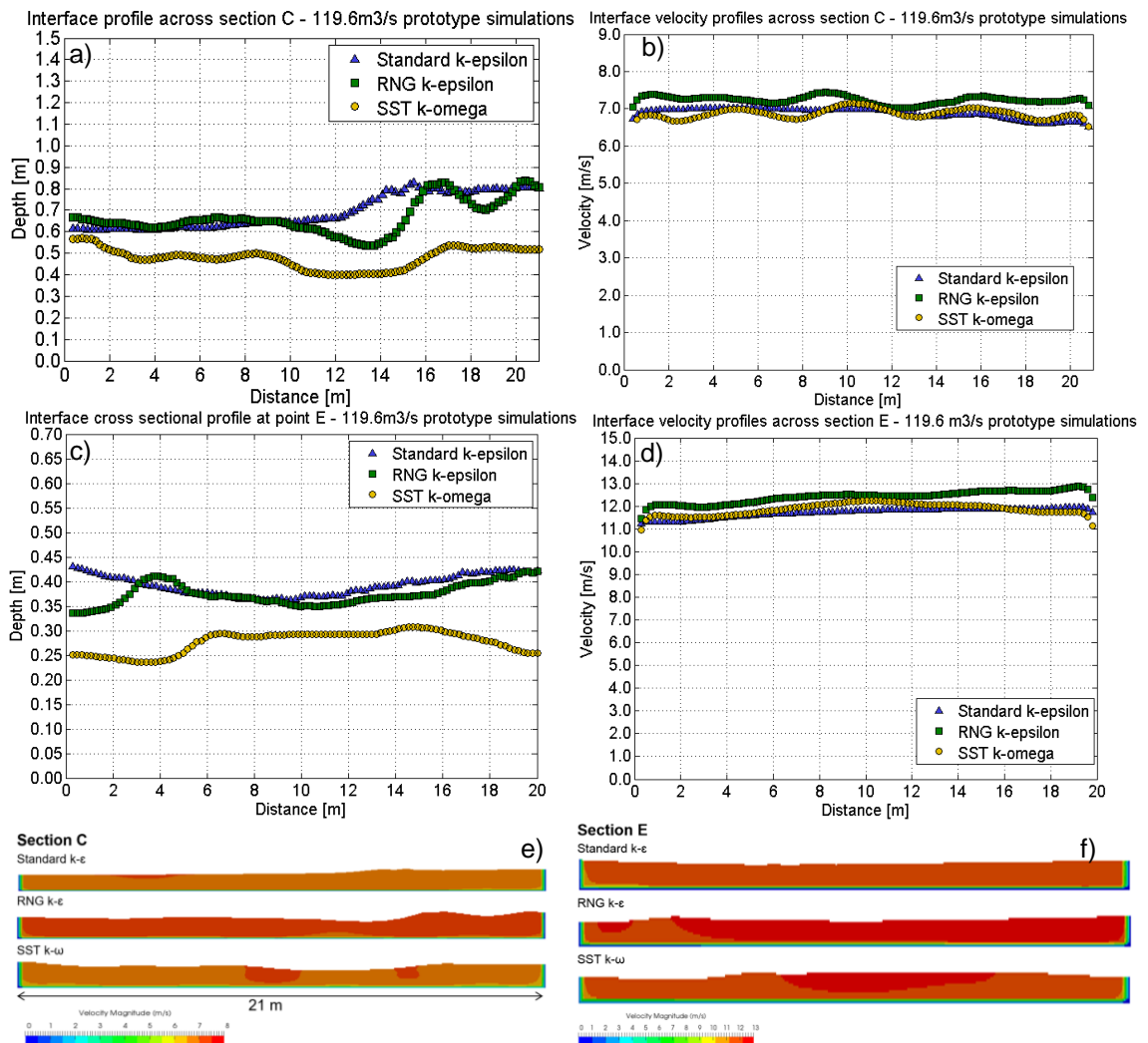


Figure 7.4: Cross-sectional profiles using the three turbulence models: a) Interface depth through point C; b) Interface velocity through point C; c) Interface depth through point E; d) Interface velocity through point E; e) Flow areas coloured by velocity at sections through point C and f): through point E

Figure 7.4 c) and d) show the interface depth and velocity profiles through point E, which is located at the end of the spillway channel. Figure 7.4 f) shows the flow area coloured by velocity magnitude contours. At this location, the $k - \epsilon$ models show a similar wave profile and depth. The SST $k - \omega$ model shows the shape of a wave located towards the centre of the channel, and the overall depths are from 0.05 m to 0.15 m lower than those predicted by the $k - \epsilon$ models. The

Chapter 7. Comparison of Prototype and Physical Model Predictions

velocity profiles are very comparable in all cases, the RNG $k - \epsilon$ model presents the highest values.

Similarly to the scaled case, cross-sectional profiles of depths and velocities at the free surface were averaged along each section and a representative value of mean velocity and depth was obtained. Table 7.3 presents the section-averaged values of depths and velocities, along with the percentage difference in depth and velocity in the RNG $k - \epsilon$ model and SST $k - \omega$ model in respect of the Standard $k - \epsilon$.

Table 7.3: Section-averaged values of depths and velocities and percentage difference of model predictions from the RNG $k - \epsilon$ and SST $k - \omega$ models with respect to the Standard $k - \epsilon$ in prototype scale simulations

Section	Standard $k - \epsilon$		RNG $k - \epsilon$		SST $k - \omega$		%Diff. Standard vs RNG $k - \epsilon$		%Diff. Standard $k - \epsilon$ vs SST $k - \omega$	
	Depth [m]	Vel. [m/s]	Depth [m]	Vel. [m/s]	Depth [m]	Vel. [m/s]	Depth [%]	Vel. [%]	Depth [%]	Vel. [%]
A	0.61	4.77	0.55	4.85	0.49	4.57	-10.81	1.63	-20.49	-4.28
B	0.64	4.97	0.47	5.26	0.46	4.79	-26.85	5.93	-28.83	-3.58
C	0.69	6.75	0.67	7.10	0.48	6.71	-3.87	5.22	-30.68	-0.59
D	0.50	9.12	0.48	9.46	0.35	9.22	-3.17	3.73	-30.50	1.00
E	0.39	11.54	0.37	12.22	0.28	11.69	-4.83	5.87	-29.46	1.28

Results on Table 7.3 indicate that as observed in the cross-sections plots, simulations using the three turbulence models exhibit a different trend to that presented at the physical model scale. Compared to the Standard $k - \epsilon$ model, the RNG $k - \epsilon$ exhibits consistently lower depths and higher velocities in all sections. Such differences are generally low, from 1 to 10 %, with a maximum of 26% decrease in depth at section B. Therefore, the two models present acceptably close predictions. These results are interesting from the point of view that in simulations at physical model scale the RNG $k - \epsilon$ presented higher depths and lower velocities than the Standard $k - \epsilon$ model. In addition, the SST $k - \omega$ model predicts very comparable velocities to the Standard $k - \epsilon$ model, at some sections being only 1% higher or between 0.6 and 4 % lower. The depth predictions with the SST $k - \omega$ model are from 20 to 30% lower than in the Standard $k - \epsilon$. This also reveals a different trend to that observed at model scale, where the predictions from the SST $k - \omega$ model provided significantly lower depths and velocities than those predicted by the $k - \epsilon$ family (ranging from 40 % to 20 % lower).

In summary, predictions using the three turbulence models present greater agreement at prototype scale than they did at physical model scale. The two models from the $k - \epsilon$ family exhibit results within 10 % difference, which is generally in line with results from these models at physical model scale. Contrastingly, the simulation using the SST $k - \omega$ model presents closer results to those predicted with the $k - \epsilon$ family models than it did at physical model scale, with velocities being within 4% difference. However, this model still appears to predict in average 28% lower depths than in those predicted with the $k - \epsilon$ family models.

7.3.3. Interface Capturing Scheme

Similarly to the sensitivity analysis completed at physical model scale in Section 6.9.4, the CICSAM scheme for interface capturing was employed to model the 119.6 m³/s prototype flow in Fluent. The simulation predictions using the PLIC and the CICSAM schemes were plotted on the same graph for comparison. Free surface profiles through sections A and B are shown on Figure 7.5 a) and those through sections C, D, and E on Figure 7.5 b). The free surface velocity profiles at sections through B, C, D and E are presented on Figure 7.5 c). Figure 7.5 a) shows that at section A the simulations using the two interface capturing schemes produce virtually equivalent predictions. The dips and crests of the waves are shown to be occurring at the same locations and they also present very comparable heights. At section through point B the two schemes also present very comparable profiles with consistent depths. Figure 7.5 b) confirms that the free surface profiles through sections C, D and E predicted with the two schemes are practically equivalent Figure 7.5 c) shows that the velocity profiles at the different sections predicted using the two schemes demonstrate consistent values. Velocity values present the greatest difference at section E where the CICSAM predictions show velocities approximately of 13 m/s in the entire section and the PLIC scheme shows a decrease of around 1 m/s in the areas from the centre of the channel to the spillway walls.

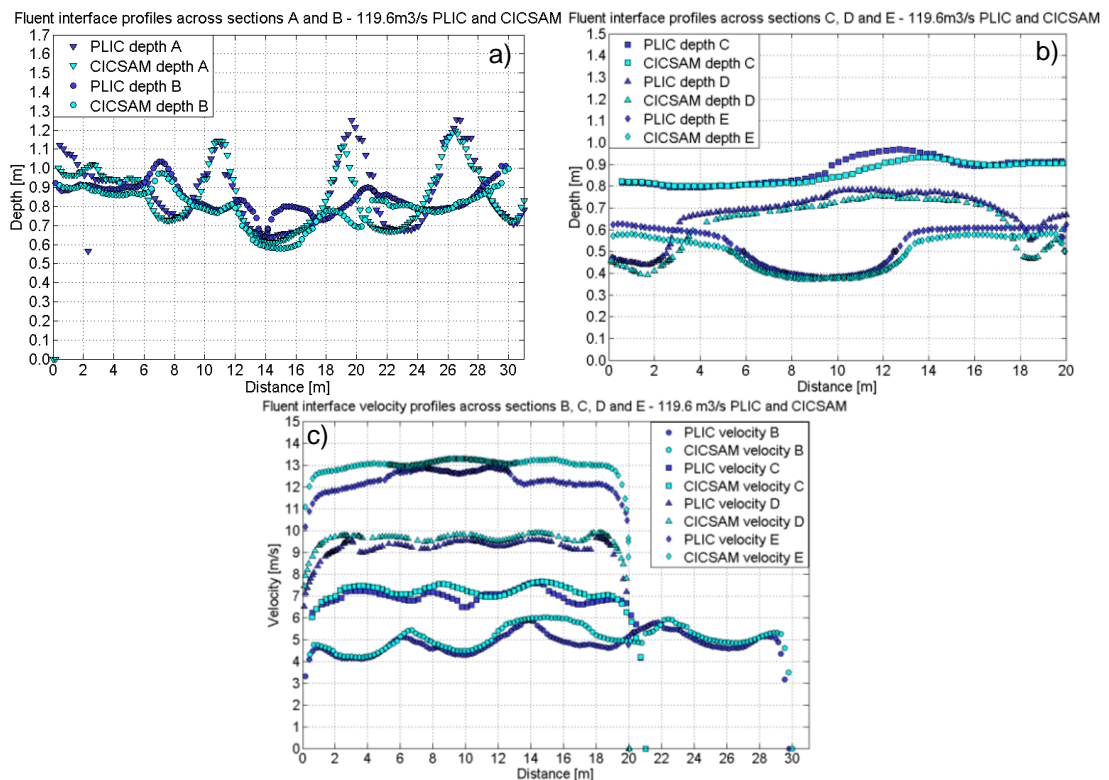


Figure 7.5: Cross-sectional profiles computed with Fluent simulations using the PLIC and the CICSAM schemes; a) interface depth at sections through points A and B and b) through C, D and E; c) interface velocity profiles at sections through points B to E

The predictions from the PLIC and CICSAM schemes therefore appear to be effectively very similar, with free surface profiles being almost equal and with minor variations in the velocity predictions, (of less than 1 m/s) at the end of the spillway channel. Therefore the implementation of any of the two schemes would provide very similar results at this scale. These results contrast

with those obtained at physical model scale, in Section 6.9.4, where the simulations using the PLIC scheme provided a superior characterisation of the waves' features compared to those using the CICSAM scheme.

In summary, results show that similarly to the sensitivity in respect of cell size and turbulence model, the model sensitivity to the interface capturing scheme also depends on the scale of the flow situation, being lower at prototype scale.

7.3.4. Discussion

The sensitivity analyses conducted at prototype scale indicate that the numerical model sensitivity to the tested numerical aspects can present variations depending on the scale of the process modelled.

In Fluent, the cell size sensitivity analysis shows that at the two scales the mesh of intermediate resolution provides very comparable results to those predicted with the mesh of highest resolution. This occurs at the model and prototype scales, where the GCI of the mesh of intermediate resolution is sufficiently low at both scales. In OpenFOAM the situation is different. In the scaled case, OpenFOAM showed to be more mesh dependent than Fluent, which as noted in the discussion section 6.9.5, this has also been highlighted in other studies. However, at prototype scale, the predictions of the mesh of intermediate resolution appear to be very close to those predicted with the mesh of highest resolution. The GCI indices at prototype scale obtained with the mesh of intermediate resolution present values of similar order and lower than those predicted with the mesh of finest resolution at model scale. These results are positive from the perspective that they indicate that a process occurring at real hydraulic structure scale, both solvers would be able to reproduce the flow situation with an equivalent cell size.

The turbulence model sensitivity analysis at prototype scale reveals the scale of the flow situation modelled affects the suitability of the turbulence model applied. At model scale, the predictions from the SST $k - \omega$ model presented significant discrepancies to those predicted with the $k - \varepsilon$ family. The SST $k - \omega$ model appeared to underestimate depths by approximately 40 % and velocities by 20 %. In addition, this model was not able to reproduce the complex configuration of cross-waves generated by the labyrinth weir appropriately. In contrast, at prototype scale the SST $k - \omega$ model presents comparable depths to those predicted by the RNG $k - \varepsilon$ model and are in average 27 % lower than those from the Standard $k - \varepsilon$ model. In addition, at prototype scale the velocities predicted by the SST $k - \omega$ model are in line with those predicted by the two $k - \varepsilon$ family models. The most substantial change observed at prototype scale is that the cross-waves generated by the labyrinth weir are well reproduced by the SST $k - \omega$ model. The predicted cross-waves present good agreement with those reproduced by the two $k - \varepsilon$ models which were validated at model scale, and therefore they are believed to be correctly reproducing the prototype flow situation. This is particularly relevant considering that the SST $k - \omega$ model was not capable of reproducing the flow structures correctly at model scale (and especially when the mesh with finest resolution was utilised in the scaled simulations). The observed changes in the numerical predictions when implementing the SST $k - \omega$ model are distinctive but not completely

unexpected considering the dramatic change in turbulence levels of the two processes modelled (at model and at prototype scale). Because the Reynolds numbers are approximately 125 times larger in the prototype than in the model, regarding turbulence, the flow situations modelled at the two scales constitute remarkably different processes. This could explain the fact that the turbulence models predictions are dissimilar for the flow situation at model scale and then converge at prototype scale, since some turbulence models are more appropriate to be applied for certain ranges of Reynolds numbers.

The results from the two $k - \varepsilon$ family models also present certain changes at prototype scale compared to the trend they exhibited at model scale, however such variations are minor. At model scale the RNG $k - \varepsilon$ model presented a consistent trend of higher depths and lower velocities in respect to the Standard $k - \varepsilon$ model. The observed differences in the predictions were minor, from 0.2 to 10%. At prototype scale, the trend observed at model scale is inverted and the RNG $k - \varepsilon$ model shows greater velocities and lower depths. Nevertheless, the discrepancies at this scale are small and approximately of the same order as in the model scale case.

The implementation of the CICSAM algorithm and comparison with the PLIC scheme shows that similarly to other numerical implementations, the sensitivity to the interface capturing scheme also decreases with the increase of scale of the flow situation. At model scale, the predictions obtained with the implementation of the CICSAM scheme demonstrated less prominent waves, and this was especially distinct in the sections located within the cross-waves configuration. Therefore, the model was found to present sensitivity to the interface capturing scheme employed. The PLIC scheme demonstrated improved predictions of the cross-waves heights and features which were in closer agreement with the experimental measurements. At prototype scale, the results employing the two different schemes demonstrate very close agreement, with only marginal discrepancies. Therefore, this study reveals that at prototype scale both schemes provide virtually equivalent predictions.

7.4. Flow in the Spillway Channel

7.4.1. Low Flow Rate: 40 m³/s

Prototype scale simulations were conducted to model the 40 m³/s flow rate over the labyrinth weir and spillway channel. Figure 7.6 a) and b) show the free surface wave structures and velocity contours for the scaled and prototype cases predicted with OpenFOAM and Fluent respectively. The wave structures present changes in the prototype compared to the scaled case. At the prototype scale, the cross-wave configuration becomes elongated and the points where the crests cross are located further downstream compared to the scaled case. In addition, the interface velocities present larger values on the prototype than on the scaled simulations. The OpenFOAM predictions show significant increases in velocity magnitude in the area immediately downstream the weir, where the cross-waves are located. The Fluent predictions show small velocity increases in the cross-wave region but significant velocity increases at the end of the spillway channel in the prototype case compared to the scaled case.

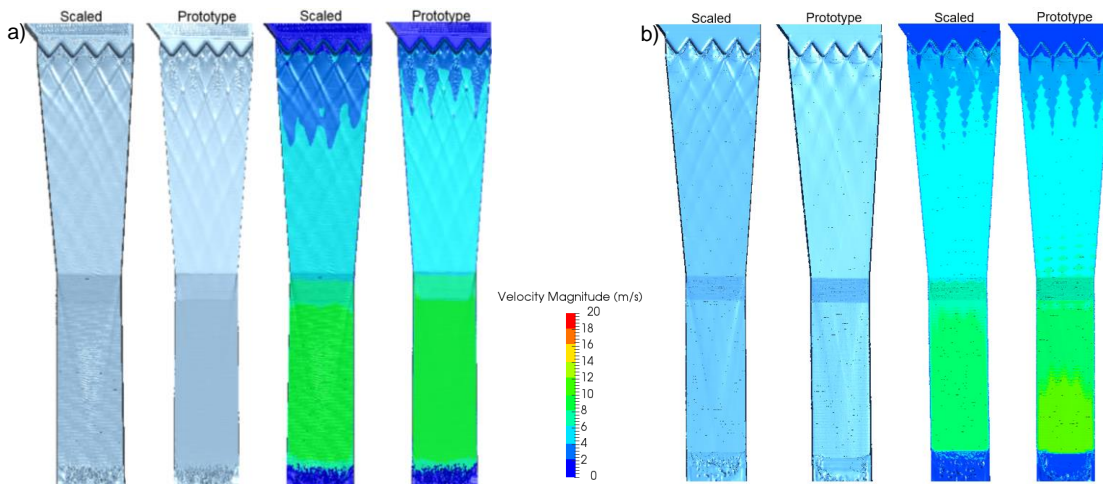


Figure 7.6: Scaled and prototype model predictions of wave structures and interface velocity contours predicted with: a) OpenFOAM and b) Fluent for a flow rate of 40 m³/s

In order to quantify the level of elongation of the cross-waves occurring at prototype scale, the distance between three waves' crossing points and the weir crest were examined. Figure 7.7 a) indicates the location of the three distances measured, namely x_1 , x_2 and x_3 . x_1 corresponds to the plan distance from the downstream apex of the labyrinth weir crests to the crossing point of the waves generated from the first and second downstream crests. The distance x_2 is that from the weir downstream apex to the point where the waves originated from the second and third downstream crests cross, and the distance x_3 is that from the downstream apex to the crossing point of the waves generated from the second and fourth downstream crests. Figure 7.7 b) c), d), e), f) and g) show the waves profiles along distances x_1 , x_2 and x_3 showing the position of the waves' crossing points at the physical model and at prototype scale predicted with the two solvers. The reference for coordinate $x = 0$ m is the outside apex of the weir downstream crests and that for $z = 0$ m is the base of the weir. Figure 7.7 b) shows that in OpenFOAM the wave profile to the first crossing point x_1 is well defined in the scaled case but the waves appear to be more broken at prototype scale. However, it is possible to locate the prototype scale wave crossing point approximately 1 m downstream of that in the scaled case which means there is approximately an elongation of 21%. Figure 7.7 c) shows that in Fluent, the first wave crossing points are less well defined than in OpenFOAM, but these can be approximately located 2 m downstream the weir in the scaled case and 2.2 m at the prototype scale. Figure 7.7 d) and f) show the wave profiles of distances x_2 and x_3 in OpenFOAM, where it is observed that the prototype waves' approximately show an elongation of 18% and 21% respectively. Figure 7.7 e) and g) show the corresponding profiles in Fluent of distances x_2 and x_3 where the wave crossing points are less distinctly defined than in OpenFOAM. The approximate elongation is of 9 % for distance x_2 and of about 5 % for x_3 .

In summary, OpenFOAM presents an elongation of approximately 20 % of all distances and Fluent shows approximately 10 % elongation of the first two distances, reducing to 5 % in the third.

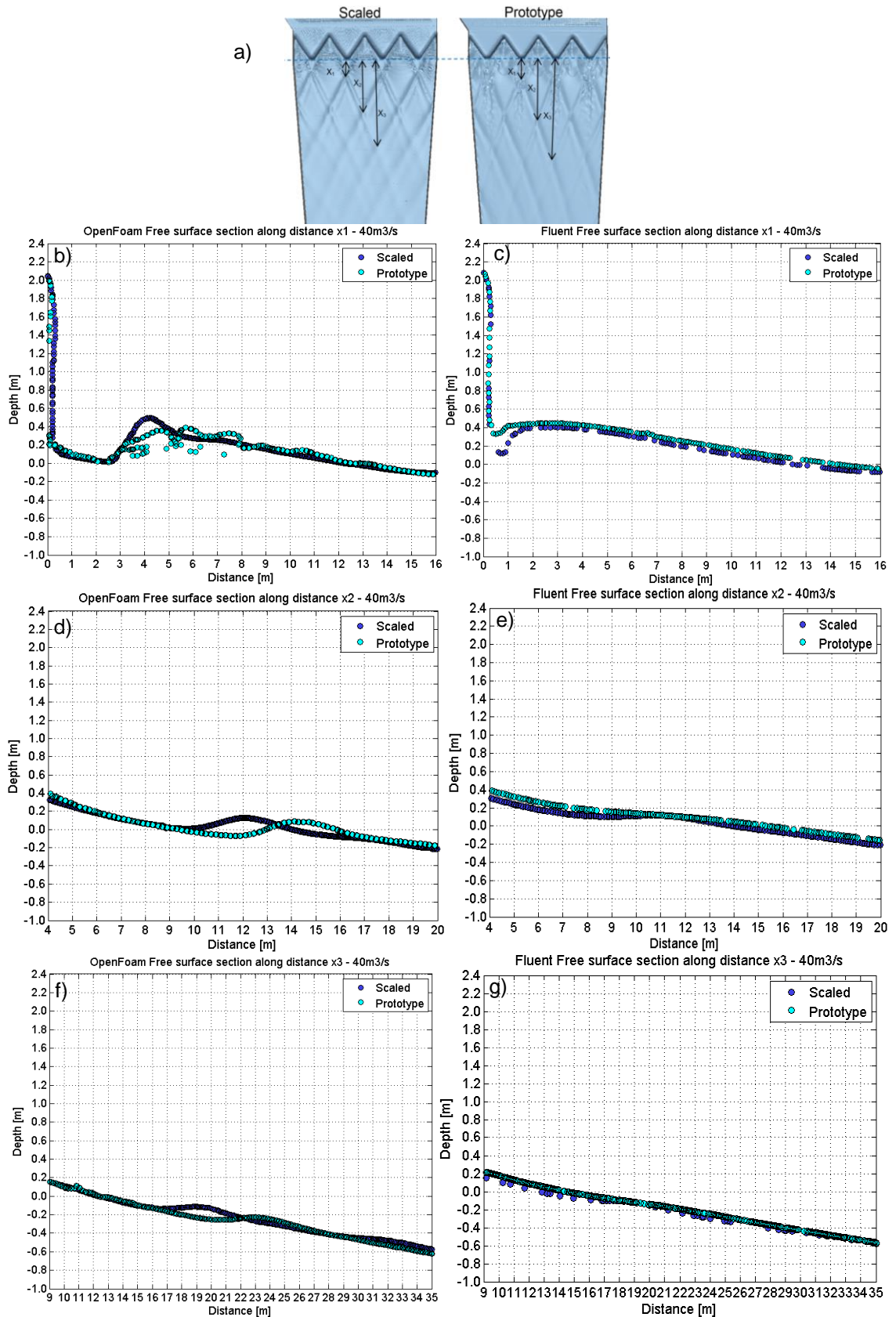


Figure 7.7: a) Scaled and prototype wave structures showing three distances to wave crossing points from the weir crest; b) Free surface profile along distance x_1 predicted with OpenFOAM and c) with Fluent; d) Free surface profile along distance x_2 predicted with OpenFOAM and e) with Fluent; f) Free surface profile along distance x_3 predicted with OpenFOAM and g) with Fluent

Figure 7.8 a) and b) show the interface cross sectional profiles of depth at sections through points A and B at the two scales predicted with OpenFOAM and Fluent respectively. In OpenFOAM

sections through point A show comparable wave features at the two scales, with the prototype depths being significantly lower. Predictions of depth at section through point B exhibit less differences between the predictions at the two scales. The Fluent results appear to show overall lower depths and less prominent flow features at the prototype scale compared to the scaled case. Figure 7.8 c) and d) show the free surface profiles at sections C, D and E, where the waves have faded, and the free surface is flatter. At these sections the difference in depth predicted at the two scales is more easily appreciable. At section D both solvers present the prototype depths to be between 0.05 m and 0.1 m lower. At section D both solvers present a central wave feature at model scale which is preserved at prototype scale but appearing slightly shallower. At section E, prototype simulations from both solvers predict the highest depth occurring at the centre of the channel with a lower depth profile compared to the model scale predictions, which present an overall flat profile of higher depth.

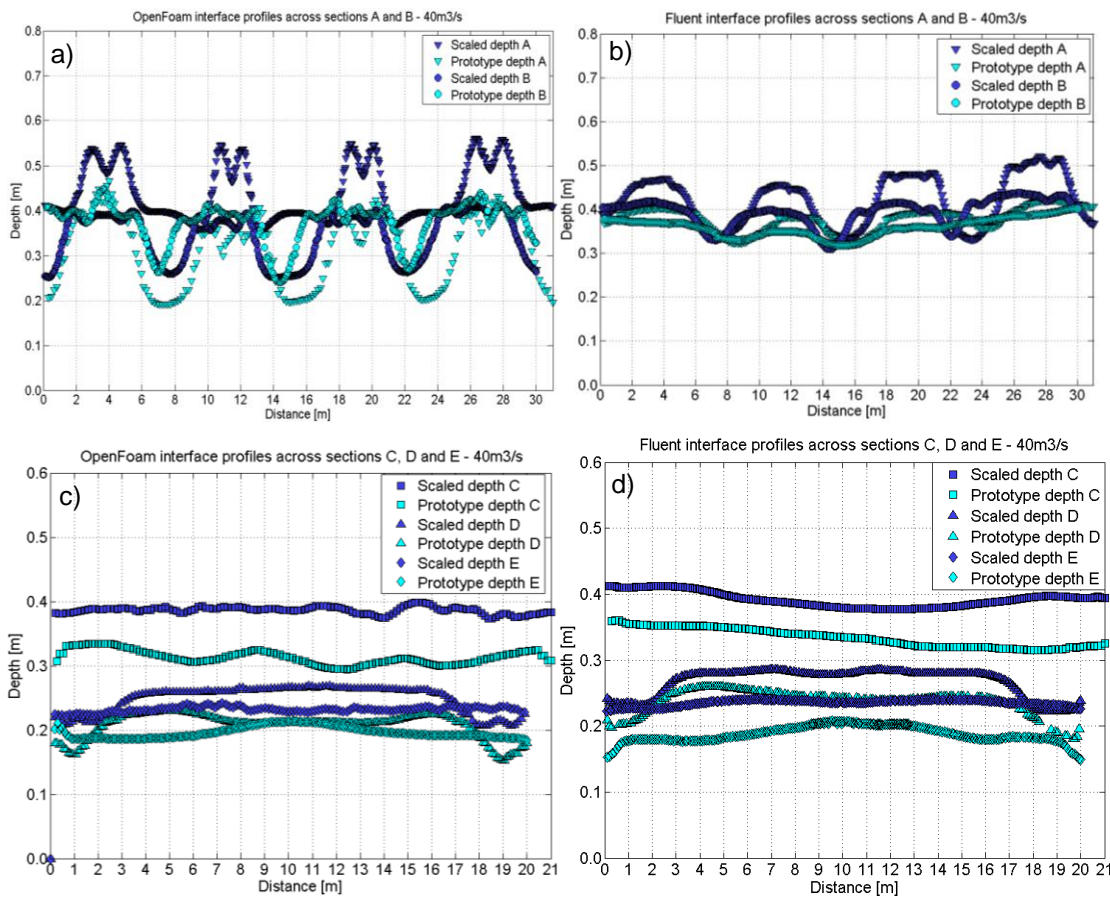


Figure 7.8: a) Interface cross-sectional profiles at sections A, B at the two scales predicted with OpenFOAM and b) with Fluent; c) Interface cross sectional profiles at sections C, D and E predicted with OpenFOAM and d) with Fluent

Interface velocity profiles at sections through experimental locations B, C, D and E are shown on Figure 7.9 a) and b) for OpenFOAM and Fluent respectively. At sections B, C, and D, the two solvers present a very consistent trend of increase in velocity at the prototype scale. At sections B and C the increase is of 0.5 to 1 m/s, while at D results at the two scales are very comparable. Results at the two scales at section E, located at the end of the channel, are different in the two solvers. The OpenFOAM sections at the two scales exhibit very similar predictions; however,

Fluent shows remarkable increases, of up to 2 m/s higher at prototype scale. This has already been highlighted at the free surface velocity contours presented on Figure 7.6.

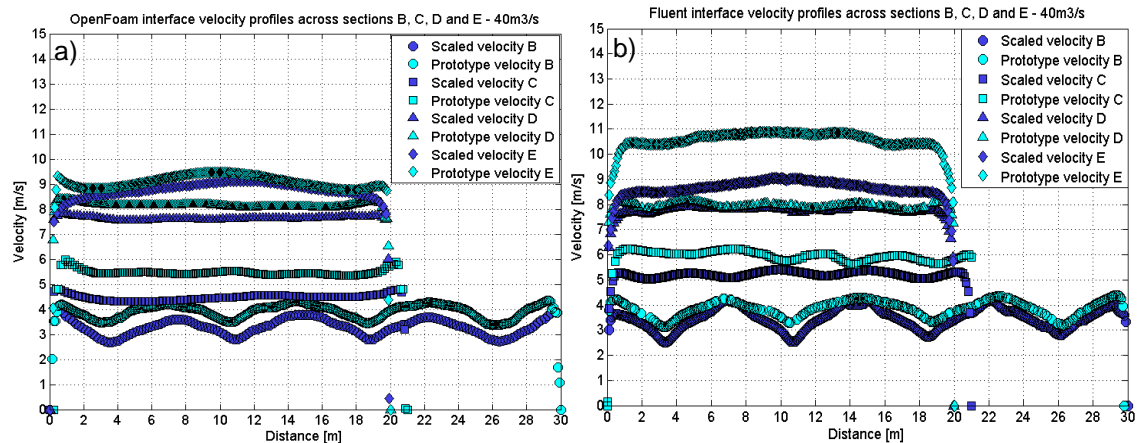


Figure 7.9: Interface cross-sectional velocity profiles at sections B, C, D and E predicted by: a) OpenFOAM and b) Fluent

In summary, in the low flow rate of $40 \text{ m}^3/\text{s}$, the average decrease in depth and increase in velocity at prototype scale observed in OpenFOAM are of approximately 18 % and 14 % respectively. These in Fluent are of 14 % and 12 % respectively. Therefore, changes at prototype scale are generally of similar order in the two solvers, being marginally larger in OpenFOAM.

7.4.1.1. Calculation of the Froude, Reynolds and Weber Numbers at Spillway Channel Sections

In order to further examine the observed discrepancies in depths and velocities at the two scales, the Froude, Reynolds and Weber numbers were calculated at sections through points D and E of the spillway channel, where the channel width is constant and equal to 20 m. Calculations were made by averaging the values of water depth and free surface velocity along the cross sections. It is important to take this into consideration when comparing the values of the force ratios with those obtained in other studies. Table 7.4 shows the model and prototype scale Froude numbers at sections D and E as well as the prototype-to-model Froude number ratio Fr_r .

Table 7.4: Froude numbers and prototype-to-model Froude ratios at sections E and D calculated from scaled and prototype simulations for $40 \text{ m}^3/\text{s}$

Section	OpenFOAM Scaled Fr [-]	OpenFOAM Prototype Fr [-]	OpenFOAM Fr_r [-]	Fluent Scaled Fr [-]	Fluent Prototype Fr [-]	Fluent Fr_r [-]
D	4.88	5.71	1.17	4.76	5.21	1.09
E	5.4	6.51	1.20	5.71	7.63	1.34

Results in Table 7.4 reveal that, as previously observed in the flow cross sections, there are certain differences between the flow conditions at the two scales. At section D the Froude numbers at the prototype and model present certain differences. At section E, OpenFOAM presents around the same ratio of prototype-to-model Froude number as at section D, however, Fluent presents greater discrepancies. The variations in velocity at the two scales at the end of the channel predicted by Fluent have previously been observed in the free surface coloured by velocity in Figure 7.6 as well as in the free surface velocity cross sectional profiles on Figure 7.9 b). Therefore in this area the flow conditions in the scaled model and in the prototype present considerable differences.

Chapter 7. Comparison of Prototype and Physical Model Predictions

In order to compare the turbulence levels at the two scales at the same sections, the Reynolds numbers were calculated at the two scales and are presented on Table 7.5. There is a number of Reynolds number formulations for open channel flows. The form utilised here is that with greater consensus in the literature, described in Scott and Lowe (2003) which has been presented in Section 2.2.2.4, Eq. 2.4. The prototype-to-model Reynolds number ratio was also calculated. As stated in Section 2.2.3.1, in a Froude number similarity model, the theoretical Reynolds number prototype-to-model ratio can be calculated as per Eq. 2.13. In the case of the physical scale model of study with scale factor 25, the Reynolds number ratio Re_r obtained with the Froude number similarity Law is equal to 125.

Table 7.5: Reynolds numbers and prototype-to-model Reynolds ratios at sections E and D calculated from scaled and prototype simulations for 40 m³/s

Section	OpenFOAM Scaled Re [-]	OpenFOAM Prototype Re [-]	OpenFOAM Re_r [-]	Fluent Scaled Re [-]	Fluent Prototype Re [-]	Fluent Re_r [-]
D	14759.8	1658881.6	112.4	16056.2	1847527	115.1
E	14788.5	1736395.4	117.4	15957	1929139.3	120.9

Results on Table 7.5 show that at section D the Reynolds numbers predicted by the two solvers at the two scales are of similar order, with the prototype values being from 112 to 114 times larger than those in the physical model. At section E, OpenFOAM shows similar results to those at section D. However, as anticipated, Fluent shows a larger difference between the two scales. The Reynolds number ratios are in both sections slightly lower than the theoretical although they are of similar order.

The Weber numbers at the two scales were also calculated at the same sections of the spillway channel. Similarly to the Reynolds number ratio, the prototype-to-model Weber number ratio was calculated. As per Eq. 2.14, for a scale factor of 25, the Weber number ratio according to the Froude number law of similarity is 625. Weber numbers at the two scales as well as ratios are shown on Table 7.6.

Table 7.6 Weber numbers and prototype-to-model Weber ratios at sections E and D calculated from scaled and prototype simulations for 40 m³/s

Section	OpenFOAM Scaled We [-]	OpenFOAM Prototype We [-]	OpenFOAM We_r [-]	Fluent Scaled We [-]	Fluent Prototype We [-]	Fluent We_r [-]
D	316.2	189478.9	599.3	349	206487.5	592
E	338.6	219488.5	648.2	389.1	280568.8	721

Table 7.6 shows that at the two sections both solvers present similar values of Weber number, although these are slightly larger in Fluent. The Weber number ratios predicted with the two solvers are generally close at section D but the Fluent results present higher values at section E, which are expected given the previously discussed variations in velocity at the two scales.

7.4.2. Intermediate Flow Rate: 78.9 m³/s

Prototype simulations of the 79.8 m³/s case were undertaken in OpenFOAM. A comparison of interface features and velocity contours at the two scales is shown on Figure 7.10. It is observed that at the prototype scale the free surface cross-waves become more pronounced and their length increases. Figure 7.10 indicates that at this flow rate the velocity at the free surface is also

higher in the prototype simulations. This is most distinct in the first section of the spillway channel, before the first change in gradient.

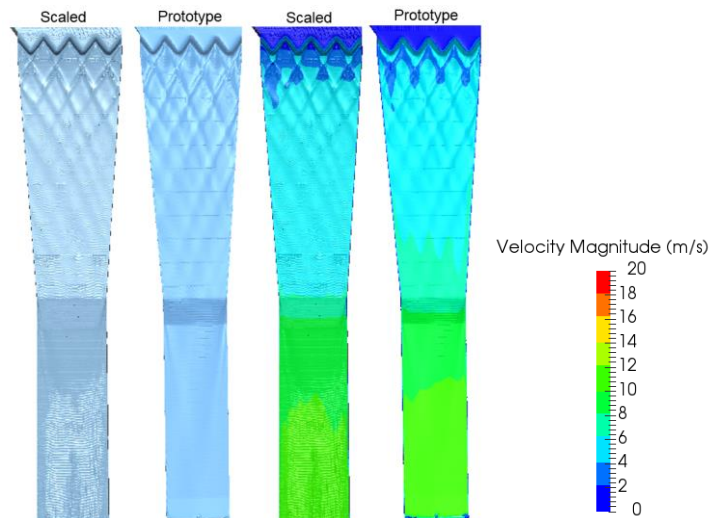


Figure 7.10: Interface velocity contours and wave structures in scaled and prototype simulations for $79.8 \text{ m}^3/\text{s}$

In this intermediate flow rate, the cross-wave configuration at prototype scale also presents elongation compared to that at physical model scale. The free surface profiles of the waves along the distances x_1 , x_2 and x_3 at the two scales are presented on Figure 7.11.

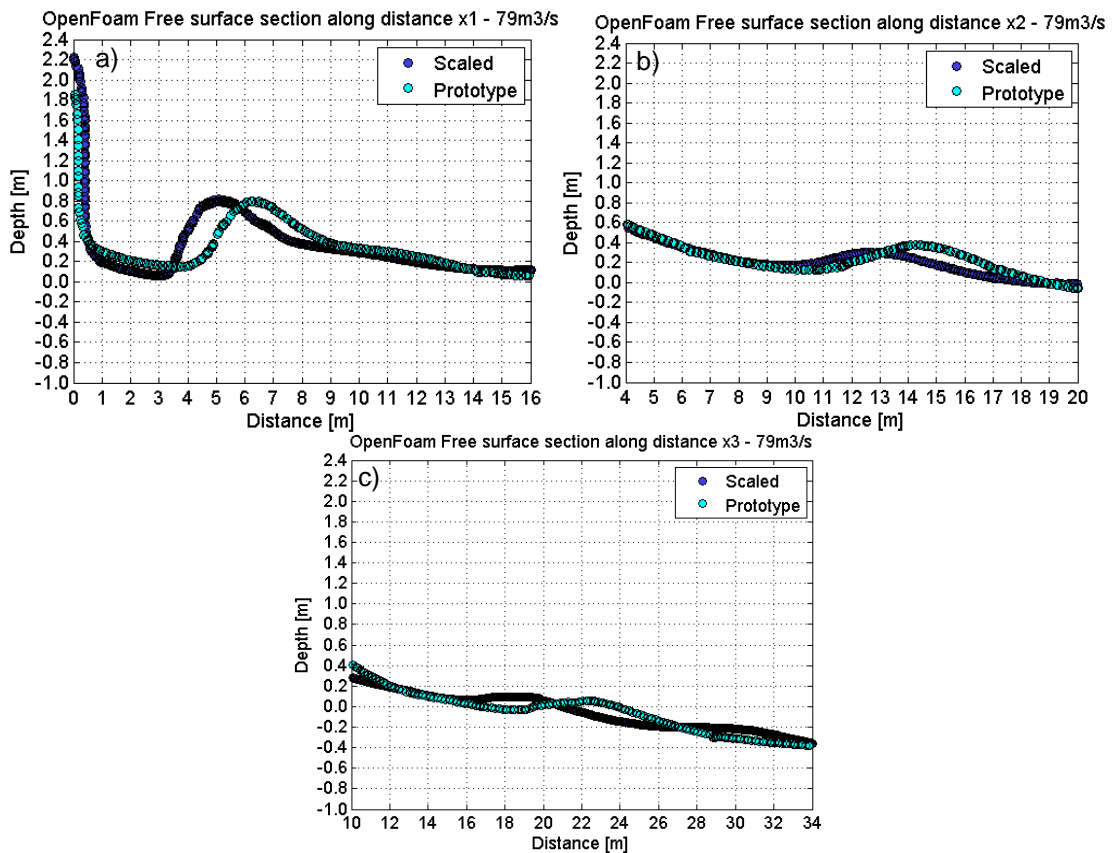


Figure 7.11: a) Free surface profile along distance x_1 ; b) Free surface profile along distance x_2 ; c) Free surface profile along distance x_3

Figure 7.11 indicates that there is certain elongation of the three distances x_1 to x_3 (identified by the misalignment of the wave peaks). This is about 1.5 m in x_1 and x_2 and approximately of 3 m

in x_3 , which represent 28%, 12% and 15% of elongation respectively in the prototype with respect to the scaled case.

Scaled and prototype time-averaged values of depth and velocity at several measurement locations were computed at the different measurement points (A-E). These are shown on Figure 7.12 a) and b) respectively. Results reveal a consistent trend with that observed in the previous flow rate, consisting in lower depths and higher velocities at prototype scale at all locations. The difference in depth varies with the location. The largest differences occur at locations A and B where there is presence of cross-waves and hence more variation in the free surface depth for a single point. Velocity magnitude values are always larger in the prototype and the difference between the scaled and prototype varies from 0.2 to 1 m/s depending on the location.

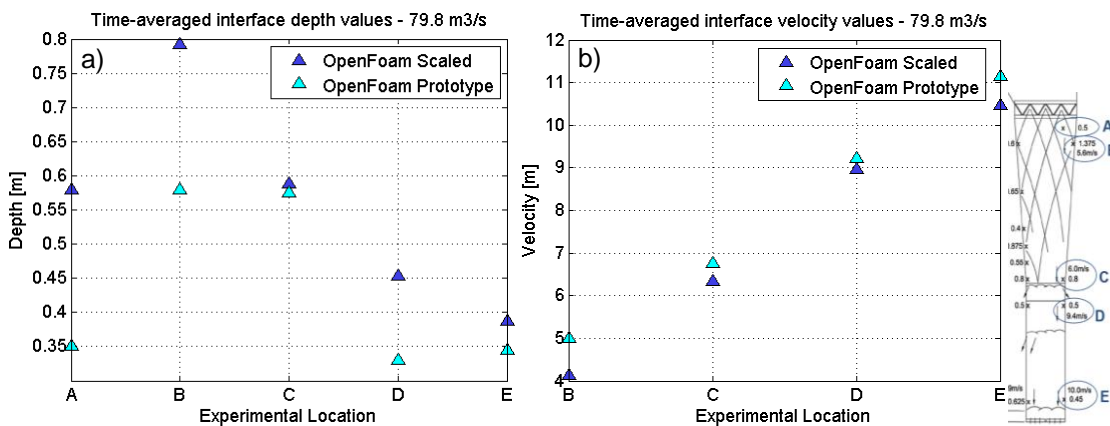


Figure 7.12: Time-averaged values of: a) interface depth and b) interface velocity magnitude at different experimental locations

Free surface cross-sectional profiles were plotted and compared at the two scales. Figure 7.13 a) shows the free surface profiles through points A and B at the two scales and Figure 7.13 b) shows those through points C, D and E. As already highlighted in Figure 7.12 a), there are considerable variations in depth along sections through point B and slightly closer agreement at the two scales in sections through point A.

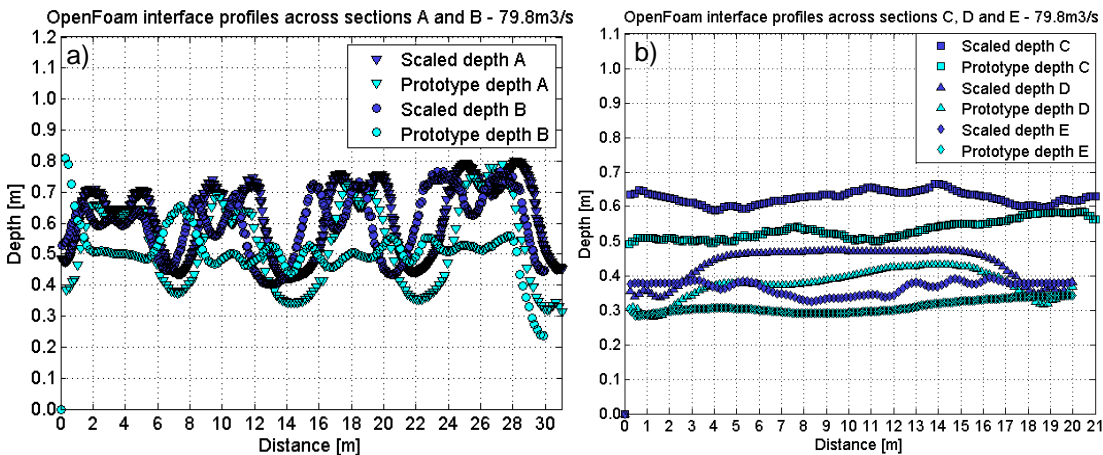


Figure 7.13: Cross sectional profiles of interface depth at sections through: a) points A, B, and b) points C, D and E.

Sections through points C and E show the prototype depth to be approximately 0.1 m lower than that in the physical scale with the free surface profile not presenting significant variations. Sections

through point D reveal that at the model scale, there is the creation of a central wave, similarly to that created at 40 m³/s. However, in this case, at prototype scale, in addition to being lower, the wave is not central but is shifted towards the left wall of the spillway.

Free surface velocities at the two scales at each section B-E are shown in Figure 7.14. It is observed that velocities at prototype scale are consistently larger than those at model scale. The largest difference occurs at section B, in the cross-waves area. At section C and E, the prototype velocities are approximately 0.5 m/s higher. At section D the profiles present very comparable velocity predictions.

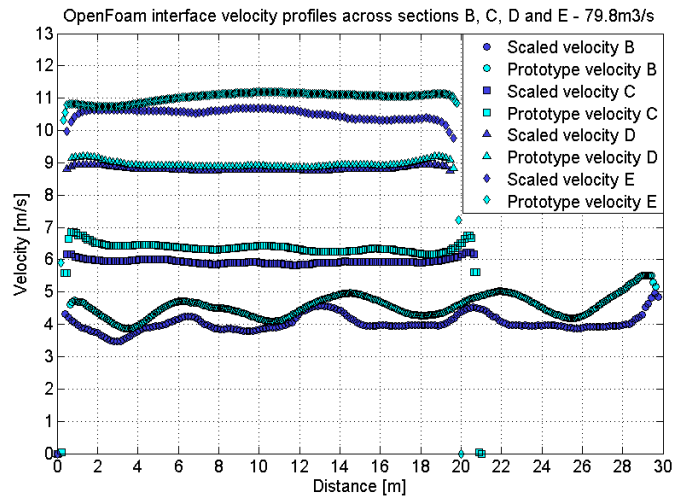


Figure 7.14: Interface cross-sectional velocity profiles at sections B, C, D and E

In summary, the average decrease in depth at prototype scale at all sections is approximately 14 % and the average increase in velocity is 7 %. Such percentage differences are reduced compared to those shown in the lowest flow rate.

7.4.2.1. Calculation of the Froude, Reynolds and Weber Numbers at Spillway Channel Sections

The Froude numbers at the two scales as well as the prototype-to-model Froude number ratios were calculated at sections through D and E. These are presented on Table 7.7. In this case simulations show closer agreement between the Froude numbers at both sections than for the 40 m³/s flow rate. The Froude number prototype-to-model ratios show values closer to 1 than those in the previous flow rate.

Table 7.7: Froude numbers and prototype-to-model Froude ratios at sections E and D calculated from scaled and prototype simulations for 79.8 m³/s

Section	Scaled Fr [-]	Prototype Fr [-]	Fr _r [-]
D	4.28	4.67	1.10
E	5.53	6.3	1.14

Reynolds and Weber numbers were calculated in the same two sections of the spillway channel. These are presented on Table 7.8 and Table 7.9 respectively. Results show that for this flow rate the prototype-to-model ratios of both Reynolds and Weber number are lower than in the previous flow rate.

Chapter 7. Comparison of Prototype and Physical Model Predictions

Table 7.8: Reynolds numbers and prototype-to-model Froude ratios at sections E and D calculated from scaled and prototype simulations 79.8 m³/s

Section	Scaled Re [-]	Prototype Re [-]	Re _r [-]
D	29328.5	3248154	110.8
E	29687.9	3293421	110.9

Table 7.9 Weber numbers and prototype-to-model Froude ratios at sections E and D calculated from scaled and prototype simulations 79.8 m³/s

Section	Scaled We [-]	Prototype We [-]	We _r [-]
D	741.14	414682.5	559.5
E	886.9	511632.3	576.9

7.4.3. High Flow Rate: 119.6 m³/s

Wave structures and free surface velocities at model and prototype scale for the 119.6 m³/s case predicted with OpenFOAM and Fluent are shown in Figure 7.15 a) and b) respectively. At this high flow rate, the OpenFOAM prototype wave structures depict more pronounced and prominent waves compared to those in the scaled case. In Fluent, the prominence of the waves appears to be similar at the two scales. The two solvers predict an elongated configuration of the wave crests positions at prototype scale. Furthermore, as observed in the 79.8 m³/s case, apart from elongation of the cross-waves, prototype predictions of this flow rate also reveal changes in the position of the waves further downstream in the spillway channel. This is appreciated after the first change in gradient of the spillway channel, where the waves present different positions at the two scales.

In the OpenFOAM predictions, the free surface velocities exhibit notably higher values in the prototype compared to the scaled case. This is especially manifested in the first section of the spillway channel immediately downstream the weir and continues downstream until the first the change in gradient. In contrast, the Fluent simulations show more comparable velocities in the spillway first section but exhibit small differences towards the bottom end of the spillway channel. In the first spillway section, up to the first change in gradient, the OpenFOAM prototype velocities are very comparable to those predicted by Fluent with slightly lower velocities at the end of the channel.

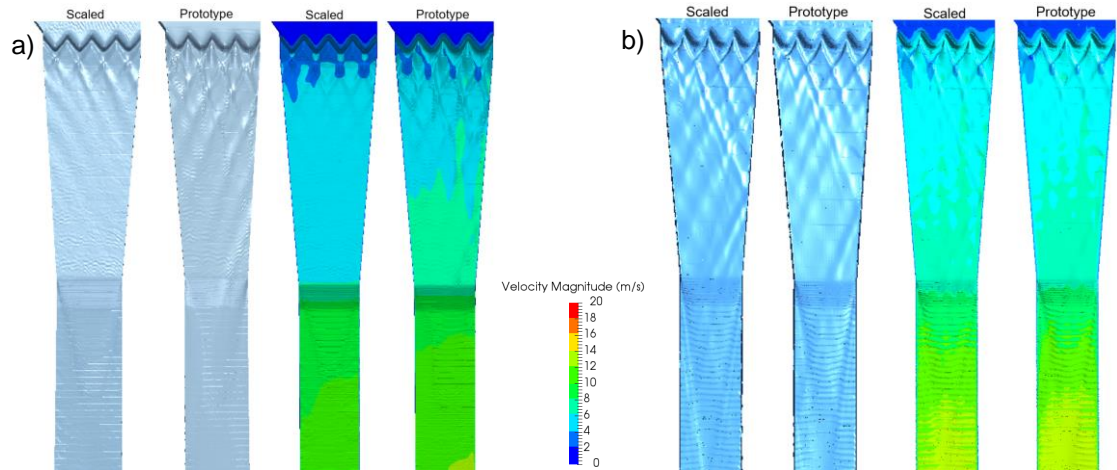


Figure 7.15: Scaled and prototype model predictions of wave structures and interface velocity contours predicted with: a) OpenFOAM and b) Fluent for a flow rate of $119.6 \text{ m}^3/\text{s}$

As observed in Section 6.10.3 the OpenFOAM scaled $119.6 \text{ m}^3/\text{s}$ case was not reproducing the prominence of the wave's peaks as accurately as Fluent. The differences between the two solvers were attributed to the mesh cell size and interface capturing scheme (OpenFOAM at physical model scale showed higher sensitivity to cell size than Fluent and the impact of the interface capturing scheme was also greater at physical model scale, see section 6.9). As indicated in the prototype scale sensitivity analyses in section 7.3, it appears that simulations at prototype scale are less sensitive to such numerical implementations than those at model scale. For this flow rate, the size of the cells where the free surface is located is the same at the two scales, and the prominence of the waves is superiorly captured at prototype scale. Therefore, the different sensitivity to model implementations at the two scales explains the additional differences that OpenFOAM presents at the two scales compared to Fluent. That is, both solvers show increase in velocities at prototype scale but in OpenFOAM these are reasonably greater and prototype simulations of this solver also exhibit greater changes in waves prominence.

In order to quantify the displacement of the waves in this case, the reference distances to three waves' crossing points x_1 , x_2 and x_3 as previously indicated on Figure 7.7 a) have been examined. Figure 7.16 shows the free surface profiles along distances to crossing points x_1 , x_2 and x_3 predicted with the two solvers. Results show that in all cases, the OpenFOAM predictions exhibit larger levels of elongation than those from Fluent. Figure 7.16 a) and b) show the distance x_1 up to the first crossing point and several metres downstream of it. The OpenFOAM plot show the scaled crossing point to be approximately 6.3 m downstream of the weir crest, while that in the prototype is around 7.7 m. This implies there is 22% of elongation at this crossing point. The wave elongation predicted with Fluent to the first crossing point is approximately 10%. Figure 7.16 c) and d) show the free surface profiles along the distance x_2 from the weir downstream crests to the second crossing point. Similarly to the distance x_1 , in this case OpenFOAM presents a wave elongation of 19 %, with the prototype scale crossing point being 2.5 m downstream of that at model scale. In addition, the prototype scale shows a presence of an air pocket. The Fluent profiles to the second crossing point present an elongation at prototype scale of only 1 m, and hence of 6 %. Figure 7.16 e) and f) show the profiles along distances to the third crossing point x_3 . The elongation of the distance to this point predicted with OpenFOAM is the greatest and

Chapter 7. Comparison of Prototype and Physical Model Predictions

approximately of 25 %. However in Fluent, the distance x_3 appears to have minimal difference (approximately 1 %), since the prototype crossing point is only 0.2 m downstream of that at model scale.

Figure 7.16 a) to f) also show that the distances to the three crossing points predicted by the OpenFOAM prototype scale simulations are in all cases, generally well correlated with those predicted in the Fluent prototype scale. The OpenFOAM scaled simulations of 119.6 m³/s case have been previously observed to be exhibiting shorter distances x_1 to x_3 than Fluent (see Section 6.10.3). Distances x_2 and x_3 were 3 and 4 m longer in Fluent than in OpenFOAM and Fluent was confirmed to have closer agreement with the experimental measurements. This explains the greater elongation of the waves observed in OpenFOAM compared to Fluent at prototype scale. Consequently, the reduced values of elongation at prototype scale (from 1 to 14%) are considered to be more realistic than those predicted in OpenFOAM.

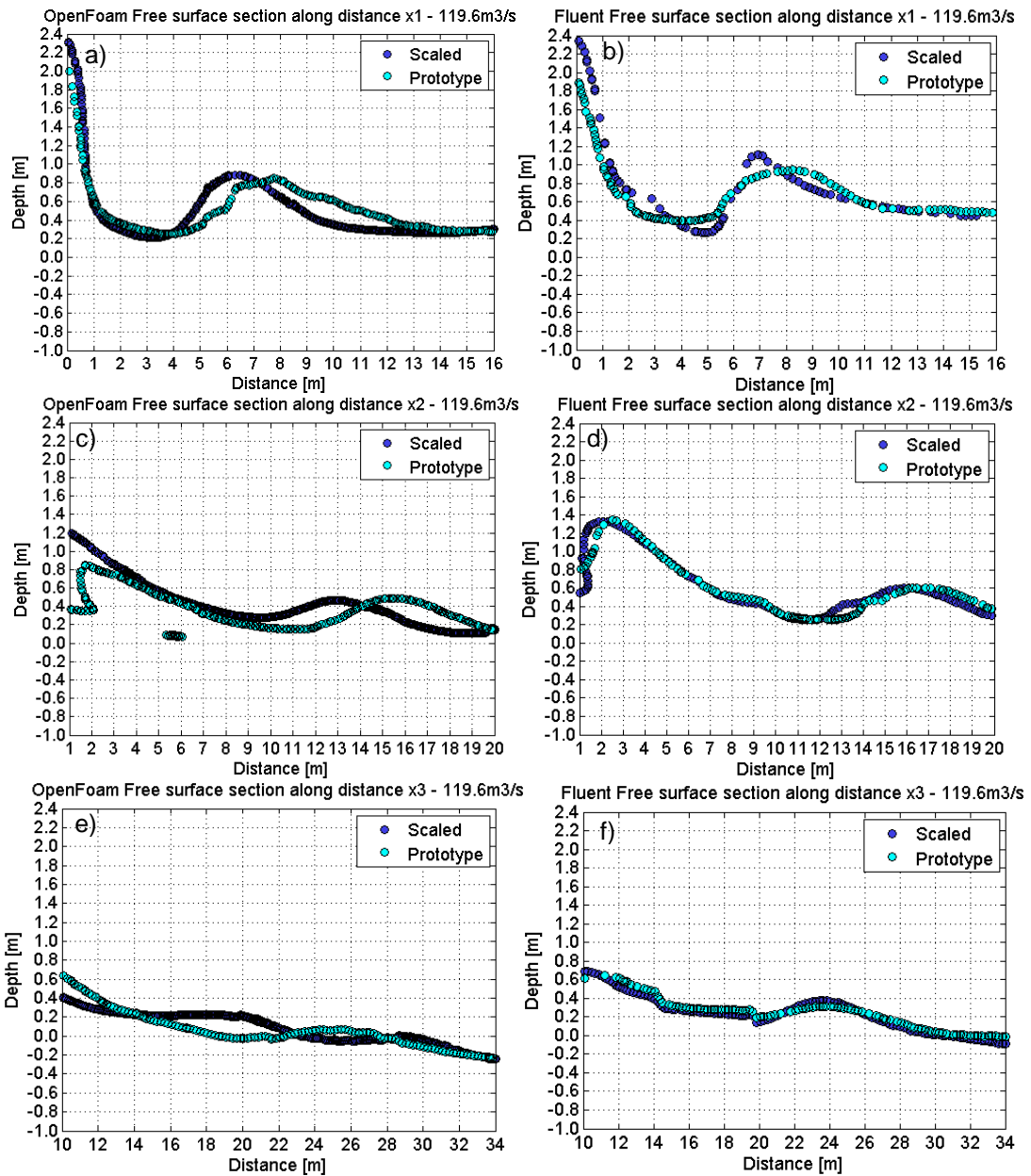


Figure 7.16: a) Free surface profile along distance x_1 predicted with OpenFOAM and b) with Fluent; c) Free surface profile along distance x_2 predicted with OpenFOAM and d) with Fluent; e) Free surface profile along distance x_3 predicted with OpenFOAM and f) with Fluent

In order to further examine the elongation of the waves and the changes in position of the wave features further downstream of the channel, the free surface features observed in the physical model were compared to those in the numerical predictions at the two scales. In the cross-waves' area it is observed that the numerical simulations at the two scales and physical model results of the 119.6 m³/s case exhibit a dominant wave originating from the first upstream crest which impacts the left wall of the spillway. This wave reflects downstream, and the reflective wave crosses the first change in gradient line approximately at the centre of the channel. In the prototype, the original wave from the first upstream crest impacts the spillway wall further downstream, which results in the reflective wave crossing the first change in gradient line at a point further to the right to that at model scale. This situation is illustrated with the indication of the wave features with black dashed lines in Figure 7.17.

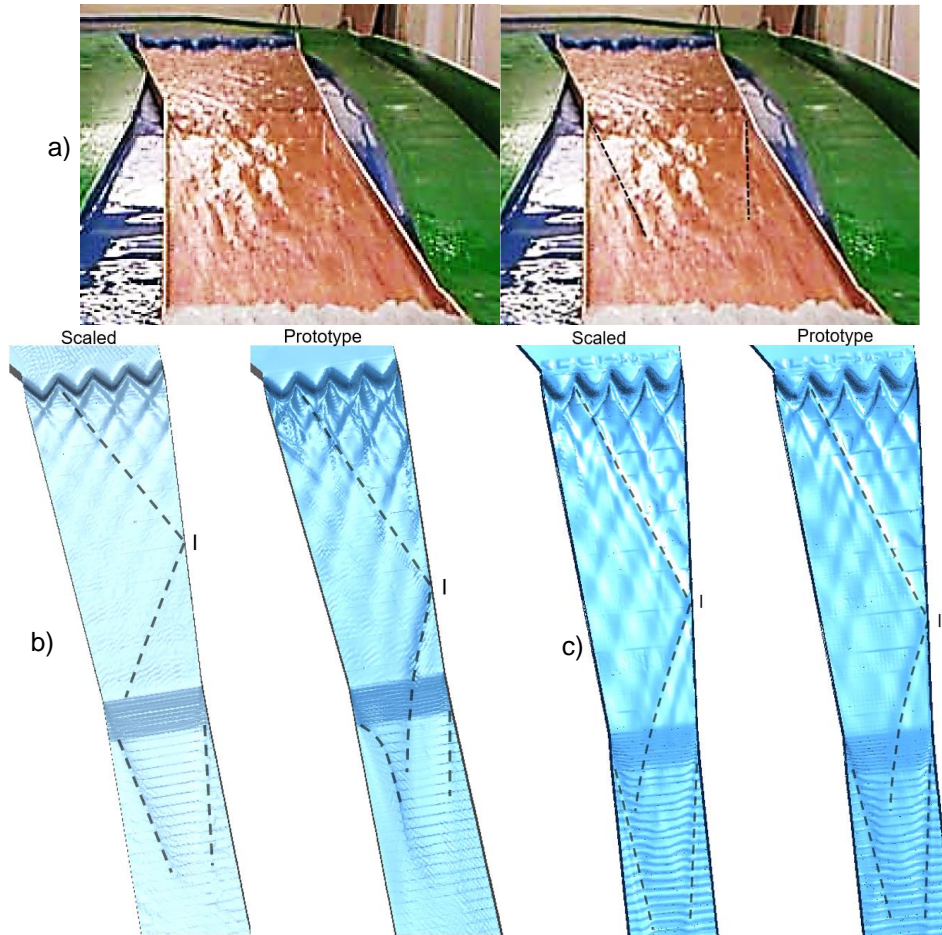


Figure 7.17: a) Physical model photograph of the free surface features at the lower section of the channel and with the dominant wave features indicated with dashed lines; b) Predictions of free surface features in the scaled and prototype cases with the main features indicated with dashed lines from OpenFOAM and c) Fluent. The impact point of the dominant wave is indicated with an "I"

Figure 7.17 a) shows that in the physical model, there is a central wave developed after the second change in gradient. The OpenFOAM predictions of the free surface features are presented on Figure 7.17 b). The free surface developed at the model and prototype scales are presented with the indication of the dominant features occurring in the two cases. In the scaled simulations the waves are less apparent, however, it is possible to observe that the waves crossing points are further upstream, which generate the central wave downstream of the second change in gradient. At prototype scale the dominant wave impacts the spillway left wall further downstream, indicated by the impact point "I" which results in the wave crossing further to the spillway left side at the first change in gradient. This reflects in a wave shifted towards the spillway left wall after the second change in gradient. Figure 7.17 c) presents the Fluent predictions of free surface features at the two scales and with the dominant features marked with dashed lines. Although the impact point at model scale is located further downstream than that in OpenFOAM, the same situation is reproduced, where the impact point at model scale is located upstream of that at prototype scale.

Free surface cross-sectional profiles of depth and velocity were extracted at several sections of the spillway channel. The cross sectional free surface profiles through measurement points A and B obtained with OpenFOAM and Fluent are presented on Figure 7.18 a) and b) respectively. Figure 7.18 a) indicates that the OpenFOAM prototype predictions at section A present waves of

larger size, with higher peaks than in the scaled case. At this section the prototype waves also present lower dips in between waves' crests than in the scaled case. In addition, the prototype scale predictions show presence of air pockets. The section through point B presents closer agreement at the two scales but with the depth being generally lower throughout the profile at prototype scale. Figure 7.18 b) shows there is overall good correlation between Fluent predictions of the free surface profile through point A at the two scales, with both cases predicting presence of air pockets at this section. At section through point B the prototype scale predictions show lower depths along most of the section. Free surface depth profiles through points C, D and E were extracted at the two scales and plotted in Figure 7.18 c) and d) for OpenFOAM and Fluent respectively. To enhance understanding of the free surface features in the plots, the wave structures at the two scales with the location of the different sections are shown in Figure 7.18 e). In Figure 7.18 c) the OpenFOAM predictions show that at section through point C the prototype depth is lower than that at model scale but near the spillway left wall shows higher depths, which is where the reflective wave crosses. As previously observed, at section D the prototype scale shows the shape of the reflective wave propagating from left to right while the scaled case shows the central wave, equivalent to that observed on the 79.8 m³/s and 40 m³/s scaled simulations. At section E the waves show similar wave features and depths at the two scales. Figure 7.18 d) shows that a similar situation is predicted on the Fluent simulations, however at section C the reflective wave is also predicted on the scaled case, which shows higher depths. At section D, there is a slight shift in the prototype wave compared to the scaled wave, but it is not as distinct as in OpenFOAM. At section E the prototype presents a distinct dip at the centre of the channel while the scaled case is more levelled, similarly to the scaled OpenFOAM predictions.

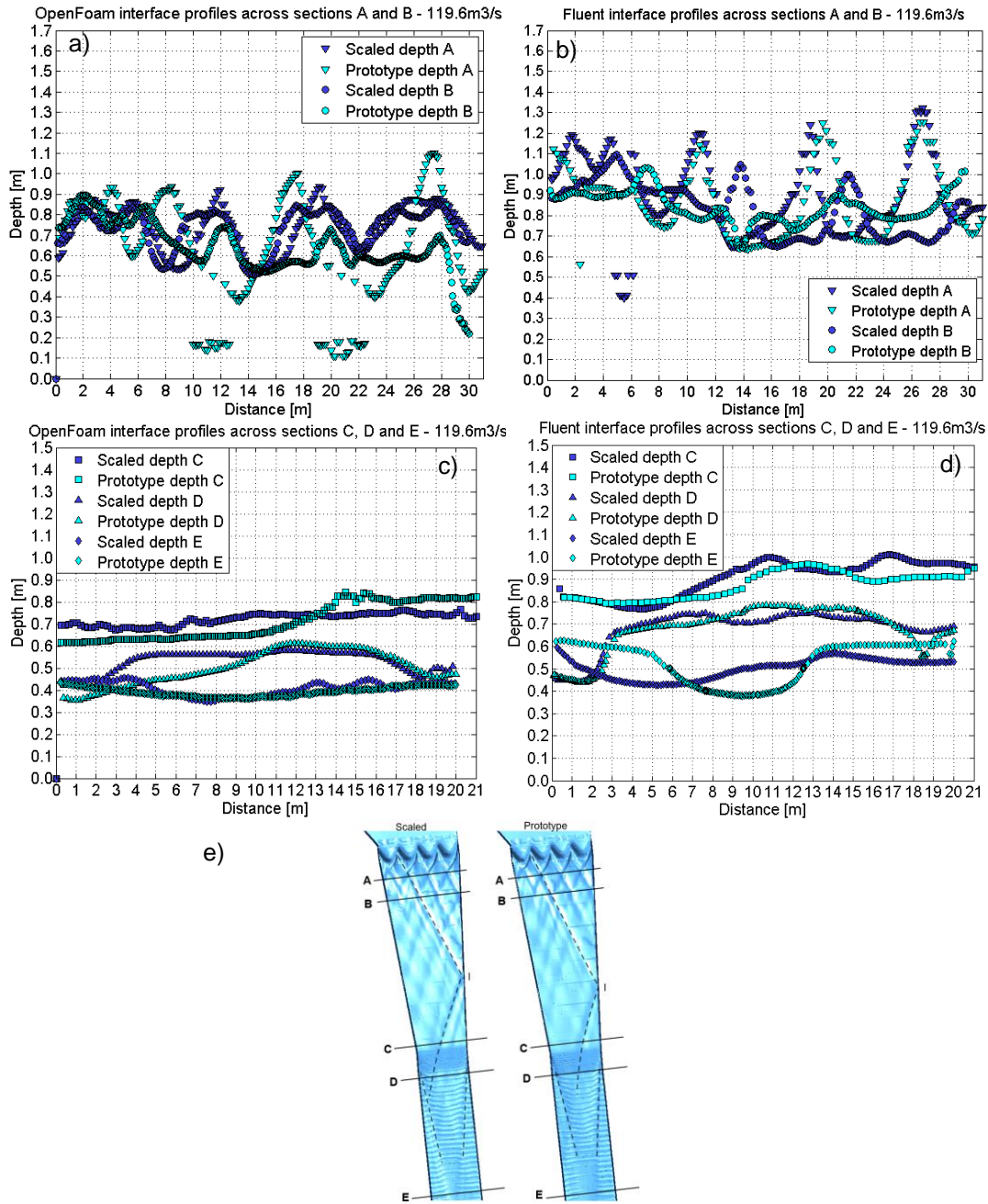


Figure 7.18: a) Interface cross-sectional profiles at sections A, B at the two scales predicted with OpenFOAM and b) with Fluent; c) Cross sectional profiles of interface depth at sections through points C, D and E predicted in OpenFOAM and d) Fluent; e) Free surface features indicated on the scaled and prototype cases with the location of the sections

Free surface velocities at sections through measurement points B to E at the two scales are presented in Figure 7.19 a) and b) for OpenFOAM and Fluent respectively. The OpenFOAM sections exhibit significant increases in velocity at section B, located in the area with presence of cross-waves. There are certain increases in velocity at section C, but overall these are lower than 1 m/s. At section D and E velocity profiles in the prototype are marginally higher than those at model scale. The Fluent predictions show very comparable velocity profiles at the two scales at sections B, C and E with slightly more noticeable increases in velocity at section D. Therefore, in this flow rate the velocity predictions at the two scales present close agreement in most of the sections.

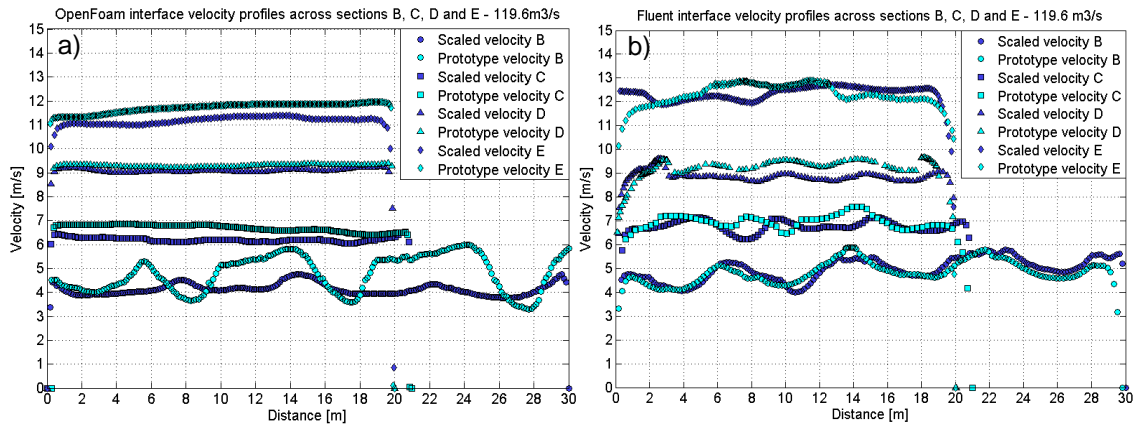


Figure 7.19: Interface cross-sectional velocity profiles at sections B, C, D and E predicted with: a) OpenFOAM and b) Fluent

In summary, at this flow rate the average decrease in depth and increase in velocity at prototype scale registered in OpenFOAM are approximately 9% and 6% respectively. In Fluent these are 3% and 2% respectively. Such percentage differences are lower than in the previous flow rate. These values are of similar order in the two solvers but are lower in Fluent than in OpenFOAM. As previously indicated, the greater differences at the two scales in OpenFOAM are generated by the slightly less accurate predictions of depths and of prominence of free surface features in the OpenFOAM scaled case.

7.4.3.1. Calculation of the Froude, Reynolds and Weber Numbers at Spillway Channel Sections

In order to further examine the flow conditions and discrepancies at the two scales, the Froude, Reynolds and Weber number were calculated along sections through points D and E, located in the third section of the spillway channel. The Froude numbers calculated at the two scales with the two solvers are shown in Table 7.10 with the prototype-to-model ratio of Froude number at the two sections. Results show that consistently the Froude number ratios have decreased compared to those calculated for the 40 m³/s and 79.8 m³/s, reflecting the greater agreement between the predictions at the two scales. The Froude numbers at both sections present very close agreement in both solvers, being of approximately 4 at section D and increasing to around 6 at section E.

Table 7.10: Froude numbers and prototype-to-model Froude ratios at sections E and D calculated from scaled and prototype simulations 119.6 m³/s

Section	OpenFOAM Scaled Fr [-]	OpenFOAM Prototype Fr [-]	OpenFOAM Fr _r [-]	Fluent Scaled Fr [-]	Fluent Prototype Fr [-]	Fluent Fr _r [-]
D	3.96	4.2	1.06	3.47	3.69	1.06
E	5.54	5.93	1.07	5.53	5.57	1.01

Reynolds numbers were calculated at sections D and E and are presented in Table 7.11. Results show the Reynolds numbers are comparable and of approximately the same order in the two solvers, with slightly larger values in Fluent. The prototype-to-model ratios show values very close to the theoretical (according to Froude law of similarity) for this case of 125, which occurs as a result of the Froude numbers being almost equivalent at the prototype and model for this flow rate.

Chapter 7. Comparison of Prototype and Physical Model Predictions

Table 7.11: Reynolds numbers and prototype-to-model Reynolds ratios at sections E and D calculated from scaled and prototype simulations 119.6 m³/s

Section	OpenFOAM Scaled Re [-]	OpenFOAM Prototype Re [-]	OpenFOAM Re _r [-]	Fluent Scaled Re [-]	Fluent Prototype Re [-]	Fluent Re _r [-]
D	36584.5	4435906.3	121.3	44473.5	5454601	122.6
E	34977.4	4414064	126.2	47059.8	5897852	125.3

The Weber numbers at the two sections calculated with the two solvers at the two scales are shown on Table 7.12. These show generally values of similar order for the two sections in the two solvers. The prototype-to-model Weber number ratios in this case are also very close to the theoretical of 625.

Table 7.12 Weber numbers and prototype-to-model Weber ratios at sections E and D calculated from scaled and prototype simulations 119.6 m³/s

Section	OpenFOAM Scaled We [-]	OpenFOAM Prototype We [-]	OpenFOAM We _r [-]	Fluent Scaled We [-]	Fluent Prototype We [-]	Fluent We _r [-]
D	957.5	594750	621.1	1156.7	730585	631.6
E	1110.3	733947.5	661	1667.4	1050236.3	629.9

Results for 119.6 m³/s show that for this larger flow rate, the Froude law of similarity is very well accomplished (especially compared to the two previous lower flows). The increase in water depth and velocity associated with the larger flow rate make the forces which haven't been matched (viscosity and surface tension) to be negligible at physical model scale, and hence a close agreement is achieved between prototype and scaled cases. Therefore, it is possible to match well the Froude numbers through different sections of the channel.

7.4.4. PMF: 159.5 m³/s

Model and prototype scale simulations were undertaken of the PMF flow of 159.5 m³/s. A comparison of the scaled and prototype free surface structures and velocities predicted with OpenFOAM and Fluent is shown on Figure 7.20 a) and b) respectively. As observed in the high flow rate case, the prototype scale cross-waves generated by the labyrinth weir present an elongated and prominent configuration compared to that at model scale. This situation is especially perceivable in OpenFOAM. In this case, the velocity contours also indicate velocities are higher in the prototype than in the scaled case. Similarly to the previous flow rates simulated, the OpenFOAM predictions present larger differences between the velocities at the two scales than those from Fluent.

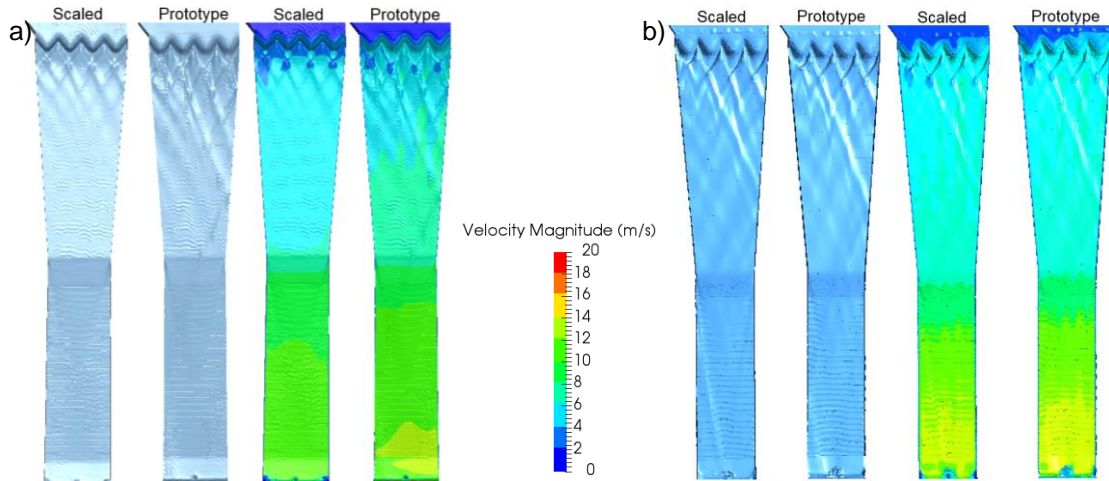


Figure 7.20: Scaled and prototype model predictions of wave structures and interface velocity contours predicted with a) OpenFOAM and b) Fluent for a flow rate of $159.5 \text{ m}^3/\text{s}$

As previously, in order to quantify the elongation of the waves on the prototype compared to the scaled case, distances from the weir downstream crests to three different wave crossing points were measured. These were the distances x_1 , x_2 and x_3 as indicated on Figure 7.7 a). The free surface profiles along the three distances computed at the two scales with the two solvers are presented on Figure 7.21. The free surface profiles along distance x_1 are shown on Figure 7.21 a) and b). The OpenFOAM results show the distance x_1 is elongated approximately 33% in the prototype, with the waves' crossing point being 6 m downstream of the weir downstream crest at model scale and 8 m in the prototype scale. As in the previous case, the Fluent predictions show less elongation of the waves, with the crossing point being approximately 8.9 and 9.4 m downstream the weir crest, and hence the elongation being of 6%. Figure 7.21 c) and d) show the waves profiles on the distance to the second crossing point x_2 , where it is shown that the OpenFOAM predictions have an elongation of approximately 36%, with the crossing points at model and prototype scale at 12.7 m and 17.3 m downstream the weir crest respectively. The Fluent results present a significantly lower displacement with the waves crossing points being only 0.8 m apart and hence elongation being of only 6%. Figure 7.21 e) and f) shows that the elongation of the distance x_3 is the largest in both solvers, however being remarkably larger in OpenFOAM than in Fluent. In OpenFOAM the crossing points at model and prototype scale are located 18.2 m and 25.8 m downstream the weir crest respectively. This implies an elongation of 41.8%, while the Fluent waves' crossing points, separated 1.8 m present 8% of elongation.

In this case OpenFOAM presents the greatest elongation of the three distances of all flow rates, ranging from 30 to 40%. Fluent presents comparable elongation percentages to the other flow rates, ranging from 5 to 8%. Similarly to the $119.6 \text{ m}^3/\text{s}$ case, the greater elongation occurring in OpenFOAM (as well as greater differences in velocity) is explained by the less accurate predictions of this solver at physical model scale. At physical model scale, the PMF presented the greatest difference in the distances x_1 to x_3 between the two solvers, being 3 to 6 m longer in Fluent than in OpenFOAM (see Section 6.10.4). Furthermore, the OpenFOAM PMF predictions at physical model scale presented underestimations of the wave's crossing points peak heights as well as velocities and depths. As previously specified, these were generated by the higher sensitivity of this solver to the cell size and to the interface capturing scheme at physical model

scale. The OpenFOAM prototype predictions present less sensitivity to such implementations and hence demonstrate greater correlation with the Fluent predictions at prototype scale. The Fluent prototype distances x_1 to x_3 are approximately 1 m longer than those predicted in the OpenFOAM prototype simulations.

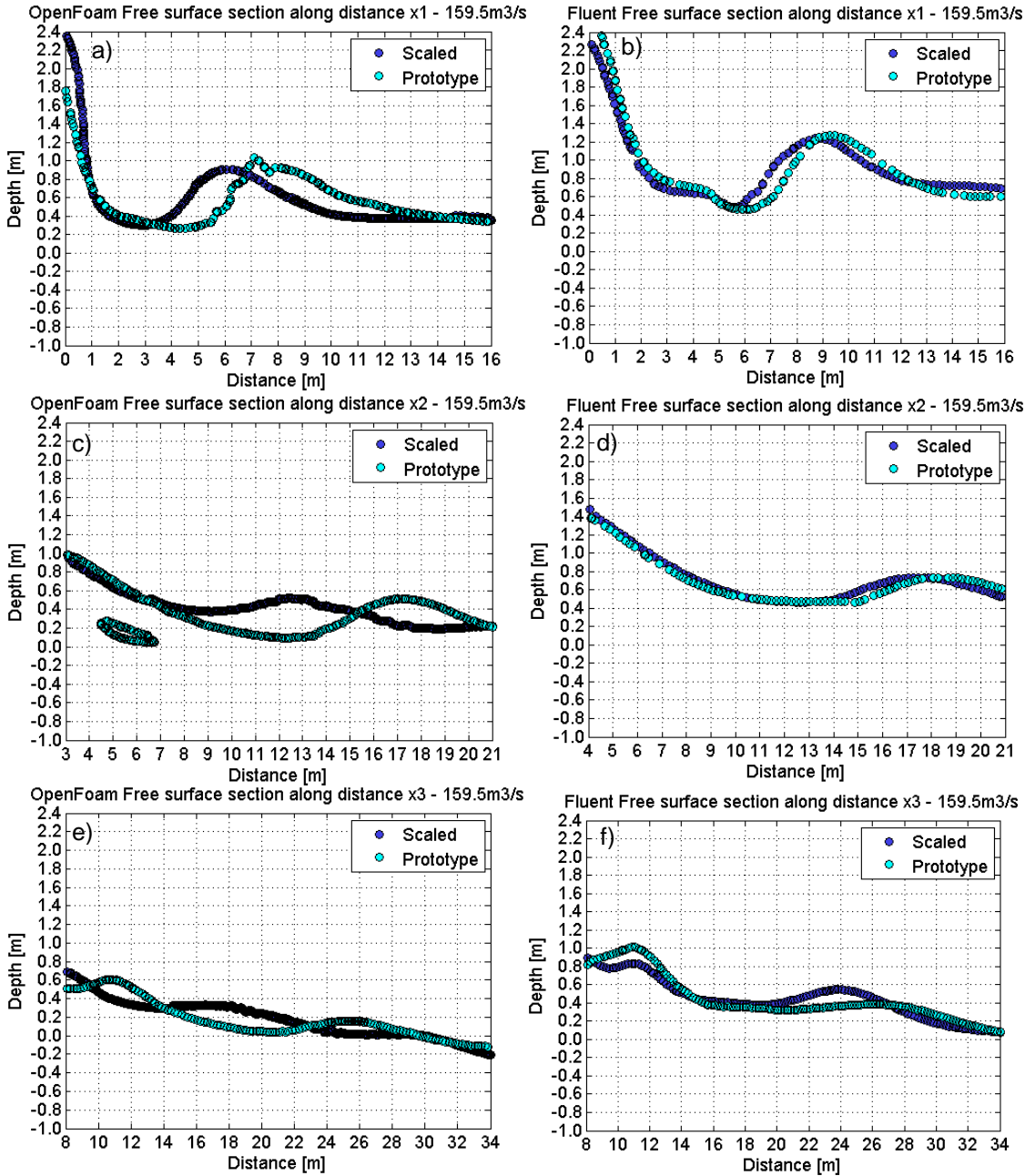


Figure 7.21: a) Free surface profile along distance x_1 predicted with OpenFOAM and b) with Fluent; c) Free surface profile along distance x_2 predicted with OpenFOAM and d) with Fluent; e) Free surface profile along distance x_3 predicted with OpenFOAM and f) with Fluent

In order to inspect the changes in position of the waves further downstream of the spillway channel, the dominant cross-waves were examined at the two scales. Figure 7.22 a), b) and c) show the free surface dominant features generated in the physical model and predicted by Fluent and OpenFOAM respectively. Figure 7.22 a) shows the section of the spillway downstream of the second change in gradient developed in the physical scale model. The physical model predicts the development of a central wave, which as observed in previous flow rates, it becomes narrower

further downstream. The contours of the wave have been indicated with black dashed lines. Figure 7.22 b) and c) reveal that in the scaled simulations, this feature is well reproduced in both solvers, indicated by the dashed lines. In Figure 7.22 b) it is observed that the prototype scale simulations from Fluent depict the dominant wave shifted to the left of the spillway channel. In Figure 7.22 c) the OpenFOAM prototype scale predictions present a very comparable wave configuration to that at prototype scale predicted with Fluent, with the dominant wave shifted towards the left side of the spillway channel compared to the scaled case. Because the Fluent scaled simulations present greater wave prominence, the change in waves' position is more appreciable in this solver than in OpenFOAM.

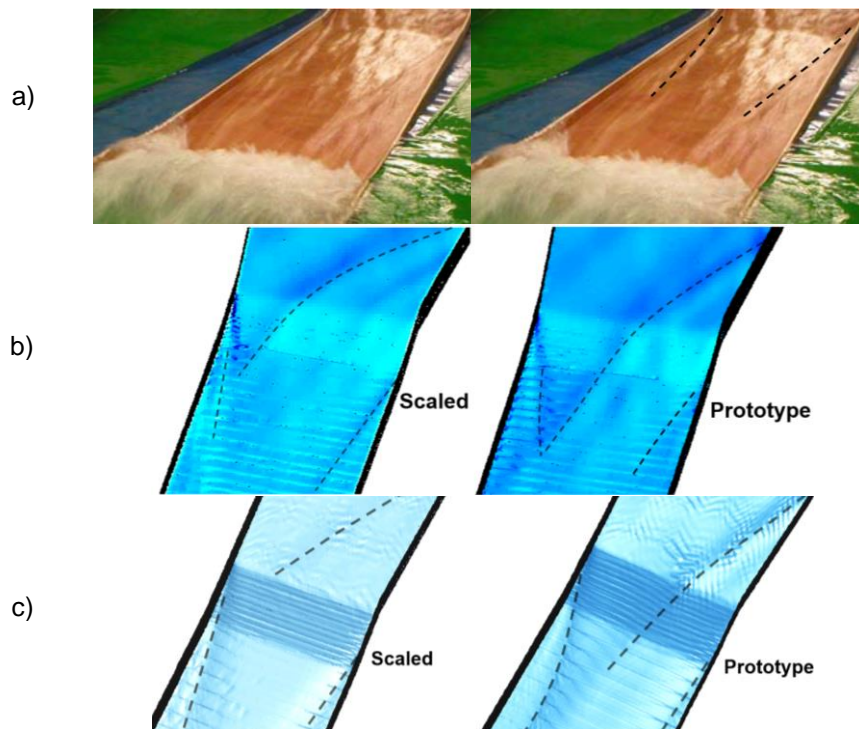


Figure 7.22: a) Physical model photograph of the free surface features at the lower section of the channel and with the dominant wave features indicated with dashed lines; b) Predictions of free surface features in the scaled and prototype cases and with the main features indicated with dashed lines from Fluent and c) OpenFOAM

To further illustrate the wave propagation from its generation until the end of the channel at the two scales, a photograph of the channel flow situation in the physical scale model is compared to the scaled and prototype simulations in Fluent, (where the waves are more visible). This is shown on Figure 7.23 a) and b) respectively. As previously identified, the central wave in the physical model has been distinguished and confirmed in Figure 7.23 a) where it is also possible to observe the dominant waves crossing the channel from the first upstream crest to the spillway left wall. Figure 7.23 b) shows again, from a different perspective, the changes in the waves positions at prototype scale. The impact point "I" is located slightly further downstream of that in the scaled case, and this establishes the reason of the shift in position of the wave further downstream of the spillway, which is particularly distinct in the section with the steepest channel base, in between the two changes in gradient.

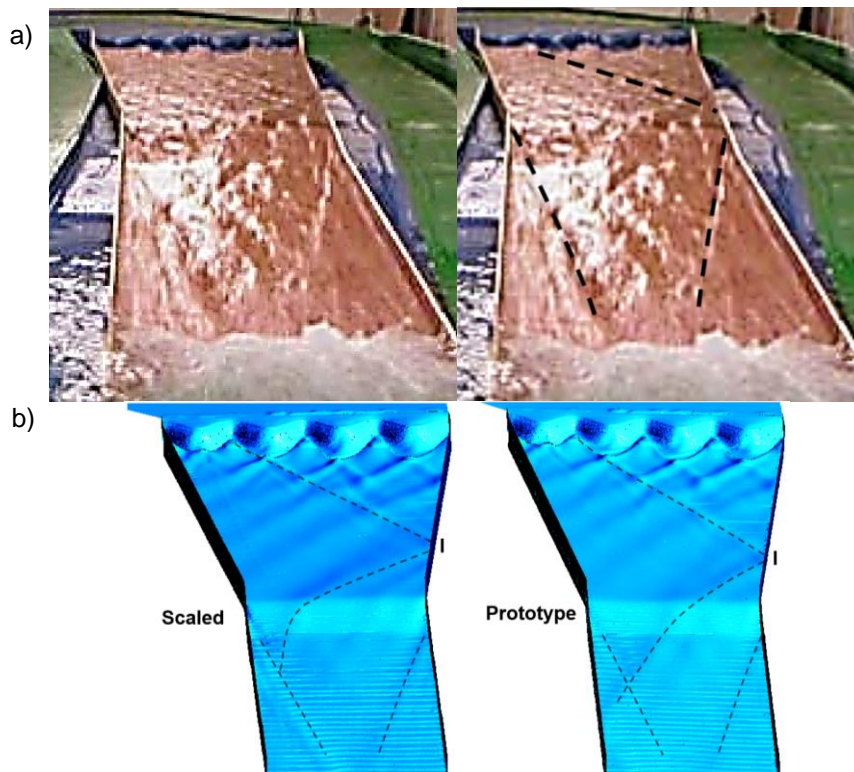


Figure 7.23: a) Physical model photograph of the free surface features at the lower section of the channel and with the dominant wave features indicated with dashed lines; b) Fluent predictions of free surface features in the scaled and prototype cases and with the main features indicated with dashed lines. The impact point of the dominant wave is indicated with an “I”

Cross-sectional free surface profiles at different sections of the spillway channel predicted with the two solvers were extracted at the two scales and plotted on the same graph for comparison. Free surface profiles at sections through measurement points A and B are shown on Figure 7.24 a) and b) for OpenFOAM and Fluent respectively. In the OpenFOAM predictions at section through point A, the prototype scale waves' crossing points exhibit higher peaks than those at model scale. In addition, the prototype scale profile depicts presence of air pockets. This confirms the greater prominence of the waves at prototype scale in OpenFOAM which has already been observed on Figure 7.20. At section through point B, the free surface depths are generally higher at model scale, but they are comparable with those at prototype scale. The Fluent predictions display high peaks at the waves' crossing points at profile through point A, with overall agreement between the heights of the waves at the two scales. Similarly, the profiles at section through point B present significant correlation between the depths predicted at the two scales. Figure 7.24 c) and d) show the free surface profiles at sections through points C, D, and E predicted with OpenFOAM and Fluent respectively. For an enhanced understanding of the free surface profiles at the various sections, Figure 7.24 e) shows their location along with the dominant wave features on the spillway channel. The OpenFOAM profiles at section C, located just before the first change in gradient, indicate that the model scale depth profile is higher than the prototype. The free surface features at both scales show a dominant wave located at the left side of the spillway. However in the scaled case, the wave is more advanced in its trajectory and has already crossed the centre of the channel. At section D, just after the second change in gradient, the change in position of the waves is similar to that noted in the previous flow rate. The scaled case depicts the central wave observed on Figure 7.22 and Figure 7.23 while the prototype scale flow shows

the shifted wave towards the left wall. At the end of the channel at section E, both scales predict a similar wave profile, where the dominant waves have faded. The Fluent predictions at section through point C demonstrate very consistent profiles to those predicted with OpenFOAM at the two scales, with the model scale wave significantly more advanced towards the centre of the channel and the prototype scale wave being still closer to the spillway left wall. This situation is further illustrated at sections through point D, where analogously to OpenFOAM, the Fluent predictions show the central wave predicted in the model scale simulations and the prototype wave is shifted towards the left wall of the spillway. At section through point E, the scaled simulations show a central dip, and the prototype profile exhibits an overall flat profile.

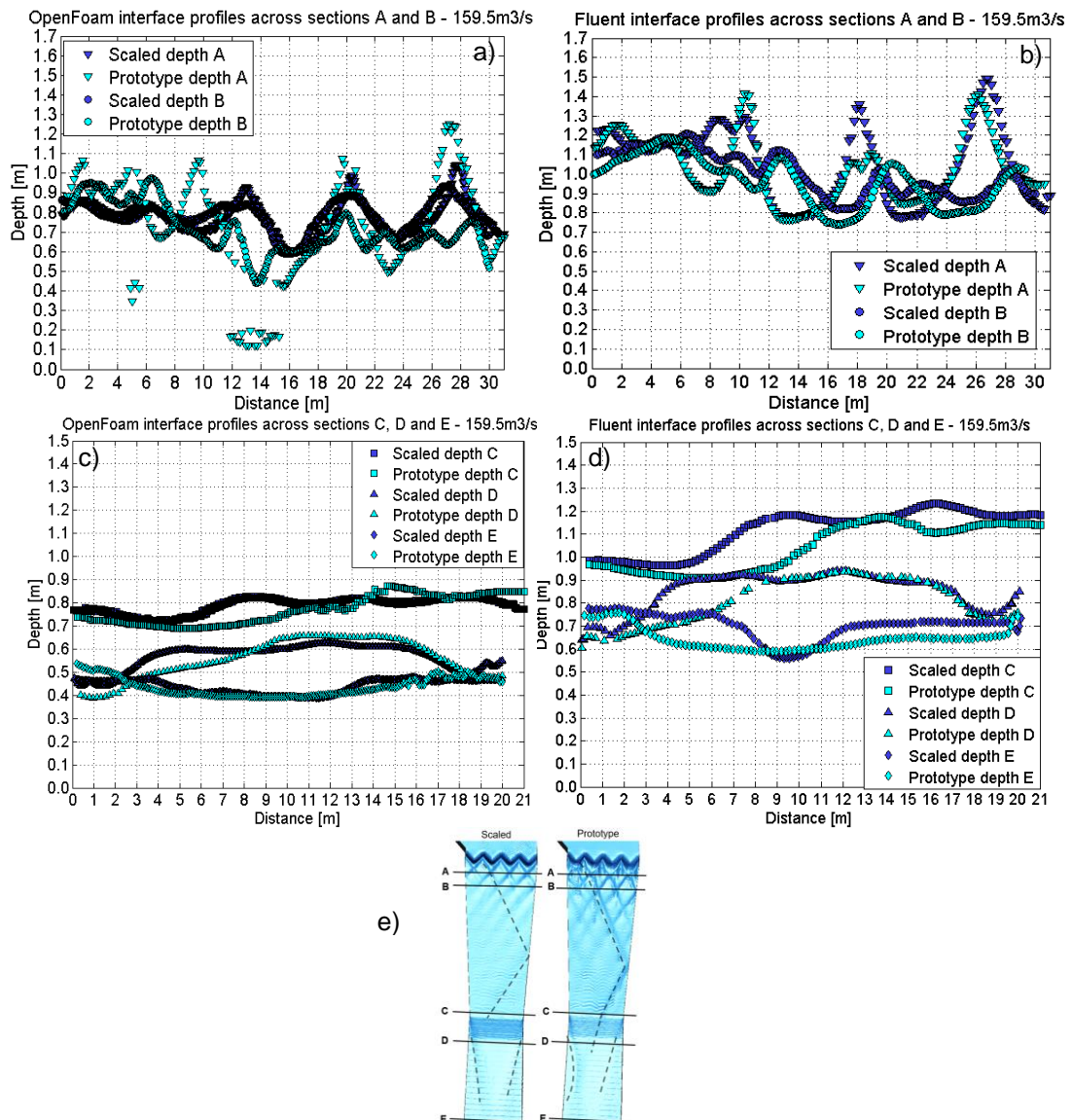


Figure 7.24: a) Interface cross-sectional profiles at sections A, B at the two scales predicted with OpenFOAM and b) with Fluent; c) Cross sectional profiles of interface depth at sections through points C, D and E predicted in OpenFOAM and d) Fluent; e) Free surface features indicated on the scaled and prototype cases with the location of the sections

In summary, despite the differences in the predictions from the two solvers at model scale of the PMF, (see section 6.10.4) and the consequently greater elongation of the waves at prototype scale predicted in OpenFOAM, the changes in position of the waves further downstream are

equivalent in both solvers. In other words, at prototype scale, the two solvers present comparable wave displacement at the second and third sections of the spillway channel.

The free surface velocity profiles at several sections of the spillway channel from OpenFOAM and Fluent are shown on Figure 7.25 a) and b) respectively. The OpenFOAM velocity predictions show that the greatest variation in velocity occurs at section through point B, where the prototype flow has a velocity of approximately 1 m/s larger than that at model scale. At sections C and E the prototype velocities present a slight increase in respect of the model scale velocities and at section D the velocities are very comparable, although that in the prototype is marginally higher. This situation is consistent with that observed for the 119.6 m³/s case. In Fluent, the velocity profiles at the two scales exhibit lower discrepancies than in OpenFOAM, with velocity profiles presenting very good correlation in sections B, C and D with only very minor increases in values at the prototype scale. At section through point E, the prototype velocity demonstrates greater differences, in some instances being of approximately 1 m/s increase.

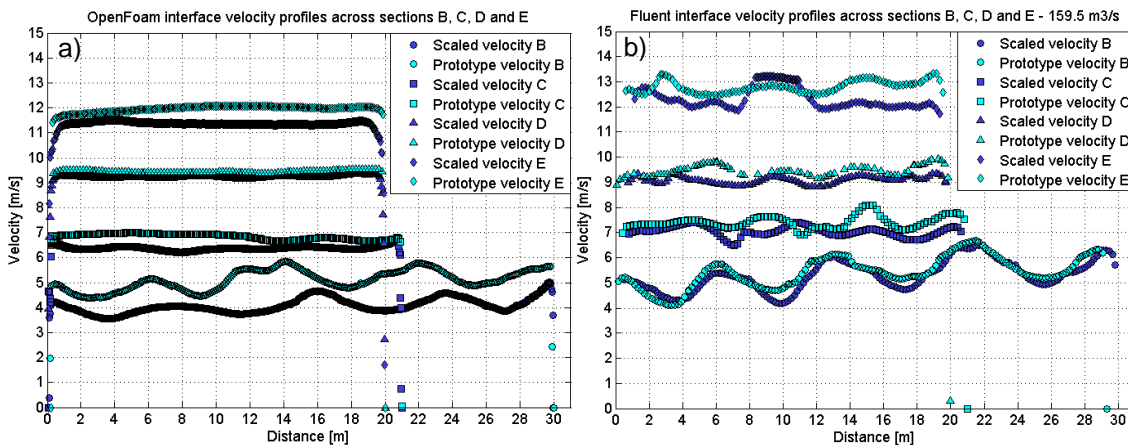


Figure 7.25: Interface cross-sectional velocity profiles at sections B, C, D and E predicted with: a) OpenFOAM and b) Fluent

To conclude, in this flow rate the average OpenFOAM decrease in depth and increase in velocity at prototype scale are approximately 4 and 7 % respectively. These in Fluent are 6 and 4 % respectively. Such percentages are generally close to those shown for the high flow rate but in this case are slightly higher. Such differences are explained by the fact that changes in position of the waves at prototype scale in this case are more notorious in the two solvers. Consequently, although scale effects due to viscosity are lower for larger flow rates, changes in position of the waves cause slightly greater discrepancies at the two scales compared to the high flow rate.

7.4.4.1. Calculation of the Froude, Reynolds and Weber Numbers at Spillway Channel Sections

The Froude numbers were calculated at sections D and E of the spillway channel to compare the values at the two scales. Table 7.13 shows the Froude numbers at sections D and E calculated with the two solvers at the two scales. Generally, the Froude numbers appear to be slightly lower in Fluent compared to OpenFOAM in the two sections and scales. The OpenFOAM results show that for this flow rate the Froude numbers become the closest between prototype and model of all flow rates modelled, with the prototype-to-model Froude number ratio being the closest to 1.

This is expected since larger velocities and depths translate to more negligible effects of viscosity and surface tension, allowing to obtain a well accomplished Froude similarity with reduced scale effects. The Fluent results at section D also show the prototype-to-model Froude number ratio appears to be the closest to 1 of all cases modelled, being the same value as for the 119.6 m³/s case. At section E it is slightly higher but it is still considerably close to 1.

Table 7.13: Froude numbers and prototype-to-model Froude ratios at sections E and D calculated from scaled and prototype simulations 159.5 m³/s

Section	OpenFOAM Scaled Fr [-]	OpenFOAM Prototype Fr [-]	OpenFOAM Fr [-]	Fluent Scaled Fr [-]	Fluent Prototype Fr [-]	Fluent Fr [-]
D	3.89	4.05	1.04	3.16	3.36	1.06
E	5.44	5.77	1.06	4.75	5.07	1.07

The Reynolds numbers at sections D and E were calculated with the simulation results from the two solvers at the two scales. These are presented in Table 7.14, where in this case the OpenFOAM results show very comparable values of prototype-to-model ratios to those obtained in the 119.6 m³/s case, being only marginally larger. The Fluent prototype-to-model ratios also exhibit very similar values to those calculated for the 119.6 m³/s case, with values only minimally lower in this case. In both cases they are considerably close to the theoretical value of 125. The Fluent results show greater Reynolds numbers than those in OpenFOAM. At section D the values from the two solvers are closer than at section E, where as previously observed, the Fluent simulations predict larger velocities.

Table 7.14: Reynolds numbers and prototype-to-model Froude ratios at sections E and D calculated from scaled and prototype simulations 159.5 m³/s

Section	OpenFOAM Scaled Re [-]	OpenFOAM Prototype Re [-]	OpenFOAM Re [-]	Fluent Scaled Re [-]	Fluent Prototype Re [-]	Fluent Re [-]
D	39340.4	4973494.1	126.4	56517.9	6857031.6	121.3
E	38149.4	5008078.8	131.2	63037.3	7736279.2	122.7

Table 7.15 shows the Weber numbers calculated at sections D and E from simulations from both solvers and at the two scales. The Weber numbers calculated with the Fluent simulations are larger than those calculated with OpenFOAM. This occurs at the two scales and sections. In OpenFOAM the prototype-to-model ratio is larger in this case than in the 119.6 m³/s flow rate. In Fluent the ratios are very comparable to the 119.6 m³/s case and in both cases they are generally in the same order as the theoretical prototype-to-model ratio value of 625.

Table 7.15: Weber numbers and prototype-to-model Froude ratios at sections E and D calculated from scaled and prototype simulations 159.5 m³/s

Section	OpenFOAM Scaled We [-]	OpenFOAM Prototype We [-]	OpenFOAM We [-]	Fluent Scaled We [-]	Fluent Prototype We [-]	Fluent We [-]
D	1047.4	681486.9	650.6	1527.5	950526.9	622.3
E	1235.5	857711	694.3	2276.3	1442937.6	633.9

7.4.5. Summary

The comparison of the various flow rates at the spillway channel at model and prototype scales revealed several key findings. In order to understand and provide a correct interpretation of the observed differences at the two scales, it is necessary to consider the findings of Section 6.10 (that is, predictions of the two solvers at model scale). There are two main aspects which have been considered throughout this chapter. The first one is the difference that the two solvers exhibit

Chapter 7. Comparison of Prototype and Physical Model Predictions

between the flow predictions at the two scales (i.e. the percentage of scale effects predicted by each solver). The second is the influence of the flow rate size on such differences (i.e. on the scale effects). The differences in the scale effects predicted by the two solvers for the same flow rate are explained by the accuracy of the physical model scale simulations of the two solvers. The impact of the flow rate size on the scale effects is expected from theory.

For 40 m³/s, the two solvers presented generally comparable differences between the flows at the two scales. Predictions of velocity and depth from the two solvers were overall comparable at physical model scale. The scale effects in depth and velocity demonstrated in the two solvers for this flow rate are the greatest of all flow rates. The average decrease in depth and increase in velocity in OpenFOAM are of approximately 18 % and 14 % respectively. Those in Fluent are of 14 % and 12 % respectively. In the prediction of the wave elongation, OpenFOAM predicts approximately 10% greater elongation than Fluent, which could be related to the fact that the two solvers presented slight variations in their predictions at model scale, given the different interface capturing scheme implemented.

The 79.8 m³/s flow rate was simulated in OpenFOAM. In this flow rate, the wave elongation is between 10 and 20%. The average decrease in depth at prototype scale is approximately 14 % and the average increase in velocity is 7 %. Therefore, these are lower than in the lowest flow rate.

The 119.6 m³/s case showed slightly greater discrepancies between scale effects predicted by the two solvers. In OpenFOAM, the decrease in depth and increase in velocity at prototype scale are in average of approximately 9% and 6% respectively. In Fluent these are 3 % and 2 %. The average elongation predicted in OpenFOAM is about 22% while in Fluent is about 6%. Therefore, the differences at the two scales predicted by the two solvers differ more than in the 40 m³/s case. The greater scale effects predicted at prototype scale by OpenFOAM are explained by the less accurate predictions of this solver at physical model scale for this flow rate. This was due to the higher sensitivity to model implementations of this solver at physical model scale compared to prototype scale. In Section 6.10.3 it was observed that the Fluent cross-wave configuration at physical model scale was more closely correlated with the physical model results than that from OpenFOAM and presented elongation in respect to that in OpenFOAM. The reduced sensitivity to model implementations at prototype scale in comparison to model scale caused the OpenFOAM predictions at prototype scale to be closer to those from Fluent at prototype scale (more than the OpenFOAM scaled simulations are to the Fluent scaled).

The 159.5 m³/s case presented a similar situation to the 119.6 m³/s but with significantly larger discrepancies in the predictions of wave elongations by the two solvers. OpenFOAM predicts elongation to be from 30 to 40 % while Fluent predicts it to be from 5 to 8 %. This significant difference in the elongation predicted by the two solvers is due to the greater discrepancies that the two solvers present in the cross-wave configuration at physical model scale. In this flow rate, the Fluent configuration at model scale presented significant elongation in respect to that in OpenFOAM and showed closer agreement with the physical model (see Section 6.10.4). In this flow rate, the OpenFOAM decrease in depth and increase in velocity at prototype scale are

approximately 4 and 7 % respectively. These in Fluent are 6 and 4 % respectively. These are similar to the 119.6 m³/s but they are not lower because of the more significant changes in the waves positions occurring in this flow rate.

7.4.6. Discussion

7.4.6.1. Scale effects on Depths and Velocities

In this section, the simulations at physical model scale are compared to those at prototype scale for a range of flow rates. The trends in the differences between prototype and model for different flow rate sizes are examined and summarised. A consistent increase in velocity and decrease in water depth in the prototype scale with respect to the model scale flows has been observed in all flow rates. This trend is seen consistent in the predictions from the two solvers. In addition, the increase in velocity and decrease in depth are observed to reduce for increasing flow rate. The percentage difference in depth and velocity between prototype and model scale are calculated at sections through measurement points A to E. A summary table of the percentage difference in depths and velocities at the two scales at the different sections of the spillway channel is presented in Table 7.16. The percentage difference in depth at sections A, B, C, D, and E are referred to as dh_A , dh_B , dh_C , dh_D , and dh_E . The percentage difference in velocity at sections B to E are referred to as dv_B , dv_C , dv_D , and dv_E .

Table 7.16: Percentage difference in depth and velocity in the prototype in respect of model scale at different sections of the spillway channel

	Q [m ³ /s]	dh_A [%]	dh_B [%]	dh_C [%]	dh_D [%]	dh_E [%]	dv_B [%]	dv_C [%]	dv_D [%]	dv_E [%]
OpenFOAM	40	28.82	14.44	18.58	16.35	15.52	18.39	23.48	7.06	7.53
Fluent	40	13.13	12.80	14.64	11.00	19.64	12.27	14.27	3.14	19.82
OpenFOAM	79.8	14.00	14.46	14.25	13.19	15.57	12.88	9.13	1.60	4.58
OpenFOAM	119.6	16.17	12.92	4.15	5.88	3.93	7.57	10.57	2.76	4.92
Fluent	119.6	1.21	0.05	8.01	5.38	0.34	0.20	3.24	3.34	0.53
OpenFOAM	159.5	6.87	8.98	2.69	1.94	0.77	8.60	10.05	2.99	5.75
Fluent	159.5	2.44	5.66	8.11	6.31	5.65	3.55	4.81	3.08	3.68

The values from Table 7.16 are plotted in two bar charts for an enhanced understanding of the values. Figure 7.26 a) shows the differences in depth and Figure 7.26 b) shows the differences in velocity at prototype scale compared to model scale in the various flow rates and for the two solvers. The OpenFOAM results are denoted by “OF” and the Fluent results are those indicated with “FI”.

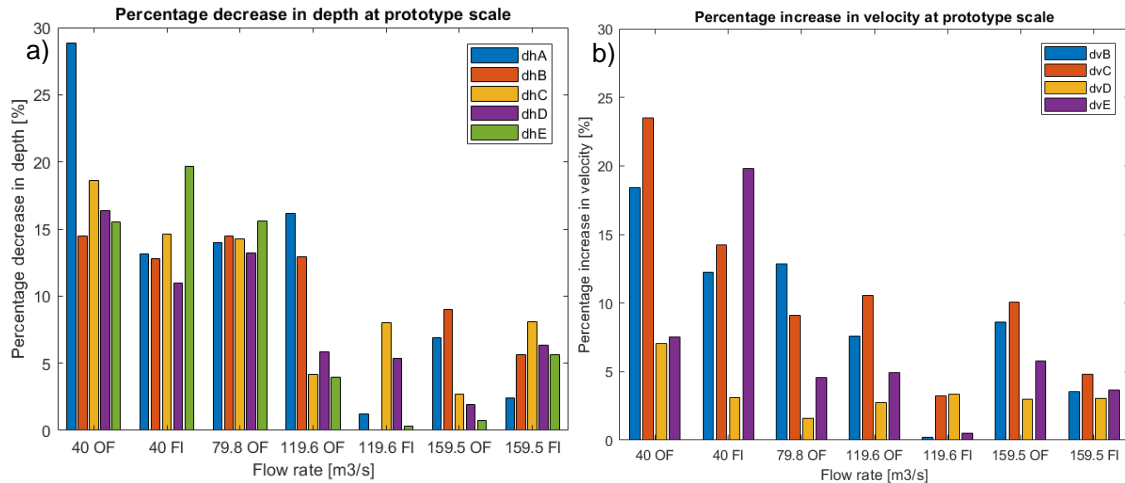


Figure 7.26: a) Percentage decrease in depth and b) percentage increase in velocity at the various sections for each flow rate and solver

The percentage difference at all sections were averaged for each flow rate and thus, an indicative value of general decrease in depth and increase in velocity in the prototype flow was obtained for each flow rate. On Figure 7.27 a) and b) the averaged percentage decrease in depth and increase in velocity are presented respectively, for all flow rates. In OpenFOAM, the decrease in depth consistently decreases for increasing flow rate. In Fluent, the decrease in depth also decreases for larger flow rates, with a remarkable variation between the decrease in depth at 40 m³/s and that at 119.6 m³/s. However, the percentage difference is not shown to be the lowest for the PMF case, which shows to be around the same order as that in the 119.6 m³/s flow rate, with a minor increase (3 % and 5.6 %). The averaged increase in velocity exhibits a similar trend to the decrease in depth. The OpenFOAM results exhibit a general decreasing trend for increasing flow rate, however it shows levelled values of velocity increase for flow rates from 79.8 m³/s to the PMF, with the lowest occurring at 119.6 m³/s. Similarly, the Fluent predictions also show the greatest increase in velocity for the lowest flow rate and it exhibits a distinct reduction of velocity difference at the two scales for the 119.6 m³/s, as previously observed. Following the same pattern as depth percentage difference, there is a small increase in velocity percentage difference in the PMF case compared to the 119.6 m³/s case, however the values are of the same order (1.8 % and 3.8 %). The slight increase in the percentage differences of the PMF flow rate compared to the 119.6 m³/s, is due to the larger displacement of the waves in the PMF compared to the other flow rates. It is important to note that the decreases in depth and increases in velocity are not showing a proportional change as they would be expected to follow to preserve flow continuity because of two reasons. The first one, the percentage differences at each section are calculated from averaged values of depth and velocity at the free surface at each section, and as observed in Chapter 6.10, in some sections the velocities and depths present significant variations within a section. The second reason is due to the fact that the values shown on Figure 7.27 a) and b) correspond to averaged values obtained from the average percentage difference at the various sections along the spillway channel. Therefore, they constitute a general indication of the overall flow differences in the spillway channel at the two scales.

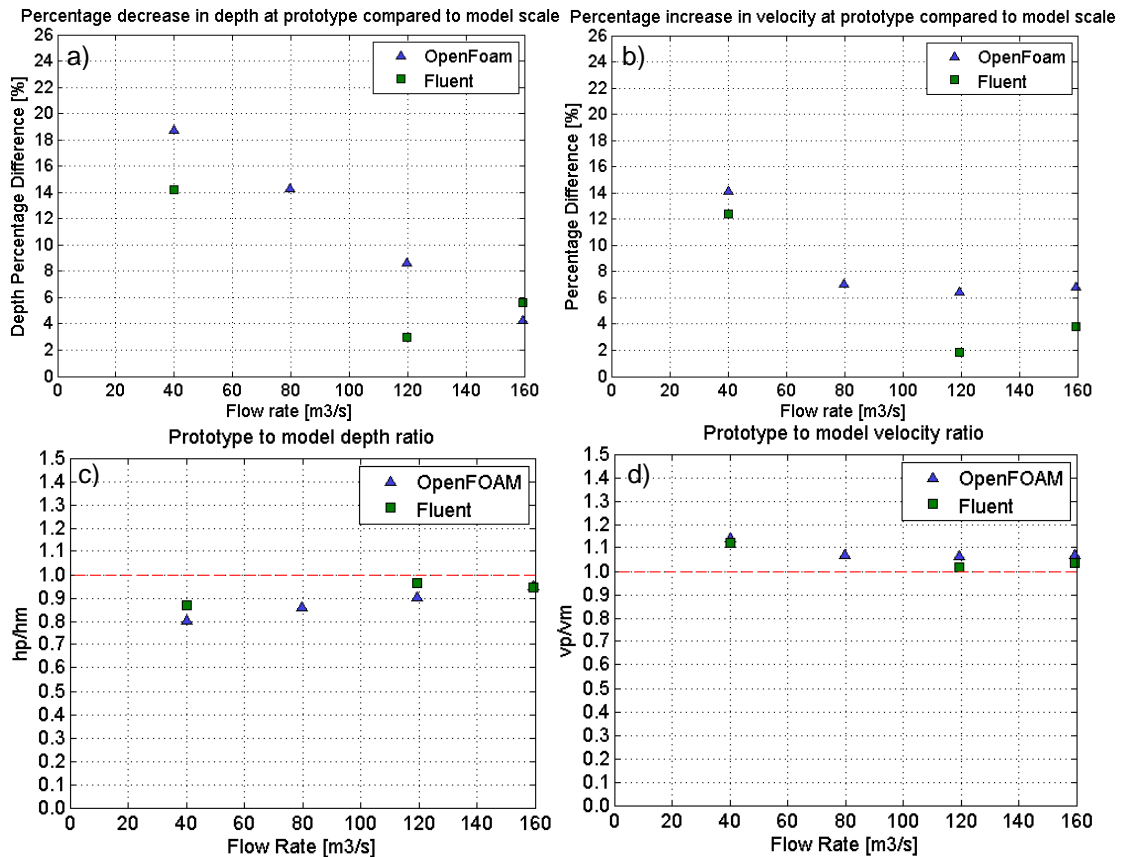


Figure 7.27: a) Percentage decrease in depth in the prototype with respect to model scale; b) Percentage increase in velocity in the prototype with respect to the model scale; c) Prototype-to-model ratio of water depth; d) prototype-to-model ratio of velocity

In order to obtain a further indication of the changes in the flow conditions at the two scales, the prototype-to-model ratio of interface depth and velocity was calculated at each section and the ratios at all sections for each flow rate were averaged to obtain a representative ratio. Figure 7.27 c) and d) present the averaged prototype-to-model depth and velocity ratios respectively. As previously indicated, the values of depth and velocity at the two scales converge for increasing flow rate. On Figure 7.27 c) it is observed that the depth ratios are always below 1, and they approach 1 for increasing flow rate, indicating the prototype depths are lower in all cases. The ratio with greatest difference to 1 is that obtained for the lowest flow rate. Figure 7.27 d) show the same trend in the velocity prototype-to-model ratio as has previously been observed, where the ratios converge to 1 for greater flow rates, and the largest difference occurs for the lowest flow rate. As expected, the velocity ratios are always greater than 1, demonstrating the values of velocity in the prototype are always greater. In order to examine the scatter of the ratios at each section for each flow rate, the prototype-to-model ratios of depth and velocity at each section of the channel were plotted and presented on Figure 7.28 a) and b). Results show the greatest scatter occur for the lowest flow rate, which presents the greatest deviation from 1 in both ratios. For increasing flow rate there is generally a decrease in the scatter in all sections.

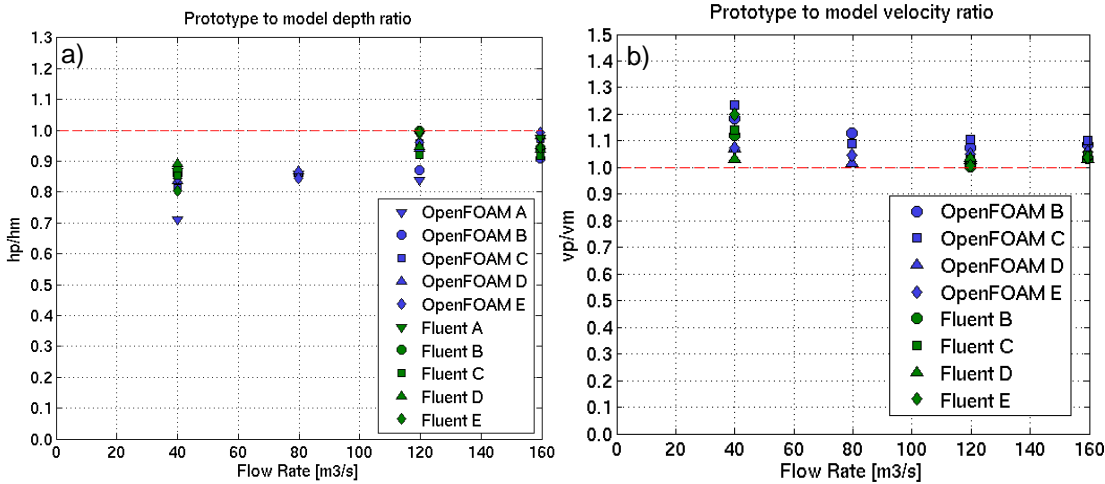


Figure 7.28: a) Prototype-to-model ratio of water depth at each experimental location; b) prototype-to-model ratio of velocity at each experimental location

The results obtained in the study conducted in this chapter are in line with what would be physically expected: for larger flow rates, the velocities and depths in the physical model are larger and hence the relevance of viscosity and surface tension forces is reduced in the Froude similarity physical model. For lower flow rates, the effects of viscosity and surface tension are greater, and since the Reynolds and Weber number are not matched, (and as observed, they are remarkably different at the model and prototype scale), these have effects on the flow which are not accounted for in the Froude law of similarity. For this reason, there is the need to establish limits to ensure the assumptions of such law of similarity are acceptable to model flows in a physical model of a spillway channel.

Although to the knowledge of the author, an analysis of such characteristics has never been conducted before, the available studies in the literature where a related work has been undertaken demonstrate well correlated results to those obtained here. Ercicum *et al.* (2016) conducted an experimental study with measurements of three identical physical hydraulic models at three different scales and also collected measurements from the prototype. In that study the rating curve of a PKW was computed with the three physical models and at prototype scale and it was found a decrease in depth in the full scale, which, in order to obtain the same flow rate, it had to be paired with an increase in velocity. This process was demonstrated experimentally to derive limits to minimise scale effects on the PKW rating curve. Here, the same process is confirmed numerically on the flow over the spillway channel. The observed discrepancies highlight the need for the derivation of refined limits to minimise scale effects related to depths and velocities in physical models of spillway channels. This task is undertaken and presented in Chapter 8.

7.4.6.2. Calculation of Prototype-to-model Ratios of Froude, Reynolds and Weber Numbers

The calculation of the Froude numbers at sections D and E of the spillway channel showed that for the lowest flow rate, the discrepancies between the Froude numbers in the prototype and model are greatest. For increasing flow rate, the Froude numbers at the two scales converge, becoming almost equal for 119.6 m³/s, with the prototype-to-model Froude number ratios being practically 1. For the PMF case they remain very close to the unity with a marginal increase. This

minimal increase is expected to be due to the change in flow conditions in the prototype and model due to the wave displacement, which is observed to be greater for the PMF than for the 119.6 m³/s case. In all cases the Froude numbers are larger in the prototype than in the model, and this is indicated in Figure 7.29 a) and b) where the prototype-to-model ratios of Froude numbers are shown at sections D and E respectively. The ratios are always greater than unity and they converge to it for increasing flow rate. The prototype-to-model Reynolds number ratios at the two sections are shown on in Figure 7.29 c) and d). As previously observed, the prototype-to-model ratios of Reynolds number are lower than the theoretical of 125 according to Froude law of similarity, and they approach this value for increasing flow rates. Because the Froude similarity is best accomplished for 119.6 m³/s, the Reynolds number ratio is also closest to its theoretical value for this flow rate. In the PMF, the OpenFOAM predictions exhibit slightly larger values than 125. Figure 7.29 e) and f) present the prototype-to-model Weber number ratio at sections D and E respectively. At section D results exhibit lower values than the theoretical of 625 for the 40 m³/s and 79.8 m³/s and, in the same way as the Reynolds and Froude ratios, they approach the theoretical for 119.6 m³/s and the PMF. At section E, there is also agreement between the ratios predicted with the two solvers, with the Fluent 40 m³/s presenting the greatest values. This is expected to be due to the greater discrepancies between prototype and model, previously observed at this section.

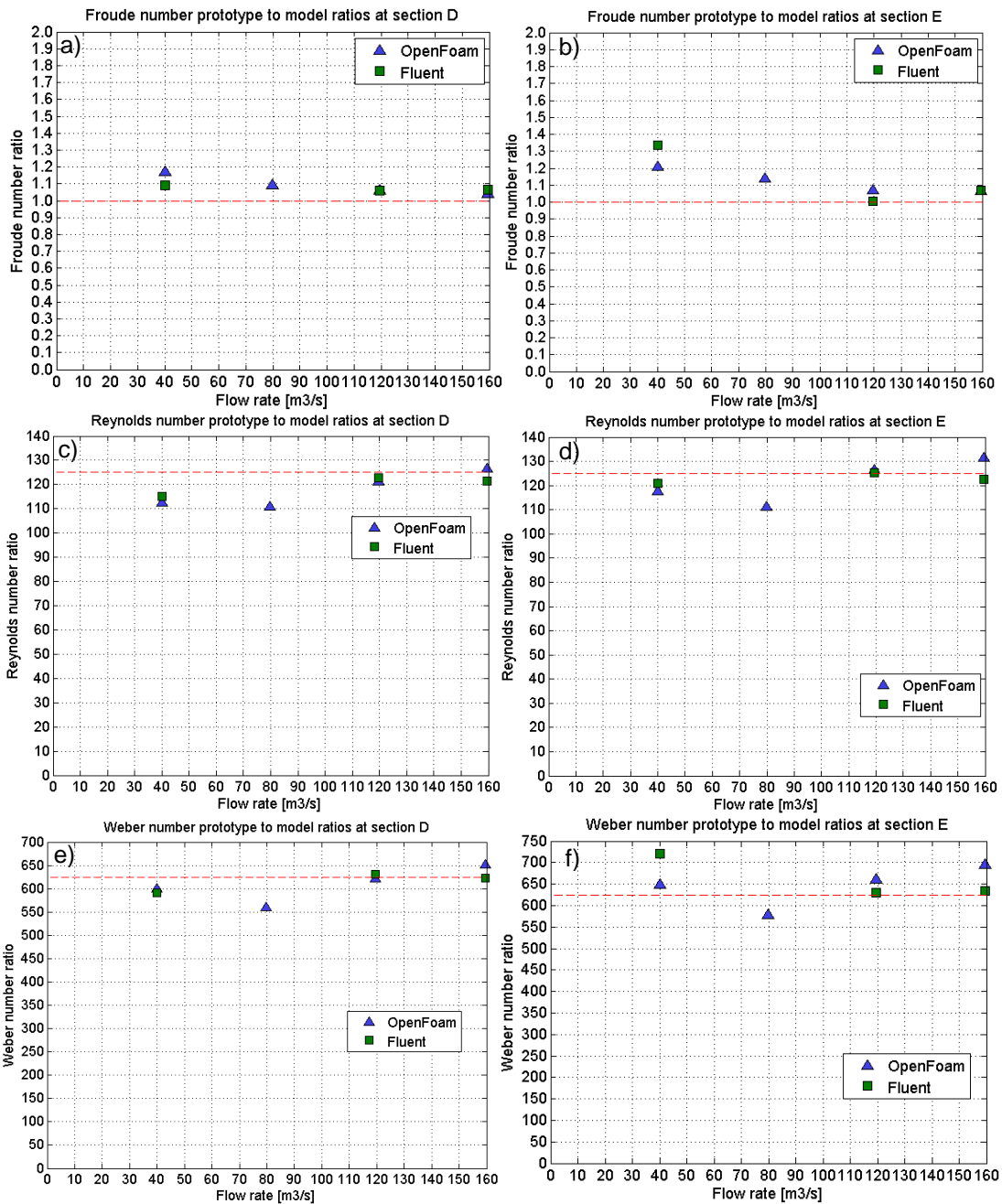


Figure 7.29: Prototype-to-model ratios of: a) Froude number at section D; b) Froude number at section E; c) Reynolds number at section D; d) Reynolds number at section E; e) Weber number at section D; f) Weber number at section E

7.4.6.3. Wave Elongation

Table 7.17 summarises the percentage elongation occurring in the three distances analysed x_1 , x_2 , and x_3 for all flow rates and in the two solvers. In Fluent, the elongation in the distances nearest to the weir x_1 and x_2 decreases for increasing flow rate, being lowest in the PMF. The distance x_3 does not present an evident trend and its elongation is larger for the PMF than for 40 m³/s. Therefore, the Fluent simulations show the flow characteristics near the weir are more similar at the two scales for the largest flow rates. The OpenFOAM simulations do not present a clear trend between flow rate and elongation of the waves.

Table 7.17: Percentage of displacement in the distances x_1 , x_2 , and x_3 for all flow rates

	40 m ³ /s Percentage Elongation [%]			79.8 m ³ /s Percentage Elongation [%]			119.6 m ³ /s Percentage Elongation [%]			159.5 m ³ /s Percentage Elongation [%]		
	x_1	x_2	x_3	x_1	x_2	x_3	x_1	x_2	x_3	x_1	x_2	x_3
OpenFOAM	20.9	18.9	20.5	28	11.5	15.2	22.2	19.2	25	33.3	36.2	41.8
Fluent	10	9.1	5.4				10	6.3	0.8	5.6	4.5	7.5

The elongation percentages in Table 7.17 are presented in form of a bar chart in Figure 7.30. Although there is no defined trend in the OpenFOAM elongation predictions, elongation is approximately 20% in the two lowest flows, slightly increasing for the 119.6 m³/s and being the largest in the PMF. The values of elongation predicted by Fluent generally decrease for increasing flow rates ranging from 8 to 6%, with the distances nearest to the weir, (x_1 and x_2) reducing for the PMF case.

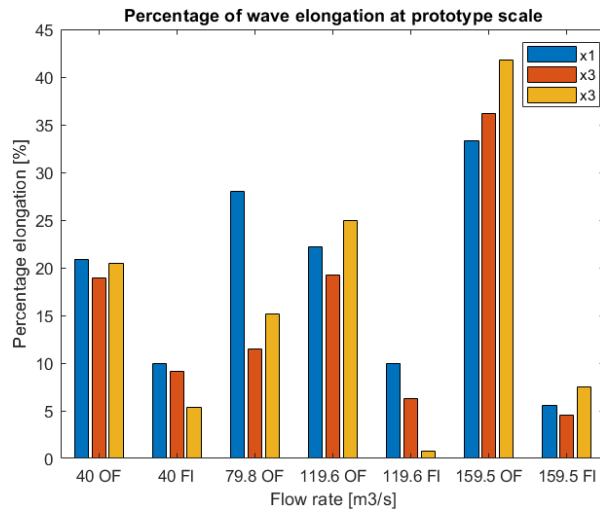


Figure 7.30: Percentage elongation of distances x_1 , x_2 and x_3 in the cross-wave configuration for each flow rate and solver

As previously discussed, OpenFOAM exhibits the largest elongation in the PMF case. This is expected since at physical model scale the OpenFOAM simulations demonstrated a significantly compressed (and less accurate) cross-wave configuration in comparison to that in Fluent. The sensitivity analyses confirmed that OpenFOAM performs better at prototype scale than at model scale (being less sensitive to numerical implementations), providing predictions of wave features closer to those from Fluent. Consequently, the larger values of elongation that OpenFOAM presents for the largest flow rate are considered to consist in overestimations. The values of elongation predicted by OpenFOAM for 40 m³/s and 79.8 m³/s of around 20 % are judged to be credible since the wave structures predicted with this solver at physical model scale were accurate. Results therefore suggest, that it is highly possible that if a mesh of higher resolution was employed to model the two largest flow rates, and in particular the PMF, a similar percentage of elongation to that occurring in the two lowest flows would be predicted, i.e. approximately 20 %.

7.4.6.3.1. Flow Conditions in the vicinity of the Labyrinth Weir

It is probable that the elongation of the waves' crossing point distance x_1 immediately downstream of the weir is due to changes in the characteristics of the flow at the crest of the weir at the two scales. Such changes could induce variations in the wave behaviour downstream of the weir. If

this was the case, it would also agree with the fact that in the Fluent predictions, (which show greater performance) the elongation of the distances near the weir decreases for increasing flow rate. In order to examine the flow characteristics in the vicinity of the labyrinth weir crest, velocity and pressure contour plots were extracted along an upstream and a downstream weir crest. This analysis was conducted utilising the weir modelling domain (described in Section 6.2) which contains very high resolution surrounding the entire labyrinth weir. This investigation was predominantly performed in OpenFOAM since this solver presents the largest elongation of the waves in the prototype compared to the model scale. Velocity and pressure contours were also extracted from the Fluent simulations of two flow rates for comparison. Figure 7.31 shows the location of two planes perpendicular to the two labyrinth weir crests where pressure and velocity were extracted to investigate the flow characteristics at the two scales. These are the first upstream crest and the second downstream crest, referred to as *crest II* and *crest III* respectively.

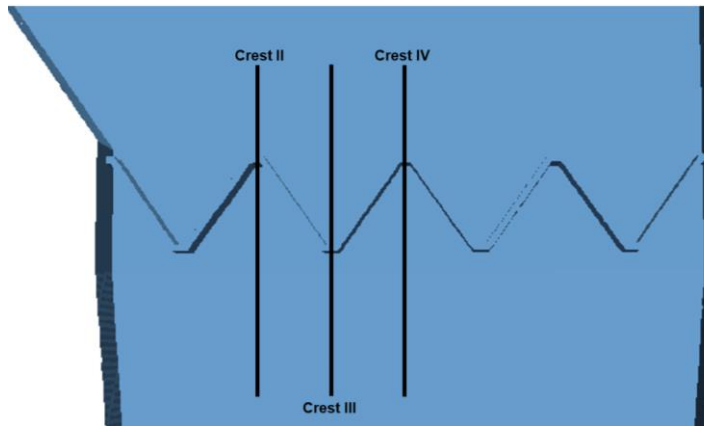


Figure 7.31: Location of planes perpendicular to weir crests II and III utilised to examine the flow conditions upstream and downstream the labyrinth weir

Planes perpendicular to crest II were extracted from the model and prototype scale PMF simulations from OpenFOAM and velocity and pressure contours were plotted. Figure 7.32 shows the velocity contours along the plane perpendicular to the upstream crest II at the two scales, where the displacement of the nappe is illustrated by the shape of the free surface. Results show that the velocity distributions between the reservoir base and the upstream wall of the weir exhibit significant differences at the two scales. Upstream the weir, the scaled case presents lower velocities, which are from 0 to 1 m/s. In the prototype scale, the velocities in this area are from 1 to 1.5 m/s. At the crest, the model scale simulations reveal velocities from 2 to 2.5 m/s while the prototype velocities at the crest range from 2.5 to 4 m/s. Just downstream of the crest, in the area surrounding the free surface, the prototype velocity is over 5 m/s and these high velocity values propagate downstream. The maximum velocities occurring at the scaled case located just downstream the weir next to the free surface range from 4 to 4.45 m/s. The shape of the vortex generated immediately downstream of the crest between the spillway base and the weir shows differences at the two scales, given the variations in the velocity distribution. At the model scale simulations, the centre of the vortex with lower velocities appears to be elongated in the vertical (water depth) direction, whereas in the prototype, the vortex appears to be elongated horizontally (in the flow direction).

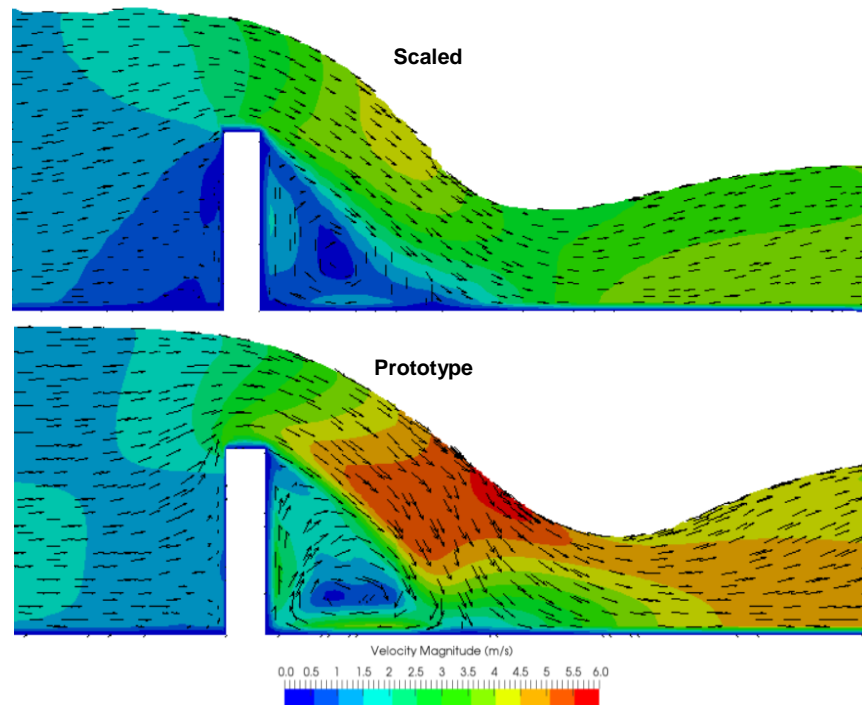


Figure 7.32: Planes along upstream crest II coloured by velocity contours and showing vectors with flow direction at the model scale and prototype scale for $159.5 \text{ m}^3/\text{s}$ in OpenFOAM

Figure 7.33 shows the contours of pressure at plane along crest II at model and prototype scales with an enhanced view of the contours occurring at the crest for each case. Results at model scale present higher pressures at the crest. Closer to the brink, the pressures are reduced because of the streamline curvature. At prototype scale the pressure distribution presents significantly lower values at the crest and the contour configuration is significantly stretched in the flow direction. At the downstream face of the weir, the prototype pressure contours present significant curvature and slightly higher values of pressure compared to the scaled case, which exhibits higher negative values. Negative values at the downstream face of the weir are expected when the nappe is not detached but clings on the weir (Crookston and Tullis 2010). The pressure contours at the weir crest and its vicinity present considerable changes at the two scales, which could explain the observed displacement of the nappe.

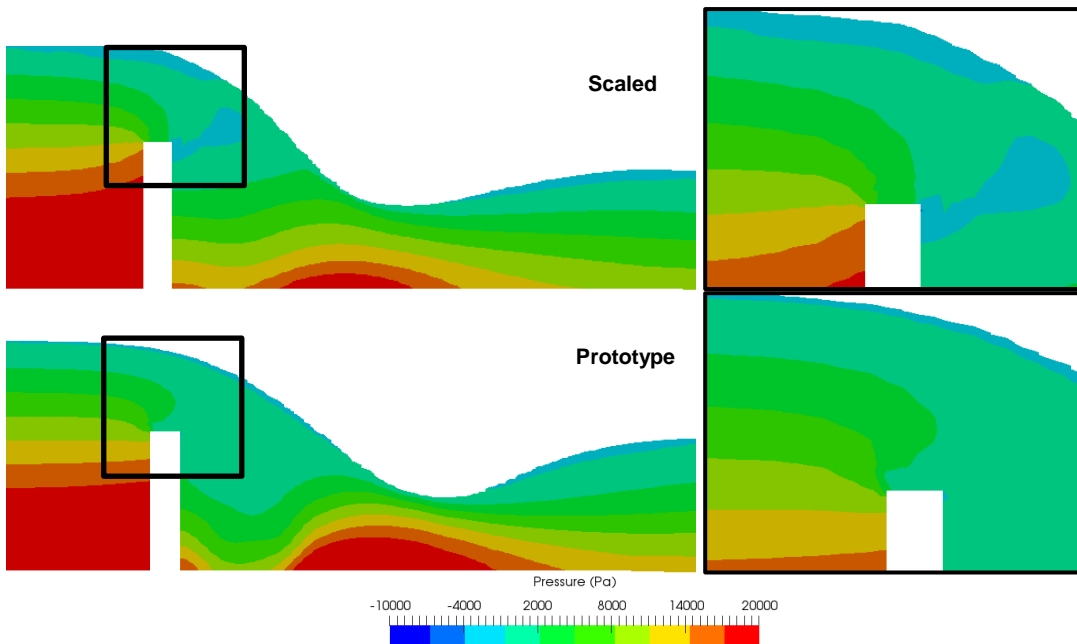


Figure 7.33: Planes along crest II coloured by pressure contours at plane through crest II at model and prototype scale with an enhanced view of the pressure contours at the crest for $159.5 \text{ m}^3/\text{s}$ in OpenFOAM

In order to examine variations in the flow behaviour at the upstream and downstream crests, the velocity and pressure contours were extracted at a plane perpendicular to the downstream crest III. Figure 7.34 shows a summary plot of the scaled and prototype velocity and pressure contours in the vicinity of crest III. Figure 7.34 a) and b) show the model and prototype scale velocity contours with vectors of flow direction. Figure 7.34 c) and d) show the model and prototype scale pressure contours in the area surrounding the downstream crest. The predictions at the two scales show a similar pattern to that observed in the upstream crest II. The velocities upstream of the weir crest at model scale are considerably lower than those at prototype scale, and hence the velocities at the crest are also lower. Immediately downstream of the weir, the prototype develops areas of higher velocity, both near the base of the spillway, with velocities up to 5 m/s and further downstream near the free surface up to 5.5 m/s . The maximum velocities in the scaled case occur further downstream on the spillway channel, with highest values of 5 m/s . Figure 7.34 c) and d) show that in this downstream crest, the pressure distributions are lower than those obtained at the upstream crest II, but similarly, the pressures are larger at model scale than at prototype scale. Downstream the weir the pressure contours at the two scales present small variations. Figure 7.34 a), b), c) and d) also reveal the nappe shapes at the two scales are significantly different at this section. In the scaled case the nappe bottom is considerably closer to the weir than that at prototype scale which appears to be displaced further downstream in the spillway channel.

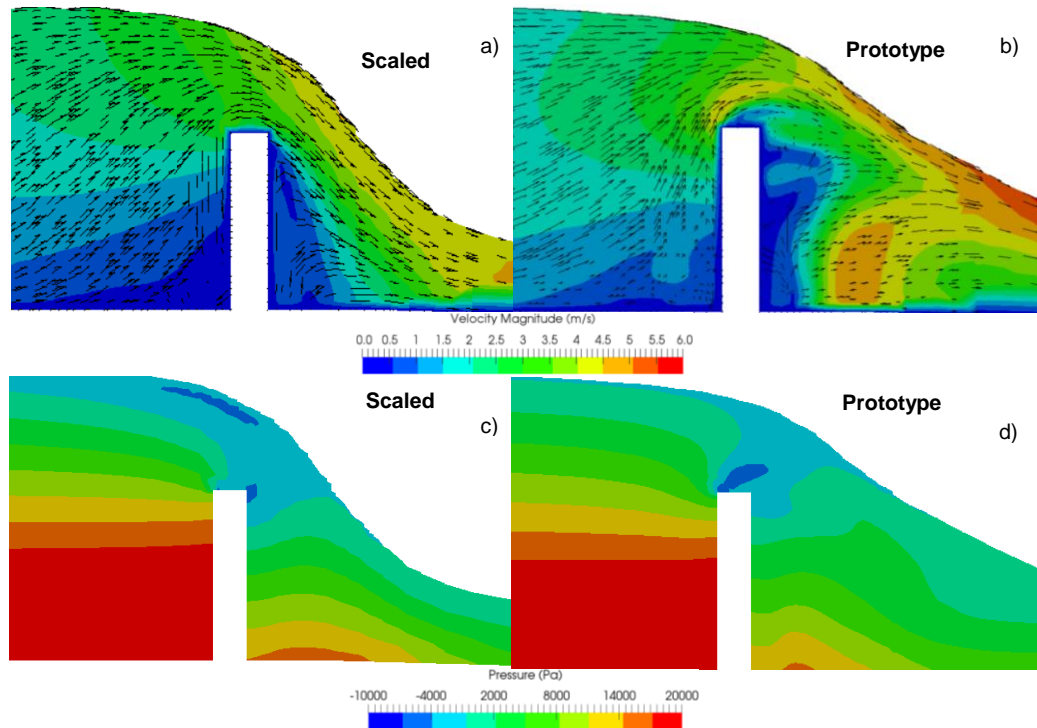


Figure 7.34: a) Plane along crest III coloured by velocity contours at model scale and b) at prototype scale; c) Plane along crest III in the area surrounding the weir crest coloured by pressure contours at model and d) at prototype for $159.5 \text{ m}^3/\text{s}$ in OpenFOAM

To further investigate the discrepancies in velocity and pressure at the two scales, dimensionless distributions of velocity and pressure were plotted for the flow at crests II and III. A sketch of a generic crest of the labyrinth weir is presented on Figure 7.35 where H is the total head, h is the water depth upstream the weir, and d is the water depth on the weir crest.

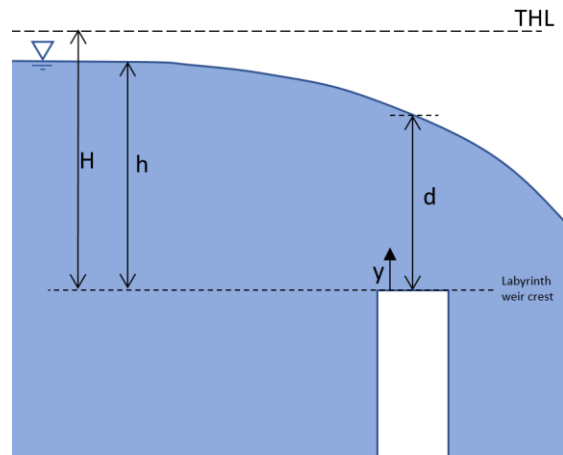


Figure 7.35: Sketch of a generic labyrinth weir crest

The pressure distribution at the weir crest was normalised by dividing by the hydrostatic pressure. The water depth of the points where velocity and pressure were extracted, y , was normalised with the depth at the crest d . Normalised velocity plots at the crest were obtained by dividing the velocity values by the maximum velocity occurring in the crest profile. Figure 7.36 shows the dimensionless distributions of pressure and velocity of the flow over crests II and III for $159.5 \text{ m}^3/\text{s}$. Figure 7.36 a) and c) demonstrate that as previously observed in the pressure contours, the pressure distribution obtained in the scaled simulations shows larger values at the crest base. Consequently, the scaled pressure distributions present a profile closer to the hydrostatic. Figure

7.36 b) and d) show that the prototype velocity distributions of the flow over the two crests present higher values at the crest base.

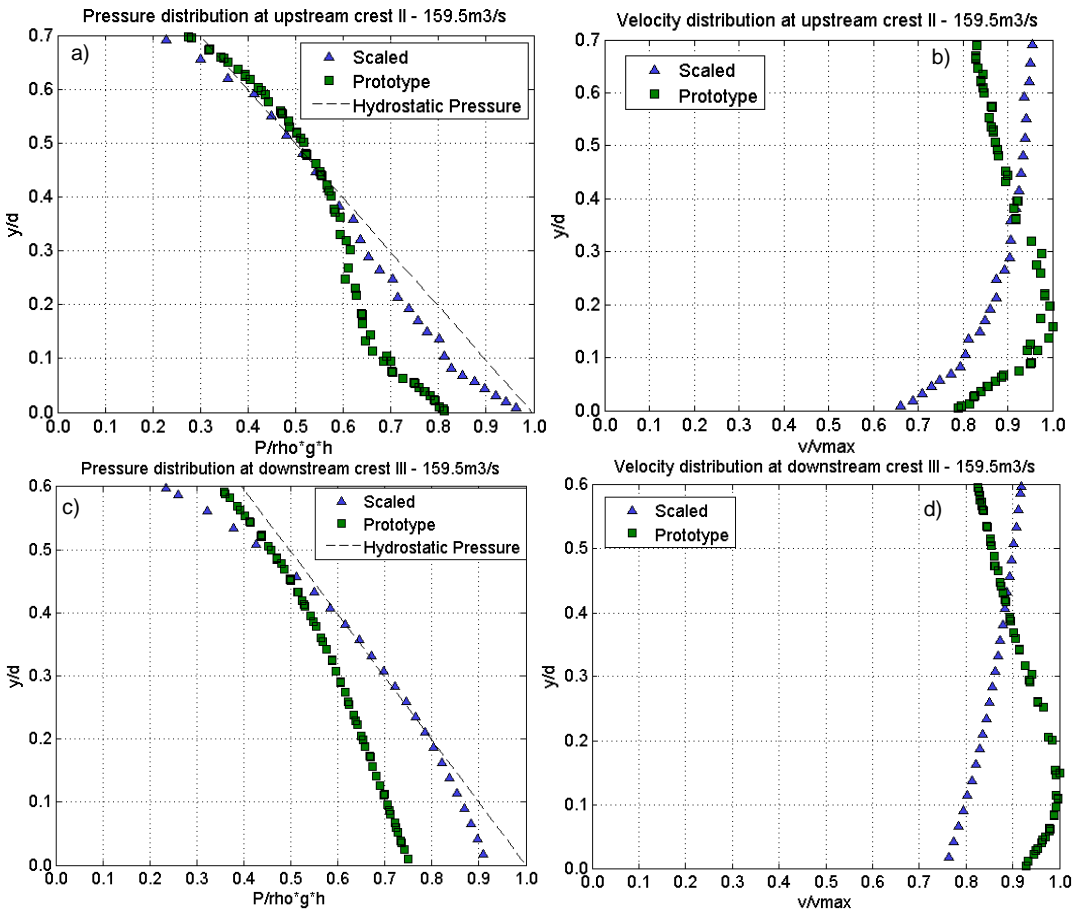


Figure 7.36: a) Pressure distribution and b) velocity distribution of flow over crest II; c) Pressure distribution and d) velocity distribution of flow over crest III for 159.5 m³/s in OpenFOAM

The comparison of pressures and velocities was also conducted with the lowest flow rate, 40 m³/s in order to investigate whether a relationship exists between the discrepancies at the two scales and the size of the flow rate. Figure 7.37 shows the velocity and pressure contours at a plane along upstream crest II at the two scales. It is observed that the nappe behaviour presents changes at the two scales, where the upstream head above crest is higher and the velocities are lower in the scaled case. Similarly to the 159.5 m³/s case the velocity contours in the vicinity of the crest show higher values at prototype scale. The model scale simulations present values from 0 to 1 m/s just upstream the weir and those at prototype scale are from 1 to 1.5 m/s. At the weir crest the velocity contours range from 1 to 2.5 m/s in the scaled case and from 1.5 to 3 m/s at the prototype scale. Downstream the weir crest the prototype velocities reach values higher than 4.5 m/s while the maximum velocities at the model scale are 4 m/s. In addition, at model scale the velocity vectors present almost a vertical direction while those at prototype scale appear to be more horizontal, and hence moving the wave crest further downstream. Figure 7.37 c) and d) show the pressure contours at the weir crest present slightly larger values at model scale than at prototype scale. At the weir downstream wall next to the crest, the pressures at the two scales present negative values and these are slightly larger at model scale.

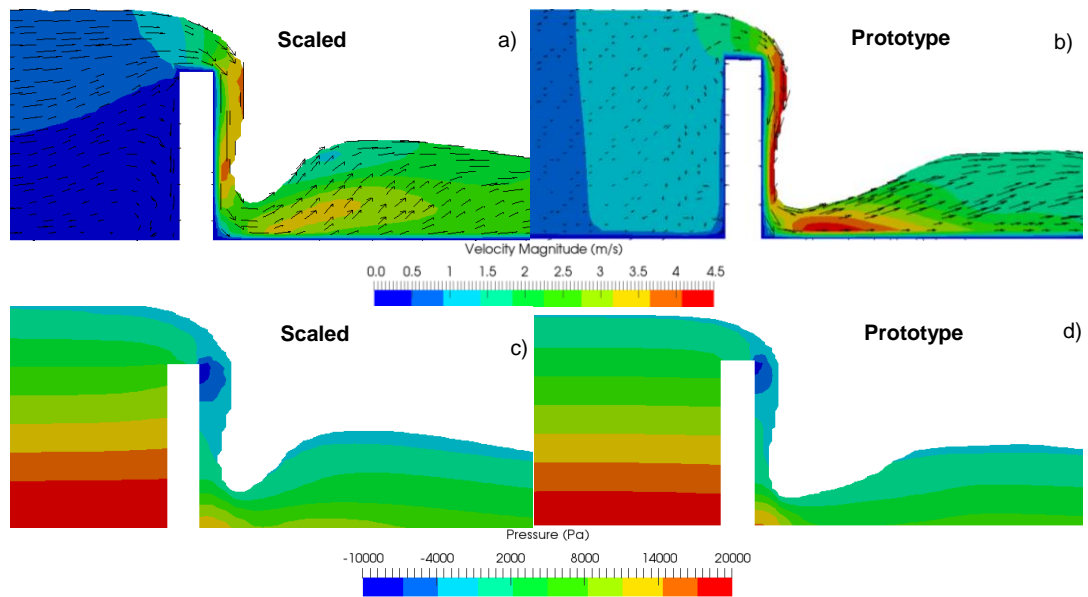


Figure 7.37: a) Plane along crest II coloured by velocity contours at model scale and b) at prototype scale; c) Plane along crest III in the area surrounding the weir crest coloured by pressure contours at model scale and d) at prototype scale for 40 m³/s in OpenFOAM

Pressure differences at the two scales appear to be moderately higher in the PMF case but generally of similar order in the two flow rates. Therefore there is no distinct trend observed between the discrepancies of flow situation at the two scales and the flow rate size.

Velocity and pressure contours predicted with Fluent were extracted along crest II for 40 m³/s and 159.5 m³/s cases for comparison. The Fluent predictions present less elongation for all flow rates and hence less differences in the velocity and pressure profiles at the two scales are expected. Figure 7.38 shows the velocity and pressure contours predicted with Fluent at model and prototype scales along crest II for 40 m³/s. In this case the differences in the flow conditions at the two scales are smaller than those observed in OpenFOAM. The main discrepancies consist in the lower velocities in the reservoir at model scale, which cause larger heads over crest. However, the scaled simulations present slightly larger velocities on the nappe and immediately downstream of the weir compared to prototype scale. As previously observed in OpenFOAM, the predictions at the two scales present discrepancies in the wave profiles. The cross-wave crest appears shorter and higher at model scale and flatter and elongated at prototype scale. Similarly to OpenFOAM, the model scale predictions present differences in the pressure distribution at the crest, as well as slightly larger negative values at the downstream wall of the weir.

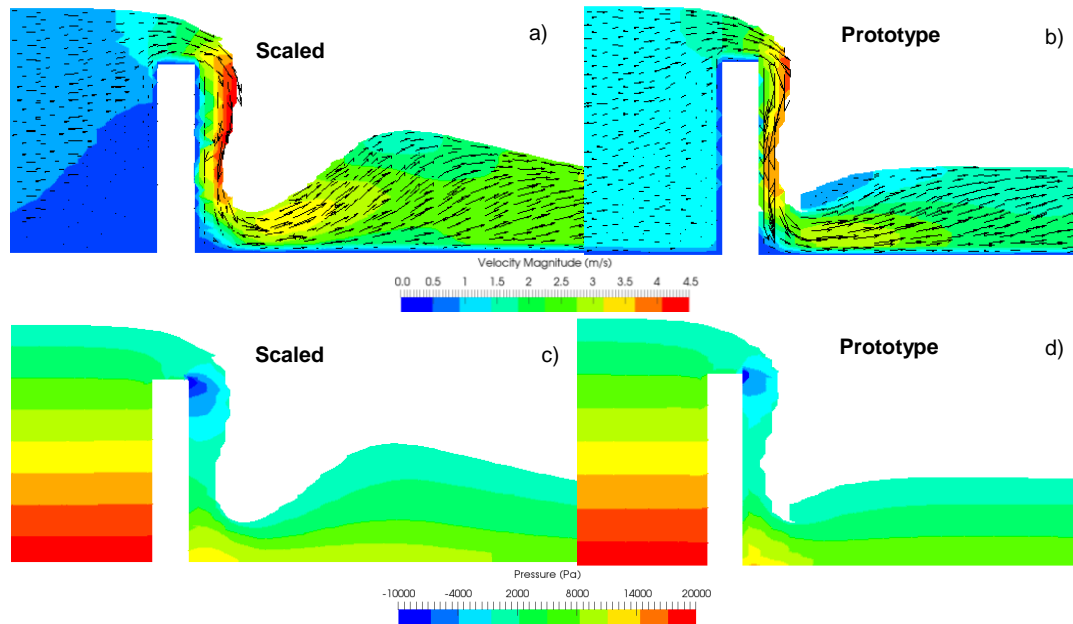


Figure 7.38: a) Plane along crest II coloured by velocity contours at model scale and b) at prototype scale; c) Plane along crest III in the area surrounding the weir crest coloured by pressure contours at model scale and d) at prototype scale for 40 m³/s in Fluent

Velocity and pressure contours at a plane perpendicular to Crest II were also extracted for 159.5 m³/s, these are presented on Figure 7.39. In this flow rate, there are considerably less differences between the velocity contours at the two scales than for 40 m³/s. This is especially evident at the crest and in the reservoir. The velocity contours at the nappe are very comparable at the two scales, with some minor differences in the distributions. The prototype values appear slightly lower at the downstream wall of the weir and near the base. However the prototype nappe presents a larger area of high velocity. The pressure contours are very comparable at the two scales, presenting only marginal differences at the downstream side of the crest, where there are marginally higher negative values at the prototype. The pressure distribution at the crest is generally consistent at the two scales. The nappe shape appears to be very similar at the two scales.

Therefore, these results confirm that the greatest differences in the flow characteristics at the two scales occur for the lowest flow rate. The Fluent predictions at the two scales are very comparable for greater flow rate, which agrees with the fact that scale effects are reduced for increasing flows.

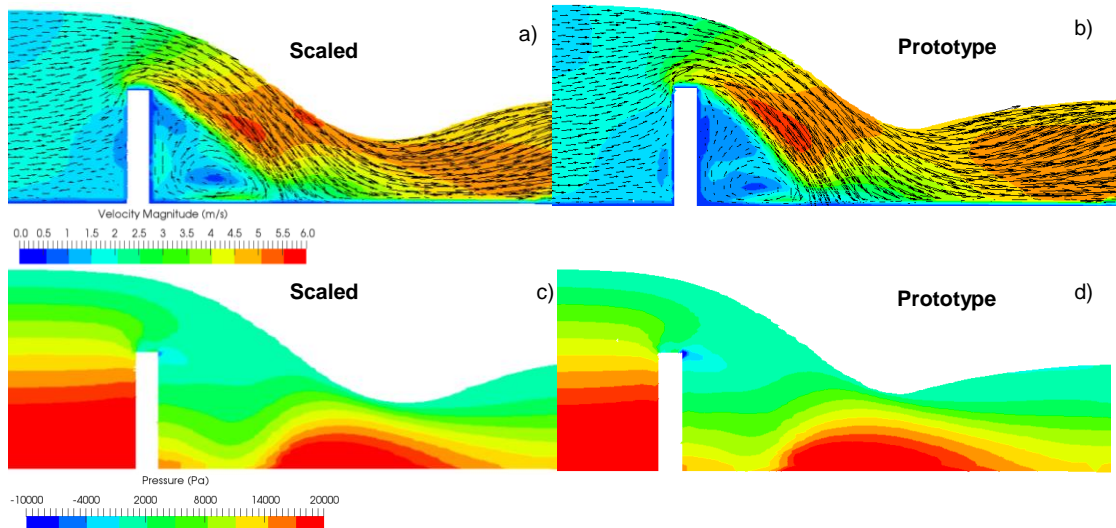


Figure 7.39: a) Plane along crest II coloured by velocity contours at model scale and b) at prototype scale; c) Plane along crest III in the area surrounding the weir crest coloured by pressure contours at model scale and d) at prototype scale for $159.5 \text{ m}^3/\text{s}$ in Fluent

Results indicate the two solvers provide different predictions of the flow characteristics in the vicinity of the weir which explain the different estimations of elongation of the waves occurring at prototype scale in the two solvers. OpenFOAM predicts more dramatic changes occurring at prototype scale with more significant increases in the nappe. The velocities predicted at physical model scale for the two flow rates are higher in Fluent. The resolution of the mesh of the weir domain is high, and hence the inaccuracies in the results from OpenFOAM (already observed with the predictions of the rating curve obtained with this mesh in Section 6.11) are not judged to be related to mesh resolution. Such less accurate predictions are likely to be due to the different implementations in the two solvers, i.e. the interface capturing scheme. However, further investigations would be required in order to determine the precise reason for the discrepancies in the predictions of the two solvers.

The analysis above also revealed that the increase in the nappe at prototype scale makes the impact angle of the weir jet on the chute to be lower at prototype scale. The lower impact angle may lead to lower energy dissipation and result in the observed higher velocities immediately downstream of the nappe at prototype scale.

The observed discrepancies in pressure at the crest of the labyrinth weir at the two scales have been observed in other studies. In Pfister *et al.* (2013a) the pressure distribution on the flow at a cylindrically crested PKW was extracted at different scales. In that study, it was found that the pressure distribution from small scale physical models presented larger values than those at prototype scale and the pressure distributions from small scale simulations were more resembling to the hydrostatic distribution. The results observed here are in line with these findings. Differences in pressure distribution at the weir crest at the two scales have been proven to be responsible for variations in flow behaviour downstream the weir and hence influencing the nappe characteristics (Ercicum *et al.* 2013b; Pfister *et al.* 2013a). In the literature, the observed differences in the crest pressure distribution have been confirmed to be the main cause of variations in the nappe trajectory at the two scales. The different crest pressures also have effects on the air entrainment in the nappe, resulting in a reduced nappe trajectory at model scale. In the

present case, the air entrainment which will be occurring at prototype scale is not fully captured with the numerical model. Therefore, the differences in aeration are not appreciated but the changes in crest pressure inducing different nappe shapes at the two scales are evident. Consequently, it would be reasonable to consider that the differences observed at the two scales downstream of the weir are induced by the different pressure distribution at the weir crest.

The most common minimum head over crest value recommended to ensure the same nappe behaviour in the prototype is reproduced in the physical model of sharp crested weirs has been defined to be 0.06 m (Ettema *et al.* 2000; Novak *et al.* 2010) and the same value was derived for PKWs (Epicum *et al.* 2013b; Leite-Ribeiro *et al.* 2012). These limits have previously been reviewed in Section 2.2.3.3. The heads upstream the weir in the physical model simulations are 0.02 m in Fluent and 0.03 m in OpenFOAM for 40 m³/s and 0.05 m in OpenFOAM and 0.06 m in Fluent for 159.5 m³/s. The available limits from the literature therefore suggest that it is likely that the heads over the weir at model scale are too low and hence there is presence of scale effects. This causes differences in the nappe behaviour at the two scales which correlate with elongation of the distances to waves' crossing points downstream of the weir. In Fluent the head over crest for the PMF case coincides with the literature limit of 0.06 m and presents minimal nappe displacement (and hence elongation) of the distance to the first crossing point x_1 .

In order to investigate the greater differences that OpenFOAM presents at the different scales (compared to Fluent), an investigation of the flow characteristics in the vicinity of the weir in OpenFOAM was conducted and is presented in Appendix A. In such study, the scale effects in the flow over the weir crest and immediately downstream of it are examined. This was undertaken with OpenFOAM PMF simulations on the weir domain at additional scales 1:50 and 1:10 to analyse the change in the flow conditions at the different scales.

7.4.6.3.2. Discussion Summary

The investigation conducted on wave elongation revealed several key findings. Results indicated that OpenFOAM presents greater percentages of elongation than Fluent. Considering the results obtained in Section 6.10, it was judged that the greater elongation predicted by OpenFOAM in the largest (and second largest) flow rate was a result of an overestimation. In the two largest flow rates, OpenFOAM at physical model scale was observed to provide a less accurate characterisation of the cross-waves configuration, with that appearing to be significantly compressed (especially in the PMF) compared to that in Fluent. Fluent provided a considerably more accurate representation of the cross-waves. The elongation predicted in OpenFOAM for the two smallest flow rates is approximately of 20 % and it is believed to be possible, since the predictions of these flows at physical model scale are accurate (and similar in the two solvers for the 40 m³/s). It is likely that finer mesh resolution in OpenFOAM to model the two largest flow rates at physical model scale would provide similar levels of elongation than for the two lowest flows (i.e. 20 %). Elongation in Fluent varies from approximately 8 % for 40 m³/s to 6 % for the PMF.

Possible causes of the observed elongation were investigated using the mesh containing the labyrinth weir modelling domain with higher resolution at the weir and approach channel than those utilised to model the spillway channel. Predictions at the two scales present different pressure and velocity distributions at the weir crest which are distinctly likely to be responsible for differences in the nappe shape at the two scales. The increased nappe observed at prototype scale has also been observed in the literature where it has been confirmed to be linked with changes in pressure distribution at the crest. In this study, these changes in the nappe behaviour are observed to be causing elongation of the waves, reflected in longer x_1 and x_2 distances at prototype scale. With Fluent the velocity and pressure plots at the two scales presented greater differences for the lowest flow rate than for the PMF, demonstrating an elongation of the distances x_1 and x_2 of around 8% for 40 m³/s and 5% for the PMF. In OpenFOAM, changes at the two scales occurring for the low and PMF flows were of similar order. This agrees with the hypothesis that a finer mesh would provide similar levels of elongation for all flow rates in OpenFOAM. The reason why OpenFOAM predicts approximately 10 % more elongation than Fluent is likely to be because of the solver implementations, especially the interface capturing scheme utilised in the two solvers. However, further investigations would be required to verify the precise reason for such discrepancies between the two solvers.

To conclude, the predictions from Fluent have demonstrated superior accuracy than those from OpenFOAM (evidence is shown in Chapter 6). In addition, the predictions from Fluent exhibit a decrease of the scale effects on the nappe shape for increasing flow rate, which is expected since the forces which are not matched at the physical model and prototype become negligible for larger flows. For the PMF, scale effects on the nappe shape are very small with the elongation of the first distances x_1 and x_2 of approximately 5%, which could be considered negligible. Therefore, the Fluent results present agreement with the literature that upstream head above crest over 0.06 m minimises scale effects on the nappe shape. Consequently, the outstanding item to investigate consists in the changes in the position of the waves occurring further downstream in the spillway channel. These are considered in Chapter 8.

7.5. Labyrinth Weir Rating Curve

7.5.1. Results

Similarly to the scaled case, prototype simulations were conducted using the weir modelling domain to model the four flow rates in the two solvers. Rating curves at prototype scale were extracted following the same procedure as described in Section 6.11 for the scaled case. The rating curves at the two scales are presented on Figure 7.40.

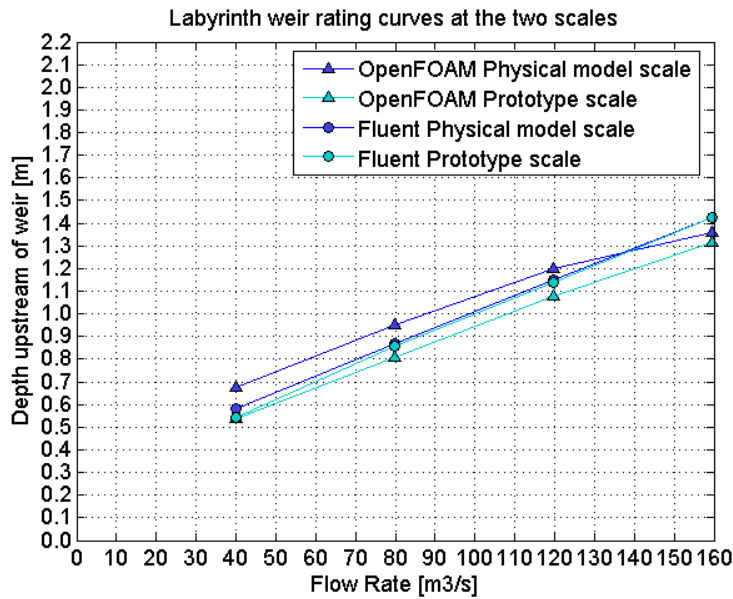


Figure 7.40: Labyrinth weir rating curve computed at model and prototype scale with the two solvers

Figure 7.40 shows that the rating curves at prototype scale present the same pattern observed in the prototype flows on the spillway channel. These consist in higher velocities and lower depths than those at model scale with discrepancies between the results at the two scales reducing for larger flow rates. The Fluent rating curves at the two scales present significantly less differences than those from OpenFOAM but both solvers present the same trend in the prototype scale predictions. For 40 m³/s the decrease in depth in the prototype scale is of approximately 6.3 % in Fluent and of 20 % in OpenFOAM. For a 159.5 m³/s the difference in depth predicted with Fluent is of 0.1 % and in OpenFOAM is of 3.2 %. These results are in line with previous studies. Matthew (1991) and Pfister *et al.* (2013a) identified the overestimation of water head upstream weir in Froude physical models for low heads over crest due to the effects of viscous and surface tension forces in the model.

7.5.2. Discussion on Existing Limiting Criteria

The scale effects in the prediction of weir rating curves due to the overestimation of the viscous and surface tension forces in Froude physical models have been investigated in a number of occasions in the literature. As water velocities and water depths increase, the effects of the viscous and surface tension forces decrease (Heller 2011). Several studies attempted to obtain guidelines and limitations to be applied to ensure the effects of such forces have minimal effect on results. A review of such studies has been presented on Section 2.2.3.1. In summary, limits to minimise scale effects in the rating curve of Froude physical models of a range of weirs lie between heads upstream crest of 0.02 m to 0.06 m. Erpicum *et al.* (2013b), Erpicum *et al.* (2016) and Pfister *et al.* (2013a) consist in more recent works with a weir configuration more similar to that in the present study, based on a PKW. In these studies it is recommended that the overflow head relative to the weir crest in the physical scale model should be at least 0.03 m. In addition, Tullis *et al.* (2017) conducted a similar experimental study with a single-cycle labyrinth weir at 3 different scales and recommends a dimensionless head ratio (normalised by the weir height, H/P) larger than 0.3. For the labyrinth weir of study this corresponds to a minimum head over crest of

0.02 m. Here, the minimum value of 0.03 m is taken as reference given the greater amount of studies supporting it for the case of non-linear weirs.

Table 7.18 shows a summary of the scaled heads over weir for the different flow rates. In the lowest flow rate of 40 m³/s the scaled head over the weir crest predicted with OpenFOAM is 0.03 m which coincides within the recommended limit. However, the depth value predicted by Fluent is slightly lower, with 0.02 m. The remaining flow rates, larger than 40 m³/s are all within the minimum head limiting criterion. For flows lower than 40 m³/s the heads would be too low and viscous and surface tension forces would have a considerable effect on results.

An alternative criterion to ensure scale effects are minimal would be to ensure the Weber number at the crest is above a minimum derived. The determination of a minimum Weber number is based on empirical criteria, as undertaken in Erpicum *et al.* (2016). Based on experiments on physical models of PKW at different scales and considering the minimum head derived to avoid scale effects on the rating curve (0.03 m), a minimum Weber number of 54 was obtained. It is important to bear in mind that in that study, the critical velocity was utilised in the calculation of the Weber number. Other studies like Machiels *et al.* (2011) or Ettema *et al.* (2000) suggested the physical model Weber number, should be higher than 50. These studies considered the mean flow velocity for the calculation of the Weber number. To verify whether the results are in compliance with such criteria, the Weber number at the weir crest of the model scale simulations was calculated using Eq. 2.5. A summary of Weber number at the crest of the weir computed with the two solvers for each flow rate is shown on Table 7.18.

Table 7.18: Summary of depth, velocity and Weber number at physical model scale

Variable	OpenFOAM				Fluent			
Flow rate [m ³ /s]	40	79.8	119.6	159.5	40	79.8	119.6	159.5
Head over weir [m]	0.03	0.04	0.05	0.05	0.02	0.03	0.05	0.06
We [-]	5.4	22.9	50.3	73.0	4.8	18.4	40.8	64.9

The calculated Weber numbers show that only the largest flow rate would adhere to the empirical criterion of minimum Weber number 54 and the second largest, 119.6 m³/s in OpenFOAM for the criterion of minimum Weber of 50. Such limits are based on empirical grounds as opposed to previous experiments on specific types of structures. For this reason, these provide a valuable indication of the order of the minimum Weber number of the flow which should be expected to minimise scale effects, but refined limits would be beneficial. This needs to be considered especially for 79.8 m³/s, which complies with the minimum head criterion but it does not appear acceptable given the difference in depth between the results at the two scales and the low Weber number. There is therefore the need to determine a limit to minimise scale effects in the rating curve of the labyrinth weir of study. This is conducted in Chapter 8.

7.6. PMF in the Comprehensive Domain

7.6.1. Introduction

In this section, prototype scale PMF simulations of the low and high tail water levels at prototype scale are conducted. Simulations of two tail water level scenarios were undertaken at prototype scale to examine how the spillway flow interaction with tail water compares with that at model

scale. Simulations were conducted utilising the same meshes as in the model scale which were scaled up to real scale. All results are presented in comparison with those from the model scale simulations.

7.6.2. Low Tail Water Level

An instant representation of the free surface at prototype scale for the low tail water scenario is shown with that at model scale on Figure 7.41 a). The instant representations correspond to the free surface at a time equal to 130 s when the system had become stable. The free surface boundary is approximated with a dashed red line at both scales on Figure 7.41 b). An enhanced view of the hydraulic jump formed when the spillway flow meets the tail water is presented on Figure 7.41 c).

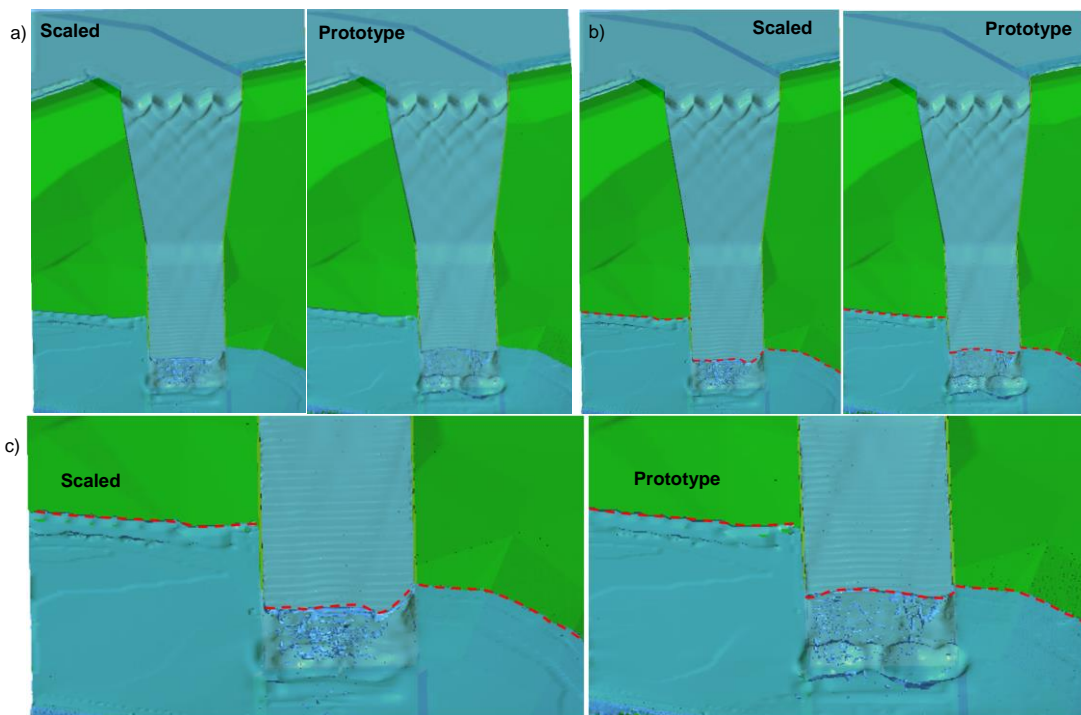


Figure 7.41: a) Instant representation of the free surface at model and prototype scale simulations and b) with red dashed lines indicating the location of the tail water; c) Enhanced view of the hydraulic jump

Figure 7.41 shows the tail water level at the surrounding terrain is at the same height at the two scales, since it was achieved by the boundary conditions of the weir downstream of the domain. However, the position of the hydraulic jump has moved upstream at the prototype scale. Despite the arbitrary nature of the hydraulic jump, involving velocity oscillations with time, the position of the hydraulic jump at both scales is maintained fixed with time once the system has become stable. In order to observe the characteristics of the hydraulic jump and tail water at the two scales, the free surface coloured by velocity contours was examined. Figure 7.42 indicates the tail water velocity contours present similar values at the two scales, particularly in the area next to the spillway sides. The velocity values shown at the tail water remain generally stable with time with only very minor variations in the vicinity of the jump. Downstream of the spillway channel and stilling basin the velocity presents changes in the distribution at the two scales. As previously noted, the velocities at the spillway channel are larger at prototype scale. This could be creating

changes in the velocity distribution in the tail water as well as changes in the position of the hydraulic jump at the two scales.

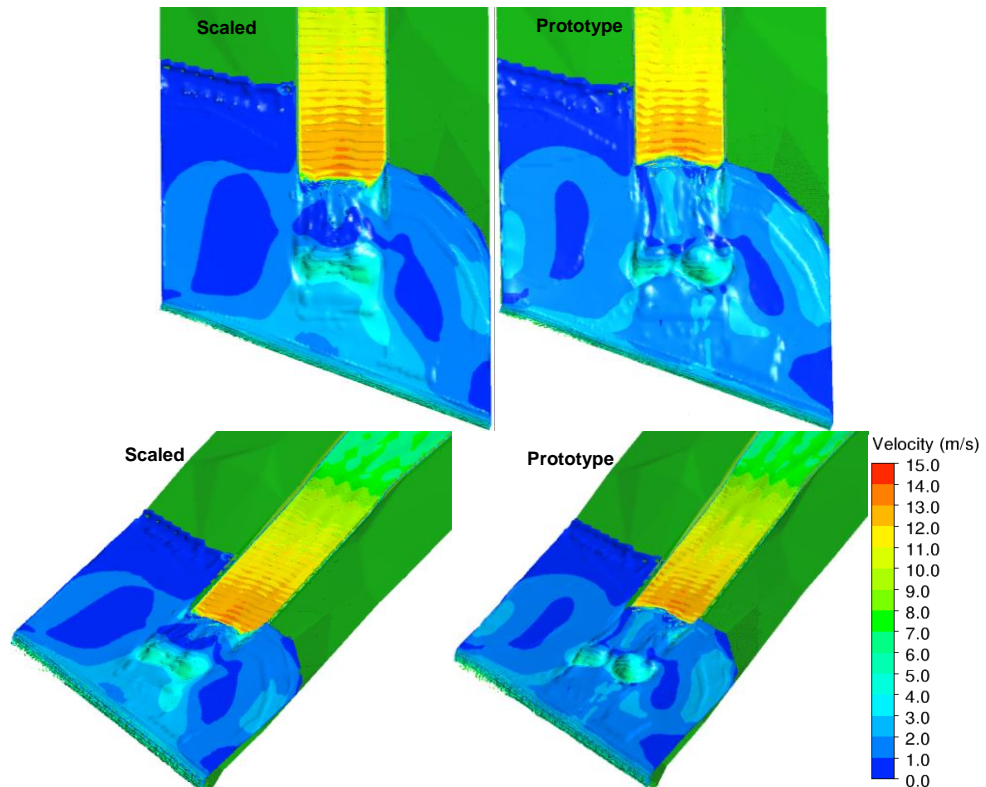


Figure 7.42: Instant representation of the free surface coloured by velocity contours at model and prototype scales from two different views

Similarly to the model scale simulations in Chapter 6, the flow characteristics were extracted at three planes along the spillway and hydraulic jump. These are planes 1, 2 and 3, where plane 2 crosses the channel in the centre through the baffle block and planes 1 and 3 are located 5 m to the right and left of the spillway channel respectively. Figure 7.43 indicates the location of the three planes.

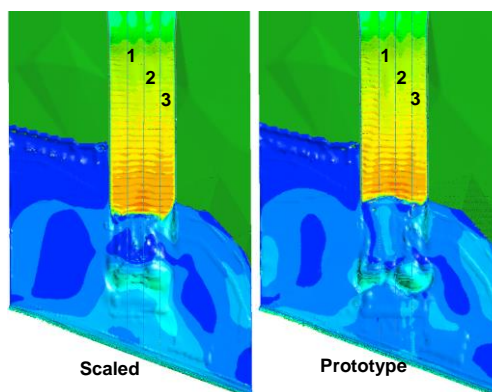


Figure 7.43: Location of planes 1, 2 and 3 in the spillway channel at model and prototype scales

Free surface depths and velocity profiles were extracted at the two scales at the three planes, these are presented on Figure 7.44 a) to e). In the three free surface depth sections in Figure 7.44 a), c) and e) it is observed that the prototype scale jump occurs approximately 5 m upstream of that at model scale. This is unexpected from the perspective that the tail water level downstream of the structure is located at the same height at the two scales (which corresponds to that needed to be achieved to model the low tail water scenario in the PMF, i.e. 133 m AOD).

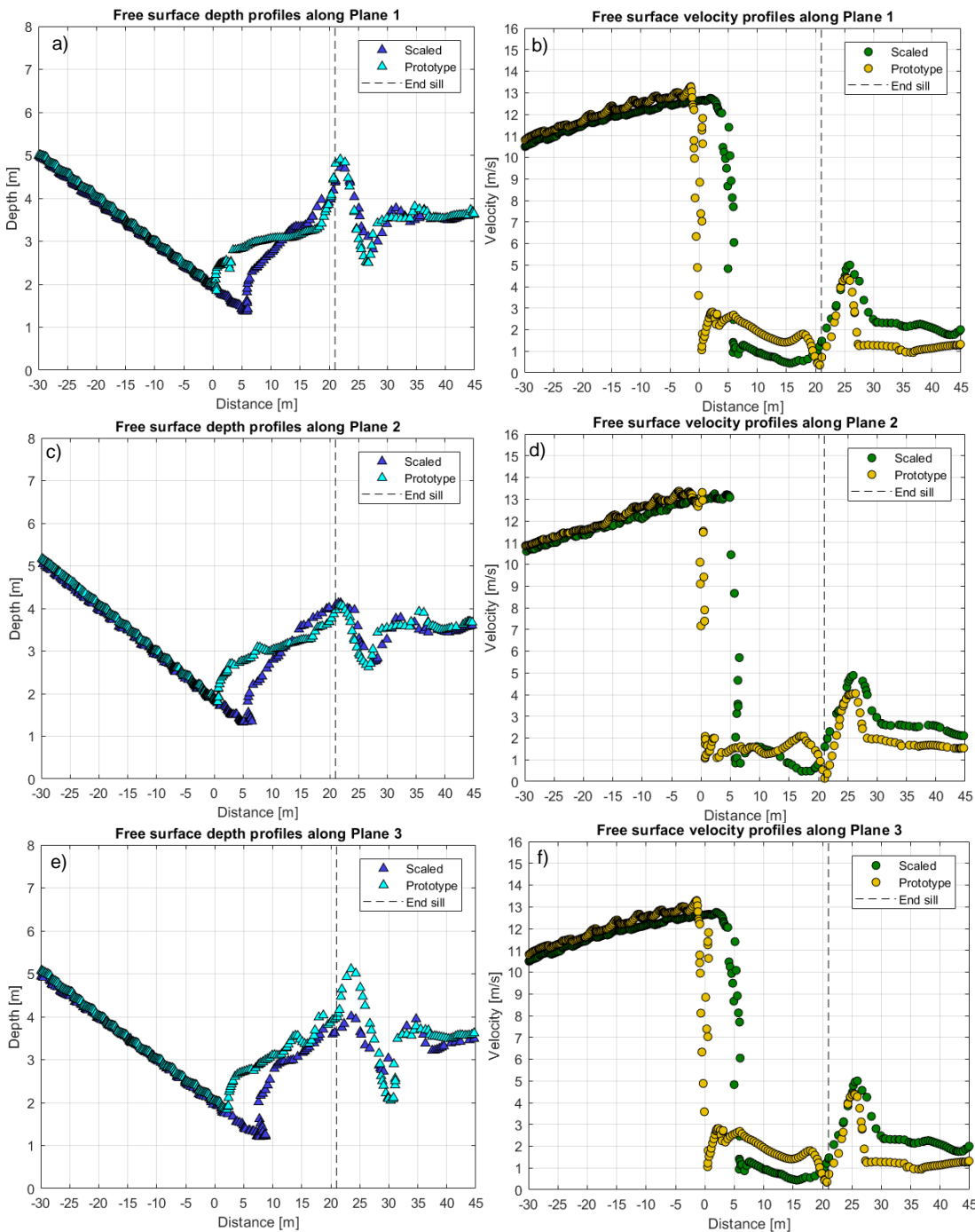


Figure 7.44: Free surface depth and velocity profiles at the two scales at: a) and b) Plane 1; c) and d) Plane 2; e) and f) Plane 3

Figure 7.44 b), d) and f) show the velocity in the spillway channel is slightly higher at prototype scale, (as previously observed in Section 6.10.4). The velocity profiles at the three sections present very comparable results. The prototype flow meets the tail water several metres upstream of the model scale flow and in the first section of the hydraulic jump the velocities are still higher at prototype scale. The two scales present the peak of velocity approximately 5 m downstream of the end sill. At the velocity peak, the model scale velocities are slightly higher than those at prototype scale at all sections. Immediately downstream of the peak the model scale velocities become around 1 m/s higher than those at prototype scale. Further downstream, the velocities at the two scales present a converging trend for increasing downstream distance from the hydraulic jump.

Figure 7.45 shows the time series of the free surface depth and velocity profiles at plane 2 in the vicinity of the hydraulic jump for 10 consecutive seconds at model and prototype scale. Results show that the position of the hydraulic jump at the two scales remains constant once the system is stable. Velocity variations with time in the vicinity of the jump are generally negligible. The minimal changes observed in the predictions of the free surface depth and velocity are due to the occurrence of air pockets in the vicinity of the hydraulic jump, which slightly vary with time.

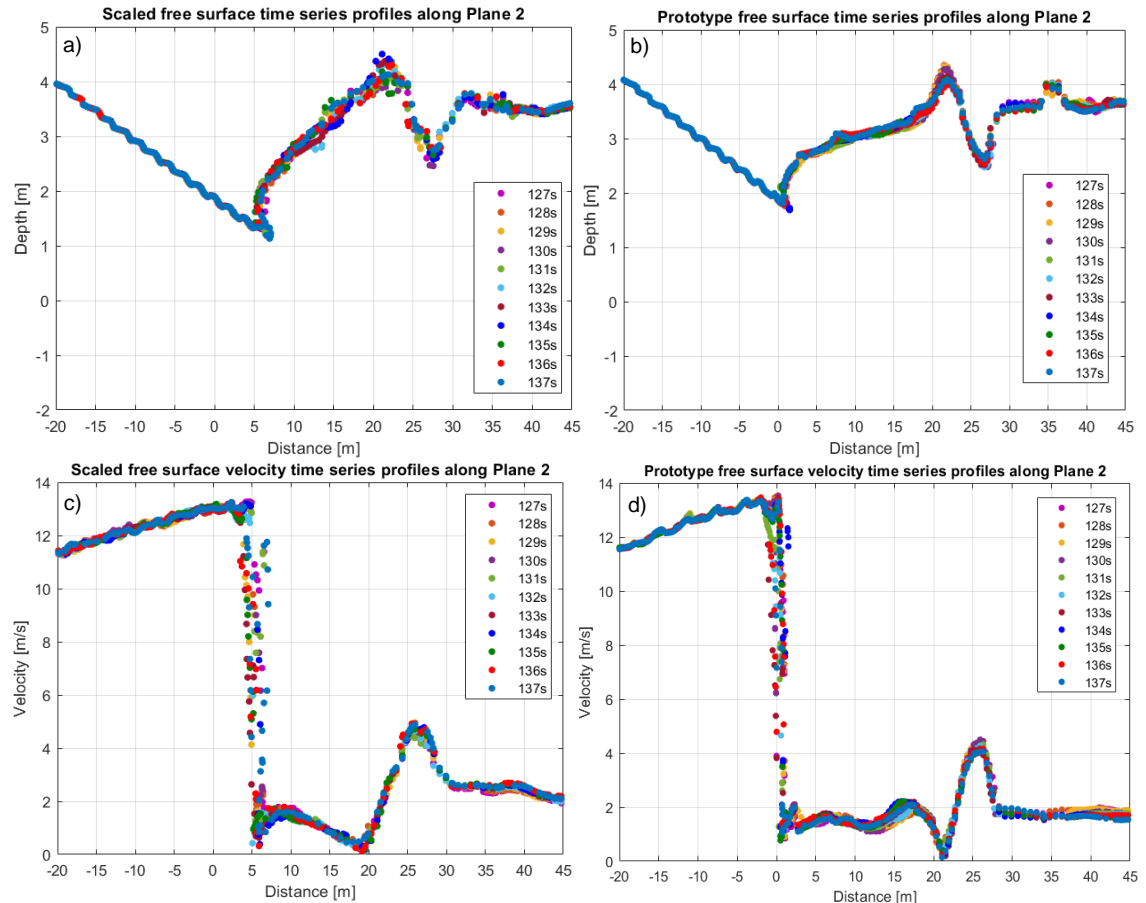


Figure 7.45: Hydraulic jump free surface time series profiles at plane 2 for: a) scaled case and b) prototype and free surface velocity time series profiles for c) scaled case and d) prototype

The water phase was extracted at the three planes and was coloured by velocity contours and plotted with velocity vectors at the two scales at 130 s once the system had become stable and velocity changes were minimal. These are presented on Figure 7.46. Results show at plane 1 the velocities at model scale are lower in the spillway channel and at the first section of the hydraulic jump. Downstream the jump the free surface velocities at prototype scale are lower, but these at the base of the terrain, immediately downstream of the end sill, are about 1 m/s higher in the prototype. The velocity vectors are similar at the two scales but immediately downstream of the end sill, the prototype scale predicts an area of higher velocity at the base of the terrain. The air pockets observed are not stable and present changes with every time step. Plane 2, located at the centre of the channel, presents higher inflow velocities at prototype scale but the velocity at the hydraulic jump indicates similar values at the two scales. Similarly to plane 1, the velocity at the base of the terrain downstream of the hydraulic structure, is slightly higher at prototype scale, but the values are not higher than 3 m/s. Predictions at plane 3 present similar velocity contours at the two scales but the prototype scale shows more vertical vectors, causing slightly higher

water height downstream the end sill. The velocities at the base of the terrain are very comparable at the two scales.

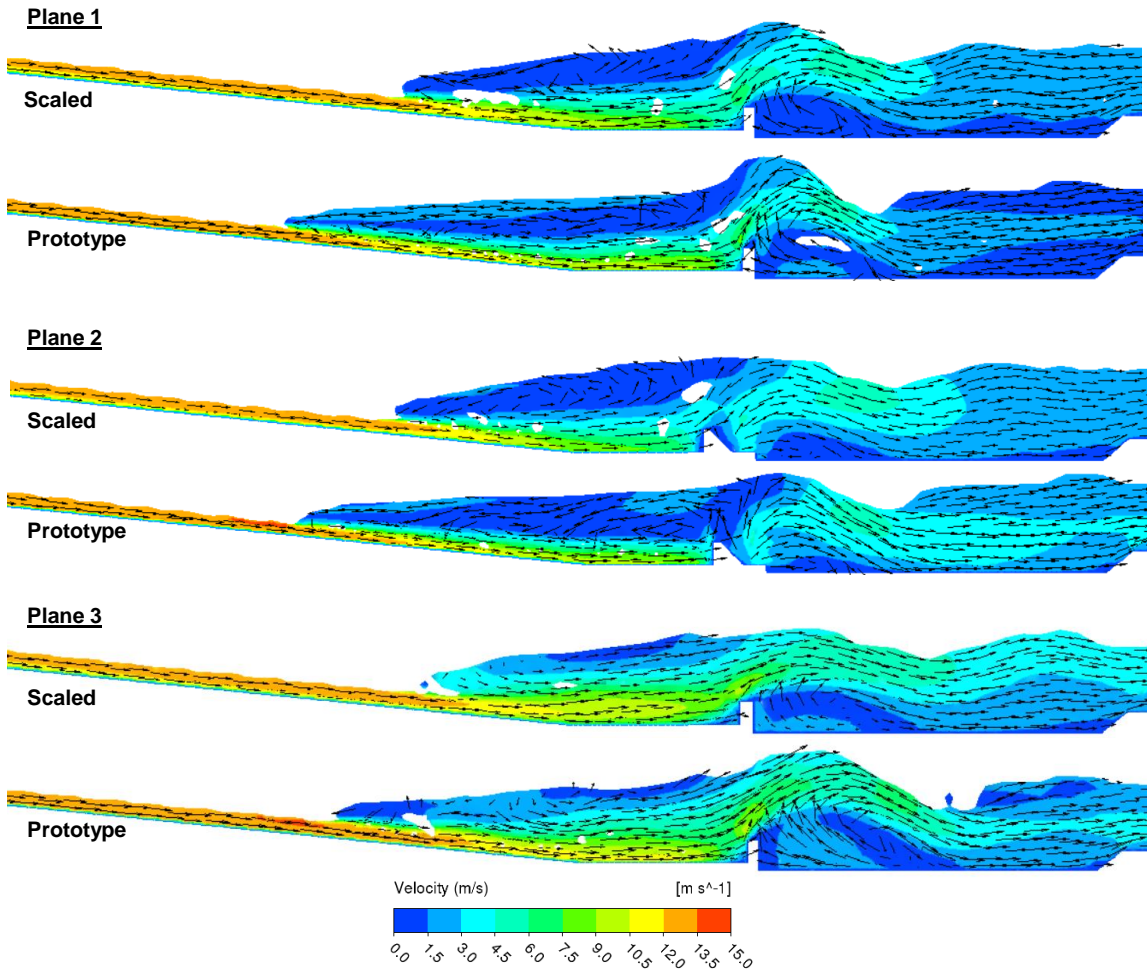


Figure 7.46: Water-phase profiles in the vicinity of the hydraulic jump showing velocity vectors and contours across Plane1, 2 and 3 at model and prototype scales

7.6.3. High Tail Water Level

The high tail water level was modelled at prototype scale and compared with that at physical model scale. An instant representation of the free surface at the two scales is presented in Figure 7.47 for a time equal to 290 s.

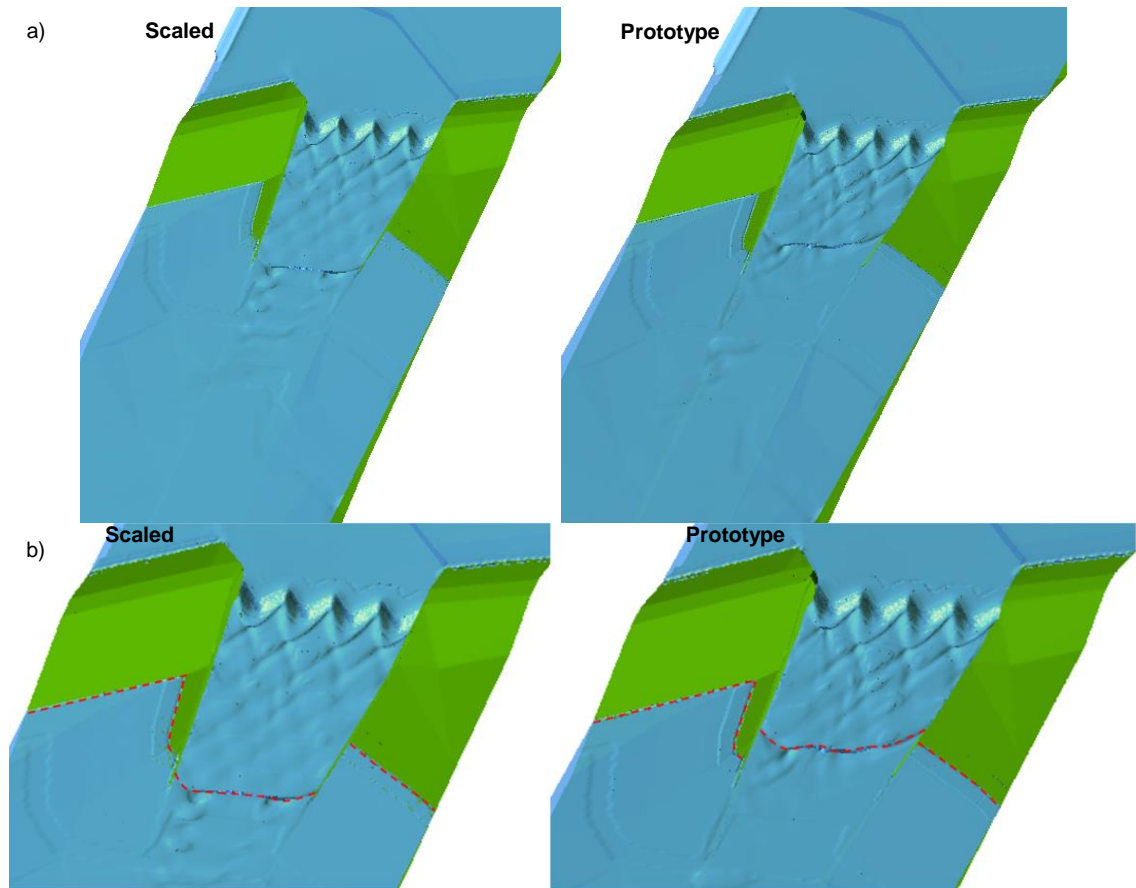


Figure 7.47: a) Instant representation of the free surface at model and prototype scale simulations and b) Enhanced scale of the hydraulic jump with red dashed lines indicating the location of the tail water

Figure 7.47 indicates that similarly to the previous case, the interaction between the spillway flow and the tail water presents different characteristics at the two scales. The tail water is at the same level at both scales, and this is observed by the position of the tail water surface in the irregular surrounding terrain. However, within the spillway channel, the hydraulic jump is located at a different point in the channel at the two scales. At prototype scale, the jump presents a more advanced position upstream of the channel compared to the scaled case. This is especially more noticeable on the left side of the spillway, but it also occurs on the right side. In addition, the shape of the hydraulic jump presents differences at the two scales.

Figure 7.48 shows the free surface coloured by velocity contours at the two scales from three different views. Figure 7.48 a) shows the free surface in plan view, and Figure 7.48 b) shows an enhanced view of the area where the spillway flow meets the tail water with the location of three planes of analysis. In the plots for the three planes, the point taken as $x = 0$ m corresponds to that of measurement location B and the $z = 0$ m coordinate is the base of the spillway at such location. Results illustrate the different position of the hydraulic jump at the two scales and the slightly higher velocity at prototype scale. At the tail water area outside the spillway channel on the surrounding terrain, both the velocity and the position of the tail water surface are equivalent at the two scales.

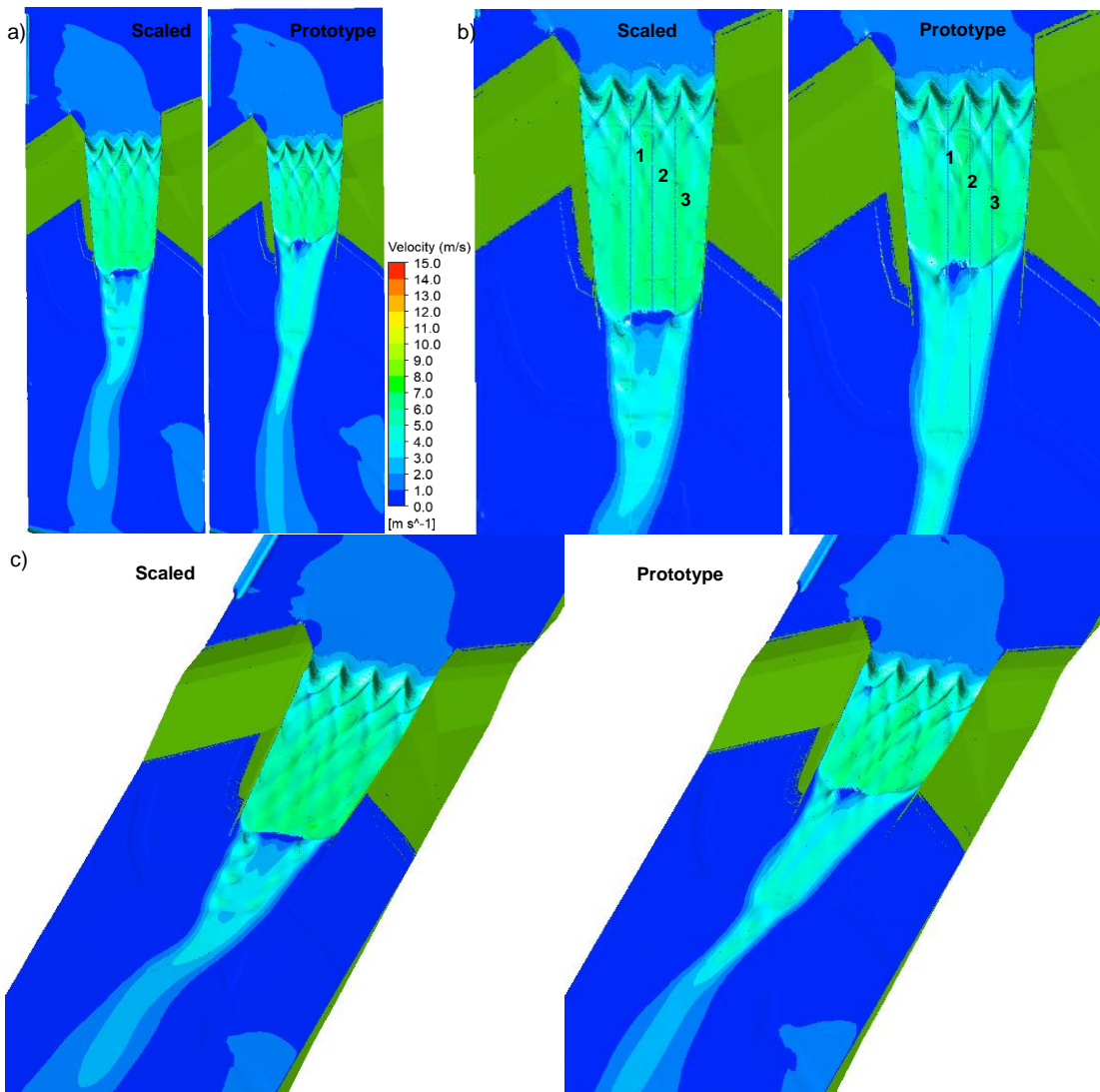


Figure 7.48: a), c) Instant representation of the free surface coloured by velocity contours at model and prototype scales from different views; b) Location of the three planes for analysis

Similarly to the previous case, free surface profiles of depth and velocity were extracted along planes 1 to 3 indicated in Figure 7.48 b). Free surface depth and velocity profiles at the two scales along the three planes are shown on Figure 7.49 a) to f).

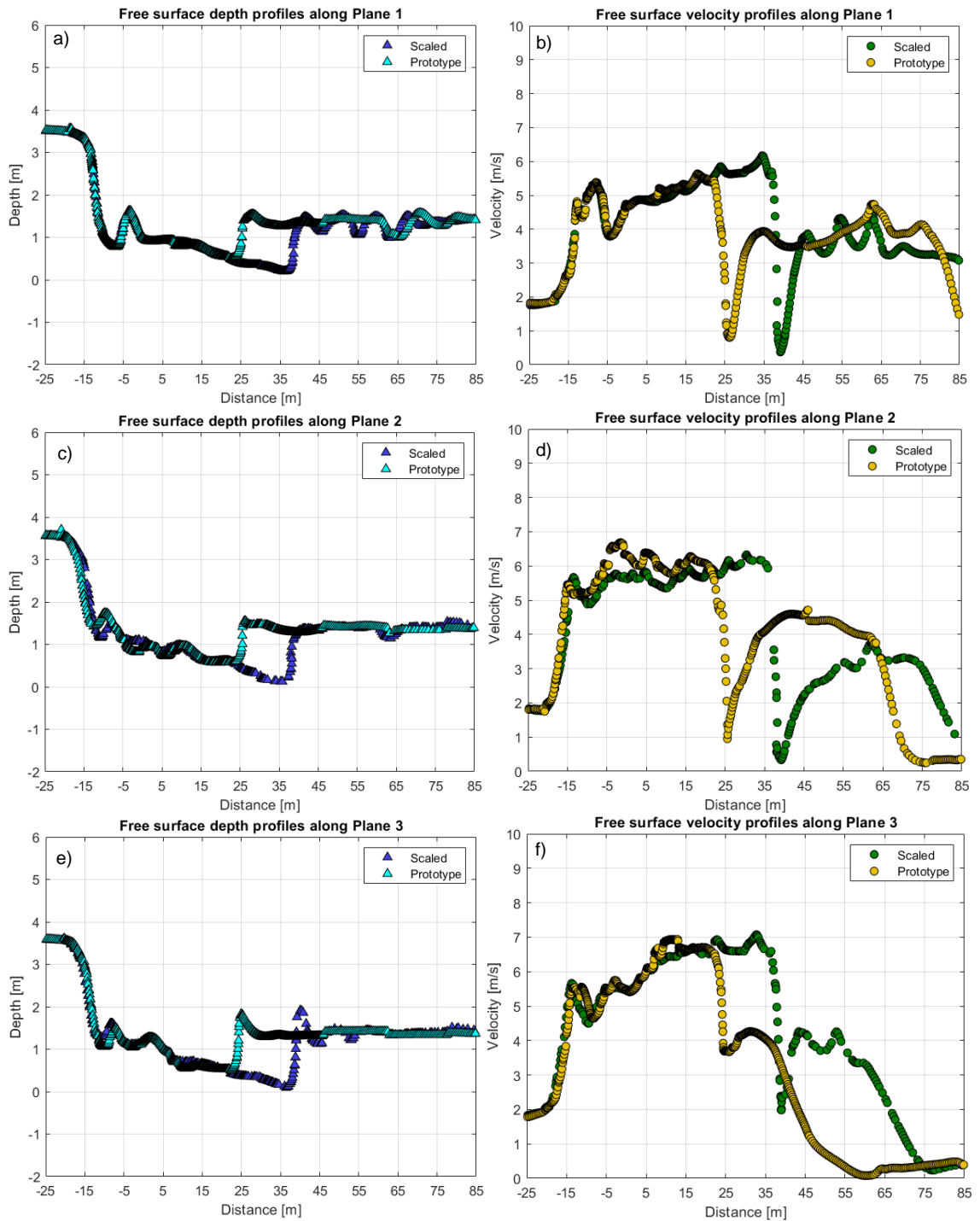


Figure 7.49: Free surface depth and velocity profiles at the two scales at: a) and b) Plane 1; c) and d) Plane 2; e) and f) Plane 3

Results show that at the three planes, the hydraulic jump at prototype scale occurs approximately 15 m upstream of that at physical model scale at the three planes. In the physical model scale simulations, the location of the hydraulic jump does not vary along the spillway channel width, remaining constant in the three planes at around 40 m downstream from the point taken as 0 m reference. The position of the prototype jump is also at a similar point in the three planes, approximately 25 m downstream from the reference 0 m point.

Velocities of the inflow in the spillway channel are similar at the two scales, only marginally higher at prototype scale. As observed in Figure 7.48 the free surface velocities at the tail water present

slightly different distribution at the two scales which is reflected in the plots along the three planes in Figure 7.49. Free surface velocities at the two scales vary with generally higher velocities at prototype scale but these appear to converge with increasing distance downstream from the hydraulic jump.

Free surface depth and velocity time series were extracted along plane 2 at the two scales. These are shown on Figure 7.50.

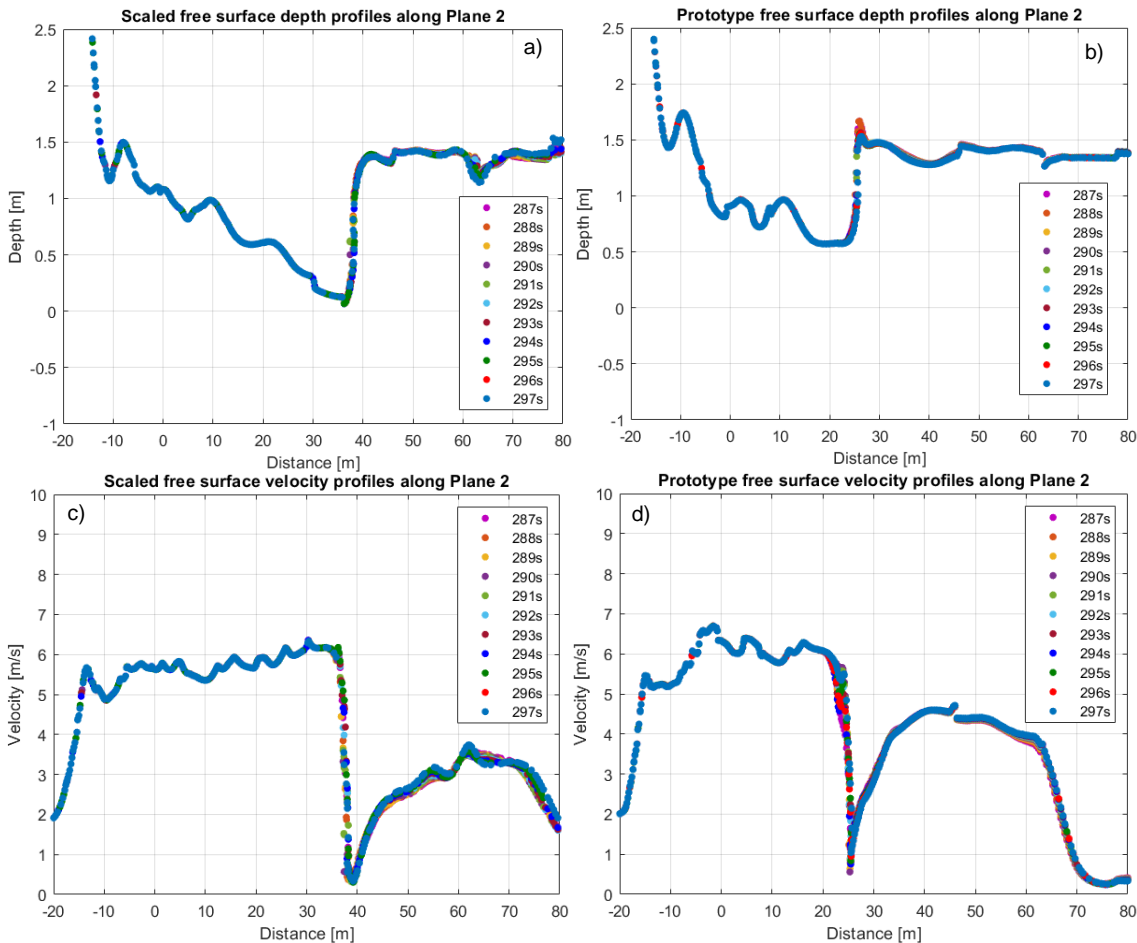


Figure 7.50: Hydraulic jump free surface time series profiles for: a) scaled case and b) prototype and free surface velocity time series profiles for c) scaled case and d) prototype

Figure 7.50 shows that the system can be considered stable from approximately 287 s at both model and prototype scales. As previously observed, the hydraulic jump at prototype scale occurs around 15 m upstream of that at model scale. In this case there is less variation between the results at each time than in the low tail water case since there is practically no presence of air pockets occurring in the hydraulic jump.

Figure 7.51 indicates the predictions of the water phase coloured by velocity and with velocity vectors indicated at planes 1 to 3 at the two scales. Results demonstrate the velocity vectors at the two scales are generally similar at planes 1 and 2 and they present some minor variations at plane 3. The previously observed upstream advancement of the hydraulic jump at prototype scale in comparison to the model scale is paired with slight changes in the velocity distribution at the two scales. At plane 1, the velocities at the base of the spillway are generally similar with only minor variations in the velocity distribution. At planes 2 and 3 the advancement of the hydraulic

jump at prototype scale appears to move the higher velocities further upstream and hence, the velocities around the first and second changes in gradient are lower at prototype scale. At the third section of the spillway channel, the velocities are comparable at the two scales.

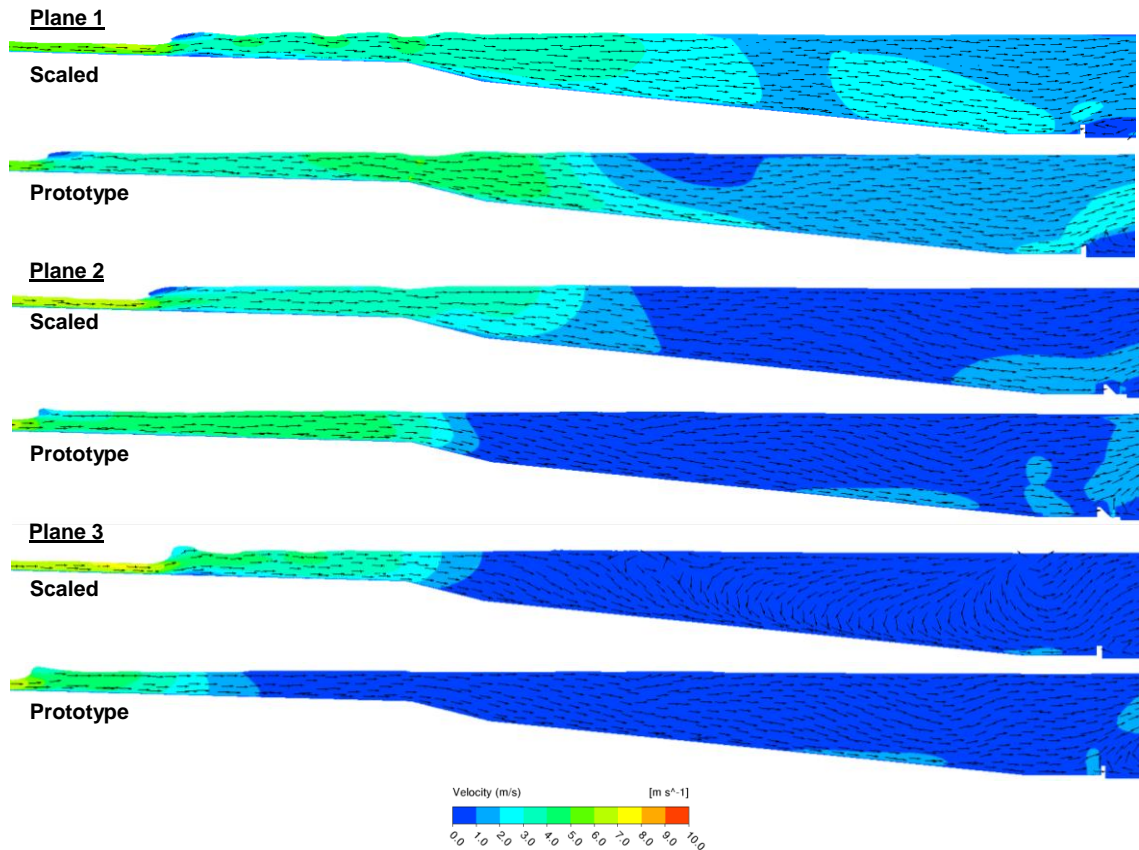


Figure 7.51: Water-phase profiles in the vicinity of the hydraulic jump showing velocity vectors and contours at Plane 1, 2 and 3 at model and prototype scales

7.6.4. Discussion

In this chapter, the low and high tail water levels were simulated in the comprehensive modelling domain for the PMF flow at prototype scale. The comparison of simulations at prototype scale with those at model scale presents interesting findings. In the two scenarios analysed, the prototype scale simulations reveal changes in the location of the hydraulic jump at the two scales, with the prototype hydraulic jump being located upstream of that at model scale. In addition, the tail water presents differences in the velocity distribution and vectors at the two scales.

In both cases the hydraulic jump at prototype scale occurs several metres upstream of that at model scale. In the low tail water case, the difference in the location at the two scales is 5 m while in the high tail water case is approximately 15 m. The downstream boundary conditions are equivalent at the two scales since the same mesh has been implemented at the two scales in the two scenarios. Although further investigations would be required to determine the precise reason for the advancement upstream of the jump at prototype scale, it is likely to be generated by the greater inflow velocities at prototype scale. Even though in the PMF the changes are small compared to the lower flow rates, the velocity is still slightly higher at prototype scale, which could be modifying the dynamics of the tail water. Differences in the inflow velocity could generate

changes in the velocity distribution and vectors in the tail water at prototype scale which could be causing the advancement upstream of the jump.

The changes in the velocity distribution and vectors of the tail water at prototype scale are thus expected to be caused by the greater inflow velocities at prototype scale. Additionally, these might also be originated by the changes in the position of the waves highlighted in Section 7.4.

In summary, with the available information, it could be speculated that the slightly larger inflow velocities as well as changes in the waves positions at prototype scale could result in the observed differences in velocity distribution at the tail water as well as in the position of the hydraulic jump. However, additional analysis would be required in order to confirm such hypothesis.

7.7. Conclusions

The first part of this chapter considered the sensitivity of the prototype scale simulations to mesh cell size, turbulence modelling, and interface capturing scheme. The overall conclusion of this part of the study was that the prototype scale simulations present less sensitivity to model settings than those at model scale. The 3D VOF models implemented in the two solvers were considered to be mesh independent for the mesh of intermediate resolution. Results with the different implementations present higher consistency at prototype scale than at model scale, exhibiting only minor variations between predictions.

Having examined the sensitivity of numerical implementations at prototype scale, prototype scale simulations were undertaken for each of the flow rates previously modelled at model scale, and comparisons at the two scales were made. The main findings of this study are outlined as follows:

- The simulations of the four flow rates on the spillway channel revealed that the prototype scale predictions consistently exhibit higher velocities and lower depths than those for the equivalent flow rates at physical model scale. In line with theory, the discrepancies between prototype and model are reduced for increasing flow rate, where the effects of the forces which are not matched in the Froude physical model (viscosity and surface tension) become negligible.
- Simulations of the spillway channel flow at prototype scale also revealed elongation of the configuration of cross-waves generated by the labyrinth weir. The elongation of the waves is manifested in different degree in the two solvers. In Fluent, the elongation of the distances to the cross-waves crossing points is generally less pronounced, of approximately 8% to 6 %, and decreases for the PMF case. In OpenFOAM, the elongation predicted for the lowest two flow rates is approximately 20 %. The elongation predicted for the largest two flows, and in particular, in the PMF, show increased values. These larger values are considered to be overestimations caused by the less accurate predictions of the cross-wave configuration at model scale of OpenFOAM for the largest flow rates. Therefore values of 20% in approximately all flow rates are judged to be more feasible. Results imply OpenFOAM presents about 10 to 15% larger elongation than Fluent. Because of the

greater accuracy that the Fluent predictions provide at physical model scale, the elongation predicted by this solver at prototype scale is taken as reference.

- An investigation of the wave elongation occurring at prototype scale was undertaken which indicated that the elongation is very likely to be caused by differences in the pressure distribution at the crest of the weir paired with variations in the velocity distribution. These generate displacement of the nappe which result in elongation of the cross-waves at prototype scale. In Fluent, the lowest flow rate presents largest nappe displacement as well as most significant changes in the flow characteristics at the crest and immediately downstream the weir. The PMF presents minimal nappe displacement as well as minor elongation of the distances to the first and second crossing points of the cross-waves x_1 and x_2 . Therefore, in Fluent the scale effects on the nappe shape decrease for increasing flow, which is expected. The head over crest predicted in Fluent for the PMF at the model scale simulations coincides with the limit value recommended in the literature to minimise changes in nappe trajectory in physical models of 0.06 m. That from OpenFOAM for the PMF appears to be slightly under the recommended value. Further analysis could be conducted in order to acquire the precise value for which scale effects on nappe behaviour become negligible in Fluent, with simulations of an intermediate scale.

Additionally, this investigation revealed that the nappe increase at prototype scale and consequent lower impact angle of the weir jet on the spillway base, may result in lower energy dissipation. This could therefore be a further cause for the observed higher velocities in the spillway channel at prototype scale.

- In all flow rates apart from the lowest (where the waves fade by the first spillway change in gradient) predictions from both solvers indicate changes in position of the dominant waves at the end of the first and second and third sections of the spillway channel. The differences in the waves positions at the two scales implies the waves observed at model scale may not be reproduced in the same way in the prototype. This could have implications on structure design and consequently requires further research.
- The comparison of the labyrinth weir rating curve at model and prototype scale indicated the occurrence of lower heads over crest at prototype scale, especially for the lowest flows. The heads upstream crest at the two scales converge for increasing flow rate. Such results confirmed strong agreement with existing literature studies where the weir rating curve was obtained with physical models at different scales. The computed heads upstream crest for the largest two flow rates are found to be complying with existing limiting criteria based on similar structures. The smallest flow rates modelled are shown to be slightly under these.
- The final section of this chapter considered the comparison at prototype and model scales of the interaction of the spillway flow with low and high tail water levels. It was identified that there are small variations in the velocity distributions and vectors of the tail water at the two scales in the two scenarios modelled. The discrepancies

Chapter 7. Comparison of Prototype and Physical Model Predictions

observed at the two scales are not significant and are attributed to the greater inflow velocities as well as to changes in the wave positioning at prototype scale compared to the model scale. Simulations at prototype scale present an upstream advancement of the hydraulic jump compared to that at model scale. Such advancement is of approximately 5 m in the low tail water level and of about 15 m in the high tail water level. Further investigations are needed in order to determine the exact cause of the advancement upstream of the hydraulic jump position at prototype scale.

8. Investigation of Scale Effects and Estimation of Limiting Criteria

8.1. Introduction

In this chapter, the discrepancies observed in the various flow aspects at the different scales are analysed in extended detail. The different aspects examined consist in the depths and velocities in the spillway channel, the labyrinth weir rating curve, and the wave displacement. The values of certain flow parameters for which scale effects are negligible are estimated and compared with existing limits suggested in the literature.

The first part of this chapter concerns the discrepancies in depths and velocities in the spillway channel at the different scales. Predictions at two sections of the spillway are utilised to establish a range of Reynolds numbers to mitigate scale effects. In the second part of this chapter, the changes in the position of the waves occurring at the mid sections of the spillway channel at the different scales are examined. The final part of this chapter concerns the estimation of limits to minimise scale effects in the labyrinth weir rating curve. The minimum upstream head above the crest for which scale effects are negligible is derived.

Predictions from the 3D VOF method simulations implemented in Fluent are considered in order to undertake the analysis of the flow aspects at the different scales and to derive the limiting criteria. Fluent was used exclusively due to the superior performance of the predictions of the VOF implemented in this solver compared to in OpenFOAM. An additional investigation conducted using the predictions from OpenFOAM on the rating curve is presented in Appendix B. In that complementary study, the OpenFOAM predictions of the rating curve were examined by calculating the rating curve at scale 1:10.

8.2. Water Depths and Velocities

8.2.1. Introduction

The previous chapter showed that the flows simulated at model and prototype scale present certain variations in depth and velocity, especially for the lowest flow rates. For the largest flow rates, the flow characteristics at the two scales present close agreement. In this section, a range of Reynolds numbers for which scale effects in the spillway channel are negligible will be estimated and compared with currently available limits established in the literature.

8.2.2. Limiting Criteria

In order to estimate a limits to minimise discrepancies between model and prototype scale predictions, the Froude numbers are considered at model and prototype scales. As shown in Chapter 7, the Froude numbers at the two scales converged to the same value for largest flow rates. The largest flow rate modelled, had values of prototype-to-model Froude number ratios very close to 1, similar to those in the second largest flow rate 119.6 m³/s. However, the Froude number prototype-to-model ratios in the PMF case were not closer to 1 than for the second largest

Chapter 8. Investigation of Scale Effects and Estimation of Limiting Criteria

flow rate because of the change in position of the waves' phenomenon, which will be studied separately in Section 8.3. In a scenario where there is no significant change in position of the waves, the flow conditions are assumed to present increasing agreement for larger flow rate.

In order to further investigate changes occurring in the flow characteristics with changing scales, the PMF flow rate was simulated at two additional scales. These are an intermediate scale between the model and prototype, 1:10 and a smaller scale than the physical model, 1:50. The PMF simulations on the spillway channel modelling domain were conducted utilising the Froude number similarity law for each scale. The scale factors corresponding to scale 1:10 are presented on Eq. 8.1 to 8.5.

$$L_p = 10L_m \quad 8.1$$

$$v_p = \sqrt{10}v_m \quad 8.2$$

$$Q_p = 10^{\frac{5}{2}}Q_m \quad 8.3$$

$$t_p = \sqrt{10}t_m \quad 8.4$$

$$p_p = 10p_m \quad 8.5$$

The scale factors for the simulation at scale 1:50 are shown on Eq. 8.6 to 8.9.

$$L_p = 50L_m \quad 8.6$$

$$v_p = \sqrt{50}v_m \quad 8.7$$

$$Q_p = 50^{\frac{5}{2}}Q_m \quad 8.8$$

$$t_p = \sqrt{50}t_m \quad 8.9$$

$$p_p = 50p_m \quad 8.10$$

The prototype-to-model Froude number ratio was calculated at sections through experimental locations D and E for the three flow rates (40, 119.6 and 159.5 m³/s) in addition to those from the PMF case at 1:10 and 1:50 scale simulations. The prototype-to-model Froude number ratio was plotted against the Reynolds number of the scaled simulation at each section. Results are presented in Figure 8.1. It is observed that the prototype-to-model Froude number ratio approaches 1 for increasing Reynolds number of the simulations. When the Froude number of the scaled simulation is 95% of that in the prototype, the results are considered to have negligible scale effects. Taking into consideration the slight increase in the prototype-to-model Froude number ratio in the PMF is caused by the changes in wave positions, it is judged that model Reynolds numbers approximately larger than 4×10^4 would provide predictions of depth and velocity with negligible scale effects.

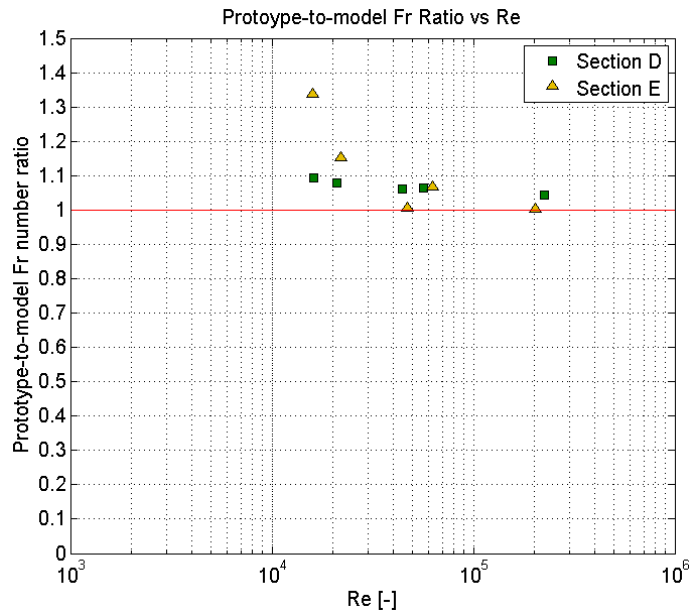


Figure 8.1: Prototype-to-model Froude number ratio versus Reynolds number

To the author's knowledge, an analysis involving the examination of multiple flow rates and scales on a spillway channel to investigate scale effects in physical modelling has not been conducted before. Scale effects associated with flows occurring in spillway channels have not been considered in many occasions. An available example in the literature for open channel flows exists in Novak *et al.* (2010) where a general Reynolds number range to avoid scale effects due to viscosity forces was recommended to be approximately between $10^{3.5}$ and $10^{4.5}$. The upper limit of Reynolds number of this range, (31623) in Figure 8.1 could be approximated to be at a point between 1 and 10 % difference between prototype and model. Therefore, the results obtained in this analysis indicate broad agreement with the available limits suggested in the literature. It is important to highlight that the derived limit value of Reynolds number is a reference value in order to reproduce the macro flow properties at physical model scale. For this reason, this limiting criterion is not applicable to reproduce the air entrainment levels of the prototype at model scale.

8.3. Changes in Waves Positions in the Spillway Channel

8.3.1. Introduction

In Chapter 7, changes in position of the waves at the mid sections of the spillway channel were predicted to occur at prototype scale, compared to model scale, by the two solvers. The observed elongation of the distances to crossing points x_1 and x_2 correlated with changes in the pressure profiles at the crest of the labyrinth weir, which affect the nappe trajectory and cause elongation of the distances from the weir to the immediately downstream waves' crossing points. In Fluent, elongation of x_1 and x_2 was minimised for the largest flow rate. However, elongation of the distance to the furthest downstream crossing point, x_3 , did not correlate with the nappe displacement. Moreover, the observed changes in position of the waves further downstream of the spillway channel were not mitigated for the largest flow rate. Differences in positioning of the waves with changes in scale have not been previously identified in the literature and could have implications on structure design.

In the next subsections, the changes in position of the waves occurring in the spillway channel are investigated. In the first subsection, changes in the characteristics of the flow in the spillway channel are examined at the different scales. The second subsection considers the existing variations in the waves' positions.

8.3.2. Changes in the Flow Characteristics in the Spillway Channel

In order to analyse the changes in position of the waves induced at the spillway channel, two additional PMF simulations of the spillway channel were undertaken at scales 1:10 and 1:50. The results of these simulations were aimed to provide insight on the change in position of the waves with changes in simulation scale.

The free surface features generated at the four scales are presented on Figure 8.2. The crest of the dominant cross-wave originated from the first weir upstream crest is depicted with a dashed line at each scale. The impact point at which this wave encounters the spillway left wall and reflects downstream is indicated with a letter "I". The reflective wave resulting from the impact point is also indicated with a dashed line. Results show that as the simulation scale factor is increased, the impact point is located further upstream in the spillway channel. This results in the reflective wave crossing the first spillway change in gradient at a different point along the channel width. The distance from the impact point in the spillway channel to the downstream crests of the labyrinth weir has been measured in the four cases. At scale 1:50 this distance is approximately 46.2 m, at scale 1:25 is 47.9 m, at scale 1:10 is 48.4 m and at prototype scale is 54.4 m.

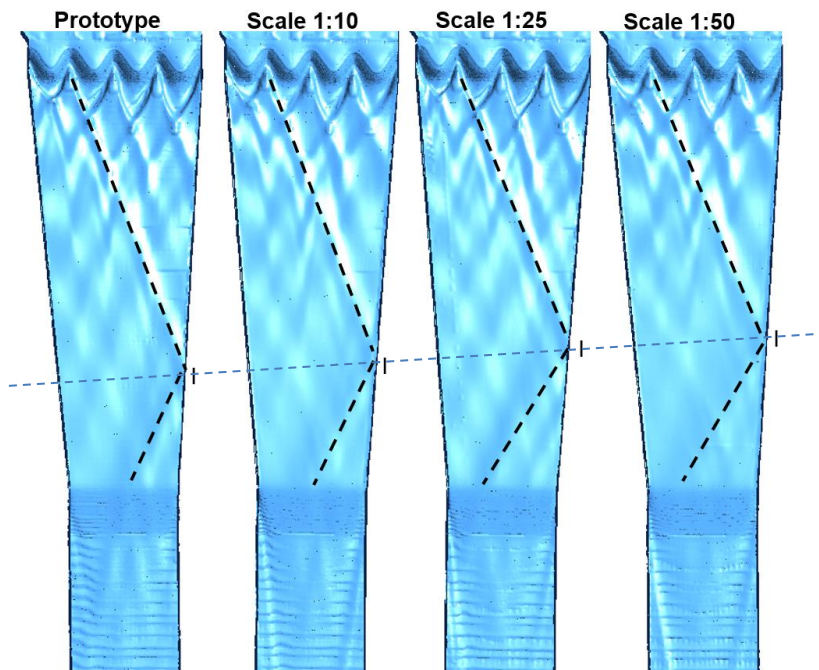


Figure 8.2: Wave structures predicted for the 159.5 m³/s flow rate at the four scales simulated

Cross-sectional flow areas were extracted across the spillway channel at the point where the dominant cross-wave impacts the spillway left wall. These are presented on Figure 8.3 a) where it is shown that the velocity values are higher for decreasing scale factor. The velocity vectors are also shown and these demonstrate good agreement at all scales. Figure 8.3 b) shows the free surface features coloured by velocity for the four simulation scales. In the first section of the

spillway, before the first change in gradient, the prototype velocities show noticeably larger velocities than those at the smaller scales. Velocities at prototype and at 1:10 and 1:25 scales also present differences in the vicinity of the first change in gradient, where the prototype velocities are from 7 to 9 m/s and at larger scale factor simulations are from 6 to 9 m/s. In the third section of the spillway, downstream of the second change in gradient, the velocity difference between the prototype scale and the larger scale factor simulations appears to be more prominent than in first section. a)

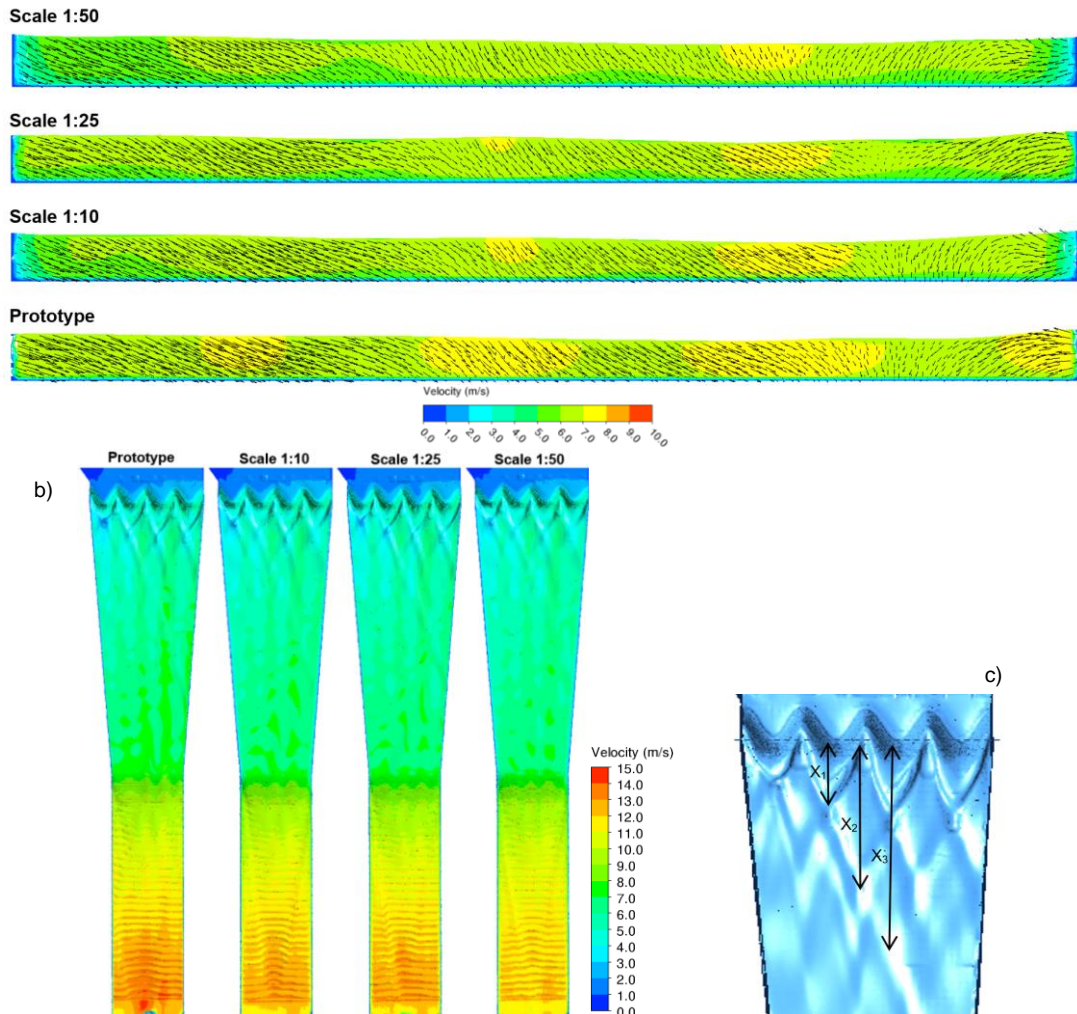


Figure 8.3: a) Flow areas coloured by velocity contours with velocity vectors across the spillway channel at the impact point of the dominant wave; b) Free surface features coloured by velocity; c) location of distances x_1 , x_2 and x_3

Figure 8.2 and Figure 8.3 also show that there is only small difference between the distance x_1 and x_2 at the different scales, indicated in Figure 8.3 c). However, the distance x_3 shows the largest difference at the four scales. Therefore, there is an increase in the variation of the flow characteristics with greater distance downstream of the weir.

Figure 8.4 a) shows the flow areas coloured by velocity at the spillway channel sections across the first cross-waves crossing point (that at end of distance x_1). Results show that the velocity disagreements at the different scales at the plane across the first crossing point, are generally minor. The main differences at this section consist in the distribution of the largest velocity values at the four scales, and overall the values are similar. Figure 8.4 b) shows the flow areas at the

third crossing point (that at end of distance x_3). Results reveal the discrepancies in velocity contours at the different scales at the third cross-wave crossing point are considerable. Velocities are larger on the left side of the spillway and increase for lower simulation scale factor, with greater variations between velocity predictions at the different scales than further upstream in the channel. At this section the velocity vectors present similar patterns at all scales. This explains that although there is little displacement at the first wave crossings, and the conditions in the vicinity of the weir are comparable at the different scales, further downstream in the spillway channel more significant changes occur in flow velocity and wave positions. Therefore, the larger the distance downstream of the weir, the greater the differences in the flow characteristics at the four scales.

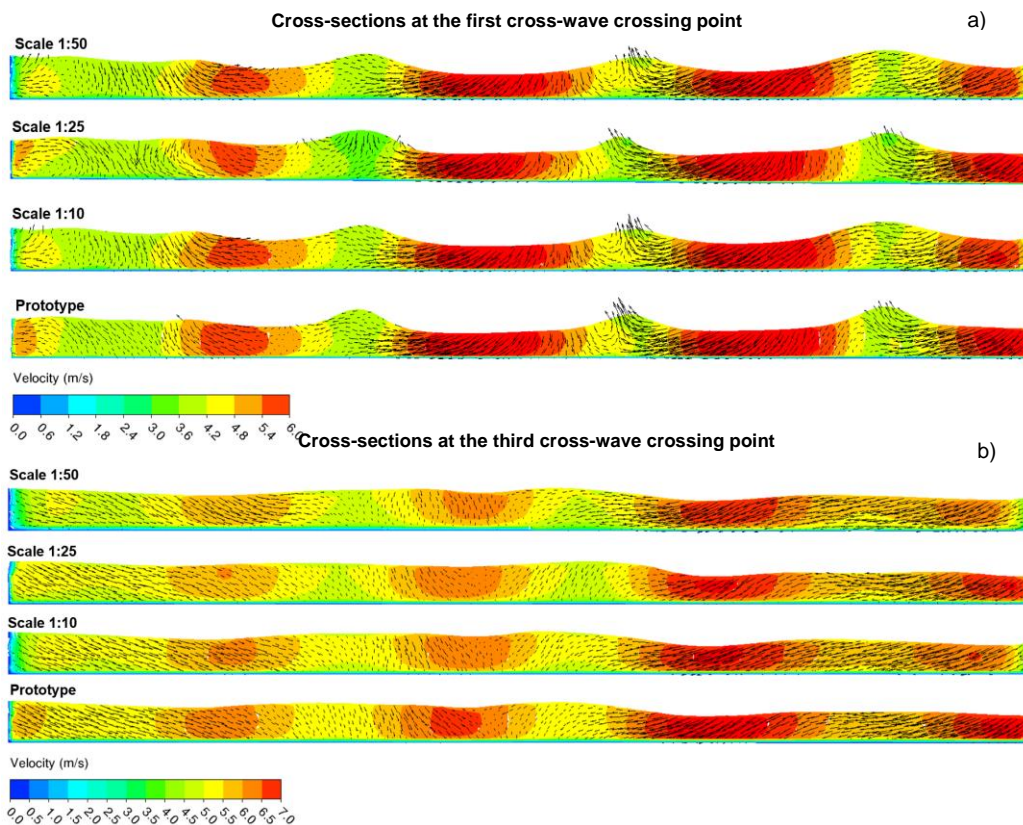


Figure 8.4: Flow areas coloured by velocity at: a) the first cross-wave crossing point; b) the third cross-wave crossing point

In summary, this subsection substantiated that the predictions at the four simulated scales present small changes in the flow conditions in the vicinity of the weir and several metres downstream of it. However, with increasing distance downstream of the weir, the flow situation in the spillway channel results in more significant velocity variations at the four scales. The velocities at scale 1:50 are the lowest and for smaller simulation scale factor the velocity values give increasing agreement with these at prototype scale. The changes in the position of the dominant wave which impacts the left spillway wall progressively further downstream for increasing simulation scale factor, could therefore be related to such increases in velocity values.

Both velocities and wave structures present greater differences at the various scales with increasing downstream distance. The precise cause of increase in velocity differences with downstream distance is not completely of knowledge. It could be estimated that because in the scaled cases the turbulent levels are significantly lower than at prototype scale, (particularly at

the scale 1:50) the viscous forces which could still be relevant in the scaled cases, slow down the propagating dominant cross-wave. The variations in the turbulence levels at the various scales present increasing differences in the turbulent structures as the flow situation evolves downstream the spillway channel.

8.3.3. Changes in the Waves' Positions in the Spillway Channel

In order to examine the change in position of the dominant waves with changes in simulation scale, the free surface profiles were extracted across the two sections with the most prominent changes at the four scales. These are sections through point C and D, located 1 m upstream of the first change in gradient and 1 m downstream of the second change in gradient respectively. The free surface profiles at the two sections are presented on Figure 8.5 a) and b).

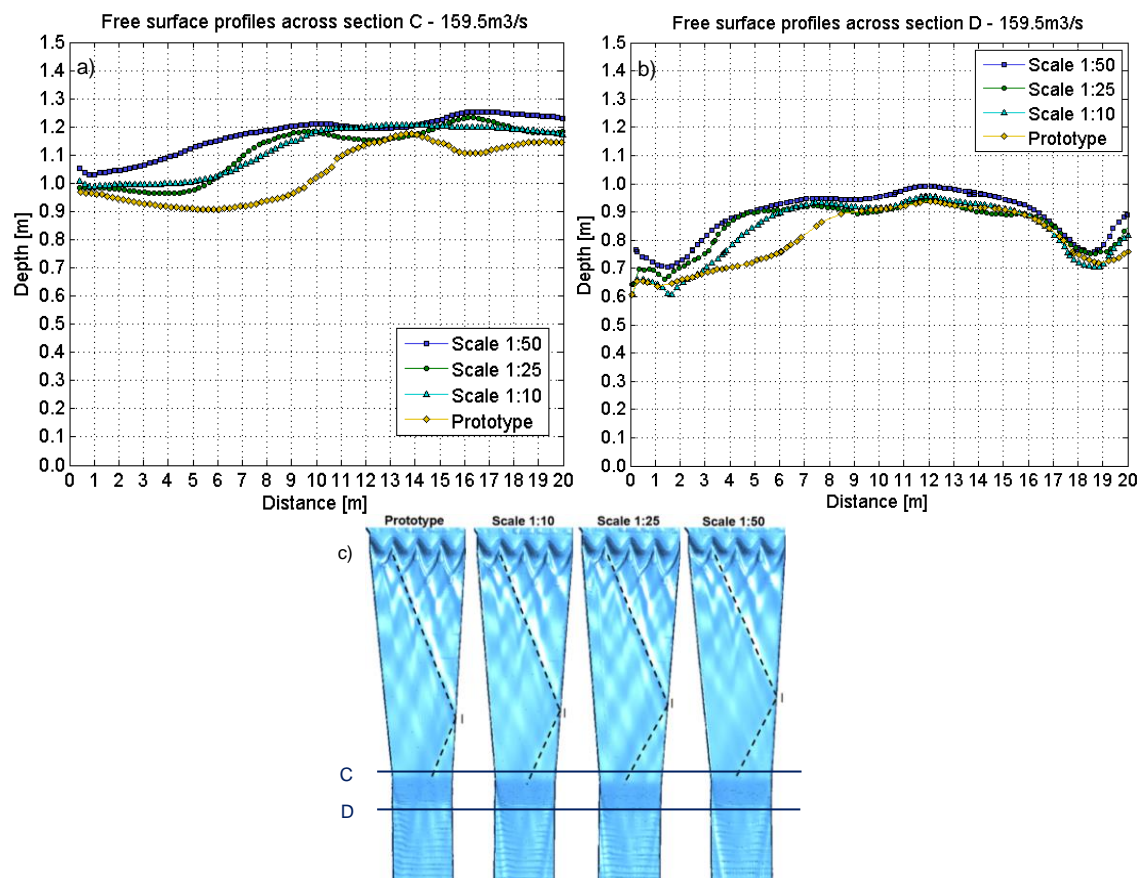


Figure 8.5: Interface cross-sectional profiles at sections: a) C and b) D extracted from simulations at the four scales; c) Location of the sections C and D on the free surface features at the different scales

Figure 8.5 a) and b) show that the dominant wave is consistently closer to the spillway left wall for larger simulation scale. As previously observed in Figure 8.2, the impact point of the spillway dominant wave moves further downstream in the spillway channel for decreasing scale factor, with the prototype being the one located furthest downstream. This induces changes in the waves' positions downstream of the spillway channel. The changes illustrated on Figure 8.5 demonstrate a progressive advancement of the wave as the scale factor is increased. At section C, generally simulations at all scales apart from that at scale 1:50 reproduce similar wave features, although at scales 1:25 and 1:10 the main waves are moved towards the centre of the channel. At section D, the 1:50 and 1:25 scales present a generally central wave profile, while that at scale 1:10

Chapter 8. Investigation of Scale Effects and Estimation of Limiting Criteria

presents a slightly more similar profile to that predicted at prototype scale, which shows the wave shifted towards the spillway left side. The profiles at the two sections also show a decrease in the flow depth for decreasing scale factor, since as previously noted, the flow velocity is increased for lower scale factors.

To obtain an estimation of the displacement for a given fixed location, the point in the cross-sectional distance corresponding to the dominant cross-wave crest was approximately placed at each section. The location of the peaks of the waves along the spillway channel widths at sections C and D at each scale was extracted. The displacement was thus calculated as the percentage difference in the location of the dominant crest at each scale in respect of that at prototype scale. Such measurements and calculations are summarised together with the distance from the weir downstream apexes to the impact point at each scale on Table 8.1.

Table 8.1: Impact point distance from the weir and location of dominant cross-wave at sections C and D with percentage difference compared to the prototype and distance ratio at the four scales

Scale	Impact Point Distance[m]	Impact point % Difference	Wave Peak Section C [m]	Wave Peak Section C % Difference	Wave Peak Section D [m]	Wave Peak Section D % Difference
Prototype	54.4		13.8		8.5	
1:10	48.4	11	10.2	26	7	18
1:25	47.94	12	9.2	33	4	53
1:50	46.24	15	9	35	4	53

The calculations on Table 8.1 show an estimation of the wave displacements at the three different scales compared to the prototype wave. The impact point distance shows overall the distances differ between 11 and 15 % from the prototype. At section C the waves' changes in position reveal that simulations at scale 1:50 present around 35 % difference from that in the prototype while scale 1:25 shows around 33 % of that in the prototype. Scale 1:10 shows the wave crest to be displaced approximately 26 % from that in the prototype. At section D simulations at scales 1:50 and 1:25 both show a percentage difference of 53% and simulations at scale 1:10 present only 18 % difference.

For a criterion consisting in the scaled simulation being equal or less than 5 % different to the prototype value, none of the scales simulated here would be large enough to reproduce the correct position of the waves observed in the prototype. In order to examine the relationship between the wave displacement at the different scales with the turbulence levels of the flow modelled, the calculated displacement was plotted against the Reynolds number at sections C and D. Figure 8.6 shows the wave displacement in respect of the prototype at each scale against the Reynolds number at each scale at the two sections. As expected, results show that the wave displacement between the simulated scales and the prototype decreases with increasing Reynolds number. Although with the current knowledge of the observed phenomenon it is not possible to determine exact limits to minimise scale effects, it is possible to estimate that in order to have less than approximately 20% in change in position of the waves, the Reynolds number in the physical model should be larger than 2 to 4×10^5 .

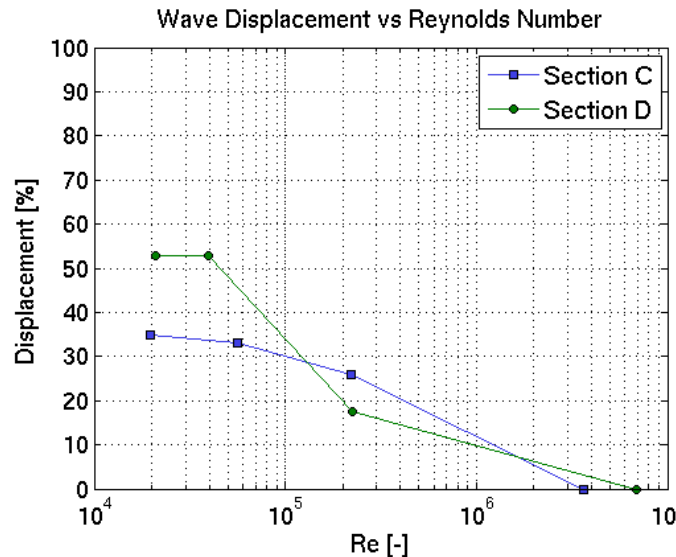


Figure 8.6: Wave displacement at sections C and D at scales 1:50, 1:25 and 1:10

The discrepancies shown by this analysis therefore provide an indication of the typical displacement of the waves which might be induced by scale effects in a structure similar to the one of study. The observed change in position of the waves is not a comprehensively understood phenomenon and requires further investigation. This study demonstrated that for decreasing scale factor of the simulation (and hence increasing Reynolds number), the predictions exhibit reduced scale effects and become closer to those at the real size prototype.

8.4. Labyrinth Weir Rating Curve Calculations

8.4.1. Introduction

In the present section, numerical predictions of the rating curve at physical model scale and at prototype scale are utilised to estimate limits on the upstream head above crest to minimise the observed scale effects. This is conducted by following a procedure previously implemented in the literature.

8.4.2. Determination of Minimum Height Upstream Weir

In Erpicum *et al.* (2016) the minimum heads over the crest to mitigate scale effects in the rating curve of a PKW were derived from rating curves predicted with physical models at several scales. In such study the uncertainty in the measurements of upstream head above crest was assumed to be 1 mm at each scale. The rating curves at the different scales were then plotted and the upstream head above crest in the prototype was considered to be equal to those at the different model scales if it was within the 1 mm error bands for each scale.

In Pfister *et al.* (2013a) the curve of a potential flow was used for the derivation of limits to minimise scale effects in the curve of a cylindrical weir. A potential flow is such that does not have effects of viscosity and surface tension and hence its rating curve is obtained by applying $\sigma = \nu = 0$. In Pfister *et al.* (2013a) the minimum heads over a cylindrical weir are derived by plotting the rating curves at the different scales with that of a potential flow and selecting the upstream head above

crest for which the minimum depth provides a coefficient of discharge which is 95% or 98% of that in the potential flow curve.

In the present study, the approach described in Epicum *et al.* (2016) is implemented using the numerically predicted curves. The prototype curve is compared to the physical model scale curve. The uncertainty is also considered to be 1 mm. Therefore, the uncertainty of the predictions is 25 mm in the physical model scale. The uncertainty bands are calculated for the rating curve at model scale and the minimum head is derived as the scaled head upstream the crest for which the prototype curve intersects with the uncertainty band range. The uncertainty bands at model scale have been calculated by adding and subtracting 0.025 m to the model scale curve. Figure 8.7 shows the predictions of the rating curves at prototype and model scale with the uncertainty bands for the model scale predictions. The prototype rating curve crosses the lower uncertainty band of the model scale curve for a flow rate of 59.1 m³/s at an upstream water head of 0.69 m, which corresponds to a scaled-down depth of 0.0277 m.

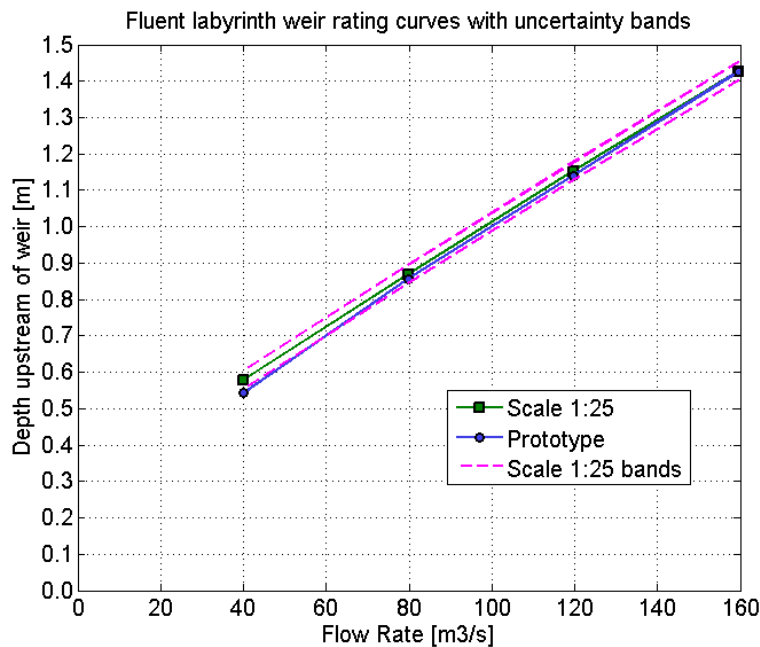


Figure 8.7: Rating curves at physical model scale (1:25) with uncertainty bands and prototype scale

These results indicate that in order to predict the rating curve of a labyrinth weir of similar characteristics to the one of study, the minimum head over the crest should be 0.03 m. This value appears to be in line with those derived in Epicum *et al.* (2016), Epicum *et al.* (2013b), Leite-Ribeiro *et al.* (2012), Pfister *et al.* (2012) and Pfister *et al.* (2013a) for PKW, also coinciding in the minimum head over crest value of 0.03 m. The scaled depth obtained is also broadly correlated to the dimensionless head approximated by Tullis *et al.* (2017) of $H/P > 0.3$ to minimise scale effects in labyrinth weirs, with the present study normalised value being 0.384.

8.5. Conclusions

In this chapter, the scale effects observed in several flow aspects of the hydraulic structure of study were investigated in extended detail using the 3D VOF model simulations conducted in Fluent. As discussed in Chapter 6, the 3D VOF model implemented in OpenFOAM was not

considered to be appropriate to draw conclusions on scale effects, and therefore it was not utilised in this chapter.

The discrepancies observed in velocities and depths in the spillway channel at the two scales were examined and a value of Reynolds number to be exceeded to prevent scale effects was derived. A minimum upstream head above the labyrinth weir crest to ensure negligible scale effects in the prediction of the rating curve was also estimated. In addition, the changes in the position of the waves occurring at the mid sections of the spillway channel were further analysed. The estimated limits to minimise scale effects were compared with available limits in the literature. The main conclusions from this chapter are outlined as follows:

- A minimum Reynolds number to ensure negligible discrepancies between depths and velocities at model and prototype scale was estimated. This was undertaken by plotting the prototype-to-model ratios of Froude number against the Reynolds number of the scaled simulation for each flow rate. In addition, PMF simulations of the flows in the spillway channel at scales 1:10, and 1:50 were conducted and prototype-to-model Froude number ratios were calculated and considered. The Reynolds number for which the Froude numbers at model scale were approximately 95 % of that at prototype scale was found to be 4×10^4 . This value appears to be broadly correlated with the literature range suggested for general open channel flows of $10^{3.5}$ to $10^{4.5}$. The derived limit constitutes new valuable guidance for physical modelling of spillway channels.
- The observed changes in waves positions at prototype scale compared to model scale were investigated for the PMF case. The changes in the flow characteristics in the spillway channel with changes in simulation scale were examined by undertaking additional PMF simulations at scales 1:10 and 1:50 in the channel domain. Results revealed that the velocity profiles and flow conditions in the channel area immediately downstream of the weir were comparable at the four scales. However, more significant changes in velocity and waves' positions occur with increasing downstream distance from the weir. The discrepancies in velocity and position of the wave structures at the various scales compared to the prototype scale consistently reduced for decreasing scale factor of the simulation. The precise cause for the increasing discrepancies with increasing distance downstream of the spillway channel is still not fully understood and requires additional research. It could be estimated that the substantial increases in turbulence levels at prototype scale compared to the different scales (particularly scale 1:50) are generating changes in velocity and flow structures. The aspect which was confirmed in this study was that for decreasing scale factor of the simulation, the wave displacement and velocity differences in respect of the prototype were reduced. Therefore, results imply that if the physical model scale factor is excessively large, the waves' features observed at physical model scale might not be reproduced in the same way in the prototype.
- The changes in position of the waves with different simulation scales are a newly discovered scale effects aspect which had not been identified in previous studies. In the present work, an attempt was made to quantify the wave displacement at the various

scales modelled. The percentage wave displacement at the three scales, 1:10, 1:25 and 1:50 were calculated at two sections of the spillway channel with presence of the dominant cross-wave and were plotted against the Reynolds number. It was estimated that Reynolds numbers over 2 to 4×10^5 would provide less than 20 % of change in position of the waves. Such values are an estimation based on the investigations conducted in this study. The wave changes in position with changes in scales are not considered to be well enough comprehended in order to establish specific limits to minimise them. Further investigations of such phenomenon are required with extended simulations which could also be complemented with experimental studies.

- A minimum upstream head above crest to minimise scale effects in the determination of the labyrinth weir rating curve with a physical model was derived. The minimum upstream head above crest estimated using the numerical predictions of the curves at model and prototype scales was 0.03 m. This value is very well correlated with previous derivations of this parameter by other studies employing experimental techniques for non-linear weirs. Therefore a minimum upstream crest of 0.03 m may be considered as a reference to ensure negligible scale effects in the prediction of labyrinth weir rating curves with physical models.
- The points above demonstrate that appropriately validated CFD VOF formulations such as the RANS Standard $k - \varepsilon$ model in conjunction with the PLIC scheme are appropriate tools to investigate and quantify scale effects in physical models as well as to estimate limits to minimise these. In addition to providing new guidance to mitigate scale effects in physical models, the numerical model has also demonstrated the capability of revealing the existence of aspects such as the change in position of the waves at the various scales. These discoveries constitute remarkably important information for the research of complex hydraulic free surface flows.

9. Conclusions and Further Work

9.1. Summary

The purpose of this thesis was to assess the capabilities of the CFD VOF method to characterise the complex hydraulic free surface flows over and downstream of a labyrinth weir and utilise the numerical predictions to investigate the scale effects induced in a physical model.

The present changes in climate and consequent increased frequency and severity of extreme flooding events result in the critical need for design and refurbishment of hydraulic infrastructure. The principal means of hydraulic modelling for the design of hydraulic structures consist in physical hydraulic models. However, in the recent years, interest in numerical modelling has grown amongst the hydraulic structures community. Several numerical modelling techniques have been proposed for hydraulic modelling, but these require further investigation and validation. Determination of the extent to which the leading approaches are capable of reproducing an experimental flow of interest is therefore of significant importance. In particular, the CFD VOF has been proven to be a robust method for the prediction of hydraulic free surface flows in several studies. Additionally, particle-based meshless approaches present strong potential but have been applied in a more limited number of occasions to model hydraulic flows, therefore the investigation of their capabilities is of remarkable interest. This led to objective 1, which consisted in the investigation of two major numerical modelling approaches based on different frameworks, namely the VOF and the SPH, to model a dam break flow over an obstacle. Such numerical models were evaluated on their reliability to accurately predict the flow situation. The initial VOF analysis was essential for the implementation of this method to simulate a more complex hydraulic flow in the subsequent chapters. The SPH modelling of this case provided valuable knowledge of this technique for its future use in the modelling of hydraulic free surface flows.

The aforementioned rising of the flood levels and associated need for rehabilitation of ageing structures also caused an increased interest in the implementation of labyrinth weirs. The application and investigation of such non-linear weirs has been predominantly based on physical hydraulic models. Consequently, although several numerical modelling studies exist, most of the research conducted on labyrinth weirs has been based on physical model studies. In addition, of all studies concerning labyrinth weirs, only a very reduced number regard the characteristics of the complex, fully 3D flows generated downstream of labyrinth weirs. This gave rise to the second objective, which embraced the application of the previously tested 3D VOF method to simulate the flow over and downstream a labyrinth weir. The purpose was to evaluate the capability of the numerical method to reproduce various complex flow aspects, including rating curve, depths, velocities and wave structures downstream the weir. This task also involved the analysis of the sensitivity of various numerical implementations to remove model uncertainty and inform best practice.

One of the main challenges of developing physical hydraulic models is designing them such that scale effects are kept to a minimal level and the flow behaviour in the prototype is appropriately reproduced. Limits to minimise scale effects have been derived by means of physical modelling

studies for a number of flow phenomena and hydraulic structures. However, the literature indicates there is the need for limits to minimise scale effects to be derived specifically for labyrinth weirs. The ability of numerical approaches to model real scale prototype structures offers the possibility to quantify scale effects of a physical model, once the numerical model has been appropriately validated. From this conceptualisation, Objectives 3 and 4 were formulated. Objective 3 involved the simulation of the free surface flow over the prototype scale labyrinth weir and spillway and the identification of discrepancies between model scale and prototype scale predictions in the different flow aspects. Objective 4 concerned the extended investigation of the observed scale effects and estimation of limiting criteria to minimise them in the modelling of the different flow aspects of the flow induced by the labyrinth weir, using the numerical predictions. The estimated limits were compared with existing limits derived for similar structures.

The four research objectives were achieved by employing the various numerical approaches and solvers. Physical model measurements from a 1:25 Froude similarity model as well as experimental data from the literature were utilised to validate the numerical methods. The conclusions drawn from the analyses conducted to achieve each of the objectives are outlined in the following section.

9.2. Conclusions

Each of the conclusions detailed in sections 9.2.1 to 9.2.4 relate to objectives 1 to 4 respectively. These are presented as follows:

9.2.1. 2D and 3D VOF and SPH Modelling of an Experimental Dam Break Flow

The first objective was to evaluate the capabilities of the VOF and the SPH techniques to model an experimental dam break flow over a triangular obstacle. This experimental case involved the fine flow layer traveling over the triangular obstacle, the interaction of the dam break flow with a pool of water downstream of the obstacle, and the generation of a reflective wave. 2D and 3D simulations were conducted with the two numerical approaches, where the VOF simulations were undertaken in the OpenFOAM and Fluent solvers and the SPH simulations were conducted in the DualSPHysics code. Sensitivity analyses were performed for the 2D simulations of the two numerical approaches in respect of several numerical implementations. In the VOF, sensitivity to the cell size, time step size, turbulence model and interface capturing scheme was assessed. In addition, a simulation using the Eulerian-Eulerian multiphase model was conducted to compare with the VOF method. In the SPH, sensitivity analyses were conducted in respect of time step algorithm, viscosity treatment and kernel definition. The outcomes from this initial VOF modelling study provided crucial knowledge on the solvers utilised and on the best practice for their implementation in the subsequent and more complex simulations comprised in this thesis. The SPH modelling results of this case constitute a valuable accomplishment for the future SPH simulation of hydraulic flows. The main findings from this study are outlined as follows:

- The 2D and 3D VOF models implemented in Fluent and OpenFOAM were capable of correctly reproducing the flow features and the free surface depths measured in the

experiment. The analysis indicated the use of variable time stepping in the 2D and 3D VOF methods provides accurate results in OpenFOAM. However, variable time stepping is not recommended in Fluent. The implementation of fixed time stepping in the 2D and 3D VOF methods in Fluent provides very accurate predictions. A mesh with cell size 1×10^{-2} m (x, y) by 2.5×10^{-3} m (z) with a time step size of 1×10^{-3} s was found to be appropriate for the dam break case modelled in the two solvers. The numerical predictions showed no significant changes when using the SST $k - \omega$ compared to the Standard $k - \varepsilon$ turbulence models. The model showed effectively equivalent results with the implementation of two different interface capturing schemes (PLIC and CICSAM). The use of the Fluent Eulerian-Eulerian multiphase model significantly improved the flow delay observed in Fluent when using variable time stepping.

- The SPH simulations indicated the 2D SPH model using a particle spacing value (dp) of 1×10^{-3} m provides an acceptable estimation of the flow characteristics and free surface features. Numerical predictions were not found to be sensitive to viscosity treatment or kernel definition, however, they were strongly dependent on the time step algorithm. The Symplectic algorithm is recommended for the modelling of this flow situation. The 3D SPH predictions present a satisfactory representation of the interface and flow features for a particle spacing value of 5×10^{-3} m. Additional investigations with simulations of higher resolution would be needed in order to fully determine the capabilities of this technique. The main limitation encountered in the SPH technique consist in its highly computational nature, which makes the application of further refinements exceptionally challenging. Further developments may consist in the implementation of GPU simulations which present a strong potential to provide a powerful computational resource for the particular solver utilised.

9.2.2. 3D VOF Modelling of the Labyrinth Weir and Spillway Physical Model

The hydraulic structure in which this thesis focused was the Eller Beck flood storage reservoir, consisting of an embankment dam, an approach channel, a labyrinth weir and a spillway. The second research objective was to model the free surface flow over the physical model of the scheme with the 3D VOF method. The numerical model performance assessment was conducted in respect of various flow aspects with physical model measurements and observations. These include, prediction of depths and velocities in the spillway channel, characterisation of the complex 3D configuration of cross-waves downstream the weir, calculation of the labyrinth weir rating curve, and representation of the interaction of the spillway flow with several tail water levels. Various modelling domains were created in order to study the different flow processes occurring in the structure with sufficient precision. This involved the creation of a workflow for the acquisition of the complex modelling domains of the hydraulic structure and associated meshes. 3D VOF simulations of several flow rates were undertaken with Fluent and OpenFOAM and the performances of the two solvers were assessed. Additionally, the models' sensitivity to several numerical implementations were analysed. The main outcomes are listed as follows:

- Having conducted a mesh independence study, it was discovered that the two solvers require different mesh configurations in order for the VOF to provide accurate representations of the free surface features. The VOF method implemented in Fluent performs superiorly with lower cell size at the base of the spillway while in OpenFOAM the optimal predictions are obtained with several layers of cells of finer cell size parallel to the spillway base.
- This analysis also revealed the VOF method implemented in OpenFOAM is more sensitive to cell size than in Fluent, requiring cell sizes of 4×10^{-3} m or lower to achieve mesh independence. Fluent provides mesh independent results with a cell size of 8×10^{-3} m or lower.
- The sensitivity analysis in respect of turbulence model demonstrated the RNG and Standard $k - \varepsilon$ models present negligible differences in the predictions of the flows, both appearing to be reproducing the flow phenomena with equivalent accuracy. With the mesh resolution used, the SST $k - \omega$ model does not indicate to be capable of accurately predicting the flow situation. It is expected that predictions from this model would improve with a further mesh refinement although further investigation would be required to identify the precise cause of such low performance.
- The comparison of the PLIC and CICSAM schemes for interface reconstruction revealed a superior performance of the PLIC compared to the CICSAM scheme to predict the cross-waves shapes and waves' crossing points heights.
- The modelling of the various flow rates on the spillway channel with the two solvers indicated that the 3D VOF RANS Standard $k - \varepsilon$ model with the PLIC scheme implemented in Fluent produces an accurate characterisation of the free surface features for all flow rates. The 3D VOF RANS Standard $k - \varepsilon$ model with the MULES scheme implemented in OpenFOAM is capable of accurately reproducing the free surface features for the two lowest flows but presented a less well defined free surface for the two largest flow rates.

For the lowest flow rate, the VOF models implemented in the two solvers generally exhibited consistency in their predictions of depth and velocity and they both presented a very accurate representation of the complex free surface cross-waves generated by the labyrinth weir. For the medium flow rate, OpenFOAM showed very close agreement with the experimental measurements of depths and velocities as well as with the free surface features. For $119 \text{ m}^3/\text{s}$, the velocity and depth predictions from Fluent were well correlated with the physical model measurements and presented accurate characterisations of the free surface structures. The free surface depths and wave structures predicted in OpenFOAM were less accurate. The PMF predictions from OpenFOAM presented lower values of depth and velocity in addition to a compressed configuration of cross-waves compared to those predicted with Fluent. The Fluent predictions confirmed close agreement with the experimental measurements and wave structures for this flow rate. The simulation results obtained with the different implementations and the various flow rates revealed that the existing disagreement

between the predictions from the models implemented in the two solvers in the larger flow rates were caused by the difference in the interface capturing scheme as well as the varying cell size sensitivity that the two solvers exhibit. Increases in mesh resolution as well as the application of a more advanced interface capturing scheme are expected to improve the OpenFOAM flow representations of the largest flow rates.

- The labyrinth weir rating curve predicted with Fluent presented close agreement with the experimental curve. The OpenFOAM rating curve prediction appeared to be slightly overestimating the upstream head above the weir crest for most flow rates.
- Predictions of the interaction of the spillway flow with the various levels of tail water confirmed close agreement with the physical model measurements. The low tail water scenario verified a good correlation with the physical model predictions of depth, velocity and location of the hydraulic jump. The medium and high tail water scenarios indicated close agreement between the numerically predicted spillway flow interaction with the tail water and that shown in the physical model. The discrepancies found between numerical predictions and physical model measurements were based in the position of the tail water in the spillway surrounding terrain. These were caused by the variations in the shape of the irregular terrain in the physical and numerical models.

9.2.3. Comparison of Prototype and Model Scale Predictions

The third objective was to model the prototype scale flow over the labyrinth weir and spillway and examine the discrepancies between model and prototype scale predictions in the different flow aspects. In addition, the previously tested numerical implementations at model scale were applied at prototype scale to determine whether the model sensitivity to these would vary with changing scale. The main findings are listed as follows:

- The testing of the various numerical implementations at prototype scale confirmed that compared to simulations at physical model scale, the prototype scale predictions present significantly less sensitivity to all the implementations tested. At prototype scale, results from both solvers were verified to be satisfactorily mesh independent with the mesh of intermediate resolution, of cell size 0.1 m at the base and 0.2 m in the area surrounding the free surface. The implementation of the three turbulence models at prototype scale showed very similar results from the $k - \varepsilon$ family models and less difference between these and the SST $k - \omega$ model than simulations at physical model scale. The predictions obtained using the PLIC and the CICSAM schemes verified that at prototype scale there is little impact of the interface capturing scheme on the simulation results.
- The simulations from both solvers of the various flow rates on the spillway channel indicated consistently higher velocities and lower depths at prototype scale compared to those for the equivalent flow rates at physical model scale. Predictions from the two solvers demonstrated discrepancies between the two scales are reduced for increasing flow rate. This is expected from theory since for increasing flow rate the effects of the

forces which are not matched in the Froude physical model (viscosity and surface tension) become increasingly less significant.

- The comparison between physical model and prototype scale simulations in the spillway channel also revealed elongation of the configuration of cross-waves generated by the labyrinth weir at prototype scale. The elongation of the waves is manifested to a different degree in each of the two solvers. In Fluent, the elongation of the distances to the cross-waves crossing points is around 8 to 6 % and it decreases for the PMF. In OpenFOAM, elongation is estimated to be slightly greater than that in Fluent. Given the established superior accuracy of the Fluent predictions (especially for the largest flows at physical model scale), they are considered to be the reference value.
- The investigation of the cause for wave elongation indicated that it is distinctly likely that it is generated by differences in the pressure distribution at the crest of the weir paired with variations in the velocity distribution at the crest and consequently immediately downstream of the labyrinth weir. These generate displacement of the nappe which result in elongation of the cross-waves at prototype scale. In Fluent, the lowest flow rate presents largest nappe displacement and most significant changes in the flow characteristics are at the crest and downstream of the weir at prototype scale. The PMF prototype predictions present reduced nappe displacement as well as minimal elongation of the distances to the first and second crossing points of the cross-waves. The upstream head over the crest predicted with Fluent for the PMF at the model scale simulations coincides with the limit value recommended in the literature to preserve nappe trajectory in physical models. That equivalent head in OpenFOAM for the PMF appears to be slightly under the recommended value, which is in line with the lower confidence in the accuracy of OpenFOAM results observed elsewhere. Consequently, the Fluent predictions are estimated to be in agreement with the current limits. More precise limits could be derived by conducting Fluent simulations of an intermediate scale between prototype and model.

Additionally, this analysis revealed that the nappe increase at prototype scale and consequent lower impact angle of the weir jet on the spillway base, may result in lower energy dissipation. This is seen as a further possible cause for the observed higher velocities in the spillway channel at prototype scale.

- Prototype scale simulations also indicated the occurrence of changes in the position of the dominant waves located at mid sections of the spillway channel. These were not correlated with the pressure distribution at the crest of the labyrinth weir and were not reduced for increasing flow rate. The differences in the waves positions at the two scales implies the waves observed at model scale may not be reproduced in the same way in the prototype. This could have implications on structure design and consequently requires further research.
- The comparison between the labyrinth weir rating curve at model and prototype scales indicated the occurrence of lower upstream heads above crest at prototype scale, with differences being greatest for the lowest flow rates. The upstream heads at the two scales

converged for increasing flow rate. Such results confirmed strong correlation with existing literature studies where the weir rating curve was obtained with physical models at different scales.

- The comparison between the interaction of the spillway flow with the tail water at prototype and model scales revealed the presence of small variations in the velocity distributions of the tail water as well as differences in the position of the hydraulic jump at the two scales in the two scenarios modelled. The discrepancies observed at the two scales are attributed to the greater inflow velocities as well as to changes in the wave positioning at prototype scale compared to model scale. The upstream advancement of the hydraulic jump at prototype scale is of approximately 5 m in the low tail water level and of about 15 m in the high tail water level. Further investigations would be required in order to determine the exact cause of the advancement upstream of the hydraulic jump position at prototype scale.

9.2.4. Estimation of Limiting Criteria and Comparison with Established Values

The fourth objective of this thesis was to further inspect the observed discrepancies between the numerical predictions at the two scales and estimate a range of limiting criteria to minimise scale effects observed in the modelling of the several aspects of the flow induced by the labyrinth weir. The purpose was to conduct an extended investigation of the results to estimate such values using the numerical predictions and to compare these with available literature limits. Limits to minimise scale effects on the physical model predictions of flows in the spillway channel as well as on the weir rating curve were estimated. Additionally, the changes in the position of the waves in the mid sections of the spillway channel were further analysed. The analysis undertaken in this chapter was based exclusively on the Fluent predictions given their superior performance compared to OpenFOAM. The flows occurring in the spillway channel at the different scales were investigated with the modelling of the PMF at two additional scales, namely 1:10 and 1:50. The main findings are outlined as follows:

- A minimum Reynolds number to ensure negligible disagreement between depths and velocities in the spillway channel at model and prototype scale was estimated. This was conducted by plotting the prototype-to-model Froude number ratio predictions at two spillway channel sections against the Reynolds number at model scale. Predictions from PMF simulations at scales 1:10 and 1:50 were also considered. The Reynolds number for which the Froude numbers at model scale were approximately 95 % of that at prototype scale was found to be 4×10^4 . This value appears to be of similar order to the literature minimum range estimated for general open channel flows of $10^{3.5}$ to $10^{4.5}$ and constitutes new valuable guidance for physical modelling of spillway channels.
- The changes in position of the waves observed at mid sections of the spillway channel were investigated with the PMF modelling of scales 1:10 and 1:50. Results at the four scales revealed the velocity profiles and flow conditions in the vicinity of the weir and in the area immediately downstream, were generally comparable at the four scales.

However, more significant changes in velocity and waves' positions occurred with increasing downstream distance from the weir. The discrepancies in velocity and position of the wave structures between the various scales and at prototype scale consistently reduced for decreasing scale factor of the simulation. This implies a physical model constructed with an excessively large scale factor could present considerable changes in the waves structures compared to the prototype. The precise cause of such increasing discrepancies is still not fully understood and requires extended analysis. It could be initially estimated that the substantial increases in turbulence levels at prototype scale (compared to the smaller scales, especially 1:50) generate greater velocities and changes in wave structures. The changes in position of the waves with different simulation scales are a newly discovered scale effects aspect which had not previously been identified in the literature. In the present work, an attempt was made to quantify the wave displacement at the various scales modelled. Further investigations of such phenomenon are required with extended simulations which could also be complemented with experimental studies.

- Limits to be ensured for the prediction of the labyrinth weir rating curve with a physical model were investigated with simulations at physical model scale and at prototype scale. The estimated upstream head over crest to ensure negligible scale effects was 0.03 m, which is very well correlated with derivations of this parameter conducted in other studies of non-linear weirs employing experimental techniques. Therefore, this value may be considered as a reference to ensure negligible scale effects in the prediction of labyrinth weir rating curves with physical modelling.
- The points above demonstrate that appropriately validated CFD VOF formulations such as the RANS Standard $k - \varepsilon$ model in conjunction with the PLIC scheme are suitable tools to investigate and quantify scale effects in physical models as well as to estimate limits to minimise these. In addition to providing new guidance to mitigate scale effects in physical models, the numerical model also revealed the existence of the change in position of the waves at the various scales. These discoveries constitute remarkably important information for the research of complex hydraulic free surface flows.

9.3. Implications of Key Findings

The research conducted in this thesis has confirmed that the 3D VOF method implemented with a turbulence model of the $k - \varepsilon$ family and an average cell size of 8×10^{-3} m in conjunction with the PLIC scheme in the ANSYS Fluent solver is capable of correctly predicting the rating curve of a labyrinth weir. This model is also able to provide a remarkably accurate characterisation of a range of flows downstream of the labyrinth weir, and appropriately predict the interaction of the spillway flow with the tail water. Therefore, this model can be implemented in the future to simulate a flow situation of similar nature and inform structure design. This study also indicated that if a significant amount of air is entrained in the weir nappe or in the hydraulic jump generated at the tail water, the model predictions are likely to not be capable of reproducing the correct amount of air entrained in the water phase with this method.

The conclusions drawn imply that cell size and interface capturing scheme are principal causes of discrepancy between predictions of the VOF methods implemented in the two solvers. Although further analysis may be beneficial to identify any further causes for such disagreements, especial attention must be paid to these two implementations when employing numerical simulations for design of hydraulic structures to ensure uncertainty is removed.

This study substantiated the capability of the 3D VOF to be utilised as a tool to investigate physical model scale effects. This includes the quantification of discrepancies between prototype and model, and derivation of minimum values to mitigate scale effects in physical models. The verification that this process can be successfully executed numerically implies it can be implemented in a multitude of hydraulic problems with significant potential for time and economic savings.

9.4. Recommendations for Further Work

The present work has been undertaken based on the time and resources available for its development. Consequently, several means could be embraced to further refine and develop the research presented. Possible conceptions are outlined as follows:

- The implementation of the newly devised IsoAdvector interface capturing scheme available in the latest versions of OpenFOAM to simulate the largest two flow rates over the labyrinth weir and spillway.
- The investigation of the observed changes in position of the waves with changes in scales. This could be undertaken with a larger simulation scale (for example 1:5) in the case of study and could be potentially complemented with experimental techniques.
- The implementation of various wall functions to observe their performance and establish the model sensitivity to these.
- The implementation of a further meshing strategy. This could be especially advantageous for the OpenFOAM simulations which require greater refinement. For example, the OpenFOAM meshing utility “snappyHexMesh” could be applied to create a more refined mesh of the spillway channel with availability of appropriate time and computational resources to generate a mesh of higher resolution. Another technique which could be explored consists in the solution-adaptive mesh refinement technique which allows the refinement of the mesh cells in an area of interest, based on a solution value of a physical variable. In the present case, this would be applied to the free surface.
- The implementation of an air entrainment model to reproduce the nappe aeration for the largest flow rates and the air entrained in the hydraulic jump generated at the tail water. This would require the utilisation of a solver with availability of such model (for example like Flow3D) and the corresponding calibration of the air entrainment parameters by conducting several simulations and comparing with experimental measurements.
- The derivation of experimental cross sections of the flow in the spillway channel in order to enhance the experimental dataset. This could be undertaken by using the available point data from the physical model and empirical relationships.

Chapter 9. Conclusions and Further Work

- The implementation of grass roughness in the spillway surrounding terrain. Simulations with and without roughness could be compared and main differences could consist in valuable outputs for future design problems.
- The turbulence model sensitivity analysis could also be conducted in Fluent at model and prototype scale. Results would reveal how the sensibility to turbulence modelling compares at the two scales with the two solvers.
- The derivation of the precise upstream head above crest for which Fluent simulations demonstrate negligible nappe displacement by conducting intermediate scale VOF simulations with this solver.

Additional analyses could be conducted to cover novel aspects which have not been regarded as part of this work. Possible developments include:

- The computation of the dimensionless head-discharge curve of the labyrinth weir based on the calculation of the coefficient of discharge from empirical relationships. This could be conducted by modelling additional flow rates for completeness, and results could be compared with the curves available in the literature.
- The calculation of the relative residual energy at the base of the labyrinth weir for the flow rates simulated and plot it with the existing data from the literature, such as Lopes *et al.* (2011) to examine how it compares.
- The SPH modelling of the labyrinth weir of study. To the author's knowledge, the SPH technique has not previously been implemented to simulate the flow over a labyrinth weir before and therefore its application and validation would be of remarkable interest.

References

- Ackers, J., Bennet, F., Karunaratne, G., Maccarthy, S. and Thornton, C. 2012. Physical and CFD modelling of a labyrinth spillway for Penwhirn reservoir. *In: Dams: Engineering in a Social & Environmental Context*, London. ICE Publishing.
- Aldaş, K. and Yapıcı, R. 2014. Investigation of Effects of Scale and Surface Roughness on Efficiency of Water Jet Pumps Using CFD. *Engineering Applications of Computational Fluid Mechanics*, **8**(1), pp.14-25.
- Aliabadi, S. K. and Tezduyar, T. E. 1993. Space-time finite element computation of compressible flows involving moving boundaries and interfaces. *Computer methods in applied mechanics and engineering*, **107**, pp.209-223.
- Ansys, I. 2009. *ANSYS FLUENT 12.0 Theory Guide*. ANSYS FLUENT.
- Ansys, I. 2017. *ANSYS Fluent* [online]. [Accessed 07/08/2017]. Available from: <http://www.ansys.com/Products/Fluids/ANSYS-Fluent>.
- Aulisa, E., Manservigi, S., Scardovelli, R. and Zaleski, S. 2007. Interface reconstruction with least-squares fit and split advection in three-dimensional Cartesian geometry. *Journal of Computational Physics*, **225**(2), pp.2301-2319.
- Aureli, F., Dazzi, S., Maranzoni, A., Mignosa, P. and Vacondio, R. 2015. Experimental and numerical evaluation of the force due to the impact of a dam-break wave on a structure. *Advances in Water Resources*, **76**, pp.29-42.
- Aydin, M. C. and Ulu, A. E. 2017. Antivortex Effects on Two-Cycle Trapezoidal Labyrinth Side Weirs. *Journal of Irrigation and Drainage Engineering*, **143**(7).
- Baird, W. F., Caldwell, J. M., Edge, B. L., Magoon, O. T. and Treadwell, D. D. 1980. Report on the damages to the sines breakwater, Portugal. *Coastal Engineering*, **184**, pp.3063-3077.
- Barenblatt, G. I. 1996. *Similarity, self-similarity and intermediate asymptotics*. Cambridge: Cambridge University Press.
- Bayon, A., Toro, J. P., Bombardelli, F. A., Matos, J. and López-Jiménez, P. A. 2017. Influence of VOF technique, turbulence model and discretization scheme on the numerical simulation of the non-aerated, skimming flow in stepped spillways. *Journal of Hydro-environment Research*.
- Bayon, A., Valero, D., García-Bartual, R., Vallés-Morán, F. J. and López-Jiménez, P. A. 2016. Performance assessment of OpenFOAM and FLOW-3D in the numerical modeling of a low Reynolds number hydraulic jump. *Environmental Modelling & Software*, **80**, pp.322-335.
- Beg, M. N. A., Carvalho, R. F. and Leandro, J. 2018. Effect of surcharge on gully-manhole flow. *Journal of Hydro-environment Research*, **19**, pp.224-236.
- Behr, M. 2001. Stabilised space-time finite element formulations for free-surface flows. *Communications for Numerical Methods in Engineering*, **11**, pp.813-819.
- Belytschko, T., Krongauz, Y., Organ, D., Fleming, M., Krysl, P. 1996. Meshless methods. An overview and recent developments. *Computer methods in applied mechanics and engineering*, **139**, pp.3-47.
- Belytschko, T., Lu, Y. Y. and Gu, L. 1994. Element free galerkin methods. *International Journal for Numerical Methods in Engineering*, **37**, pp.229-256.
- Berberovic, E., Van Hinsberg, N. P., Jakirlic, S., Roisman, I. V. and Tropea, C. 2009. Drop impact onto a liquid layer of finite thickness: dynamics of the cavity evolution. *Phys Rev E Stat Nonlin Soft Matter Phys*, **79**(3 Pt 2), p036306.

References

- Bilhan, O., Aydin, M. C., Emiroglu, M. E. and Miller, C. J. 2018. Experimental and CFD analysis of circular labyrinth weirs. *Journal of Irrigation and Drainage Engineering*, **144**(6), pp.1-11.
- Biscarini, C., Di Francesco, S. and Manciola, P. 2010. CFD modelling approach for dam break flow studies. *Hydrology and Earth System Sciences*, **14**, pp.705-718.
- Blancher, B., Montarros, F. and Laugier, F. 2011. Hydraulic comparison between Piano Key Weirs and labyrinth spillways. *In: Labyrinth and Piano Key Weirs - PKW 2011*, Liege, Belgium. Taylor & Francis Group.
- Bøckmann, A., Shipilova, O. and Skeie, G. 2012. Incompressible SPH for free surface flows. *Computers & Fluids*, **67**, pp.138-151.
- Bombardelli, F. A., Hirt, C. W., Garcia, M. H., Matthews, B. W., Fletcher, C. a. J., Partridge, A. C. and Vasquez, S. 2001. Discussion of Computations of curved free surface water flow on spiral concentrators. *Journal of Hydraulic Engineering*, **127**(7), pp.629-631.
- Bombardelli, F. A., Meireles, I. and Matos, J. 2010. Laboratory measurements and multi-block numerical simulations of the mean flow and turbulence in the non-aerated skimming flow region of steep stepped spillways. *Environmental Fluid Mechanics*, **11**(3), pp.263-288.
- Borman, D., Sleigh, A., Coughtrie, A. and Horton, L. 2014. Hydraulic free surface modelling with a novel validation approach. *In: 9th South African Conference on Computational and Applied Mechanics, Somerset West*.
- Boussinesq, M. J. 1887. *Essai sur la theorie des eaux courantes. Memories presentes par divers savants a l'academie des sciences XXIII*.
- Brinded, P., Gilbert, R., Kelham, P. and Peters, A. 2014. Eller Beck Flood Storage Reservoir – the challenges of low impact flood storage design. *In: 18th Biennial Conference of the British Dam Society at Queen's University, Belfast*. ICE Publishing.
- Bruwier, M., Ercicum, S., Piroton, M., Archambeau, P. and Dewals, B. J. 2015. Assessing the operation rules of a reservoir system based on a detailed modelling chain. *Natural Hazards and Earth System Science*, **15**(3), pp.365-379.
- Buckingham, E. 1914. On physically similar systems; Illustrations of the use of dimensional equations. *Physical Review*, **4**, pp.345-376.
- Burcharth, H. F. 1987. The lessons from recent breakwater failures: developments in breakwater design. *In: Technical Congress On Inshore Engineering, , Vancouver, Canada*.
- Celik, I., B, Ghia, U., Roache, P. J., Freitas, C. J., Coleman, H. and Raad, P. E. 2008. Procedure for Estimation and Reporting of Uncertainty Due to Discretization in CFD Applications. *Journal of Fluids Engineering*, **130**(7), pp.1-4.
- Chanson, H. 1989. Study of air entrainment and aeration devices. *Journal of Hydraulic Research*, **27**(3), pp.301-319.
- Chanson, H. 1996. *Air bubble entrainment in free-surface turbulent shear flows*. Bath: Academic Press.
- Chanson, H. 2004a. Air-water flows in water engineering and hydraulic structures. Basic processes and metrology. *In: F. YAZDANDOOST and J. ATTARI, eds. Hydraulics of Dams and River Structures*. London: Taylor & Francis Group.
- Chanson, H. 2004b. *The hydraulics of open channel flow: an introduction; basic principles, sediment motion, hydraulic modelling, design of hydraulic structures*. Oxford [UK]: Elsevier Butterworth Heinemann.

- Chanson, H. 2008. Physical modelling, scale effects and self similarity of flows on stepped spillways. *In: ASCE, ed. World Environmental and Water Resources Congress, Ahupua'a.*
- Chanson, H. 2009a. Current knowledge in hydraulic jumps and related phenomena. A survey of experimental results. *European Journal of Mechanics - B/Fluids*, **28**(2), pp.191-210.
- Chanson, H. 2009b. Turbulent air–water flows in hydraulic structures: dynamic similarity and scale effects. *Environmental Fluid Mechanics*, **9**(2), pp.125-142.
- Chanson, H. 2013. Hydraulics of aerated flows: qui pro quo? *Journal of Hydraulic Research*, **51**(3), pp.223-243.
- Chanson, H. and Carosi, G. 2007. Turbulent time and length scale measurements in high-velocity open channel flows. *Experiments in Fluids*, **42**(3), pp.385-401.
- Chanson, H. and Chachereau, Y. 2013. Scale effects affecting two-phase flow properties in hydraulic jump with small inflow Froude number. *Experimental Thermal and Fluid Science*, **45**, pp.234-242.
- Chanson, H. and Murzyn, F. 2008. Froude similitude and scale effects affecting air entrainment in hydraulic jumps. *In: World Environmental and Water Resources Congress, Ahupua'a.* ASCE, pp.1-10.
- Charney, J., G., Fjortoft, R. and Von Neumann, J. 1950. Numerical integration of the barotropic vorticity equation. *A quarterly journal of geophysics*, **2**, pp.238-254.
- Chaudhry, M. H. 1993. *Open Channel Flow*. Englewood Cliffs, New Jersey: Prentice Hall.
- Chen, Q., Zang, J., Kelly, D. M., Williams, C. J. K. and Dimakopoulos, A. 2015. Particle-in-cell numerical solver for free surface flows with fluid-solid interactions. *In: 30th Intl Workshop on Water Waves and Floating Bodies Bristol (UK).*
- Chesterton, J. O. and Warren, A. L. 2016. SC130003/R. *Reservoir Safety Research Strategy*. Delivering benefits through evidence, Bristol: Environmental Agency.
- Chow, V. T. 1959. *Open-Channel Hydraulics*. New York: McGraw-Hill.
- Courant, R., Friedrichs, K. and Lewy, H. 1928. On the partial difference equations of mathematical physics. *Mathematische Annalen*, **100**, pp.32-74.
- Crespo, A. J. C., Domínguez, J. M., Rogers, B. D., Gómez-Gesteira, M., Longshaw, S., Canelas, R., Vacondio, R., Barreiro, A. and García-Feal, O. 2015. DualSPHysics: Open-source parallel CFD solver based on Smoothed Particle Hydrodynamics (SPH). *Computer Physics Communications*, **187**, pp.204-216.
- Crespo, A. J. C., Gómez-Gesteira, M. and Dalrymple, R. A. 2008. Modelling Dam Break Behaviour over a Wet Bed by a SPH Technique. *JOURNAL OF WATERWAY, PORT, COASTAL, AND OCEAN ENGINEERING*, (134), pp.313-320.
- Crookston, B. and Tullis, B. 2010. Hydraulic performance of labyrinth weirs. *In: 3rd International Junior Researcher and Engineer Workshop on Hydraulic Structures, Brisbane.*
- Crookston, B. M. 2010. *Labyrinth Weirs*. PhD thesis, Utah State University.
- Crookston, B. M., Paxson, G. S. and Savage, B. M. 2012. Hydraulic Performance of Labyrinth Weirs for High Headwater Ratios. *In: J. MATOS, S. PAFLIARA and I. MEIRELES, eds. 4th IAHR International Symposium on Hydraulic Structures 9-11 February 2012, Porto, Portugal.* IAHR.
- Crookston, B. M. and Tullis, B. P. 2012a. Arced labyrinth weirs. *Journal of Hydraulic Engineering*, **138**(6), pp.555-562.

References

- Crookston, B. M. and Tullis, B. P. 2012b. Discharge Efficiency of Reservoir-Application-Specific Labyrinth Weirs. *Journal of Irrigation and Drainage Engineering*, **138**(6), pp.564-568.
- Crookston, B. M. and Tullis, B. P. 2012c. Labyrinth Weirs: Nappe Interference and Local Submergence. *Journal of Irrigation and Drainage Engineering*, **138**(8), pp.757-765.
- Crookston, B. M. and Tullis, B. P. 2013a. Hydraulic Design and Analysis of Labyrinth Weirs. I Discharge Relationships. *Journal of Irrigation and Drainage Engineering*, **139**(5), pp.363-370.
- Crookston, B. M. and Tullis, B. P. 2013b. Hydraulic Design and Analysis of Labyrinth Weirs. II: Nappe Aeration, Instability, and Vibration. *Journal of Irrigation and Drainage Engineering*, **139**(5), pp.371-377.
- Cruchaga, M., Celentano, D. and Tezduyar, T. 2001. A moving Lagrangian interface technique for flow computations over fixed meshes. *Computer methods in applied mechanics and engineering*, **191**, pp.525-543.
- Dabling, M. and Crookston, B. M. 2012. Staged and notched labyrinth weir hydraulics. *In: B. P. TULLIS and J. R., eds. 4th International Junior Researcher and Engineer Worksop on Hydraulic Structures, Logan, UT. Utah State Univ.*
- Dabling, M. and Tullis, B. 2013. Staged labyrinth weirs and their effects on the outflow hydrograph. *In: Labyrinth and Piano Key Weirs II - PKW 2013: Taylor & Francis Group.*
- Dabling, M. R. and Tullis, B. P. 2017. Modifying the downstream hydrograph with staged labyrinth weirs. *Journal of Applied Water Engineering and Research*, pp.1-8.
- Dabling, M. R., Tullis, B. P. and Crookston, B. M. 2013. Staged Labyrinth Weir Hydraulics. *Journal of Irrigation and Drainage Engineering*, **139**(11), pp.955-960.
- De Padova, D., Mossa, M., Sibilla, S. and Torti, E. 2013. 3D SPH modelling of hydraulic jump in a very large channel. *Journal of Hydraulic Research*, **51**(2), pp.158-173.
- Defra. 2017. *Central Government Funding for Funding for Flood and Coastal Erosion Risk Management in England*. UK Government Publications, DEFRA.
- Denner, F. and Van Wachem, B. G. M. 2014. Compressive VOF method with skewness correction to capture sharp interfaces on arbitrary meshes. *Journal of Computational Physics*, **279**, pp.127-144.
- Dhaubhadel, M. N. 1996. Review: CFD applications in the automotive industry. *Journal of Fluids Engineering*, **118**, pp.647-653.
- Donea, J., Huerta, A., Ponthot, J.-P. and Rodriguez-Ferran, A. 2004. Arbitrary Lagrangian-Eulerian Methods. *In: E. STEIN, R. D. BORST and T. J. R. HUGUES, eds. Encyclopedia of Computational Mechanics*. John Willey & Sons Ltd ISBN: 9780470846995, pp.1-25.
- Duarte, F., Gormaz, R. and Natesan, S. 2004. Arbitrary Lagrangian–Eulerian method for Navier–Stokes equations with moving boundaries. *Computer Methods in Applied Mechanics and Engineering*, **193**(45-47), pp.4819-4836.
- Dufresne, M., Vasquez, J. and Bercovitz, Y. 2018. Complementarities Between Physical Modelling and Computational Fluid Dynamics for an Ecological Continuity Project. *In: 7th IAHR International Symposium on Hydraulic Structures, Aachen, Germany.*
- Ebner, L., Askelson, S., Thompson, E. and Cox, N. 2016. Numerical Modelling of the Spillways for the Dam Raise at Isabella Dam. *In: C. B. T. (EDS.), ed. Hydraulic*

- Structures and Water System Management. 6th IAHR International Symposium on Hydraulic Structures, 27-30 June, Portland, USA.* Utah State University.
- Elsayed, K. and Lacor, C. 2011. Numerical modeling of the flow field and performance in cyclones of different cone-tip diameters. *Computers & Fluids*, **51**(1), pp.48-59.
- Environment Agency. 2016. *Post incident reporting for reservoirs. Annual report 2015.* Bristol.
- Epicum, S., Dewals, B., Archambeau, P. and Piroton, M. 2017a. 15 years of composite modelling to enhance hydraulic structures studies. *In: SimHydro 2017 - Choosing the Right Model in Applied Hydraulics*, Sophia Antipolis, France.
- Epicum, S., Dewals, B. J., Archambeau, P. and Piroton, M. 2015. Composite Hydraulic modelling to design a complex dam spillway. *In: IAHR World Congress*, The Hague, the Netherlands.
- Epicum, S., Dewals, B. J., Vuillot, J.-M., Archambeau, P. and Piroton, M. 2012. The Taoussa Project: An example of effective composite modelling. *In: 4th IAHR International Symposium on Hydraulic Structures, Porto, Portugal.*
- Epicum, S., Laugier, F., Khanh, M. H. T. and Pfister, M. 2017b. Labyrinth and Piano Key Weirs III PKW 2017. *In: International Workshop on Labyrinth and Piano Key Weirs Qui Nhon, Vietnam.* CRC Press.
- Epicum, S., Silvestri, A., Dewals, B., Archambeau, P. and Piroton, M. 2013a. Escoloubre Piano Key weir: Prototype versus scale models. *In: Second international workshop on labyrinth and piano key weirs*, Chatou, Paris, France.
- Epicum, S., Silvestri, A., Dewals, B. J., Archambeau, P. and Piroton, M. 2013b. Escoloubre Piano Key Weir: Prototype versus scale models. *In: Labyrinth and Piano Key Weirs II - PKW 2013*, Chatou, France. CRC Press.
- Epicum, S., Tullis, B. P., Lodomez, M., Archambeau, P., Dewals, B. J. and Piroton, M. 2016. Scale effects in physical piano key weirs models. *Journal of Hydraulic Research*, **54**(6), pp.692-698.
- Ettema, R., Arndt, R., Roberts, P. and Wahl, T. 2000. *Hydraulic Modeling: Concepts and Practice.* New York [US]: American Society of Civil Engineers.
- Evans, M. W. and Harlow, F. H. 1957. *The particle-in-cell method for hydrodynamic calculations.* Physics and Mathematics, New Mexico [USA]: Los Alamos Scientific Laboratory of the University of California.
- Falvey, H. T. 2003. *Hydraulic Design of Labyrinth Weirs.* Virginia, USA: ASCE Press.
- Ferrari, A. 2010. SPH simulation of free surface flow over a sharp-crested weir. *Advances in Water Resources*, **33**(3), pp.270-276.
- Ferrari, A., Dumbser, M., Toro, E. F. and Armanini, A. 2009a. A new 3D parallel SPH scheme for free surface flows. *Computers & Fluids*, **38**(6), pp.1203-1217.
- Ferrari, G. E., Politano, M. and Weber, L. 2009b. Numerical simulation of free surface flows on a fish bypass. *Computers & Fluids*, **38**(5), pp.997-1002.
- Fowler, H. J. and Kilsby, C. G. 2003. Implications of changes in seasonal and annual extreme rainfall. *Geophysical Research Letters*, **30**(13).
- Fromm, J. E. 1961. *Difference approximations for fluid dynamics.* Los Alamos, New Mexico: Los Alamos Scientific Laboratory of the University of California.
- Frostick, L. E., Mclelland, S. J. and (Eds), T. G. M. 2011. *Users Guide to Physical Modelling and Experimentation. Experience of the HYDRALAB Network.* Leiden [The Netherlands].

References

- Fuentes-Pérez, J. F., Silva, A. T., Tuhtan, J. A., García-Vega, A., Carbonell-Baeza, R., Musall, M. and Kruusmaa, M. 2018. 3D modelling of non-uniform and turbulent flow in vertical slot fishways. *Environmental Modelling & Software*, **99**, pp.156-169.
- Fujii, K. 2005. Progress and future prospects of CFD in aerospace—Wind tunnel and beyond. *Progress in Aerospace Sciences*, **41**(6), pp.455-470.
- Galavís, A., González, D., Alfaro, I. and Cueto, E. 2008. Improved boundary tracking in meshless simulations of free-surface flows. *Computational Mechanics*, **42**(3), pp.467-479.
- Gaskell, P. H. and Lau, K. C. 1988. Curvature-compensated convective transport: Smart, a new boundedness-preserving transport algorithm. *International Journal for Numerical Methods in Fluids*, **8**, pp.617-641.
- George, W. K. and Gibson, M. M. 1992. The self preservation of homogeneous shear flow turbulence. *Experiments in Fluids*, **13**, pp.229-238.
- Gerritsen, H., Sutherland, J., Deigaard, R., Sumer, M., Fortes, C. J. E. M., Sierra, J. P. and Schmidtke, U. 2011. Composite modelling of interactions between beaches and structures. *Journal of Hydraulic Research*, **49**(sup1), pp.2-14.
- Ghadimi, P., Farsi, M. and Dashtimanesh, A. 2012. Study of Various Numerical Aspects of 3D-SPH for Simulation of the Dam Break Problem. *J. of the Braz. Soc. of Mech. Sci & Eng.*, **34**(4), pp.486-491.
- Gomez-Gesteira, M., Rogers, B. D., Crespo, A. J. C., Dalrymple, R. A., Narayanaswamy, M. and Dominguez, J. M. 2012. SPHysics – development of a free-surface fluid solver – Part 1: Theory and formulations. *Computers & Geosciences*, **48**, pp.289-299.
- Gopala, V. R. and Van Wachem, B. G. M. 2008. Volume of fluid methods for immiscible-fluid and free-surface flows. *Chemical Engineering Journal*, **141**(1-3), pp.204-221.
- Greenshields, C. J. 2017. *OpenFOAM: The OpenFOAM Foundation User Guide* version 5.0, OpenFOAM Foundation Ltd.
- Hager, W. H. 1999. *Wastewater hydraulics - Theory and Practice*. Heidelberg, Germany: Springer-Verlag.
- Hager, W. H., Pfister, M. and Tullis, B. 2015. Labyrinth weirs development until 1985. *In: 36th IAHR World Congress*, The Hague, The Netherlands. IAHR.
- Harlow, F. H. and Nakayama, P. I. 1968. *Transport of turbulence energy decay rate*. Los Alamos, New Mexico: Los Alamos Scientific Laboratory of the University of California.
- Harlow, F. H. and Welch, J. E. 1965. Numerical calculation of time dependent viscous incompressible flow of fluid with free surface. *Physics of Fluids*, **8**(12), pp.2182-2189.
- Hay, N. and Taylor, G. 1970. Performance and design of labyrinth weirs. *Journal of the Hydraulics Division*, **96**(11), pp.2337-2357.
- Heiner, B. 2013. *Composite modelling of the halfway wash fish barrier*. Hydraulic Laboratory Technical Memorandum, Denver, Colorado: U.S. Department of the interior.
- Heller, V. 2011. Scale effects in physical hydraulic engineering models *Journal of Hydraulic Research*, **49**(3), pp.293-306.
- Heller, V. 2016. Self-similarity and Reynolds number invariance in Froude modelling. *Journal of Hydraulic Research*, **55**(3), pp.293-309.

- Heller, V., Hager, W. H. and Minor, H.-E. 2007. Scale effects in subaerial landslide generated impulse waves. *Experiments in Fluids*, **44**(5), pp.691-703.
- Hieu, P. D. and Tanimoto, K. 2006. Verification of a VOF-based two-phase flow model for wave breaking and wave–structure interactions. *Ocean Engineering*, **33**(11-12), pp.1565-1588.
- Hinchliff, D. L. and Houston, K. L. 1984. Hydraulic design and application of labyrinth spillways. In: *USCOLD Lecture Dam Safety and Rehabilitation*, Denver, Colo. USCOLD.
- Hirt, C. W., Amsden, A. A. and Cook, J. L. 1974. An arbitrary lagrangian-eulerian computing method for all flow speeds. *Journal of Computational Physics*, **14**, pp.227-253.
- Hirt, C. W. and Nichols, B. D. 1981. VOF method for the dynamics of free boundaries. *Journal of Computational Physics*, **39**, pp.201-225.
- Hsu, M.-H., Chen, C.-H. and Teng, W.-H. 2002. An arbitrary lagrangian-eulerian finite element method for solving three-dimensional free surface flows. *Journal of Hydraulic Research*, **39**(5), pp.481-491.
- Huang, M., Wu, L. and Chen, B. 2012. A piecewise linear interface capturing Volume of Fluid method based on unstructured grid. *Numerical Heat Transfer*, **61**, pp.412-437.
- Huang, W., Yang, Q. and Xiao, H. 2009. CFD modeling of scale effects on turbulence flow and scour around bridge piers. *Computers & Fluids*, **38**(5), pp.1050-1058.
- Hughes, J. P. and Graham, D. I. 2010. Comparison of incompressible and weakly-compressible SPH models for free-surface water flows. *Journal of Hydraulic Research*, **48**(sup1), pp.105-117.
- Hughes, S. A. 1993. *Physical models and laboratory techniques on coastal engineering*. Advanced series on ocean engineering. London: World Scientific.
- Hughes, T. J. R., Liu, W. K. and Zimmermann, T. K. 1981. Lagrangian-Eulerian finite element formulation for incompressible viscous flows. *Computer methods in applied mechanics and engineering*, **29**, pp.329-349.
- Hugues, S. A. 1993. *Physical models and laboratory techniques in coastal engineering*. Advanced Series on Ocean Engineering. Singapore: World Scientific Publishing.
- Icold. 2013. *Guidelines for use of numerical models in dam engineering (Bulletin 155)*. Paris: Commission Internationale des Grands Barrages.
- Idelsohn, S. R., Storti, M. A. and Onate, E. 2001. Lagrangian formulations to solve free surface incompressible inviscid fluid flows. *Computer methods in applied mechanics and engineering*, **191**, pp.583-593.
- Institution of Civil Engineers. 2015. *Floods and Reservoir Safety, 4th Edition*. London: ICE Publishing.
- Issa, R. I., Grosman, A. D. and Watkins, A. P. 1986. The computation of compressible and incompressible recirculating flows. *Journal of Computational Physics*, **62**(66-82).
- Jeffrey, A., Guinot, V., Reeve, D. E. and Novak, P. 2010. *Hydraulic Modelling - An introduction: Principles, Methods and Applications*. Abingdon [UK]; New York [US]: Spon Press.
- Jiang, C., Schroeder, C., Selle, A., Teran, J. and Stomakhin, A. 2015. The affine particle-in-cell method. *ACM Transactions on Graphics*, **34**(4), pp.51:1-51:10.

References

- Jonkman, S. N. 2005. Global Perspectives on Loss of Human Life Caused by Floods. *Natural Hazards*, **34**, pp.151-175.
- Kamphuis, J. W. 2000. Designing with models. *In: Proceedings 27th International Conference on Coastal Engineering*: ASCE, pp.19-32.
- Kelly, D. M., Chen, Q. and Zang, J. 2015. PICIN: A Particle-in-Cell Solver for Incompressible Free Surface Flows with Two-Way Fluid-Solid Coupling. *SIAM Journal on Scientific Computing*, **37**(3), pp.B403-B424.
- Khanh, M. H. T. 2013. The piano key weirs 15 years of research development prospect. *In: Labyrinth and Piano Key Weirs II*, Paris, France. CRC Press.
- Khatsuria, R. M. 2005. *Hydraulics of Spillways and Energy Dissipators*. Civil and Environmental Engineering. New York: Marcel Dekker.
- Kim, D. G. and Park, J. H. 2005. Analysis of flow structure over ogee spillway in consideration of scale and roughness effects by using CFD model. *KSCE Journal of Civil Engineering*, **9**(2), pp.161-169.
- Klajj, C. M., Hoekstra, M. and Vaz, G. 2018. Design, analysis and verification of a volume-of-fluid model with interface-capturing scheme. *Computers & Fluids*, **170**, pp.324-340.
- Kobus, H. and Abraham, G. 1980. *Hydraulic Modelling*. Hamburg.
- Koshizuka, S. and Oka, Y. 1996. Moving-particle semi-implicit method for fragmentation in incompressible fluid. *Nuclear Science and Engineering*, **123**, pp.421-434.
- Kvočka, D., Falconer, R. A. and Bray, M. 2016. Flood hazard assessment for extreme flood events. *Natural Hazards*, **84**(3), pp.1569-1599.
- Lauder, B. E. and Spalding, D. B. 1974. The numerical computation of turbulent flows. *Computational methods in applied mechanics and engineering*, **3**, pp.269-289.
- Lee, E. S., Moulinec, C., Xu, R., Violeau, D., Laurence, D. and Stansby, P. 2008. Comparisons of weakly compressible and truly incompressible algorithms for the SPH mesh free particle method. *Journal of Computational Physics*, **227**(18), pp.8417-8436.
- Leite-Ribeiro, M., Pfister, M., Schleiss, A. J. and Boillat, J.-L. 2012. Hydraulic design of A-type Piano Key Weirs. *Journal of Hydraulic Research*, **50**(4), pp.400-408.
- Leonard, B. P. 1991. The ULTIMATE conservative difference scheme applied to unsteady one-dimensional advection. *Computer methods in applied mechanics and engineering*, **88**, pp.17-74.
- Lopes, R., Matos, J. and J., M. 2006. Discharge capacity and residual energy of labyrinth weirs. *In: International Junior Researcher and Engineer Worksop on Hydraulic Structures (IJREWHS '06)*, Brisbane, Australia. Division of Civil Engineering, Univ. of Queensland, pp.47-55.
- Lopes, R., Matos, J. and Melo, J. F. 2008. Characteristic depths and energy dissipation downstream of a labyrinth weir. *In: S. PAGLIARA, ed. 2nd IJERW on Hydraulic Structures, Pisa, Italy*.
- Lopes, R., Matos, J. and Melo, J. F. 2011. Flow properties and residual energy downstream of labyrinth weirs. *In: Labyrinth and Piano Key Weirs - PKW 2011*, Liege, Belgium. Taylor & Francis Group.
- Lv, X., Zou, Q. and Reeve, D. 2011. Numerical simulation of overflow at vertical weirs using a hybrid level set/VOF method. *Advances in Water Resources*, **34**(10), pp.1320-1334.

- Lv, X., Zou, Q., Zhao, Y. and Reeve, D. 2010. A novel coupled level set and volume of fluid method for sharp interface capturing on 3D tetrahedral grids. *Journal of Computational Physics*, **229**(7), pp.2573-2604.
- Machiels, O., Erpicum, S., Dewals, B. J., Archambeau, P. and Piroton, M. 2011. Experimental observation of flow characteristics over a Piano Key Weir. *Journal of Hydraulic Research*, **49**(3), pp.359-366.
- Maddrell, R. 2005. Lessons re-learned from the failure of marine structures. *In: Coastlines, Structures and Breakwaters*, London, UK. Institution of Civil Engineers.
- Magalhães, A. and Lorena, M. 1989. 736. *Hydraulic Design of Labyrinth Weirs*. National Laboratory of Civil Engineering (LNEC), Lisbon.
- Magoules, F. 2011. *Computational Fluid Dynamics*. Boca Raton [US]: Chapman & Hall/CRC.
- Maitre, E. 2006. Review of numerical methods for free interfaces. *In: G. C. D. PHASE*, ed. *Talk given at Ecole Thematique. Modeles de champ de phase pour l'evolution de structures complexes, Les Houches, France*.
- Mandelbrot, B. B. 1983. *The Fractal Geometry of Nature*. San Francisco: Henry Holt and Company.
- Mattew, G. D. 1991. Higher order one dimensional equation of potential flow in open channels. *ICE Proceedings*, pp.187-201.
- Menter, F. R. 1994. Two-equation eddy-viscosity turbulence models for engineering applications. *AIAA Journal*, **32**(8), pp.1598-1605.
- Mittal, R. and Iaccarino, G. 2005. Immersed Boundary Methods. *Annual Review of Fluid Mechanics*, **37**(1), pp.239-261.
- Mohammadzadeh-Habili, J., Heidarpour, M. and Samiee, S. 2017. Study of Energy Dissipation and Downstream Flow Regime of Labyrinth Weirs. *Iranian Journal of Science and Technology, Transactions of Civil Engineering*, **42**(2), pp.111-119.
- Monaghan, J. J. 1988. An introduction to SPH. *Computer Physics Communications*, **48**, pp.89-96.
- Monaghan, J. J. 1994. Simulating Free Surface Flows with SPH. *Journal of Computational Physics*, **110**, pp.399-406.
- Moody, L. F. 1944. Friction factors for pipe flow. *Transactions of the ASME*, **66**, pp.671-684.
- Muzaferija, S., Peric, M., Sames, P. and Schelin, T. 1998. A two-fluid Navier-Stokes solver to simulate water entry. *In: Twenty-Second Symposium on Naval Hydrodynamics*.
- Nayroles, B., Touzot, G. and Villon, P. 1992. Generalising the finite element method. Diffuse approximation and diffuse elements. *Computational Mechanics*, **10**, pp.307-318.
- New York Times. 2017. *What Happened at the Oroville Dam* [online]. [Accessed 06/11/2017]. Available from: <https://www.nytimes.com/interactive/2017/02/13/us/oroville-dam.html>.
- Nguyen, V. T. 2015. 3D numerical simulation of free surface flows over hydraulic structures in natural channels and rivers. *Applied Mathematical Modelling*.
- Nithiarasu, P. 2005. An arbitrary lagrangian eulerian formulation for free surface flows using the characteristic based split scheme. *International Journal for Numerical Methods in Fluids*, **48**, pp.1415-1428.

References

- Novak, P., Guinot, V., Jeffrey, A. and Reeve, D. 2010. *Hydraulic Modelling - An Introduction. Principles Methods and Applications*. New York: Spon Press.
- Novak, P., Moffat, A. I. B., Nalluri, C. and Narayanan, R. 2007. *Hydraulic Structures 4th edition*. USA and Canada: Taylor & Francis.
- Oertel, M. and Bung, D. B. 2012. Initial stage of two-dimensional dam-break waves: laboratory versus VOF. *Journal of Hydraulic Research*, **50**(1), pp.89-97.
- Oertel, M., Mönkemöller, J. and Schlenkhoff, A. 2012. Artificial stationary breaking surf waves in a physical and numerical model. *Journal of Hydraulic Research*, **50**(3), pp.338-343.
- Onate, E., Idelsohn, S., Zienkiewicz, O. C., Taylor, R. L. and Sacco, C. 1996. A stabilised finite point method for analysis of fluid mechanics problems. *Computer methods in applied mechanics and engineering*, **139**, pp.315-346.
- Ortega, E., Oñate, E., Idelsohn, S. and Flores, R. 2013. A meshless finite point method for three-dimensional analysis of compressible flow problems involving moving boundaries and adaptivity. *International Journal for Numerical Methods in Fluids*, **73**(4), pp.323-343.
- Osborn, T. J. and Hulme, M. 2002. Evidence for trends in heavy rainfall events over the UK. *The Royal Society*, **360**(1), pp.1313-1325.
- Osher, S. and Sethian, J. A. 1988. Fronts Propagating with Curvature Dependent Speed. Algorithms Based on Hamilton-Jacobi Formulations. *Journal of Computational Physics*, **79**, pp.12-49.
- Park, I. R., Kim, K. S., Kim, J. and Van, S. H. 2009. A volume-of-fluid method for incompressible free surface flows. *International Journal for Numerical Methods in Fluids*, **61**(12), pp.1331-1362.
- Patankar, S. V. and Spalding, D. B. 1972. A Calculation procedure for heat, mass and momentum transfer in three-dimensional parabolic flows. *International Journal for Heat Mass Transfer*, **15**, pp.1787-1806.
- Paxson, G., Crookston, B., Savage, B., Tullis, B. and Lux, F. 2008. The hydraulic design toolbox: Theory and modelling for the Lake Townsend spillway replacement project. *Association of State Dam Safety Officials (ASDSO)*.
- Paxson, G. and Savage, B. 2006. Labyrinth spillways: Comparison of two popular U.S.A. design methods-and-consideration of non standard approach conditions and geometries. In: J. MATOS and H. CHANSON, eds. *International Junior Researcher and Engineer Workshop on Hydraulic Structures, Brisbane, Australia*. Univ. of Queensland.
- Pedersen, Ø., Fleit, G., Pummer, E., Tullis, B. P. and Rüter, N. 2018. Reynolds-Averaged Navier-Stokes Modeling of Submerged Ogee Weirs. *Journal of Irrigation and Drainage Engineering*, **144**(1).
- Peskin, C. S. 1977. Numerical Analysis of Blood Flow in the Heart. *Journal of Computational Physics*, **25**, pp.220-252.
- Peskin, C. S. 2002. The immersed boundary method. *Acta Numerica*, pp.1-39.
- Pfister, M., Battisacco, E., De Cesare, G. and Schleiss, A. J. 2013a. Scale effects related to the rating curve of cylindrically crested Piano Key weirs. In: *Second international workshop on labyrinth and piano key weirs*, Chatou, Paris, France.
- Pfister, M. and Chanson, H. 2012. Discussion of Scale effects in physical hydraulic engineering models. *Journal of Hydraulic Research*, **50**(2), pp.244-246

- Pfister, M., Erpicum, S., Machiels, O., Schleiss, A. J. and Piroton, M. 2012. Discussion. Discharge coefficient for free and submerged flow over Piano Key weirs. *Journal of Hydraulic Research*, **50**(6), pp.642-645.
- Pfister, M. and Hager, W. H. 2012. Deflector-jets affected by pre-aerated approach flow. *Journal of Hydraulic Research*, **50**(2), pp.181-191.
- Pfister, M., Schleiss, A. J. and Tullis, B. 2013b. Effect of driftwood on hydraulic head of Piano Key weirs. *In: Labyrinth and Piano Key Weirs II - PKW 2013*, Chatou, France. CRC Press.
- Pilliod, J. E. and Puckett, E. G. 2004. Second-order accurate volume-of-fluid algorithms for tracking material interfaces. *Journal of Computational Physics*, **199**(2), pp.465-502.
- Piroton, M., Lejeune, A., Archambeau, P., Erpicum, S. and Dewals, B. J. 2003. Numerical-experimental interaction in hydrodynamics: An integrated approach for the optimal management of hydraulic structures and hydrographic basins. *In: 9th Int. Conf. on Enhancement and Promotion of Computational Methods in Engineering and Science*, Macao.
- Pope, S. B. 2000. *Turbulent Flows*. Cambridge: Cambridge University Press.
- Ribeiro, M. L., Pfister, M. and Schleiss, A. J. 2013. Overview of Piano Key weir prototypes and scientific model investigations. *In: Labyrinth and Piano Key Weirs II*, Paris, France. CRC Press.
- Richardson, L. F. 1910. The Approximate Arithmetical Solution by Finite Differences of Physical Problems Involving Differential Equations, with an Application to the Stresses in a Masonry Dam. *Transactions of the Royal Society of London, Series A*, **210**, pp.307-357.
- Richardson, L. F. 1927. The Deferred Approach to the Limit. *Transactions of the Royal Society of London, Series A*, **226**, pp.299-361.
- Rider, W. J. and Kothe, D. B. 1998. Reconstructing Volume Tracking. *Journal of Computational Physics*, **141**, pp.112-152.
- Roache, P. J. 1994. Perspective: A method for uniform reporting of grid refinement studies. *Journal of Fluids Engineering*, **116**, pp.405-413.
- Roache, P. J. 1998. *Fundamentals of Computational Fluid Dynamics*. New Mexico, USA: Hermosa.
- Roenby, J., Bredmose, H. and Jasak, H. 2016. A computational method for sharp interface advection. *Royal Society Open Science*, pp.0-27.
- Roubtsova, V. and Kahawita, R. 2006. The SPH technique applied to free surface flows. *Computers & Fluids*, **35**(10), pp.1359-1371.
- Salazar, F., J., S.-M. and Onate, E. 2014. Analysis of flow pattern in labyrinth weirs. *In: Dam protections against overtopping and accidental leakage*, Madrid, Spain. Taylor & Francis Group.
- Santos, F. L. P., Ferreira, V. G., Tomé, M. F., Castelo, A., Mangiavacchi, N. and Mckee, S. 2012. A marker-and-cell approach to free surface 2-D multiphase flows. *International Journal for Numerical Methods in Fluids*, **70**(12), pp.1543-1557.
- Sarker, M. A. and Rhodes, D. G. 2004. Calculation of free-surface profile over a rectangular broad-crested weir. *Flow Measurement and Instrumentation*, **15**(4), pp.215-219.
- Savage, B., Crookston, B. and Paxson, G. 2016. Physical and numerical Modeling of large headwater ratios for a 15degrees labyrinth spillway. *Journal of Hydraulic Engineering*, **142**(11), pp.1-7.

References

- Savage, B., Frizell, K. and Crowder, J. 2004. Brains versus Brawn. The changing world of hydraulic model studies. *In: Dam Safety, ASDSO, Lexington, KY.*
- Scott, A. and Lowe, P. E. 2003. Omission of critical Reynolds number for open channel flows in many textbooks. *Journal of Professional Issues in Engineering, Education and Practice*, **129**(1), pp.58-59.
- Sethian, J. A. 1996. Theory, algorithms and applications of level set methods for propagating interfaces. *Acta Numerica*, **5**, pp.309-395.
- Shakibaeinia, A. and Jin, Y.-C. 2009. A weakly compressible MPS method for modeling of open-boundary free-surface flow. *International Journal for Numerical Methods in Fluids*, **63**, pp.1208-1232.
- Sheu, T. W. H., Chiao, C. and Huang, C. 2011. Development of a Particle Interaction Kernel Function in MPS Method for Simulating Incompressible Free Surface Flow. *Journal of Applied Mathematics*, **2011**, pp.1-16.
- Slater, J. W. 2008. *Uncertainty and Error in CFD Simulations* [online]. [Accessed 20/07/2018]. Available from: <https://www.grc.nasa.gov/WWW/wind/valid/tutorial/errors.html>.
- Soulaimani, A. and Saad, Y. 1998. An arbitrary Lagrangian Eulerian finite element method for solving three dimensional free surface flows. *Computer methods in applied mechanics and engineering*, **162**, pp.79-106.
- Souli, M. and Zolesio, J. P. 2001. Arbitrary Lagrangian-Eulerian and free surface methods in fluid mechanics. *Computational methods in applied mechanics and engineering*, **191**, pp.451-466.
- Stagonas, D., Warbrick, D., Muller, G. and Magagna, D. 2011. Surface tension effects on energy dissipation by small scale, experimental breaking waves. *Coastal Engineering*, **58**(9), pp.826-836.
- Sun, D. L. and Tao, W. Q. 2010. A coupled volume-of-fluid and level set (VOSET) method for computing incompressible two-phase flows. *International Journal of Heat and Mass Transfer*, **53**(4), pp.645-655.
- Sun, Z., Djidjeli, K., Xing, J. T. and Cheng, F. 2015. Modified MPS method for the 2D fluid structure interaction problem with free surface. *Computers & Fluids*, **122**, pp.47-65.
- Sussman, M., Smereka, P. and Osher, S. 1994. A level set approach for computing solutions to incompressible two phase flow. *Journal of Computational Physics*, **114**, pp.146-159.
- Sutherland, J. and Barfuss, S. L. 2012. Composite modelling: combining physical and numerical models. *In: IAHR World Congress, Brisbane, Australia.*
- Tabbara, M., Chatila, J. and Awwad, R. 2005. Computational simulation of flow over stepped spillways. *Computers & Structures*, **83**(27), pp.2215-2224.
- Tezduyar, T. E. 2004. Interface-Tracking and Interface-Capturing Techniques for Computation of Moving Boundaries and Interfaces. *In: 6th World Congress on Computational Mechanics in conjunction with APCOM'04, Beijing, China.* Tsinghua University Press & Springer-Verlag.
- The Royal Academy of Engineering, I., Ciwem. 2010. *Global Water Security - an engineering perspective*. London: The Royal Academy of Engineering.
- Thompson, E., Cox, N., Ebner, L. and Tullis, B. 2016. The Hydraulic Design of an Arced Labyrinth Weir at Isabella Dam. *In: 6th International Symposium on Hydraulic Structures, Portland, Oregon, USA.* Utah State University.

- Tome, M. F., Cuminato, J. A., Castelo, A. and Ferreira, V. G. 2004. Recent advances in the marker and cell method. *Archives of Computational Methods in Engineering*, **11**(2), pp.107-142.
- Tome, M. F. and Mckee, S. 1994. GENSIMAC: A Computational Marker and Cell Method for Free Surface Flows in General Domains. *Journal of Computational Physics*, **110**, pp.171-186.
- Tullis, B. 2018. Size Scale Effects of Labyrinth Weir Hydraulics. *In: 7th International Symposium on Hydraulic Structures*, Aachen, Germany.
- Tullis, B., Ercicum, S., Laugier, F. and Crookston, B. 2018. *Workshop on Nonlinear Weir Design: Theory and Practice*. Aachen.
- Tullis, B., Young, N. and Crookston, B. 2017. Physical modelling size-scale effects for labyrinth weirs with half-round crests. *In: Labyrinth and Piano Key Weirs III*, Qui Nhon, Vietnam. CRC Press.
- Tullis, B. P., Young, J. C. and Chandler, M. A. 2007. Head-Discharge Relationships for Submerged Labyrinth Weirs. *Journal of Hydraulic Engineering*, **133**(3), pp.248-254.
- Tullis, J. P., Amanian, N. and Waldron, D. 1995. Design of Labyrinth Spillways. *Journal of Hydraulic Engineering*, **121**(3), pp.247-255.
- Ubbink, O. and Issa, R. I. 1999. A method for capturing sharp fluid interfaces on arbitrary meshes. *Journal of Computational Physics*, **153**, pp.26-50.
- Unverdi, S. O. and Tryggvason, G. 1992. A front tracking method for viscous, incompressible multi-fluid flows. *Journal of Computational Physics*, **100**, pp.25-37.
- Upr Utah State University. 2017. *Utah State University Engineers Build Physical Model of Oroville Dam* [online]. [Accessed].
- Utah State University. 2017. *Miniaturizing America's Tallest Dam* [online]. [Accessed 06/11/2017]. Available from: <https://engineering.usu.edu/news/2017-10-02-oroville>.
- Van Os, A., Soulsby, R. and Kirkegaard, J. 2004. The future role of experimental methods in European hydraulic research: towards a balanced methodology. *Journal of Hydraulic Research*, **42**(4), pp.341-356.
- Van Wachem, B. G. M. and Almstedt, A. E. 2003. Methods for multiphase computational fluid dynamics. *Chemical Engineering Journal*, **96**(1-3), pp.81-98.
- Versteeg, H. K. and Malalasekera, W. 1995. *An Introduction to Computational Fluid Dynamics. The Finite Volume Method*. Harlow [UK]: Pearson Education Limited.
- Vreugdenhil, C. B. 1989. *Computational Hydraulics*. Berlin: Springer-Verlag.
- Waclawczyk, T. and Koronowicz, T. 2008. Comparison of CICSAM and HRIC High-Resolution Scheme for Interface Capturing. *Journal of Theoretical and Applied Mechanics*, **46**(2), pp.325-345.
- Wan, H., Li, R., Pu, X., Zhang, H. and Feng, J. 2018. Numerical simulation for the air entrainment of aerated flow with an improved multiphase SPH model. *International Journal of Computational Fluid Dynamics*, **31**(10), pp.435-449.
- Wcd. 2000. *Dams and Development: A new framework for decision-making. The report of the World Commission on Dams*. London: World Commission On Dams.
- Wendland, H. 1995. Piecewise polynomial, positive definite and compactly supported radial functions of minimal degree. *Advances in Computational Mathematics*, **4**, pp.389-396.

References

- Wilcox, D. C. 1988. Reassessment of the scale determining equation for advanced turbulence models. *AIAA Journal*, **26**(11), pp.1299-1310.
- Willey, J., Ewing, T., Wark, B. and Lesleighter, E. 2012. Complementary use of physical and numerical modelling techniques in spillway design refinement. *In: Commission Internationale Des Grands Barrages, Kyoto*.
- Witherden, F. D. and Jameson, A. 2017. Future Directions in Computational Fluid Dynamics. *In: 35th AIAA Applied Aerodynamics Conference, Denver, CO*.
- Witt, A., Gulliver, J. and Shen, L. 2015. Simulating air entrainment and vortex dynamics in a hydraulic jump. *International Journal of Multiphase Flow*, **72**, pp.165-180.
- Wormleaton, P. R. and Soufiani, E. 1998. Aeration performance of triangular planform labyrinth weirs. *Journal of Environmental Engineering*, **124**(8), pp.709-719.
- Xiang, M., Cheung, S. C. P., Tu, J. Y. and Zhang, W. H. 2014. A multi-fluid modelling approach for the air entrainment and internal bubbly flow region in hydraulic jumps. *Ocean Engineering*, **91**, pp.51-63.
- Xu, T. and Jin, Y.-C. 2014. Numerical investigation of flow in pool-and-weir fishways using a meshless particle method. *Journal of Hydraulic Research*, **52**(6), pp.849-861.
- Yakhot, V. and Orszag, S. A. 1986. Renormalisation Group analysis of turbulence I. Basic theory. *Journal of Scientific Computing*, **1**, pp.3-51.
- Yakhot, V., Orszag, S. A., Thangam, S., Gatski, T. B. and Speziale, C. G. 1992. *Development of turbulence models for shear flows by a double expansion technique*. NASA Contractor Report, Hampton, Virginia: Institute for Computer Applications in Science and Engineering.
- Yalin, M. S. 1989. *Fundamentals of Hydraulic Physical Modelling*. Recent Advances in Hydraulic Physical Modelling. Dordrecht, The Netherlands: Kluwer Academic Publishers.
- Yang, H., Li, R., Lin, P., Wan, H. and Feng, J. 2017. Two-phase smooth particle hydrodynamics modeling of air-water interface in aerated flows. *Science China Technological Sciences*, **60**(3), pp.479-490.
- Yeoh, G. H. and Tu, J. 2010. *Computational Techniques for Multiphase Flows*. Oxford [UK]: Elsevier Ltd.
- Youngs, D. L. 1982. Time dependent multi material flow with large fluid distortion. *Numerical Methods for Fluid dynamics*, pp.273-285.
- Zeng, J., Zhang, L., Ansar, M., Damisse, E. and González-Castro, J. A. 2017. Applications of Computational Fluid Dynamics to Flow Ratings at Prototype Spillways and Weirs. I: Data Generation and Validation. *Journal of Irrigation and Drainage Engineering*, **143**(1).
- Zhang, Y., Zou, Q. and Greaves, D. 2009. Numerical simulation of free-surface flow using the level-set method with global mass correction. *International Journal for Numerical Methods in Fluids*, **63**, pp.651-680.

Appendix A. OpenFOAM Investigation of Nappe Displacement

OpenFOAM presents more significant changes between the prototype and model in the weir vicinity which reflects in greater nappe displacement and elongation compared to Fluent. In order to provide understanding of how the documented nappe displacement phenomenon varies with changes in the scale of the flow situation in this solver, the PMF case was simulated in two further scales. Simulations at scale 1:10 were conducted utilising the scale factors outlined on Eq. 8.1 to 8.5. Simulations of the smallest scale 1:50 were undertaken by scaling down flow properties as per Eq. 8.6 to 8.10.

The velocity contours at a plane perpendicular to crest II at the four scales are shown on Figure A.1. The velocities at prototype and physical model scales (previously presented in Figure 7.32) are compared with those at 1:10 and 1:50 scale. Figure A.1 reveals that the OpenFOAM predictions present significant changes with the different scales. Consistently, with increasing the scale of the simulation, the velocities present higher values. The newly produced simulation scales 1:50 and 1:10 therefore present results which are in line with the previous observations at model and prototype scale. At 1:50 and 1:25 scale the velocity vectors reveal the presence of a vortex immediately downstream of the weir which presents a shape elongated in the vertical direction which evolves into a more rounded shape at scale 1:10 and finally into a horizontally elongated vortex at prototype scale.

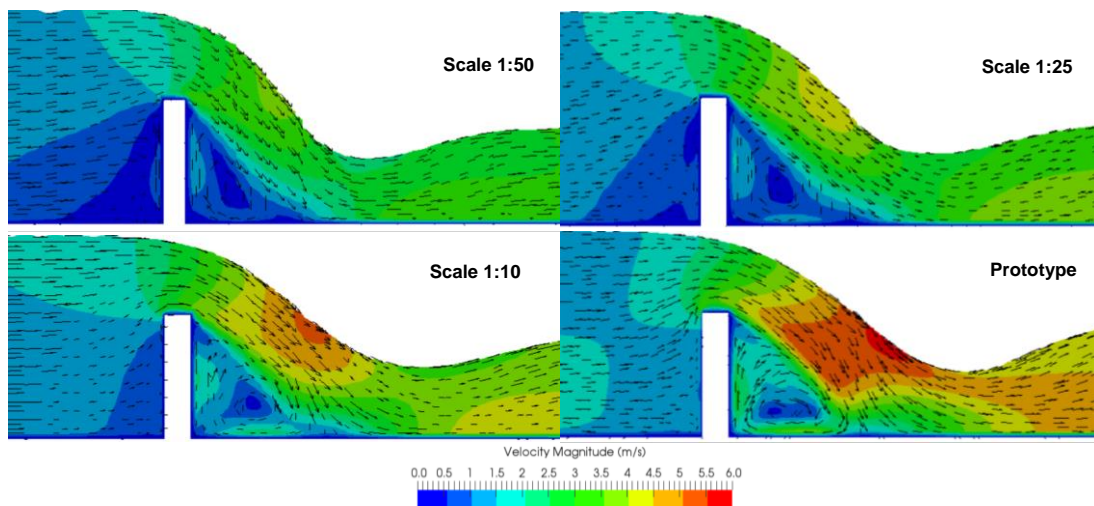


Figure A.1: OpenFOAM velocity contours and vectors along upstream crest II

Figure A.2 illustrates the pressure contours at the four scales. As previously observed, the pressures at the two additional scales enable to obtain a complete picture of the pressure distribution as the scale of the simulation is increased. At the crest, the pressure distribution at the 1:50 and 1:25 scales present higher pressures. At scale 1:10 and prototype scale the pressure distribution at the crest presents changes with reduced pressure values. In addition, the smallest scale also exhibits larger negative values at the downstream wall of the weir, next to the crest. The pressures show lower negative values at 1:25 scale but are similar to the smallest scale. At 1:10 scale the area with negative pressures at the downstream wall is reduced. At prototype scale, the negative pressure values downstream the crest are minimised.

Appendix A. OpenFOAM Investigation of Nappe Displacement

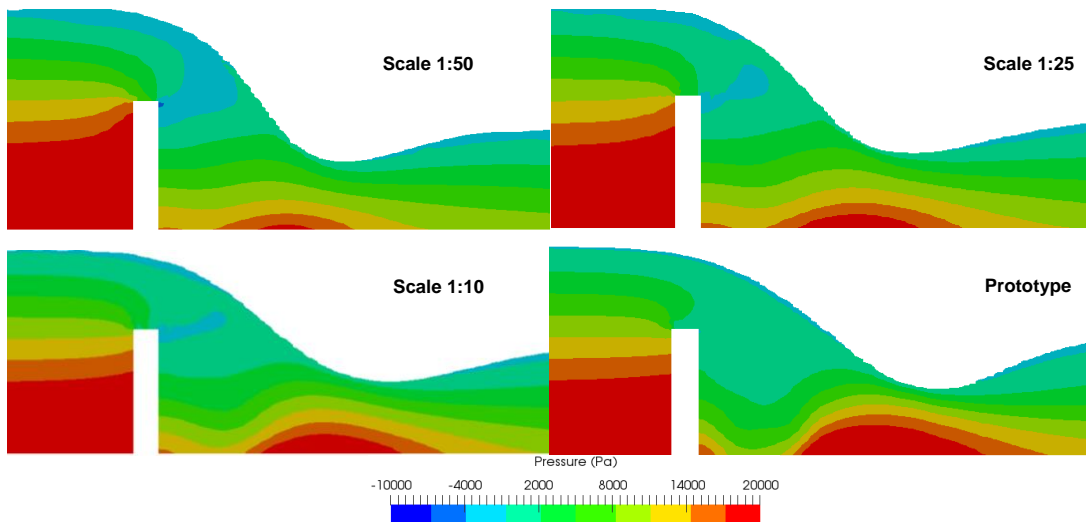


Figure A.2: OpenFOAM pressure contours along upstream crest II

In Figure A.1 and Figure A.2 the changes in the nappe shape at the different scales are clearly manifested. These results show the nappe trajectory is consistently increased for increasing simulation scale.

The bottom point of the nappe at prototype scale was taken as a reference and the displacement of such point upstream for the three scales was measured in respect of that in the prototype. The point of reference measured in each case was the lowest free surface depth before it increases downstream at the wave crossing point. Table A.1 presents the percentage displacement of the nappe bottom in respect of that in the prototype at each simulation scale and their corresponding scaled head over crest.

Table A.1: Displacement of the nappe bottom in respect of the prototype and corresponding head over crest

Scale	Head over crest [m]	Nappe displacement [%]
1:50	0.0282	48.3
1:25	0.05	24.3
1:10	0.131	0.17

These values show that as described in the literature (Ercicum *et al.* 2016; Pfister *et al.* 2013a) for increasing scale of the simulation, the scaled depth over crest is consequently larger and the nappe displacement in relation to that at prototype scale is reduced. Figure A.3 shows the percentage displacement calculated at the three scales, presented in Table A.1 plotted against the scaled head over crest. Results show that the OpenFOAM simulations would present only 5% to 10% of nappe displacement for upstream heads of 0.114 m and 0.095 m respectively.

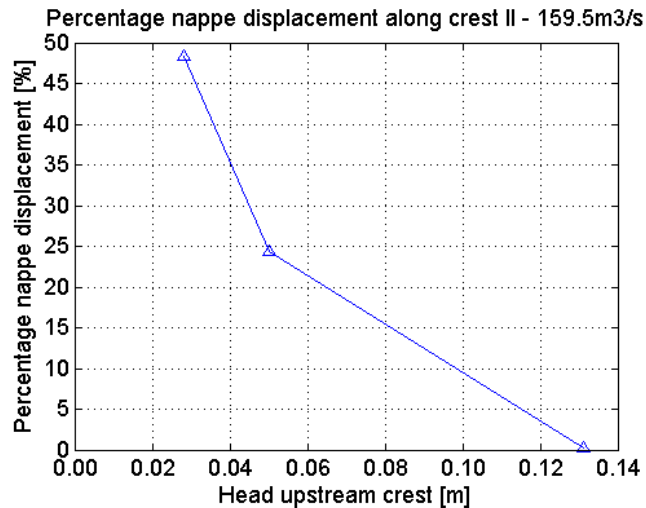


Figure A.3: Percentage nappe displacement at crest II for the PMF case predicted with OpenFOAM

As previously noted, the available limit stated in the literature of minimum head over crest to mitigate scale effects on the nappe trajectory is 0.06 m. The Fluent head over crest in the PMF flow rate coincides with this limit, and presents negligible changes in the nappe trajectory at the two scales. However, the study conducted in this section shows that in OpenFOAM the scale effects are more prominent and for a head over crest of 0.06 m the nappe displacement would still be of over 20 %.

In summary, the nappe trajectory is progressively reduced for decreasing scale factor of the simulation which leads to the bottom of the nappe being moved upstream in simulations with higher scale factors (i.e. 25 and 50). This phenomenon is therefore able to cause an impact on the configuration of cross-waves by progressively moving the cross-waves crossing points upstream for simulations with increasing scale factors. The increased nappe displacement upstream at such scales compared to prototype scale presents a correlation with the differences in pressure distribution at the weir crest in addition to the lower velocity. Consequently, as expected, such differences decrease for increasing flow rate (or decreasing simulation scale factor).

Although the OpenFOAM predictions analysed in this section are coherent from a physical point of view, these are judged to present certain overestimations, especially considering the model scale simulation results for the rating curve which overestimated heads over crest.

Appendix B. OpenFOAM Investigation of Labyrinth Weir Rating Curve

The OpenFOAM predictions of the rating curve at physical model scale were less well correlated with the experimental measurements than these from Fluent. In order to investigate how this solver performs at different scales an additional study was conducted. Simulations at scale 1:10 were conducted with the aim of estimating a minimum upstream head above crest to avoid scale effects according to the predictions from this solver. Simulations on the weir modelling domain were undertaken by scaling the prototype mesh to a scale 1:10. The Froude law of similarity was applied with the scale factor λ of 10 as per Eq. 8.1 to 8.4 and simulations of the four flow rates were conducted, that is 40 m³/s, 79.8 m³/s, 119.6 m³/s and 159.5 m³/s

Simulations on the weir modelling domain were thus undertaken of the four flow rates and the rating curve of scale 1:10 was calculated. Figure B.1 a) shows the rating curves at scales 1:10, 1:25 and at prototype scale. The 1:10 scale curve exhibits a very similar profile to that predicted at prototype scale. As expected, results converge for the largest flow rates and in this case the heads upstream the crest are almost equivalent for 119.6 m³/s and 159.5 m³/s. As it has previously been documented in Section 6.11, the OpenFOAM rating curve predicted at model scale appeared to overestimate the heads upstream the weir crest compared to the experimental curve and to that predicted with Fluent at model scale. On Figure B.1 a) the rating curve at model scale exhibits approximately a 0.10 m difference in respect to those at 1:10 scale.

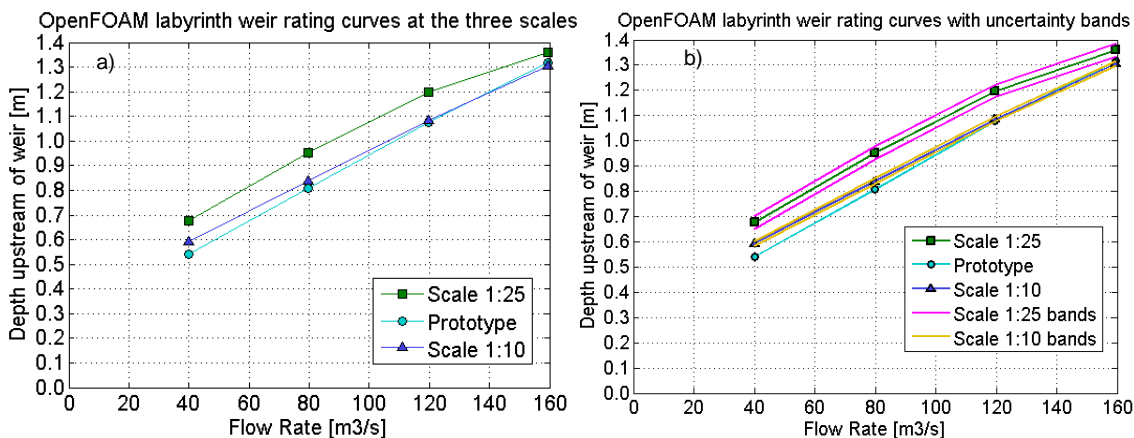


Figure B.1: a) OpenFOAM Rating curves at physical model scale (1:25), scale 1:10 and prototype scale; b) Rating curves at the three scales with uncertainty bands for scales 1:10 and 1:25

Following the same procedure as in Chapter 8 to derive minimum upstream head above crest to minimise scale effects from Ercicum *et al.* (2016), the minimum head was derived with the OpenFOAM predictions. The curves of scales 1:25 and 1:10 were compared to the prototype curve, which is the reference. The uncertainty bands at the two scales are also shown on Figure B.1 b). These were calculated by adding and subtracting 0.025 m and 0.01 m to the physical scale and 1:10 scale rating curves respectively.

Because of the larger difference in the physical model scale curve compared to the prototype scale, these two curves are expected to cross for flow rates larger than the PMF. But it would not be appropriate to predict limits based on estimations of the values of the curve for larger flow

rates since these are not available. In absence of such values, the curve at scale 1:10 is utilised to derive minimum depth. The prototype curve crosses the lower uncertainty band of scale 1:10 at a flow rate of 116.3 m³/s. This implies the curve of scale 1:10 and that from the prototype can be considered to be equal for the head upstream weir corresponding to this flow rate and above. The scaled-down head at this point is 0.1056 m, which indicates that this is the minimum head to avoid scale effects according to the predictions from OpenFOAM. Such value is considerably larger than 0.03 m which is the value found in the relevant studies from the literature. Therefore, as previously identified, the OpenFOAM minimum head values derived with the 1:10 scale curve appear to be significantly higher and less realistic than those derived with the Fluent predictions at model scale.